

Mechanisms and Machine Science

Lifang Zheng
Chaoyang Sun
Kheng-Lim Goh *Editors*

Proceedings of MEACM 2020


Mechanical Engineering and Applied
Composite Materials

 Springer

Mechanisms and Machine Science

Volume 99

Series Editor

Marco Ceccarelli , Department of Industrial Engineering, University of Rome Tor Vergata, Roma, Italy

Editorial Board

Alfonso Hernandez, Mechanical Engineering, University of the Basque Country, Bilbao, Vizcaya, Spain

Tian Huang, Department of Mechatronical Engineering, Tianjin University, Tianjin, China

Yukio Takeda, Mechanical Engineering, Tokyo Institute of Technology, Tokyo, Japan

Burkhard Corves, Institute of Mechanism Theory, Machine Dynamics and Robotics, RWTH Aachen University, Aachen, Nordrhein-Westfalen, Germany

Sunil Agrawal, Department of Mechanical Engineering, Columbia University, New York, NY, USA

This book series establishes a well-defined forum for monographs, edited Books, and proceedings on mechanical engineering with particular emphasis on MMS (Mechanism and Machine Science). The final goal is the publication of research that shows the development of mechanical engineering and particularly MMS in all technical aspects, even in very recent assessments. Published works share an approach by which technical details and formulation are discussed, and discuss modern formalisms with the aim to circulate research and technical achievements for use in professional, research, academic, and teaching activities.

This technical approach is an essential characteristic of the series. By discussing technical details and formulations in terms of modern formalisms, the possibility is created not only to show technical developments but also to explain achievements for technical teaching and research activity today and for the future.

The book series is intended to collect technical views on developments of the broad field of MMS in a unique frame that can be seen in its totality as an Encyclopaedia of MMS but with the additional purpose of archiving and teaching MMS achievements. Therefore, the book series will be of use not only for researchers and teachers in Mechanical Engineering but also for professionals and students for their formation and future work.

The series is promoted under the auspices of International Federation for the Promotion of Mechanism and Machine Science (IFTToMM).

Prospective authors and editors can contact Mr. Pierpaolo Riva (publishing editor, Springer) at: pierpaolo.riva@springer.com

Indexed by SCOPUS and Google Scholar.

More information about this series at <http://www.springer.com/series/8779>

Lifang Zheng · Chaoyang Sun · Kheng-Lim Goh
Editors

Proceedings of MEACM 2020

Mechanical Engineering and Applied
Composite Materials

 Springer

Editors

Lifang Zheng
School of Mechanical Engineering
University of Science and Technology
Beijing
Beijing, China

Chaoyang Sun
School of Mechanical Engineering
University of Science and Technology
Beijing
Beijing, China

Kheng-Lim Goh
Newcastle University Singapore
Singapore, Singapore

ISSN 2211-0984

Mechanisms and Machine Science

ISBN 978-3-030-67957-6

<https://doi.org/10.1007/978-3-030-67958-3>

ISSN 2211-0992 (electronic)

ISBN 978-3-030-67958-3 (eBook)

© The Editor(s) (if applicable) and The Author(s), under exclusive license to Springer Nature Switzerland AG 2021

This work is subject to copyright. All rights are solely and exclusively licensed by the Publisher, whether the whole or part of the material is concerned, specifically the rights of translation, reprinting, reuse of illustrations, recitation, broadcasting, reproduction on microfilms or in any other physical way, and transmission or information storage and retrieval, electronic adaptation, computer software, or by similar or dissimilar methodology now known or hereafter developed.

The use of general descriptive names, registered names, trademarks, service marks, etc. in this publication does not imply, even in the absence of a specific statement, that such names are exempt from the relevant protective laws and regulations and therefore free for general use.

The publisher, the authors and the editors are safe to assume that the advice and information in this book are believed to be true and accurate at the date of publication. Neither the publisher nor the authors or the editors give a warranty, expressed or implied, with respect to the material contained herein or for any errors or omissions that may have been made. The publisher remains neutral with regard to jurisdictional claims in published maps and institutional affiliations.

This Springer imprint is published by the registered company Springer Nature Switzerland AG
The registered company address is: Gewerbestrasse 11, 6330 Cham, Switzerland

Preface

Dear Distinguished Authors and Guests,

The 2020 International Conference on Mechanical Engineering and Applied Composite Materials (MEACM 2020) was held on October 24–25, 2020, in a virtual environment.

MEACM 2020 was hosted by the University of Science and Technology Beijing, sponsored by X ACADEMY. The conference program covered invited, oral presentation session and poster session from scientists working in similar areas to establish platforms for collaborative research projects in this field. The conference aimed to bring together leaders from mechanical engineering and applied composite materials to exchange and share their experiences, present research results, explore collaborations and spark new ideas, with the purpose of developing new projects and exploiting new technology in this field. We hope that the conference has resulted in significant contribution to the knowledge on mechanical engineering and applied composite materials.

To this end, this book contains the papers presented at MEACM 2020. All papers were accepted through a peer-review process conducted by the conference program committee and international reviewers.

On behalf of the organizing committee, we would like to thank the editors at Springer Nature for their generous support to the publication of the MEACM 2020 book. Without their excellent editorial work, MEACM 2020 will not be published so timely and successfully.

Finally, we would like to thank all authors and participants of MEACM 2020 for their contributions to making this conference a success. We look forward to your participation in the 5th MEACM in 2021.

With our warmest regards,

Beijing, China
Beijing, China
Singapore

Prof. Lifang Zheng
Prof. Chaoyang Sun
Prof. Kheng-Lim Goh
Conference Organizing Chair

Contents

Effect of Equal Channel Angular Pressing on the Microstructure and Properties of Pure Mg and the Deformation Mechanism	1
Zhuoliang Li and Hua Ding	
Research on Ice-Induced Vibration Test of Inland Icebreaker	15
Siyu Wang and Yuan Du	
Critical Analysis of Productivity of Well 2L After Foam-Acid Diversion	21
Chinedu J. Okere, Lihui Zheng, Guandong Su, Hao Liu, Qifan Chang, and Obiora J. Obiafudo	
Investigation of Spin Pinned Effect in Ni/NiFe/Ni Trilayers Via Ferromagnetic Resonance Spectroscopy	37
Yu Liu and Zhongwen Lan	
Residual Stress Evaluation of Metallic Component Based on the Synthetic Nonlinear Coefficient	45
Yuhua Zhang, Silong Quan, and Guoquan Liu	
Molding Process of Automotive Hemp Fiber Reinforced Composites . . .	53
Z. H. Zhu and H. W. Wu	
Trajectory Control of Mobile Robot Based on Novel Gesture Detection	59
Shubo Liu, Guoquan Liu, Shun'an Cao, Liyu Cheng, and Hang Zou	
Development of Personalized Wind Handling System Using Infrared Ray Sensor	69
Jungryeong Chae, Cheng Hao, Taeuk Lim, and Wonsuk Jung	
Key Design Technologies of New Cable-Stayed and Steel Truss Composite Bridge	75
Liping Xu, Qingquan Wang, and Anmin Wang	

The Role of Composite Materials to Rehabilitate Plant Piping	89
Meshal Alsaiani	
Study on Piezoelectric Stack Performance for Linear Ultrasonic Motor	95
Hongbing Wang and Chunhua Sun	
Study on Vibration and Acoustic Characteristics of Ship Stern Structure by Propeller Excitations	105
Fuzhen Pang, Cong Gao, Haichao Li, and Ruizhao Gu	
Nonlinear Wave Loads' Prediction on Ultra Large Containerships	115
Xiaoyu Li, Kaihong Zhang, Huilong Ren, and Sijun Chen	
The Design of a Backpack System to Meet the Requirements of New Type of Individual Combat	127
Yu Zhao and Wei-Jie Xu	
Study on Decarbonization of ZGMn13Cr2 During Heat Treatment	137
Ke Zhu, Qiang Li, Jianmin Zeng, and Siyong Zhao	
Numerical Simulation of Aluminum Alloy Connecting Rod with Multi-wedge Cross Wedge Rolling	145
Ke-Xing Zhang, Xiao-Lian Zhao, Ao-Ping He, Jian-Min Zeng, Ke-Zhun He, Jun-Sheng Liu, and Gang Xiao	
Effect of Water Temperature on Quenching Residual Stress of Aluminum Alloy Thick Plate	151
Xiao-Lian Zhao, Ke-Xing Zhang, Ao-Ping He, Jian-Min Zeng, Ke-Zhun He, Jun-Sheng Liu, and Gang Xiao	
Study on the Motion and Friction Mechanism of Flexible Roller in Space Roll Ring	157
Bin Wang and Jikui Liu	
Analysis on the Influence of Bearing Stiffness on Critical Speed of Rotor System of a New Scroll Compressor	167
Jiang Pu, Xu Zhou, Ya-feng Su, and Xiu-hua Zhang	
Experimental and Simulation Data-Driven Rolling Bearing Fault Size Quantitative Diagnosis in Big Data Era	173
W. T. Huang, H. Zhai, J. N. Luo, Y. C. Jiang, and W. J. Wang	
Research on Assembly Error Transmission of Small Displacement Spinor Based on State Space Model	189
Chunqi Chen, Wei Wu, and Jianzhong Shang	
Synthesis of Fluorescent Carbon Dots from Glucose and Calcium Carbonate and Their Application in the Beverage	197
Meiyu Zhang, Xiaoliang Hao, Zhigang Fang, Yun Gao, and Tongtong Li	

Fault Location Method of Multiple Bearings in Shafting Based on SPWVD-CNN 205
 W. T. Huang, H. Zhai, Y. Lei, and W. J. Wang

Investigate the Damage of Kinetic Energy High-Velocity Bird Impact on Three Different Model Spar by Using the Coupled Eulerian-Lagrangian (CEL) Approach 215
 Muhammad Hassam Saeed and Noaman Muhammad

Effects of Y₂O₃ on Microstructure and Wear Resistance of Laser Cladding Ni-Based Coating on 42CrMoA Alloy Steel 225
 Yunfeng Li, Yan Shi, and Qingtang Wu

Effect of Nb/Sn and B Combinatorial Micro-alloying on the Microstructure and Corrosion Properties of As-Cast TiFe-Based Alloys 235
 J. W. Li, Z. Y. Wang, S. X. Liu, H. S. Cao, Z. H. Dan, and H. Chang

Sputter Deposited Nanocomposite Cr-Based Films and Their Characterization 245
 A. Vyas and Z. F. Zhou

Study on Compressive Properties of Cylindrical Graphene Oxide Cement-Based Composites 257
 Qiong Liang, Zhanyuan Gao, and Dong Ruan

Split Tensile Test of Brazilian Disc Specimen of Graphene Nanoplatelets Reinforced Cement-Based Composite Materials 267
 Yanfa Sun, Zhanyuan Gao, and Dong Ruan

Review on the Preparation Processes of Natural Fiber Reinforced PLA Composites 277
 Z. H. Zhu and H. W. Wu

Fabrication of Nickel/Nano-Lu₂O₃ Co-Electrodeposited Coating with Good Corrosion and High Temperature Oxidation Resistance 283
 Yanli Dou, Yi Liang, Ruishan Yang, Guangguang Qian, Xiaojie Wei, and Hong Xu

Impact of Micromechanical and Carbon Fiber Properties on the Elastic Modulus of CFRP Woven Composites 295
 Md. Mazedur Rahman and Saiaf Bin Rayhan

Microstructure and Performance Control of Copper/Stainless Steel Wire-Feeding Laser Welding Joint 305
 Xiaoyan Gu, Ziwei Cui, and Jiaxu Shao

Research on Ultrasonic Welding of Ultra-Thin Copper and Stainless Steel Dissimilar Metals with Nickel Foil as Intermediate Layer 319
 Xiaoyan Gu and Wei Gao

Numerical Prediction of the Permeability Tensor Components for 2D Woven	331
M. Kiauka, I. Kolodiazhnyj, and A. Borovkov	
Wire Rope Mathematical Model Development	345
D. A. Lobachev, V. L. Leontiev, Yu. A. Gorskiy, Ya. A. Belolipeckaya, P. A. Gavrilov, and O. I. Klyavin	
Development of Approaches to Modeling the Processes of Joining Sections and Operation of Drilling Equipment	363
T. V. Sergeeva, G. V. Monahovskiy, N. A. Kharaldin, O. I. Klyavin, A. A. Kraev, and O. V. Knyazeva	
Research and Application of Quality Control Strategy for CNC Workshop	375
Qing Gao, Zhengming Tang, Tianfu Liu, Weiyi Wang, and Meilan Luo	
Research on Teaching Design of Machining Technology in Higher Vocational Education	385
Danqing Liu	
Microstructure and Mechanical Properties of CuCrZr Alloy at High Temperature	395
Wenjing Zhang, Zongwu Li, Haofeng Xie, Zhen Yang, Guojie Huang, Xue Feng, Xujun Mi, Limin Wang, Lijun Peng, and Yu Hou	
Size Effect Study of Tensile Strength and Elongation of Copper Foil	403
Yu Hou, Haofeng Xie, Xujun Mi, Wenjing Zhang, Zhen Yang, Guojie Huang, Xue Feng, Lijun Peng, Shuihui Huang, and Dongmei Liu	
Analysis of the Influence of Different Mechanical Delaminating Process on the Electrochemical Performance of MXene Films	411
Xingmin Liu and Yi Qu	
Effect of Solution Heat Treatment on Microstructures and Stress Rupture Properties of DZ406 Alloy	421
Wei jie Xing, Changkui Liu, Xiaotong Guo, Gang Zhu, Wenxia Zhao, Xinlang Zuo, and Zhen Zheng	
Design of Embedded Intelligent Online Monitoring System of OLTC Based on Vibration Analysis	435
Changqing Peng, Rongyan Shang, Wenquan Huang, Min Deng, and Ruiming Fang	
Management Strategy Under the Intelligent Manufacturing Initiative of Chinese Coal Machine Equipment Enterprises	447
Peng He, Lixia Zeng, and Jie Dai	

Study on the Thermodynamic Calculation Model and Solution Method Along the Steady Operation of Long Transport Pipeline 457
Yin De, Yi Zhao, Rongqiang Zhong, Lirong Yao, and Ying Xu

Effect of Hot Isostatic Pressing on Microstructure of 24CrNiMo Steel Produced by Selective Laser Melting 467
Jing Liang, Ziyang Lin, Xiuyuan Yin, Suiyuan Chen, Changsheng Liu, Yang Guo, Shixing Yan, and Shiyun Dong

Numerical Simulation of Melting Flow in Crude Oil Water Based on Fluent 477
Yi Zhao, Deyin Zhao, Rongqiang Zhong, Lirong Yao, and Xiaoqing Li

Effects of Nickel on Microstructure and Properties of Direct Laser Deposited 00Cr25-XNiMo4 Duplex Stainless Steel 485
Jing Liang, Lizhao Wang, Yunfei Gao, Suiyuan Chen, Changsheng Liu, Chuang Li, Shixing Yan, and Shiyun Dong

Effect of Equal Channel Angular Pressing on the Microstructure and Properties of Pure Mg and the Deformation Mechanism



Zhuoliang Li and Hua Ding

Abstract Commercial pure magnesium material (>99.8 wt%) was selected in the study and ECAP processes were conducted at different temperatures. The result shows that the yield strength of the material was significantly enhanced after ECAP processes. The yield strength decreased with the increase in deformation temperature because of the grain growth. At 100 °C, basal slipping was the dominated deformation mechanism of the pure Mg material. With the increase of the deformation temperature, fine equiaxed grains were obtained due to recrystallization. When the temperature of ECAP reached 200 °C, twinning occurred in the samples. The result showed that basal perfect dislocations dissociated and realigned under the applied stress at a certain temperature and a certain grain size. The dissociation of the dislocations led to the nucleation of the twins. The twins grew up stably under the induce of the activation dislocations if the grain size reached to a critical value. The critical grain size of the growth of twins is about 5.9 μm according to the calculations.

Keywords Equal channel angler pressing · Pure magnesium · Deformation mechanism · Twinning

1 Introduction

As the lightest structural materials at present, Mg and Mg alloys received extensive attention from the researchers because of their high specific strength and high specific stiffness. However, the relatively low strength and poor ductility due to the

Z. Li · H. Ding (✉)

School of Material Science and Engineering, Northeastern University,
Shenyang 110819, China
e-mail: dingh@smm.neu.edu.cn

Z. Li · H. Ding

Key Laboratory of Lightweight Structural Materials, Northeastern University,
Shenyang 110819, Liaoning, China

close-packed hexagonal structure limited the application of Mg and Mg alloys [1]. As a kind of important severe plastic deformation process, ECAP (equal channel angular pressing) process can solve the problem mentioned above in Mg and Mg alloys which are lack of slip systems. Thus ECAP process has received extensive attentions from the researchers, especially on Mg and Mg alloys.

Up to now, much work has been done to reveal the effects of ECAP process on deformation mechanism of Mg alloys. Agnew et al. [2] studied AZ and ZK series Mg alloy in the temperature range of 200–300 °C. Texture strongly impacts the plasticity of metals and the equal channel angular extrusion process has been demonstrated to induce unusual textures and enhance the room temperature ductility of magnesium alloys. The results showed that ZK series alloy gradually evolved to the $\langle 1010 \rangle$ //ED fiber texture, while AZ series evolved to the $\langle 2567 \rangle$ //ED slant texture with the slant angle of about 20°. Xia et al. [3] conducted a two-stage ECAP process on AZ31 Mg alloy with different back pressure and different temperature conditions. Ultra fine grains with the grain size below 1 μm were successfully obtained after the two-stage process of ECAP. Much work has been done to study the mechanical properties and microstructural evolution of Mg materials fabricated by ECAP [4–7], and also many researchers focus on the deformation mechanism of Mg alloys during ECAP process. Galiyev et al. [8] conducted a relatively systematic study on the ZK60 magnesium alloy. The results showed two kinds of dominant mechanisms at different temperature range when Mg alloy was deformed at the temperature above 200 °C. The deformation mechanisms could be divided into three stages according to the difference of deformation temperature. When the temperature was below 200 °C, the plastic deformation was limited to basic and pyramidal plane twinning. In the temperature range of 200–250 °C, slip could also occur on the prismatic plane and twinning was restrained, and the ductility was obviously increased. The deformation behavior of Mg alloys was controlled by diffusion processes at the temperature above 250 °C. Studies on ZA85 magnesium alloy fabricated by ECAP was conducted by Lin et al. [9]. The result showed that the dominant deformation mechanism for the specimens at 300 and 350 °C was grain boundary sliding controlled by grain boundary diffusion. And the deformation mechanism for the experimental alloy was dislocation creep at the temperature of 400 °C. Tang et al. [10] studied the microstructure evolution of AZ80 magnesium alloy fabricated by ECAP. Their results showed that coarse Mg grains were separated and surrounded by deformation networks with UFGs (ultra fine grains). And the $\text{Mg}_{17}\text{Al}_{12}$ second-phase strengthening made great contribution to the yield strength of the material. The author believed that deformation twinning occurred in the UFGs and this led to an outstanding mechanical property. Studies from Su et al. [11] showed that the grain refinement mechanism for AZ31 Mg alloy during ECAP was induced by a combination of mechanical shearing and subsequent continuous recovery, recrystallization and growth of grains and subgrain cells to result in refined and equiaxed grains. It could be inferred that temperature plays a key role in the effectiveness in grain refinement of Mg alloy by ECAP.

Up to now, many different series of Mg alloy were studied and their deformation mechanisms were revealed [12–14]. However, researchers didn't always receive

similar results because different alloy elements have different effect on Mg alloys and always resulted in different deformation mechanisms during ECAP process. Thus pure Mg material becomes the best choice to reveal the basic and universal deformation mechanism theories of the material during ECAP. In recent years, some work has been done on pure Mg material and the ECAP process, nevertheless most of the studies focused on the changes of the mechanical properties and microstructure evolution of pure Mg material after different fabrication processing [15–18]. Elucidation of deformation mechanisms are still limited. Byer et al. [19] prepared single crystal Mg material by using focused ion beam grind technology. No twinning appeared in the single crystal Mg structure after micro-compression tests. Multiple slip systems become active on the pyramidal planes, resulting in significant hardening. The author believed that little size effect on strength for these length scales (2.5–10 μm). Lilleodden [20] studied the changes of the strength and ductility of the single crystal Mg material during deformation process. The results showed that significant plasticity and hardening occurred, due to six active pyramidal π_2 slip systems and twinning was not a relevant mechanism of deformation at during micro-compression experiments. Nevertheless, single crystal deformation was circumscribed and not all kind of mechanisms of Mg material can be revealed. Fan et al. [21, 22] also focused on the pure Mg material and their studies showed that the ductility of pure Mg material was enhanced obviously after ECAP process. They analyzed the change and the influence of the internal friction after ECAP process. The intense tangle of dislocations and the significant increase of grain boundary area contribute to the decrease of strain-dependent internal friction for ECAP processed pure Mg. Jimenez et al. [23, 24] focused on the transitions among different types of slips in pure Mg during compressive deformation by electron backscattered diffraction-aided slip trace analysis. Their work elucidated that a transition from non-basal to basal dominated flow took place with the decreasing of grain size and increasing of temperature. Nevertheless other mechanisms during deformation didn't get enough attention in their work.

More attention is still needed on pure magnesium material especially the deformation mechanism of pure Mg. In this study, the deformation mechanism of Mg material by ECAP was focused on. Pure Mg was selected to remove the effect of alloy elements on the deformation mechanism. Deformation mechanism of pure Mg during ECAP process at different temperature conditions was elucidated and the effect of ECAP processes on the microstructure and mechanical properties of pure Mg was studied. In addition, as an important mechanism in the deformation process of Mg materials, the nucleation and growth condition of deformation twinning was intensive analyzed by calculation in the present study.

2 Experiment

Commercial pure Magnesium was selected in this study. The Mg ingot was forged after a solution treatment for 24 h at the temperature of 400 °C. Total reduction rate of the forging process was 50%. Bulk samples with the size of 8.5mm × 8.5mm × 90 mm were cut from the ingot along the longitudinal direction. The ECAP process was conducted in the temperature range from RT to 200 °C with a back pressure of 100 MPa. Each sample was pressed through the channel (with the angle of 90°) at the speed of 2 mm/min. And a 4-pass' ECAP process was conducted on each sample. The compressive specimens with the size of Φ4mm × 6mm were cut from the sample after ECAP process along the pressing direction. And the initial strain rate of the compressive tests was 10^{-3}s^{-1} . The samples after ECAP process were polished using abrasive paper of 1000#, 2000# and 3000# orderly and electrolytic polishing (perchloric acid: ethanol = 1:9) followed. An acetic-picric acid solution was used for etching on the polished surface of the samples. An Olympus DSX500 optical microscope and a Ultra Plus field emission scanning electron microscope were used for microstructure analysis. And a TD-3500 X-ray diffractometer and a Tecnai G220 transmission electron microscope were used as well to obtain the XRD and TEM results.

3 Results and Discussion

Figure 1 shows the results in compressive test of the samples before and after ECAP processes at different temperatures. The yield strength of the material increased obviously after ECAP process. The values raised from ~45 to ~100 MPa. The yield strength of the material decreased along with the increase of the deformation temperature. When the true strain was in the range of 0.02–0.12, the compressive curves of the samples at relatively lower temperatures (100 and 150 °C) increased linearly. In contrast, the stress showed evident concave phenomenon for the sample processed at 200 °C and the sample prior to ECAP process. It is indicated that in this range of true strain condition, twinning occurred inside the material at these two temperatures [25]. In addition, when the temperature reached 150 °C, it is obvious that the samples obtained much better ductility than those processed at any other conditions.

It could be seen from the optical micrograph (Fig. 2) of the samples before and after ECAP that the microstructure was coarse (~75 μm) and deformation twinning existed because of the previous forging process. The grains were significantly refined after 4 passes of ECAP at different temperatures, which could explain the increment in the yield strength of the material after ECAP. The average grain sizes of the samples ECAPed at the temperature of 100 °C, 150 °C and 200 °C were 4.5 μm, 5.1 μm and 8.7 μm, respectively. It is noticed the microstructure was inhomogeneous after the ECAP process at the relatively low temperature (100 °C).

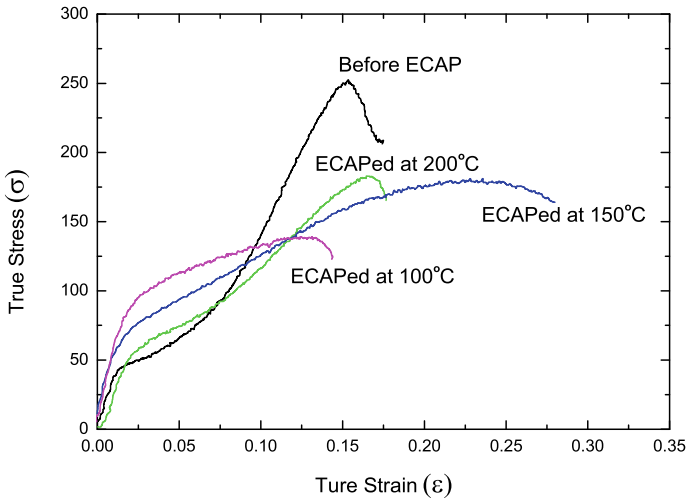


Fig. 1 True strain and true stress curves of the compressive samples

Fine (1–3 μm) and coarse (16–25 μm) grains existed together. Large amount of equiaxed fine grains appeared inside the samples which indicated that dynamic recrystallization occurred during ECAP process, but part of coarse grains formed in the forging process were retained, which illustrate dynamic recrystallization had not completely conducted at this temperature. And this should be the main reason why the ductility of the samples was poor in the compressive tests. When the deformation temperature reached 150 $^{\circ}\text{C}$ (Fig. 2c), dynamic recrystallization was completed. Coarse grains disappeared and the microstructure of the samples turned to be uniform. Most of the grains were equiaxed with a size of 4–7 μm and no deformation twins were observed inside the material. So that the ductility increased significantly. After 4 passes of ECAP process at 200 $^{\circ}\text{C}$ (Fig. 2d), the grains grew up obviously at the relatively high temperature. In the mean time, twins were observed in the samples processed at 200 $^{\circ}\text{C}$. It is clear that grain growth had greater influence on the strength of the material, although the existence of twins could improve the strength to some extent. Thus the yield strength of the samples decreased. The ductility slightly decreased compared with the samples ECAPed at 150 $^{\circ}\text{C}$. It was revealed that the existence of the twins tended to become the stress concentration area, and micro-cracks almost always appeared at the twin boundaries especially in the sharp corner during the compressive process of Mg materials [26], hence the ductility of the sample at 200 $^{\circ}\text{C}$ was decreased.

Figure 3 shows the IPF pictures of pure Mg bulk samples after ECAP process using EBSD method. The grains were obviously refined after passes of ECAP. At the deformation temperature of 100 $^{\circ}\text{C}$, coarse grains and fine equiaxed grains coexist in the material. Large amount of low angle grain boundaries existed inside the coarse grains. It could be inferred that the coarse grains would have the potential of converting to fine grains. Thus the microstructure would be significantly refined

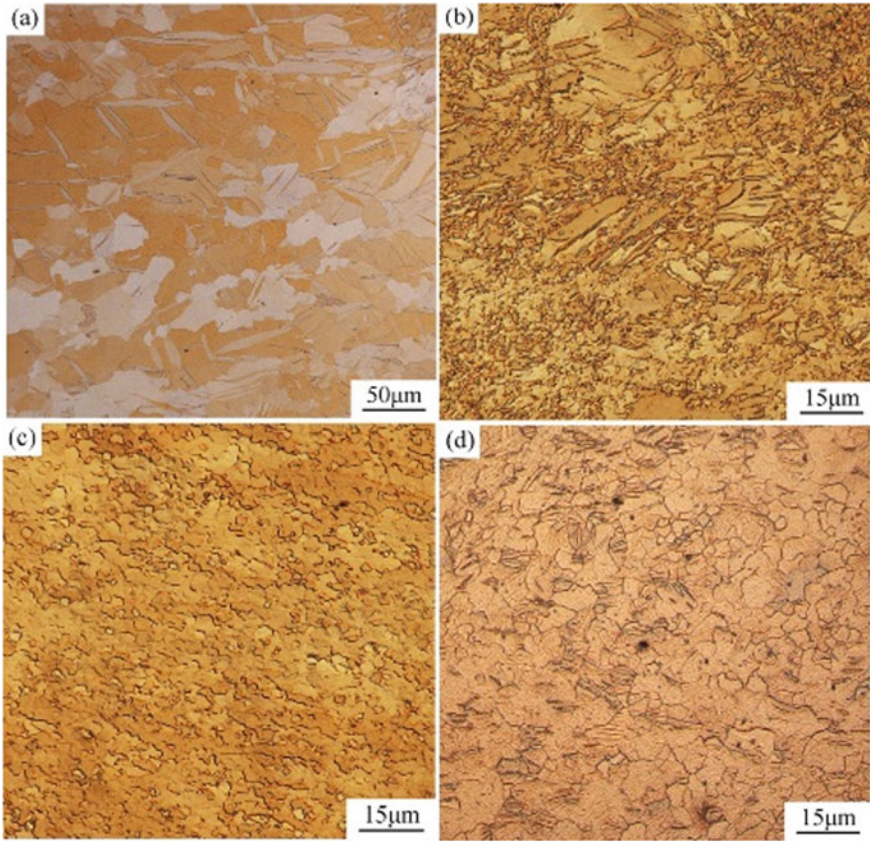


Fig. 2 Microstructures of the sample before and after ECAP **a** before ECAP, **b** 100 °C, **c** 150 °C, **d** 200 °C

with the further passes of ECAP process and/or higher deformation temperatures. As shown in Fig. 4, most of the grain boundaries in the samples after ECAP process at 100 °C were low angle grain boundaries. And the low angle grain boundaries transformed into high angle boundaries gradually with the increase of the temperature of ECAP. In different deformation temperature conditions, the percentages of high angle grain boundary were 24.7%, 51.9% and 55.5%, respectively. Qi and Krajewski [27] demonstrated that grain misorientation had a strong effect on the amount of sliding, increased with grain boundary energy. Yang's study [28] showed that the occurrence of grain boundary sliding (GBS) was evident on the surface of deformed AZ31 specimens during tensile tests at the temperature of 225 °C. The fine grains and high percentage of high angle grain boundaries could facilitate the occurrence of GBS and weakened the texture significantly. Ma et al. [29] also reported the benefit of high percentage of high angle grain boundaries to GBS. With the increase of deformation temperature, the content of high angle grain

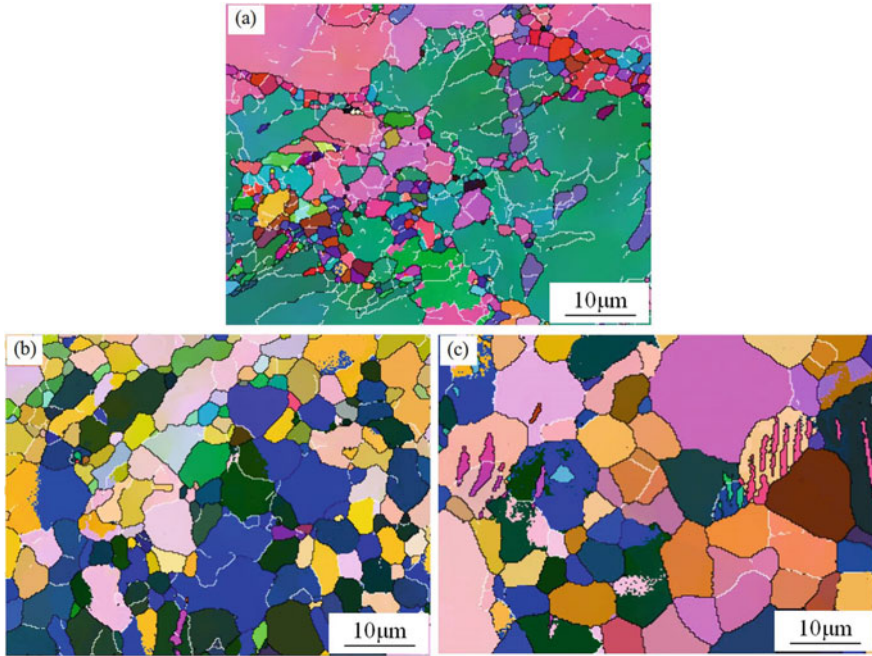


Fig. 3 IPF pictures of the samples after ECAP at different temperature **a** 100 °C, **b** 150 °C, **c** 200 °C

boundary was enhanced, and grain boundary sliding process became stronger, so that the ductility of the material was significantly increased [30, 31]. The experimental results above demonstrated that obviously dynamic recrystallization occurred interior the material during ECAP process. Dynamic recrystallization became stronger with the increasing of the ECAP temperature. Thus the main deformation mechanism of the material was basal slip at relatively low temperature (100 °C) and dynamic recrystallization became the primary mechanism gradually with the increase of the temperature. Furthermore, the inverse pole figures (Fig. 5) showed that the texture was weaker at the higher temperature. The higher the temperature, the stronger dynamic recrystallization and grains rotated during ECAP processes. The weakened texture caused by dynamic recrystallization and grain rotation led to the easier movement of the grains during the following compressive deformation and have positive influence on the ductility of the material [32, 33].

The XRD results of the samples after ECAP at different temperatures were illustrated in Fig. 6. It could be obtained by calculation that the interior dislocation densities of the samples after ECAP processes at the temperature of 100 °C, 150 °C and 200 °C were $5.15 \times 10^{14} \text{ m}^{-2}$, $1.01 \times 10^{14} \text{ m}^{-2}$ and $2.85 \times 10^{14} \text{ m}^{-2}$, respectively. Along with the increase of the deformation temperature, the dislocation density tended to decrease first and then increased. At the temperature of 100 °C, the main deformation mechanism of pure Mg material was basal slip, dynamic

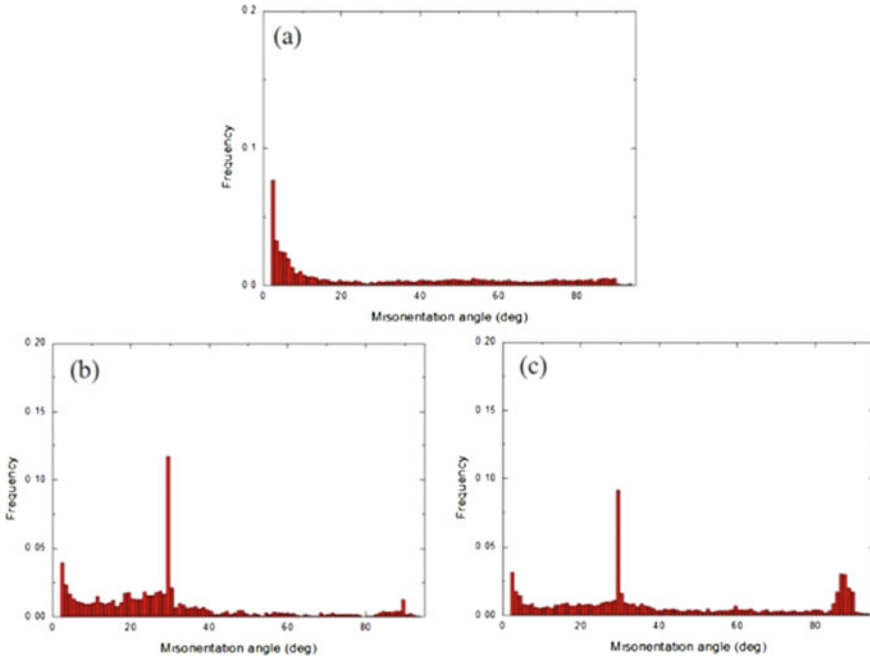


Fig. 4 Misorientation figures of the samples after ECAP processes at the temperature of **a** 100 °C, **b** 150 °C and **c** 200 °C

recrystallization didn't conduct completely. The interior dislocation density was relatively high, so that the material obtained high yield strength. Along with the enhance of the deformation temperature, recrystallization process of the material became stronger and the dislocation density decreased rapidly, thus the yield strength of the material decreased as well. When the deformation temperature reached 200 °C, recrystallization conducted more rapidly. When the deformation temperature was above 150 °C, ECAP process didn't finish when recrystallization conducted utterly. As the continuous ECAP process, the dislocation multiplication occurred inside the material and the dislocation density enhanced.

Figure 7 shows the TEM results of the samples after ECAP at different temperatures. At the temperature of 100 °C (Fig. 7a), slip traces in the samples indicated that the slip was an important mechanism of deformation at this temperature condition. Figure 7b showed the microstructure of the sample after ECAP process at 150 °C. The dislocations distributed uniformly like a net. At the temperature of 200 °C, the dislocations of the sample after ECAP process mainly distributed in two forms. Some of the dislocations were net-like distributed (Fig. 7c) and others inerratic distributed align (Fig. 7d). Normally, the basal plane dislocations formed and moved easily in Mg materials. The net-like basal $\langle\alpha\rangle$ perfect dislocation (Fig. 7c) would dissociated into two Shockley dislocations which nipped a stacking fault with a certain energy [34]. This created the conditions for the nucleation of

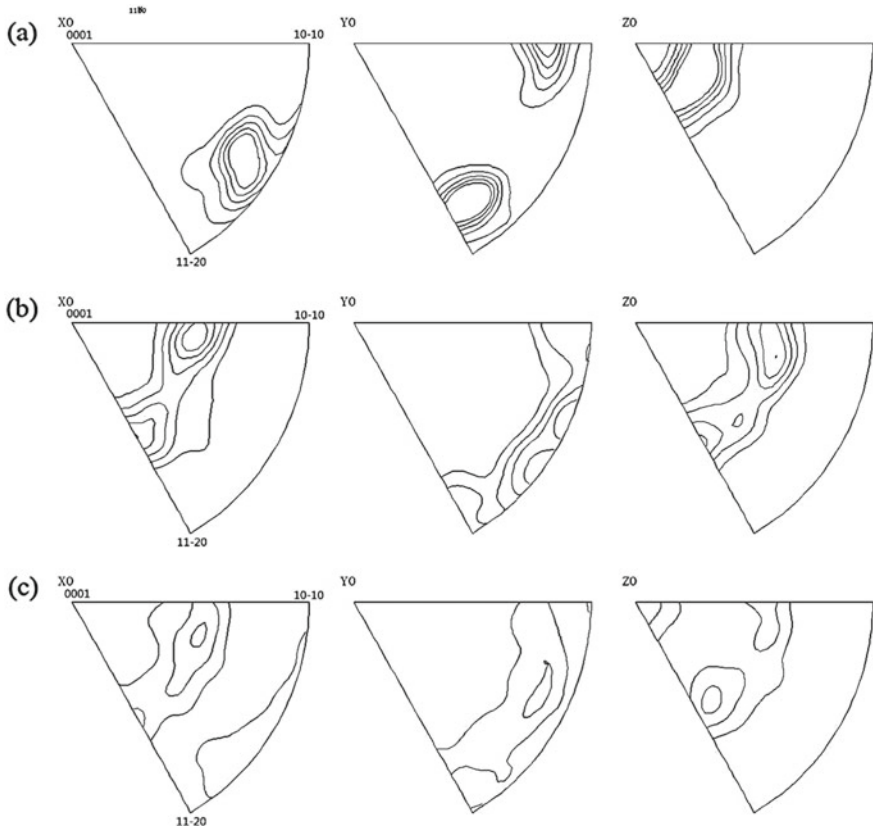


Fig. 5 Inverse pole figures of the samples after ECAP **a** 100 °C Max = 8.95, **b** 150 °C Max = 6.01, **c** 200 °C Max = 3.59

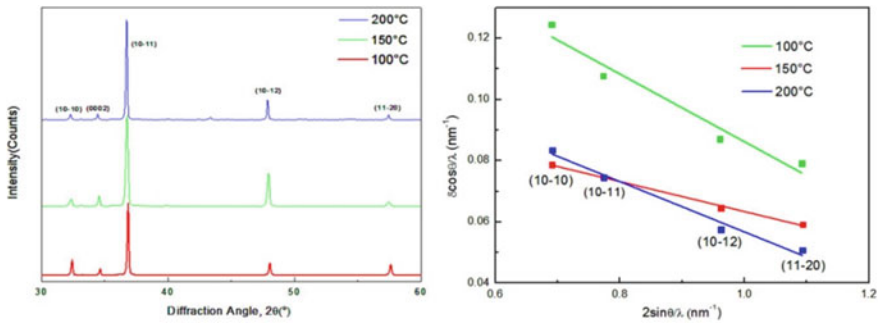


Fig. 6 XRD profiles of the samples after ECAP process and the relationship between $2\sin\theta\lambda$ and $\delta\cos\theta\lambda$

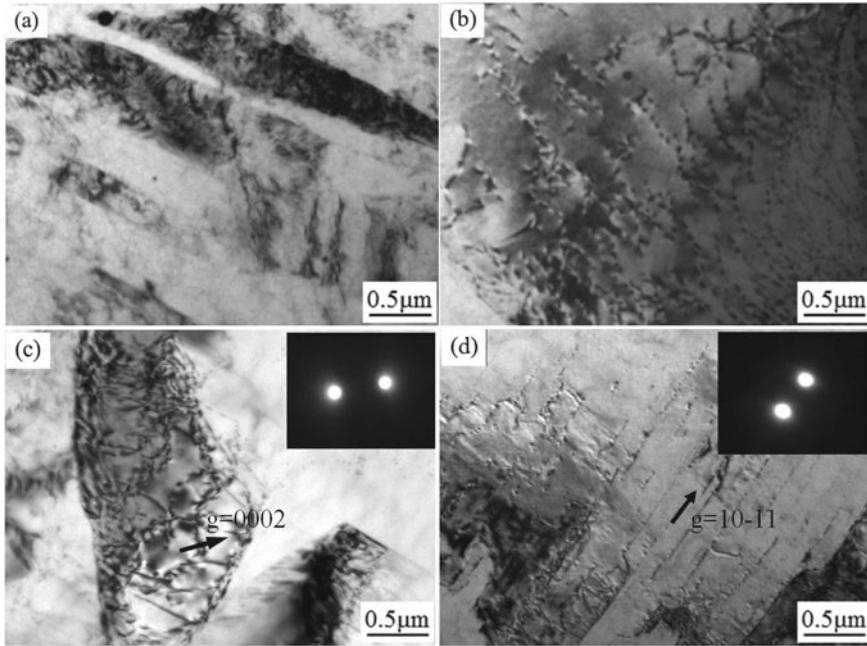


Fig. 7 TEM figures of the samples after ECAP **a** 100 °C, **b** 150 °C, **c** 200 °C, **d** 200 °C

twins. According to the Peierls-Nabarro lattice model, the screw dislocations in the magnesium materials usually had a higher Peierls energy than the edge dislocations, so that the edge dislocations could be moved much easier [35, 36]. The $\langle\alpha\rangle$ perfect dislocations dissociated and the obtained partial dislocations ($1/3\langle 10-10\rangle$) moved to a inerratic distribution under the severe shear deformation of ECAP process. These dislocations would have an activation effect on the growth of twins.

At the temperature of 200 °C, twins were observed in the samples while not in the samples at 100 and 150 °C. At the relatively low temperature (100 °C) of ECAP, the microstructure was inhomogeneous and recrystallization didn't conducted utterly. Coarse grains in the initial samples still existed and the twins in the samples were from the previous forging process. With the increase of the ECAP deformation temperature (150 °C), recrystallization completed and the grains in the material became fine and equiaxed. No twins were observed in the refined structure. With the further increase of the temperature (200 °C), the grains grew obviously and twinning occurred inside the material. On the other hand, Figueiredo et al. [37] and Jimenez et al. [24] both proved that there was a transition from twinning to slip-dominated flow with the decreasing of grain size. It demonstrated that twinning occurred when the grain size beyond a critical grain size. Li et al. [25] estimated the critical grain size of twinning appeared theoretically according to the relationship between the yield strength and grain size by twinning and that by dislocation slip. The result showed that the critical grain size should be $\sim 3 \mu\text{m}$. However, the

result above cannot always met with the reality because the slope k in Hell-Petch relationship was not always the same under different deformation conditions [38]. According to Jimenez's study [24], when the average grain size was 5 μm , basal dominated flow took place and no obvious twinning appeared in the material. And in Figueiredo's study [37], twinning also didn't observed in the samples with the grain size of 2.7 μm . Therefore, it seems more reasonable to discuss the critical grain size form the perspective of twinning dislocation mechanism.

According to the theoretical model of Yu et al. [39], the dislocations which are perpendicular to the slip plane of the twins would play a role of 'promoters' to activate the growth of the twins. These 'promoters' stimulated on the twinning slip planes layer by layer, leading to the growth of the twins step by step at the length of one burgers vector a time toward the slip direction. The activation dislocations between layer and layer could be expressed as,

$$P_{infection} \approx d^2 \rho P_{promoter}^1$$

According to the Taylor hardening model [40],

$$\sigma = \sigma_0 + \kappa b \rho^{\frac{1}{2}}$$

Then,

$$d = \left(\frac{\kappa E b}{\sigma - \sigma_0} \right) \cdot P_{promoter}^{-\frac{1}{2}}$$

where b is the burgers vector length of the promoter, E is the Young's modulus of magnesium, κ is a dimensionless constant of order 1 [40].

The critical grain size for the stable growth of the twins was 5.9 μm by calculation. When the grains of pure Mg were refined to the submicrometer scale, micro-twins would occur inside the grains [41]. As a result, twinning only occurs when the grain size is smaller than submicrometer or beyond 5.9 μm . Nucleation and growth of twins could take place because of the grains in the samples after ECAP at 200 $^{\circ}\text{C}$ were larger than the critical grain size. So that twinning occurred during deformation processes. In contrast the grains of the samples of 150 $^{\circ}\text{C}$ were too small to satisfy the critical size of the stable growth of the twins. Thus twins were not observed in the samples. In addition, perfect dislocations would dissociate during the process of twinning nucleation. Large amount of atoms migrated in these dissociation processes. Therefore the dissociation process was a process of thermal activation and a certain energy input was needed. The energy input was not enough for the dissociation of the perfect dislocation at the relatively low temperature (100 and 150 $^{\circ}\text{C}$), thus there was no twinning nucleation and growth observed in the samples at the low temperature conditions although some grains in the samples were beyond the critical grain size.

From the above, the pure Mg material was significantly refined after ECAP process. The deformation mechanism for pure Mg during ECAP was a combination of slip and recrystallization. The dominated deformation mechanism of pure magnesium material was basal slip during ECAP deformation at relatively low temperature. Recrystallization occurred interior the material had not conducted utterly, so that the microstructure was inhomogeneous, coarse grains still existed and surrounded by fine grains. With the increase of the deformation temperature, the recrystallization process became stronger and completed in 4-pass ECAP process. Instead of slip, recrystallization became the dominant mechanism at this temperature condition. Along with the continuous ECAP process, the interior dislocation multiplied rapidly. When the ECAP temperature reached 200 °C, the grains grew up obviously. The $\langle\alpha\rangle$ perfect dislocations dissociated and the partial dislocations dissociated from the $\langle\alpha\rangle$ perfect dislocations moved to an inerratic distribution under the function of applied stress. Large amount of activation dislocation distributed align and promoted the nucleation and growth of the deformation twins.

4 Conclusion

1. After ECAP processes, the grains of pure Mg material were significantly refined and the yield strength was obviously increased. Along with the rise of the deformation temperature, the grains grew up and the yield strength of the material decreased. The samples ECAPed at 150 °C showed the remarkable good ductility because of the fine and equiaxed grains and the relatively weak texture.
2. The deformation mechanisms of ECAP processes were different along with the change of the deformation temperature. Basal slip was dominated at the lower temperature. Recrystallization became the main mechanism gradually with the increase of deformation temperature. When the temperature of ECAP reached 200 °C, twinning occurred.
3. When deformation temperature raised to a certain extent, basal perfect dislocation of the pure magnesium material dissociated and twins were nucleated. The nucleated twins would grow up stably if the grains of the material beyond the critical grain size. And the calculated results indicated that the critical grain size of twins was about 5.9 μm .

References

1. Avedesian, M.M., Baker, H.: Magnesium and Magnesium Alloys, p. 3. ASM International, Materials Park, OH, USA (1999)
2. Agnew, S.R., Mehrotra, P., Lillo, T.M., Stoica, G.M., Liaw, P.K.: *Mater. Sci. Eng., A* **408**, 72–78 (2005)
3. Xia, K., Wang, J.T., Wu, X., Chen, G., Gurvan, M.: *Mater. Sci. Eng., A* **410–411**, 324–327 (2005)
4. Yin, S.M., Wang, C.H., Diao, Y.D., Wu, S.D., Li, S.X.: *J. Mater. Sci. Technol.* **27**(1), 29–34 (2011)
5. Yuan, Y., Ma, A., Gou, X., Jiang, J., Arhin, G., Song, D., Liu, H.: *Mater. Sci. Eng., A* **20**, 125–132 (2016)
6. Mostaed, E., Fabrizi, A., Dellasega, D., Bonollo, F., Vedani, M.: *J. Alloys Comp.* **638**, 267–276 (2015)
7. Yu, X., Li, Y., Wei, Q., Guo, Y., Suo, T., Zhao, F.: *Mech. Mater.* **86**, 55–70 (2015)
8. Galiyev, A., Kaibyshev, R., Gottstein, G.: *Acta Mater.* **49**, 1199–1207 (2001)
9. Lin, C.Y., Bor, H.Y., Chao, C.G., Liu, T.F.: *J. Alloys Comp.* **556**, 26–31 (2013)
10. Tang, L.L., Zhao, Y.H., Islamgaliev, R.K., Tsao, C.Y.A., Valiev, R.Z.: *Mater. Sci. Eng., A* **670**, 280–291 (2016)
11. Su, C.W., Lu, L., Lai, M.O.: *Mater. Sci. Eng., A* **434**, 227–236 (2006)
12. Gu, C.F., Toth, L.S., Field, D.P., Fundenberger, J.J., Zhang, Y.D.: *Acta Mater.* **61**(2013), 3027–3036
13. Karami, M., Mahmudi, R.: *Sci. Eng. A* **607**, 512–520 (2014)
14. Shen, J.H., Gartnerova, V., Kecskes, L.J., Kondoh, K., Jager, A., Wei, Q.M.: *Sci. Eng. A* **669**, 110–117 (2016)
15. Liu, Q., Ding, X., Liu, Y., Wei, X.: *J. Alloys Comp.* **690**, 961–965 (2017)
16. Liu, L., Chen, X., Pan, F., Gao, S., Zhao, C.: *J. Alloys Comp.* **688**, 537–541 (2016)
17. Li, W.J., Deng, K.K., Zhang, X., Nie, K.B., Xu, F.J.: *Mater. Sci. Eng., A* **20**, 367–375 (2016)
18. Ding, R., Chung, C., Chiu, Y., Lyon, P.: *Mater. Sci. Eng., A* **527**, 3777–3784 (2010)
19. Byer, C.M., Li, B., Cao, B., Ramesh, K.T.: *Scripta Mater.* **62**, 536–539 (2010)
20. Lilleodden, E.: *Scripta Mater.* **62**, 532–535 (2010)
21. Fan, G.D., Zheng, M.Y., Hu, X.S., Xu, C., Wu, K., Golovin, I.S.: *J. Alloys Comp.* **549**, 38–45 (2013)
22. Fan, G.D., Zheng, M.Y., Hu, X.S., Xu, C., Wu, K., Golovin, I.S.: *Mater. Sci. Eng., A* **556**, 588–594 (2012)
23. Jimenez, C.M.C., Aldareguia, J.M.M., Carreno, F., Prado, M.T.P.: *Acta Mater.* **88**, 232–244 (2015)
24. Jimenez, C.M.C., Aldareguia, J.M.M., Prado, M.T.P.: *Acta Mater.* **85**, 1–13 (2015)
25. Li, J.Z., Xu, W., Wu, X.L., Ding, H., Xia, K.: *Mater. Sci. Eng., A* **528**, 5993–5998 (2011)
26. Yu, Q., Qi, L., Chen, K., Mishra, R.K., Li, J., Minor, A.M.: *Nano Lett.* **12**, 887–892 (2012)
27. Qi, Y., Krajewski, P.E.: *Acta Mater.* **55**, 1555 (2007)
28. Yang, Q., Feng, A.H., Xiao, B.L., Ma, Z.Y.: *Mater. Sci. Eng., A* **556**, 671–677 (2012)
29. Ma, Z.Y., Mishra, R.S., Mahoney, M.W., Grimes, R.: *Metall. Mater. Trans. A* **36A**, 1447–1457 (2005)
30. Liu, F.C., Ma, Z.Y., Zhang, F.C.: *J. Mater. Sci. Technol.* **28**, 1025 (2012)
31. Caballero, O.A., Ruano, E.F., Rauch, F.: *Carreno. Mater. Des.* **137**, 128 (2018)
32. Jamili, M., Zarei-Hanzaki, A., Abedi, H.R., Minarik, P., Sotani, R.: *Mater. Sci. Eng., A* **690**, 244–253 (2017)
33. Johannes, J.B., Mishra, R.S.: *Mater. Sci. Eng., A* **464**, 255–260 (2007)
34. Fan, T.W., Luo, L.G., Ma, L., Tang, B.Y., Peng, L.M., Ding, W.J.: *J Appl. Mech. Tech. Phys.* **55**(4), 672–681 (2014)
35. Fan, T.W., Tang, B.Y., Peng, L.M., Ding, W.J.: *Scripta Mater.* **64**, 942–945 (2011)

36. Fan, T.W., Zhang, Q., Ma, L., Tang, P.Y., Tang, B.Y., Peng, L.M., Ding, W.J.: *Eur. J Mech. A/Solids* **45**, 1–7 (2013)
37. Figueiredo, R.B., Poggiali, F.S.J., Silva, C.L.P.: *J. Mater. Sci.* **51**, 3013–3024 (2016)
38. Barnett, M.R., Keshhavar, Z., Beer, A.G., Atwell, D.: *Acta Mater.* **52**, 5093–5103 (2004)
39. Yu, Q., Shan, Z.W., Li, J., Huang, X.X., Xiao, L., Sun, J., Ma, E.: *Nat. Lett.* **463**, 335–338 (2010)
40. Taylor, G.I.: *Proc. R. Soc. London A* **145**, 362–387 (1934)
41. Yu, Q., Mishra, R.K., Minor, A.M.: *JOM* **64**, 1235–1240 (2012)

Research on Ice-Induced Vibration Test of Inland Icebreaker



Siyu Wang and Yuan Du

Abstract Series of tests were implemented to explore the ice-induced vibration behavior of a river icebreaker. The ice thickness of experimental site is in the scope of 300–400 mm. According to the ice situation on the river, three typical ice conditions are divided in the current research. The vibration test system is mainly composed of data acquisition system, accelerometers and digital cameras. Ice condition and speed of icebreaker are chosen as the main research objects of the test. On the basis of time domain curve and acceleration spectra, some interesting points are found. The investigation results show that: Compared with other two typical ice conditions, the peak value of complete ice area is the biggest. In addition, more characteristic frequencies appear when the working condition is complete ice area. When the icebreaker drives at a faster speed, the ice-induced vibration response also increases.

Keywords Vibration · River icebreaker · Tests · Typical ice conditions · Ice-induced

1 Introduction

With the development of polar resources, people are increasingly interested in the interaction between ice and ships. Su et al. [1] presented a numerical method to simulate the interaction between ice and ship. The comparison between numerical method and experiment data from the ice trails of icebreaker matched well. Zhang et al. [2] proposed a Smoothed Particle Hydrodynamics (SPH) method to simulate the failure procedure of ice and interaction between ice and ship. The numerical data has been compared with experimental data of a scaled icebreaker model.

The vibration of hull structure leads to discomfort of passengers and abnormal working condition of instrument. Many researches have been conducted about the

S. Wang · Y. Du (✉)
Harbin Engineering University, Harbin, China
e-mail: duyuan@hrbeu.edu.cn

vibration characteristic of hull structures. Zhou et al. [3] investigated the ice load of a model-scale ship when the model was towed through ice field in the ice tank. Luo et al. [4] investigates the resistance of ships navigates in the marginal ice zone by conducting model tests in the towing tank, the ice was modelled by paraffin. Yue et al. [5] conducted a full-scale test on a platform in Bohai Bay to study the ice forces and ice-induced vibration of platform structure. Huang and Liu [6] put up a dynamic model to analyze the ice-induced vibration (IIV) of offshore structures. Pang et al. [7–10] investigated vibration characteristic of doubly curved shells, annular sector plates and rectangular plates on the basis of a new semi-analytical method.

The researches mentioned above are mainly about hull vibration, ice load of offshore structures and tests of model-scale ship. Many full-scale measurements of offshore structure have also been conducted. However, few researches have been implemented to study the vibration response of the ice-breaker when the ship sails in the ice area.

In the current research, the data measured when the ice-breaker was working in ice-infested river is displayed. In the meantime, the effects of ice condition and speed of icebreaker on vibration response of ship have also been discussed.

2 Experiment Procedure

The test was conducted when the temperature was in the scope of $-4-0$ °C. The portable vibration test system was used to collect and store vibration signals. The accelerometers were attached to the ice-breaker through magnetic base. Digital cameras were placed at the bow and portside of the ice breaker to record the interaction between ship and ice region. The signal measurement and acquisition instrument of ice-breaking test are shown in Fig. 1.

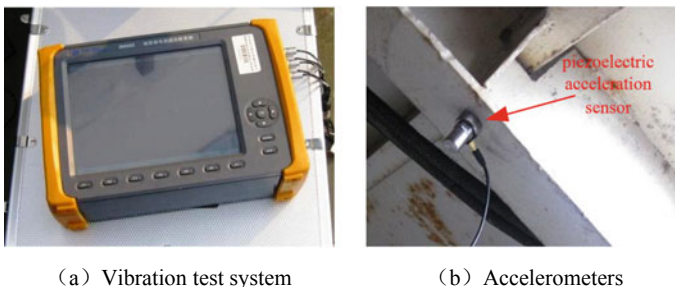


Fig. 1 The instrument used in the test

2.1 Ice Situation

According to the ice situation on the surface of river, complete ice area, floating ice area and open area are divided into three typical ice conditions. The interaction situation between icebreaker and ice sheets are displayed in Fig. 2. The ice conditions of the tests and speed of the ice-breaker were chosen as the main research objects of tests. In summary, the test condition table of icebreaker is shown in Table 1.

2.2 Layout of Key Point

The center of local plate situated on the driving deck (5250 mm from the bow, 675 mm from the centerline) and the center of local plate on the main deck (3650 mm from the bow, 675 mm from the centerline) are respectively defined as point A and B to investigate the influence of ice condition and speed of icebreaker on vibration response of ship.

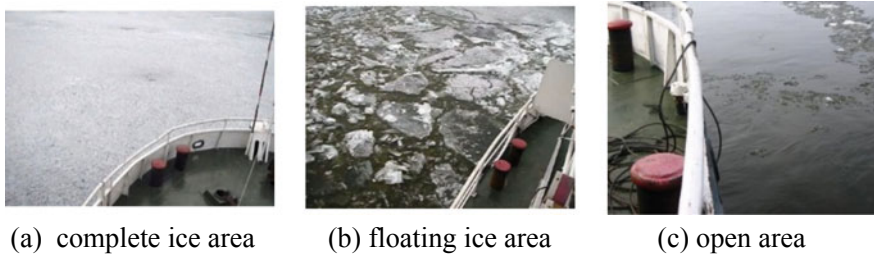


Fig. 2 The typical ice conditions

Table 1 Ice conditions and speed of the icebreaker

Test condition	Description of ice	Speed of ice-breaker/kn	
		3 ~ 4	7 ~ 8
Condition 1		Complete ice area (Thickness 250–300 mm)	
Condition 2		Floating ice area	
Condition 3		Open area	

2.3 *The Process of Dealing with Vibration Acceleration Signal*

Wavelet noise reduction and Fourier transform were combined to deal with the random vibration signal of ice-induced vibration. The fixed time-window function $g(t - \tau)$ was used to cut off objective function $x(t)$, Fourier transform was conducted with local time domain signal.

3 Experimental Phenomenon and Discussion

The key point A was selected as research subjects to discuss the influence of ice conditions on vibration response of ship, the speed was fixed between 3 and 4 kn. The key point B was defined as observation point to investigate the effects of icebreaker speed when the river icebreaker sailed in complete ice area.

3.1 *The Effects of Ice Condition*

Figure 3 indicates the time domain curve of acceleration of test point A. Maximum acceleration response value of the floating ice area is smaller than complete ice area. In addition, the variation of acceleration amplitude in the floating ice area is slower than the complete ice area condition.

Figure 4 demonstrates acceleration amplitude spectrum of the test point A. When the icebreaker navigates in open area, both the number and value of peaks are the smallest. However, the maximum peak value doesn't increase obviously when the ice condition is complete ice area. When the observed frequency is near 73 Hz, the peak value of complete ice condition is even less than the floating ice area.

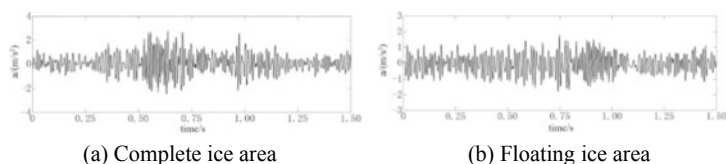


Fig. 3 Acceleration time domain curve of key point A

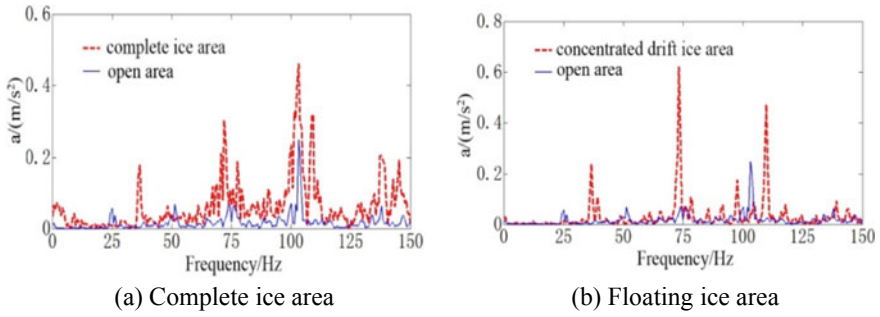


Fig. 4 Vibration amplitude spectrum of the key point A

3.2 The Effects of Icebreaker Speed

When the icebreaker navigates with different speeds in complete ice area, the time domain curve of key point B is displayed in Fig. 5. It is easy to find that peak acceleration changes dramatically with different speeds. Figure 6 presents acceleration amplitude spectrum of test point B. When the speed of icebreaker increases, the peak acceleration also increases. Whereas, the number of peaks decreases.

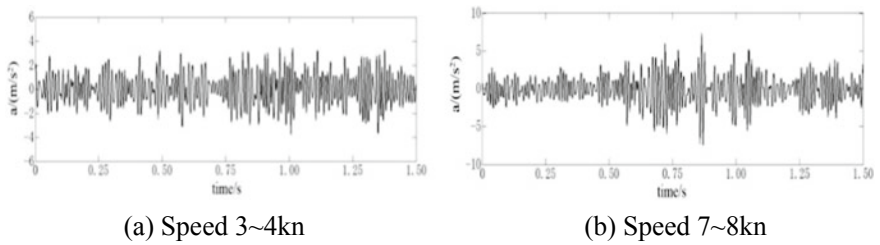


Fig. 5 Acceleration time domain curve of key point B

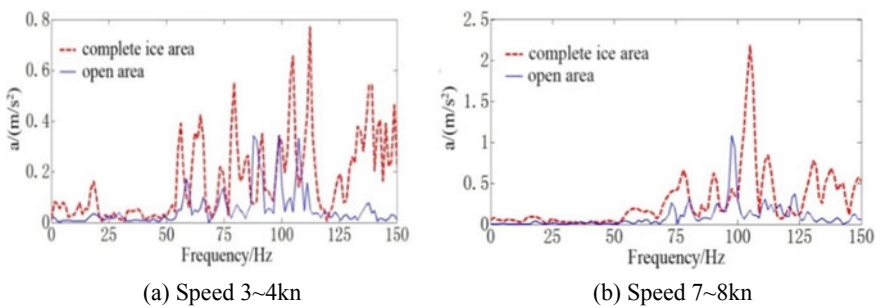


Fig. 6 Acceleration amplitude spectrum of key point B

4 Conclusion

On the basis of vibration acceleration signal of key points A and B, we can reach the conclusions as below:

1. When the ice condition is complete ice area, both the acceleration peak value and the number of acceleration peaks are more than other two ice conditions.
2. Whereas, when the ice condition is floating ice area the vibration peak value is smaller than complete ice area. What's more, vibration response excited by ice-breaking load of floating ice area condition is more sparse than complete ice area condition.
3. When the ice breaker sails with various speeds, the vibration response induced by ice breaker mainly appears in low and middle frequency. With the augment of icebreaker speed, the vibration response gradually increases.

References

1. Su, B., et al.: A numerical method for the prediction of ship performance in level ice. **60**(3), 177–188 (2010)
2. Zhang, N., et al.: A numerical study on ice failure process and ice-ship interactions by smoothed particle hydrodynamics. **11**(2), 796–808 (2019)
3. Zhou, L., et al.: Ice forces acting on towed ship in level ice with straight drift. Part I: analysis of model test data. **10**(1), 60–68 (2018)
4. Luo, W.-Z., et al.: Experimental research on resistance and motion attitude variation of ship-wave-ice interaction in marginal ice zones. *Mar. Struct.* **58**, 399–415 (2018)
5. Yue, Q.J., Guo, F.W., Karna, T.: Dynamic ice forces of slender vertical structures due to ice crushing. *Cold Reg. Sci. Technol.* **56**(2–3), 77–83 (2009)
6. Huang, G., Liu, P.: A dynamic model for ice-induced vibration of structures. *J. Offshore Mech. Arct. Eng.* **131**(1), 011501 (2009)
7. Pang, F., et al.: Free and forced vibration analysis of airtight cylindrical vessels with doubly curved shells of revolution by using Jacobi-Ritz method. *Shock Vib.* **2017** (2017)
8. Pang, F., et al.: A modified Fourier solution for vibration analysis of moderately thick laminated annular sector plates with general boundary conditions, internal radial line and circumferential arc supports. *Curved Layered Struct.* **4**(1), 189–220 (2017)
9. Pang, F., et al.: A series solution for the vibration of Mindlin rectangular plates with elastic point supports around the edges. *Shock Vib.* **2018** (2018)
10. Pang, F., et al.: A semi analytical method for the free vibration of doubly-curved shells of revolution. *Comput. Math. Appl.* (2018)

Critical Analysis of Productivity of Well 2L After Foam-Acid Diversion



Chinedu J. Okere, Lihui Zheng, Guandong Su, Hao Liu, Qifan Chang, and Obiora J. Obiafudo

Abstract Foam acid diversion is a widely adopted well stimulation technique based on its superior efficiency and applicability to reservoir layers with varying permeability. However, no study has critically analyzed the performance of a well after foam acid diversion operation from a field perspective. In this study, Well 2L was used as case study, and the field data obtained from the Nigerian Petroleum Development Company were carefully analyzed using pressure transient equations. A clustered column chart was used to compare the performance of the well before and after acid foam diversion. Combining the results of previous researches, the causes of formation damage due to the initial decline in the productivity of Well 2L was established. The results indicated that, first, a rapid decline in production of Well 2L before foam acid diversion was due to formation damage by drilling and completion operations previously carried out on the well. Second, after foam acid diversion, the productivity of Well 2L remarkably increased by 70%, suggesting that the application of foam acid diversion significantly improves oil recovery .

Keywords Foam acid diversion · Formation damage · Productivity · Well stimulation · Pressure transient well test · Well 2L

C. J. Okere (✉) · L. Zheng · G. Su · H. Liu · Q. Chang
College of Petroleum Engineering, China University of Petroleum,
Beijing 102249, Beijing, China
e-mail: zhenglihui@cup.edu.cn

O. J. Obiafudo
Department of Industrial Production Engineering, Nnamdi Azikiwe University,
Awka 420110, Anambra, Nigeria

Nomenclature

Symbol

\emptyset	Porosity
B	Formation volume factor
BHP	Bottom hole pressure
BS & W	Base sediment and water
b/d	Barrel per day
C^3	Clustered column chart
C_t	Compressibility factor
H	Total reservoir thickness
h_p	Height of perforation
h_t	Height of interval
J	Productivity index
K	Formation permeability
K_H	Horizontal permeability
K_v	Vertical permeability
M	Honer's plot slope
mD	Milli Darcy
P_{avg}	Average pressure
Ppt	Part per thousand
P_{wf}	Flowing well pressure
P_{ws}	Static well pressure
ΔP_s	Pressure drop due to skin
Q	Production flowrate
S_d	Skin effect due to damage
S_p	Skin due to incomplete perforation
t_p	Total production time
μ	Viscosity

1 Introduction

Acidizing treatment have been a preferable method in the oil and gas industry for restoring and improving the permeability of formations due to their compatibility with various types of formation. The major goal of any acidizing operations is to improve well productivity thereby eliminating formation damage caused by previous operations, and improving the characteristics of the reservoir such as porosity and permeability [1, 2]. The choice of chemical diversion process has had tremendous success in reservoir stimulation [3, 4]. The use of foam as a treating agent for acid diversion during stimulation process have been widely adopted. Studies have shown that a common type of acid used in sandstone formation is the

foamed acid [5]. Foams exist in either gaseous or liquid phase. Nitrogen gas (N_2) is used as the gaseous phase while the liquid phase is usually formed from a hydrofluoric acid (HF). Scholars like Zou et al. [6] and Songyan et al. [7] suggested that in foamed acidizing operation, the rate of fluid loss is relatively low, with extremely large viscosity and it can effectively mitigate formation damage in formations with different permeability. As the foam enters the layers of the rock it causes an increase in gas saturation and a decrease in liquid saturation at the near wellbore zone [8].

Experimental study by Siddiqui et al. [9] revealed that when foams are injected, they reside in layers of varying permeability and least damaged zones of the interval, while other injected acid will be at zones where little or no foam has entered. The presence of foam in a high permeability or undamaged region will significantly reduce the relative permeability of liquid in that region, thereby converting acid saturated layers into the foam-saturated layers. Foam acidizing treatments can be applied in three types of formations: first, in formations having a mixture of oil-water layers in which the foam blocks the water zone and prevent more water cut after acidizing. Second, in formations which will be retreated, where corroded channels formed due to previous acidification are blocked by the acid-foam solutions. Finally, in formations with thick oil layers (with varying permeability within the layers), where the foam blocks high permeability layers by diverting the acid to the low permeable regions.

A major disadvantages of foam diversion is that over time, the bubbles breaks resulting in the flow of gaseous phase which could lead to a poor diversion process [10]. Despite several experimental reports on the successful application of foam acid diversion techniques, no study has critically demonstrate this success from a field perspective.

Herein, we analyze the reservoir performance of Well 2L via a well test analysis of some Oilfield data, performance comparison chart and a review of the effect of formation damage by previous operations. This study will provide a reliable basis for understanding foam acid diversion operation and serve as a guide for formation damage analysis of oil field data.

2 Method

In order to evaluate the degree of formation damage in a well due to permeability impairment, the skin factor is use to quantitatively represent the degree of formation damage. The Permeability and skin factor are estimated from a pressure transient well test analysis. Pressure transient well testing is carried out to develop a detailed reservoir model for predicting and analyzing the characteristics of the reservoir behavior, formation permeability, skin factor, shape of the drainage area, optimum reservoir recovery rate, reservoir recovery evaluation, and the type of reservoir boundary [11].

2.1 Reservoir Formation Damage Evaluation Method

Using pressure transient well test analysis of the buildup test data of Well 2L, permeability of the formation and other parameters of the reservoir was calculated. At early time region (ETR) and transient flow regime, the permeability (K) from the Cartesian plot of the buildup test data is given by:

$$K = -\frac{162.6q\mu\beta}{mh} \quad (1)$$

The total skin effect (S) due to multiple flow rates is evaluated as:

$$S = 1.151 \left[\frac{P_{ws}(\Delta t=1h_r) - P_{wf}(\Delta t=0)}{m} - \text{Log} \left(\frac{K}{\phi\mu c_t r_w^2} \right) + 3.23 \right] \quad (2)$$

The skin effect due to partial perforation (S_p)

$$S_p = \left(\frac{h_t}{h_p} - 1 \right) \left(\text{In} \left[\frac{h_t}{r_w} \sqrt{\frac{K_H}{K_V}} \right]^{-2} \right), \quad (3)$$

where

$$K_H/K_V = 1 \quad (4)$$

Therefore, from Eq. (3), the skin effect due to formation damage (S_d) at the near wellbore region is:

$$S_d = \frac{h_p}{h_t} (S - S_p) \quad (5)$$

Additional pressure drops due to total skin effect (ΔP_s)

$$\Delta P_s = S \left[\frac{141.2q\beta\mu}{Kh} \right] \quad (6)$$

The productivity index (J) of the well is defined as

$$J = \frac{q}{P_{avg} - P_{wf}} \quad (7)$$

The flow efficiency (E) is evaluated using Eq. (8)

$$E = \frac{P_{avg} - P_{wf} - \Delta P_s}{P_{avg} - P_{wf}} \times 100 \quad (8)$$

Thus, the formation damage ratio (DR) is given by

$$DR = \frac{1}{E} \quad (9)$$

The well's transmissibility (T) is calculated using Eq. (10)

$$T = \frac{Kh}{\mu} \quad (10)$$

3 Description of Operations and Historical Development of Well 2L

The Oredo oil and gas field is one of the onshore oil and gas producing fields in Niger Delta basin that is located in the north-western Niger Delta, about 85 km South-West of Benin, Edo state, Nigeria. It was developed by the Nigerian Petroleum Development Company (NPDC) a subsidiary of the Nigerian National Petroleum Corporation.

3.1 History of Well 2L

Well 2L was drilled to a depth of 350 m and completed in April 1999 with two string dual (TDS) on A8.2 sands. When the well became fully operational in February 2000, the production rate was 700–800 stb/d and sand of about 2 ppt with a water cut of 22% was noticed in December 2000. Interval Gravel Pack (IGP) was installed across both intervals during a well intervention operation in 2002 to control high sand production after an initially installed eposand consolidation was ineffective. The water cut rose steadily to about 51% in April 2004 thus necessitating a water exclusion job in May 2004. After the water exclusion job, the water cut subsided to 8.1%. The well was observed to have experienced a drastic drop in production from 36.4 stb/d/psi in March 2000 to 3.48 b/d/psi in February 2004 due to the encroachment of external water into the formation. In order to improve its productivity, Well 2L was stimulated by a foam acid diversion treatment, the diversion operation was carried out according to the sequence below;

- A drift was inserted at the nipple of the well to ensure that the tubing was free.
- As diesel were circulated, the coiled tubing surface was run to the tubing tail to obtain a clean hole.
- Then the acidizing chemicals were injected into the perforated region based on the standard operational procedures.
- The well was shut-in for about 720 h and a pressure build up test was carried out with the bottom hole pressure at various intervals.
- The well was opened for production and the production rates, GOR, sand level and water were carefully monitored.

3.2 History of Reservoir Modifications in Well 2L Due to Various Field Operations

The reservoir of Well 2L composed of unconsolidated sandstone formation with well-developed natural fractures which is mainly composed of quartz, feldspar, mica and clay minerals [12]. During the production cycle of a well, the reservoir undergoes several changes in the weathering and behavior of the reservoir due to the impact of operations such as drilling and completion, and acidizing operations. When drilling, stresses induced to the rock leads to geo-mechanically damage and the original properties of the reservoir (such as porosity and permeability) are altered at the near wellbore zone. During high sand production, sands grain accumulates at the casing (lowering the permeability zone) and creates cavities in the reservoir which may lead to a formation collapse or a significant pressure drop at near wellbore region [13–15].

4 Results and Discussion

Details of the reservoir characteristics of Well 2L before foam acid diversion is presented in Table 1 below:

The characteristics of Well 2L of a sandstone reservoir having a porosity of about 19%, a permeability of 1698 mD, and productivity index of 85% indicating that the well can provide a good fluid transport ability. Other characteristics such as the drainage area, average reservoir pressure, oil viscosity, oil volume factor and water–gas ratio as shown in Table 1, justified the decision for investing in Well 2L. The completion operation was carried out in April 1999 to meet the sand control requirements of Well 2L, the interval gravel pack was installed to arrest high sand production. At a performance shot density of 12 spf, the perforation skin was not affected.

From Table 2, a line graph of the gross production of Well 2L before acid foam diversion is shown in Fig. 1.

Table 1 Reservoir characteristics of Well 2L

Description	Value	Field unit
Sandstone reservoir	A8.2	–
Wellbore radius	0.362	ft
Permeability	1698	mD
Porosity	18.7	%
Perforation depth	37.784	ft
Temperature	185	°F
Productivity index	0.854	bb/d/psi
Compressibility factor	8.91×10^{-5}	psi ⁻¹
Gas liquid ratio	139.2	scf/bbl
Gas saturation	0.705	–
Water-gas saturation	1.100	–
Drainage area	2010.4	ft ²
Oil viscosity	0.238	Cp
Water salinity	94,712	ppm
Oil volume factor	1.805	bbl/stb
Average reservoir pressure	4377	psi

Table 2 Production data for Well 2L before foam acid diversion

Date	Size (inch)	BHP (psi)	Gross production (stb/d)	BS & W (%)	GOR (scf/bbl)	Sand (ppt)
02/2000	20	460	780	1	200	2
02/2001	22	460	950	1	200	2
12/2001	24	500	1300	2	250	4
03/2002	36	360	2500	9	150	7
08/2002	40	310	3200	16	150	9
02/2003	44	280	3170	18	150	9
11/2003	42	280	3080	22	180	8
04/2004	42	290	3000	52	200	7
12/2004	24	250	1750	23	300	4
05/2005	36	150	850	10	175	2

At the time Well 2L became operational in February 2000, the gross production rate was 780 stb/d at a bottom hole pressure of 460 psi with a gas to oil ratio of 200 scf/bbl. There was a significant increase in the gross production over the years resulting to an obvious curve (Fig. 1) as it attained a stable production rate of 3200 stb/d in August 2002, however in May 2005, the production declined significantly to 850 stb/d. In order to improve the performance of the well, the production team designed a well intervention scheme which includes well testing and stimulation program.

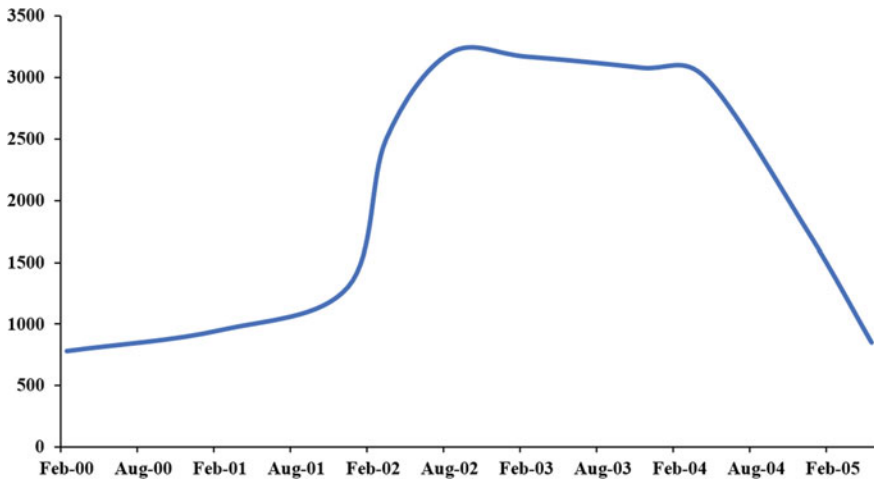


Fig. 1 Gross production history of Well 2L before acid foam diversion

In 2005, a pressure build-up test was carried out in Well 2L (Table 3). The well was shut-in for about 720 h and the bottom hole pressure at different intervals were recorded for analysis.

From the results of the well test (Table 3), it is obvious that the rate of pressure drops in the well indicates a significant impairment of the well interval due to existing formation damage. A high formation permeability value of 774 mD (Table 4) which indicates a high rate of fluid flow through the formation, but a skin effect of 14.65 implies an impairment to flow indicating the presence of damage within the near wellbore region and thus the reason for performing the acid foam diversion operation on the well. The flow efficiency of the well at approximately 37% is very low, and this implies that Well 2L was producing below its capacity and needed to be stimulated. The high formation transmissibility of about 26,093.2 mD.ft/cp shows there is an easy flow of fluids through the layers of the formation and the reservoir rock can produce fluids. Prior to acid foam diversion operation, the well's production rate was 650 stb/d (from field survey) and the positive skin factor shows that the well was significantly damaged with a pressure drop due to total skin effect to be 102 psi (Table 4).

The result of Table 5 is presented in Fig. 2.

After the acid foam diversion, the average production rate of the well increased significantly to 2150 b/d in October 2005 which was about 70% increment from last production rate before acidizing. To analyze the gross production rate of Well 2L before and after acid foam diversion operation, production reports of Tables 2 and 5 were compared in a clustered column chart as shown in Fig. 3.

Table 3 Pressure buildup test data for Well 2L

Shut-in time, Δt (hrs)	Bottom hole pressure (psia)	Horner time $\frac{(t_p + \Delta t)}{\Delta t}$
0	2685	0
1	2763	721
2	2805	361
4	2819	181
5	2825	145
7	2828	104
9	2830	81
12	2831	61
20	2831	37
60	2837	13
120	2840	7
300	2842	3.4
420	2842	2.7
550	2842	2.3
620	2843	2.2
720	2843	2.0

Table 4 Results of buildup test data analysis of Well 2L after stimulation

Description	Value	Field unit
Permeability (K)	774	mD
Total skin effect	14.65	–
Skin effect due to formation damage	3.36	–
Pressure drop due to total skin effect	101.8	Psi
Pressure drop due to skin effect by formation damage	23.4	Psi
Pressure drop due skin effect by partial perforation	35.58	Psi
Productivity index	6.203	stb/d/psi
Flow efficiency	37.2	%
Formation damage ratio	3	–
Transmissibility	26,093.2	mD.ft/cp

As Fig. 3 indicates, the maximum performance of Well 2L before acid foam diversion occurred at the mid time region (i.e. between March 2002 to April 2004) of the observed period. However, at the late time region (December 2004 to May 2005), there was a sequential drop in the performance of the well due to inherent formation damage effect. After acid foam diversion operation, the production of the well increased significantly at the early time region (October 2005 to September 2006) which suggests that the acidizing operation was successful, but due to certain factors, a sudden decline in the production occurred at the mid time and late time region. These factors were extensively reviewed in the next section.

Table 5 Production data for Well 2L after acid foam diversion

Date	Size (inch)	BHP (psi)	Gross production (b/d)	BS & W (%)	Sand (ppt)
10/2005	36	150	2150	0	10
02/2006	40	180	2050	1	14
09/2006	16	310	1900	2	12
02/2007	20	280	1000	0	8
11/2007	22	250	1000	1	10
04/2008	28	200	920	0	16
12/2008	32	200	900	0	12
04/2009	36	190	800	0	10
11/2009	36	160	700	2	14
03/2010	36	170	600	1	18
12/2010	36	150	550	1	22

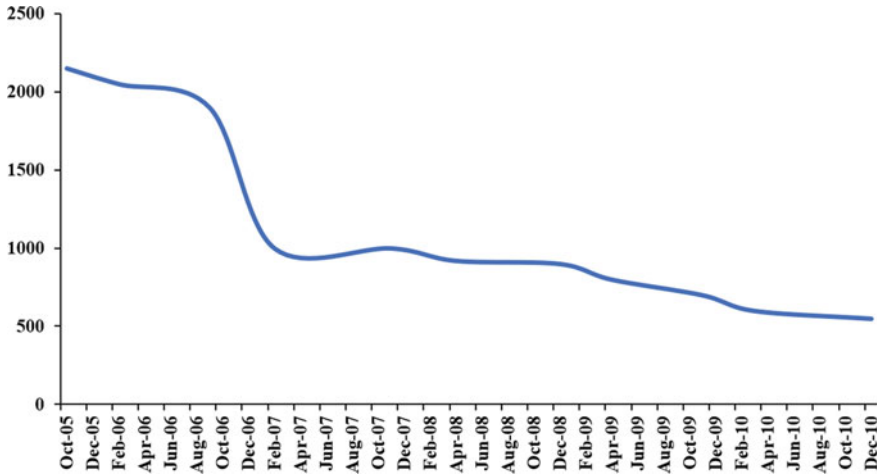


Fig. 2 Gross production rate of Well 2L after acid foam diversion

4.1 Formation Damage During Acidizing Operation

One of the recent challenges in the petroleum industries is performing matrix acidizing in complex and low permeability reservoirs like the sandstone reservoirs due to the complexity of the formation [16]. Studies have identified Injection rate, acid-formation contact time, temperature, nature of rock minerals, and the conductivity of the fractures in the formation as some of the factors influencing the success of an acid stimulation operation [17]. Acid-formation contact time and conductivity property of the fractures are the most critical factors to be considered

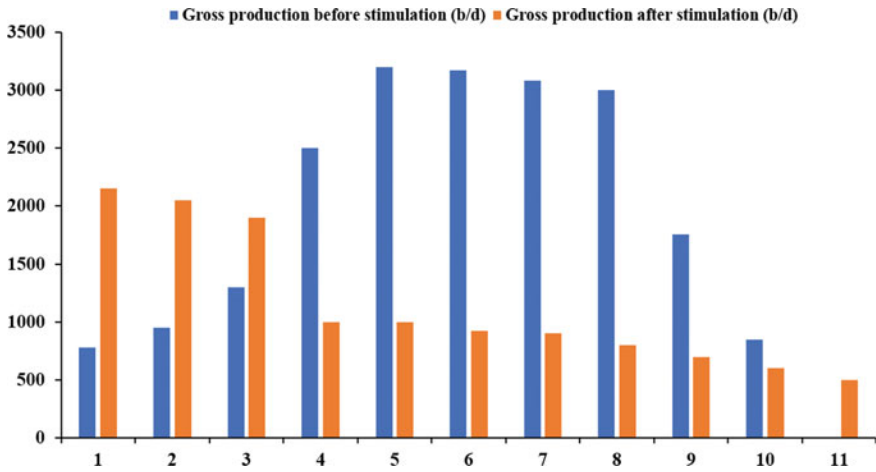


Fig. 3 Gross production of Well 2L before and after stimulation process

during acidizing process. Foam acid diversion has gain popularity because of its low rate of fluid loss and wide range of applicability in layers with variable permeability [18]. Other Factors influencing the effectiveness of acid foam diversion treatment includes, the quality of the foam, foam slug size, difference in permeability within the layers and temperature. After acid foam diversion operation was carried out on Well 2L, a subsequent decline in production rate was observed in the mid time and late time region. This effect is attributed to some possible factors which are highlighted below;

Quality of the acid foam solution. To achieve an optimum result from acid foam diversion the foam must be of a good quality. The quality of the foam in acid foam solution is a function of viscosity of the foam, foam slug size and amount of foam in the solution. Theoretically, the quality of the foam in solutions in defined as the ratio of gas volume to foam volume (gas + liquid) at a specific temperature and pressure [19]. Mathematically it is expressed as;

$$FQ = \frac{Gas\ volume}{Gas\ volume + Liquid\ volume} \tag{11}$$

where FQ is the foam quality, %; gas volume = BBLs or gallons; and liquid volume = BBLs or gallons.

Studies revealed that the quality of foam fraction in the acid solution has a significant relationship with the viscosity of foam, a graphical representation of this relationship is shown in the Fig. 4.

As Fig. 4 shows, when the foam quality is between 0 and 0.52, the spherical gas bubbles does not come into contact with each other and the viscosity is within a low range, thus there are lots of free fluids in the system, and this influence the fluid-loss

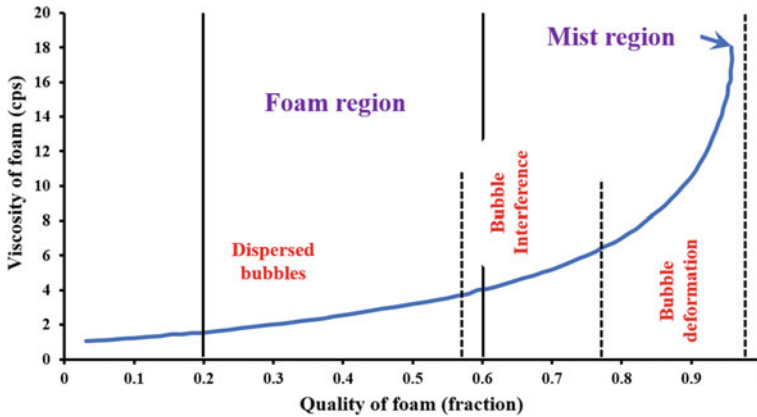


Fig. 4 Relationship between the viscosity and quality of foam [20]

ability [21]. When the quality of the foam is between 0.52 and 0.96, the gas bubbles come in contact with each other and the viscosity will be higher, in this state, the foam solution does not have proppant-suspension ability. And when the foam quality is above 0.96, there will be a significant loss in viscosity and the foam will be in mist form. A higher foam viscosity, indicates a higher acid foam oil recovery efficiency [20]. This implies that the higher the foam quality the higher the viscosity and the sweep efficiency is improved. Therefore, the most suitable and frequently used foam quality is within the range of 0.6–0.8, this was called “dry foam” which has a polyhedral molecular structure [22].

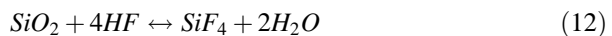
Concentration and Temperature of foam in Injected acid foam solution. The amount of foam in the acid foam solution will determine the effectiveness of the acidizing process. High foam concentration implies that more acid saturated layers will be converted into the foam-saturated layers and thus yield an effective acid diversion process. However, at downhole temperatures the performance of the acid foam solutions declines due to decrease in foam concentration and temperature effect. Many field treatments require foam effectiveness at elevated temperature in the presence of both acid and corrosion inhibitor [23]. Several researchers have recommended that at downhole conditions the concentration of the injected foam should be within 1.5 to 2 times the open hole volume of the reservoir bed while Kam et al. [23] is of the opinion that foam diversion is best applied at temperatures within the range of 150–250 °F.

Injection Techniques. The injection techniques determine the success of the acidizing process. The injection rate and strategy are critical as a poor technique could lead to significant formation damage. Selecting an optimum injection rate has been a challenging and should be based on the dissolution and removal of minerals as well as the depth of damaged zone.

The acid injection rate can also be constrained by surface injection pressure at the pump. A continuous injection of foamed acid could result to formation blockage due to the foam saturated layers. As the total skin factor increases, the initial skin factor due to formation damage decreases during acidizing while bottom hole and wellhead pressures increase. At the initial stage of the acid foam injection (within an hour), there is a rapid increase in pressure, and then it increases slowly. In high permeability layers, the flow rates of foamed acid decreases, but in low-permeability layers it increases relatively with an increase in the volume of foamed acid injected. The acid injected into different layers is more uniform during matrix acidizing by using foamed acid. However, the optimum amount of acid injection rate varies with the concentration of acid, temperature alteration and rock mineralogy. Studies from Qi et al. [24] revealed that an injection rate of 3–4 mL/min will produce an optimum acidification result while other researchers proposed a systematic procedure that requires low acid injection rates to achieve optimum stimulation with a given acid volume.

Rock mineralogy and Fracture conductivity. Rock minerals and existing fracture conductivity are key to the success of acid foam diversion operation. However, the nature of the rock mineralogy will define the optimum amount of acid injection rate. Studies revealed that in dolomite formations, in order to effectively penetrate into the pores is experienced when there is an increase in acid volume and a decrease in acid injection rate more than limestone formations [25]. Sandstone minerals are partially soluble in acid solutions and some layers restricting the flow through pore spaces are dissolved during the process, thereby allowing the formation fluids to move more freely into the well. Tight formations are most likely damaged formation during acidizing due to their low permeability and complexity of the formation [26, 27]. Therefore, the conductivity of the fractures in tight formations plays an important role in acidizing operation, acidizing becomes more efficient in high conducting fractures. Wells with permeability below one mD will produce an optimal acidizing result.

Mechanism of chemical Reactions due to contact between injected acid and the formation minerals. The chemical reaction of acid with the minerals of sandstone formation occurs in three stages, firstly, the hydrofluoric acid (HF) reacts with pure quartz layers of the sandstone in the following manner:



The result of the above reversible reaction yields an anion of silicon hexafluoride (SiF_6^{2-}), the second phase of the reaction involves the reaction of hydrofluoric acid (HF) with feldspar, chert, mica and clay minerals of the sandstone resulting in the formation of silicon hexafluoride (SiF_6^{2-}) anions and compounds of aluminum fluorides like; AlF_6^{3-} , AlF_5^{2-} , AlF_4^- , AlF_3 , AlF_2^+ , AlF^{2+} , and AlF_6^{3-} . Some of these aluminum fluorides further reacts with calcium, potassium and sodium ions at free

state to form precipitates of Calcium Fluosilicate [CaSiF_6], Potassium Fluosilicate [K_2SiF_6], Sodium Fluoroaluminate [Na_3AlF_6] and Calcium Fluosilicate [Na_2SiF_6]. The formation of these precipitates often leads to plugging effect which will eventually damage the formation. The damage increases with a corresponding increase in the amount of the precipitates formed [2, 28].

5 Conclusion and Recommendations

Formation damage can occur at different phases of a well's history from the drilling and completion phase to the development and production phase. Operations such as drilling, completion, workovers and acidizing, which exposes the formation to a foreign fluid, could result in formation damage due to re-occurring fluid/rock interactions. If a well is producing below its optimum capacity, it is necessary to identify the root-cause of the problem before corrective measures are adopted. In some cases, a critical assessment of the entire productive system may be required. If formation damage is suspected to be the actual cause of a well's low productivity, then its effect should be controlled. Based on the analysis in Well 2L, the following conclusions are made;

1. The performance of Well 2L declined significantly due to formation damage.
2. The sudden decrease in the production rate in Well 2L was due to previous activities on the well resulting from sand injection and insertion of production logging tools during the operations of the well.
3. After the application of foam acid diversion operation in Well 2L, the production increased significantly to about 70% of the previous production, which suggests that the foam acid diversion operation was effective.

The recommendation in this study becomes vital based on the conclusion deduced from Well 2L.

- During the retreatment of Well 2L, more attention should be given to the quality of the foam and the injection techniques. Solvents and acid compositions should be selected to reduce incompatibility.
- The formation of precipitates during acid foam diversion should be prevented by pre-flushing and post-flushing techniques.
- A continuous monitoring of subsequent operations in Well 2L should be carried out during future operation done on the well in order to prevent future occurrence of formation damage on the well.

References

1. Rabbani, E., Davarpanah, A., Memariani, M.: An experimental study of acidizing operation performances on the wellbore productivity index enhancement. *J. Petrol. Exploration Prod. Technol.* (2018)
2. Okere, C.J., Su, G., Zheng, L., Cai, Y., Li, Z., Liu, H.: Experimental, algorithmic, and theoretical analyses for selecting an optimal laboratory method to evaluate working fluid damage in coal bed methane reservoirs. *Fuel* **282**, 118513 (2020)
3. Nasr-El-Din, H.A., Al-Habib, N.S., Al-Mumen, A.A., Jemmali, M., Samuel, M.: A novel technique to acidize horizontal wells with extended reach. *J. Petrol. Technol.* (2005)
4. Wei, P. et al.: Fuzzy-ball fluid self-selective profile control for enhanced oil recovery in heterogeneous reservoirs: the techniques and the mechanisms. *Fuel* **275**, 117959 (2020)
5. Chengshou, C., Yaogang, Z., Haomin, J., Qiangjun, W., Fajun, R., Zhi, L., Lei, L.: New stimulation technologies on horizontal wells in Jingbian gas fields. *Nat. Gas Ind.* **20**(7) (2010)
6. Zhou, S., Li, Z., Wang, F.: Numerical simulation on the foam acidizing diversion in horizontal wells. *J. Spat. Struct.* **33**(3) (2012)
7. Songyan, L., Zhaomin, L., Lin, R.: Mathematical models for foam-diverted acidizing and their applications. *J. Petrol. Sci. Eng.* **5**(2) (2008)
8. Al Ayesh, A.H., Salazar, R., Farajzadeh, R., Vincent-Bonnieu, S., Rossen, W.R.: Foam diversion in heterogeneous reservoirs: effect of permeability and injection method. *Soc. Petrol. Eng.* (2017)
9. Siddiqui, S., Talabani, S., Yang, J., et al.: An experimental investigation of the diversion characteristics of foam in berea sandstone cores of contrasting permeabilities. *J. Petrol. Sci. Eng.* (2003)
10. Li, S., Li, Z., Li, B.: Experimental study of the effect of permeability on foam diversion. *Petrol. Sci. Technol.* (2012)
11. Zhao, X., Rui, Z., Liao, X., Zhang, R.: A simulation method for modified isochronal well testing to determine shale gas well productivity. *J. Nat. Gas Sci. Eng.* **27**, 479–485 (2015)
12. Al-Harthy, S.: Options for high-temperature well stimulation. *Oil Field Rev.* **20**(4), 52–62 (2009)
13. Ikporo, B., Sylvester, O.: Effect of sand invasion on oil well production: a case study of garon field in the Niger Delta. *Int. J. Eng. Sci. (IJES)* **4**(5), 64–72 (2015)
14. Khamehchi, E., Reisi, E.: Sand production prediction using ratio of shear modulus to bulk compressibility (case study). *Egyptian J. Pet.* **24**(2), 113–118 (2015)
15. Li, Z. et al.: Enhancing filter cake removal by engineering parameter optimization for clean development of fossil hydrogen energy: a numerical simulation. *Int. J. Hydrogen Energy* (2021)
16. Khalil, R.E., Mansour, A., Gamadi, T.: An experimental study of acid matrix treatment performance on shale core samples. Paper presented at the SPE Liquids-Rich Basins Conference-North America (2017)
17. Li, N., Dai, J., Liu, P., Luo, Z., Zhao, L.: Experimental study on influencing factors of acid-fracturing effect for carbonate reservoirs. *Petroleum* **1**(2), 146–153 (2015)
18. Chengshou, C., Yaogang, Z., Haomin, J., Qiangjun, W., Fajun, R., Zhi, L., Lei, L.: New stimulation technologies on horizontal wells in Jingbian gas fields. *Nat. Gas Ind.* **7**, 020 (2010)
19. Asad, S., Ahmad, I., Dzeti, M., Nurudeen, Y., Muhammad, B.: Influence of lauryl betaine on aqueous solution stability, foamability and foam stability. *J. Petrol. Exploration Prod. Technol.* (2019). <https://doi.org/10.1007/s13202-019-0652-7>
20. Altunina, L., Kuvshinov, V., Kuvshinov, I., Stasyeva, L.: Enhanced oil recovery from high-viscosity oil deposits by chemically evolving systems. In: Conference Proceedings, IOR 2019-20th European Symposium on Improved Oil Recovery, vol. 2019, pp. 1–11. European Association of Geoscientists & Engineers (2019). <https://doi.org/10.3997/2214-4609.201900175>

21. Fuseni, A.B., AlSofi, A.M., AlJulaih, A.H., et al.: Development and evaluation of foam-based conformance control for a high-salinity and high-temperature carbonate. *J. Petrol. Exploration Prod. Technol.* (2018). <https://doi.org/10.1007/s13202-018-0431-x>
22. Alvarez, M., Rivas, H., Navarro, G., et al.: An optional foam quality for diversion in matrix-acidizing projects. In: *SPE International Symposium on Formation Damage Control* held in Lafayette, Louisiana, 23–24, (SPE paper 58711) (2000)
23. Kam, S.I., Frenier, W.W., Davies, S.N., Rassen, W.R.: Experimental study of high-temperature foam for acid diversion. *J. Petrol. Sci. Eng.* **58** (2007)
24. Qi, N., Li, B., Chen, G., Fang, M., Li, X., Liang, C.: Optimum fluid injection rate in carbonate acidizing based on acid dissolution morphology analysis. *Energy Fuels* (2017)
25. Hassani, A., Kamali, M.R.: Optimization of acid injection rate in high rate acidizing to enhance the production rate: an experimental study in Abteymour oil field. Iran. *J. Petrol. Sci. Eng.* **156**, 553–562 (2017)
26. Al-Muhareb, M.A., Nasr-El-Din, H.A., Samuel, E., Marcinew, R.P., Samuel, M.: Acid fracturing of power water injectors: a new field application using polymer-free fluids. In: Paper presented at the SPE European formation damage conference (2003)
27. Zheng, L. et al.: The wellbore instability control mechanism of fuzzy ball drilling fluids for coal bed methane wells via bonding formation. *J. Nat. Gas Sci. Eng.* **56**, 107–120 (2018)
28. Assem, A.I., Nasr-El-Din, H.A., De Wolf, C.A.: Formation damage due to iron precipitation in carbonate rocks. *Soc. Petrol. Eng.* (2013). <https://doi.org/10.2118/165203-MS>
29. Zhang, Y. et al.: The environmental friendliness of fuzzy-ball drilling fluids during their entire life-cycles for fragile ecosystems in coalbed methane well plants. *J. Hazard. Mater.* **364**, 396–405 (2019)

Investigation of Spin Pinned Effect in Ni/NiFe/Ni Trilayers Via Ferromagnetic Resonance Spectroscopy



Yu Liu and Zhongwen Lan

Abstract Recently, increasing the application frequency of devices through spin wave resonance has received widespread attention. Exciting spin waves through the spin pinning effect of the Ni film on the surface of the Ni₈₁Fe₁₉ film is of great significance to increase the application frequency of the device. Herein, the Ni (*t* nm)/Ni₈₁Fe₁₉ (50 nm)/Ni (*t* nm) multilayer films, which were fabricated by magnetron sputtering. And the micromorphology, static magnetic properties, ferromagnetic resonance (FMR) linewidth (ΔH) are discussed in detail. As the Ni film thicknesses increased, the saturation magnetization ($4\pi M_s$) of the trilayers decreased from 7405 to 5805 Gs. When the Ni film thickness was below 10 nm, ΔH showed an upward trend, and the ΔH slightly decreased at 15 nm Ni film thickness. When Ni film thickness was less than 10 nm, the perpendicular standing spin wave (PSSW) mode appeared, which implied a strong pinning effect. With 10 nm and 15 nm Ni film, the PSSW mode disappeared, indicating that the large grain size was not conducive to the pinning effect of the film.

Keywords Microwave devices · Spin wave · Multilayer · Perpendicular standing spin wave

1 Introduction

With the continuous progress and development of communication technology, modern microwave devices are developing in the direction of miniaturization and high frequency [1–4]. However, the ferromagnetic resonance (FMR) frequency of the magnetic material determines the application frequency of the microwave device [5, 6]. Therefore, magnetic materials are required to have a higher ferromagnetic resonance frequency [7–9]. Various efforts have been made in the past

Y. Liu (✉) · Z. Lan

School of Materials and Energy, University of Electronic Science and Technology of China, Chengdu 610054, China

e-mail: liuyui15005510@163.com

© The Author(s), under exclusive license to Springer Nature Switzerland AG 2021

37

L. Zheng et al. (eds.), *Proceedings of MEACM 2020*,

Mechanisms and Machine Science 99,

https://doi.org/10.1007/978-3-030-67958-3_4

few decades to increase/regulate the ferromagnetic resonance frequency of magnetic materials, especially metal multilayer films [10–13]. Chai et al. [14] have prepared the CoFeBSm film by oblique sputtering technique and studied its frequency characteristics. As the oblique angle increased, the easy-axis ferromagnetic resonance frequency increased and the hard axis ferromagnetic resonance frequency decreased. Li et al. [15] have discussed the effect of oblique sputtering on the magnetic properties of the CoFeB film and revealed that the application frequency increased from 2.83 to 9.71 GHz as the oblique angle increased from 10° to 70° . Cao et al. [16] have studied the effect of thickness on the dynamic magnetic performance of FeCo film through VNA-FMR and electron spin resonance spectroscopy. With the increasing FeCo film thickness, the in-plane magnetic anisotropy field increases, which means an increase in the ferromagnetic resonance frequency. Zhou et al. [17] have studied the frequency characteristics of FeNi film with doped ferrite. The resonance frequency increased from 1.3 to 2.3 GHz with the increasing doped ferrite concentration.

In general, scholars have tried different methods to increase the application frequency of devices, but these methods are generally not ideal. Through the pinning effect of the Ni film with low saturation magnetization on the NiFe film, the perpendicular standing spin wave can be successfully excited, which is of great significance for improving the application frequency of the device. The saturation magnetization ($4\pi M_s$), micromorphology, and FMR linewidth (ΔH) of the Ni/NiFe/Ni films are systematic studied. The research showed that the Ni film thickness had a great influence on the $4\pi M_s$, ΔH , and micromorphology. We believed that by regulating the thickness of the Ni film layer is a reliable way to improve the frequency of microwave devices, and have a huge application prospect in high frequency applications.

2 Experimental

Ni (*t*)/Ni₈₁Fe₁₉ (50 nm)/Ni (*t*) multilayer films were deposited on Si (111) substrate by DC magnetic sputtering technique. The Ni₈₁Fe₁₉ film thickness is 50 nm. And the Ni film thickness is 2, 4, 10, 15, 10, and 20 nm, respectively. The Ni film and Ni₈₁Fe₁₉ film were deposited by the same sputtering parameters without temperature treatment. The sputtering power of thin film deposition is 20 W, the pressure is 0.3 Pa.

The micromorphology of the Ni/Ni₈₁Fe₁₉/Ni multilayer was measured by atomic force microscope (Bruker MultiMode8) films with a $2 \times 2 \mu\text{m}$ scan area. The magnetic hysteresis loop of the films were tested by vibrating sample magnetometer (VSM, Lake Shore 8604) with a 100 Oe magnetic field. The ferromagnetic resonance absorption spectroscopy were tested by ground co-planar waveguide, and the microwave frequency is 9 GHz.

3 Results and Discussion

3.1 Micromorphology

Figure 1 shows the atomic force microscope images of Ni/NiFe/Ni multilayer films. It can be seen from the atomic force microscope (AFM) image that the Ni film thickness had a great influence on the grain growth mode. When the Ni film thickness was less than 10 nm, the grain of the films with different thicknesses were smaller and the grain consistency was better. As the Ni film thickness reached 10 nm, the grains tended to grow laterally, and the surface became flatter, but the uniformity of the film grains became worse. It can be seen from the microscope image that, the grain size of the Ni/NiFe/Ni multilayer film decreased first and then increased with the increasing of the Ni film thickness, and reached the minimum value at 8 nm (Fig. 2).

With the increasing Ni film thickness, the surface roughness of the film increased first and then decreased. The surface roughness of samples with different Ni film thickness was 5.14 nm, 6.11 nm, 6.22 nm, 5.85 nm, 4.46 nm and 4.19 nm, respectively. The surface roughness of all films was greater than 4 nm, indicating that the quality of the films induced by Ni film was not good. When the film reaches 8 nm, the height fluctuation of the film grains reduces, which also caused a substantial decrease in roughness. As the Ni film thickness increased, the average grain size decreased first and then raised. The minimum value at the Ni film thickness of 8 nm was 82 nm.

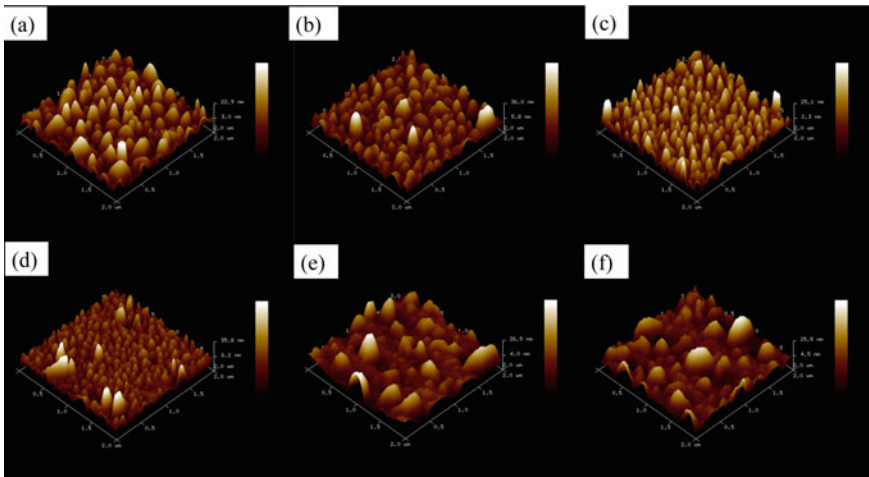
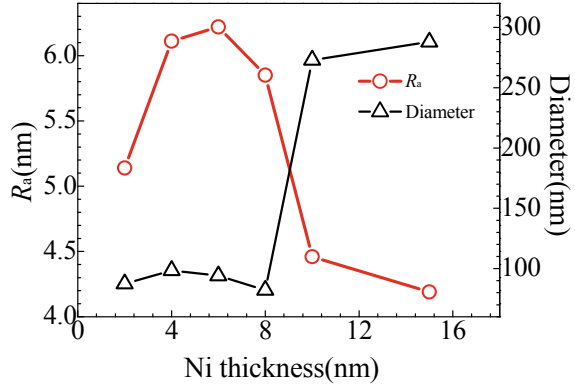


Fig. 1 The micromorphology of Ni/NiFe/Ni films with the thicknesses of Ni from 2 to 20 nm, **a** 2 nm; **b** 4 nm; **c** 6 nm; **d** 8 nm; **e** 10 nm; **f** 15 nm

Fig. 2 The surface roughness (R_a) and average grain size (D) of the Ni/NiFe/Ni trilayers



3.2 Static Magnetic Properties

Figure 3 shows the in-plane magnetic hysteresis loops of Ni/NiFe/Ni multilayer films. All films showed good soft magnetic properties, and the Ni film thickness had a huge impact on the $4\pi M_s$ and coercivity (H_c). The in-plane coercivity showed an upward trend and then a downward trend. The experimental and theoretical (calculated by the ratio of the Ni film thickness to the NiFe film thickness) saturation magnetization are shown in Fig. 4a. Both the experimental and theoretical saturation magnetization decreased as the Ni film thickness increased. Because the $4\pi M_s$ of Ni at room temperature is 6 kGs, which is smaller than the $4\pi M_s$ of NiFe film. The $4\pi M_s$ obtained by vibrating the sample magnetometer decreased from 7405 to 5805 Gs linearly. The change in saturation magnetization of the sample was mainly caused by the increased Ni film thickness. As we can see from Fig. 4 that the saturation magnetization measured by the experiment was much lower than the theoretical value, indicated that the overall quality of the multilayer film induced by the Ni film is not good. However, when the Ni film thickness is thicker than 6 nm, the decreasing trend of the saturation magnetization of the sample had slowed down, indicating that the film quality of the sample induced by the thick film has improved. The H_c first increased from 3.4 to 58.1 Oe, and then decreased to 22.6 Oe when Ni film thickness was 15 nm. It can be considered that the increase in coercivity was caused by the change in interface roughness. We believed that the increasing of the coercivity was caused by the enhancement of pinning strength, because previous studies have shown that films with good consistency and small grains are more conducive to film pinning. From the atomic force microscope photos of the thin film, it can be seen that when the thin film sample was less than or equal to 8 nm, the surface grains develop in the direction of more uniform distribution and finer grains. As the Ni film thickness was greater than 8 nm, the film was in a state of lateral growth, and the crystal grain size increased sharply, resulting in a sharp increase in coercivity.

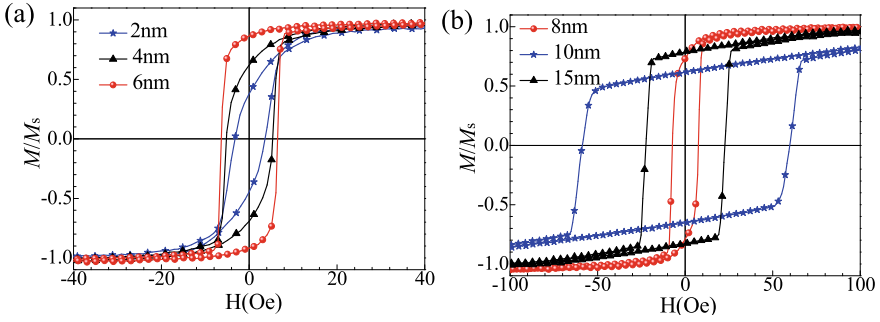


Fig. 3 The in-plane magnetic hysteresis loops of the Ni/NiFe/Ni films with different Ni film thicknesses, **a** 2, 4, and 6 nm; **b** 8, 10, and 15 nm

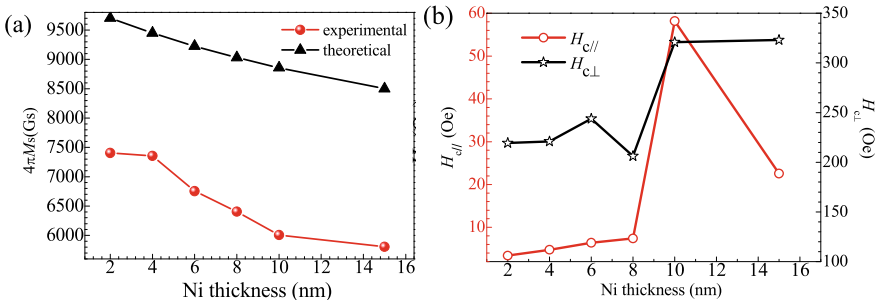


Fig. 4 **a** The $4\pi M_s$ of the Ni/NiFe/Ni trilayers; **b** the in-plane coercivity

3.3 Microwave Properties

The microwave absorption spectrums of Ni/NiFe/Ni films with different Ni thicknesses are shown in Fig. 5. It can be seen from Fig. 5, the FMR mode and PSSW mode coexisted when the Ni film is below 10 nm. There is only a high-field FMR mode with 10 nm and 15 nm Ni film. The magnetic moment of the magnetic material will precess under the combined effect of the microwave field and the DC magnetic field. For uniform magnetic materials, all magnetic moments precess uniformly. However, in some magnetic materials, the uniform precession of the magnetic moment can be converted into spin waves by the scattering caused by defects, and energy can be transferred to the crystal lattice, thereby causing the crystal lattice to vibrate. In the Ni/NiFe/Ni multilayer film, there is unevenness between the Ni and NiFe film interface, this led to the magnetic moment was pinned and the magnetic moment cannot precess. Therefore, the spin wave formed at Ni and NiFe film interface can only propagate into the material, thereby forming a PSSW mode. As the thickness of the Ni film reached 10 and 15 nm, the grains are in a state of lateral growth, and the grain size increases sharply. The large grain size

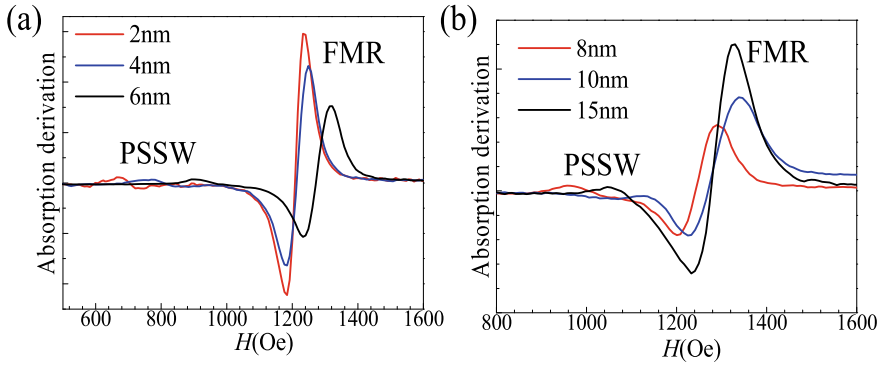


Fig. 5 a, b The microwave absorption spectra of Ni/NiFe/Ni films with different Ni thicknesses

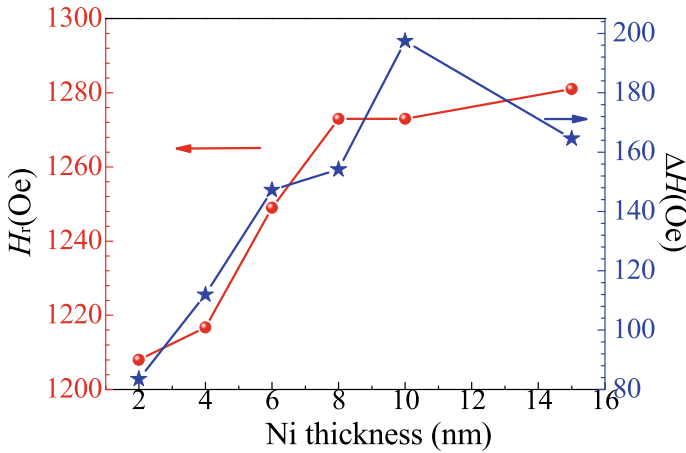


Fig. 6 The FMR linewidth (ΔH) and FMR field (H_r) of Ni/NiFe/Ni films with different Ni film thicknesses

is not conducive to the pinning effect on the film surface, and the pinning effect was weakened and cannot be limited the precession of the magnetic moment, so there is only a uniform ferromagnetic resonance mode.

The FMR linewidth (ΔH) and H_r of the Ni/NiFe/Ni multilayer films are shown in Fig. 6. The H_r and $4\pi M_s$ showed completely opposite trends. Known from Eq. (1), with a fixed microwave frequency, the H_r was always inversely proportional to the $4\pi M_s$. The linewidth of ferromagnetic resonance is calculated according to the peak-to-peak linewidth (ΔH_{pp}) from Fig. 5, and the relationship between ΔH_{pp} and the linewidth of ferromagnetic resonance can be seen from Eq. (2).

$$f_{FMR} = \frac{\gamma}{2\pi} \sqrt{(H_r + H_k)(H_r + H_k + 4\pi M_s)} \quad (1)$$

$$\Delta H = \sqrt{3} \Delta H_{pp} \quad (2)$$

With the increasing of Ni film thickness, the ΔH showed a trend of first increasing and then decreasing. The FMR linewidth increased from 83 to 197 Oe first and then dropped to 164 Oe. The FMR linewidth increased sharply when the Ni film thickness was less than 10 nm. We know that for the spin wave, the uneven magnetization may provide a scattering center, thereby exciting the magnon with non-zero wave vector (k). In a thicker film, long-distance spin waves may be caused due to the presence of a magnetization component perpendicular to the surface of the film. So, the increased ferromagnetic resonance linewidth may be caused by the enhanced coupling of magnons from $k = 0$ to $k \neq 0$. When the Ni film thickness was 15 nm, it had the lowest surface roughness compared to other samples, which can indicate that the quality of the film has improved, so the ferromagnetic resonance linewidth has decreased accordingly.

4 Conclusions

In this paper, the Ni/Ni₈₁Fe₁₉/Ni films with different Ni film thicknesses were fabricated by magnetron sputtering. With the increasing of Ni film thickness, the grain growth mode transition from vertical mode to horizontal mode and the $4\pi M_s$ decreased from 7405 to 5805 Gs. When the Ni film thickness increased from 2 to 10 nm, the ferromagnetic resonance (FMR) linewidth (ΔH) increased from 83 to 197 Oe. And the FMR linewidth drop to 164 Oe with 15 nm Ni film thickness. When the Ni film thickness was below 10 nm, the perpendicular standing spin wave appeared, which implied a strong pinning effect. With 10 and 15 nm Ni film thickness, the PSSW mode disappeared, indicating that the large grain size was not conducive to the pinning effect of the film.

References

1. Paiva, D.V.M., Silva, M.A.S., Sombra, A.S.B., Fechine, P.B.A.: Properties of the Sr₃MoO₆ electroceramic for RF/microwave devices. *J. Alloy. Compd.* **748**, 766–773 (2018)
2. Lu, Q., Yu, B., Hu, Z., He, Y., Hu, T., Zhao, Y., Wang, Z., Zhou, Z., Cui, W., Liu, M.: Surface roughness evolution induced low secondary electron yield in carbon coated Ag/Al substrates for space microwave devices. *Appl. Surf. Sci.* **501**, 144236 (2020)
3. Sharma, V., Khivintsev, Y., Harward, I., Kuanr, B.K., Celinski, Z.: Fabrication and characterization of microwave phase shifter in microstrip geometry with Fe film as the frequency tuning element. *J. Magn. Mater.* **489**, 165412 (2019)

4. Belyaev, B.A., Lemberg, K.V., Serzhantov, A.M., Leksikov, A.A., Bal'va, Y.F., Leksikov, A. A.: Magnetically tunable resonant phase shifters for UHF band. *IEEE Trans. Magn.* **51**(6), 1–5 (2014)
5. Kuanr, B.K., Veerakumar, V., Camley, R.E., Celinski, Z.: Permalloy (NiFe) nanometer square-antidot arrays: dynamic modes and use as a monolithic microwave band-pass filter. *J. Magn. Magn. Mater.* **484**, 272–278 (2019)
6. Su, Z., Bennett, S., Hu, B., Chen, Y., Harris, V.G.: Magnetic and microwave properties of U-type hexaferrite films with high remanence and low ferromagnetic resonance linewidth. *J. Appl. Phys.* **115**(17), 17A504 (2014)
7. Kobelev, A.V., Shvachko, Y.N., Ustinov, V.V.: Angular dependence of the FMR linewidth and the anisotropy of the relaxation time in iron garnets. *Phys. Met. Metall.* **117**(1), 9–15 (2016)
8. Shagaev, V.V., Lin, T.T.: Ferrite films with enhanced stability of ferromagnetic resonance frequency. *Tech. Phys.* **62**(3), 401–405 (2017)
9. Rahman, B.F., Divan, R., Rosenmann, D., Wang, T., Peng, Y., Wang, G.: Application of sub-micrometer patterned permalloy thin film in tunable radio frequency inductors. *J. Appl. Phys.* **117**(17), 17C121 (2015)
10. Anthony, R., Hegarty, M., O'Brien, J., Rohan, J.F., Mathúna, C.Ó.: Enhanced in-plane anisotropy and ferromagnetic resonance frequency in permalloy films laminated with nitrogen-doped tantalum. *IEEE Magn. Lett.* **8**, 1–4 (2016)
11. Chen, Y., Fan, X., Zhou, Y., Xie, Y., Wu, J., Wang, T., Xiao, J.Q.: Designing and tuning magnetic resonance with exchange interaction. *Adv. Mater.* **27**(8), 1351–1355 (2015)
12. Hu, S., Kiseki, K., Yakata, S., Kimura, T.: Ferromagnetic resonance in exchange-coupled NiFe/FeMn films and its control. *IEEE Trans. Magn.* **48**(11), 2889–2891 (2012)
13. Liu, Y., Sun, K., Yang, Y., Yu, Z., Zeng, Y., Chai, Z., Lan, Z.: Exchange bias effect and ferromagnetic resonance study of NiO/NiFe/NiO Trilayers with different thicknesses of NiO layers. *J. Supercond. Novel Magn.* **30**(3), 593–596 (2017)
14. Chai, G., Phuoc, N.N., Ong, C.K.: Angular tunable zero-field ferromagnetic resonance frequency in oblique sputtered CoFeBSm thin films. *Appl. Phys. Express* **7**(6), 063001 (2014)
15. Li, C., Chai, G., Yang, C., Wang, W., Xue, D.: Tunable zero-field ferromagnetic resonance frequency from S to X band in oblique deposited CoFeB thin films. *Sci. Rep.* **5**(1), 1–7 (2015)
16. Cao, D., Zhu, Z., Feng, H., Pan, L., Cheng, X., Wang, Z., Liu, Q.: Applied magnetic field angle dependence of the static and dynamic magnetic properties in FeCo films during the deposition. *J. Magn. Magn. Mater.* **416**, 208–212 (2016)
17. Zhou, C., Wang, F., Wei, W., Wang, G., Jiang, C., Xue, D.: Stripe domain and enhanced resonance frequency in ferrite doped FeNi films. *J. Phys. D Appl. Phys.* **46**(42), 425002 (2013)

Residual Stress Evaluation of Metallic Component Based on the Synthetic Nonlinear Coefficient



Yuhua Zhang , Silong Quan , and Guoquan Liu

Abstract Because the effective evaluation the residual stress of metallic specimen has very significance components, the critical refracted longitudinal wave is applied to evaluate the residual stress of metallic specimens in the paper. The nonlinear ultrasonic experiment using the critical refracted longitudinal wave has been constructed on the specimens with different stress level changing from 0 to 400 Mpa increased by 20 MPa, and the nonlinear output signal is capture to calculate the second and third order relative nonlinear coefficient. The experimental results indicate that the relative nonlinear coefficient increases slowly before 200 MPa and fortifies rapidly after 300 MPa, and the increment is about 80%. The synthetic nonlinear coefficient is proposed applying the data fusion theory. Furthermore, the stress prediction model based on the synthetic nonlinear coefficient is constructed which can effectively evaluate the stress state of specimen. Therefore the nonlinear property of LCR wave could be applied to quantitatively and nondestructively evaluate the stress state of specimens.

Keywords Residual stress evaluation · Nonlinear ultrasonic · LCR wave · Synthetic nonlinear coefficient

1 Introduction

The residual stress would critically influence the service performance and structural properties of mechanical components [1, 2]. In addition, the structure of mechanical components and parts are very complex. Thus the effective evaluation the residual stress of mechanical components has always been a difficult and necessary problem [3].

Y. Zhang (✉) · S. Quan · G. Liu
School of Mechanical and Electronic Engineering, East China University of Technology,
Nanchang 330013, China
e-mail: zhangyuhua0422@163.com

The traditional technique for residual stress measure applies the acoustic elasticity theory of ultrasonic [4]. Because the sensitivity of different ultrasonic wave for stress is different and the critical refracted longitudinal wave (LCR) has the highest sensitive to tangential stress, therefore the velocity variation of LCR wave based on the acoustic elasticity method is applied to measure the tangential residual stress [5, 6]. But in the practical application, the variation of ultrasonic velocity caused by stress change is relatively weak [3, 7]. Therefore the accurate measurement of residual stress applying the acoustic elasticity theory would be very hard [8].

According to related studies, the micro structure variation of metallic material in the process of fatigue damage process can distort the ultrasonic and higher harmonics can be produced when the ultrasonic wave spreads in the metallic materials. Recently the nonlinear ultrasonic technique has been widely used to evaluate the earlier fatigue damage, accumulated plastic deformation and so on [8–10].

Applying the nonlinear property of ultrasonic to evaluate the stress state of metallic material has attracted much attention [11–13]. Some studies had reported that the guided or Rayleigh wave can be applied to detect the stress state of specimens, but the detection depth of surface wave is relatively shallow which is only about a wavelength and very useful to the surface stress [3]. However the nonlinear property of LCR wave for stress evaluation has little researched which has the highest sensitivity for tangential stress. Therefore the LCR wave is used to nondestructively detect the stress of specimens.

2 Theoretical Background

2.1 The Detection Theory Using LCR Wave

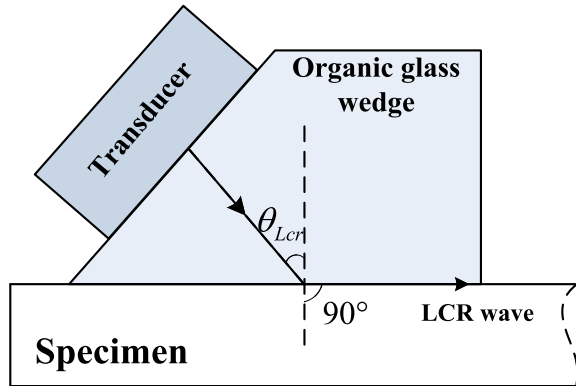
When the wave travels to the interface between two media, there is an incident angle which makes the refraction angle equal to 90° which the corresponding incident angle is the first critical angle. If the wave is from the organic glass wedge to specimen, the first critical angle can be calculated by $\theta_{LCR} = \sin^{-1}(V_1/V_2)$, where V_1 and V_2 represent the velocity of longitudinal wave in organic glass wedge and specimen. In this experiment, according to the operability of incident angle, the first critical angle is set to 30° (Fig. 1).

3 Specimens Preparation and Experimental Setup

3.1 Specimens Preparation

The material used in this research is standard 45 steel which the proportional limit is 200 MPa and the yield limit is 355 MPa. The specimens are fabricated from a

Fig. 1 The generation mechanism of LCR wave



single plate, Fig. 2 displays the dimensions of specimens with a gauge length of 160 mm and the thickness is 8 mm. There are five specimens in this study, specimen p1, p2 and p3 are training samples, while p4 and p5 are test samples.

Because the nonlinear ultrasonic experiment is conducted on specimen with different stress level, the static tensile specimen is carried on the specimen. The tensile test is paused at every 20 MPa without specimens unloaded which ensures specimens with different stress level, 0, 20, 40, 60, 80, 100, 120, 140, 160, 180, 200, 220, 240, 260, 280, 300, 320, 340, 360, 380 and 400 MPa, the nonlinear ultrasonic experiments are performed at each interruption time.

3.2 Nonlinear Ultrasonic Experiment Based on LCR Wave

The experimental arrangement applying LCR wave is displayed in Fig. 3. One longitudinal transducer is acted as the transmitter which the central frequency is 2.25 MHz to produce the ultrasonic, while the other one acts as the receiver which the central frequency is 5 MHz to receive the distorted ultrasonic. According to the generation principle of LCR wave, two longitudinal transducers are fixed on the organic glass wedges with 30 incident angle. It should be noted that the compound

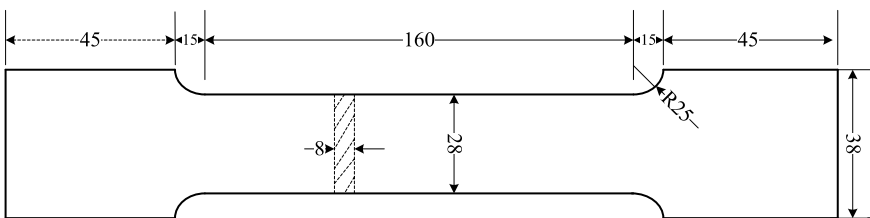


Fig. 2 The geometric configuration of 45 steel specimens

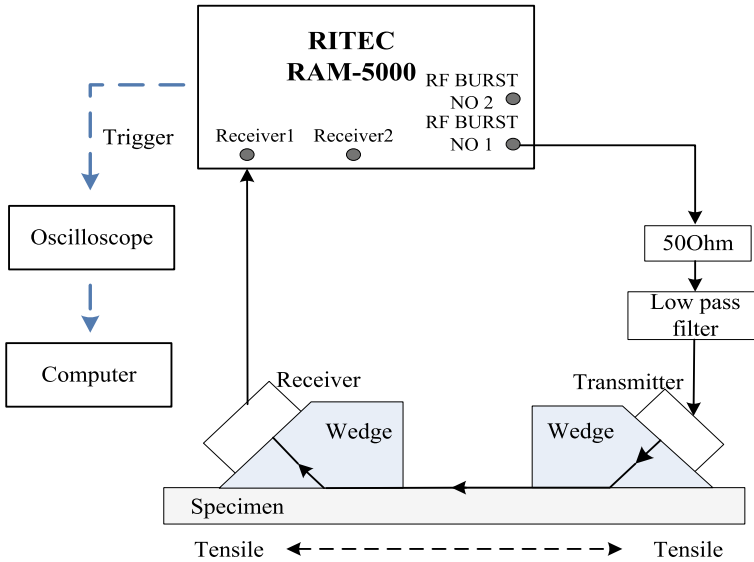


Fig. 3 The experimental arrangement applying LCR wave

lubricant is evenly painted the contact surface among wedge, specimen and transducer.

According to the nonlinear output signal collected by the oscilloscope, the value of fundamental wave, second and third harmonic is confirmed, that is A_1 , A_2 and A_3 . Based on the computational formula, the second and third order relative nonlinear coefficient could be calculated according to $\beta = A_2/A_1^2$ and $\delta = A_3/A_1^3$.

Before the actual experiment, the propagation distance of LCR wave should be firstly chosen because it has a great influence on the measured results. In our experiment the spacing of specimen is 160 mm. If other experimental conditions are the same, the specimen with 200 MPa pre-stress is applied to do the test when the propagation distance varying from 20 to 120 mm. The corresponding results are displayed in Fig. 4.

As seen from Fig. 4, the relative nonlinear coefficient shows the variation tendency of increasing firstly and then decreasing. More specifically, when the propagation distance is below 80 mm, the relative nonlinear coefficient monotonically increases. When the transmission distance is relatively small, the cumulative effect of coactions would become more obvious. The relative nonlinear coefficient reaches a maximum at 80 mm propagation distance and then decreases exceeding 80 mm distance. To achieve the best experimental results, the propagation distance of 80 mm is applied in this experiments.

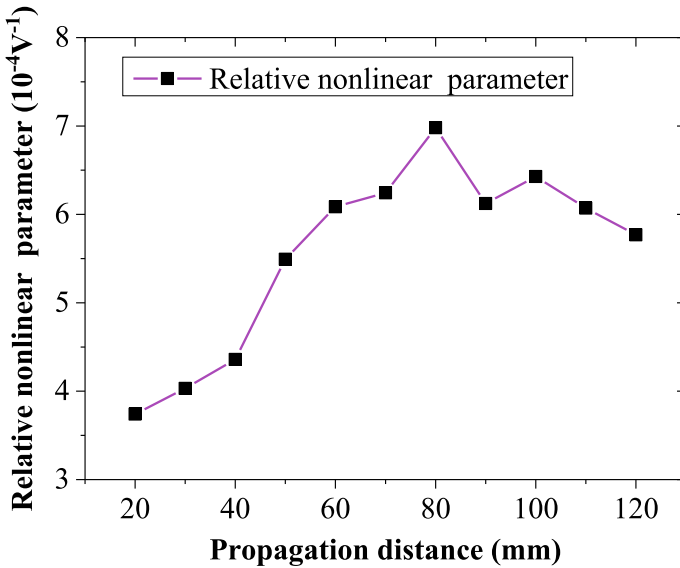


Fig. 4 The relation between the propagation distance and relative nonlinear coefficient

4 Results and Discussion

4.1 The Ultrasonic Nonlinear Coefficient Measure

For three specimens s1, s2 and s3, the related experimental results are displayed in Fig. 5, where the short vertical lines represent the error bar.

As shown in Fig. 5a, the second order relative nonlinear coefficient (β) increases slowly before 200 MPa then adds rapidly after 200 Mpa. When the stress level of specimen changes from 0 to 400 MPa, the increase amplitude of β is about 181, 176, and 189% for three specimens. Through comparison Fig. 5a, b, it can be found that the change tendency of third order relative nonlinear coefficient is very alike to β , the increment of third order relative nonlinear coefficient for three specimens are about the increase amplitude of β is about 173%, 180% and 177% respectively [3].

4.2 Residual Stress Nondestructive Evaluation

According to the analysis the relation between nonlinear coefficient and stress can be used to evaluate the stress of specimen, therefore the relational model can be built based on the experimental results displayed in Fig. 5.

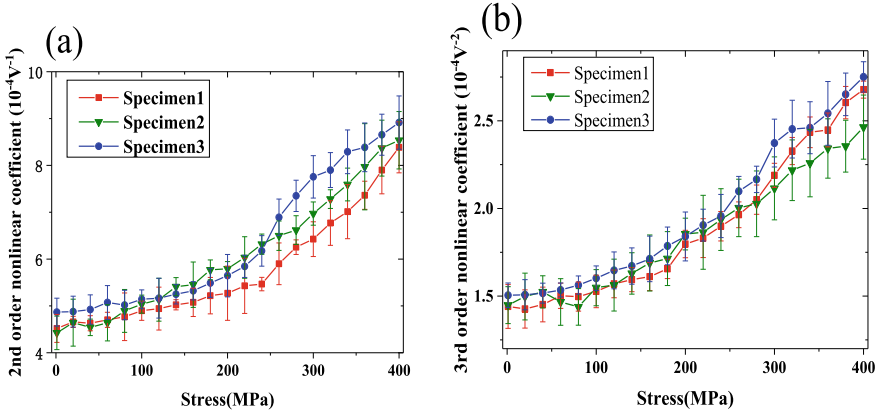


Fig. 5 The experimental results **a** the second and **b** third order nonlinear coefficient

It can be concluded from the experiments, the two nonlinear coefficient can be applied to evaluate the stress. Based on the data fusion theory, the two parameters are combined to form a new comprehensive evaluation parameter.

Based on the increment amplitude of two coefficient, the combined nonlinear parameter α can be put forward,

$$\alpha = \beta^* + \delta^* \quad (1)$$

where β^* and δ^* shows the dimensionless nonlinear β coefficient by $\beta^* = \frac{\beta_i - \beta_0}{\beta_{400} - \beta_0}$ and $\delta^* = \frac{\delta_i - \delta_0}{\delta_{400} - \delta_0}$.

According to the results displayed in Fig. 5, the relation between the stress and combined nonlinear parameter is shown in Fig. 6, where the Y-axis is stress [3]. As shown in Fig. 6, the parameter α adds gently varying before 200 MPa, then it adds quickly after 200 MPa.

The curve fitting method is used to construct the relational model. Due to the fact that the exponential function is the most suitable, thus the relational model can be constructed based on Fig. 6,

$$\sigma = 348.8\alpha^{0.3999} - 59.95 \quad (2)$$

In addition, other two specimens with stress 100, 200 and 300 MPa are applied to do the verification tests. The verification effects are illustrated in Table 1.

As illustrated in Table 1, when the stress state of specimens is 100, 200 and 300 MPa, the detection deviation is 1.33%, 2.88% and 1.26% respectively, which they are all below 4.5%. The stress evaluation results can fully explain the relationship between α and stress is very useful to evaluate the stress degree of specimen.

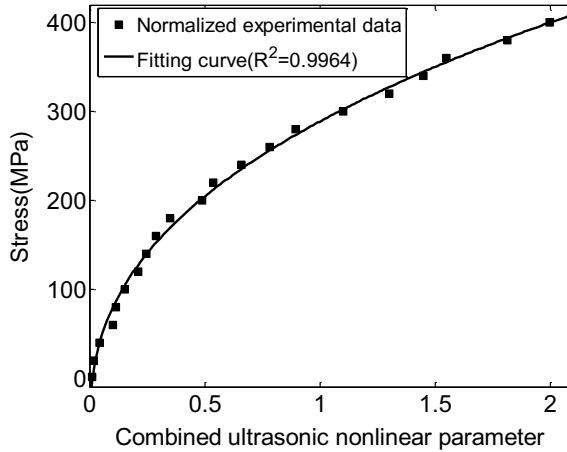


Fig. 6 Relation between α and stress

Table 1 Stress evaluation result

Stress/MPa	Combined parameter	Evaluation result/MPa	Deviation/%
100	6.3	98.67	1.33
200	7.24	205.75	2.88
300	8.45	295.33	1.26

5 Conclusion

In this paper the nonlinear characteristic of LCR wave is applied to evaluate the stress of metallic material. With increasing of stress level, the second and third order relative nonlinear coefficient increases slowly before 200 MPa and fortifies rapidly after 300 MPa, and the increment of them are about 80% according to the relation between stress and relative nonlinear coefficient. The stress prediction model based on the combined parameter can effectively predict the stress state of specimens. Therefore the nonlinear characteristic of LCR wave could be used to quantitatively and nondestructively evaluate the stress state of metallic materials.

Acknowledgements This work was supported by the East China University of Technology Research Foundation for Advanced Talents (Nos. DHBK2019166 and DHBK2019167) and the Foundation of Jiangxi Educational Committee (GJJ170484).

References

1. Huang, X., Liu, Z., Xie, H.: Recent progress in residual stress measurement techniques. *Acta Mechanica Solida Sinica* **26**(6), 570–583 (2013)
2. Rossini, N., Dassisti, M., Benyounis, K., Olabi, A.: Methods of measuring residual stresses in components. *Mater. Des.* **35**, 572–588 (2012)
3. Mao, H., Zhang, Y., Mao, H., Li, X., Huang, Z.: Stress evaluation of metallic material under steady state based on nonlinear critically refracted longitudinal wave. *Results Phys.* **9**, 665–672 (2018)
4. Song, W., Xu, C., Pan, Q., Song, J.: Nondestructive testing and characterization of residual stress field using an ultrasonic method. *Chin. J. Mech. Eng.* **29**(2), 365–371 (2016)
5. Xu, C., Song, J., Song, W., Wang, J., Tian, H.: Ultrasonic nondestructive testing and regulation technology of residual stress. In: 19th World Conference on Non-destructive Testing, pp. 1–9 (2018)
6. Song, W.: Study on technology of ultrasonic nondestructive testing and regulation of residual stress. Beijing Institute of Technology (2016)
7. Bray, D.: Ultrasonic stress measurement and material characterization in pressure vessels, piping, and welds. *J. Pressure Vessel Technol.* **124**(3), 326–335 (2002)
8. Zhang, Y., Li, X., Wang, X., Huang, Z., Mao, H., Mao, H.: Feasibility of residual stress nondestructive estimation using the nonlinear property of critical refraction longitudinal wave. *Adv. Mater. Sci. Eng.* **2017**, 1–11 (2017)
9. Walker, S., Kim, J., Qu, J., Jacobs, L.: Fatigue damage evaluation in A36 steel using nonlinear Rayleigh surface waves. *NDT & E Int.* **48**, 10–15 (2012)
10. Zhang, J., Li, S., Xuan, F., Yang, F.: Effect of plastic deformation on nonlinear ultrasonic response of austenitic stainless steel. *Mater. Sci. Eng. A* **622**, 146–152 (2015)
11. Bartoli, I., Nucera, C., Srivastava, A., Salamone, S., Phillips, R., Scalea, F., Coccia, S., Sikorsky, C.: Nonlinear ultrasonic guided waves for stress monitoring in prestressing tendons for post-tensioned concrete structures. In: European Workshop on Structural Health Monitoring; *Int. Soc. Opt. Photon.* **7292**(1), 729220 (2009)
12. Liu, M., Kim, J., Jacobs, L., Qu, J.: Experimental study of nonlinear Rayleigh wave propagation in shot-peened aluminum plates—feasibility of measuring residual stress. *NDT & E Int.* **44**(1), 67–74 (2011)
13. Kim, G., Park, S., Kwak, H.: Application of nonlinear ultrasonic method for monitoring of stress state in concrete. *J. Korean Soc. Nondestr. Test.* **36**(2), 121–129 (2016)

Molding Process of Automotive Hemp Fiber Reinforced Composites



Z. H. Zhu and H. W. Wu

Abstract Lightweight design plays a positive role in the sustainable and coordinated development of automobile industry. The molding process is a widely used molding technology for fiber reinforced composites, which has the advantages of low cost, high efficiency and good size guarantee. The process of molding process is classified and introduced in the paper according to the different premix state of natural fiber and resin.

Keywords Molding process · Automotive · Hemp fiber · Composites

1 Introduction

Nowadays, the automobile has become one of the irreplaceable means of transportation. Traditional cars are generally made of steel, which is heavy in weight and low in fuel efficiency, which is not conducive to energy conservation and environmental protection. To reduce vehicle weight and improve fuel efficiency, an effective way is to use vehicle composite materials. [1].

Natural plant fiber is one of the raw materials which can be used in automotive composites, and it has maintained a growth rate of 10–15% in the automotive industry. The density of natural fiber is relatively low, generally around 1.5 g/cm^3 , which has the potential to save material and energy consumption. From the comparison of average values, the energy consumption of natural fiber reinforced composite is about 60% lower than that of glass fiber reinforced composite.

Z. H. Zhu (✉)

School of Advanced Manufacturing Technology, Guangdong Mechanical and Electrical Polytechnic, Guangzhou, China
e-mail: 184823174@qq.com

H. W. Wu

The Key Laboratory of Polymer Processing Engineering, Ministry of Education, South China University of Technology, Guangzhou, China

Compared with synthetic fiber, Natural fiber is a kind of green material, which has attracted more and more attention. Natural fiber is green and sustainable, low-cost, lighter weight which has adequate supply of raw materials. Therefore, the application of natural fiber reinforced composites in the automotive lightweight field is more and more extensive.

The commonly used natural plant fibers mainly include hemp fiber, grass stem fiber, wood fiber, etc., among which hemp fiber has higher tensile strength and modulus. In addition, hemp fiber has the longest length among the natural fibers, and it also has the characteristics of high moisture absorption ratio modulus, good air permeability and good sound insulation performance. Therefore, hemp fiber has a wider application range than other natural fibers in the development of natural fiber vehicle composites [2].

With the development of mining and textile technology, hemp fiber can replace synthetic chemical fiber in many application scenarios and be used as reinforced fiber in automotive composite parts.

Compared with synthetic fiber reinforced composites, hemp fiber reinforced composites have the following excellent properties. Firstly, hemp fiber reinforced composites have good static mechanical and sound insulation properties, which is also green and harmless [3].

Secondly, hemp fiber is available in large quantities and at low prices. The composites is easy to be processed and formed, and the pressure requirement in the forming process is low, which can reduce the energy consumption and save the production cost.

Thirdly, the toxic and harmful particles and volatile gases will not be emitted during the manufacturing process of hemp fiber reinforced composites. To a certain extent, the application of synthetic fiber can be reduced and non-renewable energy can be saved.

At present, hemp fiber enhanced composites have been widely used as automotive interior components, such as door and door noise absorbers, bushing, etc., as well as supporting frame and instrument panel absorbers for roof seats of large vehicles [4].

2 Molding Process of Hemp Fiber Reinforced Composites

Molding process is a process in which the prepreg is put into the mold cavity of the metal mold. Then the flow prepreg filled the mold cavity under the heat softening pressure and solidified in the mold cavity by using the certain temperature and pressure generated by the hot press. The dimensional precision of the moulded products is high and the internal quality is easy to be guaranteed. In addition, the efficiency of molding production is high and the product appearance is clean and high, especially for the complex structure of the composite material components which can generally be formed once without loss of material performance. Therefore, the molding process is widely used in the manufacture of complex composite components.

The molding process is as follows. A fixed amount of mixture prepreg or billet were put into the metal mold and heated through upper and lower moulds with heating tubes under certain pressure [5]. After a certain period of cooling and stripping, the final product is obtained as shown in Fig. 1.

Compared with the injection molding process, the molding process can better overcome the weakness of the reinforcement fiber in the molding process. Moreover, the molding process only needs to place prepreg on the mold for forming. The alignment direction of the reinforcing fiber is maintained consistent and fixed during the molding process. Therefore, the situation that prepreg cannot fully fill the mold during the molding process will be greatly reduced.

Compared with the injection process, the die structure and size used in the molding process are relatively regular and simple and there is no need to set up a separate feeding device. Therefore, this process has the advantages of low cost, low forming pressure and high production efficiency, and it is easier to realize programmed and self-actuated production.

For auto parts, the area of some components is larger than other parts, and the size is required to ensure, and thus the molding process has a special advantage. In addition, the surface of the molded products is clean which needn't to be processed again and thus the molding process can produce auto parts in one time, which can reduce the production cost effectively.

Before molding, it is necessary to mix the natural fiber and matrix resin uniformly in proportion as required. According to the premixed state of the natural fiber and resin, the molding can be divided into simple premixed molding, laminated molding, fiber mesh molding, etc.

2.1 Simple Premixed Molding

Simple premix molding is mixing natural fiber and resin through a simple premix process and mold forming. This process is easy to operate and has high molding efficiency.

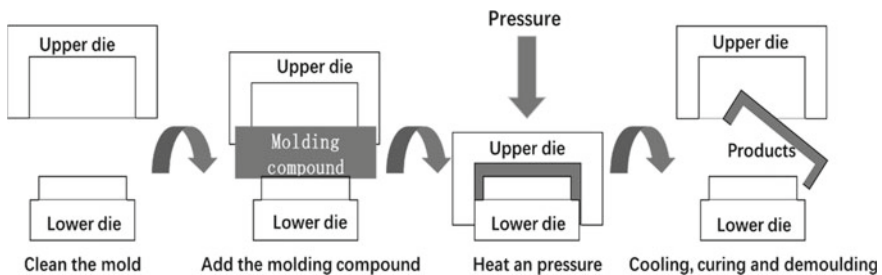


Fig. 1 Schematic diagram of molding process

Mao et al. [6] prepared PLA/bamboo fiber composites by mixing PLA and bamboo fiber, and then paving the mold and pressing it. Cui et al. [7] studied the molding process of flax fiber/polypropylene composite, and discussed the effect of the mixing ratio, forming temperature and time on the final mechanical properties of the composite.

2.2 Lamination

Lamination refers to the compounding of a film or sheet resin with natural fibers through adjusting the specification of the resin and the reinforcement and the lamination structure to prepare the different performance composite material.

Rubio-lopez studied the effects of relevant parameters for the preparation of composites by mold pressing, including heating temperature, pressure, fiber laying-number, fibers and matrix types on the static mechanical properties of biodegradable ecological composites. Research shows that it is the best process parameter when the mold pressure temperature is 185 °C and it has little influence on the tensile strength of the composite when the mold pressure is between 8 and 32 MPa [8].

Song prepared glass fiber reinforced polypropylene composites by molding process. The phase transition parameters were analyzed by differential scanning calorimetry (DSC) and the phase transition parameters were then determined. ANSYS finite element analysis was used to study the temperature field changes in the molding process [9]. The influence of preparation technology on the mechanical properties of glass fiber reinforced polypropylene composite laminates was also discussed and analyzed.

2.3 Fiber Mesh Molding

Fiber mesh molding is the felt forming process before the thermal compression molding of matrix resin fiber and natural fiber by nonwoven technology. The resin fiber and the natural fiber are mixed in different proportions to prepare mesh. After the mesh is laid by combing and loosening, it is directly molded or punched into felt and then hot-pressed according to the performance requirements.

Chen et al. [10] prepared the jute mats/PP film by laminating and molding process to obtain interior decoration materials. At the same time, orthogonal combination design and single factor method were used to optimize the molding process parameters, and the order of the influence of process parameters on the tensile strength of composite materials was obtained.

Ma [11] prepared bamboo fiber/PP fiber felt by mixing, combing the mixture of the bamboo fiber and the polypropylene fiber into a net and needling which was then hot-pressed into bamboo fiber reinforced PP composites. The hot pressing

process parameters suitable for composites and automotive interior materials were also optimized. In addition, it was found that the some surface of the hot-pressed natural bamboo fiber reinforced composites had the problem of coarse fiber warping, which caused a certain degree of influence on the addition of the later decorative layer.

2.4 Other Molding Processes

In addition to the above methods, the researchers also used a variety of joint processes for the compression molding of hemp fiber reinforced composites.

Yuan et al. [12] coated PP filament on the surface of flax to form PP/linen wrapped yarn which were then woven into three typical 2.5 dimensional woven fabrics. Then, the three woven fabrics were hot-pressed into 2.5 dimensional woven composites and the effects of different fabric structures on the tensile properties of composites were studied.

Other researchers use the method of dissolving and blending to prepare the preformed part first, and then put the preformed part into the mold for molding.

Zhang [13] prepared the pre-formed part by dissolving blending processing method firstly which was then hot-pressed into jute fiber composites by hot pressing process. The mechanical properties of the composites prepared by different jute fiber lengths and contents were studied, and the optimum hot-pressing conditions were optimized by orthogonal experiment.

3 Conclusions

Molding is a widely used molding process of composites, and the quality assurance of composite molded products is the result of inspection of process design and molding methods which reflects the synthesis of composite material manufacturing technology. The control of every step in molding process is the key to ensure qualified products.

From the above studies, it can be found that the main factors affecting the molding quality of the moulded products are prepreg properties (including resin content, fiber volume content and other technical indicators), mold precision environmental conditions (including temperature relative humidity and environmental cleanliness, etc.), lay out process control, laying quality, working state of the hot press, clamping gap control, curing process control, et al.

Nowadays, the technology development of composite moulded products is fast, the pursuit of high quality, high efficiency and low cost to complete the molding of composites and to ensure the stability of the technological state of composite components stable performance and reliability requirements is the most important research on the molding of composites.

References

1. Changchun, L.: Technical progress of natural fiber reinforced composites at home and abroad. *China Textile Leader* **03**, 80–82 (2011)
2. Zhang, Z., Ren, Z., Ye, H.: Development and prospect of hemp fiber in automobile industry. *Guangdong Agri. Sci.* **37**, 250–252 (2010)
3. Al-Oqla, F.M., Sapuan, S.M.: Natural fiber reinforced polymer composites in industrial applications: feasibility of date palm fibers for sustainable automotive industry. *J. Clean. Prod.* **66**, 347–354 (2014)
4. Danuta, M., Mateusz, B., Hubert, P.: Influence of the compression molding temperature on the mechanical properties of the basalt-reinforced PLA composites. *Rom. J. Mater.* **48**, 108–114 (2018)
5. Fatma, G.B.S., Osman, O.: The effect of compression molding parameters on the electrical and physical properties of polymer composite bipolar plates. *Int. J. Hydrogen Energy* **42**, 23054–23069 (2017)
6. Mao, H., Zhou, H., Sheng, K.: Effect of hot molding process parameters on tensile strength of POLYlactic acid/bamboo fiber composites [J]. *J. Mater. Sci. Eng.* **30**(4), 586–590 (2012)
7. Cui, P., Chu, X., Ai, H., et al.: Research on the forming technology and mechanical properties of polypropylene/flax fiber composites. *Eng. Plast. Appl.* **38**, 43–46 (2018)
8. Rubio-Lopez, A., Olmedo, A., Diaz-Alvarez, A., et al.: Manufacture of compression molded PLA based biocomposites: A parametric study. *Compos. Struct.* **131**, 995–1000 (2015)
9. Song, Q., Xiao, J., Wen, L., et al.: Effect of molding process on mechanical properties of glass fiber reinforced polypropylene composite laminates. *J. Compos. Mater.* **33**, 2740–2748 (2016)
10. Chen, C., Yongling, YU., Lihua, LU., et al.: Jute felt/PP film composite automobile interior decoration material preparation and process optimization. *J. Dalian Univ. Technol.* **30**, 303–305 (2011)
11. Ma, W.: Preparation and properties of thermoplastic natural bamboo fiber composites [D]. Zhejiang A&F University, Hangzhou (2012)
12. Yuan, S., Cao, H., Qian, K.: Preparation and tensile properties of 2.5 dimensional woven composite materials for automotive interior decoration [J]. *Glass Fiber Reinf. Plast./Compos.* **2013**(1), 120–124 (2013)
13. Zhang, R.: Study on properties of jute fiber PLA composite [D]. Qingdao University, Qingdao (2011)

Trajectory Control of Mobile Robot Based on Novel Gesture Detection



Shubo Liu, Guoquan Liu, Shun'an Cao, Liyu Cheng, and Hang Zou

Abstract In order to achieve accurate gesture control, a gesture detection module is designed based on the infrared obstacle avoidance module array, and the robot gesture trajectory control is studied. AT89S52 single chip microcomputer is used as the upper computer to complete the collection and recognition of gesture motion through gesture detection module, which sends the processed moving target vector of the robot to the lower computer MCU STC89C52 through HC-12 wireless module, and then the operation of the mobile robot is controlled by L298N. The experimental results show that the system has high gesture recognition rate, and the mobile robot can run stably under the given trajectory of gesture, which verifies the practicability of the gesture detection module design and the effectiveness of the control system.

Keywords Trajectory control · Gesture recognition · Sensor grid array · Mobile robot

With the development of modern technology, advanced human computer interaction control methods have become the research hotspots in various industries, such as voice, mind and gesture control. Among them, gesture including rich information and meaning is one of the commonly used interaction methods in daily life, which plays an important role in robot intelligent control. At present, gesture recognition can be realized by real-time hand position monitor device [1, 2] and computer vision technology based on camera [3–5]. In general, the realization of gesture recognition requires a certain amount of hardware equipment investment, whose realization is relatively complex.

The grid method of unlocking mobile phone is deeply loved by the people, which provides a new idea for the realization of robot gesture control by recognizing the running track of gestures and entering passwords through the screen of

S. Liu (✉) · G. Liu · S. Cao · L. Cheng · H. Zou
School of Mechanical and Electronic Engineering, East China University of Technology,
Nanchang Guanglan Avenue 418, Nanchang, China
e-mail: sbliu@ecut.edu.cn

the mobile phone. Thus, this paper makes a bold attempt to the new gesture detection approach, and proposes an infrared palace grid array detection module by using the infrared obstacle avoidance module as a grid point. Moreover, the mobile robot gesture trajectory control system is designed, whose practicability and effectiveness are verified through various gesture trajectory control experiments.

1 Overall Scheme Design of the System

1.1 Design of Gesture Detection Module

The infrared obstacle avoidance module can detect gesture movement within a distance of 2 ~ 30 cm, and its circuit diagram is shown in Fig. 1. The module has three pins, in which VCC is connected to 3.3–5 V power, GND pin is grounded, and DO pin is the digital output. The module has a pair of infrared emitting and receiving tubes. After the infrared rays emitted encounter obstacles, they are reflected and received.

The n -dimensional gesture detection module shown in Fig. 2 is composed of n^2 infrared obstacle avoidance module with spacing a . The row and column numbers of the array are both n that can be selected by designer. The gesture detection module has power pin VCCT, ground pin GNDT and digital output pins DO1–DOM which are connected to VCC, GND and DO in all infrared obstacle avoidance modules.

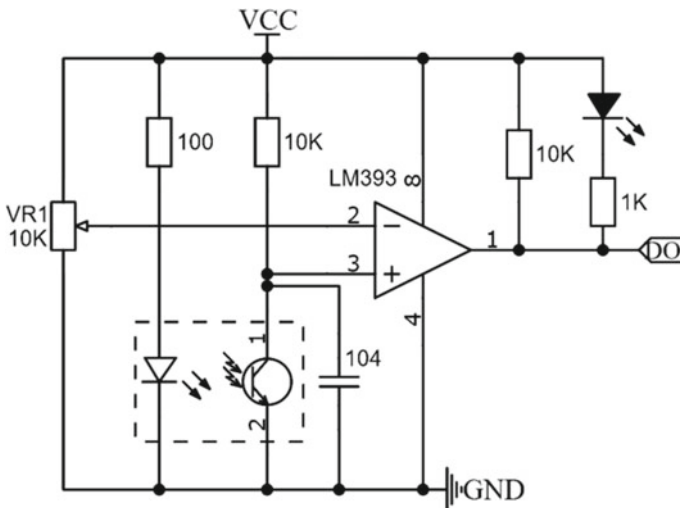
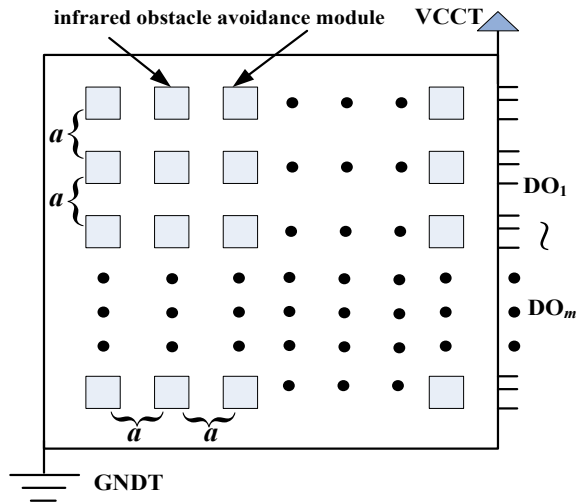


Fig. 1 Circuit diagram of infrared obstacle avoidance module

Fig. 2 Schematic diagram of the gesture detection module



1.2 Control System Structure

The overall hardware system in Fig. 3 consists of power supply module, gesture detection module, host computer controller, lower computer controller, wireless transmission, wireless reception module, mobile robot body and motor drive module. MCU AT89S52 is selected as host computer controller to collect the output of gesture detection module which is sent to MCU STC89C52 and motor drive module through wireless module HC12. Finally, the mobile robot can move according to the gesture trajectory control instruction.

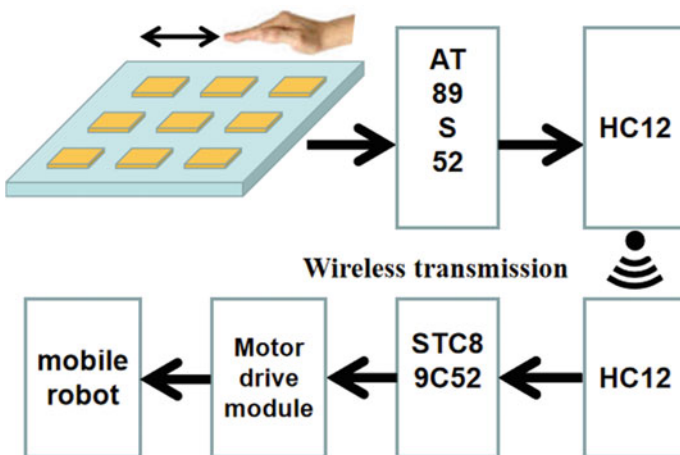


Fig. 3 Control system structure diagram

2 Hardware Circuit Design

2.1 Gesture Acquisition Circuit Design

The gesture detection module and MCU AT89S52 are powered by +5 V, and the digital output pins DO1 ~ DO9 (taking 9 square grid as example) are connected to P1.0 ~ P1.7 and P3.2 of AT89S52, respectively. If the grid point number is relatively more than that of MCU, the MCU interface should be expanded to meet the need of acquisition. The gesture detection circuit is shown in Fig. 4a.

2.2 Wireless Transmission Circuit Design

After collecting and processing the obtained gesture information, MCU AT89S52 can communicate with lower computer controller STC89C52 through HC12 to complete the motor drive of the mobile robot. The wireless transmission circuit is shown in Fig. 4b.

2.3 Motor Drive Circuit Design

The motor drive circuit is composed of STC89C52, L298N and DC motor [6]. The motor rotation is controlled through the P2.4 ~ P2.7 pins of STC89C52, among which the P2.7 and P2.6 pins control motor A, pins of P2.5 and P2.4 control motor B, and PWM output is changed by changing the pins. The duty cycle variations of

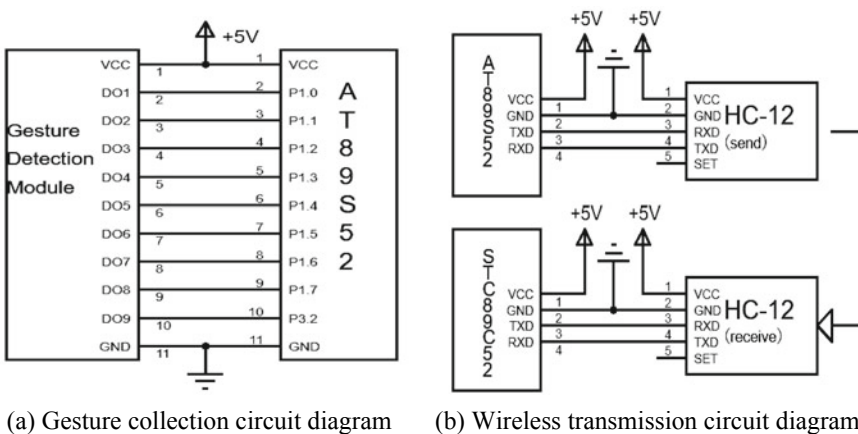


Fig. 4 System circuit diagram

L298N PWM output pins changes the forward and reverse rotation of the motors to realize the forward, steering and backward movement of the mobile robot.

3 Research on Gesture Control Strategy

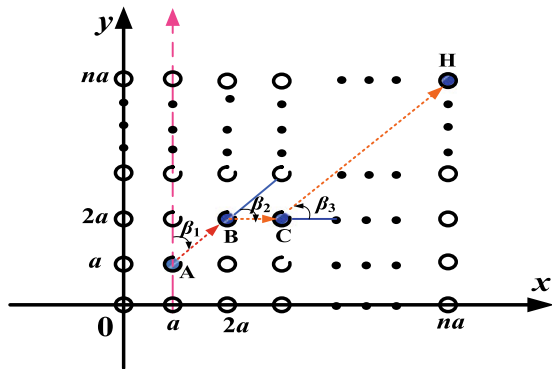
Gesture detection module starts to work when the system is powered on. If the human hand is not located in the effective detection area, the corresponding detection module pin outputs high level. Selecting the position of the infrared obstacle avoidance module at the lower-left corner as the coordinate origin (0,0), the coordinate system of the gesture controller is established as shown in Fig. 5, where each infrared module palace point is represented by a circle. The outputs of the detection module are recorded by AT89S52 in an n -dimensional matrix $L(k)$, where k is the number of gesture triggers, and the element $l_{ij} \in \{0, 1\}$ represents the output of the infrared module in row i and column j . The occlusion state of the gesture remote controller by human hand can be obtained by detecting element 0 in the matrix.

3.1 Control Problem Description

Taking the center of gravity of the robot as the origin of coordinate, and the forward direction of the mobile robot as the positive direction of y-axis, the robot coordinate system is established by selecting the forward direction of the mobile robot as the positive direction of the y-axis, in which the real-time coordinate of the robot is calculated based on the center of gravity. In fact, the robot coordinate system can continuously change as the robot moves.

Let the first triggering position of the gesture detection module be the starting point of the movement, and then multiple palace grid points will be triggered to

Fig. 5 Gesture detection module coordinate system



make the mobile robot car move according to the direction of the gesture swing. Therefore, how to calculate the target vector of the car in the motion coordinate system is an important problem to be solved in following sections.

3.2 Research on Control Algorithm

For ease of analysis, it is assumed that the gesture trajectory in Fig. 5 starts from point A(a, a), passes through intermediate points such as B(2a, 2a), C(3a, 2a), and finally reaches H(na, na) in sequence, and the robot needs to adjust the angles of $\beta_1, \beta_2, \dots, \beta_k$ during the gesture operation.

3.2.1 Point-Trigger Operation Recognition Algorithm

Point-triggered operation means that only one palace point in the gesture detection module is triggered at each time, which changes its output value from 1 to 0. The output value of the palace grid point is continuously updated in the course of hand waving. By detecting the element with $l_{ij} = 0$ in the matrix and recording the coordinate of the element $[i(k), j(k)] \in \mathbb{R}^{1 \times 1}$, the displacement vector $(x(k), y(k))$ caused by gesture motion is expressed as

$$\begin{cases} x(k) = i(k) - i(k-1) \\ y(k) = j(k) - j(k-1) \end{cases}, \quad k \geq 2 \quad (1)$$

By connecting the displacement vector of each period, the overall swing trajectory of the gesture can be obtained. At this time, the robot cannot move according to the given track of the rail unless the target vector $(x_t(k), y_t(k))$ in the motion coordinate system obtained by the following transformation formula

$$\begin{cases} x_t(k) = i \cos \theta - j \sin \theta \\ y_t(k) = i \sin \theta + j \cos \theta \end{cases}, \quad k \geq 2 \quad (2)$$

where θ is the angle between the displacement vector of the last gesture and y-axis. After receiving the target vector $(x_t(k), y_t(k))$, the mobile robot calculates the required deflection angle in the moving coordinate system and completes the steering, and then starts to move forward until the next gesture trigger command arrives. For example, If the gesture starts from point A and passes through points B and C to reach point H directly, the calculated data table is shown in Table 1.

Table 1 Results of calculated data

	Displacement before transformation	θ	Displacement after transformation
1	(a, a)	0	(a, a)
2	$(a, 0)$	$\pi/4$	$(\frac{\sqrt{2}}{2}a, \frac{\sqrt{2}}{2}a)$
3	$((n-3)a, (n-2)a)$	$\pi/2$	$(-(n-2)a, (n-3)a)$

3.2.2 Line and Area-Trigger Running Recognition Algorithm

In the process of waving the hand, multiple points may be triggered at the same time. If two points are triggered each time, it is a line trigger mode; if more than two points are triggered, or the number of trigger points changes randomly, it is defined as area trigger. At this time, there will be multiple 0 elements appeared in the grid matrix, and the average value of their coordinate points $(i(k), j(k))$ is taken as the only effective point of the gesture movement. Using formulas (1) and (2), the robot vehicle target vector $(x_t(k), y_t(k))$ in the current motion coordinate system can be obtained.

4 Experimental Research

In this experiment, an infrared sensor array with 9 points shown in Fig. 6 is used to control the trajectory of the mobile robot, where 1 is the infrared obstacle avoidance module, and 2 is the host computer AT89S52. The overall size of the PCB board is 30×30 cm, and the distance between infrared obstacle avoidance modules is 10 cm. In order to verify the effectiveness of the control system, three methods of point-trigger, line-trigger and area-trigger are tested respectively, and the Frechet Distance method in Matlab is used to calculate the similarity between the given trajectory of the gesture and the actual trajectory of the robot.

4.1 Point-Trigger Running Experiment

In this case, only one grid point is triggered at one time, and the coordinate values in the coordinate system of the gesture controller are selected as $(0,0)$, $(10,0)$, $(20,0)$, $(20,10)$, $(20,20)$, $(10,20)$, $(0,20)$.

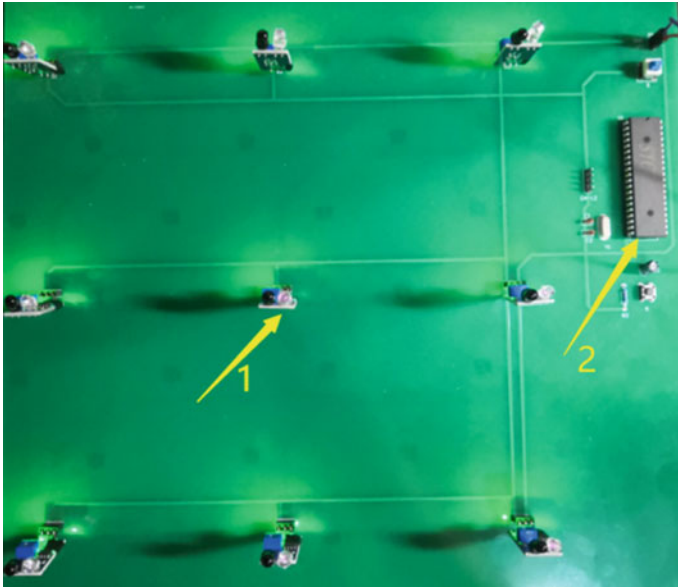


Fig. 6 Picture of grid gesture detection module

4.2 Line and Area Trigger Running Experiment

In this case, multiple different grid points are triggered each time. The trigger point coordinates and gesture swing trends are shown in Fig. 7a, b, respectively. The actual gesture movement trend is given in the form of arrow lines in the figure.

After calculation, the similarities between the actual robot trajectory and the gesture trajectory in the three sets of experiments are 92.47%, 85.41%, and 91.06%,

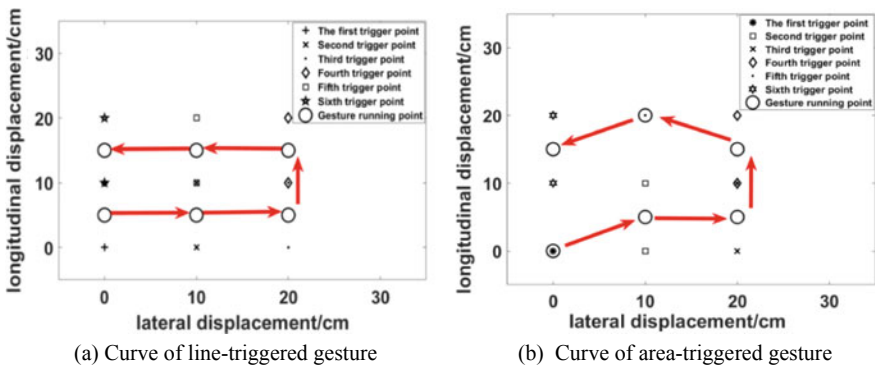


Fig. 7 Curves of line-triggered gesture and area-triggered gesture

respectively, indicating that the actual trajectory of the robot is similar to the gesture operation trajectory. The data shows that the mobile robot can move according to the given trajectory under any trigger mode, and a satisfactory control effect is achieved.

5 Conclusion

In this paper, the infrared obstacle avoidance module is used to establish a gesture detection module with a lattice structure. On this basis, a mobile robot gesture trajectory control system is built, and the gesture detection algorithm is studied. The experimental results show that the robot can move according to the given trajectory under different gesture trigger methods, indicating the rationality of the gesture detection module design and the effectiveness of the robot control system.

Acknowledgements This work was financially supported by Jiangxi Provincial Natural Science Foundation (20202BAB202008) and Foundation of Education Department of Jiangxi Province (GJJ170484, GJJ160540).

References

1. Pan, K.: Master-slave control method of dexterous hands based on data glove. *J. Syst. Simul.* **30**(7), 2600–2607 (2018)
2. Maitre, J., Rendu, C., Bouchard, K., Bouchard, B., Gaboury, S.: Basic daily activity recognition with a data glove. *Procedia Comput. Sci.* **151**, 108–115 (2019)
3. Wang, C., Liu, Z., Zhu, M., Zhao, J., Chan, S.C.: A hand gesture recognition system based on canonical superpixel-graph. *Sig. Process. Image Commun.* **58**, 87–98 (2017)
4. Gao, C., Zhang, Y.: Fingertip recognition based on a convex hull algorithm. *J. Beijing Univ. Chem. Technol. (Natural Science Edition)* **44**(2), 70–75 (2017)
5. Premaratne, P., Yang, S., Vial, P., Ifthikar, Z.: Centroid tracking based dynamic hand gesture recognition using discrete hidden Markov models. *Neurocomputing* **228**, 79–83 (2017)
6. Zhao, J., Sun, Y.: Design of S3C2440A-based velocity control system for DC motor. *Mod. Electron. Tech.* **34**(3), 157–159 (2011)

Development of Personalized Wind Handling System Using Infrared Ray Sensor



Jungryeong Chae, Cheng Hao, Taeuk Lim, and Wonsuk Jung

Abstract This paper introduces the technology for automatic control of wind volume, wind direction, and set temperature by developing a non-contact temperature sensing and control module. By combining thermal image analysis and advanced human body detection technology customized air handling system were developed according to the number and location of people. This aims to reduce electricity consumption and improve user comfort.

Keywords Air handling system · Infrared ray sensor · Wind volume and wind direction control · Non-contact temperature sensing

1 Introduction

Recently, the home appliance industry is releasing smart air conditioners that are equipped with the camera type simple human detection sensors and uniform temperature airflow control. However, the inability to detect the user's body temperature causes unnecessary cooling of large spaces, resulting in excessive power consumption, air-conditioning it is, and thermal discomfort caused by high temperatures.

In the case of Samsung Electronics 360 cassette system air conditioner and LG Electronics artificial intelligence system air conditioner, it is impossible to detect body temperature, so it is impossible to control the temperature difference according to body temperature.

Therefore, this study aims to prevent customized comfort control and over-cooling according to body temperature by detecting several people's body temperature in real time using infrared ray sensors that measure surface temperature by non-contact.

J. Chae · C. Hao · T. Lim · W. Jung (✉)
School of Mechanical Engineering, Chungnam National University,
Daejeon, Republic of Korea
e-mail: wonsuk81@cnu.ac.kr

2 Experiments

2.1 2D Array-Type Infrared Ray Sensing Part Fabrication

When the system developed in this study is attached to a general air conditioner, an air handling system that can improve comfort through customized thermal control according to the thermal information about people and surroundings was developed.

As shown in Fig. 1, the 2D matrix non-contact temperature detection sensor for measuring indoor person information was manufactured with an infrared ray sensor, a Wireless Manipulation Signal Receiver part, and a louver angle sensing part [1, 2].

2.2 Real-Time Thermal Image Processing Based on Infrared Ray Sensor

The image measured through the 2D array type infrared ray sensor for heat source detection is shown in Fig. 2a, and the system configuration for processing the thermal image from the infrared ray sensor is shown in Fig. 2b.

The thermal image processing algorithm of infrared ray sensor used the Otsu algorithm to separate the background temperature from the heat source temperature. After calculating the temperature through this, if the human body temperature is extracted as shown in Fig. 3a based on the classified temperature, the human body heat source can be separated as shown in Fig. 3b [3, 4].

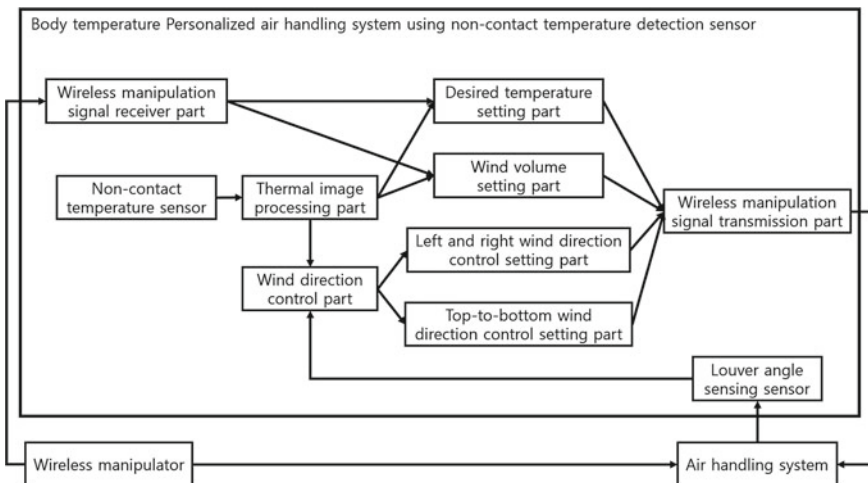


Fig. 1 Block diagram of personalized air handling system

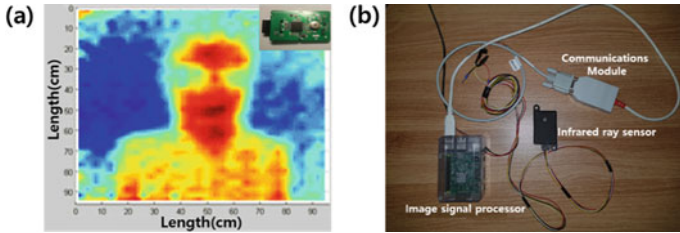


Fig. 2 a Infrared ray sensor module and image of temperature measurement and b signal processing system of thermal imagery

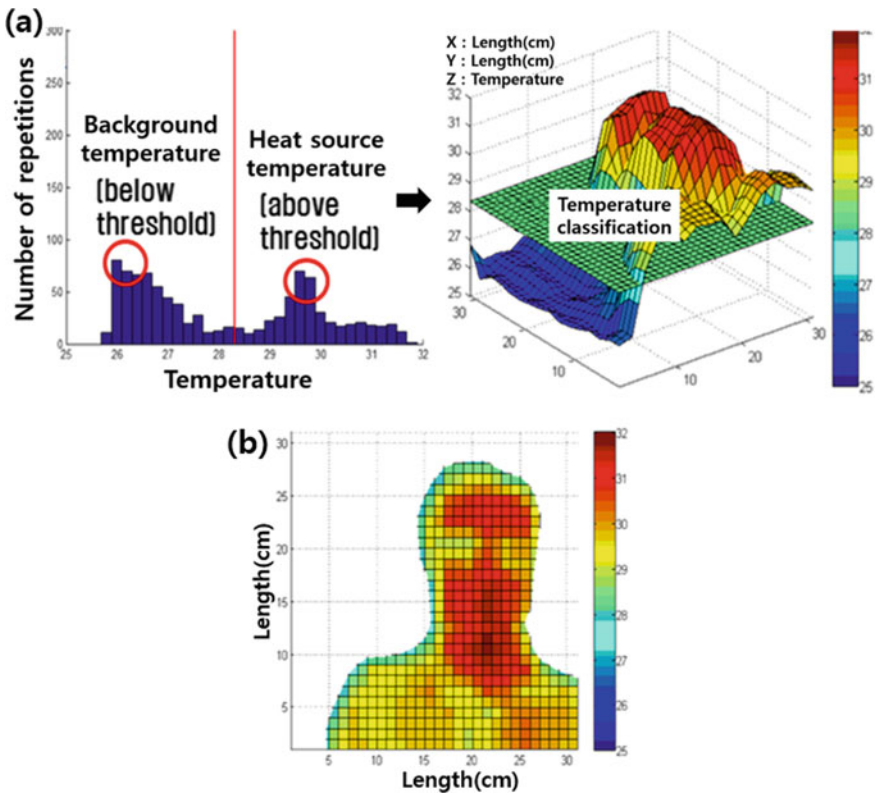


Fig. 3 a Separated temperature operation and extraction of body temperature using Otsu algorithm and b separation of body temperature by image processing algorithm

2.3 Development of Wind Direction Control and Air Handling System

In order to manipulate the wind direction of the air conditioner according to the location of the heat source, a mechanism that converts the rotational motion to the left and right reciprocating motion through a 360° rotation motor was designed as shown in Fig. 4. In addition, a servo actuator and a lever mechanism parts having left and right louver angle adjustment and angle feedback were also manufactured.

The location of the target wind direction, target setting temperature, and the target wind volume was received through the communication of the infrared image signal processor. In addition, the function of checking normal reception of measured values and transmitting power on/off signals, angle control of servo actuator through the position of the received target wind direction, and wireless transmission and reception module were used. Therefore, wind direction control and air handling controller system that sends air conditioning settings based on user's remote control input was manufactured [5].

3 Results and Discussion

Based on the center of the air conditioning vent, heat sources and anemometer for each angle were installed in the same location by 10° for a section on -30 ~ 30° section. The wind volume of the air conditioner was measured for 1 min at a location 1 m away from the maximum condition.

It was confirmed that the strong winds of about 1.49 m/s were secured up to 50°. The maximum limit for air conditioners to change wind direction from side to side is 50°. The automatic wind direction control effect according to the heat source was

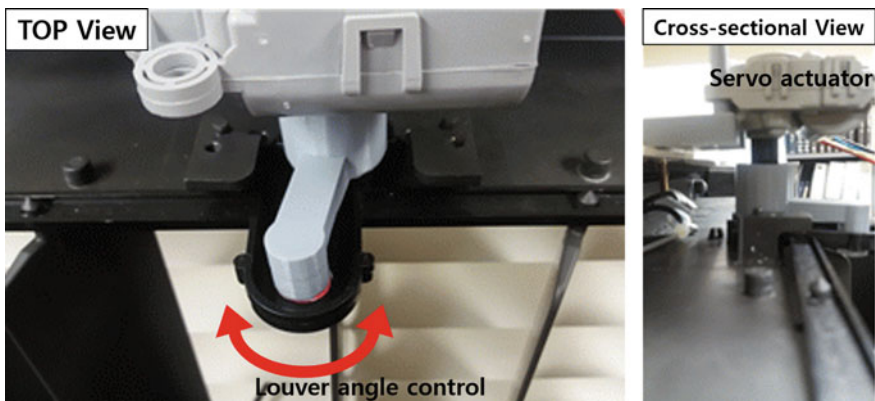


Fig. 4 Servo actuator to control louver angle of left and right

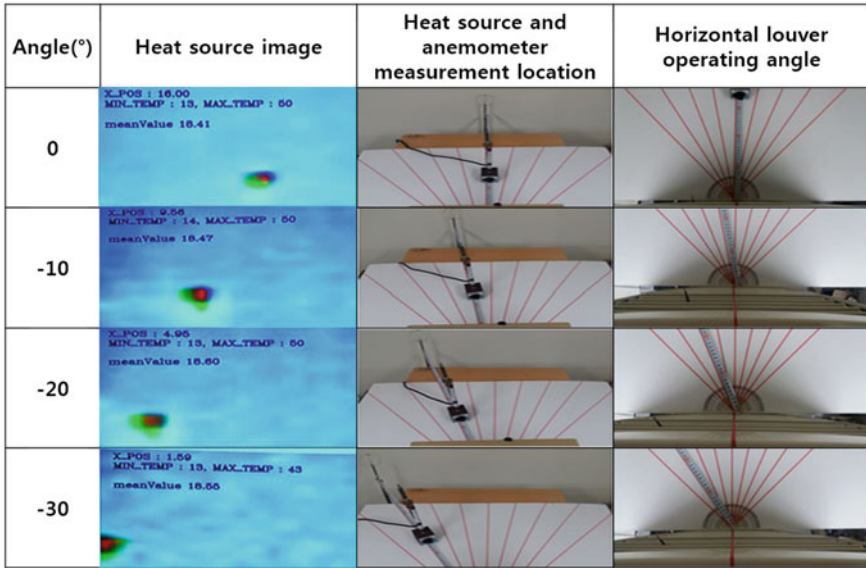


Fig. 5 Angle control of servo actuator using position of thermal imagery

measured at the center $0^\circ \sim \pm 20^\circ$ position. Before wind direction control of the heat source 0.52 m/s was measured, but after wind direction control, it was confirmed that it increased by about 3.4 times to 1.78 m/s. Therefore, it can be seen that the louver angle can be controlled according to the location of the heat source as shown in Fig. 5.

4 Conclusion

In this study, the automatic control air handling system for wind volume, wind direction and setting temperature based on non-contact temperature detection and control module was developed.

Thermal images were acquired using an infrared ray sensor, and background temperature and human body thermal data were extracted using the Otsu algorithm. In addition, the automatic wind direction control effects of heat sources could be confirmed through the development of the louver angle control and air handling system depending on the number and location of people.

Therefore, it is expected that the power consumption of the air conditioner and the thermal comfort of the person will be greatly increased through the present technology.

Acknowledgements This work was supported by research fund of Chungnam National University.

References

1. Xie, X., Long, Z.: Fuzzy PID temperature control system design based on single chip microcomputer. *Int. J. Online Biomed. Eng.* **11**(8), 29–33 (2015)
2. Raj, A., Soni, N.: Review of design of air conditioning system for commercial and domestic applications. *Int. Res. J. Eng. Technol.* **4**(7), 3124–3128 (2017)
3. Ring, E.F.J.: Progress in the measurement of human body temperature. *IEEE Eng. Med. Biol. Mag.* **17**(4), 19–24, July–August (1998)
4. Morinaka, K., Hashimoto, K.: Human information sensor. *Sens. Actuators, A: Phys.* **66**(1–3), 1–8, April (1998)
5. Cheng, C.C., Lee, D.: Smart sensors enable smart air conditioning control. *Sensors* **14**, 11179–11203, June, Issn: 1424-8220 (2014)

Key Design Technologies of New Cable-Stayed and Steel Truss Composite Bridge



Liping Xu, Qingquan Wang, and Anmin Wang

Abstract Taking Ningbo Yongjiang Sanguantang Bridge as the engineering background, the plan of new cable-stayed and steel truss combined bridge is created, according to the Construction conditions including navigation and aviation restriction and engineering geology, as a new combined bridge system from the combination of extradosed cable-stayed bridge and steel truss. This paper makes a deep study and coMPArison of four systems, such as 3 span continuous rigid frame bridge, 3 span continuous girder bridge, single cantilever rigid frame with rigid hinge, single cantilever beam with rigid hinge, and a structural system suitable for this type of bridge has been found: that is single cantilever beam with rigid hinge system. On the basis of the study and analysis of the structure system, the key technology of the anchor position at the end of the truss, and the integral static and dynamic performance and seismic performance, this paper has completed the conceptual design of the new bridge structure, and it shows that the bridge has excellent static and dynamic mechanical properties and implementable performance.

Keywords New bridge system · Cable-stayed and steel truss · Combined bridge system · Bridge structure system · Bridge key technologies

1 Introduction

1.1 Introduction

Ningbo Sanguantang bridge is planned to be located on the Yongjiang River in Ningbo City, Zhejiang Province, China, which is downstream of Chang Hong Road Tunnel. The main span of the bridge is about 465 m, and the aviation height limit is 50–56 m, so the conventional cable stayed bridge, arch bridge and suspension bridge is difficult to meet those requirements. The steel truss bridge is one of the

L. Xu · Q. Wang · A. Wang (✉)
Tongji Architectural Design (Group) Co Ltd., Shanghai 200092, China

bridge types with low height and long span capacity, which is more suitable for the project. However, the traditional steel truss girder bridge has some disadvantages in the aspects such as landscape and structure. It has too many and disorderly truss members [1], which is also difficult to construct the main span on the river, and it is not as economical as the cable-stayed bridge. Therefore, this design does not want to copy the traditional steel truss beam structure scheme, but wants to design a new bridge type scheme to meet the special bridge construction conditions, which is also consistent with the planning of modern buildings on both river sides.

The existing bridges on Yongjiang River are mainly cable-stayed bridges and suspension bridges. It is very reasonable and economical to use the cable-stayed bridge type for this span bridge, and it is convenient to use the cantilever construction technology which does not affect the channel. However, the requirement of aviation height limit makes the conventional cable-stayed bridge scheme about 40–50 m higher than the limit height, which is impossible to implement. The extradosed bridge can effectively reduce the height of the cable tower, which is about $1/8$ – $1/12$ of the main span, about $1/2$ of the general cable-stayed bridge tower. However, due to the technical limitations of the beam height ($1/30$ – $1/60$ in middle, $1/20$ – $1/40$ in fulcrum) and reasonable span of 300 m or so, it is difficult to apply the bridge type scheme here. Based on the extradosed bridge, the height of bridge tower can be reduced by using Y-shape. However, to meet the aviation height limit, the opening angle of the cable towers are more than 120° , and its horizontal length is almost about 200 m, and the influence factors such as the sag of the cable, the included angle of tower column and the ground about 30° , lead to the unreasonable mechanics of the structure.

In this scheme, the layout of the middle span of the extradosed bridge is retained. The “Y-shaped cable tower” and the whole side span form an integral structure, with a steel-truss cantilever beam, which can balance the main beam of the middle cable-stayed span. In this way, a new type of bridge structure is formed: the bridge structure of the cooperative system of cable-stayed and cantilever steel truss beam. The main span of this structure can be constructed by cantilever section like the cable-stayed bridge, which will not affect the navigation of the channel during the construction (Fig. 1).



Fig. 1 The daytime rendering of the bridge

1.2 Construction Conditions

The construction site is flat. The river here is about 390 m wide. The main river channel is located in the northwest side, and the southeast side has nearly 90 m shoal area. The deepest elevation of the river bottom is about -9.2 m, and the depth of the constant water level is within 10 m. The ground elevation of both shores is about 2.5 m. The distance between the north levee and the south is about 430 m.

The foundation soil of Yongjiang River is composed of Quaternary sedimentary layer and Cretaceous bedrock layer within 121.2 m below the ground, and soft soil foundation is distributed within the bearing layer of piles foundation.

The navigation grade of Yongjiang River is class III sea channel, with a clear width of 180 m and a clear height of 20 m. It is demanded that no pier is allowed within the river.

There is an airport 3.3 km away from the west side of the bridge. According to the aviation height limit, the building height should below 60 m.

1.3 Technical Standard

1. Road grade: urban main road; design speed of main line: 60 km/h;
2. Lane width: single lane width 3.5 m, 8 lanes.
3. Design load: automobile load: urban-A; crowd load: according to the specifications.
4. Building height: the height of the building shall meet the aviation limit of 50–56 m.
5. Navigation standard: Class III sea channel, with a clear width of 180 m and a clear height of 20 m; the highest navigable water level is 2.23 m (1985 National elevation system).

2 General Layout and Structural Design

2.1 General Layout

The main bridge adopts the cooperative system of cable-stayed and cantilever steel truss beam, with the span of $160 + 465 + 160 = 785$ m, all steel structure. The large section steel truss cantilever beam structure [2] is adopted for the anchor span on both sides, which bears the force together with the orthotropic steel deck. The double side steel box girder cable-stayed structure is adopted in the middle span.

Expansion joints are set in the joint piers of the main and approach bridges on both sides and in the middle of the mid span respectively. The longitudinal fixed and transverse movable supports are set under each truss on the middle pier [3].

The two truss supports on the top of the joint pier are all longitudinally movable and the transverse bridge is fixed to one truss while the other is released. The rigid hinge is set in the middle of the main span to transfer the longitudinal and transverse bending moment and shear force and release the temperature force.

The clear width of the carriageway is 32 m, the width of the truss structure is 3.5 m, and the width of the pedestrian and non-motor vehicle is 4.25 m respectively on both sides. The height of truss beam above the bridge deck is 26.25 m, and the elevation is arranged in two layers, and 14.25 m below the bridge deck, with a total height of 40.5 M; the longitudinal truss joint length is 20 m, and the web member between each layer is arranged according to the “N” type, and the wind support adopts the “-” type; the highest point of truss from the ground is 50.0 m. The longitudinal spacing of the stay cable on the beam is 10.0 m, while at the truss end the cable is evenly distributed and anchored in the triangle area at the end of the cantilever truss. The stay cables corresponding to each truss are arranged as the double cable plane (Figs. 2, 3).

2.2 Steel Truss

The steel trusses are arranged in two pieces. The two pieces are parallel with a center distance of 35.5 m. The facade of each truss is arranged in the form of multi fold sides. The upper part of the bridge deck is divided into two layers, with the layer height of 14.0 m. The web members of each layer are arranged in the form of “N”; the truss below the bridge deck forms a V-shape and closes to the top of the bearing platform at the middle pier, with the height of 16.0 m. The truss joint length is 20.0 m.

The upper and lower chord and the web members of the truss adopt box section, and the width is 3.5 m. The height of the top chord is 3.0 m, the height of the diagonal chord below the bridge deck and around the truss is 3.0 m, and the height of the bottom chord connected to the steel bridge deck is 3.5 m. The height of middle horizontal bar, straight and diagonal web bar is 1.60 m. The whole section of the cable anchorage area is closed, which is a solid triangle.

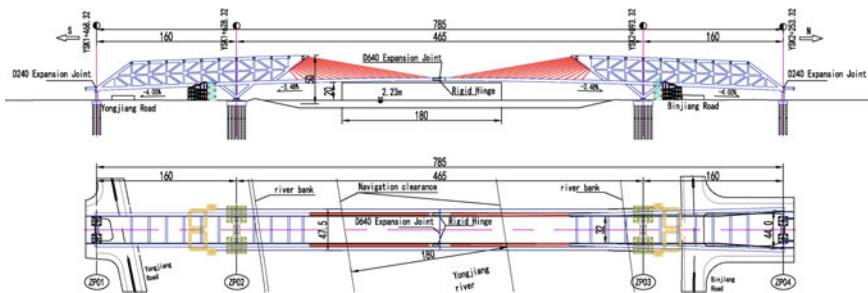


Fig. 2 The recommended bridge layout

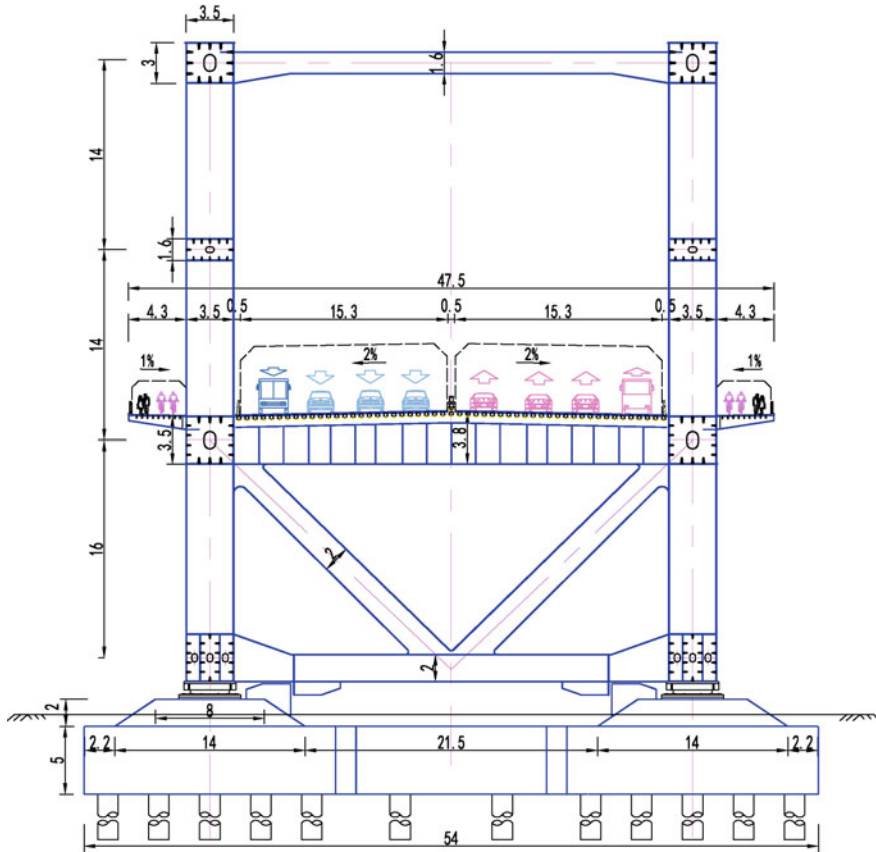


Fig. 3 The fulcrum section of the recommended bridge

The thickness of chord plate is between 30 and 50 mm. For some sections with more stress, two webs shall be added in the box room, and the thickness of additional webs shall be 30 mm. The thickness of web plate is between 20 and 40 mm.

The connection of steel truss joint adopts the integral joint and the full welding form. Q345 grade steel is mainly used, and Q420 grade steel is used for upper, lower and inclined chords near some stressed sections such as fulcrum.

2.3 Steel Girder and Steel Deck Structure

The main beam adopts a double side steel box form, and the bridge deck is of orthotropic steel deck structure. The side box girder is 3.5×3.5 m, the thickness of upper and lower flange and web is determined according to the stress demand, and

the plate thickness varies from 16 to 40 mm. The orthotropic steel bridge deck adopts U-shaped stiffening rib, the thickness of the bridge deck is not less than 16 mm, and the spacing between the diaphragms is 3.3–3.4 m. It is arranged at the same height as the side box girder, and the reinforced diaphragm beams are arranged near the corresponding truss nodes and cable anchor points. The web thickness of the common diaphragm is 12 mm, the bottom plate is 12×400 mm, the web thickness of reinforced diaphragm is 16 mm, and the bottom plate is 16×400 mm.

Q345 grade steel is used for steel deck and main girder, and Q420 grade steel is used for some parts.

2.4 Cables

The twisted parallel steel wires stay cable and cold cast anchor are adopted, and the standard strength of steel wire is 1670 MPa. There are 64 stay cables in the whole bridge, the longest one is about 142 m, and the largest one is $253 \phi 7$.

The standard spacing of stay cable in steel box girder is 10 m, the total length of non-cable section girder near the truss is 30 m, and the length of non-cable section in midspan is about 25 m.

2.5 Foundation

The main pier and side pier are both located on land, so the bored pile foundation can be directly used in the design. The foundation is designed as friction pile with a diameter of $\Phi 1.5$ m. The bearing layers of the main and side pier pile foundation are all selected at the tenth layer containing the cohesive round gravel layer, and the pile length is about 80 m. Dumbbell type arrangement is adopted for main pier and side pier cushion cap. 64 $\Phi 1.5$ m pile foundations are arranged for main pier and 18 $\Phi 1.5$ m bored piles are arranged for side pier.

3 Key Technology

The detailed study, clear elaboration and expression of bridge type, structural system and key structural problems is one of the important works to strongly support the technical feasibility of the scheme, and also one of the core technologies of the innovative scheme.

3.1 Structure System

Under the general layout condition, there are four types of structural system: (1) three span continuous rigid frame system, deck continuous, V-shape support and main pier cap consolidated, Fig. 4; (2) three span continuous beam system, deck continuous, V-shape support and main pier cap connected by large tonnage seismic isolation bearings, Fig. 5; (3) single cantilever rigid frame and rigid hinge system, rigid hinge is set in the middle of main span [4, 5], V-shape support and main pier cap consolidated, Fig. 6; (4) Single cantilever beam and rigid hinge system, rigid hinge is set in the middle of main span, V-shape support and bearing platform of main pier are connected by large tonnage seismic isolation bearing, Figs. 4, 5, 6, 7.

The main advantages of system 1 are: (1) V-shape support and main pier cap are consolidated, the main pier avoids the setting of large tonnage bearing and saves bearing cost; (2) compared with the rigid hinge system, the rigid hinge is avoided in the middle of main span, and the structure is simple; there are less number of bridge expansion joints, and more comfortable of car travel; (3) the structural rigidity is large, and the displacement of truss and midspan is small; (4) because the main pier can bear the longitudinal bending moment of the bridge, and the tension of the side pier is relatively small, which can reduce the balance weight of the structural transition pier. The main disadvantages of system 1 are: (1) due to the consolidation of V-shape support and main pier cap, the main span in the normal use stage, the temperature effect produces a large horizontal force in the pier; (2) under the E2 earthquake, the main pier is subject to a large horizontal force, so the foundation scale of the main pier needs to be large; (3) under the earthquake, the V-shape support bears a large seismic effect, which is adverse to the structural stress safety. Compared with the advantages and disadvantages of system 1, relatively speaking, the disadvantages are more prominent, the project cost is higher, and it is not beneficial to the structural safety, so this kind of structural system is not recommended.



Fig. 4 3 span continuous rigid frame system (system 1)



Fig. 5 3 span continuous girder system (system 2)

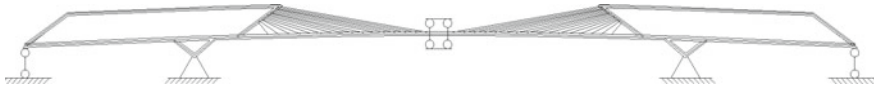


Fig. 6 Single cantilever rigid frame with rigid hinge system (system 3)



Fig. 7 Single cantilever beam with rigid hinge system (system 4)

The main advantages of system 2 are: (1) the bridge structure is continuous, the vertical stiffness of the structure is larger than that of the system with rigid hinges, there are less number of bridge expansion joints, and more comfortable of car travel. The ratio of deflection to span of the structure is $(0.620 + 0.026)/465 = L/720$, and the overall rigidity of the structure meets the requirements of the code; (2) compared with the system with rigid hinge, the setting of rigid hinge is avoided in the main span, and the structure is simple; (3) the stress system of the structure is clear, and the force transmission path is simple. The main disadvantages of system 2 are: (1) the longitudinal displacement of the structure is large, large displacement expansion joints need to be set, and the displacement distance of the support is required to be large; (2) the horizontal force under the wind load is carried by a middle pier, the horizontal force of the fixed pier under the longitudinal wind load reaches 14,000 kn, large tonnage support is required, and the pile foundation is required to be strict, and large-scale foundation needs to be set.

The main advantages of system 3 are: (1) the temperature force is released by setting the rigid hinge in the middle of the span, and the horizontal force supported by the main pier is small in the normal use stage; (2) under the longitudinal wind load, the horizontal force is supported by two middle piers respectively. The main disadvantages of system 3 are: (1) the seismic force of the main pier is very large, the horizontal reaction force of a main pier reaches 90,000 kn, and the force on the lower foundation and V-shape support is very unfavorable; (2) compared with the system without rigid hinge, the vertical stiffness and transverse stiffness of the structure are relatively small.

The main advantages of system 4 are: (1) the temperature force is released by setting rigid hinge in the middle span, and the horizontal force supported by the main pier is small in normal use; (2) under the action of longitudinal wind load, the horizontal force is supported by two middle piers respectively; (3) through setting seismic isolation bearing, the seismic effect is obviously reduced, and the horizontal reaction force of one main pier under the action of earthquake is 14,000 kn. The main disadvantages of system 4 are: compared with the system without rigid hinge, the vertical stiffness and transverse stiffness of the structure are slightly reduced, the

ratio of deflection to span of the structure is: $(0.632 + 0.018)/465 = L/715$, and the overall stiffness of the structure meets the requirements of the code.

Based on the above analysis and comparison, system 4 is finally recommended.

3.2 Structure of Cable Anchorage Zone at Truss End

The bridge adopts a truss cable-stayed cooperative system. The cable is anchored at the end of the cantilever truss, which makes the anchorage zone become the key part of the stress. In the design, the triangle area at the end is closed as a whole, and longitudinal and transverse stiffeners and diaphragms are set inside. The cable force is transmitted to the box web of the anchorage area through the anchor tube and stiffener plate, and then to the upper and lower chord of the truss through the anchor web and the longitudinal and transverse box chamber set inside (Fig. 8).

The plate and shell element model is adopted for the calculation of truss anchor cable area, the most unfavorable standard combination is adopted for the cable force of stay cable, and the boundary of truss chord is consolidated.

There are stress distribution diagram of side steel plate and main internal plate of anchor cable area (Fig. 9). It can be seen from the calculation results that the stress distribution of the main plates in the anchorage zone is relatively uniform, except that there is local stress concentration at the inner corner of the position where the anchorage web and the upper chord are connected, there is no obvious stress concentration phenomenon. The maximum stress level of the plate is not higher than 300 MPa on the lower flange plate near the position where the upper chord and the anchorage zone are connected, and the local right angle of the area can be adjusted to a small circle. The arc angle is used to eliminate the stress concentration, so the structural arrangement of the cable anchorage area is more reasonable in general.

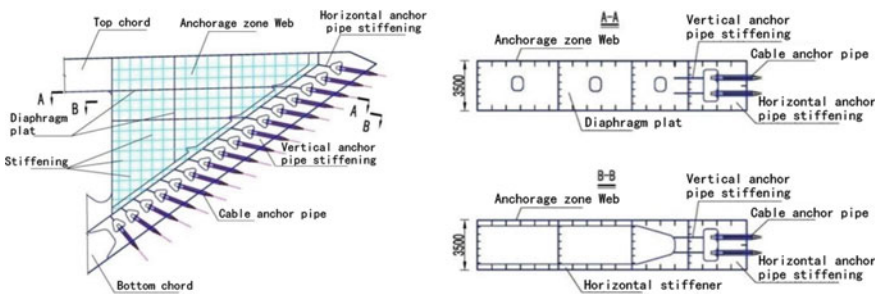


Fig. 8 The anchorage zone at the end of the truss

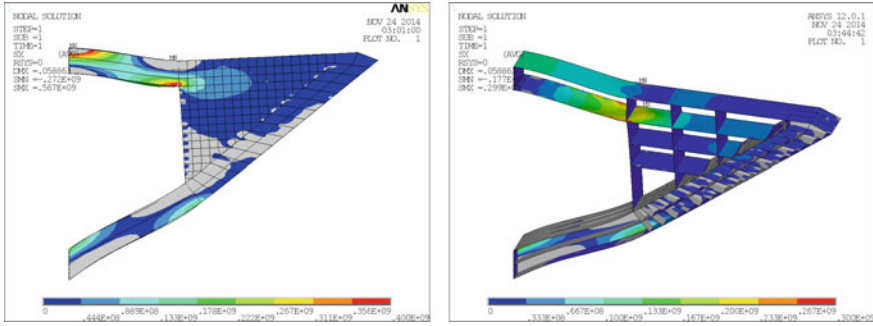


Fig. 9 The stress of the web and the stress of the inside plate

4 Overall Calculation and Analysis

4.1 Calculation Parameters and Model

The vehicle load is urban-A, two-way 8 lanes, with a reduction factor of 0.50; the pedestrian load is 4.0 m wide on both sides of the bridge deck, with a value according to the specification; the temperature rise is +25 °C, with a temperature down of -25 °C; the local temperature difference of the bridge deck is taken according to the specification; the settlement is 1 cm for the side pier, 3 cm for the middle pier; the design basic wind speed is 31.3 m/s. Unless otherwise noted, the displacement is in m, the internal force is in kn and m, and the stress is in MPa (tension is positive);

The model is calculated by Midas civil 2012 versus 8.05 program. The model has 3784 nodes and 5922 units. The cable is simulated by only tension truss element, and the other elements are simulated by beam element.

4.2 Overall Rigidity of Structure

According to the Guidelines for Design of Highway Cable-stayed Bridge (JTG/T d65-01-2007), the maximum vertical deflection value of the main girder of cable-stayed bridges caused by Lane load (excluding impact force) shall not be greater than 1/400 of the span. Under live load, the maximum vertical displacement of the middle span is $0.632 + 0.243 = 0.875 \text{ m} < 465/400 = 1.163 \text{ m}$, and the rigidity of the main beam meets the specification requirements (Figs. 10, 11).

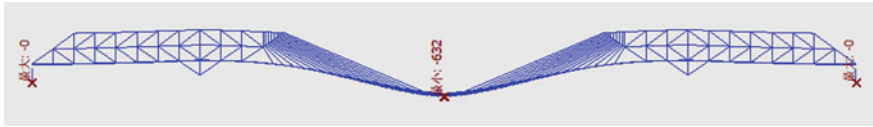


Fig. 10 The deflection under vehicle load

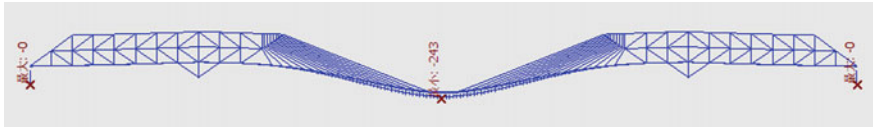


Fig. 11 The deflection under crowd load

4.3 The Static Response Under Characteristic Combination

Figures 12, 13 show the stress diagram of steel box girder under characteristic combination. In the characteristic combination at the later stage of completion of the bridge, the maximum compressive stress of the upper edge is 190 MPa, the maximum tensile stress is 38 MPa, the maximum compressive stress of the lower edge is 247 MPa, and the maximum tensile stress is 133 MPa, which meets the specification requirements; the section of the main girder near the main pier shall be made of Q420D steel

The maximum tensile force of the truss is 16,164 kn, which appears on the top chord of the truss and the top of the support; the maximum pressure is 97,360 kn, which is on the V-shape support. The maximum compressive stress is 211 MPa, and the maximum tensile stress is 230 MPa; Q420d steel is used in areas with high stress (Figs. 14, 15).

Under the action of characteristic combination, the maximum two cable force is 12,904 kn (pes7-253), and the minimum two cable force is 2801 kn (pes7-91); the safety factor of each stay cable is greater than 2.5, and the stress amplitude is less than 200 MPa according to the fatigue calculation requirements, meeting the design requirements.

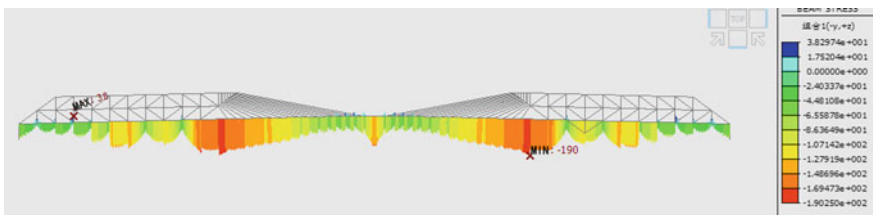


Fig. 12 The beam stress of the upper edge under characteristic combination

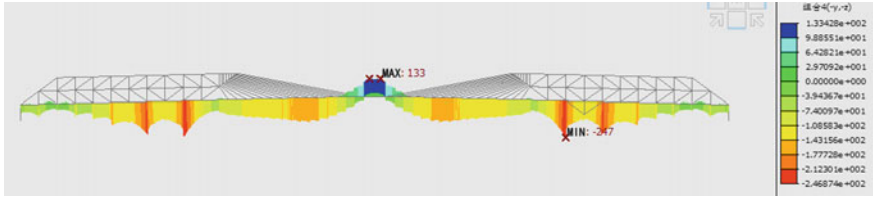


Fig. 13 The beam stress of the lower edge under characteristic combination

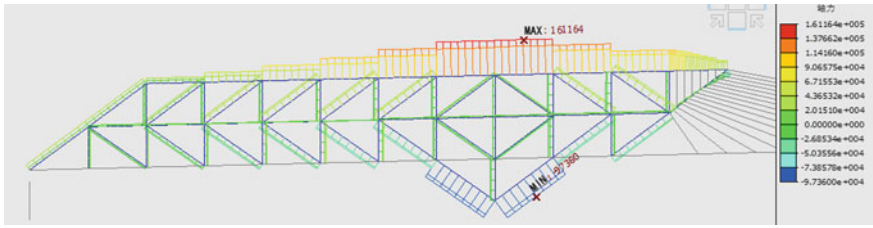


Fig. 14 The axial force of the truss under characteristic combination

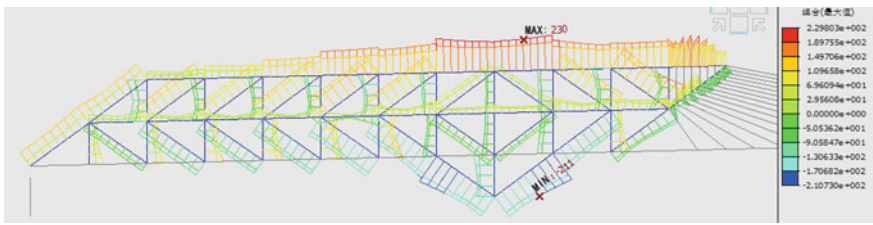


Fig. 15 The stress of the truss under characteristic combination

Table 1 The support reaction of the side and middle pier under characteristic combination (kN)

Position	Maximum support force	Minimum support force	Remarks
Side pier	10,829	827	Single support
Mid pier	129,732	111,037	

See Table 1 for reaction force of middle pier and side pier under standard combination.

4.4 *Dynamic Characteristic Analysis*

The main vibration characteristics of the structure. The first mode is out of plane translation with a period of 3.147 s and a frequency of 0.318 Hz; the second is vertical vibration with a period of 3.124 s and a frequency of 0.320 Hz; the third is first-order torsion with a period of 2.323 s and a frequency of 0.430 Hz; the fourth is second-order vertical vibration with a period of 1.967 s and a frequency of 0. The fifth order is the second-order torsional vibration with a period of 1.94 s and a frequency of 0.515 Hz.

5 Conclusion

1. Taking Sanguantang bridge in Ningbo as the engineering background, a new type of cable-stayed steel truss cooperation system bridge is designed innovatively. The span combination is $160 + 465 + 160 = 785$ m, all steel structure. Large section steel truss cantilever beam structure is adopted for the side span on both sides, which bears the force together with the orthotropic steel bridge deck, and double side steel box girder short tower cable-stayed bridge structure is adopted for the middle span. This type of bridge not only meets the navigation requirements of crossing Yongjiang River, but also meets the requirements of 50–56 m aviation height limit, and avoids the complicated truss members of traditional steel truss continuous beams, which has poor aesthetic effect.
2. In this paper, the important technical problems such as the structural system and the structure of the cable anchorage zone are analyzed and discussed in detail. The steel truss single cantilever beam and rigid hinge system is recommended for the structural system. The cable anchorage structure is set in the triangle area of the cantilever end of the closed steel truss box. The cable transmits the cable force to the box web of the anchorage zone through the anchor pipe and the stiffening plate, and then through the anchor web and its inside Part of the vertical and horizontal box chambers distribute the force to the upper and lower inclined chords of the truss.
3. The results of static, dynamic and aseismic calculation show that the strength, rigidity and stability of the main bridge can meet the stress requirements. The new cable-stayed steel truss bridge structure has good mechanical properties.

References

1. Leonhardt, F.: Bridges aesthetics and design. In: Xu, X., Gao, Y., Jiang, W. (eds) Translated, p 36. China Communications Press, Beijing (1988)
2. Yoneyama, T., Fujii, Y.: Fabrication and erection of tokyo gate bridge. In: Iabse-Jsce Joint Conference on Advances in Bridge Engineering-III, 268 (2015)
3. Li, J.: The Structural Design for Super Spherical Bearing. Chongqing University, Chongqing (2006)
4. Zhang, X., Wang, R., Lin, D., et al.: Innovative structural system design of multi cable-stayed towers of Jiashao bridge. Highway 7, 286 (2013)
5. Lu, W., Lin, D., Xiong, J., et al.: Design of purpose-made bearing for rigid hinge of Jiashao bridge. Bridge Constr. 5, 53 (2011)

The Role of Composite Materials to Rehabilitate Plant Piping



Meshal Alsaiari

Abstract This paper discusses a case study of composite materials rehabilitation on plant piping, and its influence to return the plant production after a fire. An evaluation was carried to evaluate damaged segments and propose a suitable repair mechanism. Reinstating the plant piping routes to minimize the production outage was a challenging task. Therefore composite materials repair technique was used to rehabilitate piping. This technique resulted in fast repairs. The process of composite material repair application starts with the defect identification and extent of the required repair. Based on the defect severity and geometry, a specific design of the composite materials wrap joint was developed. The composite material wrap/clamp joint design was as per ASME-PCC-2. Composite materials repair provided the piping with remarkable strength. Two wrapped locations were found to have air pockets because of improper installation, and therefore additional training is essential for the use of this composite wrap methodology.

Keywords Composite repair · Fire incident · Plant piping · Production outage

1 Introduction

Pipeline and process piping are the most efficient form of oil product transportation. The majority of these pipes are made of steel, which is vulnerable to environmental conditions. A huge amount of money is spent to minimize the deterioration of metallic pipes from corrosive environments [1]. These severe conditions lead to material failure of the metallic pipeline, mainly due to corrosion development [2, 3]. Other defects have their influence on piping integrity, such as mechanical damage due to the impact during construction and operation of metallic pipes or welding failures [4, 3]. Conventionally, defective metallic piping is repaired by piping replacement or metallic repair, where hot work is required. Recently, there has been

M. Alsaiari (✉)
Saudi Aramco, Dhahran, Kingdom of Saudi Arabia
e-mail: mishal.saiari@aramco.com

a remarkable increase in the use of fiber-reinforced polymer (FRP) composites to repair defective piping. FRP repair materials provide a considerable cost saving, and eliminate hazards associated with welding [5]. The polymers repair mechanism works when the epoxy resin covers the damaged pipe portion, and then the damaged pipe area is wrapped with FRP materials [6]. Wrapping the defective pipe portion will transfer the local defect stress to the composite repair filler layer [6, 7]. Composite materials have a solid structure with robust strength, stiffness, and corrosion resistance [8, 9]. Moreover, FRP materials can be formed and fabricated easily [8, 9]. FRP materials are susceptible to temperature, especially between composite and adhesive materials [10, 11]. Moreover, composite material bonding is affected by the surface preparation factor, which is sometimes difficult to achieve [12].

2 Overview of the Piping Failure

Fire damage occurred in an oil processing plant, damaging equipment, and piping. A specialized inspection team was assigned to perform all essential assessment examinations. The assessment found fire and mechanical damage to the piping loops. The piping systems that were mechanically damaged—from fire exposure—were replaced. The piping sections with mechanical and corrosion damage were recommended to be repaired. Rehabilitating the damaged piping with the traditional metallic repair was not possible, since the plant piping was filled with stagnant oil. As a result of this reality, composite materials repair wrap joint was employed.

3 Philosophy of the Repair Methodology

3.1 *Materials Selection*

The use of FRP materials demonstrated outstanding performance in the repair of metallic elements [13]. FRP is effective due to design flexibility and high strength materials [13]. Glass, carbon, and aramid are typical types of reinforced fibers used to repair corroded piping [14]. Glass fiber is used commonly as they are less expensive than other fibers. Carbon fiber showed better strength and stiffness but with more cost [13]. Based on this fact, composite reinforced with glass fibers was primarily utilized to repair a high number of damaged pipes. Composite reinforced with carbon fibers was also applied to high-pressure critical lines, to ensure the internal pressure was overcome safely.

3.2 Wrapping Design

The selection of design criteria for the wrapping joint, was as per ASME PCC-2 [15]. The piping system contains hazardous fluids with high pressure, and is classified as a high-risk application in ASME PCC-2 [15]. The design selection entails the piping specifications and process parameters of the corroded segment. All related data of impacted pipes were collected, evaluated, and it was recommended to install a specific wrap joint design for each of these pipes.

3.3 Composite Materials Wrap Application

The overall composite repair process for the composite wrap is summarized by the chart in Fig. 1. It entails the defect assessment, design selection, and composite installation using the spiral wrap method. Installing the composite clamp requires a clean surface, since this will impact the bonding process [12]. The failed pipe surface was cleaned mechanically to achieve the cleanliness level of NACE 3 minimum surface profile, to ensure the removal of all sharp edges and coating.

Then the resin was applied to the subject pipe repair zone. Finally, the fabric sheets utilized on the outer surface, as seen in Fig. 2. The curing time of wrap was within two hours on average. The application of all wrapping locations was successful, except for two locations that had delamination and air pockets due to improper installation.

Fig. 1 This is an illustration of the composite repair process flow

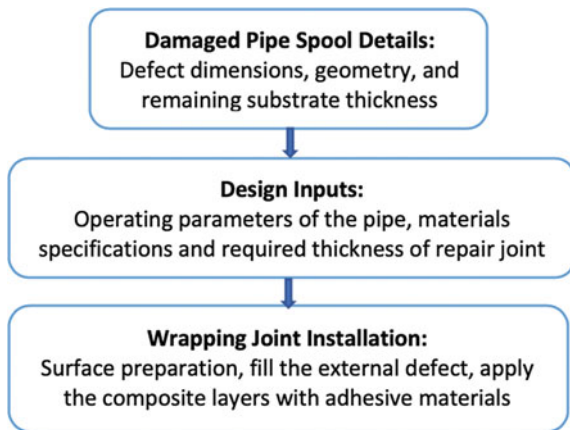




Fig. 2 This picture shows is a typical example of a defective pipe that was wrapped

4 Conclusion

This paper presents a case study of composite repair application on plant piping routes after a fire. A methodological evaluation was carried out to evaluate damaged piping and propose a suitable repair mechanism. Composite materials repair was used to rehabilitate damaged piping. This repair methodology was fast and resulted in significant savings. The process of composite material repair application starts with the defect identification and extent of the required repair. Based on the defect severity and geometry, a specific design of the composite material wrap was developed. The composite material wrap/clamp joint design was as per ASME-PCC-2. The reinforced fibers used in this case study are glass and carbon. Glass fiber was mainly used to improve the defective pipe strength because the cost was significantly lower compared to other fibers. Composites reinforced with carbon fibers were applied only to critical high-pressure lines to ensure they are safely repaired. Composite material repair provided remarkable strength to the pipes. The two wrapped locations that had suffered from delamination and air pockets because of improper installation, were repaired without any additional cost, or health and safety implications.

References

1. Ayaz, S.C.Y., Sahan, M.F.: Repair of small damages in steel pipes with composite patches. *Materwiss. Werksttech.* **47**(5–6), 503–511 (2016). <https://doi.org/10.1002/mawe.201600526>
2. Frankel, G.S.: Pitting Corrosion of Metals. *J. Electrochem. Soc.* **145**(6), 2186 (1998). <https://doi.org/10.1149/1.1838615>
3. Budhe, S., Banea, M.D., de Barros, S.: Composite repair system for corroded metallic pipelines: an overview of recent developments and modelling. *J. Mar. Sci. Technol.* 0123456789 (2019) <https://doi.org/10.1007/s00773-019-00696-3>
4. Allouti, M., Schmitt, C., Pluvinage, G., Gilgert, J., Hariri, S.: Study of the influence of dent depth on the critical pressure of pipeline. *Eng. Fail. Anal.* **21**, 40–51 (2012). <https://doi.org/10.1016/j.engfailanal.2011.11.011>
5. De Barros, S., Meniconi, L.C.M., Perrut, V.A., De Siqueira, C.E.R.: Handbook of adhesion technology. *Handb. Adhes. Technol.* (2017). <https://doi.org/10.1007/978-3-319-42087-5>

6. Chen, R., Qiu, J., Liu, B., Ren, G.: Ultimate failure of defective pipelines reinforced with composite repair systems. *J. Fail. Anal. Prev.* **19**(2), 581–589 (2019). <https://doi.org/10.1007/s11668-019-00636-8>
7. Sum, W.S., Leong, K.H., Djukic, L.P., Nguyen, T.K.T., Leong, A.Y.L., Falzon, P.J.: Design, testing and field deployment of a composite clamp for pipeline repairs. *Plast. Rubber Compos.* **45**(2), 81–94 (2016). <https://doi.org/10.1080/14658011.2016.1143082>
8. Abd-Elhady, A.A., Sallam, H.E.D.M., Mubarak, M.A.: Failure analysis of composite repaired pipelines with an inclined crack under static internal pressure. *Procedia Struct. Integr.* **5**, 123–130 (2017). <https://doi.org/10.1016/j.prostr.2017.07.077>
9. Baker, A.: Bonded composite repair of fatigue-cracked primary aircraft structure. *Compos. Struct.* **47**(1–4), 431–443 (1999). [https://doi.org/10.1016/S0263-8223\(00\)00011-8](https://doi.org/10.1016/S0263-8223(00)00011-8)
10. Andrade, B., Souza, J.P.B., Reis, J.M.L., da Costa Mattos, H.S.: A temperature-dependent global failure criterion for a composite/metal joint. *Compos. Part B Eng.* **137**(April 2017), 278–286 (2018) <https://doi.org/10.1016/j.compositesb.2017.11.015>
11. Reis, J.M.L., Coelho, J.L.V., Monteiro, A.H., Da Costa Mattos, H.S.: Tensile behavior of glass/epoxy laminates at varying strain rates and temperatures. *Compos. Part B Eng.* **43**(4), 2041–2046 (2012) <https://doi.org/10.1016/j.compositesb.2012.02.005>
12. Banea, M.D., Da Silva, L.F.M.: Adhesively bonded joints in composite materials: an overview. *Proc. Inst. Mech. Eng. Part L J. Mater. Des. Appl.* **223**(1), 1–18 (2009) <https://doi.org/10.1243/14644207jmda219>
13. Budhe, S., Banea, M.D., de Barros, S.: Composite repair system for corroded metallic pipelines: an overview of recent developments and modelling. *J. Marine Sci. Technol. (Japan)* (2019). <https://doi.org/10.1007/s00773-019-00696-3>
14. Mahdi, E., Eltai, E.: Development of cost-effective composite repair system for oil/gas pipelines. *Compos. Struct.* **202**(February), 802–806 (2018). <https://doi.org/10.1016/j.compstruct.2018.04.025>
15. The American Society of Mechanical Engineers.: ASME PCC-2 Repair of Pressure Equipment and Piping (2018)

Study on Piezoelectric Stack Performance for Linear Ultrasonic Motor



Hongbing Wang and Chunhua Sun

Abstract A piezoelectric stack for linear ultrasonic motor was developed. According to linear ultrasonic motor Requirements, the required piezoelectric ceramic was explored, and it had the characteristics of high temperature resistance, high mechanical quality factor, low voltage drive. In the sintering condition of 950 °C and 5 h, performance parameters of the developed piezoelectric ceramic, which consisted of $\text{Pb}_{0.98}\text{Bi}_{0.02}\text{Zr}_{0.51}\text{Ti}_{0.48}\text{Zn}_{0.0103}$ and is doped with 0.5%Co, were relative dielectric constant 1190, piezoelectric constant 270pC/N, electromechanical coupling coefficient 0.54 (Kp), 0.46 (Kt), Curie temperature 346 °C, dielectric loss angle tangent 0.6%. The displacement characteristics of the piezoelectric stack with different sheets were analyzed by finite element method. The results provided theoretical reference for the development of linear ultrasonic motor with piezoelectric stack.

Keywords Piezoelectric stack · Linear ultrasonic motor · Displacement characteristics

1 Introduction

Compared with traditional motors, ultrasonic motors have a series of advantages, such as small size, light weight, simple and compact structure, low speed, large torque, fast response, high motion accuracy, low noise operation, no electromag-

H. Wang (✉) · C. Sun

Department of Mechanical and Electrical Engineering, Suzhou Vocational University,
Suzhou 215104, China
e-mail: whb45@163.com

H. Wang · C. Sun

3C-Product Intelligent Manufacturing Engineering Technology Research and Development
Center of Jiangsu Province, Suzhou 215104, China

netic interference, direct linear drive, flexible structure and so on. Therefore, ultrasonic motors have developed rapidly and have wide application prospects [1, 2].

Ultrasonic motors can be classified into rotary and linear motors according to their motion forms. In recent years, the development of linear ultrasonic motor is very rapid [3–5], and there is a trend to replace electromagnetic linear motor in micro-precision drive system.

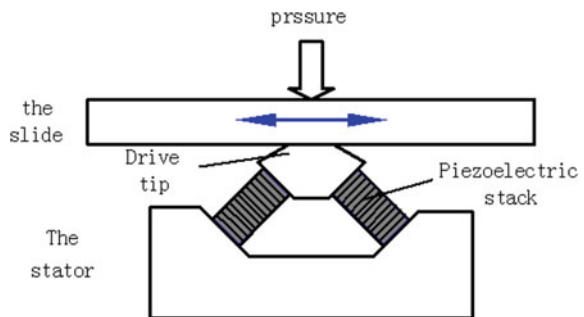
In order to develop linear ultrasonic motor with high temperature resistance, high mechanical quality factor, low voltage drive and low cost, a piezoelectric stack for linear ultrasonic motor was developed. According to linear ultrasonic motor Requirements, the required piezoelectric ceramic was developed. The displacement characteristics of the piezoelectric stack with different sheets were analyzed by finite element method.

2 Linear Ultrasonic Motor with Piezoelectric Stack

The working principle of the linear ultrasonic motor based on piezoelectric stack is shown in Fig. 1, which consists of a stator and a slide. Two groups of piezoelectric stacks on the stator are placed at 90°. The polarization and arrangement of each group of stacks are the same. When the sinusoidal and cosine AC working voltages are applied to two groups of piezoelectric stacks respectively, two longitudinal vibrations perpendicular to each other in space and 90° different in phase are excited. The two vibrations are combined at the driving head to form elliptical motion, which drives the actuator to move in a straight line by means of friction between the stator and the slide.

The designed linear ultrasonic motor based on piezoelectric stack is shown in Fig. 2. The stator of the motor was shown in Fig. 3. Applied on driving voltage 5 V, frequency 96.915 kHz and driving electric current 0.8 A, the no-load maximum speed of the motor is 25.78 mm/s, and the maximum output forces 2.14 N. The tests indicated the motor had large output force with small size and low diving voltage.

Fig. 1 The working principle of the linear ultrasonic motor



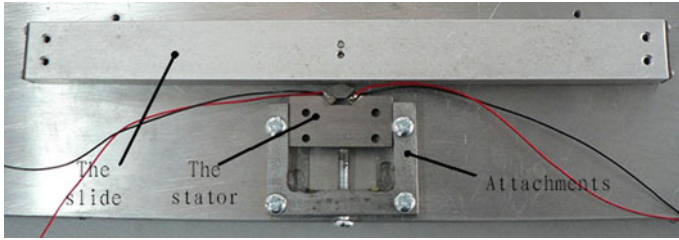


Fig. 2 The design ed linear ultrasonic motor

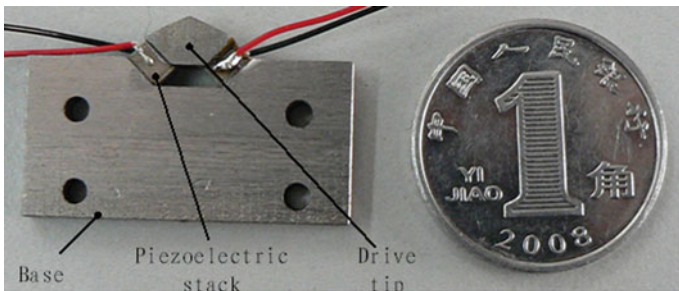


Fig. 3 The stator of the motor

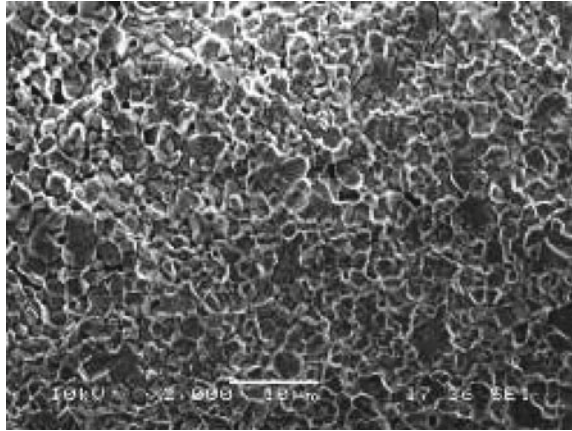
3 Formulation and Technology of Piezoelectric Ceramics

Different commercial PZT piezoelectric ceramics were selected to study the effects of different additions on the sintering characteristics and piezoelectric properties of commercial PZT piezoelectric ceramics, and to optimize the formulation and process parameters of high performance hard piezoelectric ceramics. Furthermore, according to the requirements of linear ultrasonic motor, the formula of piezoelectric ceramics is explored to make it have the characteristics of pressureless low temperature sintering and piezoelectric required.

Using piezoelectric ceramic system with pressureless low-temperature sintering and required piezoelectric properties, PZT commercial ceramic powders were sintered at 900–1000 °C pressureless low-temperature through transient liquid phase sintering and solid solution reaction, and the low-temperature sintering additives, dosage and sintering process parameters were optimized.

Figure 4 shows that SEM morphology of perovskite structure $(\text{Pb}_{0.95}\text{Sr}_{0.05})(\text{Zr}_{0.53}\text{Ti}_{0.47})\text{O}_3 + 0.5 \text{ wt\% } \text{MnO}_2 - (0.6\text{PbTiO}_3 - 0.3\text{Bi}(\text{Zn}_{0.5}\text{Ti}_{0.5})\text{O}_3 - 0.1\text{BiFeO}_3)$ piezoelectric ceramics (1050 °C/5-hour sintering). When the addition is 9 wt%, the experimental results show that the piezoelectric parameters are as follows:

Fig. 4 SEM morphology of piezoelectric ceramics microstructure



$$T_c = 298\text{ }^\circ\text{C}, \varepsilon_r = 767, \tan \delta = 0.7\%, P_r = 10.8\mu\text{C}/\text{cm}^2,$$

$$E_c = 2.11\text{ kV}/\text{mm}, d_{33} = 241\text{ pC}/\text{N}.$$

According to the brittleness of piezoelectric ceramics, the mechanical properties and comprehensive piezoelectric properties of piezoelectric ceramics are improved by strengthening the bonding force of grain boundaries and realizing the transgranular fracture mode of ceramics.

Through the experiments of different trace elements, we have realized the transgranular fracture of piezoelectric ceramics in PMN-PMS-PZT, PMN-PZT, PMN-PZN-PZT and other systems. The fracture mode is related not only to the trace elements, but also to the principal components of piezoelectric ceramics and the grain size of microstructures. Figure 5 shows the SEM results of fracture morphologies of several piezoelectric ceramics.

4 Fabrication of Piezoelectric Stack

In the sintering condition of 950 °C and 5 h, performance parameters of the developed piezoelectric ceramic, which consisted of $\text{Pb}_{0.98}\text{Bi}_{0.02}\text{Zr}_{0.51}\text{Ti}_{0.48}\text{Zn}_{0.0103}$ and is doped with 0.5%Co, were relative dielectric constant 1190, piezoelectric constant 270pC/N, electromechanical coupling coefficient 0.54 (Kp), 0.46 (Kt), Curie temperature 346 °C, dielectric loss angle tangent 0.6%. An SEM photograph of the section of multilayered piezoelectric stack is shown in Fig. 6. The piezoelectric ceramic has excellent multilayered co-firing characteristic with Ag electrode. Figure 7 shows the capacitance spectrum test results of three multi-layer co-fired piezoelectric ceramic actuators, which show good consistency.

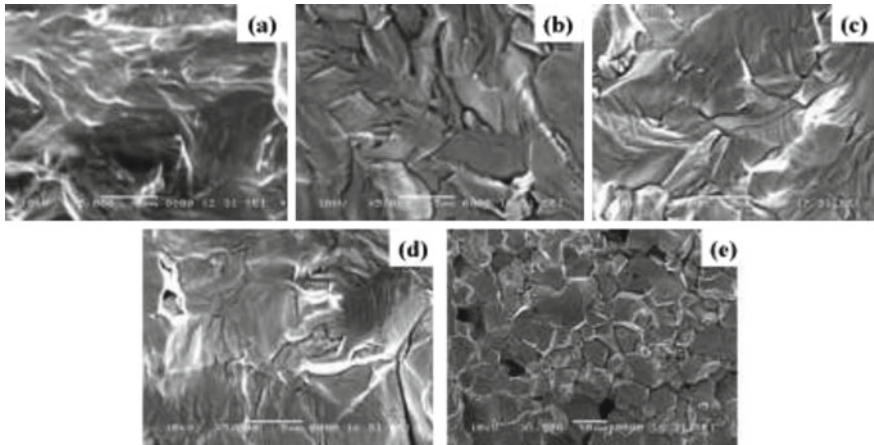


Fig. 5 SEM morphology of piezoelectric ceramics fractured surface, **a** modified PZT-PMSN, **b** PZT-PMN, **c** modified PZT-PMN-PZN, **d** modified PZT-PMN-PNN, **e** PZT-PMN-PNN

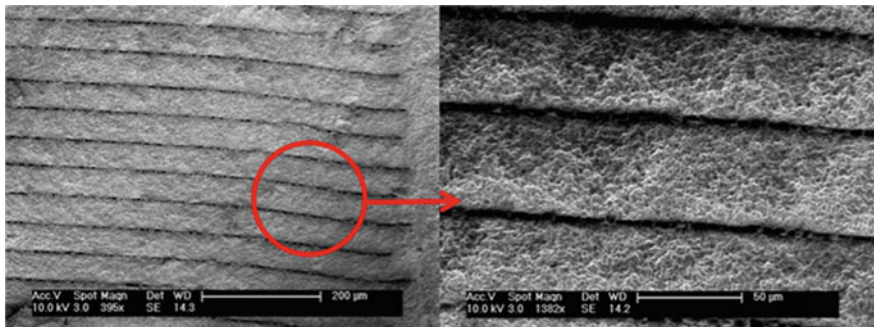


Fig. 6 SEM photograph of the section of multilayered piezoelectric stack

5 Finite Element Analysis of Piezoelectric Stack with Different Sheets

When the alternating electric field is applied to the piezoelectric crystal, the elastic waves of various modes can be excited in the piezoelectric crystal by the inverse piezoelectric effect.

Figure 8 shows the deformation of a single piezoelectric ceramic sheet under electric field. When the electric field direction is the same as the polarization direction of the piezoelectric ceramic sheet, the deformation of the piezoelectric ceramic sheet is the same as that of the polarization direction. The first kind of piezoelectric equations is shown in Eq. 1.

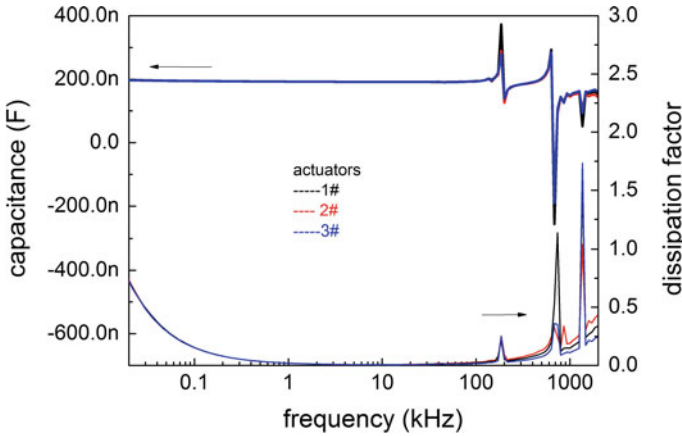


Fig. 7 Capacitance frequency spectrum of three multilayered piezoelectric stacks

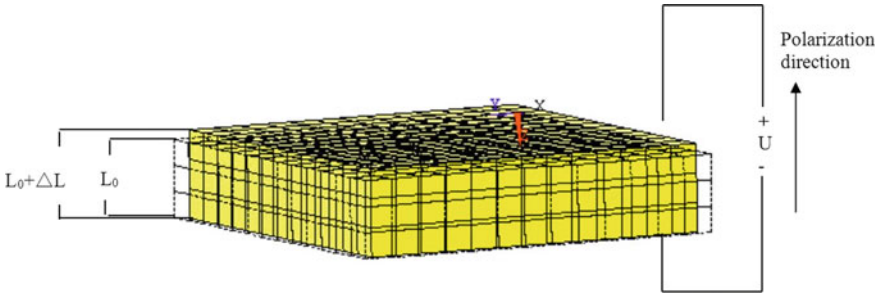


Fig. 8 The deformation of a single piezoelectric ceramic sheet

$$\begin{aligned} \{S\} &= [s]^E \{T\} + [d]\{E\} \\ \{D\} &= [d]^t \{T\} + [\epsilon]^T \{E\} \end{aligned} \tag{1}$$

The strain of piezoelectric ceramics under external electric field can be calculated by Eq. 1.

As shown in Fig. 9, the strain of a single piezoelectric ceramic sheet can be obtained by establishing a single piezoelectric ceramic sheet model in the finite element software and applying 100 V electric field. The strain of the single piezoelectric ceramic sheet is 22.9 E-9 m.

Figure 10 is the strain diagram of a double piezoelectric ceramic sheet under 100 V electric field. The strain of the double piezoelectric ceramic sheets is 45.7 E-9 m.

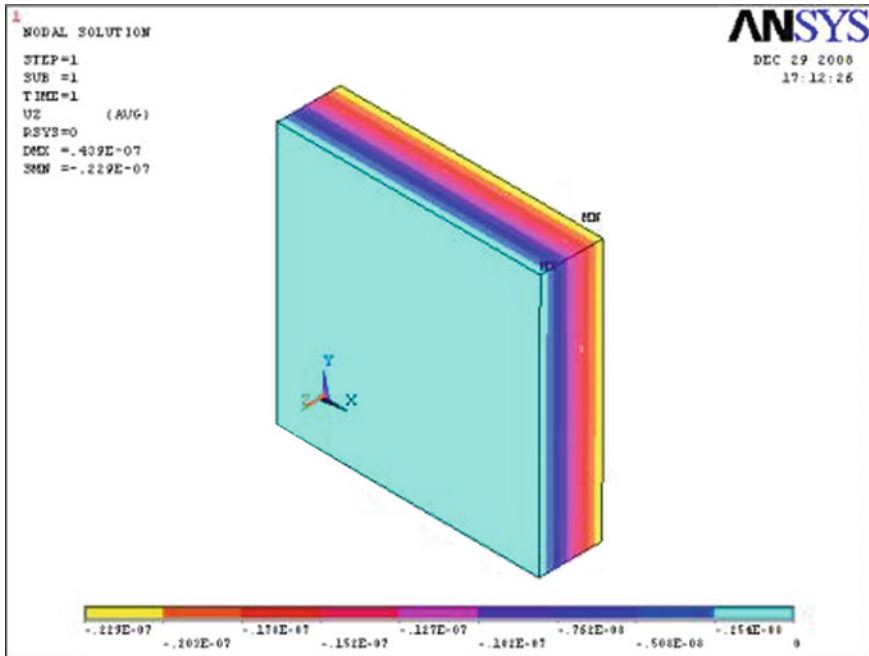


Fig. 9 The strain of a single piezoelectric ceramic sheet

Figure 11 is the strain diagram of a piezoelectric stack (including 10 piezoelectric ceramic sheets) under 100 V electric field. The strain of the double piezoelectric ceramic sheet is 229 E-9 m.

From the calculation results, the deformation of piezoelectric stack is proportional to the number of the sheets.

6 Conclusion

A piezoelectric stack for linear ultrasonic motor is designed. In the sintering condition of 950 °C and 5 h, performance parameters of the developed piezoelectric ceramic, which consisted of $Pb_{0.98}Bi_{0.02}Zr_{0.51}Ti_{0.48}Zn_{0.0103}$ and is doped with 0.5% Co, were relative dielectric constant 1190, piezoelectric constant 270pC/N, electromechanical coupling coefficient 0.54(Kp), 0.46(Kt), Curie temperature 346 °C, dielectric loss angle tangent 0.6%. The displacement characteristics of the piezoelectric stack with different sheets were analyzed by finite element method. The

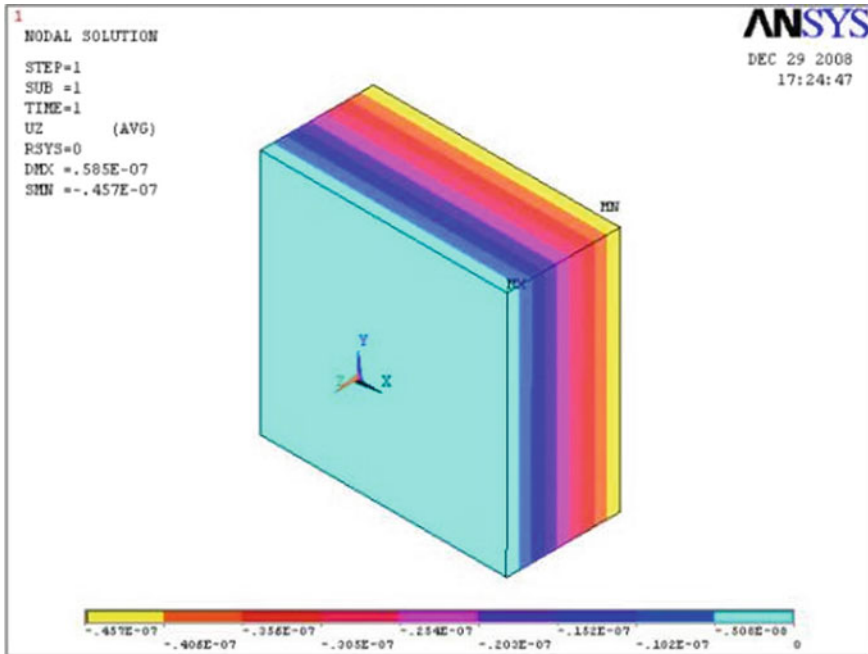


Fig. 10 The strain diagram of a double piezoelectric ceramic sheet

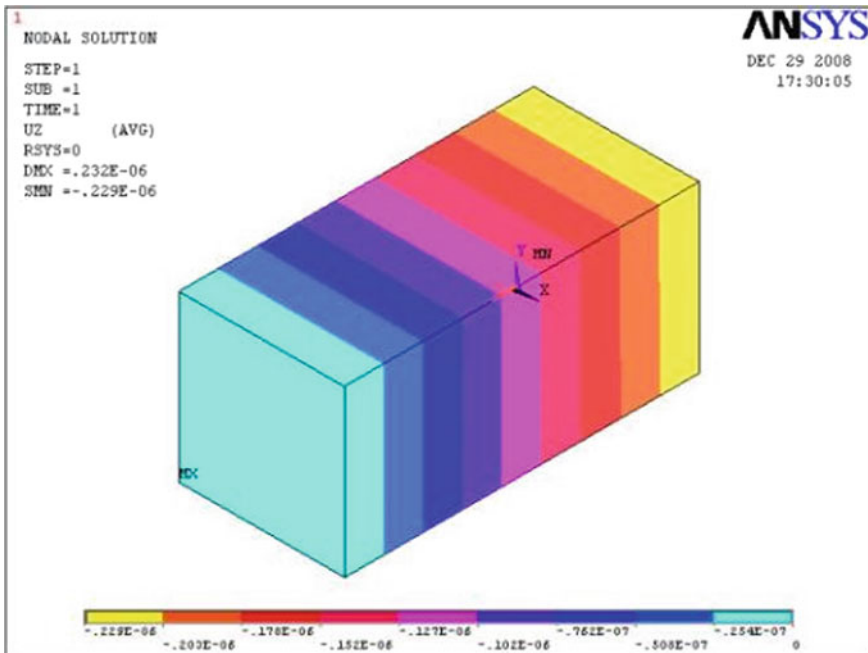


Fig. 11 The strain diagram of a piezoelectric stack

deformation of piezoelectric stack is proportional to the number of the sheets. The research results provided theoretical reference for the development of linear ultrasonic motor with piezoelectric stack.

Acknowledgements This work supported by Suzhou science and technology planning project (SYG201823); Sunzhou vocational university research project (SVU2018YY07); sponsored by Qing Lan Project.

References

1. Li, Z., Zhao, C., Huang, W., Li, Z.-L.: Several key issues in developing of cylinder type 3-DOF ultrasonic motor. *Sens. Actuators A* **136**(2), 704–709 (2007)
2. Zhao, C.: *Ultrasonic Motors Technologies and Applications*. Springer, Berlin Heidelberg (2011)
3. Asumim, K., Fukunaga, R., Fujimura, T., Kurosawa, M.K.: Miniaturization of a V-shape transducer ultrasonic motor. *Japanese J. Appl. Phys.* **48**, 07GM02 (2009)
4. Jeong, S.S., Park, T.G., Park, J.K.: Characteristics of a multilayer one-touch-point ultrasonic motor for high torque. *J. Korean Phys. Soc.* **62**, 995–998 (2013)
5. Wang, H., Zhang, Y., Li, Z., Sun, C.: A V-shaped small linear ultrasonic motor with multilayered Piezoelectric stacks. *Indian J. Eng. Mater. Sci.* **21**(5), 495–499 (2014)

Study on Vibration and Acoustic Characteristics of Ship Stern Structure by Propeller Excitations



Fuzhen Pang, Cong Gao, Haichao Li, and Ruizhao Gu

Abstract Based on the Finite Element Method (FEM) and Boundary Element Method (BEM), the coupled vibration model of propeller-shaft-hull structure is established to analyze vibration and acoustic radiation characteristics by propeller excitations in this paper. The research shows that the vibration response peak of the hull structure is similar to the natural frequency of blade passing frequency (BPF) or stern structure by propeller excitations. The vibration and acoustic radiation is mainly caused by horizontal force and fluctuating pressure. In addition, the vibration response of ship stern structure decreases obviously with the increase of shell thickness, especially in the mid-high frequency band on 100–200 Hz. Furthermore, this study can provide a reference for ship vibration and noise control.

Keywords Ship stern structure · Propeller excitations · Finite element method · Boundary element method · Vibration · Acoustic radiation

1 Introduction

Propeller noise is one of the three major noise sources of the ship, which brings bad influence on comfortable and acoustic performance [1–3]. The propeller excitations are mainly obtained by empirical formula, model test, theoretical calculation or CFD numerical calculation at present. With the development of FEM and BEM, vibration and acoustic radiation analysis of ship obtained a great deal of attention, Zhu et al. [4] studied the influence of propeller unsteady excitation on ship by FEM, in their opinion, the influence of propeller excitation on ship vibration enhanced with the increase of speed. In addition, Li [5] applied the FEM/BEM to analyse the characteristics of vibration and underwater radiated noise of hull structure caused by different forms of propeller excitation, at the same time, the influence of shafting

F. Pang · C. Gao (✉) · H. Li · R. Gu
College of Shipbuilding Engineering, Harbin Engineering University, Harbin 150001,
People's Republic of China
e-mail: congao@hrbeu.edu.cn

alignment state and hull deformation on vibration and sound characteristics was presented. The fluid-solid coupling theory [6, 7] and finite element power flow theory [8] were also used for coupled vibration characteristic analysis of shaft-propeller-shell. In terms of experiment, Pan et al. [9] explored the mechanism of propeller longitudinal excitation transmission to thrust bearing support structure and considered that the liquid film stiffness of thrust bearing is related to shaft speed.

It should be mentioned that above researches comprehensively focus on the formation and transmission characteristics of propeller unsteady excitation and its influence on hull vibration. However, there are few studies on the vibration and acoustic characteristics of surface vessels under propeller excitations, in particular, the research on propeller excitation influence in different directions is insufficient. And the calculation accuracy can be improved by acoustic-structure coupling method.

In this paper, the FEM/BEM is applied to analyse vibration and acoustic characteristics of ship stern structure in middle and low frequency bands by propeller excitations, the vibration and acoustic characteristics is analysed based on acoustic-structure coupling theory. The ship stern model is a truncated structure and the influence of fluid on structure is considered by establishing flow field. The excitation source is mainly divided into bearing force and fluctuating pressure, and the unsteady load of propeller is calculated by CFD. On this basis, the mainly component of the stern structure vibration has been explored. In addition, the influence of shell thickness and section size on the vibration characteristics of the structure is presented.

2 Theoretical Foundation and Propeller-Shaft-Hull Model

2.1 The Finite Element Theory of Structure-Acoustic Coupling

The finite element equation matrix of sound field in the fluid region is as follows:

$$\mathbf{M}_f \ddot{\mathbf{P}} + \mathbf{C}_f \dot{\mathbf{P}} + \mathbf{K}_f \mathbf{P} + \rho_f \mathbf{R} \ddot{\mathbf{U}} = \mathbf{0} \quad (1)$$

where \mathbf{M}_f is the equivalent mass matrix of the fluid; \mathbf{C}_f is the sound damping matrix; \mathbf{K}_f is equivalent stiffness matrix of fluid; \mathbf{R} is the fluid and structure coupling matrix; \mathbf{P} is the node sound pressure matrix; $\ddot{\mathbf{U}}$ is the second derivative of displacement.

The coupled vibration matrix equation between hull structure and acoustic field is as follows:

$$\mathbf{M}_s \ddot{\mathbf{U}} + \mathbf{C}_s \dot{\mathbf{U}} + \mathbf{K}_s \mathbf{U} = \mathbf{F}_s + \mathbf{F}_f \quad (2)$$

where \mathbf{M}_s is the mass matrix of ship structure; \mathbf{C}_s is the damping matrix of ship structure; \mathbf{K}_s is stiffness matrix of ship structure; \mathbf{F}_s is the force vector of ship structure.

The above two equations are combined to obtain:

$$\begin{pmatrix} \mathbf{M}_s & \mathbf{0} \\ \rho_f \mathbf{R} & \mathbf{M}_f \end{pmatrix} \begin{Bmatrix} \ddot{\mathbf{U}} \\ \ddot{\mathbf{P}} \end{Bmatrix} + \begin{pmatrix} \mathbf{C}_s & \mathbf{0} \\ \mathbf{0} & \mathbf{C}_f \end{pmatrix} \begin{Bmatrix} \dot{\mathbf{U}} \\ \dot{\mathbf{P}} \end{Bmatrix} + \begin{pmatrix} \mathbf{K}_s & -\mathbf{R}^T \\ \mathbf{0} & \mathbf{K}_f \end{pmatrix} \begin{Bmatrix} \mathbf{U} \\ \mathbf{P} \end{Bmatrix} = \begin{Bmatrix} \mathbf{F}_s \\ \mathbf{0} \end{Bmatrix} \quad (3)$$

By discretizing coupling matrix equation between ship structure and fluid, the displacement and the sound pressure at the structure surface can be obtained.

2.2 The Introduction of Model

Figure 1 shows the FEM/BEM models of stern structure, which is from transverse bulkhead to ship stern, and the propulsion shafting is cut from thrust bearing base. The model is 23 m, including 4 transverse bulkheads and 3 decks, and the diameters of two propellers are 5 blades, which speed are 110 r/min and simplified as concentrated mass points. The flow field is divided into internal flow field and external flow field, the non-reflecting boundary condition is set at truncation of flow field, and the grid is set as acoustic unit type. The hull structure is connected with surrounding flow field by coupling. The calculated frequency band is 10–200 Hz, of which interval is $\Delta f = 2$ Hz.

2.3 Load and Examination Point

Propeller bearing force is mainly divided into thrust, horizontal, vertical force and fluctuating pressure, the influence of bending moment on structural acoustic vibration characteristics is not considered in this study.

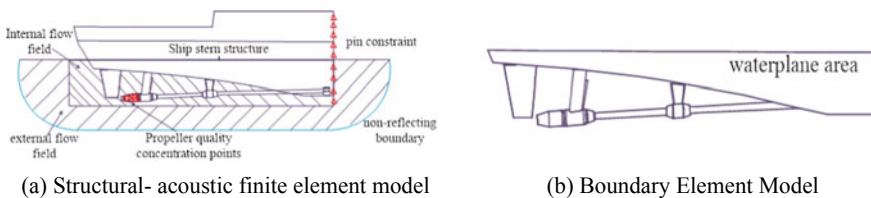


Fig. 1 The FEM/BEM model

Figure 2 presents the frequency domain curve of propeller bearing force, the blade passing frequency is $f = 9n$ Hz ($n = 1, 2, 3 \dots$). It can be seen that the propeller bearing force has a peak at blade passing frequency.

As shown in Fig. 3, the thrust, horizontal and vertical force are respectively represented by f_y, f_x and f_z , the fluctuating pressure is loading on two red areas right above the propeller, and the area is the square of the propeller’s diameter. The sound pressure examination point is 1000 m away from starboard side to reflect the far field characteristics. In addition, the acoustic field plane is 300×300 m at water plane area.

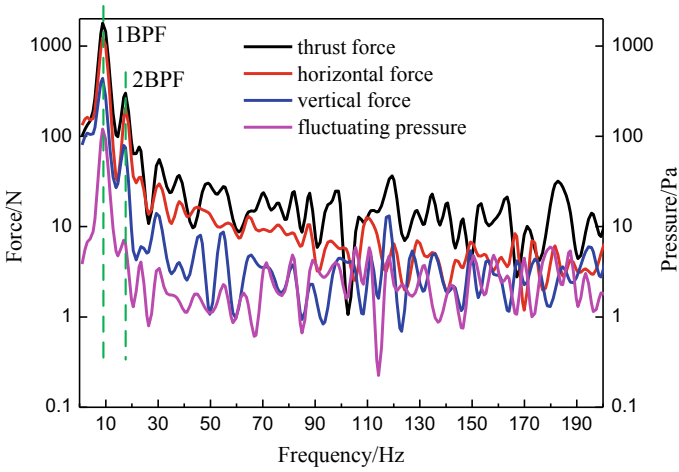


Fig. 2 Frequency domain curve

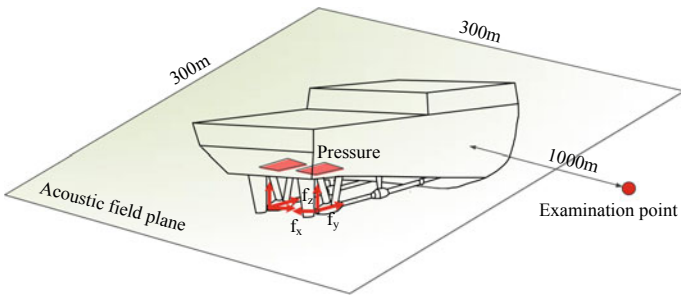


Fig. 3 Loading and examination point

3 Vibration Characteristics of Ship Stern Structure

3.1 The Wet Modes of Ship Stern Structure

The natural frequencies of typical wet modes are shown in Fig. 4, it can be seen that shafting has a higher probability of producing modes. In addition, the frequency of 1 step horizontal and vertical vibration wet mode of shafting are similar to propeller 1BPF and 2BPF respectively, which can cause resonance in structure easily.

3.2 Analysis of Vibration Responses of Stern Structure by Propeller Excitations

In this paper, the mean square vibration speed level is used as the evaluation standard to measure structural vibration, the expression is shown below:

$$L_v = 20 \lg(v/v_0) \tag{4}$$

where L_v is the mean square vibration speed level; v is the mean square vibration speed; v_0 is the reference value of mean square vibration speed, which usually taken as 10^{-9} m/s. The total level of the mean square vibration speed is defined as follows:

$$L_{v\text{total}} = 10 \lg \left(\sum_1^n 10^{L_{vi}/10} \right) \tag{5}$$

From above analysis, it is known that horizontal and vertical mode of shafting are easier to produce, Fig. 5 shows mean square vibration speed level curve of propeller excitations. The total level of thrust force, horizontal force, vertical force, fluctuating pressure and resultant force are $c + 59.3$ dB, $c + 67.3$ dB, $c + 58.3$ dB, $c + 66.9$ dB and $c + 71.2$ dB respectively, in which c is the reference value of the total level. It is horizontal force and fluctuating pressure that mainly cause the vibration of ship stern structure. The curve peaks highest at 18 Hz, which is corresponding to 1 step vertical vibration mode of shafting.

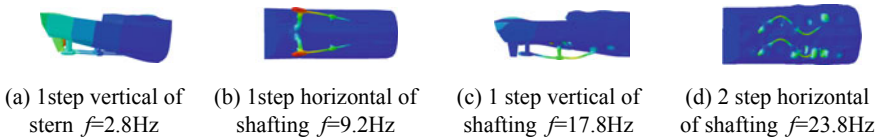


Fig. 4 Diagrams of typical modes

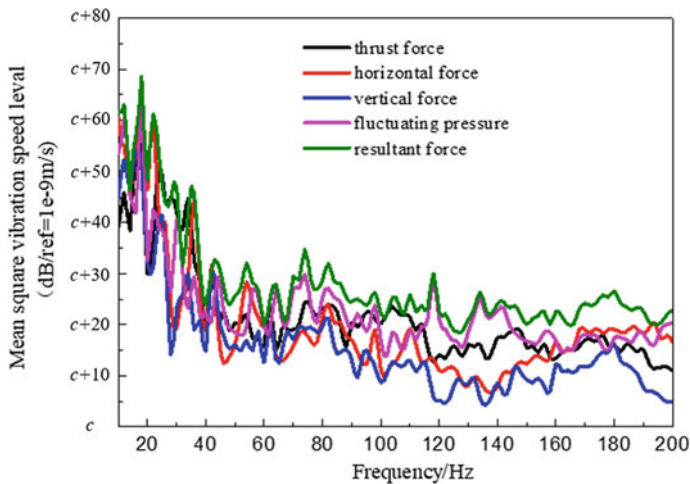


Fig. 5 Mean square vibration speed level curve

3.3 *Vibration Characteristics of Stern Structure by Propeller Excitations*

Figure 6 shows the vibration response nephograms of 18 Hz (peak) in different propeller excitations. It can be seen that the vertical vibration of boat-motherboard is easier to produce by thrust force, and horizontal force generates the horizontal vibration of shafting. The vertical vibration of shafting and boat-motherboard is easier to produce by vertical force, and the fluctuating pressure generates the large area of vertical vibration in boat-motherboard.

3.4 *Study on Vibration Responses of Ship Stern Structure with the Variation of Structure Size*

It is apparently that the vibration on boat-motherboard is easy to produce from above analysis. Therefore, it is necessary to figure out the influence on the vibration characteristics of changing the shell thickness and section size of boat-motherboard. Figure 7 indicates the mean square vibration speed level curve with the variation of shell thickness and section size. It is clearly that the vibration response of the ship stern structure decreases obviously with the increase of shell thickness, especially in the mid-high frequency band on 100–200 Hz. For each 2 mm increase in shell thickness, the total level vibration of mean square vibration speed decreases by about 1 dB. The vibration response of the ship stern structure has a tendency to decrease with the increase of section size. However, the effect is not obvious, the total level vibration of mean square vibration speed decreases by 3 dB with the section size increased from minimum to maximum (Table 1).

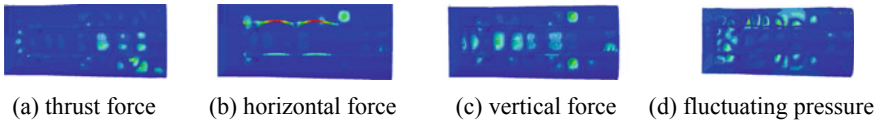


Fig. 6 Vibration response nephograms of $f = 18$ Hz

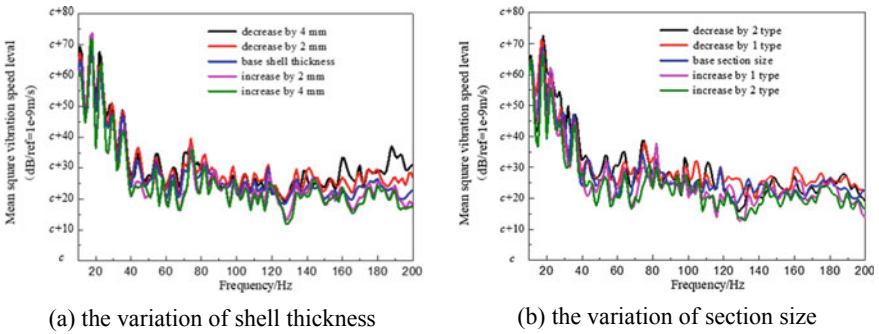


Fig. 7 Mean square vibration speed level curve

Table 1 Total level of mean square vibration speed with different structure size

The variation of shell thickness	Decrease by 4 mm	Decrease by 2 mm	Base shell thickness	Increase by 2 mm	Increase by 4 mm
Total level of mean square vibration speed	$c + 74.2$ dB	$c + 73.6$ dB	$c + 71.2$ dB	$c + 70.5$ dB	$c + 99.3$ dB
The variation of section size	Decrease by 2 type	Decrease by 1 type	Base section size	Increase by 1 type	Increase by 2 type
Total level of mean square vibration speed	$c + 73.1$ dB	$c + 72.4$ dB	$c + 71.2$ dB	$c + 70.8$ dB	$c + 70.1$ dB

4 Acoustic Radiation Characteristics of Ship by Propeller Excitations

4.1 Source Level

In this paper, the source level is used as the evaluation standard to measure structural acoustic radiation, the expression is shown below:

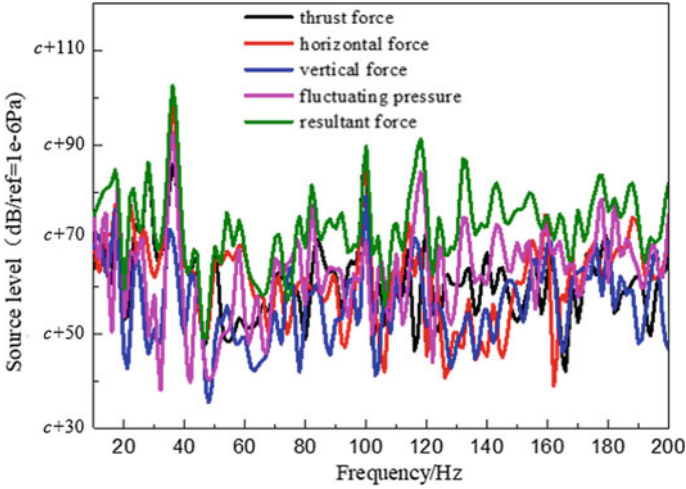


Fig. 8 Source level curve

$$L_s = 20 \lg(p/p_0) + 20 \lg r \quad (6)$$

where L_s is the source level; p is sound pressure; p_0 is the reference value of sound pressure, which usually taken as 10^{-6} Pa; r is distance from sound pressure examination point to structure. The formula of the total source level refers to the total level of the mean square vibration speed. Figure 8 shows source level curve of different propeller excitations, the amplitude of source level curve is mainly concentrated in 10–40 Hz, and the total level of thrust force, horizontal force, vertical force, fluctuating pressure and resultant force are $c + 92.1$ dB, $c + 98.8$ dB, $c + 83.8$ dB, $c + 94.5$ dB and $c + 103.9$ dB respectively, it is horizontal force and fluctuating pressure that mainly cause the acoustic radiation of stern structure.

4.2 Distribution of Sound Pressure Amplitude Along Ship Length

Figure 9 shows the distribution of sound pressure amplitude along ship length of 18 Hz (peak) in different propeller excitations. The abscissa in the figure is the longitudinal angle (θ) of the flow field relative to the ship, the direction is defined as the bow is 0° and the stern is 180° . It can be seen from the picture that the peak value appears under the bearing base by the action of thrust and horizontal force, while that appears under the propeller by the action of vertical force, fluctuating pressure and resultant force. It indicates that the thrust and horizontal force have a

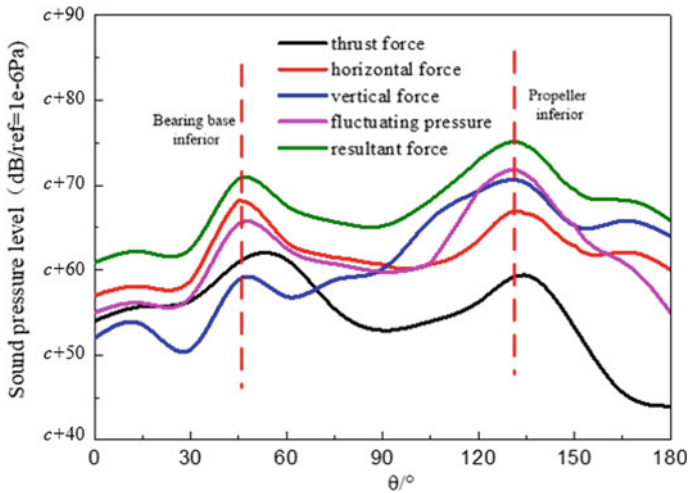


Fig. 9 Distribution of sound pressure amplitude along ship length

great influence on the propulsion shafting, which will cause the acoustic radiation of the stern shaft. In addition, the acoustic radiation caused by propeller is more pronounced under the vertical force, fluctuating pressure and resultant force.

5 Conclusion

The coupled vibration model of propeller-shaft-hull structure is established based on FEM/BEM method, and the vibration and acoustic characteristics of ship stern structure in middle and low frequency bands is analyzed on the basis of acoustic-structure coupling theory. The conclusions are as follows:

1. The frequency of 1 step horizontal and vertical vibration wet mode of shafting are similar to the propeller 1BPF and 2BPF respectively, which cause resonance in structure easily. The curve peaks highest at 18 Hz, which is corresponding to 1 step vertical vibration mode of shafting.
2. The horizontal force and fluctuating pressure mainly cause the vibration and acoustic radiation of stern structure.
3. The vibration response of ship stern structure decreases obviously with the increase of shell thickness, especially in the mid-high frequency band on 100–200 Hz. The section size has a little effect on the vibration response of the ship stern structure.
4. The thrust and horizontal force have a great influence on the propulsion shafting, which will cause the acoustic radiation of the stern shaft. In addition, the acoustic radiation caused by propeller is more pronounced under the vertical force, fluctuating pressure and resultant force.

References

1. Hua, H.X., Yu, Q.: Structural and acoustic response due to excitation from ship stern: overview and suggestions for future research. *Chinese J. Ship Res.* **12**, 6–16 (2017)
2. Merz, S., Kinns, R., Kessissoglou, N.: Structural and acoustic responses of a submarine hull due to propeller forces. *J. Sound Vib.* **325**, 266–286 (2009)
3. Pang, F.Z., Song, H.B., Miao, X.H., Wang, X.R.: Impedance analysis method applied in underwater acoustic radiation analysis of ships. *J. Vibr. Shock* **35**, 17–22 + 27 (2016)
4. Zhu, L., Pang, F.Z., Kang, F.F.: Analysis of vibration characteristics of ships under propeller excitation. *Shipbuilding China* **52**, 8–15 (2011)
5. Li, L.Y.: *Research on Propeller-Induced Ship Hull Vibration and Underwater Radiated Noise*. Harbin Engineering University, Harbin (2016)
6. Zhao, C.S., Lou, J.J., He, Q.W.: Effect of support length of stern tube bearing on vibra-acoustic radiation of underwear structure. *J. Naval Univ. Eng.* **27**(04), 11–16 (2015)
7. Li, X.J., Zhu, H.H., Xiong, W., Wu, J.D.: Coupled vibration characteristic analysis of shaft-propeller system of ship based on fluid structure interaction. *Ship Sci. Technol.* **39**(13), 19–23 (2017)
8. Liu, J.L., Lai, G.J., Cai, Y.Q., Zeng, F.M.: Research on propeller-shafting-hull coupling vibration performance based on power flow finite element method. *Shipbuilding China* **58**(02), 68–77 (2017)
9. Pan, J., Farag, N., Lin, T.: Propeller induced structural vibration through the thrust bearing. In: *Acoustics 2002-Innovation in Acoustics and Vibration*. Adelaide, Australia: Annual Conference of the Australian Acoustical Society, 2002, pp. 390–399 (2002)

Nonlinear Wave Loads' Prediction on Ultra Large Containerships



Xiaoyu Li, Kaihong Zhang, Huilong Ren, and Sijun Chen

Abstract The importance of hydroelasticity analysis of large and flexible container ships of today has been pointed out for structure design. Because of the increases of the size of container ships, whipping phenomena has been one of the important design considerations. This paper introduced a 3D nonlinear hydroelasticity theory which utilizes a 3-D Green function method and a 2-D momentum model coupled in time domain. A model system for measurement of nonlinear wave loads which is composed of a backbone and segmented container ship model has been already established, and applied to a series of large ship models, in which natural frequency of vertical bending is matched using a beam. A series of model tests have been carried out for selected cases of whipping in irregular waves. The computational results were compared with those of a model test of a 10,000-TEU containership. The Verifications and validations between model tests result and theoretical calculation have been carried out. The asymmetry of wave elevation, vertical ship motion and vertical sectional loads responses are mainly discussed, they are observed and calculated in irregular wave conditions, and the experimental results accord with simulated results, basing on which the design vertical bending moment at midship can be obtained by using the nonlinear short-term and long-term analysis, and the comparison between direct calculation and classification society rules is carried out, which has much in common.

Keywords Hydroelasticity · Slamming · Irregular sea state · Time-domain · Wave loads' prediction

X. Li (✉)

Poly Ship Technologies (Beijing) Co., Ltd., Beijing 100010, China
e-mail: xy_li8@163.com

K. Zhang · H. Ren · S. Chen

College of Shipbuilding Engineering, Harbin Engineering University, Harbin 150001, China

© The Author(s), under exclusive license to Springer Nature Switzerland AG 2021

115

L. Zheng et al. (eds.), *Proceedings of MEACM 2020*,

Mechanisms and Machine Science 99,

https://doi.org/10.1007/978-3-030-67958-3_13

1 Modeling of Nonlinear Wave

1.1 Diffraction Forces

$$\zeta_{x,y,t} = \sum_{n=1}^{\infty} (\zeta_a)_n \cos[(\omega_e)_n t + (k_0)_n x \cos \beta - (k_0)_n y \sin \beta + \varepsilon_n] \quad (1)$$

transfer functions can be used to generate a time history of the diffraction forces on different mode. The diffraction forces in harmonic waves are calculated by 3D panel method as follows:

$$F_{D^r}^t = \int_{-\infty}^{\infty} h_{D^r}^r(t - \tau) \zeta(\tau) d\tau \quad h_{D^r}^r(t) = \frac{1}{\pi} \int_0^{\infty} h_{D^r}^r(i\omega) e^{i\omega t} d\omega \quad (2)$$

where $F_{D^r}^t$ is the r -th time history diffraction force component, which can be obtained by convolution with the impulse response function $h_{D^r}^r(t - \tau)$ and wave elevation time history $\zeta(\tau)$, the integration variable t is from $-\infty$ to ∞ . The impulse response function $h_{D^r}^r(t - \tau)$ can be calculated from the frequency diffraction force transfer function $H_{D^r}^r(i\omega)$, by means Fourier analysis.

The Froude-Krylov part is related to the incident wave potential and results, they are from the integration at each time step of the associated pressure over the instantaneous wetted surface of the ship hull under the undisturbed wave profile, when nonlinearity is not included, the instantaneous wetted surface return to the mean wetted surface:

$$F_{I^r}^t = -\rho \sum_{i=1}^{\infty} (\zeta_a)_n \iint_{S(t)} (\vec{n} \cdot \vec{u}_r) \left[i(\omega_e)_n - U \frac{\partial}{\partial x} \right] (\phi_I)_n ds \quad (3)$$

where \vec{n} is the unit normal vector of each panel, which positive direction is to the inner part of the ship hull, \vec{u}_r denotes the r -th principle mode shape vector associated with the dry structure, which can be obtained by Transfer Matrix Method.

In linear theory of harmonic waves, the wave pressure is defined up to the mean waterline ($z = 0$) and will not spread upward. So when the crests pass through the hull, an approximation is assumed to account for the wave pressure above the mean waterline. It is supposed that the pressure is zero at the free surface, and it is hydrostatic between the free surface and $z = 0$.

1.2 Restoring Forces

When considering the nonlinear restoring forces, the instantaneous position should be collected at each time step. After this, the r -th restoring force can be obtained by

integration of the hydrostatic pressure over the wetted hull under the undisturbed free surface, and then minus the constant origin gravity force.

$$F_{S_t}^r = \iint_{S(t)} \bar{n} \cdot \bar{u}_r p_s ds - F_G^r$$

$$p_s = -\rho g [p_3(t) - xp_5(t) + yp_4(t)]$$

$$F_G^r = \int_L F_g(x_b) w_r(x_b) dx_b \quad (4)$$

When nonlinearity is not included, the instantaneous wetted surface return to the mean wetted surface, thus the restoring forces' calculation return to the restoring matrix multiplied by the principal coordinate column vector.

1.3 Radiation Forces

The radiation forces, which are calculated using 3D panel method, are represented in the time domain by infinite frequency added mass μ_{rs} , damping B_{rs} and radiation restoring coefficients C'_{rs} , and convolution integrals of retardation functions $K_{rs}(t)$, which are all considering velocity and radiation force memory effects.

$$F_{R_t}^r = - [\mu] \{\ddot{p}(t)\} - [B] \{\dot{p}(t)\} - [C'] \{p(t)\} - \int_0^t [K(t-\tau)] \{\dot{p}(\tau)\} d\tau$$

$$= - \sum_{s=1}^m [\mu_{rs} \ddot{p}(t) + B_{rs} \dot{p}(t) + C'_{rs} p(t)] - \sum_{s=1}^m \int_0^t K_{rs}(t-\tau) \dot{p}_s(\tau) d\tau \quad (r = 1, 2, \dots, m) \quad (5)$$

where the infinite frequency added mass μ_{rs} , damping B_{rs} and radiation restoring coefficients C'_{rs} , and convolution integrals of retardation functions $K_{rs}(t)$ are calculated separately as follows.

$$\mu_{rs} = \rho \iint_{S_H} (\bar{u}_r \cdot \bar{n}) \Psi_{1s} ds$$

$$C'_{rs} = \rho \left\{ -U_0 \iint_{S_H} (\bar{u}_r' \cdot \bar{n}') \cdot \Psi_{2s} ds + \int_{wl} (\bar{u}_r \cdot \bar{n}) [(l \times n) \cdot \bar{W}] \Psi_{2s} dl \right\}$$

$$\begin{aligned}
B_{rs} &= \rho \left\{ \iint_{S_H} (\bar{u}_r \cdot \bar{n}) \Psi_{2s} ds - U_0 \iint_{S(t)} (\bar{u}_r' \cdot \bar{n}) \cdot \Psi_{1s} ds + \int_{wl} (\bar{u}_r \cdot \bar{n}) [(l \times n) \cdot \bar{W}] \Psi_{1s} dl \right\} \\
K_{rs}(t) &= \rho \left\{ \iint_{S_H} (\bar{u}_r \cdot \bar{n}) \frac{\partial}{\partial t} \bar{\chi}_s(p, t) ds - U_0 \iint_{S_H} (\bar{u}_r' \cdot \bar{n}) \cdot \bar{\chi}_s(p, t) ds + \int_{wl} (\bar{u}_r \cdot \bar{n}) [(l \times n) \cdot \bar{W}] \bar{\chi}_s dl \right\}
\end{aligned} \tag{6}$$

For the unknown ψ_{1s} , ψ_{2s} and $\bar{\chi}_s(p, t)$, the governing equation, boundary and initial condition are shown respectively as follows. relative velocity between the

$$\begin{cases} \nabla \Psi_{1s} ds = 0 (\text{influid}) \\ \Psi_{1s} = 0 (\text{on } S_F) \\ \frac{\partial \Psi_{1s}}{\partial n} = \bar{u}_s \cdot \bar{n} (\text{on } S_H) \\ \Psi_{1s} = O(r^{-2}) (r \rightarrow \infty) \end{cases} \begin{cases} \nabla^2 \Psi_{2s} = 0 (\text{influid}) \\ \Psi_{2s} = 0 (\text{on } S_F) \\ \frac{\partial \Psi_{2s}}{\partial n} = U_0 (\bar{u}_s \cdot \bar{n}) (\text{on } S_H) \\ \Psi_{2s} = O(r^{-2}) (r \rightarrow \infty) \end{cases} \tag{7}$$

$$\begin{cases} \nabla^2 \bar{\chi}_s(p, t) = 0 & (\text{influid}) \\ \left[\left(\frac{\partial}{\partial t} - U_0 \frac{\partial}{\partial t} \right)^2 + g \frac{\partial}{\partial z} \right] (\bar{\chi}_s + \psi_{2s}) & (\text{on } S_F) \\ \frac{\partial \bar{\chi}_s}{\partial n} = 0 & (\text{on } S_F) \\ \bar{\chi}_s|_{t=0} = 0 \quad \frac{\partial \bar{\chi}_s}{\partial t} \Big|_{t=0} = -g \frac{\partial \psi_{1s}}{\partial z} & (\text{on } S_F) \end{cases}$$

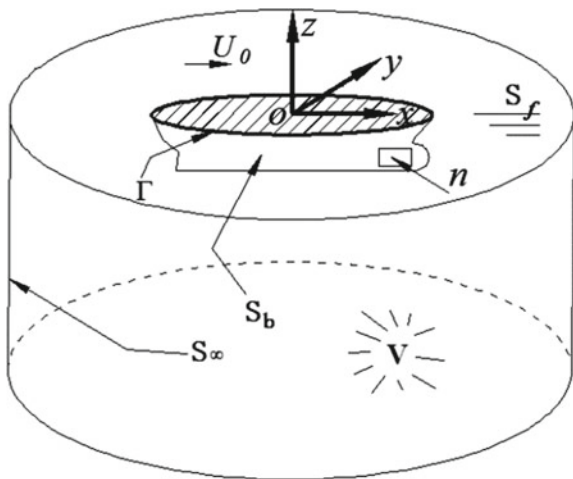
When considering the retardation function in time domain, Ogilvie [1, 2] had pointed out the relationship between $K_{rs}(t)$ and the 3D hydrodynamic coefficients in frequency domain that can be expressed as follows.

$$\begin{aligned}
K_{rs}(t) &= \frac{2}{\pi} \int_0^\infty \omega [\mu_{rs} - A_{rs}(\omega)] \sin \omega t d\omega \text{ or } K_{rst} \\
&= \frac{2}{\pi} \int_0^\infty [B_{rs}(\omega) - B_{rs}] \cos \omega t d\omega
\end{aligned} \tag{8}$$

where $A_{rs}(\omega)$ and $B_{rs}(\omega)$ represent the 3D hydrodynamic coefficients, the generalized hydrodynamic inertial matrix and damping matrix components, respectively.

For the frequency diffraction force transfer function $H_D'(i\omega)$, 3D hydrodynamic coefficients $A_{rs}(\omega)$ and $B_{rs}(\omega)$, the governing equation and boundary condition are shown respectively as follows, see Fig. 1.

Fig. 1 Fluid domain and boundary condition



$$\left\{ \begin{array}{ll} \nabla^2 \varphi_j = 0; & \text{in } V \\ \omega^2 \varphi_j + g \frac{\partial \varphi_j}{\partial z} = 0; & \text{at } z = 0 \\ \frac{\partial \varphi_j}{\partial n} \begin{cases} [i\omega \bar{u}_j + (-U \frac{\partial}{\partial x}) \bar{u}_j] \cdot \bar{n} & \text{with } j = 1, 2, \dots, m \\ -\frac{\partial \varphi_j}{\partial n}; & \text{for } j = 1 + m \end{cases} & \\ \begin{cases} \frac{\partial \varphi_j}{\partial z} = 0; \\ \nabla \varphi_j = 0 \end{cases} & \begin{array}{l} \text{with } Z = -h \\ \text{with } Z \rightarrow \infty \end{array} \\ \lim_{R \rightarrow \infty} \sqrt{R} \left(\frac{\partial \varphi_j}{\partial R} - ik_0 \varphi_j \right) = 0 & \end{array} \right. \quad (9)$$

where φ_j is the potential of the j -th motion mode, in order to calculate in the future, here $m = 9$ was selected to reduce infinite modal number to limited modal number with sufficient accuracy.

After solving the boundary integral equations, the potential φ_j can be obtained, thus the 3D hydrodynamic coefficients $A_{rs}(\omega)$ and $B_{rs}(\omega)$ can be express as follows.

$$\left\{ \begin{array}{l} A_{rs}(\omega) = \frac{\text{Re}(H_{rs})}{\omega^2} \\ B_{rs}(\omega) = \frac{\text{Im}(H_{rs})}{\omega} \\ H_{rs} = -\rho \iint_{S_0} \bar{n} \cdot \bar{u}_r - (i\omega - U \frac{\partial}{\partial x}) \varphi_s ds \end{array} \right. \quad (10)$$

The frequency diffraction force transfer function $H_D^r(i\omega)$ can be express as follows.

$$H_D^r = -\rho \zeta_a \iint_{S_0} \left(i\omega - U \frac{\partial}{\partial x} \right) \varphi_a ds \text{ with } r = 1, 2, \dots, m \quad (11)$$

The formulation presented the contribution for the vertical shear force, and bending moment of the radiation forces which may be calculated in the time domain for non-harmonic motions, accounting in a proper way the memory effects of the past history of the fluid motion.

1.4 Slamming Forces

The vertical forces associated with large bow flare and the large relative velocity between bow section and incoming wave, which occurs when the relative velocity is larger than the critical velocity, are calculated using the momentum method. The vertical force per unit length is:

$$F_f(x_b, t) = \begin{cases} \frac{dm_\infty}{dz} \left(\frac{dZ_R}{dt} \right)^2 & \frac{dZ_R}{dt} < V_{cr} \\ 0 & \frac{dZ_R}{dt} > 0 \end{cases} \quad (12)$$

where m_∞ is the added mass of the 2D section moving in vertical direction at infinite frequency using conformal mapping method and dm_∞/dz is the derivative of m_∞ with respect to the draft, and Z_R is the vertical relative motion between 2D section and wave and dZ_R/dt is the relative velocity between the 2D section and wave [3, 4].

The r-th component of generalized slamming force column matrix is expressed using an integration of slamming force along the ship length, at each instant time point with the section submerged under corresponding wave profiles.

$$F_{slam}^r(t) = \int_L F_f(x_b, t) w_r(x) dx_b \quad (13)$$

As for the wave loads calculation under severe sea state, nonlinear factors would be very important, for instance, incident wave force nonlinearity, restoring force nonlinearity and slamming force nonlinearity. In addition, the large amplitude motion can cause instantaneous wetted surface nonlinearity and hydrodynamic force nonlinearity. Nevertheless, the radiation force and the diffraction force should be calculated on the mean wetted surface because these two terms contribute less than the three main nonlinear factors.

2 Statistical Analysis

2.1 *Nonlinear Short-Term and Long-Term Statistical Analysis*

The procedures of direct calculation often include the calculation of wave loads in stochastic seas using a proper hydrodynamic theory, and the prediction of extreme wave loads following reliable stochastic analysis procedures.

A common way for predicting extreme wave loads is long-term analysis. That is, the ship is assumed to be exposed to a large number of short-term sea states during its lifetime, and the long-term extreme wave load is established as a weighted sum of all the short-term wave loads induced by the short-term sea states. Clearly, a complete long-term procedure demands tremendous computation, and a simplified procedure is desirable.

The method for analyzing short-term wave load statistics often depends on whether the wave load is linear, slightly nonlinear, or strongly nonlinear. Wave loads with strong nonlinear characteristics, especially when they involve transient slamming effects, have to be solved in time domain, and the statistical analysis is generally carried out on the wave load time histories.

Unlike the linear case where the wave load process is Gaussian and the peak values theoretically follow Rayleigh or Rice distribution depending on the wave load bandwidth, for nonlinear wave load, there is no theoretical distribution of the peak values. Several empirical probability distributions have been used for modeling of wave load peak values, such as the Generalized Gamma Distribution [5] and the Weibull distribution [6, 7]. A Weibull distribution then offers advantages because it can specialize into an exponential distribution as well as Rayleigh distribution, which is relevant to linear responses. Thus, in this paper, we choose Weibull distribution as the target distribution of short-term and long-term distribution.

Weibull distribution. The cumulative distribution function (CDF) of Weibull distribution is given by

$$F_{\text{slam}}^r(t) = \int_L F_f(x_b, t) w_r(x) dx_b \quad (14)$$

where η , β and δ are, respectively, the scale, shape and shift parameter. The Rayleigh and exponential distributions are both special cases of Weibull distribution, corresponding to $\beta = 2$, $\delta = 0$, and $\beta = 1$, $\delta = 0$, respectively.

2.2 Nonlinear Short-Term Statistical Analysis

For nonlinear short-term statistical analysis, sufficient sampled data should be prepared, the peak and the trough, separately. Then the Weibull distribution fitting is conducted, by means of maximum likelihood estimate, using the sampled data. Finally, the chi square test is used Weibull distribution test of hypothesis.

Nonlinear Long-term Statistical Analysis. For nonlinear long-term statistical analysis, it is a weighted sum of all the short-term analysis induced by the short-term sea states.

$$\begin{aligned}
 F(x) &= \frac{\sum_i \sum_j \sum_k n_0^* p_i(H_{1/3}, T_z) p_j(\beta) p_k(V) F_{0ijk}(x)}{\sum_i \sum_j \sum_k n_0^* p_i(H_{1/3}, T_z) p_j(\beta) p_k(V)} \\
 f(x) &= \frac{\sum_i \sum_j \sum_k n_0^* p_i(H_{1/3}, T_z) p_j(\beta) p_k(V) F_{0ijk}(x)}{\sum_i \sum_j \sum_k n_0^* p_i(H_{1/3}, T_z) p_j(\beta) p_k(V)}
 \end{aligned} \tag{15}$$

where $p_i(H_{1/3}, T_z)$, $p_j(\beta)$ and $p_k(V)$ are, respectively, the sea state probability, the heading angle probability and the velocity probability, and n_0^* represents the up-crossing ratio of the i -th sea state, $f_{0ijk}(x)$ and $F_{0ijk}(x)$ denote the cumulative distribution function and the probability density function under i -th sea state, j -th heading angle and k -th velocity.

3 Experimental Setup

The tests were conducted at the Laboratory of HEU Towing Tank and the Comprehensive Experimental Basin of the Underwater Robots National Key Laboratory. The Laboratory is a modern facility prepared to conduct seakeeping and maneuvering tests of ship models and offshore structures. The tank is 108 m long, 7 m wide, and 3.5 m deep, and the basin is 50 m long, 30 m wide, and 10 m deep. The wave generator is able to produce regular waves and irregular waves.

A 10,000 TEU containership was considered in the present experimental study. The ship model is a geometrically similar as the prototype. The model was made of glass fiber reinforced plastics with wooden base and was divided into seven segments in which six segments are with equal length from station No.8 to station No.20 and the rest part forms a single segment in order to arrange the self-propelled devices, such as the engine, the transmission mechanism and the propeller shaft sleeves. Each segment was fixed to the rectangular-shape steel backbone which was designed to match structural stiffness and measure section forces. A very soft latex tape which effects on bending stiffness can be negligible was applied to make water tight between segments. The use of water proofing tape should be carefully chosen in order not to induce unwanted interference on the bending stiffness. The vertical induced loads were measured at these positions. Mass distributions of those seven

segments were adjusted for the ballast loading conditions according to the assigned weight distribution. The radii of gyration of each segmented part and the whole model for pitch and roll were adjusted by using a swing table. CG, k_{xx} and k_{yy} of each segment and the whole model were adjusted within 5% tolerance. Setup configuration and main particulars of the model ship are given in Fig. 2 and Table 1, respectively.

The experimental program mainly focused on the responses in head waves, this is usually the most severe condition with respect to the vertical responses. The absolute motions of this model were measured by Large Amplitude Motion 5-DOF Instrumented Device, which allowed free heave, pitch, roll, surge and sway (in heading wave condition the horizontal motions were restrained), while wave sensors measured the relative motions and the incident wave elevation. Strain gauges were mounted on the steel backbone to measure the vertical shear force and bending moment at each position.

A discussion and limited analysis of the experimental data within this experimental program are given in another paper that deals with the results of tests in regular waves [8]. Because some of the test runs for several wave frequencies distributed along the frequency range were repeated, it was possible to analyze these records and obtain some information on the level of dispersion of the experimental data. The conclusions were that the random experiment errors are very small for the first harmonics and relatively small for the second harmonics and peaks of the structural loads.

For the three sea states, the hogging and sagging Weibull distribution fitting were conducted from the experimental records and the simulated time histories, respectively. The results were listed in Table 2. From the comparisons in Table 2, one can conclude that the numerical model is able to qualitatively capture all nonlinear characteristics of the measured responses, not only for the significant values but also for the distribution fitting values.

Thus, the nonlinear long-term analysis can be carried out based on the good agreement of the distribution parameters' fitting, under both hogging and sagging conditions. The long-term analysis results, which are calculated according to the DNV-GL rules, were listed in Table 3, which is corresponding to the exceeding probability of 10^{-8} . The results show good agreement. However, the direct calculation results were larger than the DNV-GL rules' results for the method may overestimate the loads under some significant sea states and further comparisons should be done to make more verification.

Fig. 2 Layout and setup configuration of model ship

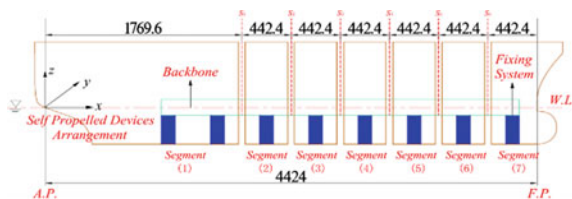


Table 1 Main particulars of model ship

Item	Prototype	Model
Scale	1/1	1/66
LBP (m)	292	4.424
Breadth (m)	48.6	0.736
Height (m)	27.2	0.412
Draft (m)	8.222	0.125
Displacement	70420 Ton	238.97 Kg
LCG from AP (m)	148.86	2.255
k_{xx} (m)	17.01	0.2577
k_{yy} (m)	73	1.106
k_{zz} (m)	73	1.106

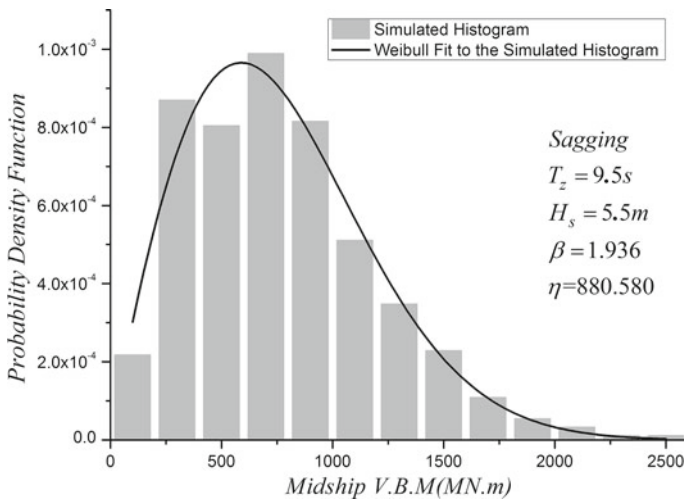


Fig. 3 Weibull shape parameter fitting of V.B.M at midship

Table 2 Weibull shape parameter fitting of V.B.M at midship results from analysis of experimental records and numerical simulated time histories

	Weibull shape parameter of vertical bending moment at midship					
	Sea state1 Hs = 5.5 m Tz = 9.5 s		Sea state2 Hs = 9.5 m Tz = 11.5 s		Sea state3 Hs = 13.5 m Tz = 12.5 s	
	Exp.	Cal.	Exp.	Cal.	Exp.	Cal.
Sagging	1.945	1.936	1.852	1.846	1.709	1.690
Hogging	2.089	2.136	2.307	2.347	2.398	2.545

Table 3 Midship design loads’ comparison between DNV-GL rules and direct calculation for containerships

	Midship design loads’ (V.B.M)	
	DNV-GL rules for containerships	Nonlinear long-term statistical analysis
Sagging (MN.m)	-11,320.2	-13,616.1
Hogging (MN.m)	4490.3	5096.5

4 Conclusions

The paper explained the results of an experimental investigation of the nonlinear effects, which is on the vertical motions and loads on a containership advancing in irregular waves, and comparisons with numerical results from a 3D Nonlinear Time-domain Hydroelasticity Method. In general, one may say that the experimental waves are basically linear, the vertical motions are slightly nonlinear, and the vertical loads are strongly nonlinear. The numerical model will qualitatively capture all nonlinear characteristics of the measured responses. Besides, there are some quantitative discrepancies.

The measured wave is basically linear. However, due to the lightly nonlinear shape of waves, the positive peaks tend to have larger magnitudes than the negative peaks.

Several conclusions concerning the nonlinear characteristics of the responses are taken from the statistical analysis of the records. The magnitudes of heave significant positive peaks tend to be around 10% larger than those of the significant negative peaks. This means that the ship emerges more than submerges. With respect to pitch motion, the ship tends to raise the bow more than to submerge it. The asymmetry of the significant peaks of the vertical shear force at midship is small. However, it is large for the vertical bending moment at midship. In these cases, the significant sagging loads are larger than the corresponding hogging loads. As an example, the vertical bending moment at midship presents magnitudes of sagging significant peaks up to 60% larger than the corresponding hogging peaks. They’re related to the “geometrical nonlinearity” of the hull especially on the bow where the ship has a large flare.

If we compare the experimental data with the results from the numerical model in terms of significant values and mean values, it will be concluded that the numerical model can capture the nonlinear tendencies of the experimental vertical motions and also of the vertical loads.

Based on the good agreement of the distribution parameters’ fitting, the non-linear long-term analysis can be successfully carried out, under both hogging and sagging conditions, and the comparisons between direct calculation and rules show good agreement, however, the direct calculation results were larger than the DNV-GL rules’ results for the method may overestimate the loads under some significant sea states and further comparisons should be done to make more verification.

References

1. Cummins, W.: The impulse response function and ship motions. DTIC Document (1962)
2. Ogilvie, T.F.: Recent progress toward the understanding and prediction of ship motions. In: 5th Symposium on Naval Hydrodynamics, Bergen, Norway (1964)
3. Hermundstad, O.A., Moan, T.: Efficient methods for direct calculation of slamming loads on ships. In: SNAME Annual Meeting (2009)
4. Fonseca, N., Antunes, E., Soares, C.G.: Whipping response of vessels with large amplitude motions. In: 25th International Conference on Offshore Mechanics and Arctic Engineering. American Society of Mechanical Engineers (2006)
5. Ochi, M.K.: Generalization of Rayleigh probability distribution and its application. *J. Ship Res.* **22**(4) (1978)
6. Sagli, G.: Model uncertainty and simplified estimates of long term extremes of hull girder loads in ships. Fakultet for ingeniørvitenskap og teknologi (2000)
7. Wang, L.-h.: Probabilistic analysis of nonlinear wave-induced loads on ships. Department of Marine Structures, Faculty of Marine Technology, Norwegian University of Science and Technology (2001)
8. Zhang, K., Ren, H., Li, H., Yan, L.: Nonlinear hydroelasticity of large container ship. In: 26th Annual International Ocean and Polar Engineering Conference, ISOPE 2016, 26 June 2016–1 July 2016, Rhodes, Greece. International Society of Offshore and Polar Engineers (2016)

The Design of a Backpack System to Meet the Requirements of New Type of Individual Combat



Yu Zhao and Wei-Jie Xu

Abstract According to the requirements of the new type of individual combat, a backpack system design requirement is formed to guide the product design. Method From the new requirements of individual combat, combined with human-machine engineering design and operational requirements, a backpack system design requirement is formed, and a new type of backpack system product design is formed through product design architecture. Result The product is trial-produced based on the design of the backpack system, and the pre-product user experience evaluation is carried out. Conclusion The backpack system products meet the requirements of the new type of individual combat.

Keywords New operational requirements · Human machine engineering · Backpack system

1 Introduction

With the continuous adjustment of international military strategy, it has added relevant requirements for small-team cooperative operations in individual operations, and such tactical requirements have proposed higher positioning for the military literacy and camp equipment of each individual soldier. According to different operational requirements and the use environment of the suspension system, each country has its unique design standards. In China, we lack research on military portable products. For which the design is generally based on the civilian backpack design and the basic ergonomic data, resulting in that the design lacks a detailed design study under the new tactical planning background. Wei-feng Hu [1] researched on the state space analysis of the backrest vibration isolation system of the suspension system from the perspective of mechanics. Yang et al. [2] researched on the design of the portable multifunctional field medicine storage and trans-

Y. Zhao (✉) · W.-J. Xu
No. 36 Research Institute of CETC, Zhejiang Jiaxing 314000, China
e-mail: 314425426@qq.com

portation box from the perspective of ergonomics. Wang [3] researched on the design of the modular lightweight carrying equipment from the perspective of modular thinking. He [4] put forward the functional fabrics for moisture conduction and perspiration. Tian [5] proposed a design plan for an innovative backpack carrying structure based on the human body size and body perception. The main goal is to research on the design requirements suitable for our military portable suspension system and then guide the subsequent product design and combining with our military new product and operational requirements.

2 First Section Suspension System Requirements for New Type Soldiers

2.1 National Military Standard Requirements

With the new training of operational tactics for our army, especially the gradual improvement of the requirements for the individual and small team operation, there are different national military standards for different services and environments. The portable suspension systems are generally concentrated in the communication field. The most representative national military standards direct at the communication field in the new operational system include: (1) GJB5662-2006 general specifications for portable communication countermeasures equipment, (2) GJB6920-2009 ordnance individual carrying equipment series, (3) GJB2667-1996 design requirements for the structure of the portable reconnaissance intelligence equipment. In these national military standard requirements, it has stipulated the detailed requirements for the carrying equipment of portable products. For example, it requires that the carrying equipment shall be made of lightweight, waterproof, mildew proof, and non-reflective materials, and the requirements for the appearance are as the same as the equipment coating color. Meanwhile, it has also stipulated the detailed requirement for the individual operational weapons and equipment in the new type individual operational requirements. The general size of which is about 0.8 m with a weight volume of about 10–20 kg. The requirement for the suspension is that the barycenter should be close to the center of the equipment bottom, equipped with double shoulder straps, chest straps, shoulder pads, waist belts and waist pads.

2.2 Analysis of the New Type Individual Operational Requirements

The analysis in this part is mainly based on the previous investigation, research and analysis of our institute. And the following typical problems current existing at this stage have been concluded after combining with the requirements of the new tactics of our army:

1. The current back pad is too heavy. The common back pad is made of metal steel pipes with large size and overweight characteristics. Meanwhile, it cannot fit the size of the human body. For which the back pad usually separated while using.
2. Diversified model of portable products, resulting in the unmatched size of the back pad and the back pad type, and it cannot achieve the modular universal carrying with so many system accessories.
3. The quick disassembly and assembly cannot be realized when individual soldiers or small teams carry out the tasks.
4. There are certain differences existing in the materials and processes of the military and civilian suspension products. Some of the current military suspension products are designed based on the design features of civilian products, resulting in many problems occurred while using.
5. Relatively high cost. Compared with the foreign Moore back pad, it cannot achieve the goal of the military-civilian suspension system.

3 Research on the Design Strategy of the New Suspension System

3.1 Architecture Requirements for the Suspension System

After organizing the pain points of the current existing suspension system by combining with the new operational requirements, and comparing the design with the U.S. Moore back pad and a certain type of antenna back frame in South Africa, the part in the design of the entire suspension system that needed to be emphasized first was the ergonomics research, followed by the research on the preliminary design materials of the system, and finally research on innovative structural design and unified design thinking. The design point that needed to be reached include:

1. The shape of the portable suspension system should be a streamlined design, and the overall design should be simple and elegant.
2. The suspension system shall overcome the defects such as the stress points of traditional back pad were concentrated on the shoulders. It shall be able to closely follow the curve of the back, and reasonably distribute the weight of the backpack to the shoulders, back and hips of the body.
3. The suspension system should adopt the ergonomic principles, based on the average height of Chinese soldiers and the average suspension size of our products, design the back pad according to the curve of the human back, and according to the characteristics of the neck, shoulders and armpits. to ensure the stability of the barycenter of the shoulder straps and back support.
4. The back ventilation design of the suspension system shall be designed with comparison. It not only required to avoid the damage to the human spine and scapular muscles, but also needed to form an upward back ventilation channel.

5. The suspension system was characterized in performance advantages, such as light weight, high load, wear resistance, portability and easy assembly.

Whether the gravity transmission of the suspension system was reasonable was the key factor for the design of the suspension system. And the solution to this problem required to understand the entire gravity transmission process of the suspension system first. The suspension object was transferred from top to bottom due to the gravity, which was finally concentrated to the lowest fulcrum. In order to make the suspension more comfortable, the position of this fulcrum should be as close as possible to the position of the weight of the suspension person. Therefore, the reasonable shape of the backpack should be large in up and small in bottom with a shape of “V” or inverted trapezoid. Meanwhile, the reasonable design of the suspension system should take the waist as the main force area, and the shoulders as the force area for grasping balance and assistance in order to reduce the force transmission links and the unnecessary physical exertion.

3.2 Research on the Module Loading

In this research, it was necessary to carry the stand-alone and other suspension equipment. In previous designs, such loading was carried out in the form of cloth bags. In this topic, it planned to adopt a buckle-type stand-alone carrying method for design, that is, stand-alone or other equipment can be loaded and used quickly. Firstly, the weight of the entire suspension system was reduced. Secondly, there were no need for users to complete the functional requirements on the backpack with disassembling. In addition, some accessories in the marching process use sub-bags. Under such circumstances, this suspension system not only can save space, but also can be used for the multi-function and multi-purpose operations.

4 Product Design of Suspension System

4.1 Back Pad Design

Referring to the Moore back pad of the US Army and the back pad system of South Africa, it has innovated and designed the back pad system that was suitable for the human body size and project requirements of our country. The back of the back pad was designed strictly in accordance with the human bone curve in the ergonomics, designing a lightweight carbon fiber back frame system suitable for the human body. Considering to satisfy the differentiated needs of military and civilian products of the back pad, it has designed a foldable bottom support in the bottom carrying design, which can be fixed to the buckle of the product. Moreover, according to the ergonomics of the suspension size measurement system method

and based on the average height of our soldiers and the average suspension size of our products, it has designed the following back pad as shown in the figure, which ensured the reasonable weight distribution and the convenience of the suspension method.

The back pad was as shown in the following figure, which was mainly composed of the inclined back pad and the support. The weight was fixed to the six grooves on the inclined back pad. The total weight of the model was 1.3 kg.

The back pad was fixed on the back through the straps fixed on the back pad, which was closely attached to the back. With certain simplification here, the rods at both ends of the back pad were used as fixed constraints. It calculated the stress condition under the background of its own weight and loading 55 kg items. The deformation and stress distribution of the back pad under its own weight were as shown in the following figure. The maximum displacement was 0.02 mm, and the maximum stress was 3.88 MPa, which occurred at the junction of the support and the inclined back pad.

The response of the back pad with 55 kg without touching the support was as shown in Fig. 3. The maximum displacement was 0.4 mm and the maximum stress was 98.2 MPa, which occurred at the connection between the inclined back pad plate and the support rod.

The response of the back pad loaded with 55 kg and placed on the support was as shown in Fig. 4. The maximum displacement was 0.04 mm and the maximum stress was 27.9 MPa, which occurred at the junction of the support and the inclined back pad.

Based on the calculation of the maximum bearing capacity of the back pad, the structure strength and mechanical properties design can meet the design requirements.

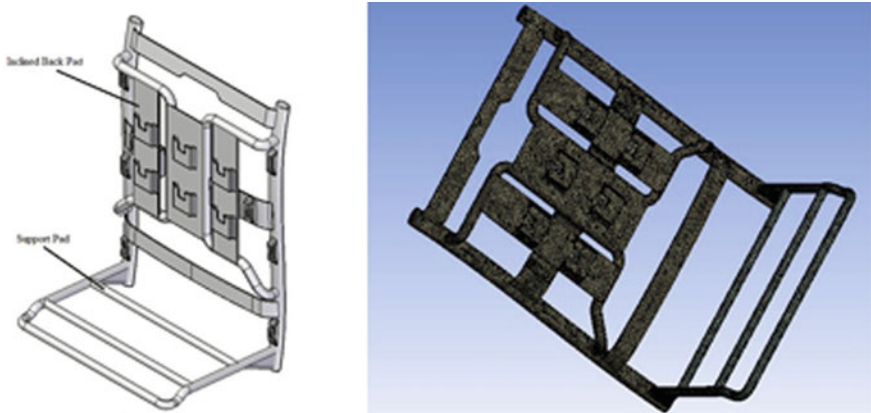


Fig. 1 Back pad model (the left is the establishing finite-element model and the right is the finite element model)

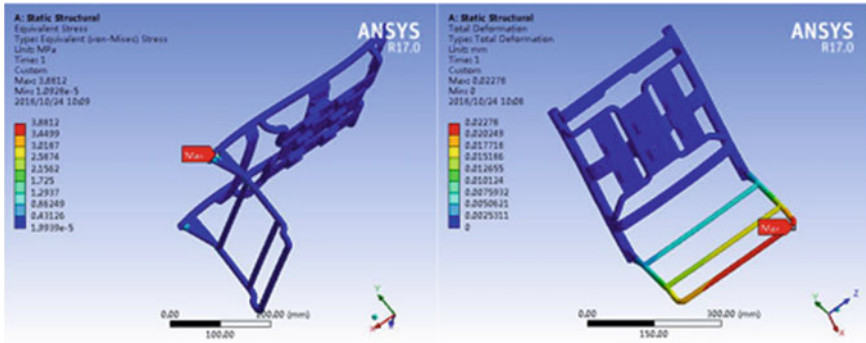


Fig. 2 The response of the back pad under its own weight (the left is the displacement distribution and the right is the stress distribution)

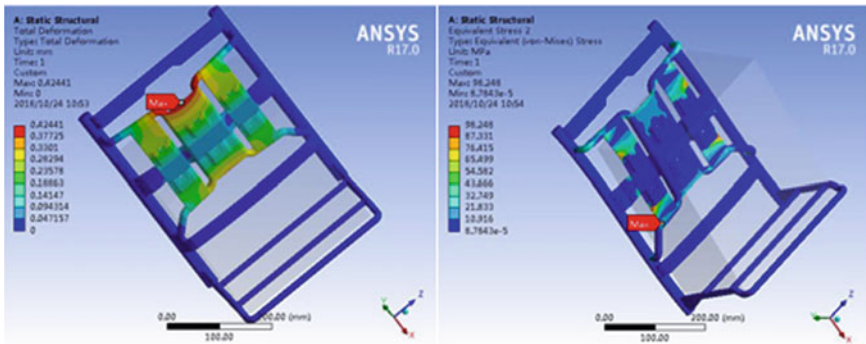


Fig. 3 Load 55 kg, the response without touching the support (the left is the displacement distribution and the right is the stress distribution)

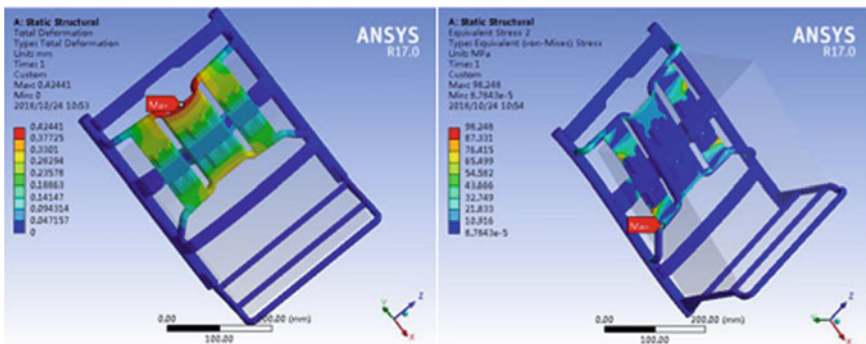


Fig. 4 Load 55 kg, the response placed on the bracket (the left is the displacement distribution, the right is the stress distribution)

4.2 Suspension Design

The suspension design is based on the structure of human body, dividing the supports of the back in segments, equipped with thickened shoulder pads, shoulder blade pads, waist pads, chest straps, and waist belts. After researching and referencing more than 50 domestic and foreign products, it adopted the Y-shaped back ventilation design, which can not only avoid the damage to the human spine and scapular muscles, but also formed an upward back ventilation channel.

The shoulder straps and lumbar pads were made of synthetic nylon padding, forming a concave-convex structure with the back pad, which avoided the pressure on the soft tissues of the shoulder socket. Meanwhile, the fixed design of the waist was changed to a semi-moving design, using the human hip bones as a lumbar support to improve the heat dissipation at back and protect the tail vertebrae.

4.3 Material Selection of Back Pad

According to market research and analysis of competing goods, chose T800 carbon fiber material, its strong tensile resistance and fiber soft the two features of machinability can completely meet the requirements of the production of new type of portable back pad. A: The junction of the bracket and the anticline. B: The connection between the inclined back pad plate and the support rod. C: The junction of the bracket and the anticline.

The data after stress experiment and static calculation of the new carbon fiber T800 backrest are shown in Table 1.

4.4 Suspension Experiment

After the product was designed, the following tests have been carried out compared with the original metal suspension system:

1. 10 healthy men of (18–25) years old each carrying a backpack with 25 kg items were divided into A and B two groups, each group had 5 people. Group A was equipped with the original ordinary suspension system, and group B was

Table 1 Static calculation of carbon fiber back pad

	Maxi-mum dis-placement (mm)	Maxi-mum stress (Mpa)
A	0.02	3.88
B	0.4	98.2
C	0.04	27.9

equipped with a new type of suspension system. All group marched at the speed of (4–5) KM per hour for 1.5 h, and then exchanged the personnel between group A and group B, marching at the speed of (4–5) KM per hour for 1.5 h, continuing to ask their feelings. Meanwhile, observed the appearance and changes of the erythema on the compressed part of the soldier's shoulders, and observed whether the structure of the new back pad was cracked.

2. After carrying a certain type of the equipment, 10 soldiers were divided into A and B two groups, each group had 5 people. Group A was equipped with the original ordinary suspension system, and group B was equipped with the new suspension system. After which it carried out the comparison between the time for disassembly and assembly of each group.

After carrying many experiments, the carbon fiber back pad was not cracked under the load of 25 kg. During the March, all users agreed that the new type suspension system has obvious improved the experience on the shoulders and back, and the erythema in the compressed part of the soldier is obviously lighter in color compared with the original one caused by the old suspension system. Meanwhile, the group B saved more time than group A in the disassembly and assembly parts.

4.5 Experimental Analysis

After carrying out many experiments, it is proved that the structural design and the material selection of the back pad have meet the current use requirements, and the weight is also better than the original metal back pad, so that soldiers can carry out the universal replacement and quick disassembly and assembly of equipment during the operation after adopting the modular design idea and the new carrying design, which saves so much time. In addition, it can also be seen from this experiment that the new suspension system can provide users with a good experience, which also proves that this product can be promoted vigorously in the civilian market.

5 Conclusion

This research is mainly based on the new operational requirements, guided by the actual analysis, proposing a new type of suspension system design strategy. Compared with the foreign suspension system products and combined with the actual situation of our military suspension system products, it has innovated and designed a new type of portable suspension system product, which will provide a good user experience for the future military suspension products and provide a strong foundation for our military portable products in international competition. Moreover, this product has entered a new journey of military-civilian integration development, creating a new situation in which the military and civilian products are mutually developed with that of countries in Europe and the United States.

References

1. Hu, W., Chen, L.: Research on the extraction and visualization of vehicle brand from gene. *Mech. Des. Res.*, 65–79 (2011)
2. Yang, D., Xu, B., Lin, S., Chen, W.: Development of portable multifunctional field medicine storage and transportation box. *Med. Med. Equip.* **9**, 63–65 (2005)
3. Wang, G., Wang, Q.: Modular light carrying Equipment. *China Pers. Protective Equip.* **8**, 47–48 (2002)
4. He, J.: Development of functional fabrics for moisture absorption and Sweat drainage. *Tianjin Univ. Technol.* **24**, 20–21 (2006)
5. Tian, F., Du, Z., Sun, X., Gao, W., Chen, S.: Human body size and somatic perception and backpack carrying structure design. *Med. Health Equip.* 15–17 (2003)

Study on Decarbonization of ZGMn13Cr2 During Heat Treatment



Ke Zhu, Qiang Li, Jianmin Zeng, and Siyong Zhao

Abstract The Oxidation and decarburization of ZGMn13Cr2 steel under different heat treatment conditions was observed, and the decarburization behavior was predicted theoretically based on the oxidation mechanism and decarburization kinetic model, and the relationship between experimental and theoretical decarburization depth was analyzed. The results show that the decarburization of ZGMn13Cr2 is serious during heating, and the depth of decarburization layer increases with the increasing of holding time at a certain heating temperature. Due to the high temperature oxidation reaction and the action of carbide, the decarburization behavior of ZGMn13Cr2 is different at different heating temperatures. When the heating temperature is 1000 °C, the predicted decarburization depth is in good agreement with that in experiment. When the heating temperature is 1050 and 1100 °C, the decarburization depth is greater than that from the kinetic model.

Keywords ZGMn13Cr2 steel · Heat treatment · Dynamic model · Oxidation · Decarburization

1 Introduction

High manganese steel, as a wear-resistant material, has been widely used in mining, metallurgy, construction and other mechanical industries. However, as-cast steel cannot be used directly because it possesses wear resistance only after heat treatment [1, 2]. When high manganese steel is heat treated in atmospheric atmosphere, decarburization will inevitably occur on its surface. In this case, the strength and hardness of decarburized layer are relatively low, which will seriously affect the

K. Zhu · Q. Li · J. Zeng (✉)

College of Resources, Environment and Materials, Guangxi University, Nanning 530004, China

e-mail: zjmg@gxu.edu.cn

S. Zhao

Guangxi Changcheng Mechanical Co., Ltd, Hezhou 542600, China

© The Author(s), under exclusive license to Springer Nature Switzerland AG 2021

137

L. Zheng et al. (eds.), *Proceedings of MEACM 2020*,

Mechanisms and Machine Science 99,

https://doi.org/10.1007/978-3-030-67958-3_15

performance of steel parts and shorten the service life of steel parts [3, 4]. Therefore, it is of great significance to study the oxidation and decarburization of high manganese steel to optimize the heat treatment process of high manganese steel. In the present work, the decarburization of high manganese steel (ZGMn13Cr2) was investigated by experiments under different conditions and the experimental results were compared with theoretical calculations.

2 Methods and Principles

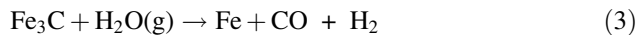
2.1 Experimental Methods

ZGMn13Cr2 was used for the experiment. The chemical composition was seen in Table 1.

Samples with size of $15 \times 10 \times 10$ mm were used in the experiment, and the sample is heat treated by a muffle furnace and the parameters were shown in Fig. 1. The mass of samples before and after heat treatment was measured with the electric balance, and the weight loss was calculated and used to estimate the oxide layer thickness. The decarburized sample was sectioned, grind, polished and corroded, and then the decarburized layer depth was measured according to the metallographic method in ISO 3887: 2017 Steels-Determination of the Depth of Decarburization, as shown in Fig. 2.

2.2 Dynamic Model of Decarbonization

The decarburization mechanism of the cast steel is that carbon reacts chemically with oxidizing gases such as O_2 , CO_2 and H_2O in atmosphere during high temperature heating, and reaction equations are as follows:



A carbon concentration gradient will be established between the surface and internal part when the carbon on the surface reacts with oxygen at high temperature, which makes the carbon atoms continuously diffuse from the high concentration

Table 1 Chemical compositions of ZGMn13Cr2 steel (w %)

C	Mn	Si	Ni	Cr	S	P
1.14	13.66	0.42	0.06	1.90	0.002	0.036

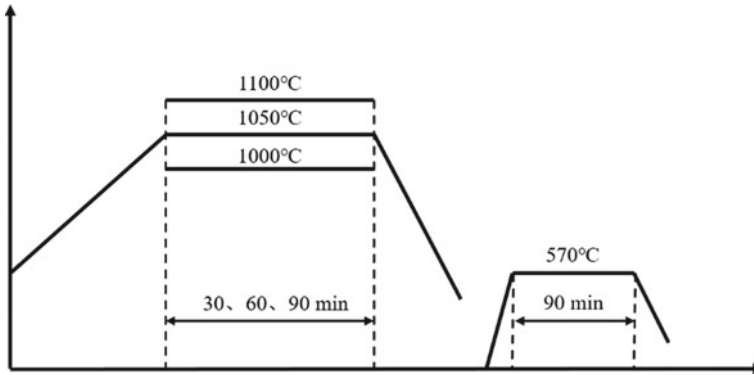
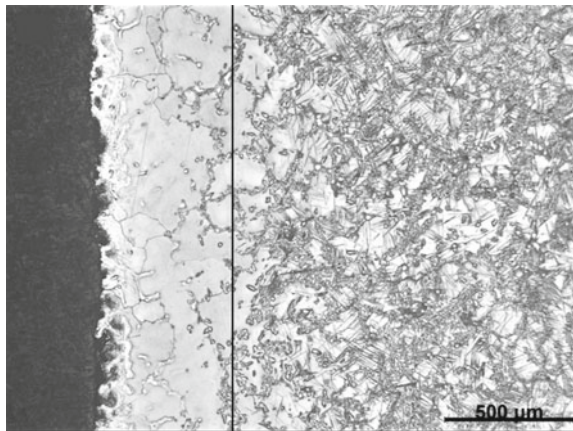


Fig. 1 Heat treatment process parameters of ZGMn13Cr2 steel

Fig. 2 Decarburization microstructure of ZGMn13Cr2 steel



area to the surface and continue to react, eventually forming a decarburization layer. With the continuous diffusion of carbon and chemical reaction, the decarburization layer also grows continuously [5]. Carbon diffusion belongs to unsteady diffusion, there is the following relationship for a $C(x, t)$ diffusion system:

$$\frac{\partial C}{\partial t} = \frac{\partial}{\partial x} \left(D \frac{\partial C}{\partial x} \right) \tag{4}$$

where, C is the carbon concentration, t is the time, D is the diffusion coefficient of carbon, x is the diffusion distance of carbon, i.e. decarburization depth.

Under certain initial and boundary conditions, the analytical solution of the equation is:

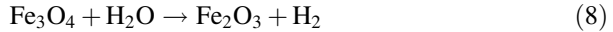
$$x = 2\operatorname{inverf}\left(\frac{C - C_s}{C_0 - C_s}\right) \sqrt{D_0 \exp\left(-\frac{Q_c}{RT}\right) t} \quad (5)$$

where, C_s is the carbon concentration, C_0 is the original carbon concentration, Q_c is the diffusion activation energy of carbon atoms (1.4×10^5 J/mol), R is the gas constant (8.314 j/(mol k)); D_0 is the diffusion constant of carbon atoms (2.0×10^{-5} m²/s), T is the absolute temperature. D is diffusion coefficient and follows Arrhenius equation:

$$D = D_0 \exp\left(-\frac{Q_c}{RT}\right) \quad (6)$$

2.3 Oxidation Mechanism

Decarburization reaction occurs during high-temperature heating. Fe on the surface will chemically react with atmosphere to form an oxide layer:



It can be seen that the reaction between Fe and O₂ will produce FeO, Fe₃O₄, Fe₂O₃, which results in formation of three-layer oxide layer from interior to surface of the casting. Some research data [6] showed that when the temperature was higher than 1000 °C, the thickness ratio of the three layer is about 95:4:1.

3 Results and Discussion

According to the density of oxide layers, the thickness ratio can be changed into the mass ratio, and then the mass of each oxide layer can be calculated according to the weight loss (the total mass of the peeled oxide layer) of the sample before and after water quenching, as shown in Table 2. Finally, the total oxide layer thickness is calculated according to the following equation:

$$x_0 = \sum \frac{M_i}{\rho_i S} \quad (10)$$

Table 2 Calculated values of mass of each oxidation layer

Temperature (°C)	Time (min)	Mass loss (mg)	M_{FeO} (mg)	$M_{\text{Fe}_3\text{O}_4}$ (mg)	$M_{\text{Fe}_2\text{O}_3}$ (mg)
1000	30	624.4	595.8	22.8	5.8
	60	929.3	886.8	34.0	8.6
	90	1191.4	1136.9	43.5	11.0
1050	30	1008.3	962.2	36.8	9.3
	60	1454.9	1388.3	53.1	13.4
	90	1838.7	1754.6	67.1	17.0
1100	30	1258.7	1201.1	46.0	11.6
	60	1706.8	1628.7	62.3	15.8
	90	2140.6	2042.7	78.2	19.8

where, x_0 is the total thickness of oxide layer, M_i is the mass of each oxide layer, mg; ρ_i is the density of each oxide layer, S is the surface area of sample.

The estimated total oxide layer thickness is shown in Fig. 3. Combining Eq. (5) with Eq. (10), the actual theoretical decarburization depth should be:

$$x' = x - x_0 \quad (11)$$

The test result was shown in Fig. 4.

Generally speaking, when the carbon content is less than 85% of the maximum carbon content, it can be regarded as decarburization [7]. So, in Eq. (5), let $C = 0.85 C_0$ and $C_s = 0$. Combined with Eq. (11), the theoretical decarburization depth can be calculated, as shown in Fig. 5.

It can be seen from the Fig. 5 that when the heating temperature is 1000 °C, the theoretical decarburization depth is basically consistent with the experimental measured value, indicating that the decarburization kinetic model can accurately predict the decarburization. When the heating temperature rises above 1050 °C, there is a deviation between theoretical and experimental values. This is mainly caused by two reasons. On the one hand, with the increasing of heating temperature, the oxidation at high temperature will be intensified, and the oxidation loss will increase. On the other hand, The higher the heating temperature and the longer the holding time, the more fully the carbide on the grain boundary is dissolved. That makes diffusion of carbon atoms easier and therefore results in more severe decarburization. Thus, at higher heating temperature, the deviation between kinetic model and experiment value increases.

Fig. 3 Estimated depth of oxidation layer of ZGMn13Cr2 steel

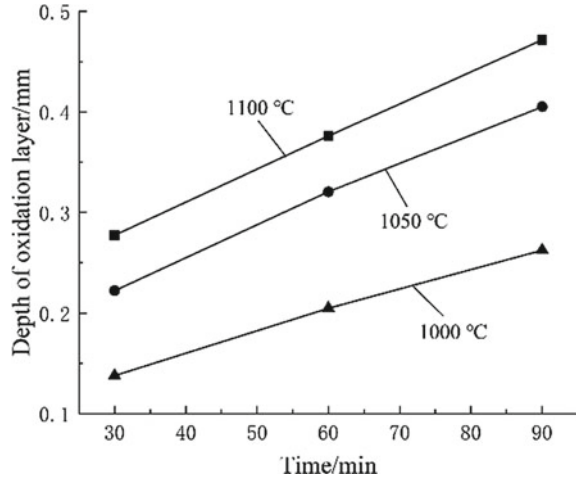
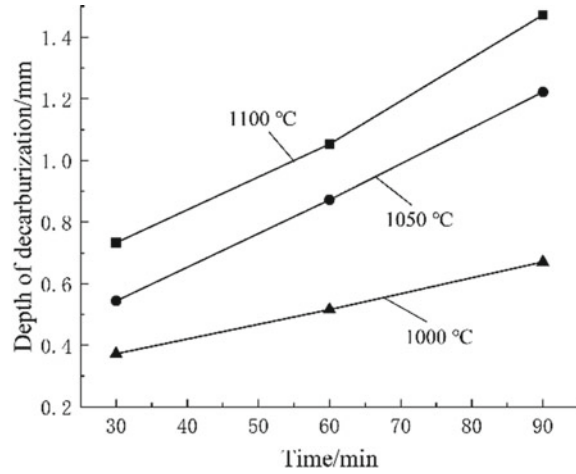


Fig. 4 Depth of decarburization layer of ZGMn13Cr2 steel

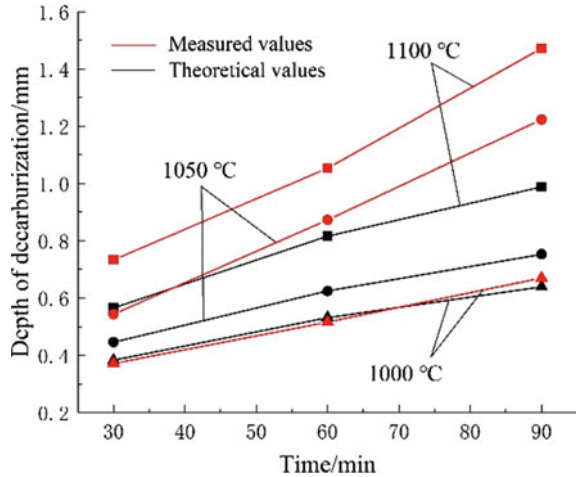


4 Conclusion

ZGMn13Cr2 has severe decarburization during heat treatment. When heated at 1000 ~ 1100 °C, the depth of decarburization layer increases with the increasing of heating temperature and holding time.

The surface of ZGMn13Cr2 will undergo oxidation reaction at the same time of reverse decarburization reaction, resulting in oxidation loss. Oxidation reaction will be intensified with the increase of water toughening temperature and holding time, and oxidation reaction has great influence on the traditional decarburization kinetic model.

Fig. 5 Comparison of theoretical and measured values decarburization depth of ZGMn13Cr2 steel



When the heating temperature is 1000 °C, the decarburization kinetic model can accurately predict the decarburization of ZGMn13Cr2. With the heating temperature rising to above 1050 °C, the decarburization kinetic model is no longer applicable due to the intensified oxidation reaction and decomposition of the carbides on the grain boundary.

Acknowledgements This work was financially supported by Major Science and Technology Projects in Guangxi (Gui Ke AA18242001).

References

1. Khanh, M.P., Thai, T.L., Nhung, T.L., et al.: Effect of element addition and heat treatment process on the properties of high manganese steel. *Int. J. Adv. Sci. Eng. Inf. Technol.* **9**(4), 1289–1295 (2019)
2. Jansa, Z., Žďánský, O., Průcha, V., et al.: Characterization of microstructure of hadfield steel. diffusion and defect data. *Solid State Data, Part B. Solid State Phenomena* **270**, 265–270 (2017)
3. Skandan, G., Kear, B.H., Sadangi, R.K.: Factors controlling decarburization in hvof sprayed nano-Wc/Co hardcoatings. *Scripta Mater.* **44**(8–9), 1703–1707 (2001)
4. Haijing, H.: The effect of chemical composition on the microstructure and properties of high manganese steel frog. *Shandong Chem. Ind.* **44**(10), 115–117 (2015)
5. Toshiharu, S., Yozo, T., Shigeyoshi, F.: The decarburization mechanism in rimming steel. *Tetsu-to-Hagane* **56**(9), 1194–1200 (1970)
6. Chen, R.Y., Yeun, W.Y.D.: Review of the high-temperature oxidation of iron and carbon steels in air or oxygen. *Oxid. Metals* **59**(5–6), 443–468 (2003)
7. Oldani, C.R.: Decarburization and grain growth kinetics during the annealing of electrical steels. *Scripta Mater.* **35**(11), 1253–1257 (1996)

Numerical Simulation of Aluminum Alloy Connecting Rod with Multi-wedge Cross Wedge Rolling



Ke-Xing Zhang, Xiao-Lian Zhao, Ao-Ping He, Jian-Min Zeng,
Ke-Zhun He, Jun-Sheng Liu, and Gang Xiao

Abstract The connecting rod is one of the most important parts in the engine, which plays a key role in the normal operation of the engine. High strength aluminum alloy was selected as raw materials for production in this program, and multi-wedge cross wedge rolling was applied for forming an engine connecting rod by numerical simulation, to explore the deformation mechanism and defect generation mechanism and its influencing factors. It is will be beneficial for subsequent forging connecting rod to provide quality assurance and provide the reference for the production of aluminum alloy connecting rod.

Keywords Cross wedge rolling (CWR) · Multi-wedge forming · Aluminum alloy connecting rod · Numerical simulation

1 Introduction

The connecting rod is one of the most widely used multi-step shaft parts, it's also one of the most important parts of the engine [1, 2]. Using the wedge rolling multi-wedge forming process can not only solve the problems such as the accurate distribution of the connecting rod blank, the continuous distribution of metal fiber streamline, etc., and mechanization automatic production can be achieved, high productivity, large quantity, which is the trend of axis type manufacturing in the future [3].

The deformation of wedge rolling is a kind of large plastic deformation, the deformation process is complex. The three dimensional stress-strain state of the rolling piece is also complicated, and the flow metal in the rolling piece may be affected by several kinds of deformation at the same time, such as compression,

K.-X. Zhang · X.-L. Zhao · A.-P. He · J.-M. Zeng (✉)

Guangxi Key Laboratory of Processing for Non-Ferrous Metal and Featured Materials,
Guangxi University, Nanning Guangxi 530004, China

K.-Z. He · J.-S. Liu · G. Xiao

Alnan Aluminum Inc., Nanning Guangxi 530031, China

© The Author(s), under exclusive license to Springer Nature Switzerland AG 2021

145

L. Zheng et al. (eds.), *Proceedings of MEACM 2020*,

Mechanisms and Machine Science 99,

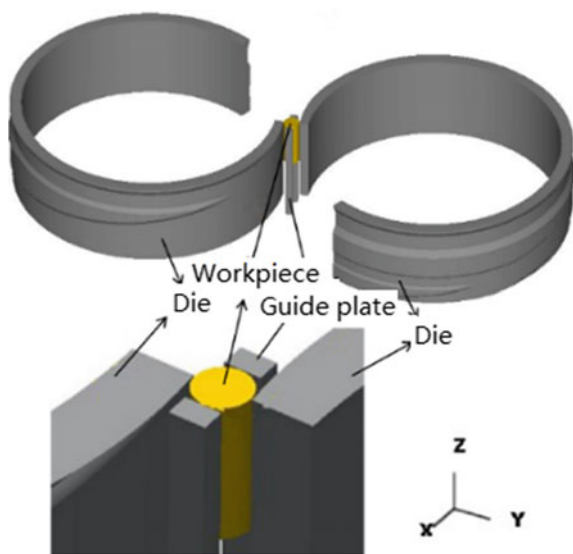
https://doi.org/10.1007/978-3-030-67958-3_16

stretching, bending, torsion, shear, etc. With the continuous development of numerical simulation method [4], the accuracy of simulation is constantly improving, and the simulation method is constantly being innovated and developed which lead to more and more reliable results of the complex plastic deformation simulation such as multi-wedge forming, and it is the main method to study the process of wedge rolling process. Through numerical simulation, adjusting the position and arrangement of the wedge on the roll and adjusting the process parameters, stable forming can be obtained, no skid, spiral mark, stacking, bending and other external defects rolling piece, and the surface quality of forming shape and size can be ensured [5]. But so far, the central defect can not directly simulated by numerical simulation. Therefore, the deformation process of the blank material must be analyzed, using the variation of the stress and strain calculation results gained by numerical simulation. The mechanism of deformation and defect will be explored, which provides a theoretical reference for further study of the precise forming and metal flow of wedge rolling multi-wedge parts.

2 Finite Element Model

Based on the DEFORM—3D finite element software platform, the finite element model of the AL6061 alloy multi-wedge connecting rod is established. The model is composed of rollers, rolling pieces, left and right baffles, as shown in Fig. 1.

Fig. 1 The finite element model of CWR



3 Results and Discussion

The connecting rod blank is a dumbbell-shaped structure, and the deformation process is very complicated during rolling. It is a typical asynchronous multi-wedge rolling process. Figure 2 demonstrates the process of the aluminum alloy connecting rod numerical simulation forming with CWR. it can be seen from the figure that there are four wedge forming stages, which include wedge 1 (Fig. 2a–b), wedge 2 (Fig. 2c and d), wedge 3 (Fig. 2e–f), wedge 4 (Fig. 2g and h).

3.1 Stress Analysis

Figure 3 shows the distribution of the equivalent stress field on the section of the connecting rod at the end of rolling. It can be seen from Fig. 3 that some parts of the surface of the blank which are in contact with the mold are in a compressive stress state and the rest are in a tensile stress state. The tensile stress of the thin rod part of the rolling part is the largest, and the tensile stress decreases with the increase of the distance from the center, which indicates that the stress of the thin rod part of the rolling is complicated, the metal flow is intense and the easiest Occurrence of the site.

3.2 Strain Analysis

Equivalent strain is an important parameter in the process of plastic deformation, the size of which can reflect the degree of plastic deformation of the blank. Figure 4 shows the distribution of the equivalent strain field of the whole and longitudinal

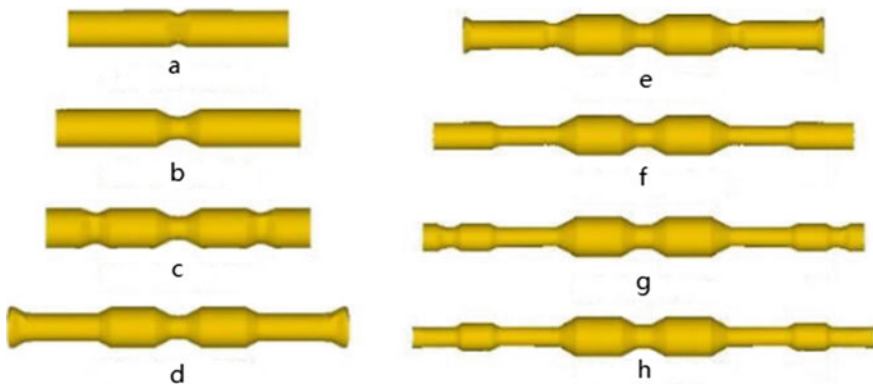


Fig. 2 Workpiece forming process of cross wedge rolling

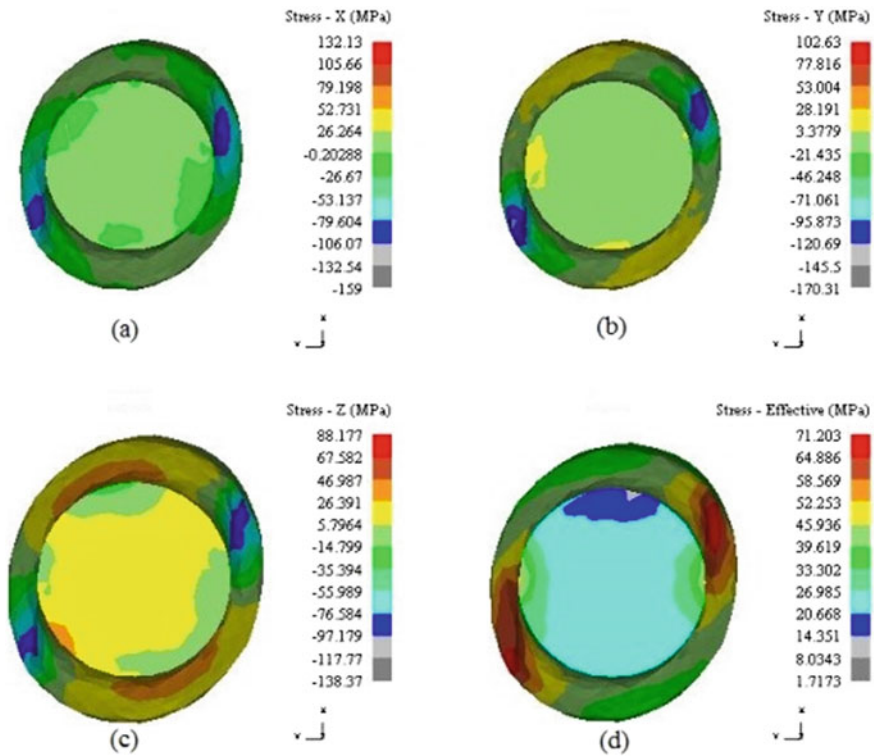


Fig. 3 Stress distribution of cross-sectional

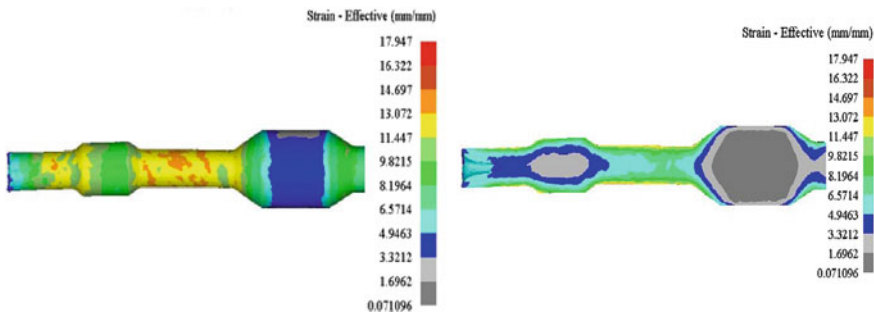


Fig. 4 Strain distribution diagram of rolled piece

section of the connecting rod blank at the end of rolling. It can be seen from Fig. 4, the middle of the thin rod equivalent strain is the largest, followed by clamping the middle of the rod to the back of the small head, and the head of the largest part of the equivalent strain of the smallest, indicating that the middle of the thin rod and

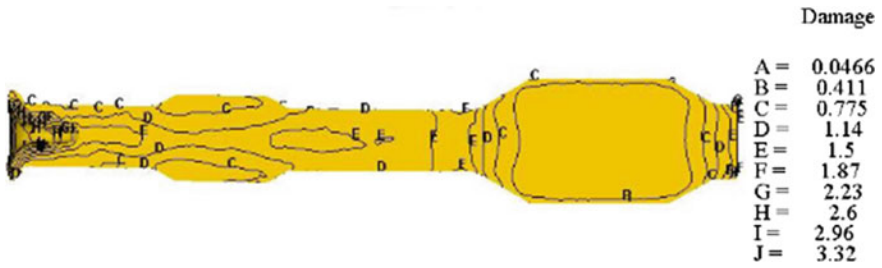


Fig. 5 Distribution of ductile damage

clamping. The deformation of the rod is severe, the deformation is large, the metal flow is complicated, and the bulk part is basically not deformed. The middle of the thin rod and clamping rods have experienced the role of two wedges, through the forming time relative to other parts of the long, strain accumulation, and thus prone to necking or cardiac defects.

3.3 Ductile Damage Analysis

Ductile damage refers to the initiation and expansion of the internal induced cavity and microcrack in the material after large plastic deformation. The accumulation of ductile damage will cause material fracture, which is called ductile fracture. When studying the internal defect, it is necessary to determine whether there is a defect in the material. At present, the Normalized Cockcroft and Latham criterion and Oyane criterion are widely used to predict whether the internal of Cross wedge rolling parts can fracture. Researchers Taoxin have just combined numerical simulations with physical experiments, and he discovered that Oyane criterion is more suitable for damage analysis of wedge rolling parts. So this subject also chooses this criterion when studying the internal defect.

The ductile damage distribution on the rolled pieces as shown in Fig. 5, the upper part of the connecting rod, the center of the middle rod, the center of the clamping rod and the end of the clamping rod are relatively large, and the head and small head are less damaged. This indicates that the center of the middle rod, the connecting rod and the clamping rod part have the possibility of centre weakness or a crack in the center The damage of the end of the mill is mainly caused by the concave center.

4 Conclusion

1. The numerical simulation of the forming process of the wedge cross wedge joint was carried out by DEFORM-3D finite element software, and the deformation and defect mechanism were explored to provide theoretical reference for the precise shape and metal flow of the wedge cross wedge.
2. During the rolling process, the middle part of the rod part and the clamping rod are deformed violently, the deformation is large, the metal flow is complicated, so it is easy to produce loose parts such as loose and crack. It is suggested that the appropriate rolling process should be taken Reduce center defects.

References

1. Hong, S.Z., Zeng, Z.P.: Application and development of cross wedge rolling process. *Die Mould Technol.* **32**(5), 97–99 (2000)
2. Lou, Y.Z., Zhang, K.S., Yang, C.P., et al.: Effect of process parameters on axial parts with super large area reduction during twice cross wedge rolling. *J. Univ. Sci. Technol. Beijing* **30** (4), 432–435 (2008)
3. Lu, H.Y., Yan, H.J., Zhang, S.J., et al.: Reserch on optimization of rolling curve for multi-step shaft in cross wedge rolling. *Foring Stamping Technol.* **44**(12), 41–48 (2019)
4. Zeng, J., Xu, C.G., Ren, W.W., et al.: Effect of process parameters on concavity depth of rolled piece by cross wedge rolling under defferent end shapes. *J. Plast. Eng.* **24**(2), 111–117 (2017)
5. Hu, Z.H., Zhang, W.: Development of part rolling technology in China. *J. Mech. Eng.* **48**(18), 7–12 (2012)

Effect of Water Temperature on Quenching Residual Stress of Aluminum Alloy Thick Plate



Xiao-Lian Zhao, Ke-Xing Zhang, Ao-Ping He, Jian-Min Zeng, Ke-Zhun He, Jun-Sheng Liu, and Gang Xiao

Abstract Based on the finite element simulation software ABAQUS, the spray quenching process of aluminum alloy thick plates were parametrically simulated by establishing a finite element model, and the influence of the water temperature on the distribution of the residual stress of the thick plate were explored by changing the water temperature. The results indicated that when the spray parameters are constant, the quenching residual stress in the aluminum alloy thick plate will decrease with the increase of the water temperature. The increase of the water temperature can effectively reduce the residual stress of the aluminum alloy thick plate with the spray pressure of 100 kPa, and the stress can be reduced by 23.9 MPa; When the spray pressure is 200 kPa, the residual stress of the aluminum alloy thick plate is the least sensitive to the change of the quenching temperature, and the stress can be reduced by 13.9 MPa.

Keywords Aluminum alloy thick plate · Quenching · Residual stress · Water temperature

1 Introduction

Al–Zn–Mg–Cu series high-strength aluminum alloys have high specific strength, low density, good toughness and excellent corrosion resistance, and are widely used in aerospace, weapon manufacturing and other fields [1–3]. In engineering production, it is inclined to use a large cooling rate, but an excessive cooling rate will cause the deformation of the aluminum alloy profile and increase the residual stress. This kind of contradiction between performance and residual stress has always

X.-L. Zhao · K.-X. Zhang · A.-P. He · J.-M. Zeng (✉)

Guangxi Key Laboratory of Processing for Non-Ferrous Metal and Featured Materials, Guangxi University, Nanning Guangxi 530004, China

K.-Z. He · J.-S. Liu · G. Xiao

Alnan Aluminum Inc., Nanning Guangxi 530031, China

© The Author(s), under exclusive license to Springer Nature Switzerland AG 2021

151

L. Zheng et al. (eds.), *Proceedings of MEACM 2020*,

Mechanisms and Machine Science 99,

https://doi.org/10.1007/978-3-030-67958-3_17

existed. Some scholars [4–6] used various methods to find ways to eliminate residual stress.

At present, there are few researches on the residual stress distribution of aluminum alloy thick plates under different water temperature. Therefore, it is of great significance to find a suitable quenching process to guide production. In this paper, ABAQUS finite element (FE) analysis software is used as a tool to explore the influence of water temperature on the residual stress distribution of aluminum alloy thick plates by establishing a parameterized model.

2 FE Analysis Modeling

In order to facilitate the calculation, this simulation simplified the model to a certain extent:

1. The model material can be regarded as an isotropic and uniform continuous medium.
2. After solution treatment, the internal stress field is zero.
3. Ignore the influence of phase change on stress during quenching and the influence of change in stress field on temperature.

The material used in the simulation of the thick plate was 7050 aluminum alloy, the size was $1300 \times 500 \times 200$ mm (length \times width \times thickness), the initial temperature was set to 477°C , and the air temperature was 20°C . The material parameters and performance parameters [7] are shown in Tables 1 and 2. The heat transfer coefficient of water under different spray pressures and the heat transfer coefficient of air are referred to [8].

Because the quenched model has the symmetry of geometry and boundary conditions, $1/8$ of the model was selected for modeling in this simulation, and symmetry constraints was imposed on the three internal surfaces. The upper surface is in contact with the quenching medium, and the two sides are in contact with air. The analysis step used in the simulation is Coupled temp-displacement, and the time period were 700 s. He default value in the length, width, and thickness direction was 20, 15, and 10, a total of 3000 grids, the element type was C3D8R. The model is shown in Fig. 1.

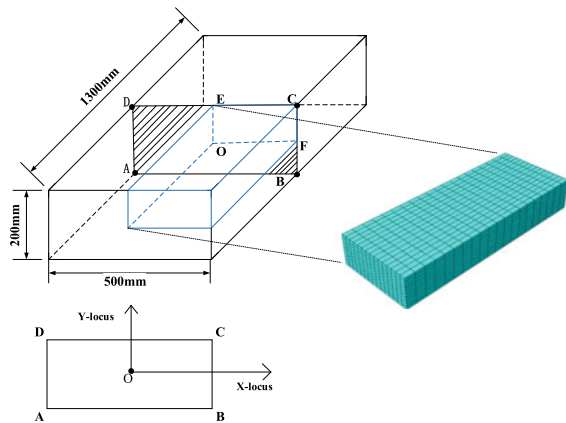
Table 1 Performance parameters

Temperature/ $^\circ\text{C}$	Elastic modulus/MPa	Poisson ratio	Temperature/ $^\circ\text{C}$	Yield strength/MPa
0	72,450	0.29	66	221
100	69,690	0.29	250	212
200	64,860	0.29	300	150
300	58,650	0.29	350	87
400	53,820	0.29	400	60
–	–	–	477	26

Table 2 Material parameters

Temperature/°C	Thermal conductivity/ (kW·m ⁻¹ ·°C ⁻¹)	Thermal expansion/ (10 ⁻⁶ ·°C ⁻¹)	Specific heat/ (J·kg ⁻¹ ·°C ⁻¹)	Density/ (g·cm ⁻³)
0	0.11	–	–	2.796
20	–	21.8	837	–
100	0.12	23.6	896	2.768
200	0.14	24.5	963	2.768
300	0.15	25.4	–	2.74
400	0.16	–	1130	2.713
477	–	–	1193	–
500	0.17	–	–	2.685
600	–	–	–	2.657

Fig. 1 FE model of aluminum alloy thick plate



3 Analysis of Results

Figure 2 shows the variation of temperature and residual stress (p_x) at the surface point E and the center point O during the quenching process over time. The spray pressure selected for quenching was 100 kPa and the water temperature was 20 °C. When the residual stress value is positive, it represents tensile stress, and when the residual pressure is negative, it represents compressive stress.

Figure 2a illustrates that the surface point E is much higher than the cooling rate of the center point O. The quenching sensitivity temperature range of 7×50 high-strength aluminum alloy is 420–230 °C, and the cooling rates of the surface point E and the center point O are 46.8 and 3.0 °C·s⁻¹ which are more than 15 times different in this temperature range. As shown in Fig. 2b, In the initial stage of quenching, the surface metal is subjected to tensile stress and the center metal to compressive stress. When the quenching process lasts for about 60 s, the stress state

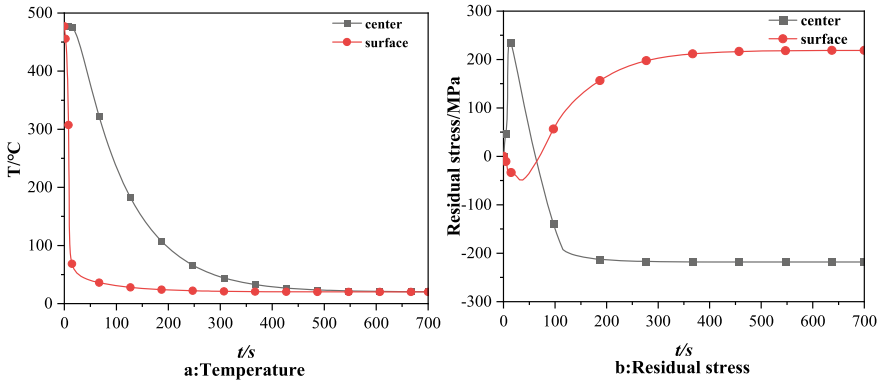


Fig. 2 Temperature and residual stress at the center and surface points versus time

of the surface metal and the core metal changes, the surface metal begins to transform from tensile stress to compressive stress, and the core metal transforms from compressive stress to tensile stress. During the entire quenching cycle, the surface point E has completed the transformation from tensile stress to compressive stress, and the center point O has completed the transformation from compressive stress to tensile stress, which is in accordance with the theory.

Figure 3 characterizes the effect of water temperature on the residual stress in the thickness direction of aluminum alloy thick plates under different spray pressures. According to Fig. 3, the distribution of residual stress at the center point is affected by the change of water temperature. When the spray parameters are constant, the influence of the water temperature on the residual stress of the aluminum alloy thick plate changes regularly. In general, the residual stress of aluminum alloy thick plates decreases with the increase of water temperature. This is because as the water temperature increases, the temperature gradient between the surface and center will be reduced, which makes the overall deformation of the thick plate more uniform, resulting in a reduction in residual stress. The effect of water temperature on residual stress of thick aluminum alloy plates is also different under different spray pressures. When the spray pressure is 100 kPa, the change of water temperature has the greatest effect on the residual stress of aluminum alloy thick plates. When the spray pressure is 100 kPa, the change of water temperature has the greatest effect on the residual stress of aluminum alloy thick plates. When the water temperature is increased from 20 to 80 °C, the stress value of center point is reduced by 23.9 MPa; when the spray pressure is 200 kPa, the change of the water temperature has little effect on the residual stress of the aluminum alloy thick plate, and the water temperature is increased from 20 to 80 °C, the stress value of center point is only reduced by 13.9 MPa.

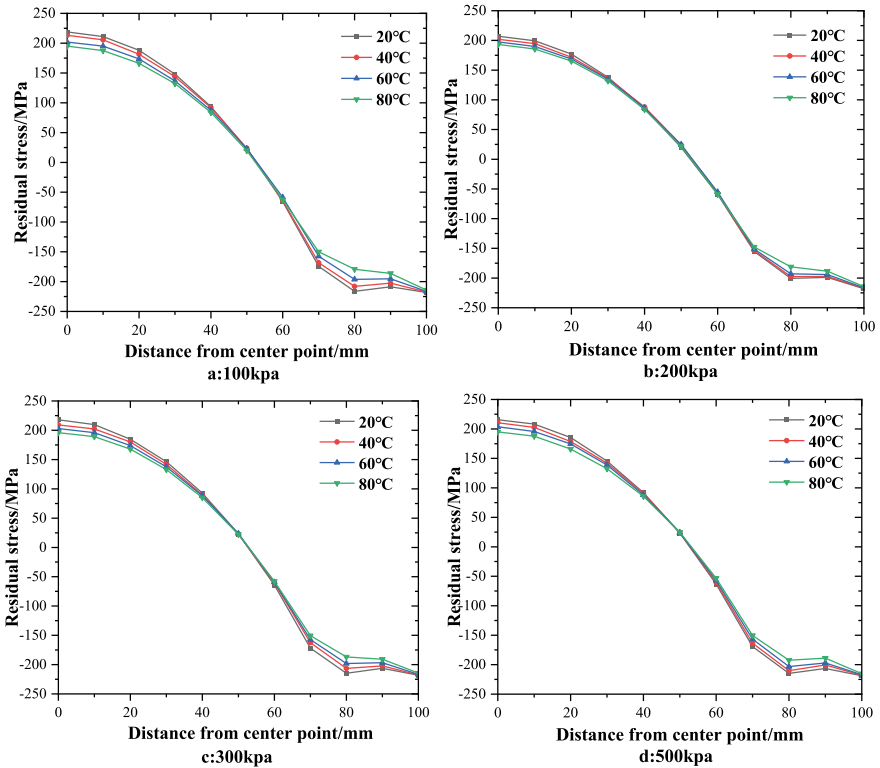


Fig. 3 The relationship between the thickness direction residual stress and the water temperature under different spray pressures

4 Conclusion

1. During the entire quenching cycle, the distribution of residual stress in the aluminum alloy thick plate has undergone complex changes. Overall, the aluminum alloy thick plate shows the stress distribution law of the surface compressive and the center tensile stress at the beginning of quenching. After quenching, the stress state of the surface area and center area of the thick plate has changed, showing the stress distribution state of the surface tensile and the center compressive stress.
2. The quenching residual stress of aluminum alloy thick plates will decrease with the increase of water temperature.
3. The effect of water temperature on residual stress of thick aluminum alloy plates is also different under different spray pressures.

References

1. Heinz, A., Haszler, A., Keidel, C., Moldenhauer, S., Benedictus, R., Miller, W.S.: Recent development in aluminum alloys for aerospace applications. *Mater. Sci. Eng. Struct. Mater. Prop. Microst. Process.* **280**(1), 102–107 (2000)
2. Staley, J.T., Liu, J., Hunt, W.H.: Aluminum alloys for aerostructures. *Adv. Mater. Process.* **152**(4), 17–20 (1997)
3. Robinson, J.S., Cudd, R.L., Tanner, D.A., Dolan, G.P.: Quench sensitivity and tensile property inhomogeneity in 7010 forgings. *J. Mater. Process. Technol.* **119**(1–3), 261–267 (2001)
4. Robinson, J.S., Truman, C.E., O'Donovan, A., Kornmeier, J.R.: Uphill quenching to reduce residual stress in a heat treatable aluminum alloy. *Mater. Sci. Technol.* **35**(15), 1864–1871 (2019)
5. Pan, R., Zheng, J.H., Zhang, Z.P., Lin, J.G.: Cold rolling influence on residual stresses evolution in heat-treated AA7xxx T-section panels. *Mater. Manuf. Process.* **34**(4), 431–446 (2019)
6. Robinson, J.S., Tanner, D.A.: Residual stress development and relief in high strength aluminum alloys using standard and retrogression thermal treatments. *Mater. Sci. Technol.* **19**(4), 512–518 (2003)
7. Koç, M., Culp, J., Altan, T.: Prediction of residual stresses in quenched aluminum blocks and their reduction through cold working processes. *J. Mater. Process. Technol.* **174**(1–3), 342–354 (2006)
8. Guo, S.: Investigation on Experimental and Simulation of Spray Quench for 7050 Aluminum Alloy Plate. Central South University, Changsha (2010)

Study on the Motion and Friction Mechanism of Flexible Roller in Space Roll Ring



Bin Wang and Jikui Liu

Abstract The space roller assembly is composed of inner ring, outer ring and planetary roller. It can reduce contact resistance, increase power transmission ability and improve electric transmission performance by increasing the number of rollers. Based on the application background of high power roll ring for space power station, this paper analyzes the rolling mechanism of flexible roller, puts forward the feasible structure design scheme of roll ring assembly, analyzes the advantages and disadvantages of the scheme, determines the flexible ring as the roller structure scheme and the retainer scheme as the roller spacing scheme; The friction between the flexible roller and the raceway and retainer is analyzed, the friction torque calculation value of the roll ring assembly is given, and the bearing, raceway lubrication and surface treatment scheme are determined. Finally, the contact stress between the flexible roller and the raceway is analyzed by theoretical calculation and finite element method.

Keywords Roll ring · Friction · Optimization · Contact resistance

1 Introduction

Conductive rings are usually used when electrical power or electrical signals need to be transmitted between two components of continuous rotation. The conductive ring can be divided into slip ring and roll ring according to the friction mode. Because of its defects in motion principle, both friction torque and electric transmission ability are difficult to meet higher application requirements. For the purpose of effectively reducing friction torque and improving life and electrical transmission performance, the roll ring is studied and [1] from the aspect of rolling motion at home and abroad.

B. Wang (✉)

School of Mechanical Engineering and Automation, Beihang University, Beijing, China

J. Liu

Beijing Institute of Control Engineering, Beijing, China

© The Author(s), under exclusive license to Springer Nature Switzerland AG 2021

157

L. Zheng et al. (eds.), *Proceedings of MEACM 2020*,

Mechanisms and Machine Science 99,

https://doi.org/10.1007/978-3-030-67958-3_18

The space application conductive ring is generally responsible for the transmission of electrical power and other related signals on the whole satellite or space station, and its reliability will affect the success or failure of the whole star mission. Therefore, when developing conductive ring at home and abroad, we must pay enough attention to its performance index.

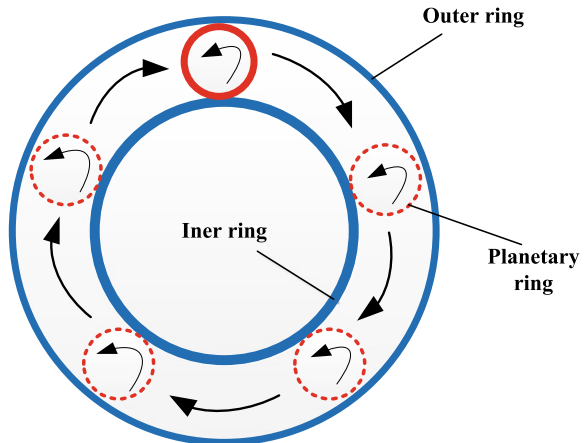
Because its structure form, motion and working principle are completely different from the slip ring of the common driving mechanism, it is necessary to carry out more in-depth technical investigation and theoretical calculation and analysis of the structural design parameters of the existing roll ring prototype to optimize a more reasonable structural form.

2 Design of Roll Ring Structure

The conductive rotating joint adopts the roll ring transmission scheme. The roll ring consists of multiple rolling components through stacking. The structure principle of the rolling component is shown in Fig. 1.

According to the above figure, the rolling component is mainly composed of inner ring, outer ring and rolling body. the inner and outer ring generally use brass substrate, the surface of the raceway is coated with anti-oxidation conductive film, which has low contact resistance; the roller can be made of beryllium bronze and other materials, which has good elastic properties and can set a reasonable preloading force between the inner and outer rings. The number of rolling components and the number of rollers in each rolling component can be determined according to the transmission power requirements and structural dimensions. Because rolling friction is used instead of sliding friction, compared with traditional slip ring, it has many advantages, such as smaller friction moment, longer life, smaller contact resistance and [2] transmission power.

Fig. 1 Roll ring rolling assembly



2.1 Roller Structure

The roller plays the role of connecting the rotating part and the fixed part in the roll ring, which is the key link to affect the performance of the electric transmission of the roll ring. According to the rigidity of rollers, the roll rings studied in the past can be divided into two categories, that is, rigid roller roll rings and flexible roller roll rings.

Rigid Roller Rigid roll ring mainly simulates the existing rolling bearing and other structures, the general process is more mature, high machining accuracy. The surface contact area between roller and stator and rotor is improved by high precision roller machining and surface treatment, and the electric transmission performance and reliability are improved by applying pretightening force to stator and rotor.

Figure 2 is a four-point contact rolling bearing roller structure. Each component adopts brass or copper base material, in order to ensure all contact of each roller, cylindrical roller adopts high precision surface processing technology and is selected on this basis. On this basis, pretightening force is applied to stator and rotor, bearing clearance is 0, loop resistance is less than 1 m Ω .

However, the experimental analysis shows that the electric transmission capacity is mainly completed through the contact area between roller and stator and rotor. In order to improve the reliability of electric transmission, it is necessary to ensure the contact area and contact pressure of the contact area. For rigid rollers, if the pretightening force is too large, the friction moment of the roll ring increases and is prone to serious wear. If the pretightening force is insufficient, the contact area and pressure are insufficient to transmit the current very well. It can be seen that the contradiction between reducing wear and friction moment and improving telex performance can not be coordinated.



Fig. 2 Four point contact ring structure

Flexible Rollers Flexible roller adopts elastic structure to solve the contact problem in rigid roller. Flexible roller can adopt beryllium bronze and other materials, which has good elastic performance and electric transmission performance. The flexible roller has low stiffness, easier to apply pretightening force, stable contact area and reliable electrical transmission performance, and has low friction torque.

The flexible ring roller developed by the Sperry Corporation of the United States is designed with a hollow star wheel, which has a very low wear rate and friction torque, and each ring can transmit 1 A of current. In continuous rotation, due to the existence of sliding friction, planetary wheels will eventually collide with each other and produce serious sliding friction and wear. One solution is to use only one flexible ring, but it will seriously restrict the current transmission capacity of the roll ring. Another solution is to add a position holding device. Each flexible ring is separated by idler wheel structure, and the same function can be realized by retainer and other schemes. However, no matter which device is used, it will increase the complexity of the ring structure and cause the weight and size of the ring to be not too small.

John at the Goddard Space Flight Research Center of the National Aeronautics and Space Administration. Venice has designed a standard gear roller, the flexible roller of this structure keeps its position through the meshing of teeth, saves the idler wheel and reduces the size of the whole machine. At the same time, because the multi-tooth contact standard planetary gear provides more contact area than the planetary gear with roll ring structure, and the contact area size can be quantitatively described by coincidence coefficient, Therefore, the flexible gear device has obvious advantages in high current transmission than the idler roll ring device. However, the subsequent studies show that the deformation of the standard planetary gear used in this scheme is prone to serious wear and friction moment after radial compression, and the insufficient compression will lead to insufficient contact area and pressure and cannot transmit the current well.

In order to overcome the disadvantages of standard gears and retain their advantages of self-positioning, the National Aeronautics and Space Administration commissioned the Systems Research Institute of the University of Mary Landy to develop a class of new tooth shapes for power transmission. Such new non-standard flexible gears are called nodal rolling gears in NASA-CR-19442 research reports. In view of the advantages of circular rolling gear transmission, the future research of the National Aeronautics and Space Administration of the United States focuses on the electric transmission device of the circular rolling gear (Fig. 3).

To sum up, the flexible roller roll ring is used as the whole machine scheme. Because the flexible roll ring structure has good technology accumulation at present, the scheme is optimized. To solve the problem of complex structure and increasing size and weight, the structure parameters are optimized.

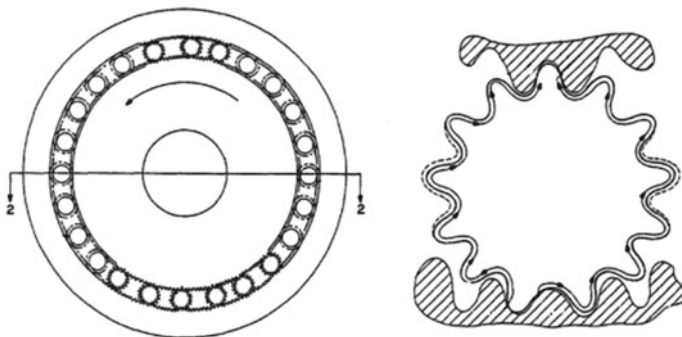


Fig. 3 Flexible planetary gear scheme

2.2 Retainer Structure

Inert Wheel According to different application needs and flexible ring structure, NASA developed a variety of flexible ring position holding devices, among which the idler wheel holder scheme is more mature and has been used in the free space station.

In the above scheme, the guide rail is fixed with the inner ring, and its rotational speed is the same as the inner ring. The idler wheel is compressed between the guide rail and the flexible ring on both sides. When the inner conductive ring rotates, the flexible ring also rotates under the drive of the inner ring. The idler wheel between the two flexible rings also needs to rotate at the same speed as the flexible ring. In order to reduce friction, theoretically between the flexible ring and the inner and outer ring, between the inert wheel and the flexible ring on both sides, and between the inert wheel and the raceway are all pure rolling.

The advantage of this scheme is that the idler wheel is small in size, sandwiched between two flexible rings and raceways, the whole machine is compact in structure and light in weight. The disadvantage is that many flexible rings and idler wheels are arranged in series for the whole cycle, and it is required that there is a certain pre-pressure between the flexible ring and the inner and outer raceways and between the idler wheels on both sides, so it is difficult to process and install the parts. In addition, because the track is connected with the inner ring, the rotational speed is different from the common rotation speed of the idler wheel and the flexible ring, so it cannot be mechanically connected with the idler wheel. Therefore, the idler wheel lacks hard limit, only two flexible rings are pressed on the track, and the mechanical reliability is poor.

Retainer The retainer is connected to the positioning wheel through the bearing, and the positioning wheel is pressed on the inner ring by pretightening force. When working, the inner ring rotates simultaneously to drive the positioning wheel and

the flexible ring to roll, and the positioning wheel guide retainer rotates according to the flexible ring rotation speed.

When the common speed of the flexible ring is the same as that of the guide wheel, there is no sliding friction in the whole roll ring assembly. When the rotation speed of each flexible ring is inconsistent with the retainer speed because of the machining error, the flexible ring with slow speed is pushed by the retainer pin shaft, and the flexible ring with fast speed is blocked by the retainer pin shaft.

2.3 Flexible Ring Structure

The flexible ring structure adopts hollow ring structure, the inner surface of the ring is cylindrical, which is in contact with the pin shaft of the retainer, and the outer side is the electric transmission working surface, which is in contact with the raceway of the inner and outer rings of the roll ring, which can be cylindrical or arc[3].

When the radius of the outer arc surface and the radius of the specific raceway arc surface are small, the contact area between the flexible ring and the raceway is at the vertex, as shown in Fig. 4a. As shown in Fig. 4b, both schemes are practical.

The flexible ring structure parameters include thickness, width, ring radius, arc radius, etc. The thickness should be as thin as possible and the ring radius should be as large as possible under the premise that the machining accuracy and structure size meet the requirements. The purpose is to reduce the stiffness. Under the same fatigue stress, the compression is large and the contact area reliability is improved.

In addition, the pretightening force of the flexible ring is fixed on the radial direction by the inner and outer raceways, and the arc radius of the inner and outer raceways is fixed on the axial direction, so the stability in the process of mechanics and motion should be considered. The arc radius of the raceway should be less than the ring radius, as shown in Fig. 5. At this time, when the flexible ring deflects because of disturbance, $d_2 < d_1$, the compression of the flexible ring increases, the flexible ring can return to its initial position under the extrusion of the inner and outer raceways.

Fig. 4 Flexible ring structure

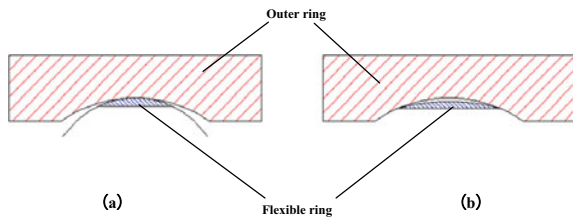
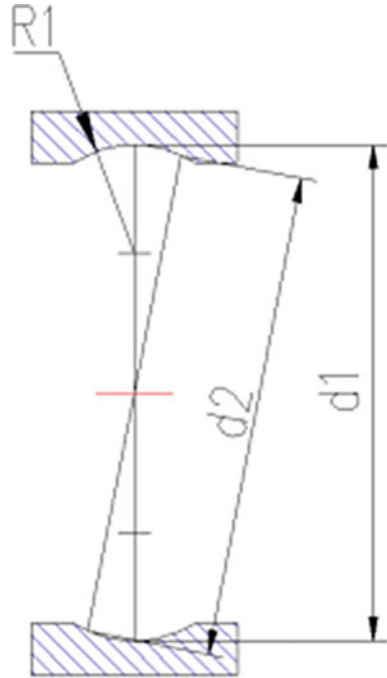


Fig. 5 Roller structure



3 Design Analysis and Optimization

3.1 Power Transmission Capacity

The power transmission capacity of the whole machine mainly includes: (1) insulation and voltage resistance between ring components and lead wires; (2) current transmission capacity of lead wires; (3) current transmission capacity at contact area between stator and rotor.

Cross section area of roller 0.89 mm^2 , which is greater than 20# conductor cross section. The transmission current of 20 conductors is 6.5 A, according to GJB/Z35-93. Each rolling assembly has two rows of rollers, each row of up to 6 rollers, and each roller is annular, the effective conductive area is twice the cross-sectional area. The total transmission current capacity of each rolling component is therefore estimated as 156 A.

3.2 Frictional Torque

Friction torque of roll ring includes friction torque of supporting bearing, friction torque of positioning wheel of retainer, friction torque of roller, etc. The friction torque of each diagonal contact bearing is about 0.05 Nm, total 0.55 Nm.

Friction torque produced by roller is related to the number of rollers, pre-pressure, structure size and other factors. In practice, each ring is not more than 0.1 Nm, according to 5 channels, there are 10 rings with loop, the friction torque is 1 Nm.

As a result, the total friction torque does not exceed 2 Nm. Adopting step motor plus harmonic reducer can easily meet the requirement of driving torque.

3.3 Fatigue Life

The roller life mainly considers the compression fatigue life of the flexible ring during the planetary rotation. The life of the roll ring is generally defined by the number of inner rings. According to the 15 years life of the low-orbit satellite, the number of turns during the life of the whole machine is as follows:

$$30 \times 365 \times 14 = 1.53 \times 10^5 \quad (1)$$

The compression times of the flexible ring can be calculated by the number of meshing times between the inner ring and the flexible ring. The same point on the flexible ring is engaged with the inner ring once, and the fatigue stress is repeated twice, so the number of stress cycles of the flexible ring is:

$$n_2 = 2 \times \frac{(W_H + W_2)}{W_1 \times n_1} \quad (2)$$

The stress cycles of the flexible ring in 15 years are 9.3×10^5 .

The contact stress of roll ring flexible ring is calculated by finite element method. The parameters of beryllium bronze material for flexible ring ($E_1 = 131$ GPa, Poisson's ratio 0.35) and brass material for ring channel ($E_1 = 110$ GPa, Poisson's ratio 0.33). The finite element model and the calculation results are shown in Fig. 6.

The simulation results of displacement load, contact stress and pretightening force in Fig. 6b show that when the compression of flexible ring is 0.28 mm (0.14 mm), the pretightening force is 3.4 N, the maximum stress is 306 MPa.

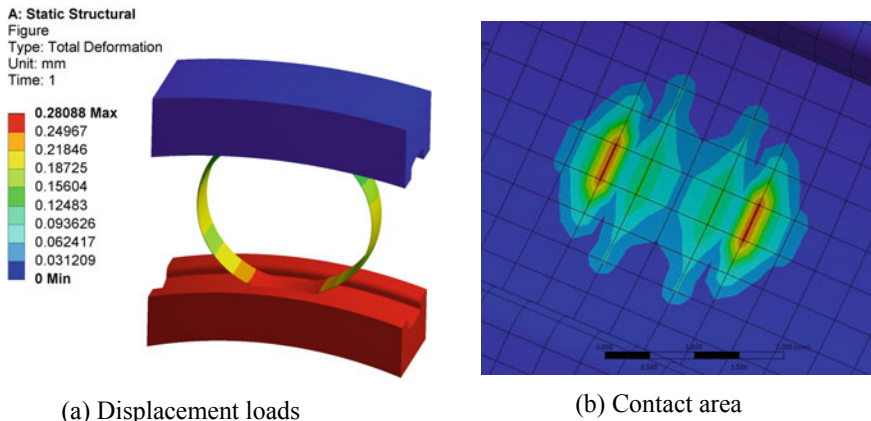


Fig. 6 Finite element calculations

3.4 Resistance and Heating

The contact resistance can be calculated according to the empirical formula (3) [4, 5]. It can be seen from the formula that the flexible ring should be subjected to sufficient pretightening force to reduce the contact resistance value from the point of view of improving the contact resistance performance. In addition, reducing the stiffness of the flexible ring can increase the deformation of the flexible ring and improve the reliability of electrical contact:

$$R_J = \frac{\rho_1 + \rho_2}{2t_p} \sqrt{\frac{H}{F_R}} \tag{3}$$

The pretightening force $F_R = 3.4 \text{ N}$, according to formula (3), the contact resistance calculated empirically is obtained (Fig. 7):

$$R_{J2} = \frac{2.2 \cdot 10^{-5} + 2.2 \cdot 10^{-5}}{2 \cdot 0.15} \sqrt{\frac{550}{3.4}} = 0.18 \text{ m}\Omega \tag{4}$$

Fig. 7 Single-loop resistance distribution



Single ring total resistance:

$$R = 2 \times R_Y + 2 \times R_H + (2 \times R_J + R_G) / 12 = 1.34 \text{ m } \Omega \quad (5)$$

Total heat generation:

$$Q = 40^2 \times 1.34 \times 10 = 21.4 \text{ W} \quad (6)$$

The on-resistance between rings is tested by GW801-H millimeter. The test results show that the circuit resistance is less than 1 m Ω .

4 Conclusions

In this paper, a new type of spacer and flexible ring structure design scheme is proposed for high power and long life application. The power transmission capacity, friction torque, life and heat of the roll ring are analyzed and optimized. The optimal design size is given. The test results show that the product design and calculation are reasonable and scientific to meet the long life engineering application of aerospace.

References

1. Liu, W., Zheng, C., Zhao, K.: Overview on development and application of roll slip ring technology. *fire control radar technology*, vol. 43, no. 2 (2014)
2. Deng, J., Zhang, L., Wu, H., Zhou, P.: Research of rolling rotation electrical transmission technology. *Mach. Des. Manuf.* (2017)
3. Sun, L., Wang, X., Wang, L.: Optimum design on roll ring. *J. Dalian Railw. Inst.* (1990)
4. Holm, R.: *Electric Contacts Handbook*. Springer, Berlin (1958)
5. Multi-Hundred Kilowatt roll ring assembly final report. NASA Report, No CR-174832 (1985)

Analysis on the Influence of Bearing Stiffness on Critical Speed of Rotor System of a New Scroll Compressor



Jiang Pu, Xu Zhou, Ya-feng Su, and Xiu-hua Zhang

Abstract As the third-generation mainstream compressor scroll compressor, most of the normal working speeds are below 7000 RPM, which greatly limits the improvement of system efficiency. The main reason is that the problem of resonance at high speed is not well solved. To avoid resonance and cross the critical speed point smoothly, this paper takes a new type of scroll compressor rotor system with a maximum working speed of 12,000 RPM being developed as the research object, and studies the bearing stiffness, one of the important factors affecting the critical speed, and obtains the influence law of several different bearing stiffness of the system, for the scroll compressor rotor system to avoid resonance and select the bearing stiffness to provide certain theoretical reference and practical guiding significance.

Keywords Scroll compressor rotor · Resonance · Bearing stiffness · Critical speed

1 Introduction

Scroll compressors are widely used in many fields because of its continuous compression process, high efficiency and energy saving, compact structure and other characteristics [1–3]. At present, the working speed of the mainstream scroll compressor is generally in the range of 6000–7200 RPM, and the system efficiency is limited. The efficiency of the system can be improved by increasing the rotor speed, but the increase in the speed makes the system more prone to vibration [4, 5]. As a high-speed rotating part of scroll compressor, the critical speed must be avoided in design and operation. Reasonable configuration of critical speed of rotor system is an important premise and foundation to ensure safe and reliable operation of scroll compressor. The stiffness of rotor bearing is one of the important

J. Pu · X. Zhang (✉)

School of Mechatronics Engineering, Guizhou Minzu University, Guiyang 550025, China

X. Zhou · Y. Su · X. Zhang

School of Mechanical Engineering, Guizhou University, Guiyang 550025, China

© The Author(s), under exclusive license to Springer Nature Switzerland AG 2021

167

L. Zheng et al. (eds.), *Proceedings of MEACM 2020*,

Mechanisms and Machine Science 99,

https://doi.org/10.1007/978-3-030-67958-3_19

parameters affecting the calculation of critical speed [6–9]. Based on the scroll compressor being developed with the maximum working speed of 12,000 RPM, the influence of bearing stiffness on the critical speed of the scroll compressor rotor system was analyzed, so as to provide certain theoretical reference for avoiding resonance of rotor system of scroll compressor and selecting bearing stiffness.

2 Modeling

2.1 3D of the Rotor System Modeled

As the support unit of the scroll compressor rotor system, the dynamic characteristics of the system will be directly affected by the bearing force and stiffness. In order to study the influence of rolling bearings on the dynamic characteristics of high-speed rotor system, a rotor system model was established, as shown in Fig. 1.

2.2 Established Finite Element Analysis of the Rotor System

The simplified model of the rotor system is shown in Fig. 2, and the physical properties of the rotor are shown in Table 1.

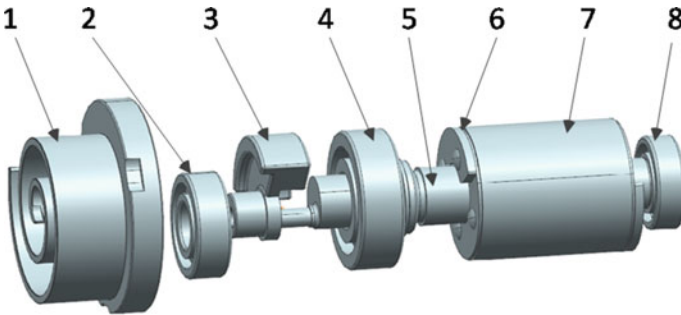


Fig. 1 Rotor structure of scroll compressor. 1. Orbiter, 2. scroll disk bearing, 3. eccentric sleeve, 4. main bearing, 5. principal axis, 6. small counter-weight, 7. motor rotor, 8. counter shaft bearing

Fig. 2 Simplified rotor model of scroll compressor

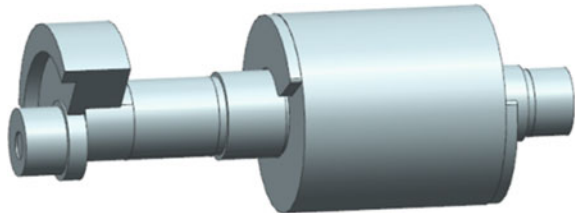


Table 1 Physical properties of components

Parts	Material	Density (kg/m ³)	MOE (N/m ²)	Poisson ratio
Spindle	40Cr	7870	2.11E+11	0.277
Motor rotor	DW310-35	7730	2.18E+11	0.26
Eccentric bushing	QT600	7890	1.73E+11	0.3
Small counterweight	CuZn36Pb1.5	8590	1.05E+11	0.1

3 Analyzed the Influence of Different Bearing Stiffness on the Critical Speed of Rotor

After the physical properties and mesh generation of the rotor are set, constraints and loads are added to the rotor. According to the installation position and assembly relation between rotor parts of scroll compressor and the actual working condition, the influence of rolling bearing damping is usually not considered. As the stiffness of the bearing changes with the change of speed, a large number of tests show that its value is generally $1 \times 10^6 - 1 \times 10^9$ N/m [10–13]. Bearing constraint is adopted to simulate the bearing elements of the rotating subsystem. Bearing stiffness is input only, and distal displacement is adopted to limit the axial displacement of the rotor. Set the rotation speed to 0–12,000 rpm and consider the effect of gyroscope. The rotor analysis model after the above setting is shown in Fig. 3.

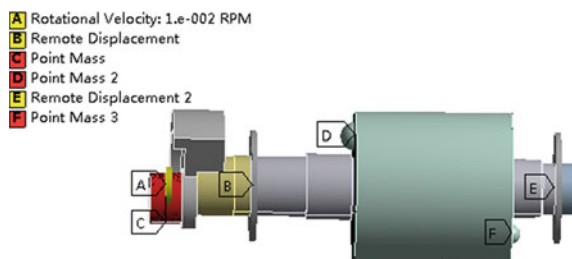
Through simulation, the bearing stiffness shown in Fig. 4 is obtained as The Campbell diagram of the rotor system with 1.0×10^6 N/m, 1.0×10^7 N/m, 1.0×10^8 N/m and 1.0×10^9 N/m respectively, and the rotor vortex frequency as shown in Table 2.

The relationship between rotor speed ω and its natural frequency f is shown in Eq. (1).

$$\omega = 60 f \tag{1}$$

According to Eq. (1), when the bearing stiffness is 1.0×10^6 N/m, the rotor has two critical speeds of 174 and 11,700 RPM within the working speed range, the former is small, and the rotor can cross this critical speed soon after starting to reach a stable operating state. The latter is close to the rotary scroll compressor motor

Fig. 3 Rotor boundary condition constraint model



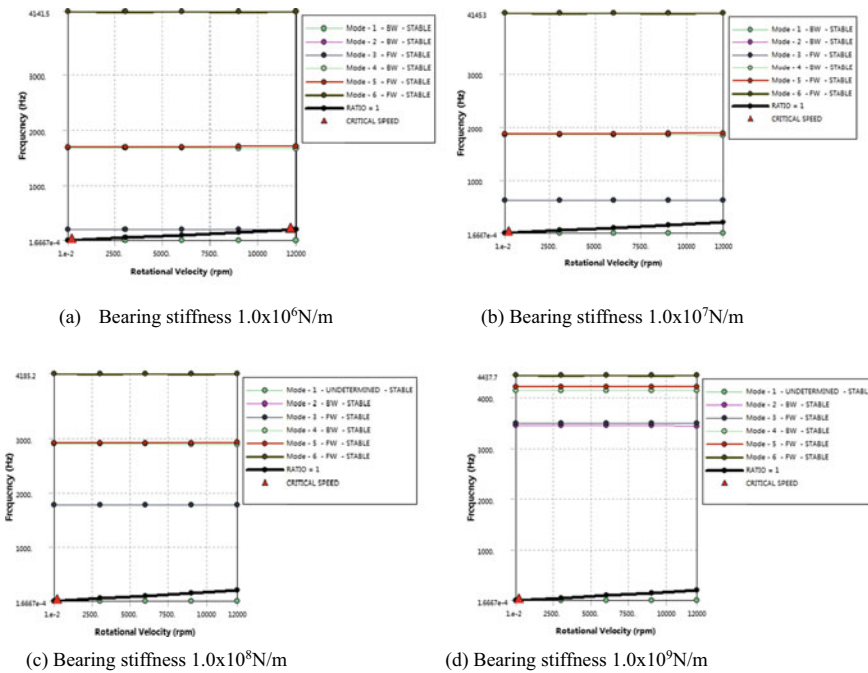


Fig. 4 Campbell diagram of rotor with different bearing stiffness

Table 2 Rotor vortex frequencies with different bearing stiffness

Modal order	1st order	2nd order	3rd order	4th order	5th order	6th order
Bearing stiffness	(HZ)	(HZ)	(HZ)	(HZ)	(HZ)	(HZ)
$1.0 \times 10^6 \text{ N/m}$	2.9	195	195	1679	1686	4141
$1.0 \times 10^7 \text{ N/m}$	2.9	611	611	1856	1864	4145
$1.0 \times 10^8 \text{ N/m}$	2.9	1775	1777	2895	2913	4185
$1.0 \times 10^9 \text{ N/m}$	2.9	3442	3494	4132	4207	4437

speed of 12,000 RPM, and the rotor operating speed that does not meet the engineering requirements should avoid the resonance area of critical speed of about 15%. Similarly, when the bearing stiffness is 10^7 , 10^8 and 10^9 N/m respectively, the scroll compressor avoids the resonance region in the whole working speed. And the critical speed value of the scroll compressor rotor increases with the increase of bearing stiffness, so the bearing stiffness of the scroll compressor motor rotor is at least 10^7 N/m. In the whole speed range, the rotor has only the critical speed at the beginning of the operation, but the high-speed rotor will quickly cross the threshold speed to reach the stable operation state, in line with the actual working state of the rotor. By studying the influence of different bearing stiffness on the dynamic

performance of the rotor, it is shown that when the working speed of the rotor system is close to the critical speed, the rotor can run smoothly by changing the bearing stiffness without changing the structure.

4 Conclusion

- (1) The analysis of the critical speed under different bearing stiffness shows that the critical speed of the scroll compressor rotor increases with the increase of bearing stiffness. Therefore, when the working speed of the rotor system is close to the critical speed, the rotor can run smoothly by changing the bearing stiffness without changing the structure.
- (2) For this rotor system, the rotor will generate resonance when the bearing stiffness is less than 1.0×10^7 N/m, and the rotor will avoid resonance when the bearing stiffness is greater than 1.0×10^7 N/m. However, too much bearing stiffness will also cause the bearing life to be weakened. Considering this, the system chooses 1.0×10^7 N/m bearing stiffness.

Acknowledgements 1. Science and Technology Planning Project of Guizhou Province [Basic science and Technology of Guizhou Province (2019) No. 1166].

2. Talent Introduction Program of Guizhou University [Guida Jihe Zi (2015) 51].

References

1. Liu, X.-W., Pang, C.-W.: Research on oil and gas separation performance of scroll Compressor for Electric Vehicle. *Fluid mach.* (1), 34–39 (2018)
2. Dong, G.: Research on Electric Car Air Conditioner General Scroll Profiles Compressor Design and Process. Chongqing University of Technology (2017)
3. Yu, Y., Li, C., Zhao, M., et al.: Modal analysis of scroll compressor in rotator system with finite element method. *J. Appl. Sci.* (2014)
4. Liu, Z.-Q.: Scroll fluid Machinery and Scroll Compressor, p. 1. CHINA MACHINE PRESS, Beijing (2009)
5. Liu, Z., Du, G.: Mechanical model of scroll compressor. *Ch. J. Mech. Eng.* (1999)
6. Jiang, Y.-F., Liao, M.-F.: Stiffness characteristics analysis on high-pressure rotor front bearing of aero-engine. *J. Propuls. Technol.* **35**(08), 1123–1130 (2014)
7. Wei, Dou, Liu, Z.: Effect of turbo-pump bearing supporting stiffness and axial position on critical speed of rotor system in liquid rocket engine. *Missiles Space Veh.* **03**, 18–22 (2013)
8. Zhou, J., Sun, W., Cui, Q.: Research of the effect of bearing stiffness and gear helix angle on vibration noise of gear reducer. *J. Mech. Trans.* **39**(05), 20–25 (2015)
9. Li, X., Zhu, H., Qin, Y.: Influence of Aft Stern tube bearing stiffness on whirling vibration of ship shafting. *J. Wuhan Univ. Technol. (Transp. Sci. Eng.)* **42**(02), 274–277 (2018)
10. Pei, L.I.U., Kunpeng, W.E.I., Xingjian, D.A.I.: Analysis and experimental study on the shaft of a 1 MW/60 MJ flywheel energy storage system. *Energy Stor. Sci. Technol.* **6**(06), 1257–1263 (2017)

11. Tang, K.-L., Zhang, X.-W., Xiong, H.-W.: The transfer matrix method of rotor system considering bearing countermoment. *Mach. Tool Hydraul.* (10), 27–29 (2005)
12. Chen, H.: *Research of Modal Analysis and Dynamic Characteristics for Turbine Rotor DJ*. North China Electric Power University (Beijing) (2017)
13. Xia, Q.: *Finite Element Analysis and Optimization of Steel Bar Cutting Machine Based on ANSYS Workbench*. Taiyuan University of Science and Technology (2015)

Experimental and Simulation Data-Driven Rolling Bearing Fault Size Quantitative Diagnosis in Big Data Era



W. T. Huang, H. Zhai, J. N. Luo, Y. C. Jiang, and W. J. Wang

Abstract Data-driven fault diagnosis based on machine learning in rolling bearing has become a hot topic in the field of fault diagnosis in recent years. Researchers have focused on the study of diagnostic methods while ignoring the connotation of data and the background of big data. Therefore, aiming at the problem that sample data is insufficient in rolling bearing fault diagnosis, the vibration response simulation signal generated by the dynamic model of the rolling bearing with four degrees of freedom is applied to the quantitative diagnosis of the rolling bearing fault size so as to enrich the data set of the rolling bearing. The VMD-BLSTM method is proposed, which extracts the information features by calculating the VMD energy entropy of rolling bearing vibration signal based on variational mode decomposition and put features into BLSTM network, in order to obtain the result of different fault size classification of rolling bearing. This method is applied to both experimental and simulation data-driven rolling bearing fault size quantitative diagnosis by estimating fault size of rolling bearing intelligently.

Keywords Variational mode decomposition · Long short-term memory · Experimental data-driven · Simulation data-driven · Fault diagnosis

1 Introduction

Rolling bearing is one of the most important common parts of rotating machinery and equipment. Its health affects the working condition and operating life of the entire mechanical equipment. The field of fault diagnosis is entering the era of big data due to the large scale requirement of diagnosis, more test points, and longer data collection period of equipment [1]. Under the background of big data,

W. T. Huang (✉) · H. Zhai · J. N. Luo · Y. C. Jiang · W. J. Wang
School of Mechatronics Engineering, Harbin Institute of Technology, Harbin 150001, China
e-mail: hwt@hit.edu.cn

J. N. Luo
Shenyang Aircraft Design Institute, Shenyang 110035, China

intelligent diagnosis gets rid of the dilemma that traditional fault diagnosis relies on experts. Relying on the large capacity, diversity and high rate of data, intelligent diagnosis could identify the fault state of equipment accurately and efficiently [2].

In recent years, data-driven fault diagnosis based on machine learning has become a hot topic in this field. Patil et al. [3] combined the discrete wavelet transform and artificial neural network to achieve a good detection of the faults of the inner and outer rings of the rolling bearing. Shen et al. [4] proposed a quantitative identification method for rolling bearing fault size based on support vector regression, which can accurately identify fault size by extracting the feature vector from the original signal as input and fault size as output. Wen et al. [5] proposed a new convolutional neural network that converts one-dimensional signals into two-dimensional images and achieves high diagnostic accuracy in fault diagnosis of bearings, centrifugal pumps and hydraulic pumps.

Now, the proposed diagnosis methods are only verified in limited open source data sets or laboratory conditions. The sizes of bearing fault provided by these data sets are small and limited. Therefore, these “small sample” datasets have some limitations. Moreover, faults based on historical data are only effective for the specific environment in which they are collected [6], which often fails to reflect the large capacity and diversity of big data, thus deviating from the original intention of data-driven fault diagnosis. For the shortcomings of insufficient sample data information in fault diagnosis and the lack of effective actual fault data of fault labels, the vibration response signal of bearing simulation is obtained by using the dynamic model of rolling bearing with four degrees of freedom, and it is applied to the quantitative diagnosis of rolling bearing fault size to enrich the bearing data set. Based on the methods of Variational Mode Decomposition (VMD) and Bidirectional Long short-term Memory (BLSTM) network, this paper changes the previous data-driven fault diagnosis by only using a small sample of a limited number of experimental data, and conducts the fault degree quantitative diagnosis of bearing through the dual data-driven experiment and simulation.

2 Dynamic Model of Surface Failure of Outer Ring Raceway of Rolling Bearing

Many scholars have studied the dynamic model of rolling bearing. Sawalhi et al. [7] proposed to simulate the bearing base with the mass-spring-damping system, and analyzed the simulation results and experimental results in time domain and frequency domain, and found a good consistency between the two results. Petersen et al. [8] proposed a multi-body dynamic analysis model, which was extended to double-row bearings to predict the vibration response of rolling bearings with raceway surface defects. Our research group [9] introduced the impact force into the vibration model and established a dynamic model of rolling bearing with four degrees of freedom.

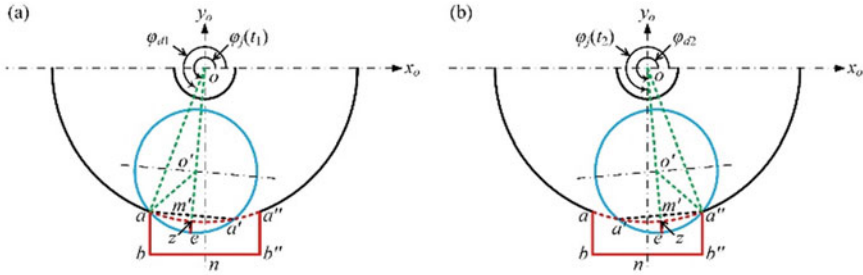


Fig. 1 The balls pass through the defect area of outer race of bearing

As can be seen from Fig. 1, without considering whether the rolling body is in contact with the bottom end of the fault, which means the influence of fault depth h_d on the motion path of the rolling body is ignored. The directional displacement of the rolling body $\delta_d(t)$ is related to the fault length l_d , which means it is related to the angle φ_d between the fault and the center of the bearing circle. When l_d changes, $\delta_d(t)$ changes accordingly, so the vibration response results obtained are also different. The expressions are as below

$$\left\{ \begin{array}{l} \delta_d(t) = r_b - \sqrt{r_b^2 - r_o^2 \sin^2(\varphi_j(t) - \varphi_a)} - r_o \\ \quad + r_o \cos(\varphi_j(t) - \varphi_a), \varphi_a \leq \varphi_j(t) < \varphi_m \\ \delta_d(t) = r_b - \sqrt{r_b^2 - r_o^2 \sin^2(\varphi_c - \varphi_j(t))} - r_o \\ \quad + r_o \cos(\varphi_c - \varphi_j(t)), \varphi_m \leq \varphi_j(t) \leq \varphi_c \end{array} \right. \quad (1)$$

where, r_b and r_o are respectively the radius of the rolling body and the outer ring raceway, φ_a and φ_c are position angles of the front and back edge of the failure area, φ_m is the position angle of the failure area in the radial plane median line, with $\varphi_m = 270^\circ$.

The vibration response signal of the actual fault bearing obtained by the EDM and the vibration response signal obtained by the dynamic model simulation are shown in Fig. 2a and b respectively. From the moment of the rolling body entering

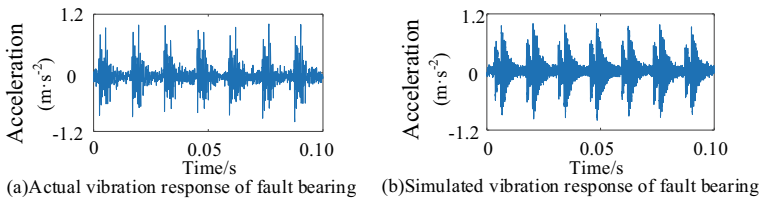


Fig. 2 Vibration response of outer race fault with size of 3.280 mm

and leaving the defect, there is little difference between the two signals. Therefore, the simulation data can be used as the database for fault diagnosis of the rolling bearing.

3 VMD Energy Entropy Signal Feature Extraction Method

3.1 Basic Principle of VMD Algorithm

Variational Mode Decomposition (VMD) is a novel non-recursive mode decomposition signal processing and the feature extraction method was proposed by Konstantin et al. [10] on the basis of Empirical Mode Decomposition (EMD).

In the VMD algorithm, Intrinsic Mode Function (IMF) is defined as an AM-FM signal, and the expression is

$$u_k(t) = A_k(t) \cos(\varphi_k(t)) \quad (2)$$

where, $A_k(t)$ represents the instantaneous amplitude of $u_k(t)$; $\varphi_k(t)$ represents the instantaneous phase of $u_k(t)$.

The basic principle of the VMD algorithm is to find K IMF components under constraint conditions so as to minimize the sum of the estimated bandwidth of IMF. Its specific structure is shown as follows:

- (1) Analytical signals of each IMF were obtained by Hilbert transformation and their unilateral spectra were solved as below:

$$\left(\delta(t) + \frac{j}{\pi t} \right) * u_k(t) \quad (3)$$

- (2) Add the prediction center frequency index item $e^{-j\omega_k t}$ to each analytical signal, and adjust the frequency spectrum of each IMF to the corresponding fundamental frequency band

$$\left[\left(\delta(t) + \frac{j}{\pi t} \right) * u_k(t) \right] e^{-j\omega_k t} \quad (4)$$

- (3) Calculate the square norm of regulated signal gradient and estimate the bandwidth of each mode signal, and the variational problem constructed by that can be expressed by Eq. (6).

$$\left\{ \begin{array}{l} \min_{\{u_k, \omega_k\}} \left\{ \sum_k \left\| \partial_t \left[\left(\delta(t) + \frac{j}{\pi t} \right) * u_k(t) \right] e^{-j\omega_k t} \right\|_2^2 \right\} \\ s.t. \sum_k u_k = x(t) \end{array} \right. \quad (5)$$

where, $\{u_k\}$ represents K IMF components after variational mode decomposition, and $\{\omega_k\}$ represents the frequency center corresponding to each IMF component. The optimization selection method of K value is as follows [11]:

For this constrained variational problem, VMD algorithm introduced quadratic penalty factor α and Lagrangian multiplication operator $\lambda(t)$ to eliminate the constraint, transforming the constrained variational problem into A non-variational constraint problem, namely, the solution of the minimum value was transformed into the problem of saddle points for solving the Lagrangian augmented function, whose expression was expressed by Eq. (9).The quadratic penalty factor α enables VMD variational problem to guarantee the signal decomposition and reconstruction accuracy under gaussian noise. The larger its value is, the smaller the bandwidth of each mode signal is. The Lagrangian multiplication operator $\lambda(t)$ guarantees the strictness of the constraint.

$$\begin{aligned} L(\{u_k\}, \{\omega_k\}, \lambda) = & \alpha \sum_k \left\| \partial_t \left[\left(\delta(t) + \frac{j}{\pi t} \right) * u_k(t) \right] e^{-j\omega_k t} \right\|_2^2 \\ & + \left\| x(t) - \sum_k u_k(t) \right\|_2^2 + \left\langle \lambda(t), x(t) - \sum_k u_k(t) \right\rangle \end{aligned} \quad (6)$$

VMD uses the multiplication operator alternating direction method to solve the saddle point of Lagrangian augmented function by updating u_k^{n+1} , ω_k^{n+1} and λ_k^{n+1} alternately which is the optimal solution. The expression of u_k^{n+1} can be expressed by Eq. (7).

$$u_k^{n+1} = \arg \min_{u_k \in X} \left\{ \alpha \left\| \partial_t \left[\left(\delta(t) + \frac{j}{\pi t} \right) * u_k(t) \right] e^{-j\omega_k t} \right\|_2^2 + \left\| x(t) - \sum_i u_i(t) + \frac{\lambda(t)}{t} \right\|_2^2 \right\} \quad (7)$$

By using Fourier transform, u_k^{n+1} in Eq. (7) is converted to the frequency domain

$$\hat{u}_k^{n+1}(\omega) = \frac{\hat{x}(\omega) - \sum_{i \neq k} \hat{u}_i(\omega) + \frac{\hat{\lambda}(\omega)}{2}}{1 + 2\alpha(\omega - \omega_k)^2} \quad (8)$$

The updated equation of frequency ω_k^{n+1} is

$$\omega_k^{n+1} = \frac{\int_0^\infty \omega |\hat{u}(\omega)|^2 d\omega}{\int_0^\infty |\hat{u}(\omega)|^2 d\omega} \tag{9}$$

The updated equation of Lagrangian coefficient Q is

$$\lambda_k^{n+1} = \lambda_k^n + \tau(\hat{x}(\omega) - \sum_k \hat{u}_k^{n+1}(\omega)) \tag{10}$$

where, τ is the fidelity coefficient. Generally, τ takes 0 to remove the noise in the decomposed vibration signal.

When the condition of Eq. (11) is satisfied, iterative update is stopped and VMD algorithm is completed.

$$\frac{\sum_k \|\hat{u}_k^{n+1} - \hat{u}_k^n\|_2^2}{\|\hat{u}_k^n\|_2^2} < e \tag{11}$$

where, e is the discriminant accuracy.

3.2 Feature Extraction of Bearing Fault Signal Based on VMD Energy Entropy

In the running process of rolling bearing, the collected signals are generally one-dimensional signals, and the state of each component can be observed through variational mode decomposition. For example, variational mode decomposition is performed on the vibration signal of a certain faulty bearing, and the calculation parameters $K = 4, \alpha = 2000, \tau = 0, e = 10^{-7}$ are set. The results are shown in Fig. 3.

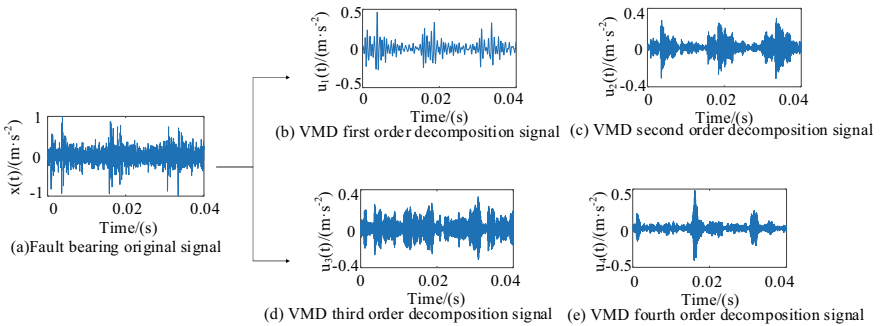


Fig. 3 The result of VMD of bearing signal

However, for different IMF corresponding $u_k(t)$, it is still difficult to extract effective features only from the time-domain signal, and the corresponding frequency components of the rolling bearing will also change under different fault conditions. Therefore, the energy entropy method based on VMD is proposed as a means to extract effective information of vibration signal of rolling bearing.

The k modal component calculation energy entropy obtained by performing VMD calculation on the rolling bearing vibration signal, can reflect the proportion of each modal component in the original signal energy, so as to obtain the fault characteristics of rolling bearing under different fault conditions.

The energy entropy calculation formula of each mode component of VMD is

$$H(u_k) = -P_k \log P_k \tag{12}$$

where, $H(u_k)$ is the energy entropy of the K th component u_k ; P_k is the proportion of energy of the K th component u_k in the total signal energy, $P_k = \frac{E_k}{E}$; E is the overall energy of the signal, $E = \sum_{i=1}^K E_i$; E_k is the energy of the K th component, u_k , $E_k = \sum u_k(t)^2$.

The energy entropy of each modal component of VMD is calculated for the vibration signal of rolling bearing corresponding to Fig. 4, and the results are shown in Table 1.

4 BLSTM Fault Quantitative Diagnosis Method

BLSTM is an improvement on a Recurrent Neural Network (RNN). HOCHREITER et al. [11] proposed the most original LSTM, which solved the problem of long-term dependence. After improving, LSTM has been applied to power transformer operation state prediction, traffic prediction and fault prediction of complex systems such as aircraft [12–14].

Fig. 4 Diagram of LSTM unit

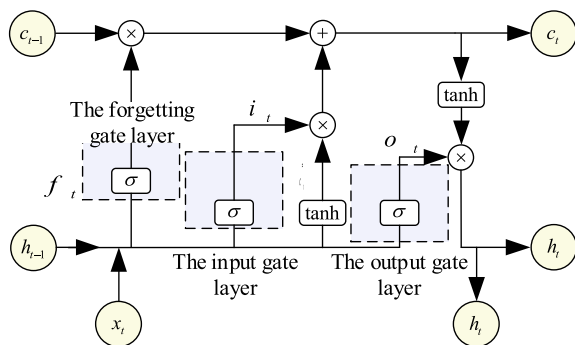


Table 1 VMD energy entropy of each intrinsic mode component of bearing signal

K	1	2	3	4
Energy entropy	0.1213	0.0352	0.3974	0.5227
Proportion	11.27%	3.27%	36.91%	48.55%

4.1 Basic Principle of LSTM

Set x as the input of LSTM cell, and h is the output of LSTM cell, c is the memory cell of LSTM cell, and \tilde{c} is the candidate memory cell of LSTM cell; i_t is the value of LSTM’s input gate, f_t is the value of LSTM’s forgetting gate, and o_t is the value of LSTM’s output gate. The unit schematic diagram of LSTM is shown in Fig. 5. Unlike the traditional single-layer RNN, the LSTM unit is specifically designed to store historical information in memory cells.

The update steps for the LSTM unit are as follows

- (1) Calculate the value f_t of the forgetting gate. The forgetting gate layer is used to control the influence of historical information on current memory cells.

$$f_t = \sigma(W_{xf}x_t + W_{hf}h_{t-1} + b_f) \tag{13}$$

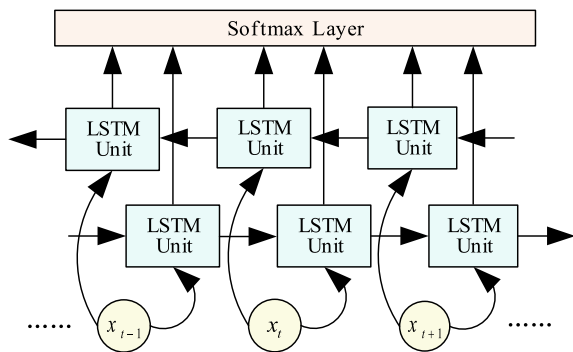
where, W_{xf} is the input weight corresponding to the forgetting gate layer, W_{hf} is the output weight of LSTM unit corresponding to the forgetting gate layer at the last moment, and b_f is the bias corresponding to the forgetting gate layer.

- (2) Calculate the value i_t of the input gate. The input gate layer is used to control the influence of current input data on memory cells.

$$i_t = \sigma(W_{xi}x_t + W_{hi}h_{t-1} + b_i) \tag{14}$$

where, W_{xi} is the input weight corresponding to the input gate layer, W_{hi} is the LSTM unit output weight corresponding to the input gate layer at the last moment, and b_i is the bias corresponding to the input gate layer.

Fig. 5 Diagram of BLSTM net structure



- (3) According to the principle of RNN, the candidate memory cell value \tilde{c}_t at the current moment is calculated

$$\tilde{c}_t = \tanh(W_{xc}x_t + W_{hc}h_{t-1} + b_{\tilde{c}}) \quad (15)$$

where, W_{xc} is the input weight corresponding to candidate memory cells, W_{hc} is the output weight of LSTM unit corresponding to candidate memory cells at the last moment, and $b_{\tilde{c}}$ is the bias corresponding to candidate memory cells.

- (4) Determine the current memory cell value of c_t

$$c_t = f_t \otimes c_{t-1} + i_t \otimes \tilde{c}_t \quad (16)$$

where, \otimes represents the dot product.

- (5) Calculate the value o_t of the output gate at the current moment

$$o_t = \sigma(W_{xo}x_t + W_{ho}h_{t-1} + b_o) \quad (17)$$

where, W_{xo} is the input weight corresponding to the output gate layer, W_{ho} is the output weight of LSTM unit at the last moment corresponding to the output gate layer, and b_o is the bias corresponding to the output gate layer.

- (6) Calculate the output value h_t of LSTM unit at the current moment

$$h_t = o_t \otimes \tanh(c_t) \quad (18)$$

This paper adopts BLSTM network structure, which is shown in Fig. 5. BLSTM is the fusion of bidirectional RNN and LSTM. Output data can be got by input data through bidirectional LSTM unit, and then pass through the Softmax layer to get the final classification result.

4.2 Quantitative Diagnosis of Rolling Bearing Fault Based on BLSTM

The vibration signal of rolling bearing can be regarded as a time series and the characteristic information extracted from the signal can also be regarded as a sequence. Therefore, BLSTM network classification method can be used to classify and estimate the fault size of rolling bearing. Based on the content introduced in Sect. 3.2, the VMD energy entropy feature sequence extracted from the rolling bearing signal was regarded as the input of BLSTM network, which was divided into training set and test set, and corresponding input features were labeled. The BLSTM network structure was defined, and relevant parameters such as input feature dimension, number of hidden neurons, training times and minimum iterative sample size were set and the model was trained. Then the test set is used to test the

trained model to get the test results, so as to make quantitative diagnosis of different failure sizes of rolling bearings.

5 Quantitative Diagnosis of Bearing Fault Driven by Experimental Data

For the fault diagnosis of rolling bearing with different fault locations and fault sizes driven by experimental data, the rolling bearing experimental data adopted in this paper comes from the CWRU bearing data center, and its signal acquisition system is shown in Fig. 6. The experimental bearing is the 6205 deep groove ball bearing produced by SKF. The fault was made by EDM (Electric Discharge Machining). The sampling frequency of the sensor is $f_s = 12,000$ Hz and the rotation speed of the shaft is $r = 1730$ r/min. In the experiment, 9 kinds of bearing vibration signal data with different fault positions and fault sizes under the motor load of 3HP were selected, the fault positions were in the outer ring, inner ring and rolling body respectively, and the fault sizes were 0.178, 0.356 and 0.533 mm respectively, there are 10 types faults plus normal bearing data, and the drive end signal data were taken.

For this data set, 100 segments of signals are randomly selected as training samples under each fault state, and 20 segments of signals are randomly selected as test samples. There are 1000 training samples and 200 test samples.

The collected signal was extracted with VMD energy entropy feature. The parameters of VMD are: $K = 4$, $\alpha = 2000$, $\tau = 0$, $e = 10^{-7}$. By calculating the energy entropy of each IMF, the characteristic sequences of 10 different faults were obtained.

BLSTM network structure is defined: the input feature dimension of BLSTM is 4, the number of hidden layer neurons is 200, the number of training times is 500,

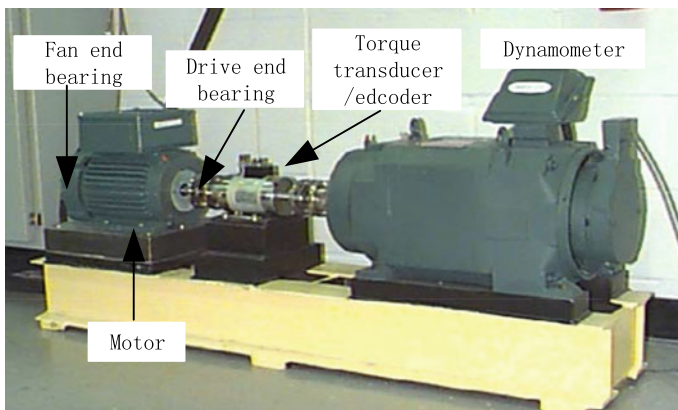


Fig. 6 CWRU bearing signal acquisition system

the minibatch size is 20, and the learning rate is 0.001. Adaptive moment estimation algorithm is used to adjust the weight parameter optimization model of neural network.

The extracted features were input into the constructed BLSTM training model and tested with the test set to obtain the final diagnosis result. Diagnostic accuracy is the ratio of the number of correct test results to the total number of test samples. Since the diagnosis time is greatly affected by hardware and software, the diagnosis time referred to in this paper is a relative value, and the diagnosis time of VMD-BLSTM method is defined as 1. The diagnosis time of other diagnostic methods is the ratio of the actual time of this method and the actual time of VMD-BLSTM method.

In order to prove that VMD-BLSTM method is applicable to quantitative diagnosis of rolling bearing fault size, this paper also lists the diagnosis results of some traditional diagnosis methods for comparison, as shown in Table 2. In order to retain more effective feature information, the first 6 modes of EMD were selected. The kernel function of Support Vector Machine (SVM) is radial basis function, and the kernel function parameters are optimized with coarse grid method, with a learning rate of 0.01. The experimental data-driven test results of each diagnostic method are the average of 10 experimental test results.

As can be seen from the comparison in Table 2, VMD-BLSTM has the highest diagnostic accuracy. The method based on EMD is limited by the algorithm itself, resulting in a large number of feature dimensions of the data, poor diagnostic accuracy and long time. Although the diagnosis time of SVM is shorter than that of BLSTM, its accuracy is lower and it is not conducive to dealing with big data problems. It can be seen that VMD-BLSTM is a feasible diagnosis method in rolling bearing fault diagnosis experiment. Therefore, VMD-BLSTM method is used in the following parts to conduct quantitative diagnosis of rolling bearing fault size.

6 Simulation Data-Driven Quantitative Diagnosis of Bearing Outer Ring Fault

Although the CWRU database can be used to verify the diagnosis methods of fault location identification and fault size estimation, the characteristics of different fault locations are easy to distinguish, and for the fault size of rolling bearings, only three different fault sizes is far from enough for the intelligent fault diagnosis in big data background. In addition, the l data obtained only under experimental conditions are

Table 2 The result of experimental data-driven fault diagnosis in different methods

Methods	EMD-SVM	VMD-SVM	EMD- BLSTM	VMD- BLSTM
Accuracy (%)	85.00	96.50	97.86	99.75
Time	0.91	0.79	1.19	1

limited. Therefore, this paper simulates the vibration response of the fault bearing according to the dynamic model of the rolling bearing mentioned above, so as to obtain the simulation signal data of the rolling bearing and enrich the database.

According to the dynamics model mentioned above, the outer ring raceway failure angle φ_d is used to determine the size of the outer ring raceway failure size l_d , a total of 22 kinds, the corresponding size parameters are shown in Table 3.

For the simulation data of each kind of outer ring fault, 100 segments of signals were randomly selected as training samples, and 20 segments of signals were randomly selected as test samples. The sampling points of each segment were 2048. Assuming that the simulation data has k kinds of outer ring faults of different sizes, there are $k \times 100$ training samples and $k \times 20$ test samples.

Firstly, 14 kinds of simulation signals of outer ring fault sizes were selected, φ_d being 0.2° , 0.4° , 0.6° , 0.8° , 1.0° , 1.4° , 2.0° , 2.5° , 3.0° , 3.5° , 4.0° , 4.5° , 5.0° and 8.0° respectively. VMD energy entropy was calculated for each signal. The BLSTM network is trained with training samples, and the test samples are input into the trained network to classify and estimate the fault size, and the result of quantitative diagnosis of rolling bearing fault size is obtained. Then the sample types were increased to 22 kinds of outer ring fault sizes, and the quantitative diagnosis results of rolling bearing fault sizes were obtained in the same way. For the VMD-BLSTM diagnostic method, relevant parameters of BLSTM are listed in Table 4, and the diagnostic results are shown in Fig. 7, where the diagnostic accuracy is the average of the five test results.

According to the diagnostic results in Fig. 7, when the BLSTM network structure with number 1 and the number of modal components $K = 4$ were adopted, the diagnostic accuracy of 14 kinds of outer ring fault sizes was significantly lower than that of CWRU experimental data. This shows that, with the increase of the type of training samples, the BLSTM network classifier with the same structural parameters presents a situation of under-fitting, resulting in a decrease in accuracy. Increasing the number of hidden neurons and training times appropriately can improve the diagnostic accuracy. However, due to the increasingly complex structure of BLSTM network, the corresponding training time will be increased accordingly, so the efficiency of diagnosis will be reduced or even unable to meet the requirements. In addition, blindly increasing the number of iterations of

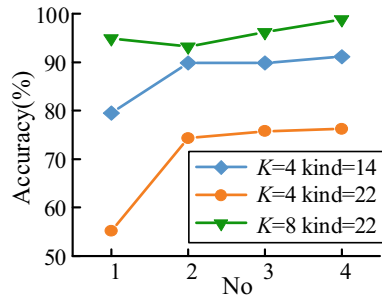
Table 3 22 kinds of fault size parameters of outer race

No	φ_d ($^\circ$)	l_d (mm)	No	φ_d ($^\circ$)	l_d (mm)	No	φ_d ($^\circ$)	l_d (mm)	No	φ_d ($^\circ$)	l_d (mm)
1	0.2	0.082	7	1.4	0.574	13	3.5	1.432	19	6.5	2.659
2	0.4	0.164	8	1.6	0.656	14	4.0	1.639	20	7.0	2.863
3	0.6	0.246	9	1.8	0.738	15	4.5	1.843	21	7.5	3.066
4	0.8	0.328	10	2.0	0.820	16	5.0	2.048	22	8.0	3.280
5	1.0	0.410	11	2.5	1.025	17	5.5	2.252			
6	1.2	0.492	12	3.0	1.230	18	6.0	2.456			

Table 4 BLSTM parameters in simulation data-driven

No	Number of hidden neurons	Number of training	Small sample handling capacity
1	200	500	20
2	800	1200	20
3	1000	1500	20
4	1500	1800	20

Fig. 7 The result of simulation data-driven fault quantitative diagnosis of rolling element bearing



BLSTM network may lead to over-fitting, so it is necessary to set the termination iteration conditions and regularization.

However, in the quantitative diagnosis of 22 kinds of outer ring fault sizes, the diagnostic accuracy for the number of modal components $K = 4$ has been reduced to completely be unable to meet the requirements of intelligent fault diagnosis. Moreover, even adjusting the relevant parameters of BLSTM network cannot substantially improve the diagnostic accuracy. In this regard, the number of modal components K is adjusted to 8, increasing the dimension of the input feature. When 8 modes of VMD energy entropy were input into BLSTM network, the diagnostic accuracy was over 90%. By increasing the dimension of the input feature, the information of the input feature is enriched and the diagnostic accuracy is greatly improved. By strengthening and optimizing the structure of BLSTM network, or adjusting the number of modal components of VMD and improving the dimension of input features, data-driven quantitative diagnosis of rolling bearing faults can be realized.

7 Conclusion

- (1) Based on a four-degree-of-freedom rolling bearing dynamic model, the bearing vibration simulation signals of bearing outer ring fault were obtained. By setting the angle of the outer ring raceway fault, the bearing vibration simulation signals of different fault sizes were obtained, which can enrich the data set of different fault sizes of the rolling bearing, and provide a database with large

capacity and diversity for intelligent fault diagnosis of the rolling bearing under big data.

- (2) Quantitative diagnosis of rolling bearing based on VMD-BLSTM method. VMD energy entropy was calculated to extract the characteristics of the vibration signal of the fault bearing, which was input into the BLSTM network to obtain the classification results, so as to quantitatively diagnose the fault size of the rolling bearing. The method has high accuracy and good practicability.
- (3) In the quantitative diagnosis of the rolling bearing driven by simulation data, as the parameters of VMD-BLSTM remain unchanged, the sample types increased, the training set became larger, the phenomenon of underfitting occurred, and the diagnostic accuracy decreased. In order to obtain high diagnostic accuracy, it is necessary to strengthen and optimize the structure of BLSTM network properly and increase the number of VMD modal components, improve the dimension of the features properly.

Through the dual data drive of experiment and simulation, the data set of the fault bearing is expanded, the fault size of the rolling bearing is quantitatively diagnosed, and the intelligent fault diagnosis of the rolling bearing under big data is realized.

References

1. Lei, Y.G., Jia, F., Kong, D.T., et al.: Opportunities and challenges of machinery intelligent fault diagnosis in big data era. *J. Mech. Eng.* **54**(5), 94–104 (2018)
2. Lei, Y.G., Jia, F., Zhou, X., et al.: A deep learning-based method for machinery health monitoring with big data. *J. Mech. Eng.* **51**(21), 49–56 (2015)
3. Patil, A.B., Gaikwad, J.A., Kulkarni, J.V.: Bearing fault diagnosis using discrete Wavelet Transform and Artificial Neural Network. I: Proceedings of the IEEE international conference on applied and theoretical computing and communication technology, 21–23 July 2016, Bengaluru, Karnataka, India, pp. 99–405 (2016)
4. Shen, C.Q., Hu, F., Liu, F., et al.: Quantitative recognition of rolling element bearing fault through an intelligent model based on support vector regression. In: 4th international conference on intelligent control and information processing, 09–11 June 2013, Beijing, China, pp. 842–847 (2013)
5. Wen, L., Li, X.Y., Gao, L., et al.: A new convolutional neural network-based data-driven fault diagnosis method. *IEEE Trans. Ind. Electron.* **65**(7), 5990–5998 (2018)
6. Sobie, C., Freitas, C., Nicolai, M.: Simulation-driven machine learning: bearing fault classification. *Mech. Syst. Signal Process.* **99**, 403–419 (2018)
7. Sawalhi, N., Randall, R.B.: Simulating gear and bearing interactions in the presence of faults: Part I. The combined gear bearing dynamic model and the simulation of localized bearing faults. *Mech. Syst. Signal Process.* **22**(8), 1924–1951 (2008)
8. Petersen, D., Howard, C., Sawalhi, N., et al.: Analysis of bearing stiffness variations, contact forces and vibrations in radially loaded double row ball bearings with raceway defects. *Mech. Syst. Signal Process.* **50–51**, 109–160 (2014)
9. Huang, W.T., Dong, Z.Z., Kong, F.C.: Vibration model of rolling bearings with inner race faults considering impact force. *J. Vib. Shock* **35**(17), 121–126 (2016)

10. Konstantin, D., Dominique, Z.: Variational mode decomposition. *IEEE Trans. Signal Process.* **62**(37), 531–544 (2014)
11. Hochreiter, S., Schmidhuber, J.: Long short-term memory. *Neural Comput.* **9**(8), 1735–1780 (1997)
12. Dai, J.J., Song, H., Sheng, G.H., et al.: Prediction method for power transformer running state based on lstm network. *High Volt. Eng.* **44**(4), 1099–1106 (2018)
13. Ma, X.L., Tao, Z.M., Wang, Y.H., et al.: Long short-term memory neural network for traffic speed prediction using remote microwave sensor data. *Transp. Res. Part C Emerg. Technol.* **54**, 187–197 (2015)
14. Wang, X., Wu, J., Liu, C., et al.: Exploring LSTM based recurrent neural network for failure time series prediction. *J. Beijing Univ. Aeronaut. Astronaut* **44**(4), 772–778 (2018)

Research on Assembly Error Transmission of Small Displacement Spinor Based on State Space Model



Chunqi Chen, Wei Wu, and Jianzhong Shang

Abstract In the assembly process of precision machinery, the error modeling of the assembly process is one of the important means to analyze the assembly error. This paper analyzes the error propagation in the assembly process, establishes a mechanical assembly error propagation model based on the small displacement spin (SDT) using the homogeneous transformation of robotics coordinates, and derives the state space expression of the mechanical assembly process. Finally, a primary and secondary mirror system is used as an example to analyze, using computer software simulation and state space equations to predict the final cumulative error of the assembly, which verifies the feasibility of the method for predicting the cumulative error of the precision assembly process.

Keywords State space · Small displacement spinor · Coordinate transformation · Error transfer

1 Introduction

In the assembly process of precision machinery, the overall error of the assembly includes the machining error and assembly error of the manufactured parts. The machining error can be measured by measuring tools, but the errors introduced during the assembly process cannot be directly measured, and the first-line assembly workers cannot intuitively know the assembly Process information causes blindness during assembly adjustment [1]. The assembly accuracy of the whole machine cannot be guaranteed only through part tolerance design, but must also be realized through assembly processes such as measurement and adjustment. Therefore, it is necessary to establish a mathematical model for the prediction and control of deviation transmission in the assembly process to quantitatively describe the impact

C. Chen · W. Wu · J. Shang (✉)

School of Intelligent Science, National University of Defense Technology, Hunan 410072, China

e-mail: Jz_shang_nudt@163.com

© The Author(s), under exclusive license to Springer Nature Switzerland AG 2021

189

L. Zheng et al. (eds.), *Proceedings of MEACM 2020*,

Mechanisms and Machine Science 99,

https://doi.org/10.1007/978-3-030-67958-3_21

of assembly adjustment process on the final accuracy of the whole machine. After the concept of small displacement spinner (SDT) was proposed, it was introduced into the tolerance field in 1996. Spinor parameters can describe the variation of a surface or its elements relative to its nominal position (tolerance zone). Each tolerance zone can be expressed in the form of a screw, which represents the slight changes that may occur within the tolerance zone [2, 3]. This paper establishes a mechanical assembly error propagation model based on the small displacement spin (SDT) using the homogeneous transformation of robotics coordinates, and uses the state space equation to describe the assembly process, which is of great significance for the control of the assembly process of precision machinery.

2 Coordinate Transformation of Space Object

The description of space objects in different coordinate systems is different, which requires us to perform coordinate transformation [4]. Define the global coordinate system, and the local coordinate system, as shown in Fig. 1. A local coordinate system can describe its position in a global coordinate system using three unit vectors of the coordinate origin and the coordinate axis. Similarly, a local coordinate system can use three unit vectors of the coordinate origin and the coordinate axis, to describe its position in the global coordinate system.

The translation vector and rotation vector transformation of coordinate system O_B relative to coordinate system O_A are expressed as ${}^A P_B$ and ${}^A R_B$ respectively, and

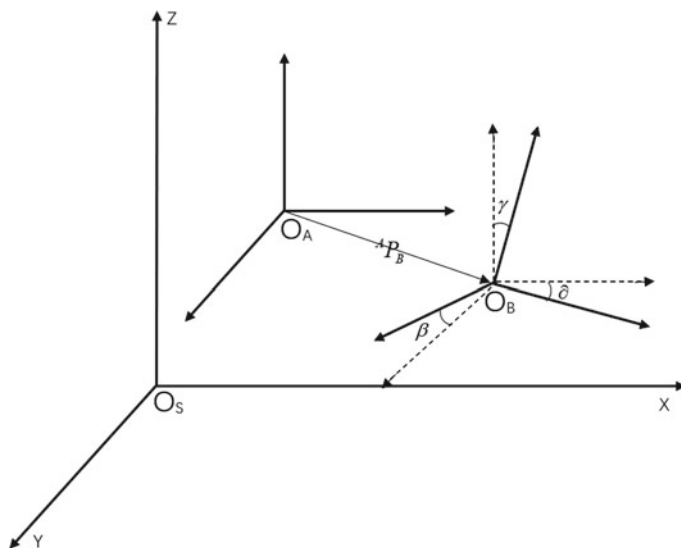


Fig. 1 Coordinate transformation

the transformation of the two coordinate systems in the global coordinate system O_S is:

$$P_{O_A} = {}^A_B R \cdot P_{O_B} + {}^A P_B \tag{1}$$

$${}^A_B R = \begin{bmatrix} \cos(x_B, x_A) & \cos(y_B, x_A) & \cos(z_B, x_A) \\ \cos(x_B, y_A) & \cos(y_B, y_A) & \cos(z_B, y_A) \\ \cos(x_B, z_A) & \cos(y_B, z_A) & \cos(z_B, z_A) \end{bmatrix} \tag{2}$$

$${}^A P_B = P_{O_B} - P_{O_A} \tag{3}$$

The above formula is expressed in the form of a matrix as:

$$\begin{bmatrix} {}^A P \\ 1 \end{bmatrix} = \begin{bmatrix} {}^A_B R & {}^A P_B \\ 0 & 1 \end{bmatrix} \begin{bmatrix} {}^B P \\ 1 \end{bmatrix} \tag{4}$$

As ${}^A_B T = \begin{bmatrix} {}^A_B R & {}^A P_B \\ 0 & 1 \end{bmatrix}$, For the K coordinate system the coordinates are passed as follows:

$$P_1 = {}_2^1 T \cdot {}_3^2 T \dots {}_k^{k-1} T \cdot P_k \tag{5}$$

3 Assembly Error Propagation Model Based on Small Displacement Spinor (SDT)

Establishing the error transmission model is the basis for the calculation of assembly error [5]. All parts in the error transmission chain studied in this paper meet the rigid body assumption, and there is no gap between the mating surfaces of the parts. Therefore, the assembly error of each part and the tolerance of the part assembly geometric feature surface can be regarded as the small displacement relative to the ideal position, which can be represented by three translation vectors $D = [\Delta x, \Delta y, \Delta z]^T$ and three rotation vectors $R = [\Delta \alpha, \Delta \beta, \Delta \gamma]^T$. Then the assembly error is expressed by the screw theory of small displacement as follows:

$$\Delta T = \begin{bmatrix} 1 & -\Delta \lambda & \Delta \beta & \Delta x \\ \Delta \lambda & 1 & -\Delta \alpha & \Delta y \\ -\Delta \beta & \Delta \alpha & 1 & \Delta z \\ 0 & 0 & 0 & 1 \end{bmatrix}$$

As shown in Fig. 2, for an assembly containing k parts, the assembly error accumulation model is:

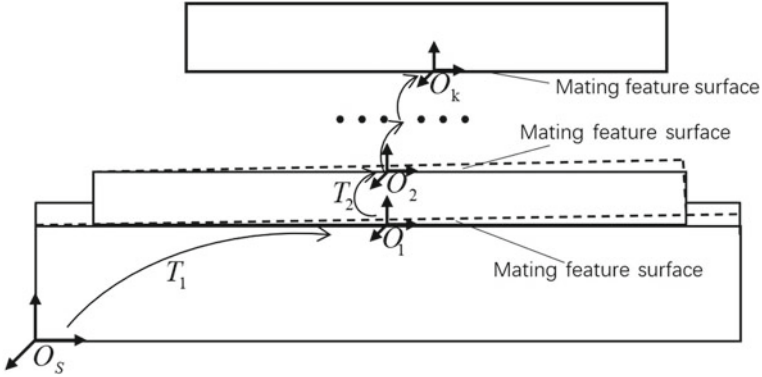


Fig. 2 Error transmission of part assembly

$$\sigma = \prod_{i=1}^k T_i \cdot \Delta s_i - \prod_{i=1}^k T_i \quad (6)$$

The part tolerance is a small amount relative to the part size. Expand the above matrix and ignore the second-order small amount to get:

$$\sigma = \begin{bmatrix} \Delta x \\ \Delta y \\ \Delta z \\ \Delta \alpha \\ \Delta \beta \\ \Delta \lambda \end{bmatrix} = \begin{bmatrix} \sum_{i=1}^k \Delta x_i - \sum_{j=2}^k (y_j \sum_{i=1}^{j-1} \Delta \lambda_i) + \sum_{j=2}^k (z_j \sum_{i=1}^{j-1} \Delta \beta_i) \\ \sum_{i=1}^k \Delta y_i - \sum_{j=2}^k (z_j \sum_{i=1}^{j-1} \Delta \alpha_i) + \sum_{j=2}^k (x_j \sum_{i=1}^{j-1} \Delta \lambda_i) \\ \sum_{i=1}^k \Delta z_i - \sum_{j=2}^k (x_j \sum_{i=1}^{j-1} \Delta \beta_i) + \sum_{j=2}^k (y_j \sum_{i=1}^{j-1} \Delta \alpha_i) \\ \Delta \alpha_1 + \Delta \alpha_2 + \cdots + \Delta \alpha_k \\ \Delta \beta_1 + \Delta \beta_2 + \cdots + \Delta \beta_k \\ \Delta \lambda_1 + \Delta \lambda_2 + \cdots + \Delta \lambda_k \end{bmatrix} \quad (7)$$

Δs_i represents the tolerance of the assembly characteristic surface of each part, $\prod_{i=1}^k T_i$ represents an ideal assembly that requires only a coordinate transformation.

4 State Space Propagation Model

The error stream of the assembly process for K parts is shown in Fig. 3, [6]. All vectors are defined as follows: $X(k) = (\Delta \alpha_k, \Delta \beta_k, \Delta \gamma_k, \Delta x_k, \Delta y_k, \Delta z_k)$ represents the accumulated deviation of K Parts After Assembly; $U(k)$ represents the

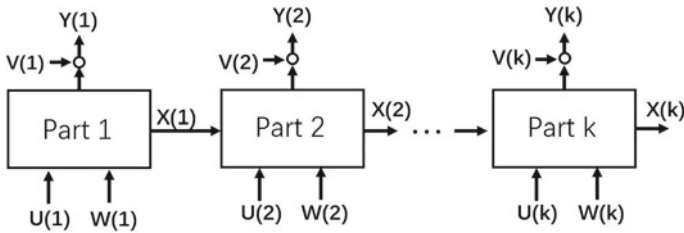


Fig. 3 Multi-part assembly process

manufacturing error of the feature surface introduced by the Assembly of K Parts; $Y(k)$ represents the observed value of the offset of K parts after assembly; $W(k)$ and $V(k)$ are independent noises.

The assembly process can be written in the form of a state space equation:

$$X(k) = A(k)X(k - 1) + B(k)U(k) + W(k) \tag{8}$$

$$Y(k) = C(k)X(k) + V(k) \tag{9}$$

It can be derived from formula (7):

$$A(k) = \begin{bmatrix} 1 & 0 & 0 & 0 & z_k & -y_k \\ 0 & 1 & 0 & -z_k & 0 & x_k \\ 0 & 0 & 1 & y_k & -x_k & 0 \\ 0 & 0 & 0 & 1 & 0 & 0 \\ 0 & 0 & 0 & 0 & 1 & 0 \\ 0 & 0 & 0 & 0 & 0 & 1 \end{bmatrix}$$

$$B(k) = E, C(k) = E$$

Matrix $A(k)$ represents the influence of rotation error on translation error during the assembly process, which is determined by the size of the part and the position of the coordinate system; matrix $B(k)$ is the input matrix, which represents the influence of part offset on assembly error, Generally it is the identity matrix; the matrix $C(k)$ is the output matrix, and the selection matrix is composed of 0 and 1, which represents the size we want to measure.

5 Case Analysis

Take a primary and secondary mirror system as an example, as shown in Fig. 4, establish an error transfer coordinate system. The assembly consists of five parts: the main mirror, the main mirror base, the connecting frame, the secondary mirror base, and the secondary mirror. The assembly requires control of the matching accuracy of the primary mirror and the secondary mirror. By analyzing the error transmission chain of the primary and secondary mirror system: primary mirror-connecting frame-secondary mirror.

The assembly parts are all surface-to-surface fits, and the tolerance characteristic surface is expressed by small displacement spin as:

$$\Delta s = \begin{bmatrix} 1 & 0 & \Delta\beta & 0 \\ 0 & 1 & -\Delta\alpha & 0 \\ -\Delta\beta & \Delta\alpha & 1 & \Delta z \\ 0 & 0 & 0 & 1 \end{bmatrix}, \left\{ \begin{array}{l} \Delta\alpha \leq \frac{T_{PAR}}{2b} \\ \Delta\beta \leq \frac{T_{PAR}}{2a} \\ -T_{SL} \leq \Delta z \leq T_{SU} \end{array} \right\}, \left\{ \begin{array}{l} -\frac{T_{PAR}}{2} \leq y \cdot \Delta\alpha + x \cdot \Delta\beta \leq \frac{T_{PAR}}{2} \\ -T_{SL} \leq \Delta z + y \cdot \Delta\alpha + x \cdot \Delta\beta \leq T_{SU} \end{array} \right.$$

Among them, T_{PAR} is the tolerance of parallelism, T_{SU} and T_{SL} are the upper and lower deviations of the part size. According to the system design parameters and accuracy requirements, the characteristic surface information is obtained as shown in Fig. 5.

As the actual geometric characteristics of the part change relative to the nominal geometric characteristics is unpredictable and random [6]. Therefore, the spinor parameter in the characteristic surface is also a random quantity. Parts are usually affected by many factors in the actual processing. Generally speaking, the processing size approximately obeys the law of normal distribution. Using matlab

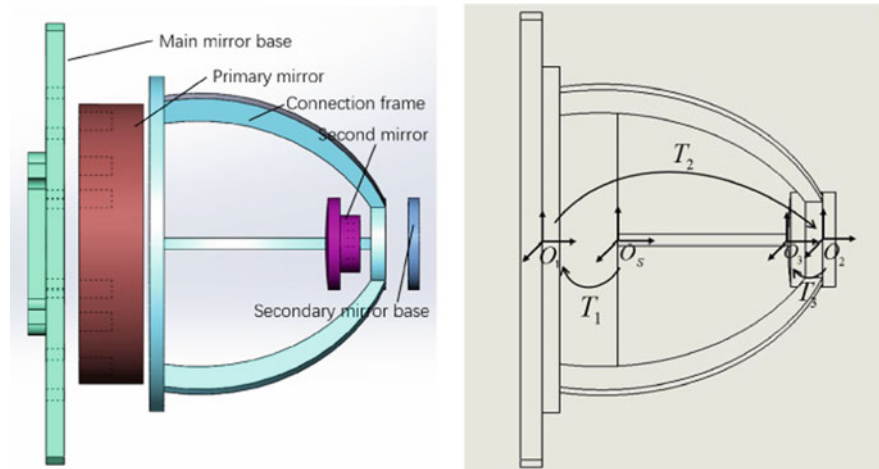


Fig. 4 A primary and secondary mirror system

Component	Coordinate transformation matrix	Feature surface information
主 镜	$T_1 = \begin{bmatrix} 1 & 0 & 0 & 0 \\ 0 & 1 & 0 & 0 \\ 0 & 0 & 1 & -12.66 \\ 0 & 0 & 0 & 1 \end{bmatrix}$	$\begin{cases} \Delta\alpha \leq \frac{0.001}{76.8} \\ \Delta\beta \leq \frac{0.001}{76.8} \\ -0.02 \leq \Delta z \leq 0.02 \end{cases} \quad \begin{cases} -0.001 \leq y \cdot \Delta\alpha + x \cdot \Delta\beta \leq 0.001 \\ -0.02 \leq \Delta z + y \cdot \Delta\alpha + x \cdot \Delta\beta \leq 0.02 \end{cases}$
连接架	$T_2 = \begin{bmatrix} 1 & 0 & 0 & 0 \\ 0 & 1 & 0 & 0 \\ 0 & 0 & 1 & 66.5 \\ 0 & 0 & 0 & 1 \end{bmatrix}$	$\Delta\alpha = 0, \Delta\beta = 0, \Delta z = 0$ $\begin{cases} \Delta\alpha \leq \frac{0.005}{50} \\ \Delta\beta \leq \frac{0.005}{50} \\ -0.1 \leq \Delta z \leq 0.1 \end{cases} \quad \begin{cases} -0.0025 \leq y \cdot \Delta\alpha + x \cdot \Delta\beta \leq 0.0025 \\ -0.1 \leq \Delta z + y \cdot \Delta\alpha + x \cdot \Delta\beta \leq 0.1 \end{cases}$
次 镜	$T_3 = \begin{bmatrix} 1 & 0 & 0 & 0 \\ 0 & 1 & 0 & 0 \\ 0 & 0 & 1 & -8 \\ 0 & 0 & 0 & 1 \end{bmatrix}$	$\begin{cases} \Delta\alpha \leq \frac{0.01}{31} \\ \Delta\beta \leq \frac{0.01}{31} \\ -0.02 \leq \Delta z \leq 0.02 \end{cases} \quad \begin{cases} -0.005 \leq y \cdot \Delta\alpha + x \cdot \Delta\beta \leq 0.005 \\ -0.02 \leq \Delta z + y \cdot \Delta\alpha + x \cdot \Delta\beta \leq 0.02 \end{cases}$

Fig. 5 Assembly error information

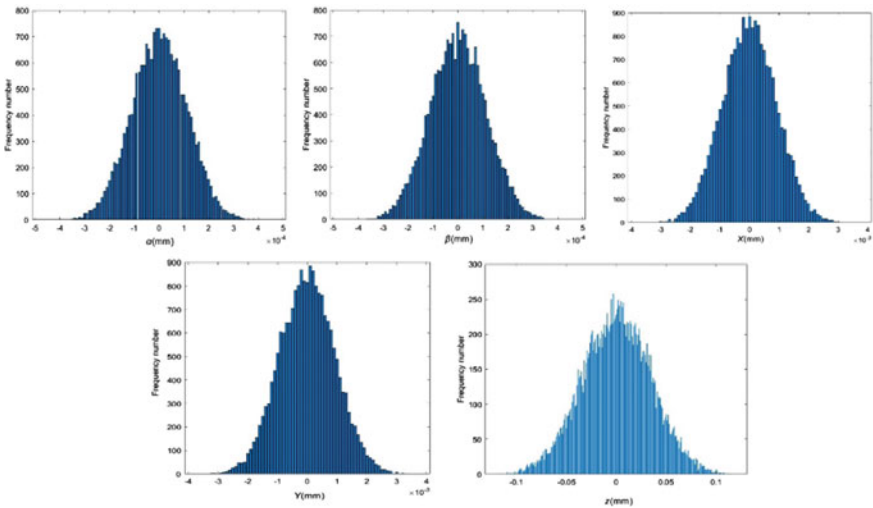


Fig. 6 Cumulative error distribution

programming to simulate the characteristic surface parameter changes of the above three parts, excluding noise, the number of simulations is 20,000 times, the results are shown in the Fig. 6.

From the computer simulation results, it can be seen that the accumulation of assembly errors along the X-axis and Y-axis is symmetrical, which is consistent

with the actual situation. The cumulative distribution range of assembly errors along the Z-axis is larger: -0.12 mm — 0.12 mm . It is the direction we need to control. Based on the small displacement spin, this paper establishes a state space model of precision machinery assembly error transmission. The state space model can be used to effectively predict and analyze the cumulative error of mechanical assembly, which is of great significance for the adjustment and control of mechanical assembly errors.

Acknowledgements This work was financially supported by the National Natural Science Foundation of China (Grant No. 51675527).

References

1. Jun, H., Junkang, G., Zhigang, L., et al.: Assembly accuracy prediction and adjustment process modeling of precision machine tool based on state space model. *J. Mech. Eng.* **49**(6), 114–121 (2013)
2. Sun, Y., Liu, Y., Ran, Y., et al.: Assembly precision method of numerical control machine tools based on meta-action. *Mech. Sci. Technol. Aerosp. Eng.* **36**(11), 1734–1739 (2017)
3. Wu, Z.: Stimulated tolerances modeling based on small displacement torsors and tolerances analysis. *Mach. Des. Manuf.* **01**, 205–207 (2010)
4. Whitney, D.E., Gilbert, O.L., Jastrzebski, M.: Representation of geometric variations using matrix transforms for statistical tolerance analysis in assemblies. *Res. Eng. Des.* **6**(4), 191–210 (1994)
5. Cai, S., Wang, H., Liu, T.: Assembly precision prediction and adjustment method based on error propagation model. *Mach. Manuf.* **45**(6), 6–10 (2016)
6. Li, X., Yu, N., Cao, Y., et al.: Angular variation analysis of spacecraft assembly based on state space model. *J. Nat. Univ. Def. Technol.* **36**(1), 104–109 (2014)

Synthesis of Fluorescent Carbon Dots from Glucose and Calcium Carbonate and Their Application in the Beverage



Meiyu Zhang, Xiaoliang Hao, Zhigang Fang, Yun Gao,
and Tongtong Li

Abstract In this text, glucose and calcium carbonate are used as raw materials to prepare carbon dots using electric thermostatic drying oven. The synthesized carbon dots solution is used for pineapple beverage. The single factor experiment and orthogonal experiment are used to determine the optimum proportion of the beverage. The results showed that for pineapple beverage the optimum proportion is that white sugar is 6%, citric acid is 0.1%, and pineapple juice is 40%, and carbon dots solution is 2.5%. Under this condition, the best flavor of beverage was obtained. It is hoped that this study could provide some suggestions for the further application of carbon dots.

Keywords Glucose · Calcium carbonate · Pineapple · Carbon dots · Fluorescence · Single factor

1 Introduction

A beverage is a liquid intended for human consumption or for livestock. It is a product that has been quantitatively packaged for direct consumption or prepared or brewed in a proportion of water and contains no more than 0.5% ethanol by mass [1, 2].

With the continuous improvement of people's life quality and level, beverages are welcomed by a wide range of consumers because of their unique advantages. And type fruit beverage can be drunk in a variety of occasions, such as family gatherings, daily life, travel [3].

In the process of beverage production, more flavouring essences and pigments are needed to obtain better taste and color. However, many of these flavouring essences and pigments are synthetic, so there are some security risks. It is found that

M. Zhang · X. Hao (✉) · Z. Fang · Y. Gao · T. Li
College of Chemical Engineering, University of Science and Technology Liaoning,
Anshan 114051, People's Republic of China
e-mail: 463622633@qq.com

some food materials can be carbonized at high temperature, and some carbonation reactions result in the formation of fluorescent carbon dots (CDs). For example, coffee brewed with hot water, bread carbonized at high temperatures, there will be some fluorescence of CDs production.

Fluorescent CDs are a new kind of carbon-based zero-dimensional nanomaterials. Since the discovery of CDs, the research of CDs has never stopped. CDs are the most important part of the research and development of new nano-materials because of their good optical properties, stable anti-external ability, non-toxic or low toxic, good solubility and so on.

In this study, food-grade raw materials glucose and calcium carbonate were used as raw materials, by one-step synthesis, CDs were obtained. Because the raw materials itself is non-toxic, the process of preparation follows aseptic operation, therefore the fluorescent CDs are relatively non-toxic. After carbonation, the better color and structure were obtained, and fluorescent CDs were added to juice beverage to explore more possible applications.

2 Experimental Procedures

2.1 Materials and Equipments

The reagents used in the experiments came from the biopharmaceutical laboratory of University of Science and Technology Liaoning. Ultrapure water was used in all the experiments. 202-20A Electric thermostatic drying oven (Jiangsu Changzhou Huapuda Mathematical Instrument Co., Ltd.); UV-vis absorption spectra (UV-2000 UV-vis spectrophotometer, Unico China); fluorescence detection (FL-2700 fluorescence spectrometer, Hitachi Japan); X-ray diffraction (XRD) (Bruker AXS, Germany); Fourier transform infrared spectrometer (FTIR) (Mettler, Switzerland).

2.2 The Synthetic Method of CDs and Preparation of Beverage

1 g glucose powder, 1 g calcium carbonate powder, and 20 ml water were weighed. Put the materials into stainless steel reactor, and then put the reactor into an electric thermostatic drying oven, set the reaction temperature to 180 °C, and heat for 8 h. After the reaction, the solution is filtered to obtain a clear liquid by the gauze, the liquid is CDs solution. Pick fresh pineapple, remove the peel, wash with the water, cut into small pieces and add 5 times water and press to juice.

2.3 Sensory Evaluation Scoring Standard

In this experiment, a compound beverage was studied. In order to better determine the best ratio, 10 trained personnel were selected. Sensory scores were scored by tasting the beverage (Table 1).

2.4 Single-Factor Experiment

In this experiment, white sugar, citric acid, pineapple juice and CDs solution were selected as the main factors. By consulting the handbook of food additives and the literature, the range of each factor was determined. In the single factor experiment, the quantity of three factors was fixed respectively, and the effect of another factor on the sensory score was investigated.

2.5 Orthogonal Experiment

Orthogonal experiments are carried out using the optimal conditions obtained from the above single factor experiment (Table 2).

Table 1 Sensory evaluation table

Index	Scoring criteria
Status	The pineapple juice is clear belongs to 10 points; there is a little sediment belongs to 5 points; turbidity is 1 to 3 points
Odor	Pineapple juice smells fresh belongs to 10 points; slightly peculiar smell belongs to 5 points; pungent smell belongs to 1–3 points
Taste	The taste of pineapple juice is smooth belongs to 10 points; a bit sour is 5 points; the taste is too sour belongs to 1–3 points

Table 2 Factor level table

Factor	White sugar(%)	Citric acid (%)	Pineapple juice (%)	CDs solution (%)
1	4	0.1	30	1.5
2	6	0.2	40	2
3	8	0.3	50	2.5

3 Results and Discussion

3.1 Characterization

Result of XRD XRD was used to detect the characterization of CDs. The obtained XRD pattern shows that there is a peak at $2\theta = 18.3^\circ$ (Fig. 1). The peak of CDs corresponds to the 002 lattice plane of the graphite structure, the CDs belongs to the amorphous carbon structure.

Determination of Optimal Excitation Wavelength Figure 2 recorded the fluorescence intensity of CDs when excitation wavelength was changed from 300 to 400 nm. When the wavelength increased, the emission intensity first increased and then decreased, and the optimal excitation wavelength was 360 nm.

3.2 Single Factor Experiment Results

Effect of White Sugar on Sensory Score With the increase of sugar content, the sensory score increased at first and then decreased. The possible reason is that the appropriate sweetness contributes to the flavor of the drink, but excessive sweetness can degrade the taste. When the sugar content is 6%, the beverage tastes best (Fig. 3).

Effect of Citric Acids on Sensory Score Citric acids help improving the taste of the beverage, but too much of citric acids will increase the acidity and decrease the sensory score. When the citric acids content is 6%, the beverage tastes best (Fig. 4).

Fig. 1 XRD spectra of CDs

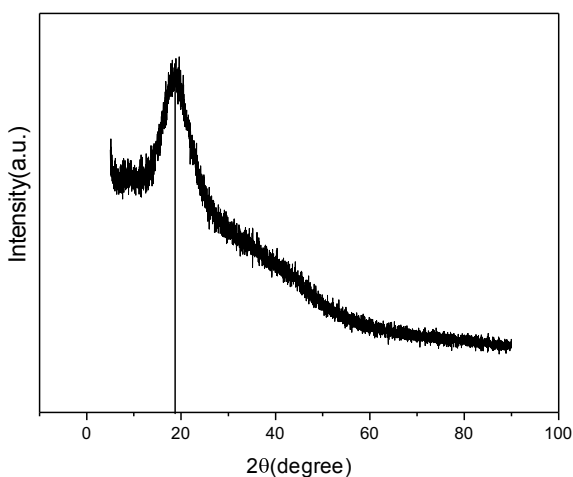


Fig. 2 Fluorescence spectra at different excitation wavelengths

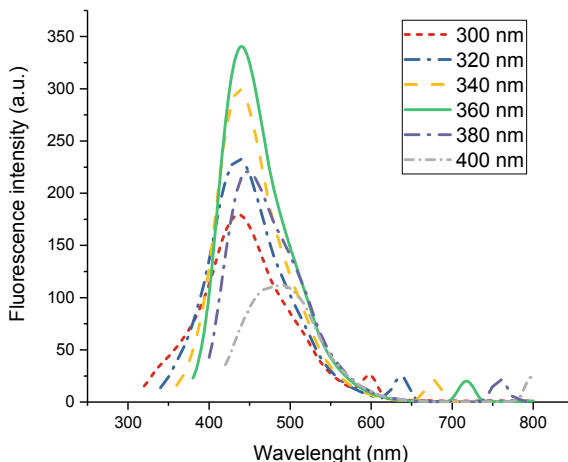
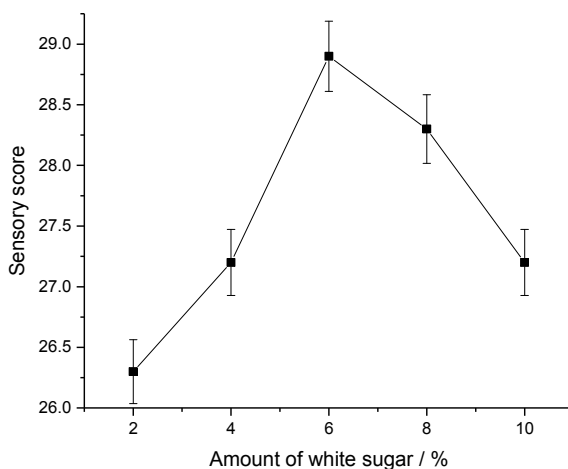


Fig. 3 Effect of white sugar on sensory score



Effect of Applepine Juice on Sensory Score Pineapple juice is good for the nutrition of the beverage, but more juice will make the beverage more viscous. When the pineapple juice content is 30%, the beverage tastes best (Fig. 5).

Effect of the CDs Solution on Sensory Score In this experiment, blue-emission CDs were synthesized. Because the synthesis of raw materials is non-toxic, preparation method is sterile, therefore the CDs solution has a higher safety. The addition of CDs solution will improve the quality of the beverage, and increase the nutrition of the beverage because of the addition of calcium ions. When the content of CDs solution is 2%, the sensory score is highest (Fig. 6).

Fig. 4 Effect of citric acid on sensory score

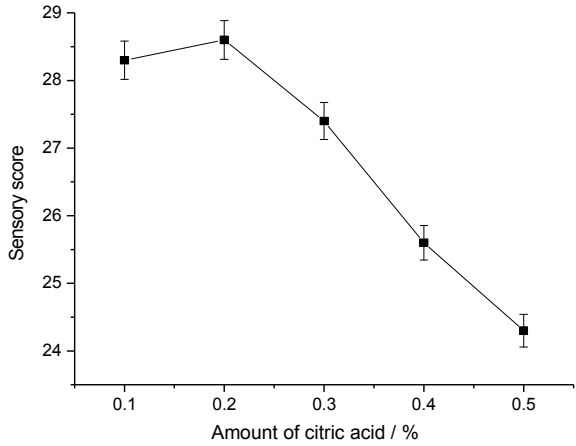


Fig. 5 Effect of pineapple on sensory score

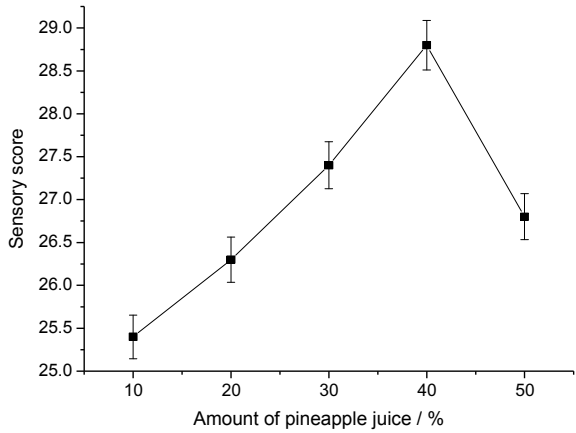


Fig. 6 Effect of CDs on sensory score

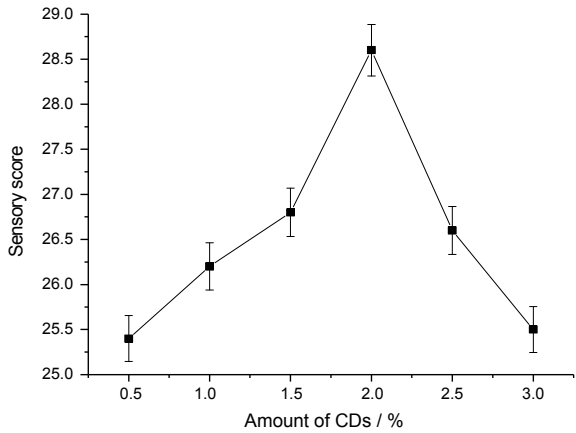


Table 3 Orthogonal experiment table

Column	1	2	3	4	Score
Factor	White sugar	Citric acid	Pineapple juice	CDs solution	
Experiment 1	1	1	1	1	28.4
Experiment 2	1	2	2	2	25.4
Experiment 3	1	3	3	3	24.7
Experiment 4	2	1	2	3	28.9
Experiment 5	2	2	3	1	24.2
Experiment 6	2	3	1	2	25.2
Experiment 7	3	1	3	2	27.3
Experiment 8	3	2	1	3	25.9
Experiment 9	3	3	2	1	26.1
Mean 1	26.167	28.200	26.500	26.233	
Mean 2	26.100	25.167	26.800	25.967	
Mean 3	26.433	25.333	25.400	26.500	
Range	0.333	3.033	1.400	0.533	

3.3 Orthogonal Experiment Results

By the analysis of the range, it can be seen that the order of influence of the four factors is: citric acid > pineapple juice > CDs solution > white sugar. According to Table 3, the optimal formula of the beverage is: A2B1C2D3, that is, white sugar is 6%, citric acid is 0.1%, and pineapple juice is 40%, and CDs solution is 2.5%. The pineapple juice under this formula is the best in terms of taste, smell and state.

4 Conclusions

In this study, a new type of CDs solution was prepared and synthesized using two raw materials: glucose and calcium carbonate. After determining its characterization and properties, the application of CDs was studied by single factor experiments and orthogonal experiments. The low toxicity of CDs was used for experiments in the food field. By the experiment, the best formula of pineapple beverage is: white sugar is 6%, citric acid is 0.1%, and pineapple juice is 40%, and CDs solution is 2.5%. It is hoped that our research can provide suggestions for more applications of fluorescent CDs.

Acknowledgements This paper is supported by the University of Science and Technology Liaoning 2020 Innovation and Entrepreneurship Training Program for College Students (202010146025).

References

1. El-Shibiny, S., Abd El-Salam M. H., Mahfouz M.B., El-Etriby H.: The use of skim milk permeate in the preparation of spray dried beverages II. Beverage based on Strawberry. *Z Lebensm Unters Forsch* **181**, 223–225 (1985)
2. Hao, X.L., Pan, X.H., Gao, Y., Wang, Y., Guo, J., Teng, Y.X.: Facile synthesis of nitrogen-doped green-emission carbon dots as fluorescent off-on probes for the highly selective sensing mercury and iodine ions. *J. Nanosci. Nanotechnol.* **20**(4), 2045–2054 (2020)
3. Kim, H.J., Lee, M.J., Park, H.J., Kim, H.J., Cho, S.K., Jeong, M.H.: Simultaneous determination of synthetic food additives in kimchi by liquid chromatography-electrospray tandem mass spectrometry. *Food Sci. Biotechnol.* **27**(3), 877–882 (2018)

Fault Location Method of Multiple Bearings in Shafting Based on SPWVD-CNN



W. T. Huang, H. Zhai, Y. Lei, and W. J. Wang

Abstract To solve the problem of multi-bearing fault diagnosis in mechanical equipment, it is necessary not only to confirm whether there is fault in shafting, but also to determine the position of the fault bearing, so as to meet the application needs in practical engineering scenarios and effectively realize further diagnosis. In this study, a fault location diagnosis method based on CNN for multiple rolling bearings under coaxial installation in shafting is proposed. First, By analyzing the vibration response signals in time domain and frequency domain, a time-frequency analysis method based on SPWVD is proposed to identify the fault signal and the coupling signal. Then, the information of fault and position can be used as the input of AlexNet network for diagnosis by stitching the time-frequency diagrams of bearing signals of each position in the shafting. The experimental results show that the accuracy of fault diagnosis of the inner and outer ring fault bearings is above 90% when the three bearings are coaxial installed in the shafting. It verifies the effectiveness of fault location based on SPWVD-CNN in the coaxial installation of multiple bearings in the shafting.

Keywords Multiple bearings in shafting · Fault location · SPWVD-CNN

1 Introduction

At present, the research on fault diagnosis of rolling bearings is mainly focused on fault detection, diagnosis or defect location of a single bearing, ignoring the diagnosis research on the coaxial operation of multiple bearings in the shafting. But in practical engineering applications, bearings are used simultaneously. For example: the installation of bearings on the main shaft of wind turbine mostly uses two or three point support; Bearings are used in aircraft engines in the form of

W. T. Huang (✉) · H. Zhai · Y. Lei · W. J. Wang
School of Mechatronics Engineering, Harbin Institute of Technology, Harbin 150001, China
e-mail: hwt@hit.edu.cn

© The Author(s), under exclusive license to Springer Nature Switzerland AG 2021
L. Zheng et al. (eds.), *Proceedings of MEACM 2020*,
Mechanisms and Machine Science 99,
https://doi.org/10.1007/978-3-030-67958-3_23

205

pairwise installation, etc. Therefore, the study of single bearing failure in isolation is obviously inconsistent with the practical application of bearing in engineering.

Shafting structure exists in many large mechanical equipment, so bearing fault diagnosis in shafting has gradually attracted the attention of some researchers. Ma et al. [1] proposed a multi-objective integrated deep learning diagnosis strategy that weighted and integrated the Convolutional Residual Network (CRN), Deep Belief Network (DBN) and Deep Auto Encoder (DAE) realized the diagnosis of rotor and bearing faults; Han et al. [2] extracted bearing contact angle by using spline interpolation algorithm to identify the specific position of bearing fault. The signal is decomposed and reconstructed by full-vector EMD, and the contact times of bearing single ring are recorded by the chamfered domain analysis, which realizes the diagnosis of fault type. Dai et al. [3] analyzed the bearing signal based on the principle of satellite positioning, and used time-amplitude curve analysis to capture the fault frequency at the moment of occurrence. This time was taken as the input condition to calculate the vibration wave source position and judge the position of the fault bearing; Sun et al. [4] used the K-means to extract feature vectors from the energy of different frequency bands after wavelet decomposition, and then used the hidden Markov Model to diagnose the fault and determine the fault location; Chi et al. [5] adopted the degree of cyclostationariness as an indicator for distinguishing the characteristics of bearing signals at different positions, and used the slope of the fitting curve of kurticity—degree of cyclostationariness of different components of fault signals as a diagnostic parameter to identify the position of fault bearing in the shafting; Based on the exclusion analysis method, Wang et al. [6] combined the multi-spectrum analysis algorithm and GEMD algorithm to diagnose the fault position in the system through the crossover results of each spectrum analysis method; Wang et al. [7] used the pulse source positioning method to calculate the difference between the sound source and each microphone in order to identify the fault location in the rotating machinery for periodic pulse signals with high noise.

There are two main reasons for the difficulty in fault diagnosis of multiple bearings in shafting: first, when multiple bearings are installed coaxially, coupling between signals would occur resulting in that the measured signals would no longer have a single fault characteristic; second, when diagnosing multiple bearings in shafting, it is necessary not only to diagnose the existence of faults, but also to confirm the fault location. This article uses the SPWVD to analyze the vibration response signal of each bearing in shafting, which could distinguish the fault signal and coupling signal. Then time-frequency images are spliced according to the bearing position in shafting. Finally, the fault bearing in shafting is diagnosed by convolution neural network.

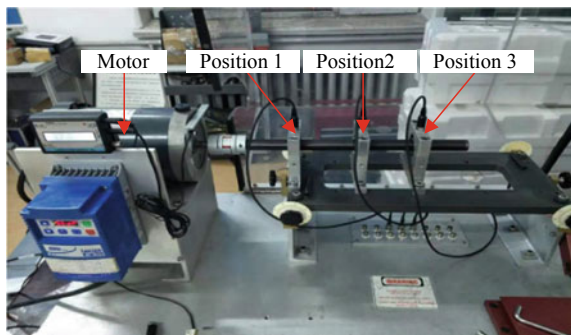
2 Analysis of Rolling Bearing Fault/Coupling Signal in Coaxial State

2.1 Time Domain Analysis of Rolling Bearing Fault/Coupling Signal

When bearing fault signals and coupling signals in coaxial state are observed from the perspective of time domain, impact signals would be generated when the ball moves to the fault area, whether the fault of the rolling bearing is in the outer or an inner raceway. This phenomenon can be regarded as an important feature of time domain analysis. Taking the coaxial installation of three bearings as an example, observing the vibration response signals measured at the motor end (Position 1), the middle position (Position 2) and the position away from the motor (Position 3) when the faulty bearing is at Position 1. The specific installation position of the bearing is shown in Fig. 1. Machinery Fault Simulator (MFS) is used to collect data and the bearing type used is 6205. The sensor's sampling frequency is set to 51,200 Hz, the sampling time is set to 5.12 s and the shaft speed is set to 1200 r/min. Data collection should be carried out after the motor is stable to avoid random interference caused by unstable operation.

The vibration response signals of the bearings at each position acquired are shown in Fig. 2. By analyzing the vibration response signals of each position, it can be seen that the vibration signals measured at the Position 1 have impact characteristics due to the presence of the faulty bearing. The bearings installed at Position 2 and 3 are all normal bearings and the measured signals should not have the characteristics of failure impact. However, because all the bearings are in the state of coaxial installation, the vibration response signals measured at the other two positions also have the characteristics of failure impact due to the coupling effect. Therefore, it's hard to determine whether the bearings at various positions in the shafting are fault or healthy but disturbed by coupling effects just according to the time-domain impact feature.

Fig. 1 Specific installation of bearings



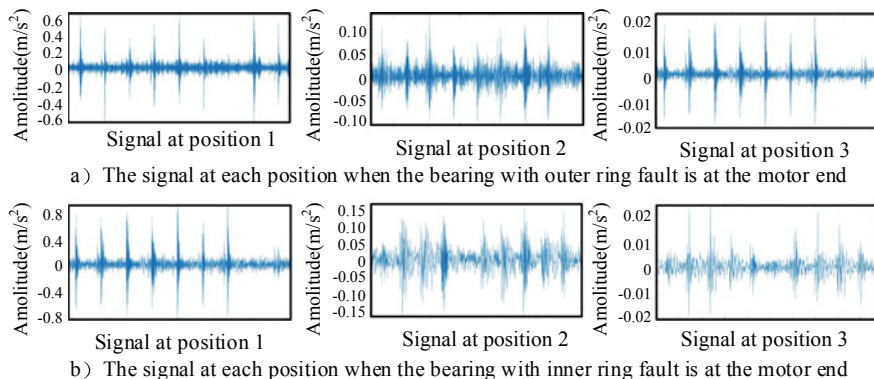


Fig. 2 Bearing vibration signals at each position

2.2 Frequency Domain Analysis of Rolling Bearing Fault/Coupling Signal

In addition to analyzing the signal from the time domain according to the impact characteristics, analyzing the characteristics of the rolling bearing vibration signal from the frequency domain is also one of the common bearing fault diagnosis methods [8].

The characteristic frequency of inner ring fault of rolling bearing is expressed as

$$fbpo = \frac{Z}{2}fr \left(1 + \frac{De}{Dp} \cos \alpha \right) \quad (1)$$

The characteristic frequency of outer ring fault of rolling bearing is expressed as

$$fbpo = \frac{Z}{2}fr \left(1 - \frac{De}{Dp} \cos \alpha \right) \quad (2)$$

where f_r is the switch frequency; D_e is the diameter of the ball; D_p is the pitch diameter of rolling bearing; Z is the number of ball; α is the pressure angle of the ball.

The outer diameter of the 6205 bearing D_o is 52 mm, the inner diameter of the bearing D_i is 25 mm, the number of the ball Z is 9, the radius of the ball r_c is 3.696 mm, the pressure angle of the ball α is 0, the rotating frequency f_r is 20 Hz. It is calculated that the characteristic frequency of the inner ring fault of the 6205 deep groove ball bearing is $f_{bpo} = 108.56$ Hz, and the characteristic frequency of the outer ring fault is $f_{bpo} = 71.44$ Hz. According to Eqs. (1) and (2), it can be seen that the factors affecting the characteristic frequency of the rolling bearing are f_r , D_e , D_p , Z and α respectively. When the same type of bearing is installed coaxially, the fault characteristic frequency of each bearing is the same. Therefore, when any bearing in

the shafting has defects, its impact vibration would cause different degrees of resonance of each bearing, resulting in the frequency spectrum of all bearings on the same shaft peaking at the frequency multiplier of the bearing's fault frequency. That is, all bearings would have fault characteristics, as shown in Fig. 3.

3 Time Frequency Processing of the Signal

The use of time domain or frequency domain methods alone lacks a comprehensive description of the signal, resulting in the inability to distinguish the fault signal and coupling of bearings in the shafting. Therefore, time and frequency are considered as rulers to represent the signal. The bearing fault signal is processed through time-frequency analysis, so that the result contains the characteristics of the original signal in both time domain and frequency domain.

Short-Time Fourier Transform, Wavelet Transform and Wigner-Ville time-frequency distribution are the common time-frequency processing methods. Due to the uncertainty principle, the signal information may be lost in the process of Fourier Transform. When using Wavelet Transform, the results of time frequency processing of the same signals are different because of the choice of the parent wavelet, which may make the optimization process of time-frequency results more complex. Comparatively speaking, the Wigner-Ville distribution is more suitable for fault diagnosis of rolling bearings [8].

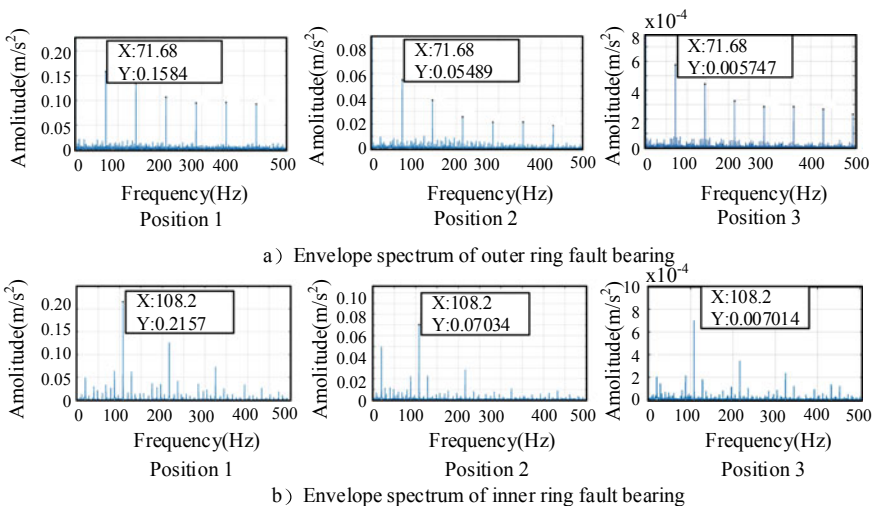


Fig. 3 Envelope spectrum of faulty bearing

The expression for the Wigner-Ville distribution is

$$Wx(\omega, t) = \frac{1}{2\pi} \int_{-\infty}^{\infty} x\left(t + \frac{1}{2}\tau\right) x^*\left(t - \frac{1}{2}\tau\right) e^{-i\tau\omega} d\tau \quad (3)$$

The problem of cross-term suppression can be solved by adding window function to τ in the processing of signals using the Wigner-Ville distribution. Adding the window function on the time axis and frequency axis, the cross term of two directions could be suppressed. This distribution is called the Smooth Pseudo Wigner-Ville Distribution (SPWVD) [9] and its expression is

$$SPWx(\omega, t) = \frac{1}{2\pi} \int_{-\infty}^{\infty} \int_{-\infty}^{\infty} h(\tau) g(s-t) x\left(s + \frac{1}{2}\tau\right) x^*\left(s - \frac{1}{2}\tau\right) e^{-i\tau\omega} ds d\tau \quad (4)$$

where $h(\tau)$ is the window function on the time axis; $g(t)$ is the smooth window function on the frequency axis.

It can be seen from Fig. 4 that the time-frequency diagram obtained by using SPWVD can clearly distinguish the characteristic differences between fault signals and coupling signals. Therefore, SPWVD time-frequency diagram can be used as an important tool for bearing fault diagnosis in shafting. Therefore, SPWVD would be used as a time-frequency analysis method to extract fault features from experimental signals in the follow-up study of this paper.

4 The Fault Location Method Based on CNN

The Convolutional Neural Network (CNN) was originally proposed by LeCun in 1989 [9]. CNN is generally composed of input layer, convolution layer, excitation layer, pooling layer and full connection layer. CNN can automatically extract image features and topological structure, and has good robustness and computing efficiency.

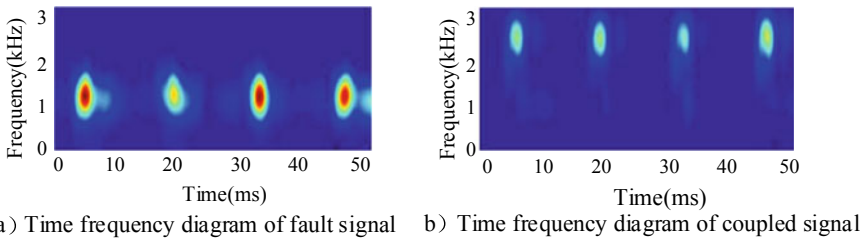


Fig. 4 SPWVD time-frequency image of bearing vibration response signal

CNN network has strong processing capacity for two-dimensional image samples. Therefore, the two-dimensional time-frequency images of experimental signals obtained by SPWVD are used as the input of CNN for network training and fault diagnosis. However, the time-frequency image only contains the fault information of a single bearing in the shafting, and no bearing position information can be obtained from it. Therefore, the time-frequency image input to CNN is spliced according to the acquired position of the bearing signal, that is, the time-frequency image generated from the signal measured at position 1 is placed at position 1, and so on. The essential idea of splicing time-frequency image is to gather the signals of each bearing in the shafting into a module, so that the splicing time-frequency image has shafting characteristics and the characteristic dimension is expanded. The splicing time-frequency image not only contains the bearing fault information, but also has the fault location information that the time-frequency image of the single channel signal does not have.

It would take a long time and a large amount of resources to rebuild a new CNN architecture. Moreover, the new CNN architecture is often not adequately trained, which leads to insufficient generalization ability of the model. Therefore, instead of training a CNN model from the ground up by completely using the fault data samples obtained by the laboratory, it would be easier to classify your own data by fine-tuning the network structure and parameters of the CNN whose architecture completed by mass data training. Compared with the new CNN architecture, the fine-tuned pre-training network has lower requirements on the quality and quantity of the follow-up training data set. And the pre-trained CNN can also reduce the training cost and speed up the training process. Therefore, AlexNet model with fewer network layers and higher training efficiency is selected as the diagnostic model. AlexNet which was proposed by Krizhevsky et al. [10] in 2012 is the first network structure that successfully demonstrates the potential of convolutional neural networks. After its appearance, CNN has gradually become the core model of image classification. Its structure is shown in Fig. 5

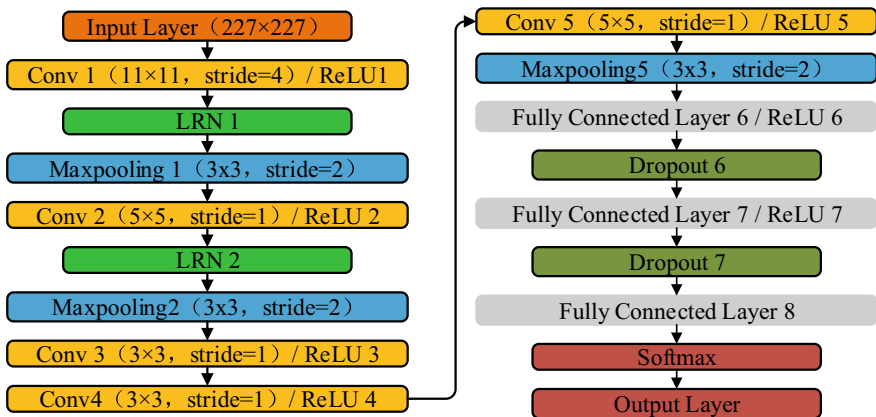


Fig. 5 The network structure of AlexNet

The effectiveness of AlexNet network for locating and diagnosing faulty bearings in shafting is verified by experiments. In the experimental design, AlexNet is used to locate and diagnose the bearing fault when the rolling bearing in the shafting has outer ring fault and inner ring fault respectively. Firstly, the data set input to the diagnostic network is set. According to the above data processing method, the spliced time-frequency image of bearing signals of each position in the shafting is obtained when the outer ring fault bearing is located in three positions respectively, as shown in Fig. 6a. The three types of time-frequency splicing diagrams are labeled with data according to the fault location. In this way, the data set is classified by AlexNet, and the location of the fault bearing in the shafting can be completed. In the same way, the experimental signals are obtained when the faulty bearing is an inner ring fault and the data set is set, as shown in Fig. 6b.

Because the AlexNet has strict requirements on the size of input image samples, the image size converter is used to adjust the time-frequency image size to 227×227 . The number of time-frequency image of each label in the training set is set to be 1000. The data sets were divided into training samples and verification samples in a ratio of 7:3. The epoch is set as 3 and the sample size for each input to the network is set as 20. In order to speed up the initial training speed, the initial learning rate is set as 1×10^{-4} and the learning rate attenuation factor is set as 0.5. Set the sample classification number to be consistent with the sample label type in the data set. According to the above setting, when the fault bearing in the shafting is an outer ring fault, the accuracy rate of positioning and diagnosis of the model is 98.45%. The change of accuracy rate and loss of the model in the training process is shown in Fig. 7a. When the fault bearing in the shafting is an inner ring fault, the parameters and data sets of the diagnosis model are set the same as when the fault bearing is an outer ring fault, and then experimental verification is carried out. Finally, when the fault bearing in the shafting is an inner ring fault, the accuracy of positioning and diagnosis of the model is 94.67%. The change of accuracy and loss of the model in the training process is shown in Fig. 7b.

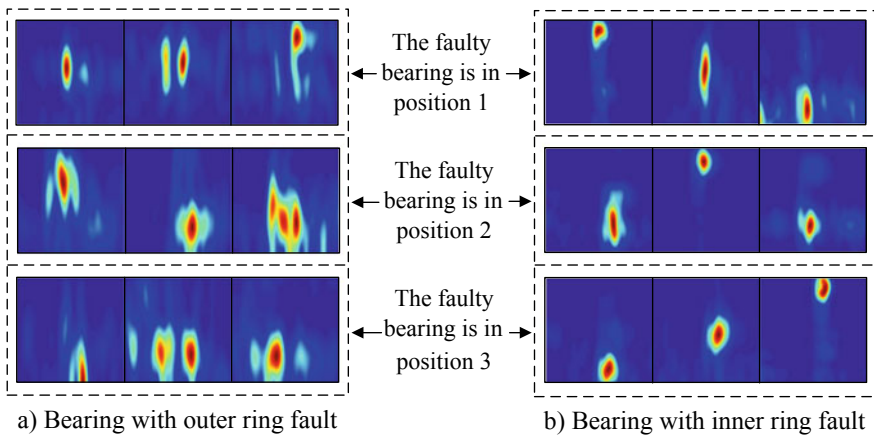


Fig. 6 AlexNet diagnostic data set

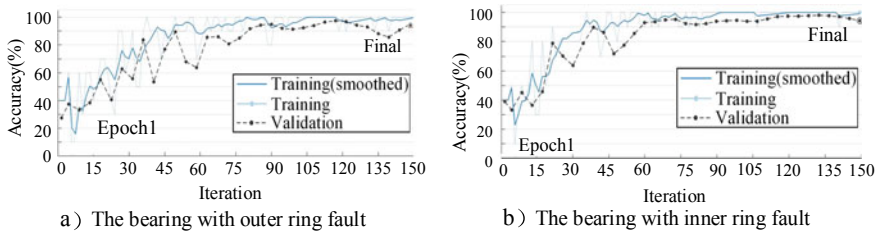


Fig. 7 Accuracy of bearing locating fault in shafting

5 Conclusion

In this paper, the fault diagnosis of multiple bearings under coaxial installation in shafting is studied. After analyzing various signals in shafting in time domain and frequency domain respectively, a signal time-frequency analysis method based on SPWVD is proposed to distinguish fault signals and coupling signals in shafting. Aiming at the problem of bearing fault location diagnosis in shafting, the method of splicing the time-frequency image of bearing signal obtained at each position according to the position of bearing in shafting is proposed, so that the splicing time-frequency image contains both fault information and position information. Then the spliced time-frequency image is used as the input of AlexNet network for fault location diagnosis. The experimental results show that the accuracy of fault location is 98.45% when the fault bearing in the shafting is an outer ring fault. When the fault bearing in shafting is an inner ring fault, the fault location accuracy is 94.67%.

In future studies, we would diagnose the severity of fault bearings in shafting and improve the accuracy of fault diagnosis of convolutional neural network under different working conditions through transfer learning.

References

1. Ma, S., Chu, F.: Ensemble deep learning-based fault diagnosis of rotor bearing systems. *Comput. Ind.* **105**, 143–152 (2019)
2. Han, J.H., Yan, W., Cao, J.H.: Research of fault diagnosis method of multi low speed high—loaded bearings installed on same axis. *J. Mech. Trans.* **4**, 164–169 (2018)
3. Dai, Y.M., Zhang, H.S., Fang, K.: Fault diagnosis of rocket turbine pump bearing based on navigation and position principle. *J. Astronaut.* **40**(3), 286–294 (2019)
4. Sun, Q.L., Liu, C.L., Zhen, C.G.: Application of hidden markov model in fault diagnosis of rolling bearing. *J. Eng. Thermal Energy Power* (10) (2018)
5. Chi, Y.W.: Analysis of vibration characteristic and intelligent fault diagnosis of rolling bearings. Zhejiang University (2018)
6. Wang, L.: Study of spectrum and GEMD envelop spectrum analysis for rolling machinery fault location. Taiyuan University of Technology (2014)

7. Wang, Y., Wu, C.Q., Cui, S.S.: Sound source localization method applying to check fault place of machine. *Mach. Electron.* **11**, 39–41 (2007)
8. Luo, J.N.: Research on experimental and simulation data-driven fault severity assessment of rolling element bearings. Harbin Institute of Technology (2019)
9. LeCun, Y., Boser, B., Denker, J.S, et al.: Backpropagation Applied to Handwritten Zip Code Recognition, vol. 1, no. 4, pp. 541–551 (1989)
10. Krizhevsky, A., Sutskever, I., Hinton, G.E.: ImageNet classification with deep convolutional neural networks. *Commun. ACM* **60**(6), 84–90 (2017)

Investigate the Damage of Kinetic Energy High-Velocity Bird Impact on Three Different Model Spar by Using the Coupled Eulerian-Lagrangian (CEL) Approach



Muhammad Hassam Saeed and Noaman Muhammad

Abstract This study aims the experimental and numerical high-velocity bird strike on the aircraft's spar and analysis the kinetic energy (K.E.) of the bird. The experiment is having different designs of spar resist against the bird strike at high velocity. The striking velocity of the bird is 300 m/s in this study, using two materials, one is aluminium, and the second is a composite material. The vertical plate, top and bottom horizontal plates of the spar are made by aluminium, and composite plates make other structures. In the first model, plates are parallel to the top and bottom and between them. In the second V shape plates fix on vertical aluminium, V shape's single edge is the outer side. The third is similar to the first but cover with aluminium cover. Abaqus explicit finite element software is used to simulate the strike of a bird. Experiment using Coupled Eulerian-Lagrangian (CEL) approach. Where the bird modelled the Murnaghan EOS, the material parameters are identified by the optimisation process. The simulated dynamic response of bird strike on spar are compared with the experimental result to verify the numerical model. At last, compare the different designs and dissolving power of K.E. of the bird.

Keywords Bird strike · Kinetic energy · Spar · Coupled Eulerian-Lagrangian · Composites · Impact analysis

M. H. Saeed

School of Mechanical Engineering, Jiangsu University, Zhenjiang, China

N. Muhammad (✉)

School of Energy and Power Engineering, Jiangsu University, Zhenjiang, China

© The Author(s), under exclusive license to Springer Nature Switzerland AG 2021

215

L. Zheng et al. (eds.), *Proceedings of MEACM 2020*,

Mechanisms and Machine Science 99,

https://doi.org/10.1007/978-3-030-67958-3_24

1 Introduction

Nearly the last thirty years, airline is the most common way of travel. It is smoother and quicker than other modes of transport. Military aircraft play a significant role in the war. An engine and a wing are the core parts of an aircraft. All are adaptive and boost the aircraft to reach its destination. Mostly these two parts are the only ones to face the attack of birds. Bird impacting is a significant threat to civilian and military aircraft. The primary wing, horizontal and vertical stabiliser, it has many essential roles in the whole flight. The primary wing transport the aircraft fuel. Due to these factors, civil aviation ensures that after the bird strikes, airplane land safely on his destination or nearby airports. Wing also follows the essential safety requirements for security of the airplane. Part 25 of the Law allows an airplane to be capable of completing a flight where the effect of a 4 lb (1.82 kg) bird (8 lb (3.64 kg) on a frame of a bird's empennage) might cause structural damage but does not reach within a wing, where the bird's speed (Design Cruise Velocity) of an airplane has been defined at sea level [1]. The bird's liquid behaviour, according to ShuchangLong, happens when it reaches a comparatively rigid structure at high velocity. The bird is a model on a reliable feature by smooth particulate hydrodynamics (SPH) technique in his research. At the time of the experiment, the atoms were converted into particles [2]. Sd. Abdul Kalam is concerned with a hydrodynamic model sensitivity study, carried out by numeric simulation, and his results show that the hemispheric ended bird form with porosity 0.1 results are very close to the theoretical results [3]. In the wing spar is mainly a part that combines all together, which provides the left to take off. It can bear the bird's impact and dissolve the kinetic energy (K.E) of the bird. Dahai Research on K.E. of the bird during shock and deformation needs to be studied (K.E) [4]. According to the studies, a bird impacts the leading edge after failing the leading edge bird strike on the spar and analysing spar damage [5]. Ernie Illyani Basri study about design and simulation validation based on finite element optimisation for tubercle leading edge and internal stress on the spar [6]. The optimisation of the aircraft's wing spar beam was done by comparing the crack growth's tiredness for various cross-sectional types but constant cross-sectional areas of the spar. Usually, Coupled Eulerian-Lagrangian (CEL) methods are prevalent and occur at high speed. Salvatore's utilising CEL examines and extends the formation of structural deformation and damage by analysing unique impact places and different angle [7]. In this study, the bird's hitting velocity is 300 m/s. In this analysis, one is aluminium using two components, and the second is a composite material. The vertical plate and the spar's top and bottom horizontal plates are made of metal, and other frame is made of composite plates. In the first model, the plates are parallel to and between the top and the bottom. In the second V, plates mounted on vertical aluminium. The outer side consists of a single V-shaped tip. The third is same as the first but coated by aluminium cover. Abaqus explicit finite element software elements are used for the simulation of bird strikes. Coupling Eulerian-Lagrangian (CEL) experiment. Experiment. The material parameters of the bird are calculated by the optimisation method when modelled on the Murnaghan EOS.

2 Bird Impact Theory

As per the event of impact into three categories: elastic impact theory, plastic impact theory, and Hydrodynamic impact theory. These theories are classified based on impact of velocity. In this study, birds behave like fluid, Hydrodynamic theory treated with the fluid. When a bird impacts a body, there is a common characteristic in pressure background determined by transducers away from the centre's impact but decreases in pressure amplitude at increasing radial distance from the impact centre. To calculate the time of bird takes to travel through its length and it is expressed by logically as

$$T = \frac{L}{U_0}$$

L is the length of the object; T is the impact period and U_0 is the initial velocity impact. In this period, the bird effect is classified into four groups. "Figure 1 shows all of these groups."

3 Bird Modelling

The bird behaves like a fluid during impact and designed as a cylinder made by water, but since there are cavities and internal organs containing air, bird is commonly made as made of 90% fluid and 10% air. Here geometry, which represents a real bird that is also a cylindrical shape, has both ends, is the semi sphere. By using of empirical formulas derived by the Australian Transport Safety Bureau, 2002. Federal Aviation Regulations which certification required 4 Ib bird here bird is also 4 Ib and properties of bird is shown in (Table 1) which is derived by empirical formulas. ρ (kg/m³) = 942.7 density is calculated by empirical formulas C_0 (m/s) = 1480 Speed of sound in water = 1480 m/s in this experiment is made by water, and it is constant.

$$\text{bird mass} = 4 \text{ IB} = 1.82 \text{ Kg}$$

$$\text{Density} = 959 - 63 * \log_{10}(\text{mass of bird}) = 942.7 \text{ kg/m}^3$$

$$\text{Diameter of bird} = 0.0804 * \text{mass of bird}^{0.035} = 0.098 \text{ m}$$

$$\text{Length of bird} = 4 * \left[\frac{\text{mass of bird}}{\pi \cdot \text{density} \cdot \text{Diameter of bird}^2} - \frac{\text{Diameter of bird}}{6} \right] = 0.189 \text{ m}$$

$$\text{Total length of bird} = 0.098 + 0.189 = 0.287 \text{ m}$$

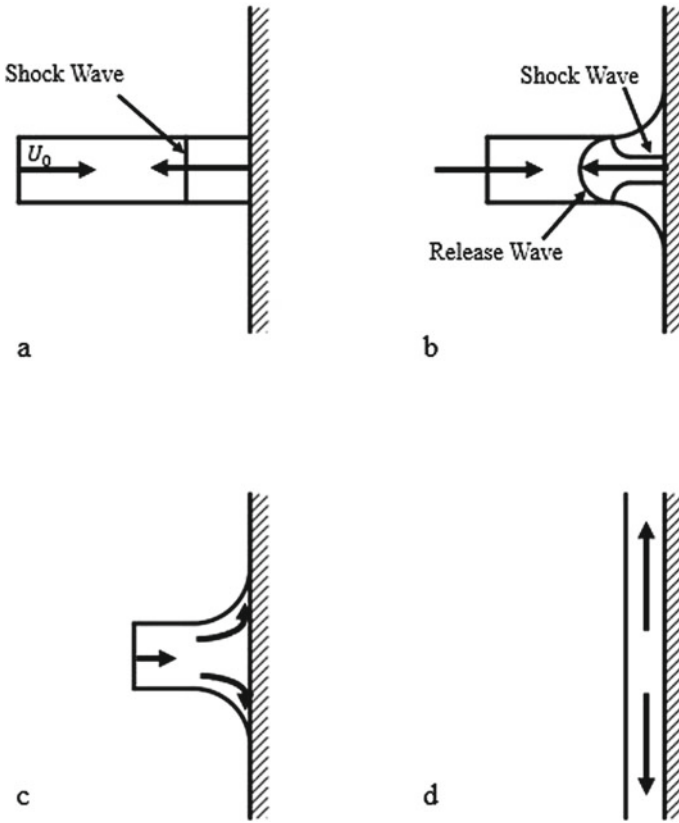
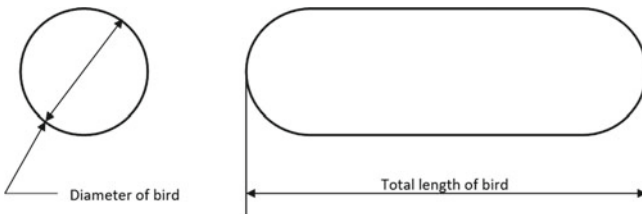


Fig. 1 a Initial impact phase; b Shock propagation; c Steady state flow; d Pressure decay process

Table 1 Material properties of the bird

Properties	Values
ρ (kg/m ³)	942.7
Γ_0	0
C_0 (m/s)	1480
S	0



4 Marital Damage Modes

To conduct the research on the bird's high-velocity impact on spar it performed using finite element analysis (FEA). In composite material, three forms of damage are considered: fibre loss, ply fracture delamination. They are implementing an acceptable failure parameter and constitutive equation to the model, the structural characteristics of marital composite and alloy. In this research, aluminium inner structure [8] and plates are composite materials T300 [9]. Simulate our study using the Johnson-Cook damage model for aluminium, and Hashin's law is for the composite model. These damage models can predict the material's behaviour, and both available finite element (F.E.) tools to model material forming simulations. The Johnson-Cook model analyses statistical effective and mostly usable modelling and simulation work. The Johnson-Cook material model is a universal material relation for metals commonly used in impact simulation and problem-related penetration. It has a wide range of potential applications. The composite layer is damaged mostly with impact velocity on it. For the impact, that time, more than one stress acting on the composite layer, Hashin's law deals with the different types of failure models and appraises the failure. According to the Hashin's law, which used to study these criteria are the developers for the unidirectional polymeric composite layer. It will also be much rough calculation refer to many types of laminate and non-polymer composite normally Hashin's applies on two-dimensional approaches for point stress.

5 Test Model

The modern technological development took place in aviation too, in the result, the aircraft is faster than it needs a strong wing, which is more reliable and low weight. This experimentation uses FEA like ABAQUS/Explicit, which is suitable for research. It provides a nearly accurate result of the experiment. In this study using Abaqus FEA is the CEL approach. This study over aims spar design must be lightweight and able to bear the impact of the bird. In this bird strike, our velocity is 300 m/s. This study uses two materials, aluminium [8], and second is a composite material [9]. The spar's vertical plates, top and bottom horizontal plates are made by aluminium, and the other structures are made of composite plates. In the first (model-a), plates are parallel to the top and bottom, and between them, "Fig. 2a shows that model". In the second (model-b), V shape plates fix on vertical aluminium. The single edge of V shape is the outer side "Fig. 2b shows that model". The third (model-c) is like the first but covered with aluminium. "Figure 2c shows that model". Fix all of these spar models with fixtures and apply the boundary condition on fixtures. Set the target on the centre of the spar, then bird impact equally on the spar "Fig. 2d shows all process".

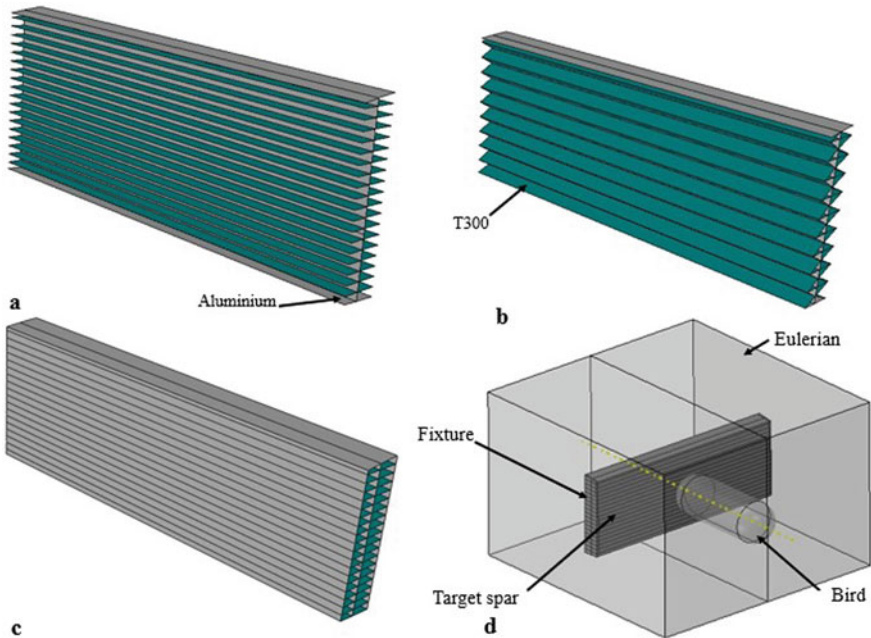


Fig. 2 Test models

5.1 Validation of CEL

To validate our work credibility and approach gives the result of bird impact on the wing is near to spar's real bird impact. Validate our methodology to compare the real experiment, which is presented in [10]. The result of the bird impact in reference study. Where gelatin bird lode in the gas gun with bird 4lb (1.82 kg). Which is fire on aluminium plate Al6061 at a velocity of bird is round about 150 m/s. The aluminium plate is fixed on a rigid body frame. The dimension of the plate is 550 * 550 * 6.35 mm. The diameter is free from the rigid frame is 0.4064 m, after bird impact on plate. Like bowel shape using the CEL approach in Abaqus explicit, its damage replaced the body frame by the boundary condition. After getting the resulting CEL, compare with the experiment results, "Fig. 3 shows the result of an experiment and CEL bird impact."

6 Result

This simulation carried out in three different types of spars. All details are described in the above part of the paper. The striking velocity of the bird in 300 m/s. The bird's mass is 1.82 k.g. When the bird strikes on the model, the bird's K.E is

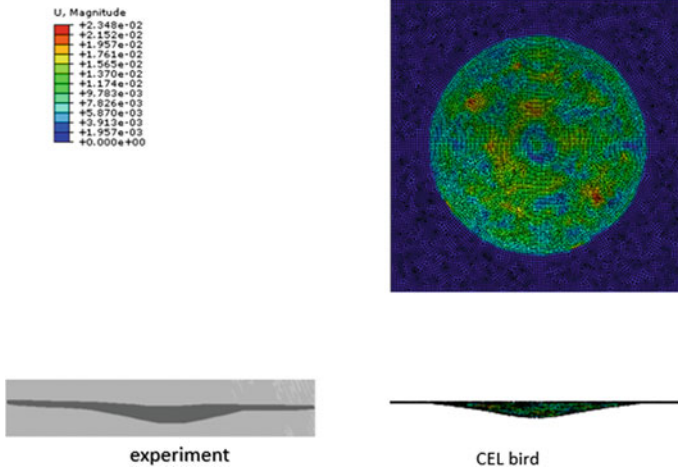


Fig. 3 Results comparison

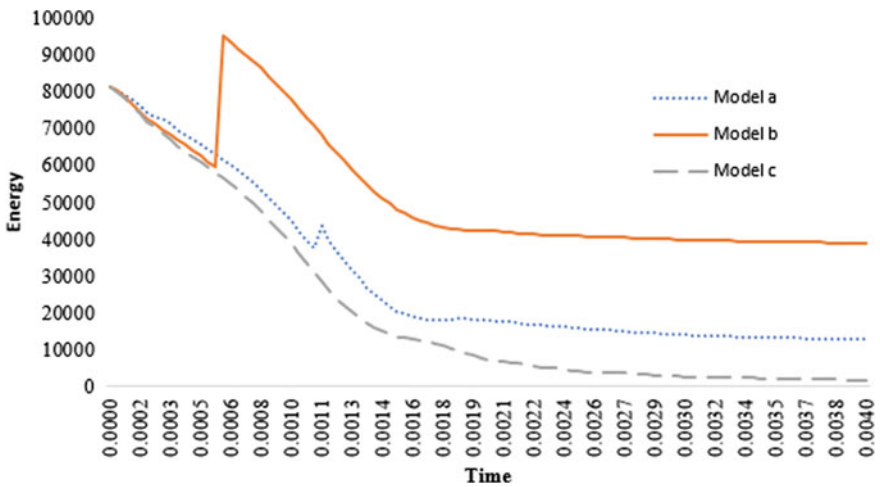


Fig. 4 Kinetic energy graph

decreasing. Due to K.E’s absorption in the material. Three different spar designs have a different type of response against the bird strike the K.E “Fig. 4 shows kinetic energy graph.”

7 Conclusion

This research aims to stimulate the bird strike’s impact on the spar and assess the damage at velocity 300 m/s. Our validation proves that the CEL method is given nearly accurate results to the experiment. Finite element computational simulations of the bird effect were carried out using the CEL technique to represent the bird body. The bird was modelled using the EOS with water properties. Based on the numerical simulation results, “Figs. 5, 6 and 7, shows the results,” model-c is given better results than others. The outer covers absorb the K.E. of the bird, and the

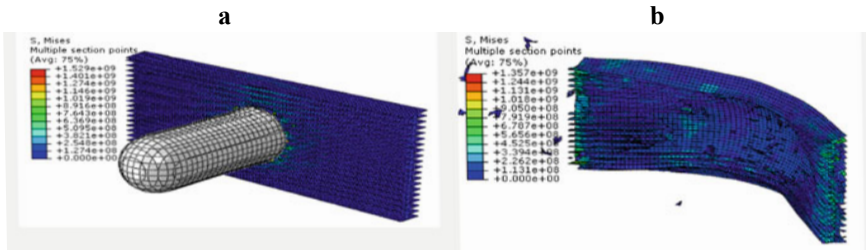


Fig. 5 Bird strike simulation in model-a at 300 m/s, a t = 0.12 ms; b t = 4 ms

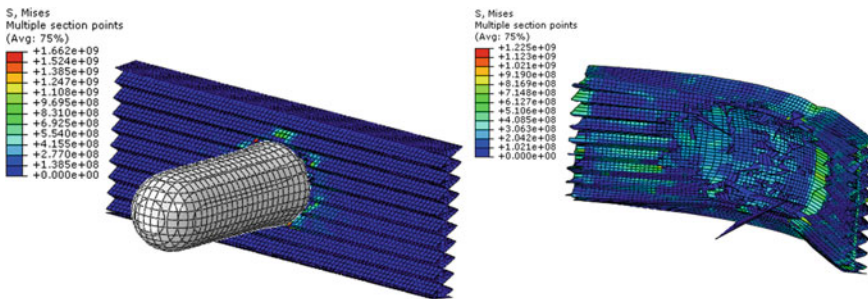


Fig. 6 Bird strike simulation in model-b at 300 m/s, a t = 0.12 ms; b t = 4 ms

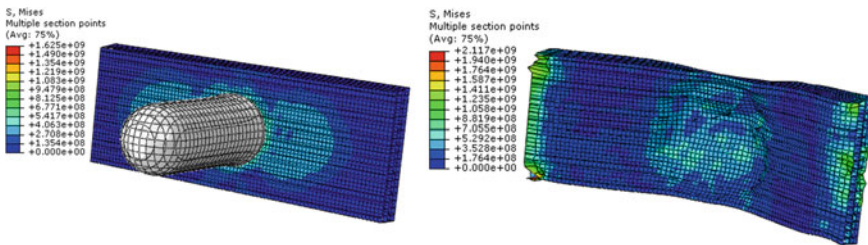


Fig. 7 Bird strike simulation in model-c at 300 m/s, a t = 0.12 ms; b t = 4 ms

composite material plates help absorb energy. Model-a gave the result better than model-b. The composite plates help to cut the bird into pieces and divide the K.E. The aluminium plate of the spar, which is vertically absorbed more K.E than the composite material.

References

1. Federal Aviation Administration (FAA). Federal Register: Rules and Regulations (2012). <https://doi.org/10.1017/cbo9781107415324.004>
2. Long, S., Mu, X., Liu, Y., Wang, H., Zhang, X., Yao, X.: Failure modeling of composite wing leading edge under bird strike. *Compos. Struct.* **255**(September 2020), 113005 (2021). <https://doi.org/10.1016/j.compstruct.2020.113005>
3. Abdul Kalam, S., Vijaya Kumar, R., Ranga Janardhana, G.: SPH high velocity impact analysis-influence of bird shape on rigid flat plate. *Mater. Today Proc.* **4**(2), 2564–2572 (2017). <https://doi.org/10.1016/j.matpr.2017.02.110>
4. Zhang, D., Fei, Q.: Effect of bird geometry and impact orientation in bird striking on a rotary jet-engine fan analysis using SPH method. *Aerosp. Sci. Technol.* **54**, 320–329 (2016). <https://doi.org/10.1016/j.ast.2016.05.003>
5. Yu, Z., Xue, P., Yao, P., Zahran, M.S.: Analytical determination of the critical impact location for wing leading edge under birdstrike. *Lat. Am. J. Solids Struct.* **16**(1), 1–17 (2019). <https://doi.org/10.1590/1679-78255352>
6. Basri, E.I., et al.: Conceptual design and simulation validation based finite element optimisation for tubercle leading edge composite wing of an unmanned aerial vehicle. *J. Mater. Res. Technol.* **8**(5), 4374–4386 (2019). <https://doi.org/10.1016/j.jmrt.2019.07.049>
7. Saputo, S., Sellitto, A., Riccio, A., Di Caprio, F.: Crashworthiness of a composite wing section: numerical investigation of the bird strike phenomenon by using a coupled Eulerian-Lagrangian approach. *J. Mater. Eng. Perform.* **28**(6), 3228–3238 (2019). <https://doi.org/10.1007/s11665-019-03944-0>
8. Zhu, Q., Zhang, C., Curiel-Sosa, J.L., Quoc Bui, T., Xu, X.: Finite element simulation of damage in fiber metal laminates under high velocity impact by projectiles with different shapes. *Compos. Struct.* **214**(February), 73–82 (2019). <https://doi.org/10.1016/j.compstruct.2019.02.009>
9. Dababneh, O., Kipouros, T., Whidborne, J.F.: Application of an efficient gradient-based optimisation strategy for aircraft wing structures. *Aerospace* **5**(1), 1–27 (2018). <https://doi.org/10.3390/aerospace5010003>
10. Welsh, C.J.: Aircraft transparency testing—artificial birds. Technical Reports Arnold Air Force Station, Tennessee Air Force Systems Command (1986)

Effects of Y_2O_3 on Microstructure and Wear Resistance of Laser Cladding Ni-Based Coating on 42CrMoA Alloy Steel



Yunfeng Li, Yan Shi, and Qingtang Wu

Abstract In the paper, Ni45 alloy coating was produced by laser cladding on 42CrMoA alloy steel using the 5 kW CO_2 laser, four-axis CNC machines and the coaxial powder feeding system. It were investigated that the effects of Y_2O_3 on microstructure and wear resistance of the Ni-based coating. The macromorphology and microstructures were characterized by using optical microscopy, SEM, and microhardness tester. The wear properties were evaluated on the friction-wear tester. The results show that the microstructure was first refined and then coarsened with the increase of Y_2O_3 addition. When the Y_2O_3 addition is 0.3 wt%, the coating showed the finest microstructure. Meanwhile, the wear rates of coating were gradually decreased.

Keywords Laser cladding · Y_2O_3 · Microstructure · Wear resistance

1 Introduction

Laser cladding has been widely used in industrial manufacturing [1]. Meanwhile, the laser cladding can be mainly divided into two ways on the basis of the methods of adding powder. One of two ways is Pre-placed laser cladding. The pre-placed method can make ensure that the content of additions (rare earth, carbide etc.) isn't decreased in composite coating during the laser cladding process.

Y. Li · Q. Wu (✉)

Laboratory of Ultra-Precision Fabrication, Changchun Institute of Equipment and Processes, No. 738 Huguang Road, Changchun 130012, Jilin, People's Republic of China
e-mail: wqtwj@sohu.com

Y. Li · Y. Shi

School of Mechanical and Electric Engineering, Changchun University of Science and Technology, Changchun 130022, People's Republic of China

Y. Shi

National Base of International Science and Technology Cooperation for Optics, Changchun 130022, People's Republic of China

At present, rare earth elements (REs) and their oxides (REO) have been widely used in various industrial fields [2, 3]. Many scholars have investigated the influence of rare earth (such as Y_2O_3 , CeO_2 , La_2O_3 et al.) on microstructure, physical and chemical properties of composite coating by pre-placed laser cladding for the past many years. Of these, the effects of micron- CeO_2 and nano- CeO_2 powders have been investigated by laser cladding. The results show that the microstructure and properties of the coatings with the addition of micron- CeO_2 and nano- CeO_2 were better than the coating without CeO_2 added [4–6]. Meanwhile, some researchers also investigated the effects of La_2O_3 on microstructure and properties in clad layer [7–9].

In addition, the Y_2O_3 has been discussed in many studies. Liu Qibin et al. [10] study the effect of Y_2O_3 on microstructure of composite coating. The result indicate that the best effect of rare earth in synthesizing HA and β -TCP was acquired with the content of Y_2O_3 from 0.3 to 0.6%. Anil Kumar Das et al. [11] develop the micro-hardness and wear resistance of alloyed layer with and without the Y_2O_3 in the mixed powder of Ti+SiC+h-BN on the Ti–6Al–4V substrate by laser surface alloying. The micro-hardness and wear resistance of alloyed layers are enhanced significantly with Y_2O_3 addition. According to the report by Li H.C. et al. [12], the optimal addition of Y_2O_3 have the best effect on microstructural refinement and cracking resistance of CaO-SiO₂ coatings.

Although the above papers already have investigated the influence of rare earth in clad layer by the pre-placed method, there are many disadvantages about it. The deformations, cracks, pores and slags also can be generated in clad layer. Except as described above way of Pre-placed laser cladding, the coaxial powder injection is used to feed powder in molten pool. It can improve the absorptivity of laser energy and eliminate the pores in coating. Furthermore, the synchronized shielding gas can prevent the oxidation of the molten pool. Parisa Farahmand investigated the effects of rare earth element (La_2O_3) on the microstructure, microhardness and corrosion resistance of Ni-WC coatings by using a coaxial powder feeding system. The grain of the coating was refined with nano-WC particles and La_2O_3 [13].

From the above studies, no one has done any research about the Individual effects of Y_2O_3 in Ni45 composite coating by the laser cladding of coaxial powder feeding. So in this paper will reveal the effect of Y_2O_3 on the microstructure, microhardness and wear resistance of the Ni45 composite coating by coaxial powder feeding laser cladding.

2 Experiment Methods

2.1 Material

The composite coating was fabricated on the substrate of 42CrMoA alloy steel. The Ni45 powder were used to clad the composite coating. The Y_2O_3 powder was added into the Ni45 powder in the mass fraction of 0.0, 0.3 and 0.6 wt%.

2.2 Equipment

The laser cladding were conducted by a process device (a 5 kW CO_2 laser, a 4-axis CNC platform and a powder feeder). The clad layers were produced by multi-track laser cladding with a overlapping rate of 40%. The laser process parameters on clad procedure were explored including 2100 W of laser power, 8.5 g/min of powder feed rate and 300 mm/min of laser scan speeds.

The cross-section of clad specimens were ground and polished. Afterwards, aqua regia was used to etch the sample. The microstructures of clad layers were characterized by a JEOL: JSM-6510F SEM microscope. A Emyrean sharp shadow X-ray Diffractometer was used to analysis the phases of the clad layers. The microhardness was measured by a MH-60 tester.

The wear teat of the clad layers sliding against GCr15 steel ring were conducted with a method in Fig. 1. Under condition of 98 N load, the GCr15 steel ring performs a 30 min wear test on the clad samples at a rotating speed of 400 r/min. The wear rate ω of the clad layers were calculated by the Eq. (1) [14]:

$$\omega = \frac{V_{loss}}{L \times N} \tag{1}$$

$$V_{loss} = B \left[\frac{\pi R^2}{180} \arcsin\left(\frac{b}{2R}\right) - \frac{b}{2} \sqrt{R^2 - \frac{b^2}{4}} \right] \tag{2}$$

$$L = 2\pi Rvt \tag{3}$$

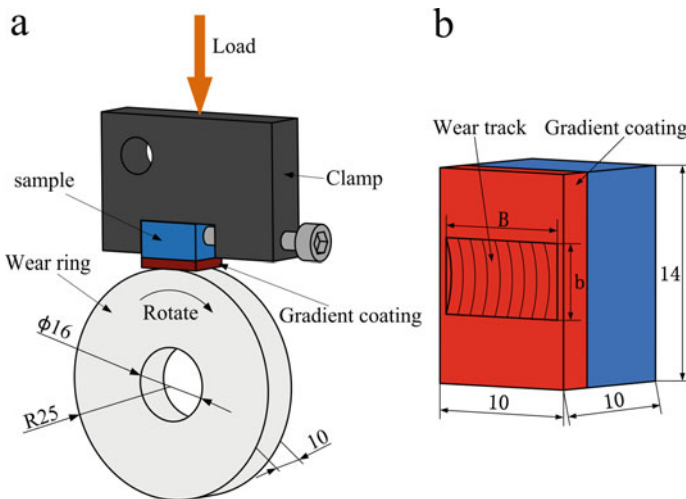


Fig. 1 Friction and wear test. a Friction and wear device, b wear track

Volume loss (V_{loss}) is calculated by Eq. (2), B and b is the length and width of the wear track (mm), R is the radius of the GCr15 steel ring (25 mm), L is the wear distance (mm) as calculated by Eq. (3), v is the rotating speed of the GCr15 steel ring (400 r/min), t is the wear time (30 min), F is the load (98 N).

3 Result

3.1 Cracks Morphology of Clad Layers

The cracks morphology of clad layers with different amount of Y_2O_3 are shown in Fig. 2, respectively. The number of cracks were decreased first and then increased with the increase of Y_2O_3 addition.

3.2 Microstructure Characteristics of Clad Layers

The microstructure of the clad layers with different amount of Y_2O_3 are shown in Fig. 3. It can be observed that the variation of solidification type were in the forms of columnar dendrites and equiaxed crystals. With increasing amount of Y_2O_3 , the length and quantities of columnar dendrites were decreased first and then increased. However, the quantities of equiaxed crystals were first increased and then decreased. The crystal size of clad layer with the amount of 0.3 wt% is most uniform and fine.

3.3 Microhardness of Clad Layers

Figure 4 show the microhardness of the clad layers with different amount of Y_2O_3 . The clad layers with the addition of Y_2O_3 possess higher micro-hardness than that of the clad layer without Y_2O_3 . With the gradual increase of Y_2O_3 addition, the microhardness gradually increased.



Fig. 2 Cracks morphology of clad layers with different amount of Y_2O_3 . **a** 0.0 wt%, **b** 0.3 wt%, **c** 0.6 wt%

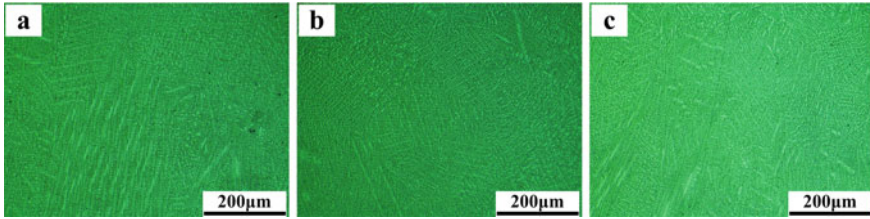


Fig. 3 Microstructure of clad layers with different amount of Y_2O_3 . **a** 0.0 wt%, **b** 0.3 wt%, **c** 0.6 wt%

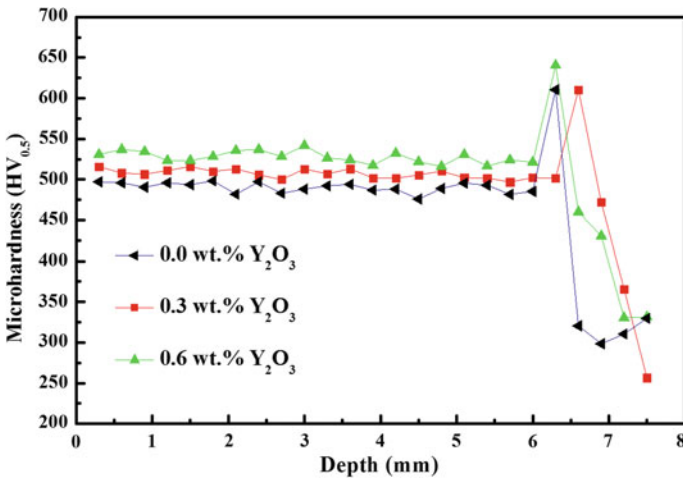


Fig. 4 Microhardness of clad layers with different amount of Y_2O_3

3.4 Wear Resistance of Clad Layers

Figure 5 shows the wear rate of the clad layers. As the content of Y_2O_3 increased, the wear rate decreased first and then increases. When the addition amount is 0.3 wt %, the wear rate does not decrease significantly. When the addition of Y_2O_3 increased to 0.6 wt%, the wear rate dropped to the lowest value.

4 Discussion

4.1 Effect of Y_2O_3 on the Microstructure of Clad Layers

Figure 6 show the microstructure of the clad layers by SEM analysis. It can be seen that the primary dendrites of clad layers with Y_2O_3 addition (Fig. 6b) became more

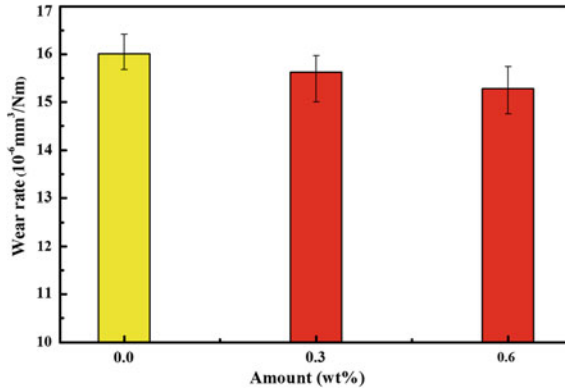


Fig. 5 Wear rate of clad layers with different amount of Y_2O_3

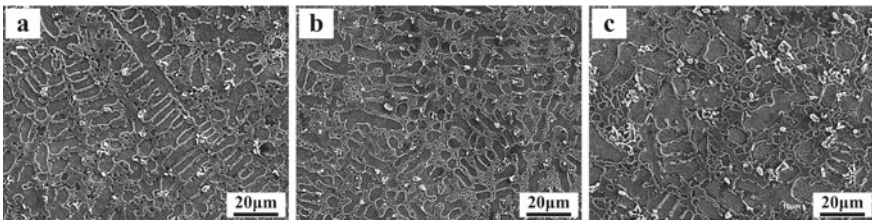


Fig. 6 Microstructure of clad layers with different amount of Y_2O_3 . **a** 0.0 wt%, **b** 0.3 wt%, **c** 0.6 wt%

fine and uniform than that of clad layer without Y_2O_3 addition (Fig. 6a). Meanwhile, the clad layer without Y_2O_3 showed a clear dendritic morphology. There was a coarse dendritic structure, and a large number of particles precipitate in the eutectic zone. When 0.3 wt% Y_2O_3 is added (Fig. 6b), the size of primary dendrites was refined significantly in the clad layer with the amount of 0.3 wt%. The dendritic and columnar grains disappeared, and uniformly distributed fine grains were formed.

At the same time, The hypoeutectic zone is largest than that of another clad layers. The eutectic structure with a larger distribution area was formed at the refined grain boundary, the particles precipitated in the eutectic zone are significantly reduced, and the particle size is significantly reduced. As the addition of yttrium oxide increased to 0.6 wt%(Fig. 6c), the microstructure was significantly coarsened, and larger columnar crystals were formed, and the particle precipitation gradually increased.

Due to the large atomic radius of Y can generate a great amount of lattice distortion and increase the total energy of system [15]. So, the Y_2O_3 are easily converged to grain boundaries for retaining the lowest free energy of the grain growth. When the Y element accumulate over the grain boundaries, it could have an

positive effect on retarding grain evolution by creating a dragging effect during the process of grain growth [16]. The Y_2O_3 can reduce the energy of solid-liquid interface in the molten pool, which cause probably the reduction of Gibbs free energy for forming a nucleus. Therefore, Y element can reduce the phenomenon of critical nucleation by generating the more number of nuclei. In a word, the grains become finer with the growing number of nucleation formed in the solidifying molten pool [17].

4.2 *Effect of Y_2O_3 in Reducing Crack Susceptibility*

According to the characteristic of rapid solidification, the high cooling speed and temperature gradient can result in forming the cracks [18]. Further to this, it can cause the propagation of cracks that the coefficient of thermal expansion of matrix and clad layer exist a larger difference. Besides, the toughness can be reduced throughout the section of clad layer owing to the inhomogeneous distribution of the coarse brittle phase and the high density of reinforcing carbide phase [19].

Due to the Y_2O_3 addition of clad layer, the grains were refined and caused the increase in the number and area of grain boundaries [16]. The crack initiation may be hindered and the dragging effect is improved on the propagation of cracks [20]. Additionally, the development of grain boundaries decrease the concentration of impurity and the density of dislocation. The stress concentration can be relieved by the above advantages. When too much Y_2O_3 was added (0.6 wt%), the clad layer showed many larger crystal grains. It could reduces the density of grain boundaries and aggravates dislocation slip. In addition, too much Y_2O_3 were enriched to the grain boundary, which greatly increased the brittleness of the grain boundary and the microhardness. The above reasons cause the clad layer with 0.6 wt% Y_2O_3 to have a greater tendency to crack.

4.3 *Effect of Y_2O_3 on the Wear Morphology of Clad Layers*

Figure 7 show the wear morphology of the clad layers by SEM. For the clad layer without Y_2O_3 (Fig. 7a), the worn surface shows obvious adhesive wear and plastic deformation, no obvious furrows are formed. When 0.3 wt% Y_2O_3 is added (Fig. 7b), a wide and deep furrow is formed on the wear surface of the coating. As the Y_2O_3 content increases to 0.6 wt% (Fig. 7c), a larger number of narrow furrows are formed on the worn surface.

When the Y_2O_3 content is 0.3 wt%, the microstructure was significantly refined. The refined structure brings dense grain boundaries and eutectic regions. The boundary has been significantly strengthened, resulting in a strong tendency of slippage of dislocations near the grain boundary, thereby increasing the possibility of slip transfer within the grain [21]. At the same time, the grain boundaries help the

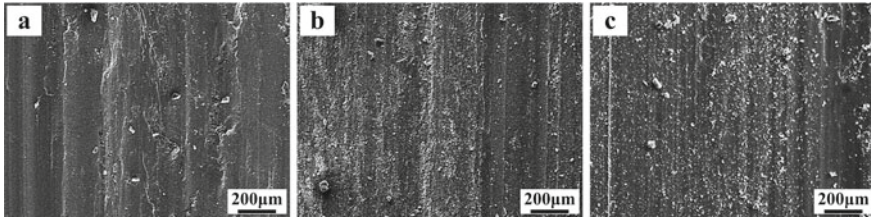


Fig. 7 Wear morphology of clad layers with different amount of Y_2O_3 . **a** 0.0 wt%, **b** 0.3 wt%, **c** 0.6 wt%

stress relaxation at the front end of the worn microcracks, and hinder the continued propagation of the cracks. However, the 0.3 wt% Y_2O_3 does not significantly increase the microhardness. So it does not show a lower wear rate. As the addition of Y_2O_3 increase, the Y_2O_3 enriched at the edge of the grain will hinder the dislocation slip of the grain boundary, thereby slowing down the amount of wear. But when the content of Y_2O_3 reaches 0.6 wt%, too much Y_2O_3 will be enriched to the grain boundary, which greatly increases the brittleness of the grain boundary and the microhardness of clad layer. So that the coating wear rate is reduced. In summary, the addition of Y_2O_3 can refine the microstructure and enhance the wear resistance of the coating.

5 Conclusions

- (1) The microscopic analysis results show that with the increase of rare earth content, the coating grains are first refined and then coarsened. When 0.3 wt% Y_2O_3 is added, the grain size of the coating is smaller.
- (2) The micro-hardness of the clad layers with the 0.3 wt% Y_2O_3 were higher than that of the clad layer without Y_2O_3 . Meanwhile, the microhardness gradually increased with the increase of Y_2O_3 addition.
- (3) The wear resistance test shows that the wear rate of the clad layer gradually decreased as the content of Y_2O_3 increased. When the amount was increased to 0.6 wt%, the wear rate of the clad layer dropped to the lowest value.

Acknowledgements The authors are also grateful for the financial aids from the Foundation of Changchun Institute of Equipment and Processes (Grant No: WDZC2019JJ015).

References

1. Hüttner, B., et al.: *The Theory of Laser Materials Processing*. Springer Netherlands (2009)
2. Zhang, Z.f., Jia, Q., et al.: Progress in the separation processes for rare earth resources. In: *Handbook on the Physics and Chemistry of Rare Earths*. Elsevier Science & Technology, vol. 48, pp. 287–376 (2015)
3. Zhang, H., Zou, Y., et al.: Effects of CeO_2 on microstructure and corrosion resistance of TiC-VC reinforced Fe-based laser cladding layers. *J. Rare Earths* **32**(11), 1095–1100 (2014)
4. Li, J.N., Chen, C.Z., et al.: Effect of nano- CeO_2 on microstructure properties of TiC/TiN + TiCN-reinforced composite coating. *Bull. Mater. Sci.* **36**(4), 541–546 (2013)
5. Wang, H.Y., Zuo, D.W., et al.: Effects of CeO_2 nanoparticles on microstructure and properties of laser clad NiCoCrAlY coatings. *J. Rare Earths* **28**(2), 246–250 (2010)
6. Zhang, S.H., Li, M.X., et al.: Laser clad Ni-base alloy added nano- and micron-size CeO_2 composites. *Optics Laser Technol.* **40**(5), 716–722 (2008)
7. Zhao, Y.H., Sun, J., et al.: Effect of rare earth oxide on the properties of laser cladding layer and machining vibration suppressing in side milling. *Appl. Surf. Sci.* **321**(3), 387–395 (2014)
8. Wang, X.H., Zhang, M., et al.: Microstructure and properties of laser clad TiC + NiCrBSi + rare earth composite coatings. *Surf. Coat. Technol.* **161**(2-3), 195–199 (2002)
9. Liu, X.B., Yu, R.L.: Effects of La_2O_3 on microstructure and wear properties of laser clad $\gamma/Cr_7C_3/TiC$ composite coatings on TiAl intermetallic alloy. *Mater. Chem. Phys.* **101**(2–3), 448–454 (2007)
10. Liu, Q.B., Zou, J.L., et al.: Effect of Y_2O_3 content on microstructure of gradient bioceramic composite coating produced by wide-band laser cladding. *J. Rare Earths* **23**(4), 446–450 (2005)
11. Das, A.K., Shariff, S.M., et al.: Effect of rare earth oxide (Y_2O_3) addition on alloyed layer synthesized on Ti-6Al-4V substrate with Ti+SiC+h-BN mixed precursor by laser surface engineering. *Tribol. Int.* **95**, 35–43 (2016)
12. Li, H.C., Wang, D.G., et al.: Effect of CeO_2 and Y_2O_3 on microstructure, bioactivity and degradability of laser cladding CaO-SiO₂ coating on titanium alloy. *Coll. Surf. B Biointerf.* **127**, 15–21 (2015)
13. Farahmand, P., Frosell, T., et al.: Comparative study of the slurry erosion behavior of laser clad Ni-WC coating modified by nanocrystalline WC and La_2O_3 . *Int. J. Adv. Manuf. Technol.* **79**(9-12), 1607–1621 (2015)
14. Li, Q.T., Lei, Y.P., et al.: Laser cladding in-situ NbC particle reinforced Fe-based composite coatings with rare earth oxide addition. *Surf. Coat. Technol.* **239**(2), 102–107 (2014)
15. Kou, S.: *Welding Metallurgy*. Wiley (2003)
16. Wang, K.L., Zhang, Q.B., et al.: Rare earth elements modification of laser-clad nickel-based alloy coatings. *Appl. Surf. Sci.* **174**(3–4), 191–200 (2001)
17. Quazi, M.M., Fazal, M.A., et al.: Effect of rare earth elements and their oxides on tribo-mechanical performance of laser claddings: a review. *J. Rare Earths* **34**(6), 549–564 (2016)
18. Lu, D.H., Liu, S.S., et al.: Effect of Y_2O_3 on microstructural characteristics and wear resistance of cobalt-based composite coatings produced on TA15 titanium alloy surface by laser cladding. *Surf. Interf. Anal.* **47**(2), 239–244 (2015)
19. Sun, S., Durandet, Y., et al.: Parametric investigation of pulsed Nd: YAG laser cladding of stellite 6 on stainless steel. *Surf. Coat. Technol.* **194**(2–3), 225–231 (2005)
20. Yin, J., Wang, C.S.H., et al.: On the development of microstructures and residual stresses during laser cladding and post-heat treatments. *J. Mater. Sci.* **47**(2), 779–792 (2012)
21. Wu, C.M.L., Yu, D.Q., et al.: Properties of lead-free solder alloys with rare earth element additions. *Mater. Sci. Eng. R Reports* **44**(1), 1–44 (2004)

Effect of Nb/Sn and B Combinatorial Micro-alloying on the Microstructure and Corrosion Properties of As-Cast TiFe-Based Alloys



J. W. Li, Z. Y. Wang, S. X. Liu, H. S. Cao, Z. H. Dan, and H. Chang

Abstract Effects of Sn, Nb and B micro-alloying on the microstructural refinements and the anti-corrosion properties have been investigated in order to obtain the finer initial cast microstructures of TiFe-based alloy ingots. Three alloys including $\text{Ti}_{73.3}\text{Fe}_{26.7}$, $\text{Ti}_{73.3}\text{Fe}_{24.6}\text{Nb}_2\text{B}_{0.1}$, $\text{Ti}_{73.3}\text{Fe}_{24.6}\text{Sn}_2\text{B}_{0.1}$ alloys have obtained by vacuum suspension melting and the effect of adding Sn, Nb, B on the structure, corrosion properties of Ti–Fe alloys has been explored by surface morphology, X-ray diffraction, grain size statistics, potentiodynamic polarization measurements and contact angle tests. The results show that the grain sizes of TiFe-based alloys can be reduced by chemical compositions designs, and the corrosion resistance can be improved as well. The grain refinements by micro-alloying can be achieved for all regions. The average grain sizes at the edge of cast ingots were confirmed to be 225 μm for $\text{Ti}_{73.3}\text{Fe}_{26.7}$ alloy, and the size of 156 μm for $\text{Ti}_{73.3}\text{Fe}_{24.6}\text{Sn}_2\text{B}_{0.1}$ alloy and 86 μm for $\text{Ti}_{73.3}\text{Fe}_{24.6}\text{Nb}_2\text{B}_{0.1}$ alloy, respectively. The refinement efficiency was 30.8 and 61.8% by the minor addition of Sn/Nb+B elements. According to the polarization curves, the corrosion potential of micro-alloyed TiFe-based alloys positively shifted more than 200 mV. The refinements are possibly ascribed to the low diffusion coefficients of micro-alloyed elements and the inhibition of the rapid growth of the grains.

Keywords TiFe-based alloys · Chemical compositions design · Microstructural refinement · Corrosion performance

J. W. Li · Z. Y. Wang · S. X. Liu · H. S. Cao · Z. H. Dan (✉) · H. Chang
College of Materials Science and Engineering and Tech Institute for Advanced Materials,
Nanjing Tech University, Nanjing 210009, China
e-mail: zhenhuadan@njtech.edu.cn

J. W. Li
e-mail: 201961203102@njtech.edu.cn

1 Introduction

Since the 1950s, titanium and titanium alloys have attracted the extensive attention of researchers because of their superior properties, such as high strength-to-weight ratio, good corrosion resistance to strong corrosive medias, nonmagnetism, and biocompatibility [1–3]. The design of chemical compositions of the titanium alloys is of importance to meet the specific demands for the practical applications. These α -phase stabilized elements, i.e. Al, C, N and O, tend to increase the phase transition temperature. On the contrary, β -phase stabilized elements, such as Fe, Mo, Mg, Cr, Mn and V decrease the phase transition temperature. Neutral elements, i.e. Sn, Zr, are considered to have little effect on phase transition temperature. The designs and optimal combination of the alloying elements can effectively manipulate the initial microstructures of the as-cast alloys, and further improve the mechanical performances of α titanium alloys, β titanium alloys and $\alpha+\beta$ titanium alloys after the specific plastic deformations to obtain the finer grains.

It has been the choices of many researchers to add Fe as β -phase stabilizing element to improve the compressive strength, tensile strength and elastic modulus of the titanium alloys. Binary $\text{Ti}_{65}\text{Fe}_{35}$ alloys prepared by arc melting and casting exhibit a high mechanical strength of 2.2 GPa, ductility of 6.7% and a Young's modulus of 149 GPa by Louzguine [4]. Peng et al. [5] reported that the tensile strength of the $\text{Ti}_{1-x}\text{Fe}_x$ alloys was significantly enhanced when they increase the Fe concentrations. Zhang et al. [6] revealed that the average columnar dendrite spacing of as-cast Ti–46Al alloy was 1,000 μm , and they refined as-cast structure of Ti–46Al alloys by Hf and B additions. Das et al. [7] investigated the addition of the element Sn to binary $\text{Ti}_{70.5}\text{Fe}_{29.5}$ alloy, and they found that the ingots of the $\text{Ti}_{67.79}\text{Fe}_{28.36}\text{Sn}_{3.85}$ alloy have ultrafine high-strength ductile eutectic and high processibility at a low cooling rate of 10 K/s. Sn element was added to improve the surface tension of the melt in the process of smelting and affect the solidification processes and the casting microstructure, thus the corrosion resistance was improved [8]. Meanwhile, Nb element can be used to refine grains and make intermediate phase precipitation strengthening [9]. Ehtemam-Haghighi et al. [10] assessed the effects of Nb contents on the microstructural and mechanical characteristics of the Ti–Fe–Nb alloys, and the Young's modulus values decreased from 129 to 84 GPa with Nb additions from 0 to 11 wt%. Tamirisakandala et al. [11] revealed that the as-cast grain sizes have been reduced by about an order of magnitude in Ti–6Al–4V and Ti–6Al–2Mo–4Sn–2Zr alloys with an addition of 0.1 wt% B. It has also been reported that a trace of ~ 0.1 wt% B addition to Ti–6Al–4V alloys can reduce the grain sizes with nearly an order of magnitude [12, 13]. B was added to improve the mechanical performances of the casting titanium alloy [14, 15]. Therefore, the combination of Fe and other minor alloying elements, such as Nb, Sn and B, is proposed here to reduce the initial grain sizes, refine as-cast microstructures and improve the properties of TiFe-based alloys.

This research aims to refine the microstructure by adding Sn, Nb and B elements to the binary $Ti_{73.3}Fe_{26.7}$ alloy and improve the corrosion performance of binary $Ti_{73.3}Fe_{26.7}$ alloy. Meanwhile, the refined microstructure is helpful to obtain the better deformed microstructures in the subsequent materials processing.

2 Materials and Methods

$Ti_{73.3}Fe_{26.7}$, $Ti_{73.3}Fe_{24.6}Nb_2B_{0.1}$ and $Ti_{73.3}Fe_{24.6}Sn_2B_{0.1}$ button ingots of about 300 g were prepared by cold crucible suspension melting furnace with mixtures of Ti (99.7 mass%), Fe (99.9 mass%), Sn (99.99 mass%), Nb (99.99 mass%) and B (99.5 mass%). The microstructure was observed on Zeiss metallographic microscope after etching in HF, HNO_3 and H_2O solution with volume ratio was 1:2:7. The potentiodynamic evaluations were implemented in 0.1 M HCl solution with scan rate of 1 mV/s and in the potential range from -1 to 1.5 V. An X-ray diffractometer (XRD, Rigaku, Geigerflex) was used to analyze the constituent phases. The contact angle tests were carried out in pure water and n-Hexadecane. The metallographic observations and corrosion evaluations were conducted at the edge, middle and central zones, respectively.

3 Results and Discussion

The Mo_{eq} [16], defined as the sum of the weighted averages of the elements (wt%), can be used as a criteria for the mechanical properties in Eq. (1):

$$Mo_{eq} = Mo + 0.67V + 0.44W + 0.28Nb + \dots + 1.25Ni + 1.7Co + 2Fe \text{ (wt.\%)} \quad (1)$$

The Mo equivalent was confirmed to be 53.4 for $Ti_{73.3}Fe_{26.7}$ alloy, and the Mo equivalent of 49.2 for $Ti_{73.3}Fe_{24.6}Sn_2B_{0.1}$ alloy and 49.76 for $Ti_{73.3}Fe_{24.6}Nb_2B_{0.1}$ alloy, respectively. According to the Mo_{eq} , Nb/Sn+B micro-alloyed alloys belong to the stable β -type titanium alloys.

Figure 1a, b, c and d are the metallographic photos of the edge zones of three alloys and the change of the average grain sizes in the edge, middle and central zones. The average grain sizes at the fine grains distributed in the edge zones were confirmed to be 225 μm for $Ti_{73.3}Fe_{26.7}$ alloy, 156 μm for $Ti_{73.3}Fe_{24.6}Sn_2B_{0.1}$ alloy and 86 μm for $Ti_{73.3}Fe_{24.6}Nb_2B_{0.1}$ alloy, respectively. The refinement efficiency was 30.8 and 61.8% by the addition of Sn, Nb and B elements. The average grain sizes of columnar crystals at the middle zones were done to be 232 μm for $Ti_{73.3}Fe_{26.7}$ alloy, 174 μm for $Ti_{73.3}Fe_{24.6}Sn_2B_{0.1}$ alloy and 100 μm for $Ti_{73.3}Fe_{24.6}Nb_2B_{0.1}$ alloy, respectively. The refinement efficiency was 25.0 and

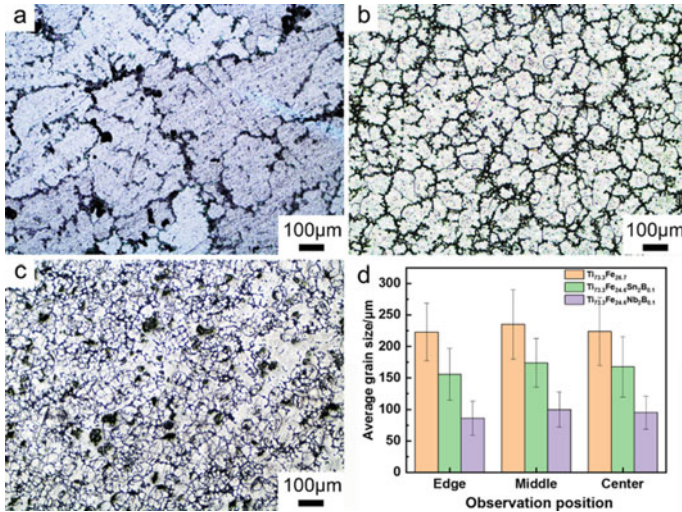


Fig. 1 Metallographic photos of as-cast $\text{Ti}_{73.3}\text{Fe}_{26.7}$ (a), $\text{Ti}_{73.3}\text{Fe}_{24.6}\text{Nb}_2\text{B}_{0.1}$ (b), $\text{Ti}_{73.3}\text{Fe}_{24.6}\text{Sn}_2\text{B}_{0.1}$ (c) alloys in the edge zones and the change of the average grain sizes in the edge, middle and central zones (d)

56.9% by micro-alloying. These of equiaxed grains at the central zones were measured to be 227 μm for $\text{Ti}_{73.3}\text{Fe}_{26.7}$ alloy, and the size of 168 μm for $\text{Ti}_{73.3}\text{Fe}_{24.6}\text{Sn}_2\text{B}_{0.1}$ alloy and 95 μm for $\text{Ti}_{73.3}\text{Fe}_{24.6}\text{Nb}_2\text{B}_{0.1}$ alloy, respectively. The refinement efficiency was 26.0% and 58.1%. The Nb+B combination is most effectively for the refinements of the initial as-cast microstructures of $\text{Ti}_{73.3}\text{Fe}_{26.7}$ alloy. Moreover, it is obviously that the grain refinement efficiency in the edge area is the highest. This may be ascribed to the high cooling rates and heat transfer of melt solutions close to the copper cold crucible.

Figure 2a, b and c show the XRD patterns of as-cast $\text{Ti}_{73.3}\text{Fe}_{26.7}$, $\text{Ti}_{73.3}\text{Fe}_{24.6}\text{Nb}_2\text{B}_{0.1}$, $\text{Ti}_{73.3}\text{Fe}_{24.6}\text{Sn}_2\text{B}_{0.1}$ alloys at the different tested zones. There are obvious diffraction peaks from β -Ti phases in the edge, middle and central zones at about 40° . The diffraction peaks are very strong corresponding to (110) planes. There is also a small diffraction peak at about 43° , the peak is arising from TiFe phases. In addition, small β -Ti diffraction peaks can be found at 58° and 74° . The three large XRD diffraction peaks were confirmed to belong to β -Ti phases in the quaternary alloys at the edge, middle and central zones, corresponding to the (110) plane, (200) plane and (211) plane. According to the diffraction patterns, a small amount of α -Ti phases precipitated in the matrix of as-cast $\text{Ti}_{73.3}\text{Fe}_{26.7}$ alloys due to the insufficient stabilities of 26.7% Fe. The diffraction peaks can be assigned to β -Ti, α -Ti, TiB_2 , TiFe phases. The presence of new phase P6/mmm TiB_2 may be one of the reasons for the grain refinements through the increases of the grain boundaries and the nucleation densities, and inhibit effect of the atomic diffusion. There are two phases, TiFe and β -Ti, in the microstructure of three alloys. The lattice parameter of the $\text{Pm}\bar{3}\text{m}$ TiFe phase ($a = 0.2983 \text{ nm}$) is slightly larger than

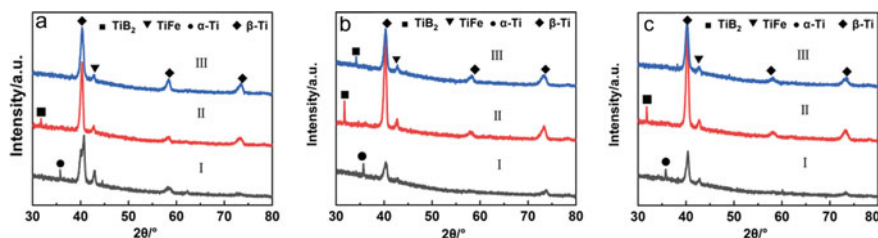


Fig. 2 XRD patterns of as-cast $\text{Ti}_{73.3}\text{Fe}_{26.7}$ (I), $\text{Ti}_{73.3}\text{Fe}_{24.6}\text{Nb}_2\text{B}_{0.1}$ (II), $\text{Ti}_{73.3}\text{Fe}_{24.6}\text{Sn}_2\text{B}_{0.1}$ (III) alloys in the edge **a**, middle, **b**, central, **c** zones

that of TiFe phase (B2, $a = 0.2975$ nm). The small black regions in Fig. 1a, b, c may be TiFe phase instead of TiB_2 phase because of the low proportion of B (0.1%) and small amount of precipitated TiB_2 phases. The lattice parameter of the Im3m β -Ti phases ($a = 0.3160$ nm) is smaller than of pure β -Ti phases (0.33065 nm) because of the shrinking lattice distortion effects of Fe [17]. On the basis of the metallographic photos (Fig. 1) and XRD patterns (Fig. 2) of as-cast Nb/Sn+B micro-alloyed alloys, it is concluded that the main phases for as-cast alloys are β -Ti. As-cast $\text{Ti}_{73.3}\text{Fe}_{26.7}$ alloy is $\alpha+\beta$ type alloy, and as-cast $\text{Ti}_{73.3}\text{Fe}_{24.6}\text{Nb}_2\text{B}_{0.1}$ and $\text{Ti}_{73.3}\text{Fe}_{24.6}\text{Sn}_2\text{B}_{0.1}$ alloys are β type alloys.

Polarization curves of as-cast $\text{Ti}_{73.3}\text{Fe}_{26.7}$, $\text{Ti}_{73.3}\text{Fe}_{24.6}\text{Nb}_2\text{B}_{0.1}$, $\text{Ti}_{73.3}\text{Fe}_{24.6}\text{Sn}_2\text{B}_{0.1}$ alloys in three different zones in 0.1 mol/L HCl solution are shown in Fig. 3. The corrosion current density and corrosion potential are obtained by Tafel slope methods. It can be found that the overall trends of the polarization curves of the three alloys in the edge, middle and central zones are similar. The corrosion current density and corrosion potential of as-cast alloys in the edge, middle and central zones of $\text{Ti}_{73.3}\text{Fe}_{26.7}$, $\text{Ti}_{73.3}\text{Fe}_{24.6}\text{Nb}_2\text{B}_{0.1}$, $\text{Ti}_{73.3}\text{Fe}_{24.6}\text{Sn}_2\text{B}_{0.1}$ alloys are shown in Table 1. According to the polarization curves, the corrosion potential at the edge region was confirmed to be -0.36 V for $\text{Ti}_{73.3}\text{Fe}_{26.7}$ alloy, -0.27 V for $\text{Ti}_{73.3}\text{Fe}_{24.6}\text{Sn}_2\text{B}_{0.1}$ alloy and -0.11 V for $\text{Ti}_{73.3}\text{Fe}_{24.6}\text{Nb}_2\text{B}_{0.1}$ alloy, respectively. The more positive the corrosion potential is and the smaller the self-corrosion current density is, the better the corrosion resistances the as-cast alloys have [18]. On the basis of the metallographic photos (Fig. 1), it is concluded that the corrosion potential of micro-alloyed TiFe-based alloys positively shifted with the decrease of grain sizes, and the corrosion resistance was improved. Therefore, their corrosion resistances are improved through the microstructural refinements by Nb/Sn+B micro-alloying on the basis of the chemical compositions designs.

Figure 4 shows the surface energy and contact angles with water of as-cast $\text{Ti}_{73.3}\text{Fe}_{26.7}$, $\text{Ti}_{73.3}\text{Fe}_{24.6}\text{Nb}_2\text{B}_{0.1}$ and $\text{Ti}_{73.3}\text{Fe}_{24.6}\text{Sn}_2\text{B}_{0.1}$ alloys at the central zones. The contact angles with water at central zones were confirmed to be 89.09° for $\text{Ti}_{73.3}\text{Fe}_{26.7}$ alloy, 92.74° for $\text{Ti}_{73.3}\text{Fe}_{24.6}\text{Sn}_2\text{B}_{0.1}$ alloy and 93.75° for $\text{Ti}_{73.3}\text{Fe}_{24.6}\text{Nb}_2\text{B}_{0.1}$ alloy, respectively. Meanwhile, it can be seen that the surface energies at the central zones were 29.89 mJ m^{-2} for $\text{Ti}_{73.3}\text{Fe}_{26.7}$ alloy, 28.79 mJ m^{-2}

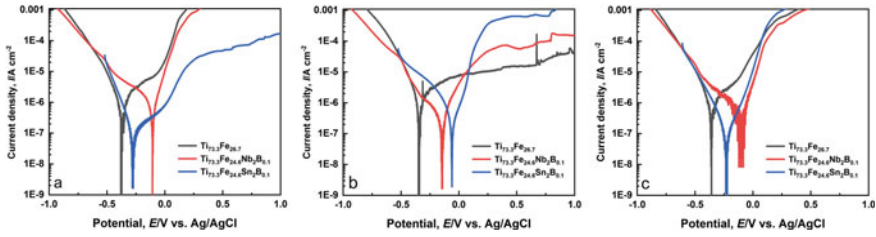


Fig. 3 Potentiodynamic polarization curves of as-cast $\text{Ti}_{73.3}\text{Fe}_{26.7}$, $\text{Ti}_{73.3}\text{Fe}_{24.6}\text{Nb}_2\text{B}_{0.1}$ and $\text{Ti}_{73.3}\text{Fe}_{24.6}\text{Sn}_2\text{B}_{0.1}$ alloys at the edge, **a** middle, **b** central, **c** zones

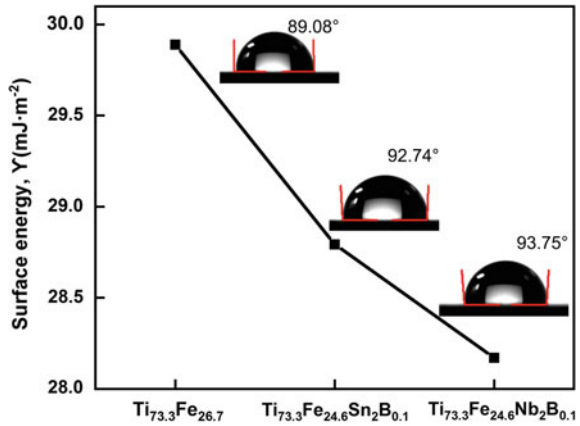
Table 1 Summary of the grain size, and the electrochemical properties of the as-cast $\text{Ti}_{73.3}\text{Fe}_{26.7}$, $\text{Ti}_{73.3}\text{Fe}_{24.6}\text{Nb}_2\text{B}_{0.1}$, $\text{Ti}_{73.3}\text{Fe}_{24.6}\text{Sn}_2\text{B}_{0.1}$ alloys in the edge, middle and central zones

Alloys	Grain size/ μm			Corrosion potential/V			Corrosion current ($10^{-7}\text{A}/\text{cm}^2$)		
	Edge	Middle	Central	Edge	Middle	Central	Edge	Middle	Central
$\text{Ti}_{73.3}\text{Fe}_{26.7}$	225	232	227	-0.36	-0.35	-0.37	5.94	4.95	8.63
$\text{Ti}_{73.3}\text{Fe}_{24.6}\text{Sn}_2\text{B}_{0.1}$	156	174	168	-0.27	-0.06	-0.23	0.74	0.25	0.52
$\text{Ti}_{73.3}\text{Fe}_{24.6}\text{Nb}_2\text{B}_{0.1}$	86	100	95	-0.11	-0.15	-0.12	5.67	5.12	2.20

for $\text{Ti}_{73.3}\text{Fe}_{24.6}\text{Sn}_2\text{B}_{0.1}$ alloy and 28.17 mJ m^{-2} for $\text{Ti}_{73.3}\text{Fe}_{24.6}\text{Nb}_2\text{B}_{0.1}$ alloy, respectively. The surface of as-cast alloys is considered to be hydrophobic because of the contact angles of large than 90° for $\text{Ti}_{73.3}\text{Fe}_{24.6}\text{Sn}_2\text{B}_{0.1}$ and $\text{Ti}_{73.3}\text{Fe}_{24.6}\text{Nb}_2\text{B}_{0.1}$ alloys. In general, the lower surface energy reflects the more stable system and the better corrosion resistance of the alloys to some extent. The larger the surface energy the smaller contact angles are, the more easily the solid surface will be wetted and the worse the corrosion resistances of the as-cast alloys will have [19]. The surface energy of $\text{Ti}_{73.3}\text{Fe}_{26.7}$ alloy was the highest and $\text{Ti}_{73.3}\text{Fe}_{24.6}\text{Nb}_2\text{B}_{0.1}$ alloy was the lowest, it suggests that the addition of Nb/Sn+B improved the corrosion resistances of as-cast TiFe-based alloys. On the basis of the metallographic photos (Fig. 1), the surface energies decreased with the decrease of grain sizes and the corrosion resistance was improved, this trends corresponded to potentiodynamic polarization curves (Fig. 3c). Hence, their surfaces are more stable through the microstructural refinements by Nb/Sn+B micro-alloying on the basis of the chemical compositions designs.

Das [8] have suggested that the Sn addition is effective to introduce a spatial heterogeneity at the interfacial areas, thus minimizing the interfacial strain between the β -Ti solid solution and the constitute TiFe compounds. Similar findings were also reported for HCP Mg alloys recently by Ma et al. [20]. It was concluded that eutectic compounds of Mg alloys are finely distributed and dispersed after adding Sn compared with Mg alloy without Sn, although the precipitated amount is very small, which indicates that Sn has the refining effect on the MgZn eutectic compounds [20]. It is also noted that the addition of Nb causes a quite large lattice mismatch between the β -Ti

Fig. 4 Surface energies and contact angles of as-cast $\text{Ti}_{73.3}\text{Fe}_{26.7}$, $\text{Ti}_{73.3}\text{Fe}_{24.6}\text{Nb}_2\text{B}_{0.1}$ and $\text{Ti}_{73.3}\text{Fe}_{24.6}\text{Sn}_2\text{B}_{0.1}$ alloys at the central zones



and TiFe phases [9, 10, 21], as revealed by the increase of the β -Ti lattice parameter, and simultaneously introduces a coherency strain as well as minimizes the coherency stress at the interface, which may be favorable to absorb dislocations from the β -Ti (Fe, Nb) phases. Hence, we consider that the Sn, Nb and B elements could form solid solution of β -type titanium alloys, which leads to the lattice distortions of Ti and hinders transference of Ti and Fe atoms. The good refinements in the microstructures in the middle and central zones of $\text{Ti}_{73.3}\text{Fe}_{24.6}\text{Nb}_2\text{B}_{0.1}$ alloys are considered to be resulted from the suppression effects of the fast growth of the grains by the low diffusion coefficients of Nb+B combinations. The diffusion coefficients of Ti and Nb are $D_{\text{Ti}} = 4.54 \times 10^{-4} e^{-31300/RT} \text{ cm}^2/\text{s}$ and $D_{\text{Nb}} = 2.91 \times 10^{-4} e^{-31030/RT} \text{ cm}^2/\text{s}$, respectively [22]. The diffusion coefficient of Nb is smaller than that of Ti. The intermediate refinements from Sn+B combination might be resulted from the surface tension and high viscosity of Sn element [7, 8]. The surface tension of Sn is about from 470 to 630 mN/m near the melting point, and those of Ti is about from 1390 to 1650 mN/m. It is obvious that the surface tension of Ti is much larger than that of Sn. From the aspects of the surface diffusion and the surface tensions, the slower surface diffusion and the smaller surface tension helps to increase the nucleation density and inhibit the fast growth of the nuclei. As a result, the finer microstructure refined by the combinatorial micro-alloying of Nb+B and Sn+B into eutectic $\text{Ti}_{73.3}\text{Fe}_{26.7}$ alloys. According to Hall-Petch [23, 24] formula in the form of $\sigma_s = \sigma_0 + kd^{-1/2}$ (σ_s : tensile strength; d : grain size), the yield strength increases drastically with the decrease of the grain sizes. Therefore, the present microstructural refinements arising from the combinatorial micro-alloying of Nb/Sn and B are highly expected to enhance the mechanical properties of the TiFe-base alloys after plastic deformations such as forging, hot-rolling and cold rolling processing.

4 Conclusion

Combinatorial micro-alloying of Nb/Sn and B has been employed to refine the initial microstructures of as-cast $\text{Ti}_{73.3}\text{Fe}_{26.7}$ alloys on the basis of the chemical composition design. As-cast $\text{Ti}_{73.3}\text{Fe}_{26.7}$ alloy is $\alpha+\beta$ type alloy, and as-cast $\text{Ti}_{73.3}\text{Fe}_{24.6}\text{Nb}_2\text{B}_{0.1}$ and $\text{Ti}_{73.3}\text{Fe}_{24.6}\text{Sn}_2\text{B}_{0.1}$ alloys are β type alloys, on the principle of Mo equivalence and XRD data. The micro-alloying of Nb+B can drastically reduce the grain sizes with high refinement efficiency, although Sn+B addition can also refine the initial microstructure with a medium level. The refinements have been achieved by both combinatorial Nb+B and Sn+B additions. The corrosion resistances of micro-alloyed TiFe-based alloys were improved due to the microstructural refinements and the formation of the small-sized grains. The initial cast microstructure with refined grains is highly expected to enhance the mechanical properties of the TiFe-base alloys.

Acknowledgements This work is financially supported by State Key Laboratory of Advanced Metals and Materials (Grants No. 2018-ZD04), State Key Laboratory of Metal Material for Marine Equipment and Application (Grant No. SKLMEA-K201806), the National Natural Science Foundation of China (Grant No. 51671106 and 51931008), Natural Science Foundation of Jiangsu Province (Grants No. BK20171424), Primary Research & Development Plan of Jiangsu Province (BE2019119), National Defense Basic Scientific Research Program of China (Grant No. JCKY08414C020) and Top-notch Academic Programs Project of Jiangsu Higher Education Institutions (Grand No. PPZY2015B128). This work is partially supported by and Priority Academic Program Development of Jiangsu Higher Education Institution (PAPD).

References

1. Chuvil Deev, V.N., Kopylov, V.I., Nokhrin, A.V., Bakhmet Ev, A.M., Sandler, N.G., Kozlova, N.A., Tryaev, P.V., Tabachkova, N.Y., Mikhailov, A.S., Ershova, A.V., Gryaznov, M.Y., Chegurov, M.K., Sysoev, A.N., Smirnova, E.S.: Simultaneous increase in the strength, plasticity, and corrosion resistance of an ultrafine-grained Ti–4Al–2V pseudo-alpha-titanium alloy. *Tech. Phys. Lett.* **43**, 466 (2017)
2. Keist, J.S., Palmer, T.A.: Development of strength-hardness relationships in additively manufactured titanium alloys. *Mater. Sci. Eng. A* **693**, 214 (2017)
3. Chausov, M., Maruschak, P., Pylypenko, A., Markashova, L.: Enhancing plasticity of high-strength titanium alloys VT 22 under impact-oscillatory loading. *Philos. Mag.* **97**, 389 (2017)
4. Louzguine, D.V., Kato, H., Inoue, A.: High strength and ductile binary Ti–Fe composite alloy. *J. Alloys Compd.* **384**(1–2), L1–L3 (2004)
5. Peng, Y., Zhu, Q., Luo, T., Cao, J.: Enhancement of the tensile strength by introducing alloy element Fe for Ti based alloy. *Solid State Commun.* **318**, 113982 (2020)
6. Zhang, L., Su, Y.Q., Yang, H.M., Luo, L.S., Guo, J.J.: As-cast structure refinement of Ti–46Al alloy by hafnium and boron additions. *China Foundry* **6**(002), 115–118 (2009)
7. Das, J., Kim, K.B., Baier, F., Löser, W., Gebert, A., Eckert, J.: Bulk ultra-fine eutectic structure in Ti–Fe–base alloys. *J. Alloys Compd.* **434–435**, 28 (2007)
8. Das, J., Kim, K.B., Baier, F., Löser, W., Eckert, J.: High-strength Ti-base ultrafine eutectic with enhanced ductility. *Appl. Phys. Lett.* **87**, 161907 (2005)

9. Zhang, L., Wang, K., Xu, L., Xiao, S., Chen, Y.: Effect of Nb addition on microstructure, mechanical properties and castability of β -type Ti–Mo alloys. *Trans. Nonferrous Metals Soc China* **25**, 2214 (2015)
10. Ehtemam-Haghighi, S., Liu, Y., Cao, G., Zhang, L.: Influence of Nb on the $\beta \rightarrow \alpha''$ martensitic phase transformation and properties of the newly designed Ti–Fe–Nb alloys. *Mater. Sci. Eng C* **60**, 503 (2016)
11. Tamirisakandala, S., Bhat, R.B., Tiley, J.S., Miracle, D.B.: Grain refinement of cast titanium alloys via trace boron addition. *Scr. Mater.* **53**, 1421 (2005)
12. Wang, W.Q., Yang, Y.L., Zhang, Y.Q., Li, F.L., Yang, H.L., Zhang, P.H.: The microstructure and mechanical properties of high-strength and high-toughness titanium alloy BTi-6554 bar. *Mater. Sci. Forum.* **618–619**, 173 (2009)
13. Luo, J., Li, M.Q., Yu, W.X.: Microstructure evolution during high temperature deformation of Ti-6Al-4V alloy. *Rare Mater. Eng.* **39**(8), 1323–1328 (2010)
14. Bram, M., Aubertin, F., Venskutonis, A., Brems, J.: Kinetics of the phase transformation and wear resistance of in-situ processed titanium matrix composites based on Ti–Fe–B. *Mater. Sci. Eng. A* **264**, 74 (1999)
15. De Graef, M., Löfvander, J.P.A., McCullough, C., Levi, C.G.: The evolution of metastable Bf borides in a Ti–Al–B alloy. *Acta Metall. ET Mater.* **40**(12), 3395–3406 (1992)
16. Weiss, I., Semiatin, S.L.: Thermomechanical processing of beta titanium alloys—an overview. *Mater. Sci. Eng. A* **243**(46) (1998)
17. Kim Y.C., Kim W.T., Kim D.H.: A development of Ti-based bulk metallic glass. *Materials Science and Engineering: A.* 375-377. 127 (2004)
18. Wood, R.J.K.: Erosion–corrosion interactions and their effect on marine and offshore materials. *Wear* **261**, 1012 (2006)
19. Zeng, D., Dan, Z., Qin, F., Chang, H.: Adsorption-enhanced reductive degradation of methyl orange by $\text{Fe}_{73.3}\text{Co}_{10}\text{Si}_4\text{B}_8\text{P}_4\text{Cu}_{0.7}$ amorphous alloys. *Mater. Chem. Phys.* **242**, 122307 (2019)
20. Ma, C.X.: Effect of Sn content on the structure and property of Mg alloy. *Forg. Stamp. Technol.* **39**(09), 116–118 (2014)
21. Park, J.M., Han, J.H., Kim, K.B., Mattern, N., Eckert, J., Kim, D.H.: Favorable microstructural modulation and enhancement of mechanical properties of Ti–Fe–Nb ultrafine composites. *Philos. Mag. Lett.* **89**(10), 623–632 (2009)
22. Pontau, A.E., Lazarus, D.: Diffusion of titanium and niobium in bcc Ti–Nb alloys. *Phys. Review B Condens. Matter.* **19**, 4027 (1979)
23. Loucif, A., Figueiredo, R.B., Baudin, T., Brisset, F., Chemam, R., Langdon, T.G.: Ultrafine grains and the Hall–Petch relationship in an Al–Mg–Si alloy processed by high-pressure torsion. *Mater. Sci. Eng. A* **532**, 139 (2012)
24. Furukawa, M., Horita, Z., Nemoto, M., Valiev, R., Langdon, T.G.: Structural evolution and validity of hall-petch relationship in an Al-3% Mg alloy with submicron grain size. *Mater. Sci. Forum* **204–206**, 431 (1996)

Sputter Deposited Nanocomposite Cr-Based Films and Their Characterization



A. Vyas and Z. F. Zhou

Abstract The Cr-C-N films with varied N concentrations (45.3–25.5 at.%), controlled by closed loop optical emission monitoring, were deposited onto Si(100) and M42 steel substrates by reactive magnetron sputtering technique. The deposited films were characterized by employing X-ray photoelectron spectroscopy (XPS) for elemental composition and bonding state, X-ray diffraction (XRD) for crystal structure, Pin-on-disc (POD) test for friction coefficient, Rockwell-C test and Scratch tests for adhesion and Nanohardness test. It is found that variation in N concentration influences the structure and thus the properties. The phase structure changes from CrN + Cr for samples with N/Cr = 1.16–0.95 (at.%) to β -Cr₂N + CrN + Cr for samples with N/Cr = 0.80–0.42. Film with N/Cr = 0.80, possesses the highest nanohardness of 27.3 GPa comprising of Cr₂N + CrN + Cr phases. The lowest achieved friction coefficient value was 0.36 and lowest specific wear rate of 2.1×10^{-8} mm³/Nm, in the pin-on-disk wear test which was mainly due to the combination of the two factors: growth of hard Cr₂N phase and high carbon content of 20.6 at.% in the film. The low friction coefficient and wear values are due to the presence of high carbon content. The scratch test provided best adhesive and cohesive properties with critical load as high as $L_{C2} = 72.9$ N for the hardest film. Rockwell-C adhesion tests demonstrated adhesion strength HF2 for the hardest film.

Keywords Cr-C-N coatings • PVD • XRD • Hardness • Adhesion • Friction • Wear

A. Vyas (✉)

Division of Science, Engineering and Health Studies, SPEED, The Hong Kong Polytechnic University, Hung Hom, Hong Kong, China

e-mail: anand.vyas@cpce-polyu.edu.hk

Z. F. Zhou

Department of Mechanical Engineering, City University of Hong Kong, Kowloon, Hong Kong SAR, China

© The Author(s), under exclusive license to Springer Nature Switzerland AG 2021

245

L. Zheng et al. (eds.), *Proceedings of MEACM 2020*,

Mechanisms and Machine Science 99,

https://doi.org/10.1007/978-3-030-67958-3_27

1 Introduction

Cr based hard coatings are traditionally used in industries where engineering tools such as drills, dies and precision metal parts to increase their performance and life due to their merits such as good hardness, strength, good adhesion to steel substrate, high wear resistance, chemical stability, etc. [1–3]. However, for the tribological properties, Cr-N coatings have high friction coefficients, and thus striving for lower coefficients of friction (COFs) has been of interest lately. Through the addition of carbon in Cr-N films, Cr-C-N films with reduced COFs can be prepared by various techniques [4–8]. Since carbon exists mostly in amorphous form in the films, mechanical properties of the Cr-C-N films are usually compromised over tribological properties or vice versa.

It is known that Cr-N coatings have a range of phase compositions (i.e. bcc Cr, fcc CrN and hexagonal β -Cr₂N), depending on the specific deposition conditions [9, 10]. The Cr₂N phase is more covalent than CrN phase, leading to higher intrinsic hardness than that of purely cubic phases [11]. The formation of hard Cr₂N phase in Cr-C-N films may provide a facile way to increase the film hardness and at the same time maintain their low coefficients of friction. The N concentration mainly determines the phase composition of Cr-N films according to the phase diagram [12], which then affects the mechanical properties.

In this work, Cr-C-N films with continuously decreased N concentrations are prepared by reactive magnetron sputtering, and the influence of N content on phase structure, mechanical and tribological properties of the Cr-C-N_x films are investigated.

2 Experimental

The Cr-C-N_x films were deposited on Si(100) wafer (for structural and mechanical analyses) and M42 tool steel (for tribological test) substrates by an unbalanced dc magnetron sputtering system (UDP 450, Teer Coating Ltd.), with a pure Cr and C targets (99% pure). The Cr and C target currents were fixed at 4.0 A respectively. The base pressure of the vacuum chamber was $\leq 5.0 \times 10^{-5}$ Pa. The target currents and bias voltage were fixed at 4.0 A and -60 V, respectively. After the preparation of a Cr interlayer (~ 0.25 μm), N₂ gas was introduced to the chamber to deposit the ternary films. The flow of N₂ gas was controlled using optical emission monitor (OEM) by regulating the reactivity of Cr⁺ with the OEM settings at 40%, 45%, 50%, 55%, 60% and 65% to get the samples A1–A6 (Table 1). The working pressure was ~ 0.26 Pa, and no additional heating or cooling of the substrate was applied during the deposition process. The deposition duration was 60 min, and the total film thickness was around ~ 1.8 μm .

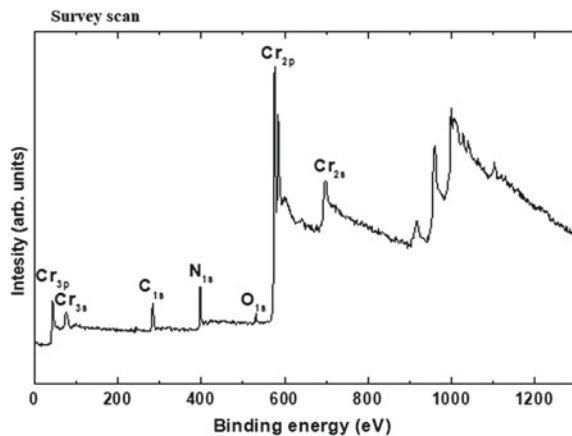
The elemental concentration of the films was determined by X-ray photoelectron microscopy (XPS, PHI 5802 system) with a monochromatic Al K α X-ray source

Table 1 OEM value, elemental concentration and phase composition of the Cr-C-N_x films

Sample	OEM (%)	Concentration (at.%)			N/Cr	Phase composition
		Cr	C	N		
A1	40	38.9	15.8	45.3	1.16	CrN + Cr
A2	45	39.5	19.2	41.3	1.04	CrN + Cr
A3	50	40.1	21.5	38.4	0.95	CrN + Cr
A4	55	44.0	20.6	35.4	0.80	Cr ₂ N + CrN + Cr
A5	60	53.2	19.7	27.1	0.50	Cr ₂ N + CrN + Cr
A6	65	60.1	14.4	25.5	0.42	Cr ₂ N + CrN + Cr

($h\nu = 1486.6$ eV). Figure 1 shows the spectra of XPS scan demonstrating chemical and bonding states in the CrCN coating. Cr, C, N are the major peaks. Existence of O is also detected which is understood to inherently exist in the coating. To investigate the crystal structure of the films, XRD using a Rigaku MiniFlex diffractometer with a Cu tube operated at 40 kV and 30 mA was employed. The measurements were carried out using Cu K α radiation with a Ni filter to remove Cu K β reflections. The nanohardness (H) and elastic modulus (E) were analyzed by nanoindentation measurements with a maximum load of 20 mN. Ten separate measurements were taken for each sample in order to get a mean value and the maximum indentation depth was kept less than 10% of the total film thickness. POD tests were conducted on coated CrCN_x steel substrate using Tungsten carbide ball having a 5 mm diameter at room temperature as well as in air at about 70–75% relative humidity. The loads used in this experiment were 2 N and a constant sliding speed of 0.0570 m/s with a total of 10800 cycles per experiment. Thereafter, specific wear rates were calculated. The wear rates were determined by using, an Archard’s classical wear equation [13]: $W = V/(S \times L)$ where, S is the sliding distance, L represents the loading force, and V is wear volume. Scratch test was conducted using progressive loading from 10 N to 80 N. The radius of stylus was

Fig. 1 XPS scan demonstrating chemical states in the CrCN coating



300 nm which was drawn over the coating surface with a continuously increasing normal force of 1 N/s until the film delaminated [14]. The maximum load was 80 N. The normal force causing cohesive and adhesive failures was defined indicated by the critical scratching load. Optical microscope was employed to investigate the morphology of the scratch tracks. The Rockwell-C test with a load of 1500 N, was conducted to evaluate adhesion of the coatings and the results were assessed on the basis of defined adhesion strength quality classification HF 1–6. HF1–4 are classified as sufficient adhesion strength and HF 5 and HF 6 are considered as poor adhesion.

3 Results and Discussion

3.1 X-Ray Diffraction for Crystallographic Structure

Figure 2 shows XRD patterns of the Cr-C-N_x samples. Phase structure of the films changes from CrN + Cr for samples A1–A3 to β -Cr₂N + CrN + Cr for samples A4–A6. The evolution of Cr-N phases is related to the reduced N content of the films (Table 1). Sample A1 (N/Cr = 1.16, atomic ratio) exhibits orientations of CrN (111) and CrN (200), while the peaks of CrN (311) and CrN (222) at higher 2 θ angles signify a high degree of crystallinity of the film. Sample A2 (N/Cr = 1.04) shows the similar pattern but with increased intensities. This observation may indicate the formation of the finer grains. For sample A3 (N/Cr = 0.95), the CrN (111) peak is reduced, but the CrN (200) peak is enhanced. The CrN peaks are significantly reduced, and β -Cr₂N (111) and Cr (110) peaks emerge for sample A4 (N/Cr = 0.80). These observations seem to be contradictory to the report that near stoichiometric CrN phase occurred at N/Cr = 0.81 [15]. It is noted that some N atoms exist as CN_x phase in the films, although diffraction peaks of CN_x are not detected due to its amorphous nature. The appearance of Cr (110) peak may come from Cr in the Cr-C-N_x film, rather than from the interlayer. However, it is reported that the presence of excess nitrogen at the interstitial sites and grain boundaries is possible [11, 15, 16]. Samples A5 (N/Cr = 0.50) and A6 (N/Cr = 0.42) have similar phases to sample A4, but CrN (111) peak is further reduced and Cr(110) peak is markedly increased, signifying the dominance of Cr phase in the samples. Coexistence of CrN-Cr₂N phases at lower N/Cr ratio agrees with the reports in [17–19].

Since no peaks of CrC or CN_x phase was observed suggesting mainly graphite/amorphous structure of CN_x, amorphous C or short-range carbide phases [15]. Also, since C has lower energy X-ray characteristic, therefore it cannot be appear in the X-ray diffraction pattern.

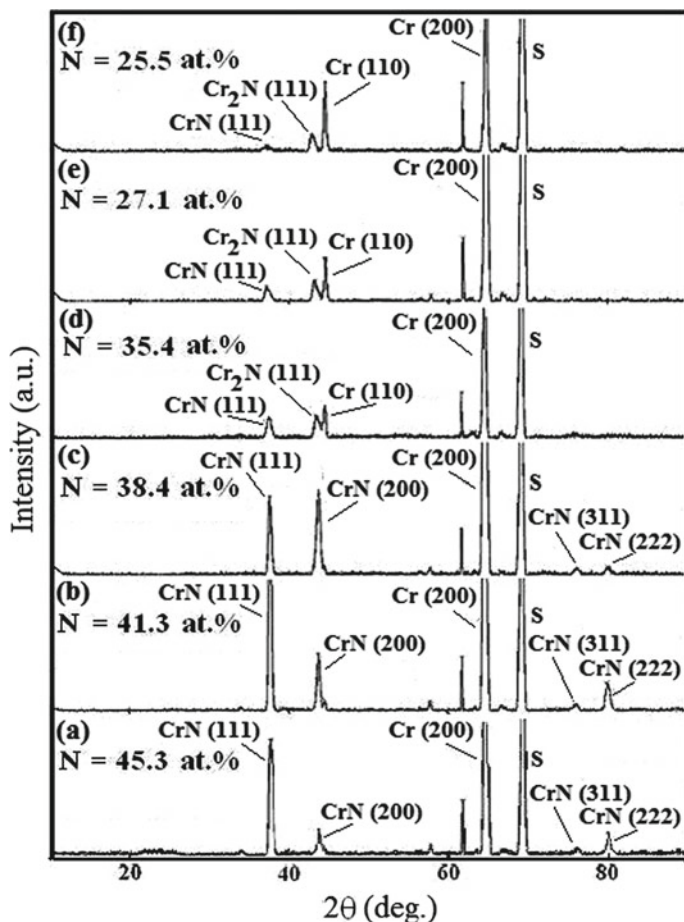


Fig. 2 XRD θ - 2θ scan patterns **a-f** Cr-C-N_x samples A1-A6, and their N at.%. The ICDD file number is 06-0694 for bcc Cr, 11-0065 for fcc CrN, and 35-0803 for hexagonal β -Cr₂N

3.2 Hardness

Decrease in grain size can improve the hardness [15]. It is found that hardness (H) and elastic modulus (E) values of the films first increase from sample A1 to A4, and then decrease for sample A5-A6 and a maximum hardness of 27.3 GPa and elastic modulus of 190 GPa, was achieved for sample A4 (see Table 2). A4 film contains CrN, significant volume of β -Cr₂N phase and high content of carbon (20.6 at.%). The enhanced hardness for this film can be explained as β -Cr₂N phase is more covalent than the CrN phase, leading to higher intrinsic hardness than that of purely cubic phases [11]. In our case the hardness of A4 sample is much higher than previous reports [16]. The further decrease in N and increase in C content results in

drop of hardness and elastic modulus, which is consistent with previous reports [20–22].

Moreover, H/E ratio, and H^3/E^2 ratio were determined where H/E ratio is a parameter which corresponds to the elastic strain to failure and can be used to predict wear resistance. Moreover, wear rate is related to resistance to the plastic deformation coefficient (H^3/Er^2) [13, 23]. The H/Er and H^3/Er^2 ratio of all the films with various N concentration is shown in Table 2. Both, H/Er and H^3/Er^2 ratios were in the range of 0.130–0.143. These ratios are high as compared to reported results [23].

L_{C1}^a , a critical load for cohesive failure and defined as the load at which the film shows first chipping on the scratch track [24].

L_{C2}^b , a critical load for adhesive failure and defined as the load at which the substrate is revealed on the scratch track.

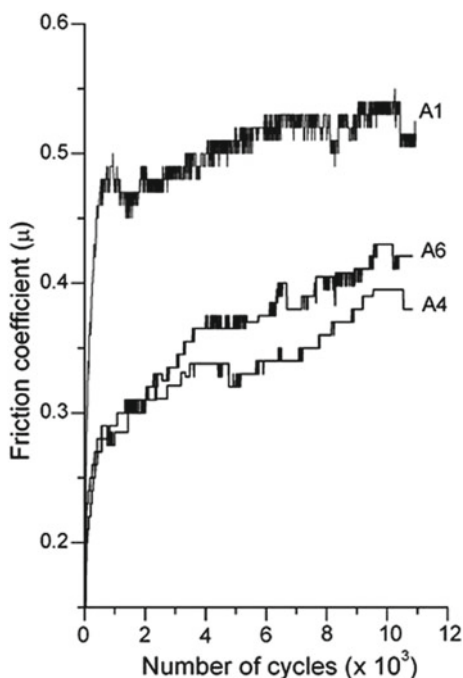
3.3 Pin-on-Disc Test to Determine Friction and Wear

Tribological test under the load of 2N were conducted on all the films by employing POD to determine coefficient of friction (COF). The COF values of the samples first decreases for the samples A1 to A4 and then increases for sample A5 and A6 (see Table 2), showing an inverse variation trend with the C content and hardness of the films. Lowest COF is obtained for sample A4 which is 0.36. Film A4 has higher hardness and COF is lower than the results reported previously [23]. Figure 3 shows details of the POD spectra for the typical samples A1, A4 and A6 with COF values ranging 0.52–0.36 and are relatively low when compared with those of the binary

Table 2 Nanoindentation, scratch and pin-on-disk test data of the Cr-C-N_x samples

Sample	H GPa	E GPa	H/E	H^3/E^2	COF (μ)	w (mm^3/Nm)	L_{C1}^a N	L_{C2}^b N	Adhesion Strength
A1	22.5 ± 0.9	172 ± 4.8	0.130	0.38	0.52 ± 0.03	4.9	19.1 20.4	37.3 47.0	HF5 HF4
A2	23.5 ± 0.5	176 ± 5.2	0.133	0.42	0.48 ± 0.022	1.1			
A3	25.0 ± 1.2	180 ± 7.3	0.138	0.48	0.38 ± 0.019	3.2	27.5 38.1 39.0 35.2	63.5 72.9 71.1 71.8	HF4 HF2 HF2 HF2
A4	27.3 ± 1.3	190 ± 7.6	0.143	0.56	0.36 ± 0.015	2.1			
A5	26.0 ± 0.9	185 ± 6.0	0.140	0.51	0.39 ± 0.016	2.9			
A6	24.0 ± 1.3	175 ± 5.9	0.137	0.45	0.42 ± 0.017	4.0			

Fig. 3 Coefficient of friction vs number of rotation cycles of the three typical Cr-C-N_x samples measured in the pin-on-disk wear test



Cr-N films [25]. It is obvious that C content (21.5–14.4 at.%) in the films plays an important role in reducing the COF values and are comparable with previous results [26]. In addition, the specific wear rates were determined to be in the range of $(1-5) \times 10^{-7} \text{ mm}^3/\text{Nm}$ for samples A1 and A2 and $(2-4) \times 10^{-8} \text{ m}^3/\text{Nm}$ for samples A3–A6. Lowest wear rate obtained is for the film A4 ($2.1 \times 10^{-8} \text{ m}^3/\text{Nm}$). Wear resistance is closely related to the films structure. The phases in our films mainly comprise of $\text{Cr}_2\text{N} + \text{CrN} + \text{Cr}$ as determined by XRD. Moreover, according to the theory on wear [13], hardness is an important factor which certainly influences the wear resistance of the film. It has been reported [26] that films rich in carbon possess low friction coefficient. In such films carbon mostly exists in graphite or amorphous form [27] leading to low hardness and have high wear rate. Contrarily, in our case, although film A4 has comparatively high carbon (20.6 at. %) retains low COF and possess high hardness with lower wear values suggesting not all of carbon is in amorphous form. It can be understood as, since the transition metals in group 4–6 has strong carbide forming ability [28] thus, multiple Cr-C phase formations are possible and existence of sole carbon in a complete amorphous form is ruled out. A solid solution with small amounts of C into interstitial sites can occur and a short-range order of complex chromium-carbide phase could be present contributing to comparatively high hardness of the film. Also, free carbon largely amorphous with no structural order can exists at grain boundaries between nitride grains analogous to what is witnessed in other binary or ternary systems.

3.4 Scratch Test and Rockwell-C for Adhesion

Both, cohesive as well as adhesive properties of Cr-C-N_x films were evaluated by scratch test, which gives information on cohesive failure, where crack occurs at a certain load (L_{C1}), and the adhesion failure, where the first delamination occurs at the edge of the scratch track at a certain load (L_{C2}) based on acoustic emission measurement. The values of both critical loads, L_{C1} and L_{C2} of all the samples are given in Table 2.

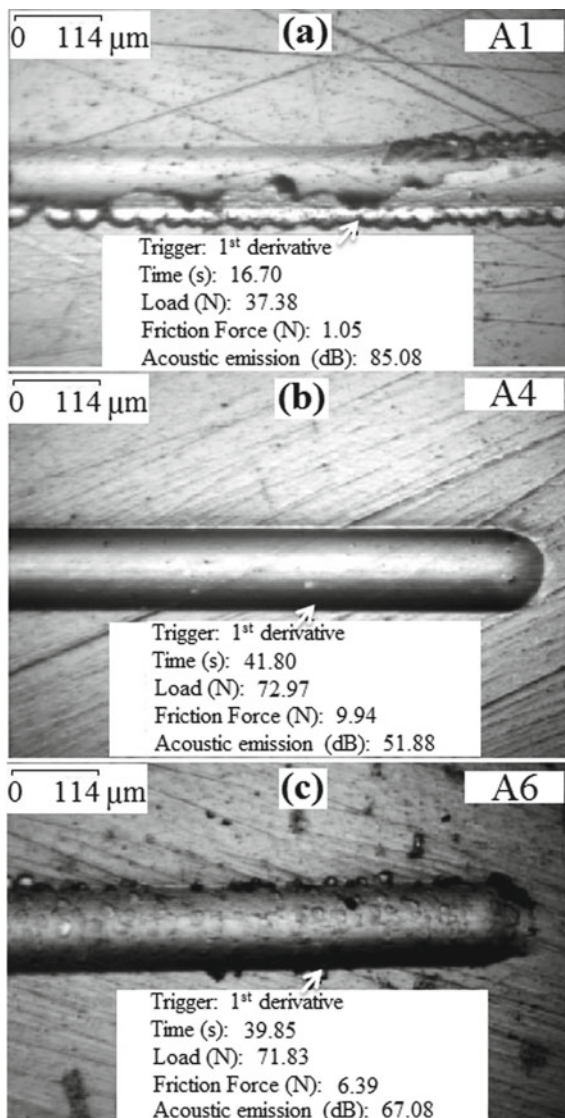
Typical optical micrographs of scratch tracks on films A1, A4 and A6 are shown in Fig. 4 indicating critical loads L_{C2} . It is found that the film A1, with the highest N/Cr ratio (1.16), demonstrates severe delamination with critical load $L_{C2} = 37.3$ N. However, films A4 and A6 with lower N/Cr ratios (0.80 and 0.42), show a remarkable increase in critical loads, $L_{C2} = 72.9$ and 71.8 N, respectively. On one hand, during the scratch test the tensile and compressive stress distributions present in the film are high, there is also a higher plastic flow of the material, therefore resulting in an increased critical load. The enhanced critical load values obtained here are much higher when compared with even multilayers CrN/CrCN which supposedly show better properties in comparison to their single layer counterparts [29]. It seems that the low N/Cr ratio is favorable for film adhesion and hardness comprising of phase mixture Cr₂N + CrN + Cr.

In order to investigate the adhesion strength, which is an important parameter to evaluate the coatings, Rockwell-C hardness test was utilized to determine the adhesion between the coating and substrate by observing the indentation impressions that causes coating spallation thus giving the scale of delamination if any. In such a way, the coating adhesion can be evaluated qualitatively on the basis of six classes from HF1–HF6 [23, 30]. Table 2 shows the classification of adhesion strength for all samples falling between HF2–HF5. Elemental concentration highly affects the adhesion of the films. Coatings A1–A3 with higher N/Cr ratios between 1.16–0.95 possess poorest adhesiveness. A1 show poorest adhesion strength quality HF 5 whereas A4 and A5 possess good strength quality HF2 and could be related to the hardness conforming well to the indentation. Figure 5a–c shows the optical micrographs after the Rockwell-C indentation test illustrating adhesion strength for the sample A1 as HF5, A4 as HF2 and A6 as HF3.

4 Conclusion

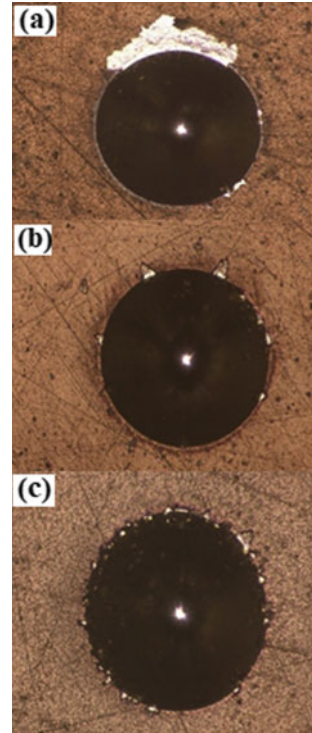
Nanocomposite Cr-C-N_x films were prepared by close-field unbalanced magnetron sputtering technique where nitrogen gas was controlled by using optical emission monitor (OEM) by regulating the reactivity of Cr⁺ with the OEM settings between 40% and 65% leading to production of films with varied elemental composition. For the sputter deposited nanocomposite Cr-C-N_x films, the phase structure changes from CrN + Cr for films with N/Cr = 1.16–0.95 to phase β -Cr₂N + CrN + Cr for

Fig. 4 Optical micrographs of the scratch tracks made at a continuous progressive load on typical Cr-C-N_x films and the critical load L_{C2}: **a** A1, **b** A4, **c** A6



films with N/Cr = 0.80–0.42. The sample A4 with N/Cr = 0.80 possesses the highest hardness of 27.3 GPa. Film A4 also has the best adhesive and cohesive properties L_{C2} = 72.9 N amongst all the films. The lowest friction coefficient value 0.36, with lowest wear rate for the same films is related to the formation of hard Cr₂N phase and the high carbon content 20.6 at.%, in the film.

Fig. 5 Typical Rockwell-C adhesion test images of samples **a** A1 **b** A4 and **c** A6



References

1. Gautier, C., Machet, J.: Study of the growth mechanisms of chromium nitride films deposited by vacuum ARC evaporation. *Thin Solid Films* **295**, 43–52 (1997)
2. Aubert, A., Gillet, R., Gaucher, A., Terrat, J.P.: Hard chrome coatings deposited by physical vapour deposition. *Thin Solid Films* **108**, 165–172 (1983)
3. Pakala, M., Lin, R.Y.: Reactive sputter deposition of chromium nitride coatings. *Surf. Coat. Technol.* **81**, 233–239 (1996)
4. Tong, C.Y., Lee, J.W., Kuo, C.C., Huang, S.H., Chan, Y.C., Chen, H.W.: Effects of carbon content on the microstructure and mechanical property of cathodic arc evaporation deposited CrCN thin films. *Surf. Coat. Technol.* **231**, 482–486 (2013)
5. Hu, P., Jiang, B.: Study on tribological property of CrCN coating based on magnetron sputtering plating technique. *Vacuum* **85**, 994–998 (2011)
6. Guan, J.J., Wang, H.Q., Qin, L.Z., Liao, B., Liang, H., Li, B.: Phase transitions of doped carbon in CrCN coatings with modified mechanical and tribological properties via filtered cathodic vacuum arc deposition. *Nucl. Instrum. Methods Phys. Res. B* **397**, 86–91 (2017)
7. Qianzhi, W., Fei, Z., Xiangdong, D., Zhifeng, Z., Chundong, W., Wenjun, Z., Li, K.Y., Lee, S.T.: Microstructure and water-lubricated friction and wear properties of CrN(C) coatings with different carbon contents. *App. Surf. Sci.* **268**, 579–587 (2013)
8. Hu, P.F., Jiang, B.L., Li, H.T.: Influence of carbon target current on friction coefficient of CrCN coating. *J. Funct. Mater.* **42**, 175–177 (2011)
9. Ehrlich, A., Kuhn, M., Richter, F., Hoyer, W.: Complex characterisation of vacuum arc-deposited chromium nitride thin films. *Surf. Coat. Technol.* **76**, 280–286 (1995)

10. Vyas, A., Shen, Y.G., Zhou, Z.F., Li, K.Y.: Nano-structured CrN/CN_x multilayer films deposited by magnetron sputtering *Comp. Sci. Technol.* **68**, 2922–2929 (2008)
11. Sanjines, R., Hones, P., Levy, F.: Hexagonal nitride coatings: electronic and mechanical properties of V₂N, Cr₂N and δ-MoN. *Thin Solid Films* **332**, 225–229 (1998)
12. Massalski, T.B.: Binary alloy phase diagrams. *ASM* **1**, 370 (1986)
13. Wu, F., Yu, L., Ju, H., Asempah, I., Xu, J.: Structural, Mechanical and Tribological Properties of NbCN-Ag Nanocomposite Films Deposited by Reactive Magnetron Sputtering. *Coatings* **8**, 50 (2018)
14. Vyas, A., Li, K.Y.: Shen YG: Influence of Deposition Conditions on mechanical and tribological properties of nanostructured TiN/CN_x multilayer films. *Surf. Coat. Technol.* **203**, 067–975 (2009)
15. Vyas, A., Shen, Y.G., Zhou, Z.F., Li, K.Y.: Nano-structured CrN/CN_x multilayer films deposited by magnetron sputtering. *Compos. Sci. Technol.* **68**, 2922–2929 (2008)
16. Shen, Y.G.: Effect of deposition conditions on mechanical stresses and microstructure of sputter-deposited molybdenum and reactively sputter-deposited molybdenum nitride films. *Materials Science and Eng. A* **359**, 158–167 (2003)
17. Lin, J., Wu, Z.L., Zhang, X.H., Mishra, B., Moore, J.J., Sproul, W.D.: A comparative study of CrN_x coatings Synthesized by dc and pulsed dc magnetron sputtering. *Thin Solid Films* **517**, 1887–1894 (2009)
18. Wei, G., Scharf, T.W., Zhou, J.N., Huang, F., Weaver, M.L., Barnard, J.A.: Nanotribology studies of Cr, Cr₂N and CrN thin films using constant and ramped load nanoscratch techniques. *Surf. Coat. Technol.* **146**, 357–362 (2001)
19. Holleck, H.: Material selection for hard coatings. *J. Vac. Sci. Technol., A* **4**, 2661–2669 (1986)
20. Ye, Y., Wang, Y., Wang, C., Li, J., Yao, Y.: An analysis on tribological performance of CrCN coatings with different carbon contents in seawater. *Tribol. Int.* **91**, 131–139 (2015)
21. Ye, Y., Wang, Y., Chen, H., Li, J., Yao, Y., Wang, C.: Doping carbon to improve the tribological performance of CrN coatings in seawater. *Tribol. Int.* **90**, 362–371 (2015)
22. Han, Z.H., Tian, J.W., Lai, Q.X., Yu, X.J., Li, G.Y.: Effect of N₂ partial pressure on the microstructure and mechanical properties of magnetron sputtered CrN_x films. *Surf. Coat. Technol.* **162**, 189–193 (2003)
23. Kong, Y., Tian, X., Gong, C., Paul, K.C.: Enhancement of toughness and wear resistance by CrN/CrCN multilayered coatings for wood processing. *Surf. Coat. Technol.* **344**, 204–213 (2018)
24. Vyas, A.: Lu, YH Shen YG, Mechanical and tribological properties of multicomponent Ti–B–C–N thin films with varied C contents. *Surf. Coat. Technol.* **204**, 1528–1534 (2010)
25. Wu, Z.L., Lin, J., Moore, J.J., Lei, M.K.: Microstructure, mechanical and tribological properties of Cr–C–N coatings deposited by pulsed closed field unbalanced magnetron sputtering. *Surf. Coat. Technol.* **204**, 931–935 (2009)
26. Choi, E.Y., Kang, M.C., Kwon, D.H., Shin, D.W., Kim, K.H.: Comparative studies on microstructure and mechanical properties of CrN, Cr–C–N and Cr–Mo–N coatings. *J. Mater. Process. Technol.* **187–188**, 566–570 (2007)
27. Era, H., Ide, Y., Nino, A., Kishitake, K.: TEM study on chromium nitride coatings deposited by reactive sputter method. *Surf. Coat. Technol.* **194**, 265–270 (2005)
28. Supakanya, K., Charnarong, S., Parinya, S., Naphatara, I.: A comparative study on the hardness of CrN, CrC and CrCN coatings. *Adv. Mater. Res.* **1016**, 145–149 (2014)
29. Bahce, E., Cakir, N.: Tribological investigation of multilayer CrN/CrCN/TaN films deposited by close field unbalanced magnetron sputtering. *Rev. Adv. Mater. Sci.* **58**, 271–279 (2019)
30. Gerth, J., Wiklund, U.: The influence of metallic interlayers on the adhesion of PVD TiN coatings on high-speed steel. *Wear* **264**, 885–892 (2008)

Study on Compressive Properties of Cylindrical Graphene Oxide Cement-Based Composites



Qiong Liang, Zhanyuan Gao, and Dong Ruan

Abstract To investigate the effects of GO and age on the compressive strength, fracture propagation of cement-based composites. GO (0–0.06%) cement mortar cylinder specimens with different dosage (60 mm in diameter and 30 mm in height) were prepared, and static compression experiments were carried out on 3d, 7d, and 28d. The results show that the compressive strength increases as the age increases. With the increase of GO content, the compressive strength of cement-based composite first increases and then decreases. When the compressive strength of 3d and 7d cylinders reached the maximum, the GO content was 0.03%, which was increased by 19.3% and 23.3% respectively compared with the blank group. When the compressive strength of the 28d cylinder reaches the maximum, the GO content is 0.04%. Compared with the blank group, the improvement was 37.2%. At the same time, the addition of GO can effectively improve the stress during fracture generation, prevent fracture expansion, and thus enhance the mechanical properties of cement matrix composites.

Keywords Graphene oxide · Cement base · Composite materials · Compressive strength · Fracture propagation

1 Introduction

At present, the static mechanical properties of GO cement matrix composites have been studied extensively at home and abroad, but the dynamic mechanical properties need to be further studied. Separated Hopkinson bar was one of the effective means to study the dynamic mechanical properties of various materials. Its specimen shape was generally a cylinder with a height/diameter ratio of 1/2, which was different

Q. Liang (✉) · Z. Gao
Tianjin Chengjian University, Tianjin 300384, China
e-mail: 504424309@qq.com

D. Ruan
Swinburne University of Technology, Melbourne, VIC 3000, Australia

from the specimen size in static compression specifications of various countries. Therefore, the static compression test of a cylinder (diameter 60 mm, height 30 mm) can not only provide a theoretical basis for the study of dynamic compressive properties of going cement-based composites but also lay a foundation for the corresponding relationship between cylinder specimens and standard specimens.

Many domestic and overseas scholars have studied the mechanical properties and microstructure of GO cement-based composites. Wang Qin [1] studied the effect of GO on the mechanical properties of cement-based composites and it turned out that, compared with the control group, the GO mass fraction of 3d,7d, and 28d compressive strength increased by 43.2%,33%, and 24.4%, respectively, at 0.05%. Zeng Ju Qing [2] also showed that when GO was mixed with cement mortar, the flexural strength and compressive strength of the cement-based composites can be significantly improved. Ge Yaping et al. [3] showed that with the increase of GO content, the compressive and flexural strength of GO cement-based composites first increases and then decreases and the effect of increasing the flexural strength far exceeds the compressive strength. Lv Shenghua et al. [4] studied the effect of the GO nanometer layer on the mechanical properties of cement mortar. When the oxygen content of GO was 25.43%, the compressive strength increased by 30.8% compared with the control sample. Gong et al. [5] conducted a study on Portland cement paste by enhancing the effect of GO, showing that the 28-day compressive strength increased by more than 40% compared with the control sample when the GO content was 0.03%. Li et al. [6] conducted 3d, 7d, and 28d compression tests on GO cement matrix composites, and GO can improve the compressive strength of cement matrix composites. Shang [7] studied the GO cement-based composites, indicating that the compressive strength increases with the increase of GO content and age.

In this paper, cylinder specimens with different GO content (60 mm in diameter and 30 mm in height) were made for static compression tests to analyze the compressive strength, crack propagation, and failure morphology of GO cement-based composites.

2 Experiment

2.1 Materials and Instruments

GO dispersion (concentration: 1 g/mL),specific parameters of GO dispersion (as shown in Table 1), polycarboxylate water-reducing agent (PC) [8–10], ordinary Portland cement, ISO standard sand.

Table 1 Related parameters of graphene oxide dispersion

Model	pH	Solid content	Relative deviation of solid content
FH-522	1–6	0.1%	±10%

Table 2 Relevant parameters of electro-hydraulic servo pressure testing machine

Model	Test force (KN)	Range of force measurement
YNS-Y1000	1000	2–100%

Specifically related parameters of CNS-Y1000 double-column electro-hydraulic servo pressure testing machine (as shown in Table 2), UJZ-15 mortar mixer, KH2200DE NUMERICAL control ultrasonic cleaner, Metro small concrete vibrator.

2.2 Static Compression Test

Specimens were prepared and maintained according to the standards in ASTM/C109. Cement-based composites were prepared according to 543.1 g cement, 263.4 g water, 1493.6 g ISO standard sand, 0.2% PC and 0, 0.01, 0.02, 0.03, 0.04, 0.05 and 0.06% GO (GO was solid content and calculated according to cement quality; PC was calculated according to cement quality). To improve the dispersity of GO nano-flakes and PC in aqueous solution, the GO dispersing liquid, water and PC were mixed and dispersed by ultrasonic cleaning machine for 30 min. Then the GO aqueous solution was poured into cement for the 30 s, mixed with sand for 60s, stopped 90s, and continued to be stirred for 60s. Then, the GO aqueous solution was injected into the mold and vibrated to form on a small concrete vibrating table. Carry out maintenance and quasi-static compression test according to ASTM/C109 standard, set the loading rate to 1.5 mm/min, and apply lubricant on the upper and lower contact surfaces of the test piece.

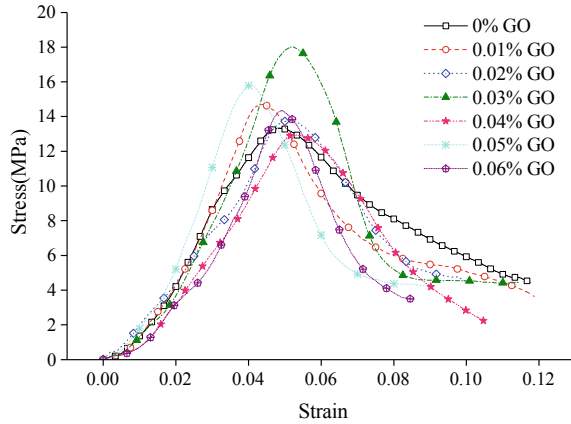
3 Results and Discussion

3.1 The Influence of GO on the Compressive Performance of 3d Cylinder

3.1.1 GO Resists the Effects of Compressive Strength

According to the uniaxial compression test, a 3d cylindrical cement mortar stress-strain curve was obtained (as shown in Fig. 1). Figure 1 shows that the stress-strain curve of go cement mortar was similar to that of ordinary cement mortar, which was composed of ascending and descending sections, and there were peak points in both. With the increase of GO, the peak stress first increases and then decreases. Among them, when the GO content was 0.03%, it reaches the maximum value, which was 19.3% higher than the blank group. When the go content was

Fig. 1 3d cylinder stress-strain curve



more than 0.03%, the peak stress of cement-based composite material was lower than the maximum peak stress. Due to the excessive dosage, GO was not easy to disperse, which was not conducive to play the regulation and template role of GO, thus reducing the compressive strength.

3.1.2 The Influence of GO on Crack Propagation

When the compressive strength of the 3d cement matrix composite reaches the maximum, the GO content was 0.03% (Fig. 2). Therefore, the blank group and the specimens with the GO content of 0.03% were selected to analyze the crack generation, peak stress, and failure. Respectively, the fracture status diagram at different positions was obtained (as shown in Fig. 3). Figure 3a–f correspond to Fig. 2a–f. Figures 2a, b and 3a, b show that, compared with the blank group, the stress of cement mortar crack with GO was increased by 3.31 MPa, with a small crack difference, while the crack at peak stress and failure are significantly different. The cement mortar with GO appears discontinuous cracks at the peak stress, and the surface fragments flake off (as shown in Fig. 3d). A large number of mortar fragments spalling occurred at the failure point, which was lower than the cement mortar spalling in the blank group (as shown in Fig. 3f), indicating that the incorporation of GO was conducive to preventing crack expansion and reducing the degree of specimen failure.

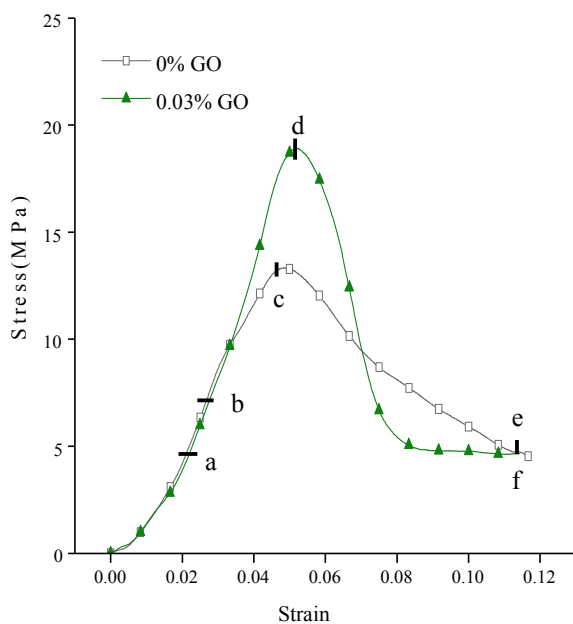


Fig. 2 Blank group and 0.04% GO stress-strain curve

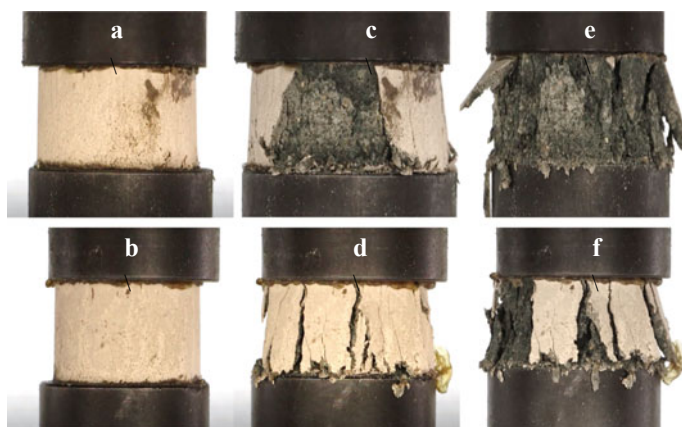


Fig. 3 Blank group and 0.03% GO crack propagation diagram

3.2 The Influence of GO on the Compressive Performance of 7d Cylinder

3.2.1 GO Resists the Effects of Compressive Strength

According to the uniaxial compression test, the stress-strain curve of 7d cylindrical cement mortar was obtained (as shown in Fig. 4). The stress-strain curve of GO cement mortar consists of an ascending section and a descending section, and both have peak points. With the increase of GO, the peak stress of cement-based composites first increased and then decreased. Among them, when the GO dosage was 0.03%, it reaches the maximum value. Compared with the blank group, it was increased by 23.3%. When GO content was more than 0.03%, the compressive strength of the cement-based composite was lower than the maximum compressive strength, indicating that GO of 0.03% was the optimal content at 7 days.

3.2.2 The Influence of GO on Crack Propagation

When the compressive strength of 7d cement matrix composite reaches the maximum, the GO content was 0.03% (Fig. 5). Therefore, the blank group and the specimens with the GO content of 0.03% were selected to analyze the crack generation, peak stress, and failure, respectively, and the fracture status diagram at different positions was obtained (as shown in Fig. 6). Figure 8a–f correspond to Fig. 5a–f. Figures 5a, b and 6a, b show that, compared with the blank group, the stress generated by cement mortar cracks with GO increased by 8.85 MPa, with a small difference in cracks, while there was a difference in peak stress and failure. The specimen with GO appeared multiple cracks on the surface at the peak stress,

Fig. 4 7d cylinder stress-strain curve

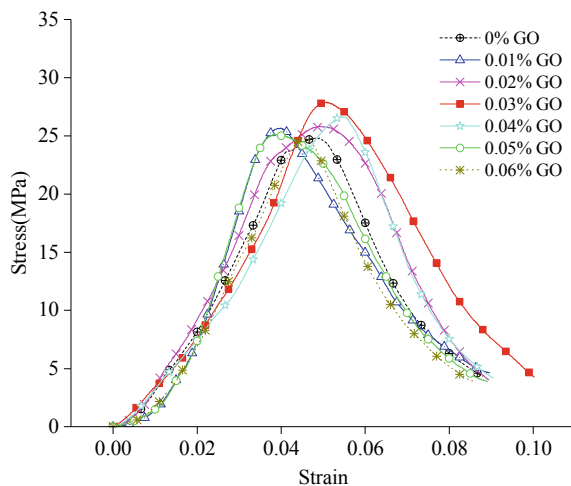
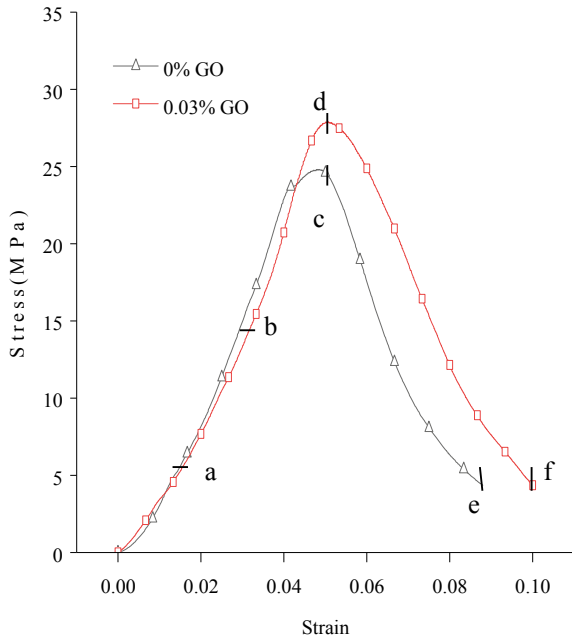


Fig. 5 Blank group and 0.04% GO stress-strain curve



and some small pieces fell off (as shown in Fig. 6d). At the crushing point, part of the cement pieces fell and the internal structure was damaged, but to a lesser degree than the blank group (as shown in Fig. 6f).

3.3 The Influence of GO on the Compressive Performance of 28d Cylinder

3.3.1 GO Resists the Effects of Compressive Strength

According to the uniaxial compression test, the stress-strain curve of 28d cylindrical cement mortar was obtained, as shown in Fig. 7. The stress-strain curve of GO cement mortar was composed of an ascending section and a descending section, and both of them have peak points. With the increase of GO, the peak stress first increases and then decreases. Among them, when the GO dosage was 0.04%, it reaches the maximum value. Compared with the blank group, the improvement was 37.2%. It shows that the compressive strength of 28d is improved more than that of 3d and 7d. When GO content was greater than 0.04%, the compressive strength of cement-based composites was lower than the maximum compressive strength.

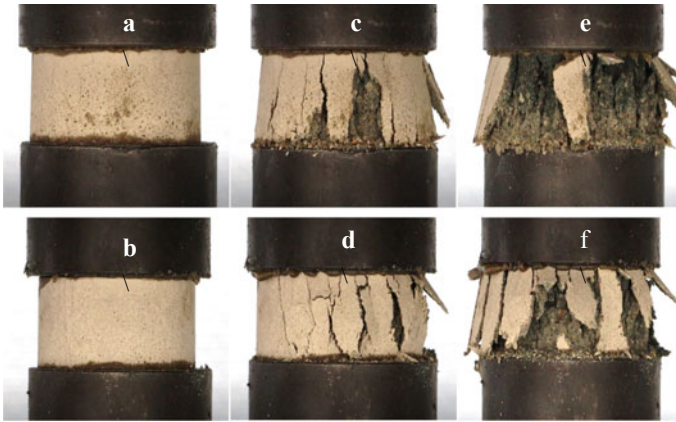
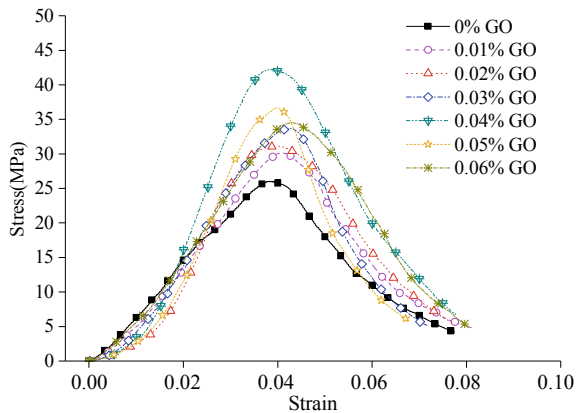


Fig. 6 Blank group and 0.03% GO crack propagation diagram

Fig. 7. 28d cylinder stress-strain curve



3.3.2 The Influence of GO on Crack Propagation

When the compressive strength of 28d cement matrix composite reaches the maximum, the GO content is 0.03% (Fig. 8). Therefore, the blank group and the specimens with the GO content of 0.03% were selected to analyze the crack generation, peak stress, and failure, respectively, and the fracture status diagram at different positions was obtained (as shown in Fig. 9). Fig. 9a–f correspond to Fig. 8a–f. Figures 8a, b and 9a, b show that, compared with the blank group, the stress generated by cement mortar crack with GO increased by 13.8 MPa. At the peak stress, discontinuous cracks appeared on the surface of the specimen with GO, and the number of cracks and some small pieces of cement fell off (as shown in Fig. 9d). At the point of failure, inclined cracks and nonpenetrating cracks appeared

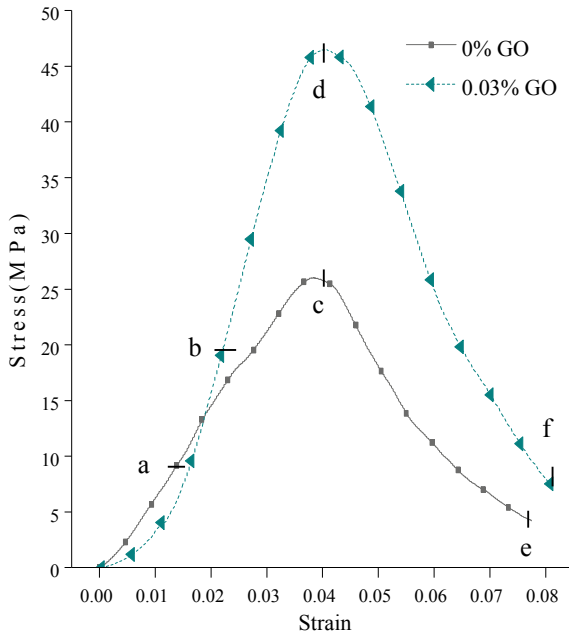


Fig. 8 Blank group and 0.04% GO stress-strain curve

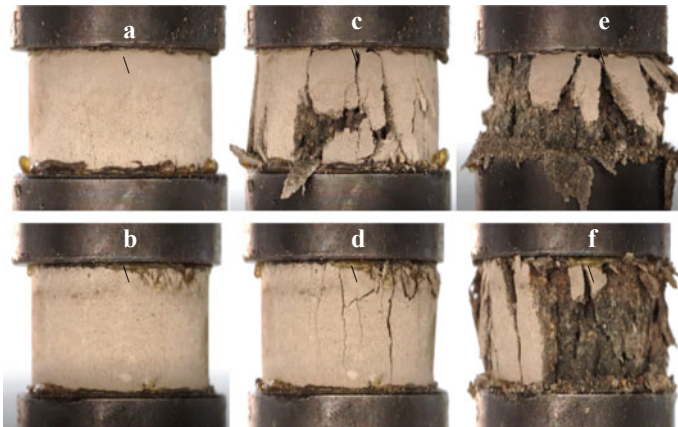


Fig. 9 Blank group and 0.03% GO crack propagation diagram

in the specimens with GO, showing good integrity (as shown in Fig. 9f), and the degree of failure of the internal structure of the specimens was lower than that of 3d and 7d.

4 Conclusion

With the increase of age, the compressive strength of the cylinder specimen increases. With the increase of GO content, the compressive strength of the cylinder specimen first increased and then decreased, and the increased amplitude of the compressive strength was greater than that of 3d and 7d at 28d. Among them, when the compressive strength of 3d and 7d cylinders reached the maximum, the GO content was 0.03%, which was increased by 19.3% and 23.3% respectively compared with the blank group. When the compressive strength of the 28d cylinder reaches the maximum, the GO content is 0.04%. Compared with the blank group, the improvement was 37.2%. The above changes in mechanical properties are mainly since the addition of GO can effectively improve the fracture stress of cement-based composites, prevent the expansion of cracks, and reduce the damage degree of specimens, thus improving the mechanical properties of cement-based composites.

References

1. Wang, Q., Wang, J., Lv, X., et al.: Effect of Graphene Oxide on Microstructure and Mechanical Properties of Cement-based Composites. *New Carbon Materials* **30**(4), 349–356 (2015)
2. Zeng, Q.J., Xu, D.Y., Pan, H.Z., et al.: Research on the fluidity, mechanical properties and mechanism of Go Cement-based composites. *J. Jiangsu Univ. Sci. Technol.* **33**(3),126–130 (2019)
3. Peng, H., Ge, P.Y., Yang, T.Z., et al.: Mechanical properties and microstructure of go reinforced cement matrix composites. *Mech. Prop. Microstruct. Go Reinf. Cem. Matrix Compos.* **35**(8), 2132–2139 (2018)
4. Lv, S.H., Zhou, F.Q., SunT., et al.: Effects of GO nanometer layers on the mechanical properties of cement hydration crystals and colloidal sand. *J. Build. Mater.* **17**(5), 749–754 (2014)
5. Gong, K., Pan, Z., Korayem, A.H., et al.: Reinforcing Effects of Graphene Oxide on Portland Cement Paste. *J. Mater. Civ. Eng.* **27**(2), A4014010.1–A4014010.6 (2015)
6. Li, X., Li, C., Liu, Y., et al.: Improvement of mechanical properties by incorporating graphene oxide into cement mortar. *Mech. Adv. Mater. & Struct.* (2016)
7. Shang, Y., Zhang, D., Yang, C., et al.: Effect of graphene oxide on the rheological properties of cement pastes. *Constr. Build. Mater.* **96**, 20–28 (2015)
8. Wang, X.Y., Cai, R.J., Cao, J., et al.: Mechanical properties and microstructure of multilayer go-cementmatrix composites. *J. Appl. Mech.* **37**(2), 860–865 (2020)
9. Lv, S.H., Zhang, J., Zhu, J.J., et al.: Effects of go on microstructure regulation and compressive strength of cement matrix composites. *J. Chem. Ind.* **68**(6), 2585–2595 (2017)
10. Lv, S.H., Sun,T., Ma, Y.J., et al.: Nano-graphene oxide control and toughening of hydrated crystal structure in cement composites. *Concrete* **11**,1–6 (2013)

Split Tensile Test of Brazilian Disc Specimen of Graphene Nanoplatelets Reinforced Cement-Based Composite Materials



Yanfa Sun, Zhanyuan Gao, and Dong Ruan

Abstract Effect of Graphene nanoplatelets(GNP) on the mechanical behavior of cement-based composite materials is studied by using split tensile test of Brazilian disc. The ordinary cement mortar and 0.01–0.07% GNP cement mortar are made into disc specimen with a diameter of 60 mm and a height of 30 mm. The indirect tensile strength of the specimen was obtained by splitting tensile test under quasi-static loading, and the failure pattern was analyzed. The results show that GNP can significantly enhance the strength of cement mortar. With the increase of graphene content, the tensile strength decreases gradually. The tensile strength of cement mortar with 0.01% graphene is the largest, which is increased by 25.51% compared with the blank group.

Keywords Graphene · Cement · Tensile strength · Brazilian disc · Splitting tensile

1 Introduction

Cement-based material is a common building material, which is widely used in all kinds of engineering construction. Cement-based material is a kind of brittle material, its tensile strength is much lower than its compressive strength. It is easy to form cracks under various loads, which reduces its durability and increases its maintenance cost. The defects of traditional cement-based composites are difficult to meet the requirement of engineering technology development. In order to improve the tensile strength of cement-based materials, some high strength and high toughness materials such as steel fiber, polypropylene fiber and carbon fiber are added to cement matrix [1–3]. The above methods delay the extension and diffusion

Y. Sun (✉) · Z. Gao
Tianjin Chengjian University, Tianjin 300384, China
e-mail: yanfasun@foxmail.com

D. Ruan
Swinburne University of Technology, Melbourne, VIC 3000, Australia

of cracks from the macro perspective. Although it played a certain positive role, it failed to fundamentally solve the problem of internal cracks. Therefore, it is necessary to improve the cement-based materials at the nanoscale from the micro level in order to fundamentally solve the durability, fracture and permeability problems.

In recent years, with the rapid development of nanotechnology, a number of high-performance nanomaterials have emerged, such as graphene, carbon nanotubes and nano-silicon. Single-layer graphene is the strongest (130GPa) nanomaterial with the thinnest thickness (0.35 nm) [4]. Graphene's unique structure and excellent physical and chemical properties [5] have attracted great attention in the research field of cement-based composites [6–8]. Du et al. [9] found that adding graphene nanosheets to cement mortar significantly reduced the water penetration depth, chloride diffusion coefficient and chloride migration coefficient. This is mainly due to the resistance of GNP itself to permeability and the refinement of the micro-structure. Dimitar et al. [10] made a kind of graphene concrete, whose compressive strength and flexural strength increased by 146% and 79.5% compared with standard concrete. Xia Cui et al. [11] found that the hardness of cement matrix composites with 5%NGPs increased by 1.5 times, the wear amount per unit area decreased by 71%, and the wear depth decreased by 73%.

Because of the difficulty of specimen clamping, it is usually not necessary to measure the tensile strength of cement-based materials by direct tensile method. The Brazilian disc splitting experiment has attracted much attention because it can be used to measure the tensile strength easily and quickly. At present, there are few reports about the tensile strength of graphene cement-based composites using Brazilian disc. In this paper, ordinary cement mortar and graphene-based cement mortar with different contents were prepared to compare the compressive strength, indirect tensile strength and failure modes of different specimens by quasi-static Brazilian disc splitting test. It aimed to find out the best mixture of graphene and provide theoretical support for engineering applications.

2 Experimental

2.1 Materials

Graphene is produced by Shandong Leadernano Technology Co. Ltd, whose physical properties are shown in Table 1. The surfactant is polyvinylpyrrolidone (PVP, average molecular weight 1,300,000), which was purchased from Shanghai Aladdin Biochemical Technology Co. Ltd. Bilon-500 ultrasonic disperser is produced by Beijing BILON Experimental Equipment Co. Ltd.

Table 1 Physical properties of graphene

Thickness (nm)	Size (um)	Specific surface area (m ² /g)	Purity (%)	Conductivity (S/m)
1–5	1–10	300–600	≥ 96	≥ 400

2.2 Preparing GNP Suspensions

In order to introduce graphene into cement-based materials, aqueous solutions of graphene need to be prepared first. In the previous study on graphene dispersion process, the author found that graphene had the best dispersion effect when the mass ratio of graphene and surfactant (PVP) was 1:1, the ultrasonic power was 500 W, and the ultrasonic time was 60 min. The graphene suspension prepared by this method is shown in Fig. 1.

2.3 Specimen Preparation

According to the preparation of cement mortar is based on ASTM C109, the graphene content of cement mortar is 0.01–0.07%. The mass ratio of standard sand to cement is 2.75, and the water-cement ratio is 0.485. The Brazilian disc is 60 mm in diameter and 30 mm in thickness. The process of making the Brazilian disc is as follows: First, put the cement and standard sand into the blender and mix them evenly. In the second step, the graphene suspension was added and stirred. The third step is to load the graphene cement mortar into the mold and shake on the shaker until the surface overflows with cement. The specimen was taken out after 24 h and cured for 28 days at room temperature in saturated lime water, as shown in Fig. 2.

Fig. 1 Graphene suspension



Fig. 2 Brazil disc

The tensile strength formula:

$$\sigma_t = \frac{2p}{\pi Dh} \quad (1)$$

where σ is the tensile strength (MPa), P is the failure load (N), D is the diameter (mm) and h is the thickness (mm).

2.4 Testing Procedures

The indirect tensile strength of the specimen was measured by an electro-hydraulic servo pressure testing machine with a maximum bearing capacity of 100kN. The installation method of the specimen is shown in Fig. 3, and the loading speed is 1.5 mm/min. During the test, the load curve slowly rises, then suddenly drops and does not rise any more. This phenomenon indicates that the specimen has lost its bearing capacity, and the specimen is fractured. In the test, with the increase of vertical load, cracks first appeared in the center of the specimen. The cracks rapidly expanded and connected along the loading direction and cracked loudly. The fracture surface is shown in Fig. 4.

Fig. 3 Specimen placement mode



Fig. 4 Fracture surface



3 Results

3.1 Tensile Strength

When the tensile strength is measured by quasi-static splitting test, six sets of parallel tests are done for each specimen. The load-displacement curve rises slowly, reaches the highest point and then drops suddenly, as shown in Figs. 5 and 6. The

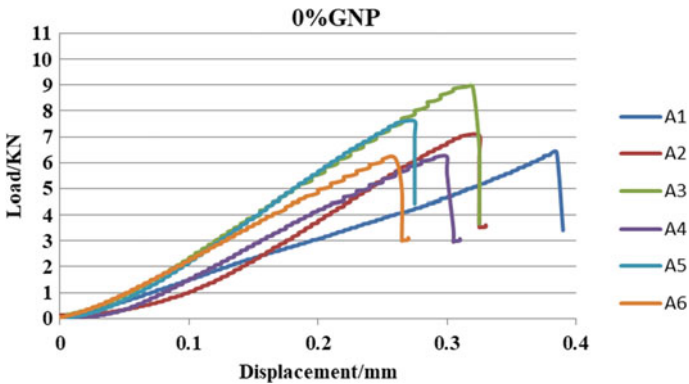


Fig. 5 0% GNP tensile strength

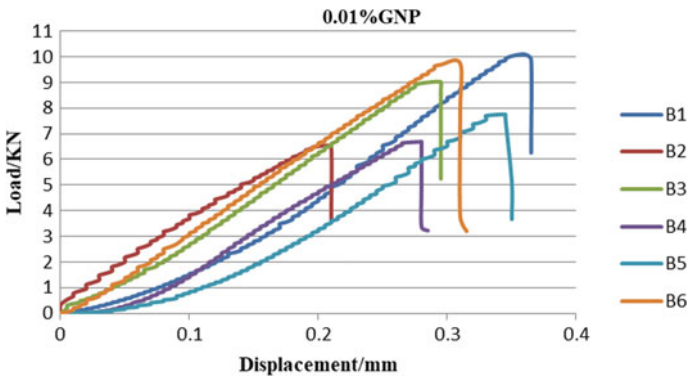


Fig. 6 1% GNP tensile strength

fracture load P of graphene specimen (0.01% GNP) is significantly higher than that of ordinary specimen, indicating that 0.01% graphene improves the bearing capacity of ordinary cement mortar. In view of the discreteness of the test results, the average values of 6 groups of test loads are taken as the final results. The maximum bearing capacity of cement mortar with different graphene content is shown in Fig. 7. It can be seen from the figure that the failure load of graphene cement mortar is higher than ordinary cement mortar. With the increase of graphene content, the failure load first increased and then decreased. When the graphene content was 0.01%, the maximum load was achieved, indicating that the graphene content at this time was the optimal value.

As shown in Fig. 8, the tensile strength of graphene cement mortar at the same age and under the same curing condition is higher than that of the blank group. With the increase of graphene content, the flexural strength curve showed a trend of first increasing and then decreasing. When the content was 0.01wt%, the

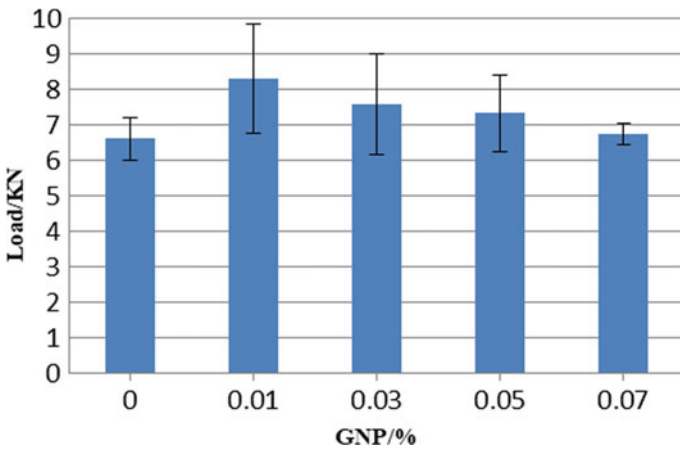


Fig. 7 Bearing capacity of cement mortar with different graphene content

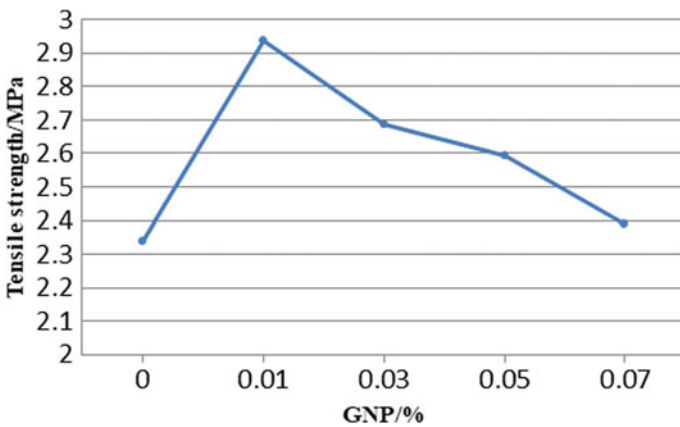


Fig. 8 Tensile strength of cement mortar with different graphene content

strength reached its peak. This shows that graphene can improve the compressive strength of cement-based composites. Within a certain range, the strength of cement-based materials also increases with the increasing proportion of graphene doping. When the dosage is too large, the enhancement effect will weaken, or even reduce the strength of cement-based materials.

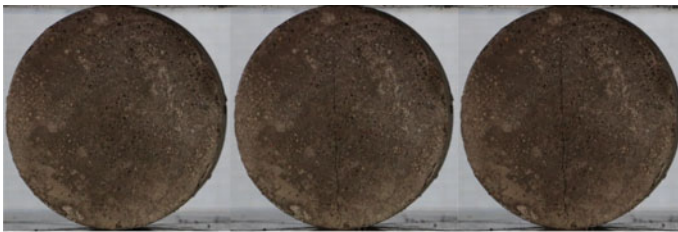
According to formula (1), the tensile strength and increase amplitude of graphene cement mortar were calculated. As shown in Table 2, graphene has a significant strengthening effect on the tensile strength of cement mortar, and the strengthening extent is closely related to the amount of graphene added.

Table 2 Growth rate of compressive strength of different graphene cement mortar

GNP	Breaking load (KN)	Tensile strength (MPa)	Growth rate
0	6.6173	2.3404	–
0.01%	8.3056	2.9375	25.51%
0.03%	7.5957	2.6864	14.79%
0.05%	7.3376	2.5951	10.89%
0.07%	6.7506	2.3875	2.01%

3.2 Failure Pattern

In the quasi-static splitting experiment, the compression failure and crack generation of the specimen are shown in Fig. 9. Figure 9a shows the splitting process of the Brazilian disk of cement mortar without graphene. The crack first appears at the center of the disc, and then expands outward rapidly, and finally runs through the whole specimen. According to Sect. 3.1, the optimum content of graphene is 0.01%. Figure 9b shows the splitting process of 0.01% GNP Brazilian disk, which is similar to Fig. 9a, and meets the requirements of splitting test. From the crack path after penetration, the crack of (a) is a straight line, while the crack of (b) shows obvious bending shape. It is obvious that the cracks in (b) encounter more obstacles in the process of propagation, and even need to penetrate the graphene sheet. As a result, more energy is required, which results in a stronger tensile strength.



(a) 0%GNP.



(b) 0.01%GNP.

Fig. 9 Splitting failure process of Brazil disk

4 Conclusions

Brazilian disc splitting test was carried out on 0% ~ 0.07% GNP cement mortar. Compared with ordinary cement mortar, the addition of graphene can significantly improve the tensile strength of cement mortar. In the range of 0.01–0.07% graphene, the tensile strength first increases and then decreases with the increase of graphene content. The best content of graphene is 0.01%, and the tensile strength is the largest, increasing by 25.51%. Too much graphene will have an adverse effect on the tensile strength.

Acknowledgements This work was financially supported by the Natural Science Foundation of China (51708391), The Natural Science Foundation of Tianjin (18JCYBJC22700).

References

1. Toth, M., Bokor, B., Sharma, A.: Anchorage in steel fiber reinforced concrete—concept, experimental evidence and design recommendations for concrete cone and concrete edge breakout failure modes. *Eng. Struct.* **181**, 60–75 (2019)
2. Truong, G.T., Kim, J.C., Choi, K.K.: Seismic performance of reinforced concrete columns retrofitted by various methods. *Eng. Struct.* **134**, 217–235 (2017)
3. Gong, J., Zeng, W., Zhang, W.: Influence of shrinkage-reducing agent and polypropylene fiber on shrinkage of ceramsite concrete. *Constr. Build. Mater.* **159**, 155–163 (2018)
4. Allen, M.J., Tung, V.C., Kaner, R.B.: Honeycomb Carbon: A Review of Graphene. *Chem. Rev.* **110**(1), 132–145 (2009)
5. Katsnelson, M.I.: Graphene: carbon in two dimensions. *Mater. Today* **10**(1–2), 20–27 (2006)
6. Rhee, I., Kim, Y.A., Shin, G.O., et al.: Compressive strength sensitivity of cement mortar using rice husk-derived graphene with a high specific surface area. *Constr. Build. Mater.* **96**, 189–197 (2015)
7. Du, H., Pang, S.D.: Enhancement of barrier properties of cement mortar by graphene nanoplatelet. *Cem. Concr. Res.* **76**, 10–19 (2015)
8. Wang, B.M., Jiang, R.S., Wang, Z.L.: Investigation of the Mechanical Properties and Microstructure of Graphene Nanoplatelet-Cement Composite. *Nanomaterials* **6**(11), 200 (2016)
9. Du, H., Pang, S.D.: Dispersion and stability of graphene nanoplatelet in water and its influence on cement composites. *Constr. Build. Mater.* **167**, 403–413 (2018)
10. Dimov, D., Amit, I., Gorrie, O., et al.: Ultrahigh performance nanoengineered graphene-concrete composites for multifunctional applications. *Adv. Funct. Mater.* **28**(23), 1705183 (2018)
11. Cui, X., Sun, S. W., Han, B.G., et al.: Mechanical, thermal and electromagnetic properties of nanographite platelets modified cementitious composites. *Compos. Part A: Appl. Sci. Manuf.* (2017)

Review on the Preparation Processes of Natural Fiber Reinforced PLA Composites



Z. H. Zhu and H. W. Wu

Abstract The common preparation processes of natural fiber reinforced PLA composites, including injection molding, extrusion molding, hot pressing molding, hot pressing molding and 3D printing molding were introduced. The advantages and disadvantages of various processes were pointed out in this paper.

Keywords Natural fiber · PLA · Composites · Process

1 Introduction

The most commonly used forming processes to prepare natural fiber reinforced biocomposites include injection molding, extrusion molding, hot pressing molding after open or intensive refining, et al. According to the characteristics and forming requirements of different plant fibers, different forming processes can be selected. For short cut plant fiber such as bamboo fiber, wood fiber, short hemp fiber, it is not necessary to consider the shearing of the fiber in the molding process, and thus the molding process is relatively more selective.

For some plant fibers with large length-diameter ratio, such as sisal fiber, hemp fiber, the main molding process is hot pressing process. It is mainly because that fiber would be cut because of the strong shearing action of a screw or rotor during the Injection molding process extrusion molding process and open refining process. Therefore, there is no guarantee that the length-diameter ratio of the fiber will be maintained at the desired large value, which will influence the overall performance of the composites.

Z. H. Zhu (✉)

School of Advanced Manufacturing Technology, Guangdong Mechanical & Electrical Polytechnic, Guangzhou, China

H. W. Wu

The Key Laboratory of Polymer Processing Engineering, Ministry of Education, South China University of Technology, Guangzhou, China

2 Preparation Processes

2.1 Lamination Process

Lamination is a common forming process for preparing composites. Its main advantage is that the forming equipment is simple and cheap, and the natural fiber will not be subjected to strong shearing action during the forming process which will lead to the reduction of length-diameter ratio, and thus maximize the comprehensive performance of the long fiber reinforced composite. Therefore, lamination process is often used in the preparation of long plant fiber reinforced composites.

Ochi [1] prepared Kenaf fiber reinforced PLA composite by hot-pressing process and studied the mechanical properties of the composite. It was found that the mechanical properties of the composite gradually improved with the increase of the content of flax fiber.

Graupner et al. [2] blended Hemp fiber Kenaf fiber and Cotton fiber with PLA fiber to prepare mixed fiber, and then prepared multi-fiber reinforced PLA laminated composites by hot-pressing process, and studied the influence of different fiber ratios on the mechanical properties of composites. It was found that different fibers have different effects on the tensile properties, bending properties and impact properties of the composites. The composites with excellent tensile properties, bending properties and impact properties can be obtained by using appropriate fiber ratio.

Plackett et al. [3] made jute fiber into fiber felt, and prepared composites by lamination process and polylactic acid (PLA) thin film hot-pressing, and studied the influence of different molding temperature on the tensile properties of composites. It was found that the tensile strength of the composite could be increased by nearly 100% with appropriate hot pressing temperature and fiber content.

2.2 Hot Pressing After Open or Close Refining

Hot pressing after open or close refining is also a common process. Compared with lamination process, the dispersion degree of plant fiber and PLA matrix is better due to the blending process of open or close refining. However, the plant fiber will be cut off due to the shearing action because of the strong shearing action of the double roller or the rotor of the mixer, and thus the length-diameter ratio of the plant fiber cannot be guaranteed.

Zhu et al. [4] prepared sisal fiber reinforced polylactic acid composite by open blending process and studied the thermal and crystalline properties of the composites. It was found that the addition of sisal fiber could increase the crystallization rate of composites. Compared with pure PLA, the crystallinity of the composites

was improved. However, the thermal stability of the composites was reduced, and the relative molecular weight of pure PLA and composites was reduced after blending.

Fu et al. [5] studied the difference of mechanical properties and degradation properties of sisal fiber reinforced PLA composite treated with alkali and grafted with L-lactide by hot pressing after blending. It was found that the degradation rate of composites was faster than that of pure PLA while the impact properties of composites were reduced and the tensile properties and bending properties were improved after graft treatment.

Cai Jun [6] prepared the sycamore fiber reinforced PLA composite by using an internal mixer. It was found that sycamore fiber could promote the crystallization of PLA, and the bending modulus of composite was positively correlated with the content of sycamore fiber. However, the impact strength of the composite decreases with the increase of the content of sycamore fiber.

2.3 Extrusion and Injection Molding

The other two common processes are extrusion molding and injection molding, which were often used in the preparation of some short fiber or powdery plant fiber reinforced PLA composites. Their main advantages are simple operation and high production efficiency. However, the equipment is expensive, and the length-diameter ratio of plant fiber will be reduced due to the strong shearing action of screw and thus the performance of plant fiber would be decreased.

Lee et al. [7] prepared bamboo fiber reinforced PLA composites by extrusion blending and hot-pressing process, and studied the changes of mechanical properties of composites with different bamboo fiber content. It was found that the tensile strength of the composite was negatively correlated with the increase of bamboo fiber content when the bamboo fiber content was low, but the mechanical properties of the composite were still better than that of the pure PLA. Oksman et al. [8] also used extrusion and blending process to prepare PLA composites with different content of flax fiber. It was found that the composites were easy to be formed and the mechanical properties were improved, while the increase of fiber mass fraction reduced the tensile strength of the composites.

2.4 3D Printing

3D printing technology, also known as additive manufacturing technology, is a new manufacturing technology that is made by computer-aided design and manufacturing, which is similar to the direct printing of products by ordinary printers. As a research hotspot nowadays, how to apply plant fiber/polymer composites to 3D printing is what the researchers are concerned about.

Filgueira [9] grafted dodecyl gallate (LG) or octyl gallate (OG) on the surface of thermal mechanical Spruce wood pulp fiber (TMP), then the PLA composite was processed wire with the diameter of into Φ 2.2 mm, in which the content of TMP were 10% and 20% respectively. Finally, a 3D printer with a nozzle of 0.4 mm was used to print the molding spline. SEM analysis showed that the cross section of unmodified TMP/PLA has uniformly distributed holes, while the size of holes in the LG modified TMP/PLA cross section is significantly smaller than that of the unmodified TMP/PLA. The tensile strength test of 3D printed spline showed that modified TMP/PLA had higher tensile strength than pure PLA, which is further verified that OG modification can effectively improve the interface binding between TMP and PLA.

Y Tao et al. [10] filled wood powder with PLA to prepare 3D printing wire rod and applied it in FDM molding successfully. The tensile properties, crystallinity and surface morphology of PLA/wood powder composites were measured and characterized by SEM, TGA and DSC respectively. The results showed that the initial bending resistance of the composite was enhanced compared with PLA, the initial thermal degradation temperature of the composite decreased slightly, and the melting temperature had almost no effect.

Scholars at home and abroad are exploring various types of natural fiber/polymer composites to be used in 3D printing and have tried different improvement methods to solve the problems encountered. The modification and addition of compatibilizer on the surface of natural fiber are the main approach. It also seems to be effective to improve the technological parameters and methods of printing. For example, Continuous fiber printing is also a new direction of improvement.

3 Conclusion

According to the above introduction, several commonly used composite molding processes have advantages and disadvantages. Injection molding and extrusion molding process have high production efficiency and are easy to be used in industry. Whereas, the expensive equipment and the strong shearing action of screw make the composites comprehensive performance decrease. The hot pressing process can produce natural fiber reinforced composites with excellent mechanical properties, while it is not suitable for industrial application due to its low production efficiency. For 3D printing, natural fiber reinforced PLA composites are mostly printed by FDM printers. Because of the poor interfacial compatibility, the poor fluidity of some fibers in the melting state and the poor mechanical properties of the products, and the increase of fiber content will affect the product quality, etc., the types of natural fibers applied are also relatively limited. Therefore, the suitable forming process must be selected according to the actual situation to achieve the ideal comprehensive properties of the composites in the preparation of natural fiber reinforced PLA composites. We believe that more and more exploration will lead to the application of more natural fiber/polymer composites in 3D printing.

Funding This research was supported by Specialized Research Fund for the Doctoral Program of Higher Education of China (grant no. 20120172130004) and National Key Basic Research Program of China (973 Program) (grant no. 2012CB025902).

References

1. Ochi, S.: Mechanical properties of kenaf fibers and kenaf/PLA composites[J]. *Mech. Mater.* **40**(4), 446–452 (2008)
2. Graupner, N., Herrmann, A.S., Müssig, J.: Natural and man-made cellulose fibre-reinforced poly(lactic acid) (PLA) composites: An overview about mechanical characteristics and application areas[J]. *Compos. Part A-Appl. Sci. Manuf.* **40**(6), 810–821 (2009)
3. Plackett, D., Andersen, T.L., Pedersen, W.B., et al.: Biodegradable composites based on l-poly lactide and jute fibres. *Compos. Sci. Technol.* **63**(9), 1287–1296 (2003)
4. Zhu, Z., Hao, M., Zhang, N.: Influence of contents of chemical compositions on the mechanical property of sisal fibers and sisal fibers reinforced PLA composites. *J. Nat. Fibers* **17**(1), 101–112 (2020)
5. Fu, W., Xu, X., Wu, H.: Mechanical and biodegradable properties of L-lactide-grafted sisal fiber reinforced poly lactide composites. *J. Reinf. Plast. Compos.* **33**(22), 2034–2045 (2014)
6. Jun, C.: Study of natural fiber modified POLYLactic acid composites. Nanjing University of Technology, Nanjing (2014)
7. Lee, S.H., Wang, S.: Biodegradable polymers/bamboo fiber biocomposite with bio-based coupling agent. *Compos. Part A-Appl. Sci. Manuf.* **37**(1), 80–91 (2006)
8. Oksman, K., Skrifvars, M., Selin, J.F.: Natural fibres as reinforcement in poly lactic acid (PLA) composites. *Compos. Sci. Technol.* **63**(9), 1317–1324 (2003)
9. Filgueira, D., Holmen, S., Melbo, J.K., Moldes, D., Echtermeyer, A.T., Chinga-Carrasco, G.: *Acs. Sustain. Chem. Eng.* **5**(10), 9338–9346 (2017)
10. Tao, Y., Wang, H., Li, Z., et al.: Development and Application of Wood Flour-Filled Poly lactic Acid Composite Filament for 3D Printing. *Materials* **10**(4), 339 (2017)

Fabrication of Nickel/Nano-Lu₂O₃ Co-Electrodeposited Coating with Good Corrosion and High Temperature Oxidation Resistance



Yanli Dou, Yi Liang, Ruishan Yang, Guangguang Qian, Xiaojie Wei, and Hong Xu

Abstract In this paper, pure nickel and Ni-Lu₂O₃ composite coatings with different content of nano-Lu₂O₃ particle were prepared using direct current electroplating. The morphology, texture, corrosion and high temperature oxidation resistance of the nanocomposite coating are investigated. The results show that the deposition amount of Lu₂O₃ particles in the composite coating increased first and then decreased with the increasing of the nano-Lu₂O₃ particles concentration in plating solution. The incorporation of nano-Lu₂O₃ particles changes the surface morphology and the preferential orientation of nickel matrix. The corrosion resistance and high temperature oxidation resistance of Ni-Lu₂O₃ composite coatings increase with the deposition amount of Lu₂O₃ particles. Compared with other samples, the composite coating of Ni/Lu₂O₃ (2.99 wt%) shows the best corrosion resistance and high temperature oxidation resistance.

Keywords Composite electroforming · Rare earth · Corrosion resistance · Lu₂O₃ particles

1 Introduction

Electroforming of nickel on the electric plastic surface has the advantage of replicating micro-structure of the matrix accurately. These electroformed nickel molds are widely used as slush mold or injection mold to prepare the parts of circuit board, automobile, or aircraft. The corrosion and oxidation resistance under high temperature are very importance to these molds. Many researchers have demonstrated the composite electroplating is a superior technique to enhance the properties of pure metal electroforming coating [1–5]. Introducing nano-sized particles as the second-phase in the coating is a way to improve the properties of nickel

Y. Dou · Y. Liang · R. Yang · G. Qian · X. Wei · H. Xu (✉)

Key Laboratory of Automotive Material, Ministry of Education, College of Material Science and Engineering, Jilin University, Changchun 130025, China

e-mail: 822291329@qq.com

© The Author(s), under exclusive license to Springer Nature Switzerland AG 2021

283

L. Zheng et al. (eds.), *Proceedings of MEACM 2020*,

Mechanisms and Machine Science 99,

https://doi.org/10.1007/978-3-030-67958-3_31

matrix [6–10]. In the past few decades, many efforts have been made to improve the performance of nickel deposits by co-deposition of nano-sized particles such as Si_3N_4 [11], TiO_2 [12], SiC [13, 14], nano-diamond [15], etc.

Among the available nano sized particles, rare earth oxide act as a promising material in corrosion protection, solid fuel electrolyte applications and environmental catalysis, etc. Campos et al. synthesized the Pt- CeO_2 composite coatings by codeposition [16]. Hui Jin [17] prepared the Ni- CeO_2 nanocomposite coatings, which was achieved by ultrasonic cavitation. The corrosion resistance of Ni- CeO_2 nanocomposite coatings was improved. Carac et al. produced the Ni-Co- CeO_2 composite coatings by electrodeposition [18], which indicated the deposition of CeO_2 in a cobalt and nickel matrix was possible, and the properties of composite coatings could be varied in a wide range. Zi-tao Zhou [19] prepared that the hardness, high-temperature oxidation resistance and the corrosion resistance of Ni-Fe-La composite coatings were significantly improved. Zhiyong Li et al. demonstrated that the electrodeposition of Cu- La_2O_3 composite coating had better electrical erosion resistance compared to pure Cu [20]. As one of rare earth oxides, Lu_2O_3 has similar chemical properties with CeO_2 and La_2O_3 . To study the effect of nano- Lu_2O_3 nanoparticles on the properties of nickel films, the preparation of thin films of Ni and Lu_2O_3 reinforced nickel matrix composites were obtained through electrodeposition.

In our work, an electroplating process of Ni- Lu_2O_3 nanocomposite coatings was developed. To examine and better understand the effect of nano- Lu_2O_3 particles content on the properties, the weight percent of nanoparticles in deposits, preferred orientation, high oxidation resistance and wear resistance of deposits were investigated in this paper.

2 Experimental

2.1 Preparation of Ni- Lu_2O_3 Composite Coatings

The Ni- Lu_2O_3 composite coatings were prepared by constant current electrodeposition. The bath component and plating conditions were listed in Table 1. The plating solution was prepared using analytical reagents and de-ionized water. The concentration of nano- Lu_2O_3 particles in the bath varied from 0.4 to 8.0 g/L. The temperature of electrolyte was maintained at 50 °C by thermostat water bath, the pH was 4.0 adjusted by sulfamic acid. A copper plate (99.9% purity) of 60 mm 70 mm × 0.2 mm was used as cathode and the sulfur-containing nickel cake produced by INCO of Canada (purity 99.9%) was used as anode. The thickness of the coating was fixed to 0.8 mm. The distance among the anode and cathode was maintaining at 20 cm. After electrodeposition, the specimens were rinsed with de-ionized water and then dried.

Table 1 Composition of the bath solution and the electrodeposition parameters

Bath composition		Plating conditions	
Component	Concentration (g/l)	Plating conditions	Value
Ni(SO ₃ NH ₂) ₂ ·4H ₂ O	420	Temperature (°C)	50
NiCl ₂ ·7H ₂ O	5	pH	4.1
H ₃ BO ₃	36	Current density (A/dm ²)	3.0
CH ₃ (CH ₂) ₁₁ NaOSO ₃	0.3	Area ratio (cathode:anode)	1:2
Nano-Lu ₂ O ₃ particles	0.4–8	Distance (between cathode and anode) (cm)	20
		Stirring rate (r/min)	800
		Thickness (mm)	0.8

2.2 Microstructural and Phase Characterizations

The content of Lu element in the composite coatings was measured by an inductively coupled plasma emission spectrometer (ICP, Plasma1000, NCS), and the mass fraction of Lu₂O₃ was obtained by calculation. The surface morphology and roughness of the composite coatings were observed by scanning electron microscopy (ZEISS, EVO 18) and three-dimensional laser confocal microscopy (LEXT OLS4100, OLYMPUS). The crystal structure of the composite deposits was investigated by X-ray diffraction (D/max-2500, Rigaku Corporation).

2.3 Corrosion Test

CHI-660D electrochemical workstation was used for electrochemical measurements. Tafel curves were obtained in 1 M NaOH or 1 M HNO₃ solution. The corrosion potential (E_{corr}) and corrosion current density (I_{corr}) for the deposits were obtained from the intersection of the cathodic and anodic Tafel curves by the Tafel extrapolation method. To study the corrosion resistance of samples, the weight loss of samples after acid etching was calculated. Oxidation at 800 °C was performed in a muffle furnace. After certain intervals of exposure, samples were withdrawn from the furnace for weighing. The weight change of samples was calculated for characterizing high temperature oxidation resistance of samples. After 20 h oxidation, the oxide scale was investigated by scanning electron microscopy (SEM).

3 Results and Discussion

3.1 The Composition of Co-Deposition Layer

The content of Lu element in the co-deposition layer tested by ICP and the content of Lu_2O_3 calculated according the data of Lu element are listed in Table 2. The content of Lu_2O_3 in the codeposition layer increase as the concentration of nano- Lu_2O_3 particles(NLP) in plating solution increase up to 4 g/L and decrease beyond this value. In the plating solution, nickel ions can be adsorbed on the surface of NLP by the electrostatic interaction under stirring situation. Then nickel ions take NLP to the cathode surface through electric force between electrodes [5]. The codeposition process of NLP and nickel ion is shown in Fig. 1. The collision probability of NLP and nickel ion increase as the content of NLP raise in plating bath under stirring situation. As a result, the number of nano- Lu_2O_3 particles arrive to the surface of cathode increase through electric field force. The nickel nanocrystalline layer formed after the discharging of nickel ion at the surface of cathode, and then the nano- Lu_2O_3 particles are embedded into the composite coatings. In addition to Ni^+ , H^+ ionized by acid and water can also act as the carrier of NLP. However, when the concentration of NLP in plating solution is beyond 4 g/L, the NLP quality content in Ni- Lu_2O_3 composites decrease. As more NLPs accumulate on the surface of cathode, the non-conductive area increase, resulting in the increasing of current density, which intensifies hydrogen evolution [21]. When the hydrogen escapes from cathode surface, the adsorption of NLP in the plating solution is inhibited. Therefore, the content of NLP in the co-deposition layer decreases when continuing to increase the concentration of NLP in plating solution.

The SEM surface morphology and confocal microscopy images of Ni- Lu_2O_3 composite coatings are shown in Fig. 2. Pure nickel coating is uneven, it shows cell-like structure with different and broad sizes in Fig. 2a. The surface of the codeposition layer of Ni/ Lu_2O_3 levels off and the size of cell-like structure becomes more smaller with NLPs addition, as shown in Fig. 2b–d. Especially in Fig. 2d, only finely grainy morphology can be observed in the coating of Ni/ Lu_2O_3 (2.99), and the surface is smooth with good compactness. To quantitative analyze the changes in the codeposition layer, the roughness data is tested by confocal microscopy and shown in Table 3. The surface roughness is decreasing with the content of NLPs increasing. When the content of NLP increases to 2.99 wt% in the composite coatings, the surface roughness decreases from 1.123 μm to 0.445 μm . The reason is that Lu_2O_3 particles co-deposit with ions at cathode in the solution under the drive of stirring and disperse in the nickel matrix, producing dispersion

Table 2 The contents of Lu element and Lu_2O_3 of deposition layer

The concentration of NLP in plating solution (g/L)	0.4	2	4	6	8
Content of Lu element in codeposition layer (wt%)	0.23	1.47	2.63	2.60	1.52
Content of Lu_2O_3 in codeposition layer (wt%)	0.26	1.67	2.99	2.96	1.73

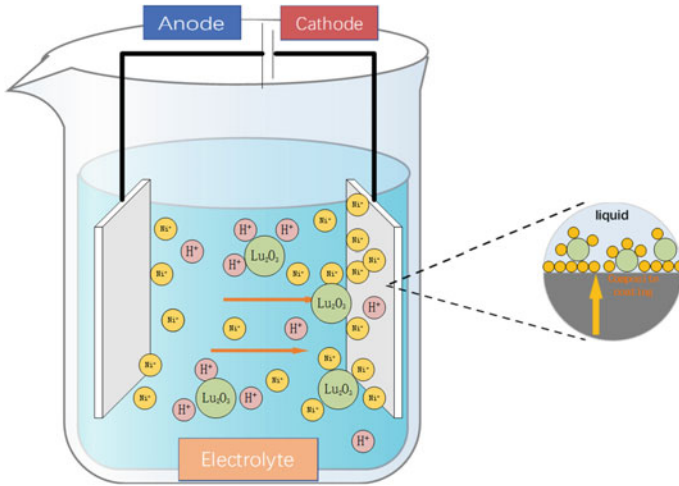


Fig. 1 Schematic diagram of co-deposition process

force and reducing the interfacial tension of crystal nucleus. Thus, the critical nucleation radius has been decreased and more crystal nuclei have been formed. Moreover, metal nickel ions can deposit directly with Lu₂O₃ particles as the base point, which can hinder the growth of nickel crystal grains [22–25]. As a result, the surface of coating is fine and uniform without cracks, holes, and other defects.

3.2 Roughness and Morphological Analysis

The XRD patterns of pure Ni and Ni-Lu₂O₃ composite coatings with different nano-Lu₂O₃ content are shown in Fig. 3a. The pure Ni coating is clearly observed to be orientated in the (111) and (200) plane direction, while Ni-Lu₂O₃ composite coatings exhibit a reinforcement of (311) and (111) lines accompanied with a reduction of the (200) line. It is worth noting that the reinforcement of the lines (311) and (111) is attributed to a reduction of (200) orientation [13]. To quantify the relative crystallographic textures associated with nickel and nickel composite coatings, the ratio of diffraction peak intensity ($I_{(111)}/I_{(200)}$) is used to characterize the texture of composite coatings. Figure 3a and b show that the grain growth in direction of the (200) decrease consistently as the content of NLP increase in coatings. Moreover, the ratio of $I_{(111)}:I_{(200)}$ varies from 0.09 to 0.58 as the content of NLP in composite coatings increase. It is attributed to the grains in the coating growing in multiple directions and avoiding coarse growth in a single direction refined the grains [26]. Therefore the diffraction peak intensity and the dominant orientated of composite coatings change with the addition of NLP [27].

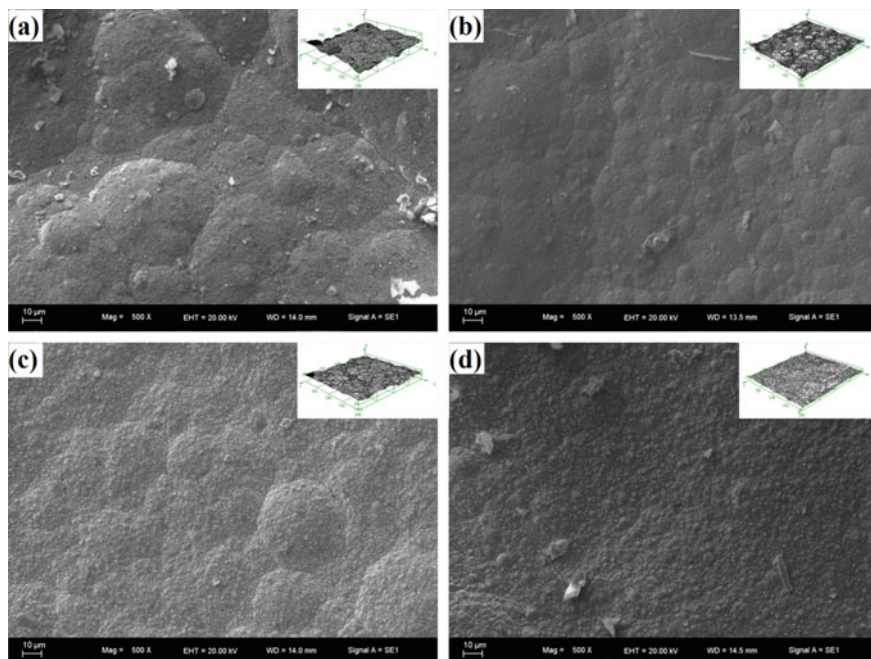


Fig. 2 SEM surface morphology and confocal microscopy images of Ni-Lu₂O₃ composite coatings. Lu₂O₃ content in the composite coatings: **a** 0 g/L, **b** 0.26 g/L, **c** 1.67 g/L, and **d** 2.99 g/L

Table 3 Relationship between surface roughness and the content of NLP of composite coatings

Sample	Content of Lu ₂ O ₃ (%)	Surface roughness (μm)
Pure Nickel	0	1.395
Ni/Lu ₂ O ₃ (0.26)	0.26	1.123
Ni/Lu ₂ O ₃ (1.67)	1.67	0.897
Ni/Lu ₂ O ₃ (2.99)	2.99	0.445

3.3 Corrosion Resistance Analysis

The corrosion performance of pure Ni and Ni-Lu₂O₃ composite coatings are investigated by polarization curve measurements in 1 M NaOH and 1 M HNO₃, respectively. Figure 4 shows the Tafel polarization curves for electrodeposited layers in 1 M HNO₃ and 1 M NaOH. The relationship between nano-Lu₂O₃ particles concentration in the composite coatings and corrosion potentials and densities is listed in Table 4. Pure nickel coating had lesser E_{corr} (-0.274 V) among the four composite coatings and also having the highest corrosion current I_{corr} (1434 μA/cm²). The composite coating (2.99wt%) presents noble E_{corr} (-0.179 V) compared with pure nickel coating, and the corrosion currents are greatly lower than pure

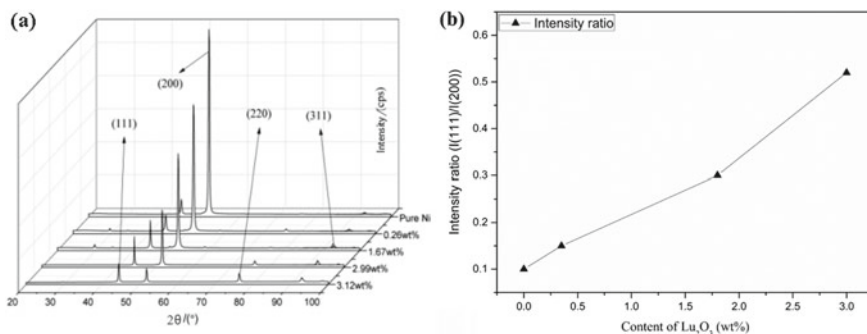


Fig. 3 XRD patterns of pure Ni coating and composite coatings (a) and the intensity ratio of (111) and (200) (b)

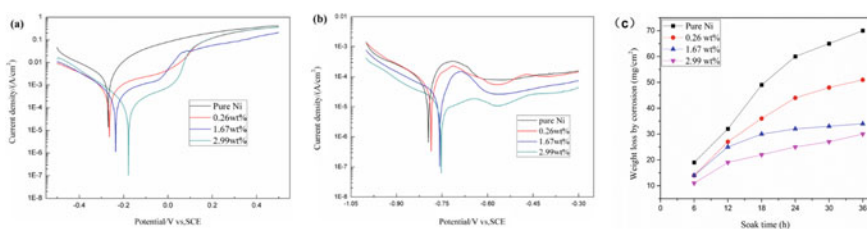


Fig. 4 Effect of the Nano-Lu₂O₃ particles concentration in the composite coatings on its polarization curves in 1 M HNO₃ (a) and 1 M NaOH (b) Correlation between weight loss of composite coatings contain different content of NLP and soaking time (c)

nickel coating, as it can be seen in Fig. 4a. This difference caused by the morphology of coatings [28]. Pure nickel coating have cell-like substances on its surface, leading to a higher corrosion activity, which can be seen by higher corrosion current. Composite coating Ni/Lu₂O₃ (2.99) presents a compact and uniform passivation protective film on its surface, and this feature has some corrosion inhibition effects. The Tafel polarization curves for electrodeposited layers in 1 M NaOH, in Fig. 4b, shows a similar regulation that E_{corr} (-0.755 V) of Ni/Lu₂O₃ (2.99) presents a higher corrosion potential than pure nickel coating E_{corr} (-0.796 V). Generally, a lower I_{corr} and a higher E_{corr} are related to a lower corrosion rate and so a better corrosion resistance [28]. As the content of NLP increase in the coating the corrosion potential increase and corrosion current densities decrease. It indicates that whether in acid or alkalinity environment, composite coating exhibits a better corrosion resistance than pure nickel coating.

The weight loss of composite coatings with different content NLP in 1 M HNO₃ is shown in Fig. 4c. The weight loss of the pure nickel, M_{loss} is 52.8 mg/cm², according to weight loss measurements, while the M_{loss} of composite coating is only 19.8 mg/cm². The weight loss measurement reveals that the corrosion rate of

Table 4 Effect of Nano-Lu₂O₃ particles concentration in the composite coatings on its corrosion potentials and corrosion current densities

Solution	Concentration of NLP in the coatings (wt%)	$E_{corr}(V)$	$I_{corr}(\mu A/cm^2)$
HNO ₃	0	-0.274	1434
	0.26	-0.267	857
	1.67	-0.239	450
	2.99	-0.179	169
NaOH	0	-0.796	210.6
	0.26	-0.788	146.2
	1.67	-0.759	53.2
	2.99	-0.755	39.1

composite coatings is much lower than that of the pure nickel, further showing that the composite coating surface with good anticorrosion performance.

The weight raise of the composite coatings with different content NLP after oxidation is used to evaluate the antioxidant performance, and the data is listed in Table 5. All samples are placed in muffle furnace at 800 °C for 12 h oxidation to accelerate the oxidation process. The weight raise of the pure nickel coating is highest (1.01 mg/cm²) compared to the composite coatings with NLP, while that of Ni/Lu₂O₃ (2.99) is only 0.83 mg/cm². This reveals that, high temperature oxidation resistance increase as the concentration of NLP increase in composite coatings. It attributes to a dense oxidation film is formation on the coating surface, which prevents the composite coatings further oxidation. The NLP provide many nucleation centers for the formation of oxidation film, which prompts oxidation film growth. Moreover, the fine nano-Lu₂O₃ particles are dispersed at the grain boundary of NiO during oxidation process. These particles hinder the diffusion progress of Ni²⁺ and O²⁻ ions in oxidation film, which reduces the oxidation rate [29–31].

The surface morphology images of deposition coatings after oxidation under high temperature are shown in Fig. 5, and the scanning results of energy spectrum of these specimens listed in Table 6. As seen in the Fig. 5a, the pure nickel coating shows obvious deep cracks and the matrix is not compact. Oxygen is easily enter into the matrix through these cracks, which makes Ni element in deep layer to be

Table 5 The weight raise of the composite coatings with different content NLP after oxidation at 800 °C

Sample	Ni	Ni/Lu ₂ O ₃ (0.26)	Ni/Lu ₂ O ₃ (1.67)	Ni/Lu ₂ O ₃ (2.99)
0 h/(mg/cm ²)	0	0	0	0
3 h/(mg/cm ²)	0.64	0.57	0.55	0.48
6 h/(mg/cm ²)	0.84	0.80	0.75	0.64
9 h/(mg/cm ²)	0.97	0.89	0.82	0.78
12 h/(mg/cm ²)	1.01	0.94	0.87	0.83

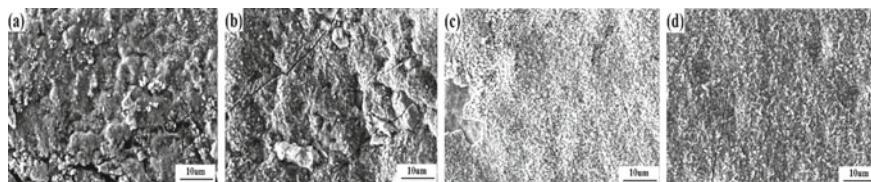


Fig. 5 SEM surface morphology of Ni-Lu₂O₃ composite coatings containing: **a** 0 g/L, **b** 0.26 g/L, **c** 1.67 g/L, and **d** 2.99 g/L at 800 °C for 12 h

Table 6 Energy spectrum results of the composite coatings with different concentration of NLP

Sample	Ni	Ni/Lu ₂ O ₃ (0.26)	Ni/Lu ₂ O ₃ (1.67)	Ni/Lu ₂ O ₃ (2.99)
O (wt%)	20.82	19.47	18.17	17.89
Ni (wt%)	79.18	80.53	81.83	82.11

oxidized. Compared with pure nickel coating, the composite coating surface with few cracks perform more flat. The compact oxidation layer is formed in Ni/Lu₂O₃ (1.67) and Ni/Lu₂O₃ (2.99), as it can be seen from Fig. 5c and d, which inhibits the continuing oxidation in deep matrix by oxygen permeating. Thus, the oxidation extent of composite coating reduces constantly as the concentration of NLP increase. The oxygen content of pure nickel coating is 20.82%, however, the composite coating containing NLP (2.99 wt%) is 17.89%, which indicates the composite coatings have better high temperature oxidation resistance than pure nickel coating. This is attributed to the NLP prompts the formation of dense oxidation film.

4 Summary

Ni-Lu₂O₃ nanocomposite coatings were successfully prepared by electroplating. The content of nano-Lu₂O₃ in the composite coatings increased with a rise in the loading of nano-Lu₂O₃ particles from 0.4 g/L to 4 g/L, and then decreased with further increasing of nano-Lu₂O₃ particles in the plating bath. The maximum weight percent of Lu₂O₃ in the composite coating reached 2.99 wt%. The addition of nano-Lu₂O₃ particles refined the grain of nickel matrix and changed the preferred orientation of Ni crystal. The Ni-Lu₂O₃ composite coating exhibited a flat surface with lower roughness and better corrosion resistance both in acid and alkali solution compared with pure nickel coating. Moreover, the high temperature oxidation resistance at 800 °C of composite coatings was gradually enhanced as content of nano-Lu₂O₃ particles increased in the composite coatings. The improvement of corrosion resistance could enlarge the application of Ni electroplated coating.

References

1. Borkar, T., Harimkar, S.P.: Effect of electrodeposition conditions and reinforcement content on microstructure and tribological properties of nickel composite coatings. *Surf. Coat. Technol.* **205**(17–18), 4124–4134 (2011). <https://doi.org/10.1016/j.surfcoat.2011.02.057>
2. Saha, R.K., Khan, T.I.: Effect of applied current on the electrodeposited Ni–Al₂O₃ composite coatings. *Surf. Coat. Technol.* **205**(3), 890–895 (2010). <https://doi.org/10.1016/j.surfcoat.2010.08.035>
3. Cai, F., Jiang, C., Wu, X.: X-ray diffraction characterization of electrodeposited Ni–Al composite coatings prepared at different current densities. *J. Alloy. Compd.* **604**, 292–297 (2014). <https://doi.org/10.1016/j.jallcom.2014.03.063>
4. Maharana, H.S., Bishoyi, B., Basu, A.: Current density dependent microstructure and texture evolution and related effects on properties of electrodeposited Ni–Al coating. *J. Alloy. Compd.* **787**, 483–494 (2019). <https://doi.org/10.1016/j.jallcom.2019.02.096>
5. Bahrololoom, M.E., Sani, R.: The influence of pulse plating parameters on the hardness and wear resistance of nickel–alumina composite coatings. *Surf. Coat. Technol.* **192**(2–3), 154–163 (2005). <https://doi.org/10.1016/j.surfcoat.2004.09.023>
6. Ramesh Bapu, G.N.K., Jayakrishnan, S.: Development and characterization of electrodeposited Nickel–Titanium Carbo Nitride (TiCN) metal matrix nanocomposite deposits. *Surf. Coat. Technol.* **206**(8–9), 2330–2336 (2012). <https://doi.org/10.1016/j.surfcoat.2011.09.078>
7. Li, B., Li, D., Mei, T., Xia, W., Zhang, W.: Fabrication and characterization of boron nitride reinforced Ni–W nanocomposite coating by electrodeposition. *J. Alloy. Compd.* **777**, 1234–1244 (2019). <https://doi.org/10.1016/j.jallcom.2018.11.081>
8. Tirlapur, P., Muniprakash, M., Srivastava, M.: Corrosion and Wear Response of Oxide-Reinforced Nickel Composite Coatings. *J. Mater. Eng. Perform.* **25**(7), 2563–2569 (2016). <https://doi.org/10.1007/s11665-016-2117-1>
9. Singh, S., Sribalaji, M., Wasekar, N.P., Joshi, S., Sundararajan, G., Singh, R., Keshri, A.K.: Microstructural, phase evolution and corrosion properties of silicon carbide reinforced pulse electrodeposited nickel–tungsten composite coatings. *Appl. Surf. Sci.* **364**, 264–272 (2016). <https://doi.org/10.1016/j.apsusc.2015.12.179>
10. Xu, Y., Ma, S., Fan, M., Chen, Y., Song, X., Hao, J.: Design and properties investigation of Ni Mo composite coating reinforced with duplex nanoparticles. *Surf. Coat. Technol.* **363**, 51–60 (2019). <https://doi.org/10.1016/j.surfcoat.2019.02.016>
11. Shi, L., Sun, C.F., Zhou, F., Liu, W.M.: Electrodeposited nickel–cobalt composite coating containing nano-sized Si₃N₄. *Mater. Sci. Eng., A* **397**(1–2), 190–194 (2005). <https://doi.org/10.1016/j.msea.2005.02.009>
12. Lampke, T., Wielage, B., Dietrich, D., Leopold, A.: Details of crystalline growth in co-deposited electroplated nickel films with hard (nano)particles. *Appl. Surf. Sci.* **253**(5), 2399–2408 (2006). <https://doi.org/10.1016/j.apsusc.2006.04.060>
13. Pavlatou, E.A., Stroumbouli, M., Gyftou, P., Spyrellis, N.: Hardening effect induced by incorporation of SiC particles in nickel electrodeposits. *J. Appl. Electrochem.* **36**(4), 385–394 (2005). <https://doi.org/10.1007/s10800-005-9082-y>
14. Zimmerman, A.F., Palumbo, G., Aust, K.T., Erb, U.: Mechanical properties of nickel silicon carbide nanocomposites. *Mater. Sci. Eng., A* **328**, 137–146 (2002)
15. Wang, L., Gao, Y., Xue, Q., Liu, H., Xu, T.: Effects of nano-diamond particles on the structure and tribological property of Ni-matrix nanocomposite coatings. *Mater. Sci. Eng., A* **390**(1–2), 313–318 (2005). <https://doi.org/10.1016/j.msea.2004.08.033>
16. Campos, C.L., Roldán, C., Aponte, M., Ishikawa, Y., Cabrera, C.R.: Preparation and methanol oxidation catalysis of Pt–CeO₂ electrode. *J. Electroanal. Chem.* **581**(2), 206–215 (2005). <https://doi.org/10.1016/j.jelechem.2005.04.002>
17. Wang, Y., Jin, H., Chen, L., L, W.: Preparation and Corrosion Resistance of Ni–Co–CeO₂ Composite Coatings. *Surf. Technol.* **46**(10), 115–119 (2017)

18. Cârâc, G., Benea, L., Iticescu, C., Lampke, T., Steinhäuser, S., Wielage, B.: Codeposition of Cerium Oxide With Nickel and Cobalt: Correlation Between Microstructure and Microhardness. *Surf. Eng.* **20**(5), 353–359 (2004). <https://doi.org/10.1179/026708404x1134>
19. Qiong, J.: Effect of Rare Earth La on the Properties of Ni-Fe Alloy Coating. *Electroplat. & Pollut. Control.* **37**(2), 14–17 (2017)
20. Li, Z.Y., Cui, Q.W., Chen, B., Xu, J., Guo, H.: Fabrication and EDM Corrosion Resistance of Copper Electroforming Layer on Tube Electrode for Aero-Engine Blade Cooling Hole in EDM Process. *Key Eng. Mater.* **764**, 133–141 (2018). <https://doi.org/10.4028/www.scientific.net/KEM.764.133>
21. Zhang, Y., Hang, T., Dong, M., Wu, Y., Ling, H., Hu, A., Li, M.: Effects of 2-mercaptopyridine and Janus Green B as levelers on electrical resistance of electrodeposited copper thin film for interconnects. *Thin Solid Films* **677**, 39–44 (2019). <https://doi.org/10.1016/j.tsf.2019.03.012>
22. Napłoszek-Bilnik, I., Budniok, A., Łosiewicz, B., Pająk, L., Łągiewka, E.: Electrodeposition of composite Ni-based coatings with the addition of Ti or/and Al particles. *Thin Solid Films* **474**(1–2), 146–153 (2005). <https://doi.org/10.1016/j.tsf.2004.08.175>
23. Li, L., Wei, X.T., Zheng, G.M., Li, L.Y., Dai, C.S.: Electroforming of TiB₂-Reinforced Copper Matrix Electrode for EDM. *Mater. Manuf. Processes* **31**(6), 776–780 (2015). <https://doi.org/10.1080/10426914.2015.1070418>
24. Qu, N.S.: Synthesis of Ni-CeO₂ Nanocomposite Coatings by Electroforming. *Appl. Mech. Mater.* **248**, 48–53 (2012). <https://doi.org/10.4028/www.scientific.net/AMM.248.48>
25. Feng, Q., Li, T., Yue, H., Qi, K., Bai, F., Jin, J.: Preparation and characterization of nickel nano-Al₂O₃ composite coatings by sediment co-deposition. *Appl. Surf. Sci.* **254**(8), 2262–2268 (2008). <https://doi.org/10.1016/j.apsusc.2007.09.014>
26. Yang, B.W., Wang, Z., Xirong, Y.: Effect of cobalt content in electroforming fluid on the properties of nickel cobalt alloy electroforming mold core. *Materials Protection* **49**(1), 59–62 (2016)
27. Yao, J.H., Li, Y.W., Lin, H., Yang, Q.X., Li, Y.K.: Factors affecting internal stress of electroformed nickel in sulfate bath. *Electroplating & Finishing* **29**(3), 20–22 (2010)
28. Soares, H.J.M., Campos, O.S., Dias, D.F., Casciano, P.N.S., de Lima-Neto, P., Correia, A.N.: Chemical, morphological and corrosion characterisations of electrodeposited Ni-Fe-P coatings. *Electrochim. Acta* **284**, 18–23 (2018). <https://doi.org/10.1016/j.electacta.2018.07.151>
29. Jin, H.M., Chen, R.F., Zhang, J.F., Felix, A.C.: High Temperature Oxidation Mechanism of Nickel and Rare Earth Effect. *Mater. Mech. Eng.* **28**(5), 7–10 (2004)
30. Jin, H.M., Jiang, S.H., Dong, W.: Study on Oxidation Dynamics and Rare Earth Effects of Sputtered Ni-0.5Y Coating. *J. Mater. Eng.* **11**, 18–21 (2003)
31. Song, T., Tan, X.X., Tan, Z.J., Han, Z.Q.: High Temperature Protective Coatings with Reactive Element. *Surf. Technol.* **46**(8), 201–207 (2017)

Impact of Micromechanical and Carbon Fiber Properties on the Elastic Modulus of CFRP Woven Composites



Md. Mazedur Rahman and Saiaf Bin Rayhan 

Abstract In recent times, Carbon fiber reinforced polymers (CFRP) are widely adopted in various industries such as automobile, aerospace, marine, infrastructure, etc. due to their excellent strength to weight ratio. On the other hand, woven textile composites are replacing unidirectional composites since the fiber can be reinforced in more than one direction. To improve the mechanical behavior of CFRP woven composite materials, it is crucial to investigate their constituent properties at micro-level considering fiber material, fiber volume fraction, yarn volume fraction, yarn spacing, fabric thickness, etc. along with the type of weaving, such as plain, twill or satin. In this present research, a computational homogenization technique based on commercial finite element code Ansys is adopted to investigate the effect of constituent properties on the elastic modulus of plain and twill woven composites considering two different carbon fibers; namely, Carbon-290 and Carbon-395. Numerical results reveal that both fiber volume fraction and yarn volume fraction have a strong effect on the prediction of in-plane elastic modulus of CFRP composites. However, fabric thickness does not impact the prediction at all, while yarn spacing has a minor effect on the outcomes. Moreover, the weaving type does not affect the predictions significantly. Finally, it is found that Carbon-290 fiber provides higher elastic modulus values for any given condition than Carbon-395 fiber.

Keywords Carbon fiber reinforced polymer (CFRP) · Woven composite · Micromechanics · Computational homogenization · Ansys

1 Introduction

When two sets of yarn, namely, warp and weft are interlaced with each other at 90°, then the produced fabric is known as woven. From the last four decades, researchers have investigated the elastic properties of woven composites by developing both

Md. M. Rahman (✉) · S. B. Rayhan
School of Mechanical Engineering, Northwestern Polytechnical University, Xi'an, China
e-mail: mazed@mail.nwpu.edu.cn

analytical means and computational homogenization methods. At an early stage, Halpin et al. [1] first investigated the stiffness of 2D and 3D composites based on classical laminate theory, which was further developed by Ishikawa and Chou [2–4] establishing the mosaic model, undulation model, and bridging model. These models were further improved and the outcomes revealed that the yarn undulation and lamina thickness have a crucial role in the elastic moduli of plain-woven composites [5]. Moreover, the yarn gap between two adjacent layers and the laminate configuration for the different number of layers have a significant impact on the elastic properties of woven composites [6].

Since the geometry of the woven composite is quite complex, it is often troublesome to analyze the elastic properties based on the above-mentioned theories. Therefore, at a later stage, the homogenization technique based on RVE has gained popularity to determine the elastic properties. Carvelli and Poggi [7] proposed a homogenization technique to predict the stiffness and strength of the composite considering lamina thickness, yarn orientation, and fiber volume fraction. Angioni and Meoa [8] carried out a comparative study, which revealed that the asymptotic expansion homogenization method can be used to predict the mechanical properties of 2D woven composites. Though some discrepancies are found for out plane properties, but the in-plane properties of the composites were precisely calculated by this method. More recently, a two-step homogenization technique was adopted to estimate the mechanical properties of woven composites [9, 10]. It was found that the two-step homogenization is one of the easiest ways to predict the elastic properties accurately. Besides, a voxel-based homogenization technique was used to estimate the thermo-mechanical properties of woven composites [11]. A good agreement was established between the predicted and experimental results.

With the availability of modern powerful computers, the finite element method (FEM) has become an essential part to solve a wide range of real-world problems including the prediction of elastic properties considering micro-level parameters. With the help of FEM, Ichihashi et al. [12] calculated the mechanical properties of woven composites. Their study revealed that weave densities have a minor impact on microfracture stress. Further investigation based on FEM proved that it can predict the in-plane, out-plane young's and shear moduli of woven composites [13]. A recent study suggests that FEM can be used to predict interlaminar shear properties, cumulative damage failure, and crack deviation, although an obstacle is found to model the ceramic matrix composite [14]. FEM is also useful to analyze other micro-scale defects like voids [15], tow misalignments [16], etc. Moreover, FEM is regularly utilized to solve multiscale analysis where a direct impact of a micromechanical property can be investigated on a large structure [17, 18]. Finally, FEM can be time-efficient in the case of utilizing preloaded geometries for regular composite material like unidirectional, woven, chopped, etc. [19, 20].

In summary, micro-level analysis of various composite materials based on computational homogenization is an efficient technique, which can provide better material with lower cost reducing the necessity of experimental testing. In this current investigation, commercial FE code Ansys Material Designer is adopted to study the impact of micromechanical parameters, namely, fiber material, fiber

volume fraction, yarn volume fraction, yarn spacing, and fabric thickness along with two types of weaving, namely, plain and twill on the CFRP based woven composites.

2 Numerical Homogenization Procedure

2.1 Material Selection

To calculate the elastic modulus numerically, commercial finite element code Ansys Material Designer is adopted. For the present study, two different carbon fibers are selected which will be embedded in the epoxy matrix. Elastic properties of the fiber materials are chosen from Ansys Material Library, which is given below, Table 1 and the elastic properties of epoxy is adopted from the literature [21], Table 2.

2.2 RVE Geometry and Parametric Study Plan

For woven composite homogenization, a preloaded geometry with twill and weave type RVE is utilized, Fig. 1. For the parametric study, other micromechanical properties, namely, fiber volume fraction (V_f), yarn volume fraction (Y_f), yarn

Table 1 Elastic moduli of fibers

Name of fibers	E_{11} (GPa)	E_{22} (GPa)	ν_{12}	ν_{23}	G_{12} (GPa)	G_{23} (GPa)
Carbon-395	395	6	0.2	0.4	8	2.149
Carbon-290	290	23	0.2	0.4	9	8.2143

Table 2 Elastic moduli of matrix [21]

Name of matrix	E (GPa)	ν
Epoxy	5.35	0.354

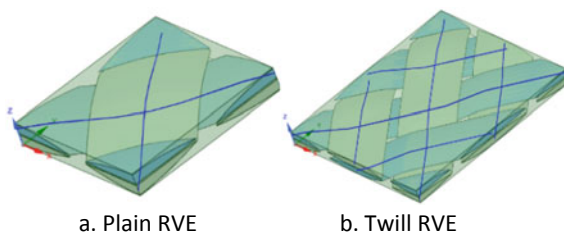


Fig. 1 RVE types of woven composites for present study

Table 3 Parametric study plan for the present study

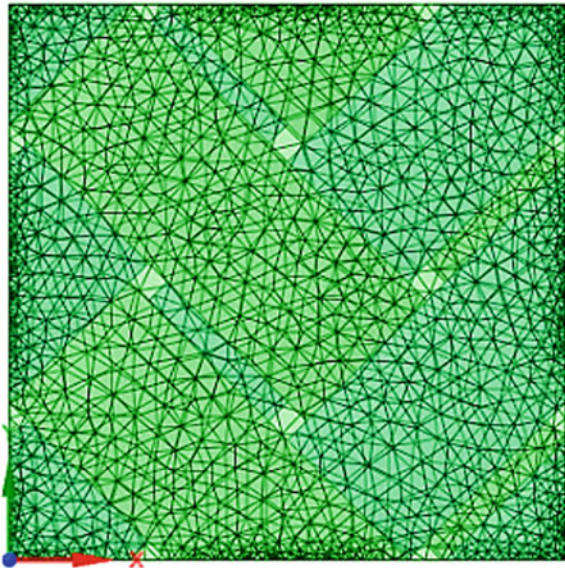
No.	Case study	Constant parameters	Value	Variable	Range
I	Effect of fiber volume fraction	Yarn volume fraction Yarn spacing Fabric thickness	0.755 1 mm 0.188 mm	Fiber volume fraction	0.2–0.7
II	Effect of yarn volume fraction	Fiber volume fraction Yarn spacing Fabric thickness	0.55 1 mm 0.188 mm	Yarn volume fraction	0.2–0.8
III	Effect of fabric thickness	Fiber volume fraction Yarn volume fraction Yarn spacing	0.55 0.755 1 mm	Fabric thickness	0.188–0.216 mm
IV	Effect of yarn spacing	Fiber volume fraction Yarn volume fraction Fabric thickness	0.55 0.755 0.188 mm	Yarn spacing	0.5–2 mm

spacing, and fabric thickness are used as variables to investigate their effects on the elastic modulus of plain and twill type woven composites made of above-mentioned fibers and matrix. The plan of the parametric study is given in Table 3. Please note that both the constant parameters and variable ranges are selected based on the experimental possibilities found in the literature [22].

2.3 Mesh Generation and Boundary Conditions

To mesh the RVE geometry, conformal periodic meshing is adopted, which is provided by the software by default, Fig. 2. The main reason for choosing the periodic meshing is that, with periodic meshing, a periodic boundary condition can be selected, which provides a better solution to the problem and no convergence problem occurs. A detailed boundary condition with periodic and non-periodic setup can be found in the Ansys Material Designer user's manual [20]. Please note that the manual input of the boundary condition is not required to attain the finite element homogenization results.

Fig. 2 Periodic mesh generation



3 Numerical Results Discussion

3.1 Impact of Fiber Volume Fraction

At first, the impact of the fiber volume fraction (V_f) on the elastic modulus of woven composites are shown in Fig. 3. For in-plane elastic modulus, it is apparent that as the fiber volume fraction increases, a steep increase in the prediction of

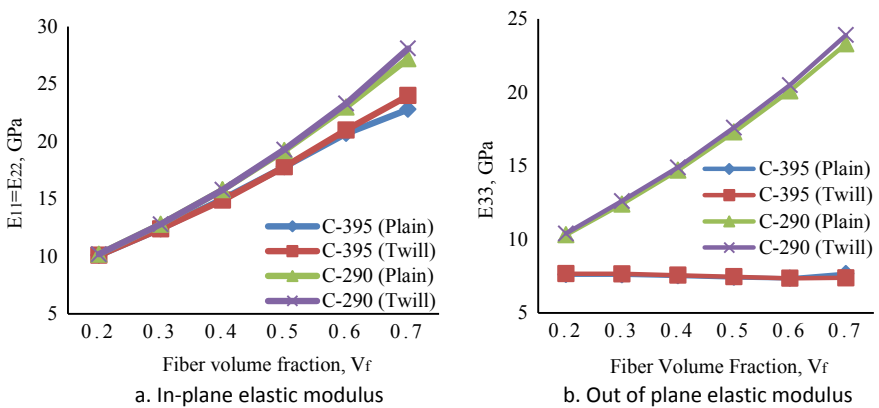


Fig. 3 Predicted elastic modulus against fiber volume fraction

elastic modulus is observed. Moreover, Carbon-290 (C-290) fiber provides a higher elastic modulus than Carbon-395 (C-395) fiber, which becomes apparent after $V_f = 0.35$. Furthermore, the weaving type (twill or plain) does not have any influence for both carbon fibers until $V_f = 0.6$.

For, out of plane elastic modulus, an interesting observation is found, Fig. 3b. For Carbon-395 fiber, V_f does not have any influence on the elastic modulus regardless of the weaving type. However, Carbon-290 fiber provides a similar trend as the previous finding, when increasing the V_f would increase the elastic modulus linearly.

3.2 Impact of Yarn Fiber Volume Fraction

Unlike the previous case study, yarn fiber volume fraction (Y_f) has a negative impact on the in-plane elastic modulus of woven composites, Fig. 4a. In the beginning, when $Y_f = 0.6$, the plain and twill type weaving prediction of elastic modulus has a difference of 4.73 and 2.95% for Carbon-395 and Carbon-290 fibers, respectively. However, this difference has been diminished as the Y_f value increases linearly. Interestingly, for out of plane elastic modulus, the calculated values are found to be constant for Carbon-395 fiber despite increasing the Y_f values. However, a declining trend is observed for Carbon-290 fiber, which linearly decreases with increasing values of Y_f .

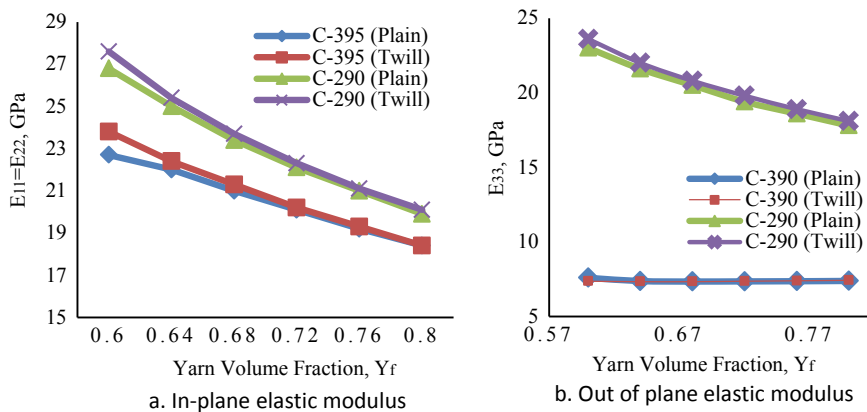


Fig. 4 Predicted elastic modulus against yarn volume fraction

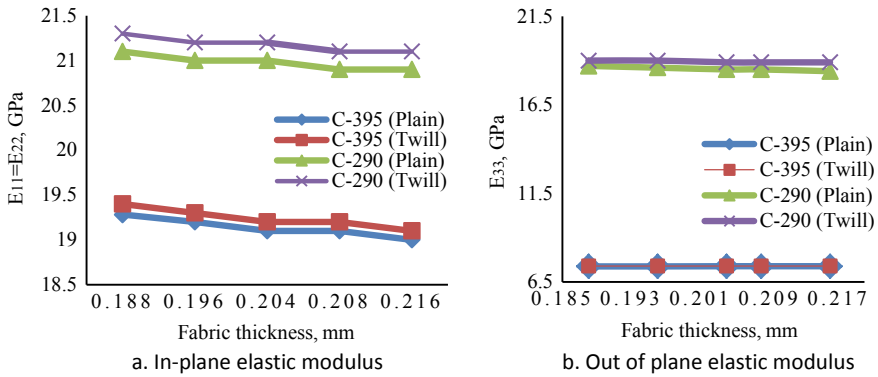


Fig. 5 Predicted elastic modulus against fabric thickness

3.3 Impact of Fabric Thickness

Numerical predictions of in-plane and out of plane elastic modulus due to the fabric thickness ranging from 0.188 mm to 0.216 mm can be found in Fig. 5. From the illustration, it is observed that for both Carbon-290 and Carbon-395 GPa fibers, no significant impact due to the increment of fabric thickness is found despite altering the weave type from plain to twill.

3.4 Impact of Yarn Spacing

Finally, the influence of yarn spacing on the calculated elastic modulus is illustrated in Fig. 6. For in-plane elastic modulus, in the beginning, changing the yarn spacing from 0.5 mm to 0.75 mm has a moderate impact on the elastic modulus of the carbon fibers and their weaving type. An increment of 7.9 and 5.5% is found for Carbon-395 (plain) and Carbon-290 (plain) fibers, respectively. However, a further increment of yarn spacing values does not affect the elastic modulus significantly.

For out of plane elastic modulus, yarn spacing has no impact on the predictions for Carbon-395 fibers, Fig. 6b. A slight influence of yarn spacing is observed at the beginning for Carbon-290 fibers, which also reduces with the increment of spacing values.

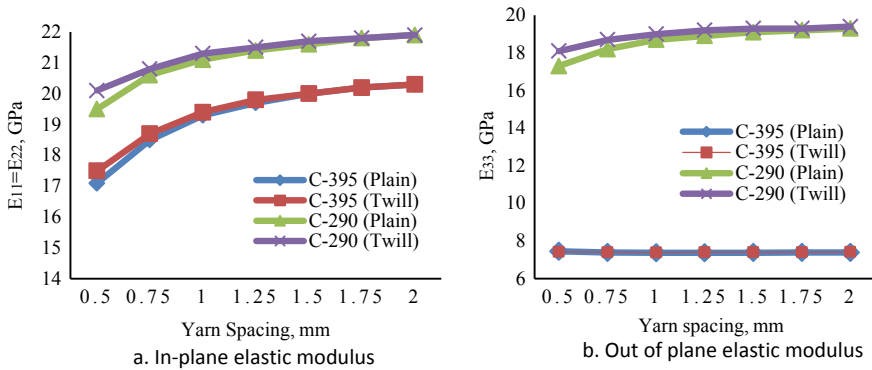


Fig. 6 Predicted elastic modulus against yarn spacing

4 Conclusion

A series of numerical simulations were conducted to analyze the impact of micromechanical and carbon fiber properties on the elastic modulus of CFRP woven composite materials. From the investigation, it is found that despite Carbon-395 fiber possesses higher longitudinal elastic modulus (E_{11}) than Carbon-290 fiber, however, it provides lower in-plane and out of plane elastic modulus while embedded in the matrix to produce CFRP woven composites. A primary reason for this phenomenon is that the transverse elastic modulus of Carbon-295 fiber is almost 97% higher than Carbon-395 fiber, which plays a crucial role for the differences found in the numerical study. Some other important findings are listed below.

- Fiber volume fraction has a strong influence on the elastic modulus prediction of woven composites. In-plane elastic modulus increases linearly with the increment of fiber volume fraction.
- Unlike the fiber volume fraction, the yarn volume fraction has an adverse effect on the elastic modulus calculation. In-plane elastic modulus decreases linearly with the increment of yarn volume fraction.
- Fabric thickness does not affect the outcomes of elastic modulus of CRFP woven composites.
- Yarn spacing has a minor effect on the estimation of elastic modulus, which also diminishes with higher spacing.
- Type of weaving (Twill or plain) has a minor impact on the prediction of elastic modulus. However, in some cases, twill weave provides slightly higher elastic modulus than plain weave.

Acknowledgements The authors are grateful to China Scholarship Council (CSC) to finance their research at Northwestern Polytechnical University, China (CSC grant No. GXZ023506).

References

1. Halpin, J., Jerine, K., Whitney, J.: The Laminate Analogy for 2 and 3 Dimensional Composite Materials. *J. Compos. Mater.* **5**(1), 36–49 (1971)
2. Ishikawa, T., Chou, T.: Elastic Behavior of Woven Hybrid Composites. *J. Compos. Mater.* **16**(1), 2–19 (1982)
3. Ishikawa, T., Chou, T.: One-dimensional micromechanical analysis of woven fabric composites. *AIAA J.* **21**(12), 1714–1721 (1983)
4. Ishikawa, T., Chou, T.: Stiffness and strength behaviour of woven fabric composites. *J. Mater. Sci.* **17**(11), 3211–3220 (1982)
5. Naik, N., Shembekar, P.: Elastic Behavior of Woven Fabric Composites: I—Lamina Analysis. *J. Compos. Mater.* **26**(15), 2196–2225 (1992)
6. Naik, N., Shembekar, P.: Elastic Behavior of Woven Fabric Composites: III—Lamina Design. *J. Compos. Mater.* **26**(17), 2522–2541 (1992)
7. Carvelli, V., Poggi, C.: A homogenization procedure for the numerical analysis of woven fabric composites. *Compos. A Appl. Sci. Manuf.* **32**(10), 1425–1432 (2001)
8. Angioni, S., Meo, M., Foreman, A.: A comparison of homogenization methods for 2-D woven composites. *Compos. B Eng.* **42**(2), 181–189 (2011)
9. Liu, X., Rouf, K., Peng, B., Yu, W.: Two-step homogenization of textile composites using mechanics of structure genome. *Compos. Struct.* **171**, 252–262 (2017)
10. Hayat, K., Lei, X., Ali, H.: Prediction of elastic behavior of woven fabric reinforced plastics composites using two-step homogenization. 2018 15th International Bhurban Conference on Applied Sciences and Technology (IBCAST) (2018)
11. Smitheman, S., Jones, L., Long, A., Ruijter, W.: Iccm-central.org. (2009). Available at: <http://iccm-central.org/Proceedings/ICCM17proceedings/papers/D11%20%20Smithman.pdf>. Accessed 18 October 2020
12. Ichihashi, H., Hamada, H., Ikuta, N., Maekawa, Z.: Finite element analysis of woven fabric composites considering interfacial properties. *Compos. Interfaces* **2**(2), 81–94 (1994)
13. Choi, J., Tamma, K.: Woven fabric composites-part I: Predictions of homogenized elastic properties and micromechanical damage analysis. *Int. J. Numer. Meth. Eng.* **50**(10), 2285–2298 (2001)
14. Choi, A., Heness, G. and Ben-Nissan, B.: Using finite element analysis to understand the mechanical properties of ceramic matrix composites. *Advances in Ceramic Matrix Composites*, pp. 375–400 (2018)
15. Jiang, H., Ren, Y., Liu, Z., Zhang, S.: Microscale finite element analysis for predicting effects of air voids on mechanical properties of single fiber bundle in composites. *J. Mater. Sci.* **54**(2), 1363–1381 (2018)
16. Mekonnen, A., Woo, K.: Effects of Defects on Effective Material Properties of Triaxial Braided Textile Composite. *Int. J. Aeronaut. Space Sci.* **21**(3), 657–669 (2020)
17. Nguyen, D., Wang, H.: Multi-Scale Analyses of Three Dimensional Woven Composite 3D Shell With a Cut Out Circle. *Appl. Compos. Mater.* **26**(1), 339–356 (2018)
18. Rayhan, S., Rahman, M.: Modeling elastic properties of unidirectional composite materials using Ansys Material Designer. *Procedia Structural Integrity* (2020)
19. Ansys Inc.: Ansys Material Designer User’s Guide. Ansys Inc., Canonsburg, PA (2018)
20. Rayhan, S., Rahman, M.: Effect of micromechanical properties on the critical buckling load of woven composite plate: A multiscale analysis. *Procedia Structural Integrity* (2020)
21. Younes, R., Hallal, A., Fardoun, F., Hajj, F.: Comparative Review Study on Elastic Properties Modeling for Unidirectional Composite Materials. *Composites and Their Properties* (2012)
22. Aliabadi, M.: *Front Matter. Woven Composites*. Imperial College Press, London (2015)

Microstructure and Performance Control of Copper/Stainless Steel Wire-Feeding Laser Welding Joint



Xiaoyan Gu, Ziwei Cui, and Jiaxu Shao

Abstract Wire-feeding laser welding of copper/stainless steel was carried out by filling nickel-based welding wire. ANSYS finite element numerical simulation software was used to analyze the temperature field of the joint, the diffusion of interface elements and the microstructure of the joint were studied. The influence of welding power on joint microcracks is analyzed. The study found that as the welding power increased, the cooling rate of the joint decreased, and the temperature gradient on the copper side weld decreased. This promoted the transformation of columnar dendrites on the copper side to equiaxed dendrites and effectively suppressed microcracks in the weld. In order to show the fracture mechanism of the joint, digital image correlation technology (DIC) is used to analyze the local mechanical behavior of the joint. The weld joint had achieved the ultimate tensile strength (UTS) of 239.5 ± 2.11 MPa, which is 84.8% of the strength of the copper base metal and all the joints were fractured in the Cu-HAZ, the fracture mode was ductile fracture.

Keywords Laser technology · Copper · Stainless steel · Digital image correlation · Mechanical properties

1 Introduction

Because of the excellent thermal conductivity and ductility, copper and copper alloys have been widely used in the power generation industry. Austenitic stainless steel has excellent resistance to erosion. Copper/stainless steel composite components not only have relatively high electric, heat performance, wear resistance and erosion resistance, but also are light weight and with high strength. The copper/stainless steel joint has been widely used in the nuclear industry, petrochemical and

X. Gu (✉) · Z. Cui · J. Shao
Ministry of Education, College of Materials Science and Engineering, Jilin University,
Changchun 130022, China
e-mail: guxiaoyan821@sina.com

© The Author(s), under exclusive license to Springer Nature Switzerland AG 2021
L. Zheng et al. (eds.), *Proceedings of MEACM 2020*,
Mechanisms and Machine Science 99,
https://doi.org/10.1007/978-3-030-67958-3_33

305

chemical industries. Although no brittle intermetallic compounds are formed between copper and stainless steel, the physical and chemical properties of copper and stainless steel (especially melting point and thermal conductivity) are quite different, and the penetration of copper along the heat-affected zone of steel may also causes hot cracks [1].

Tradition fusion welding methods such as electron beam welding, laser welding, and tungsten gas shielded welding have their own limitations. The vacuum conditions is harsh in the electron beam welding [2, 3], the beam seam has high requirements for the medium degree in the laser welding [4], current carrying capacity is limited in the gas shielded welding welding and the fusion welding process will cause serious copper burning [1]. Friction stir welding [5–9] and explosive welding [10, 11] are solid-state weilding methods that have disadvantages of strict tool compensation conditions and high safety regulations. Previous researches showed that wire-feeding laser welding was conducted with high energy density, small post-welding deformation, high welding efficiency, as well as no vacuum requirements, furthermore, it also has the advantages of reduced assembly accuracy, convenient metallurgical adjustment, and unlimited joint forms [12, 13]. Therefore, an effective combination between copper and stainless steel will be technically obtained.

In this paper, the method of wire-feeding laser welding was used to obtain copper/stainless steel dissimilar metal joints, and the interface characteristics, microstructure and performance characteristics of the joints were studied, which lays a theoretical foundation for the practical application of copper/stainless steel wire-feeding laser welding.

2 Test Materials and Methods

2.1 Experiment Materials

The base metals used in this study were T2 copper alloy and 304 austenitic stainless steel sheets. For wire-feeding laser welding, all the as-received 1 mm-thick sheets were machined to dimensions of 100 mm × 50 mm. The welding wire used was nickel-based stainless steel welding wire with a diameter of 1.2 mm. The chemical composition is shown in Tables 1, 2, and 3.

Table 1 Chemical composition of 301 stainless steel

Ingredient	C	Mn	Si	Cr	Ni	P	S
content	≤ 0.15	≤ 2.00	≤ 1.00	16.0–18.0	6.0–8.0	≤ 0.035	≤ 0.03

Table 2 Chemical composition of T2 red copper

Ingredient	Cu	Bi	Pb	Sb	Fe	As	S
content	99.90	0.001	0.005	0.002	0.005	0.002	0.005

Table 3 Chemical composition of nickel-based welding wire

Ingredient	Ni	Mn	Fe	Cu	Cr	Nb	Ti	Si
content	≥ 67	2.5–3.5	≤ 3	≤ 0.5	18–22	2–3	≤ 0.75	≤ 0.5

2.2 Experiment Equipments

Figure 1 shows the laser welding system used in the experiment. The welding machine is an RC-YLS-2000 fiber laser with a rated power of 3 KW.

2.3 Test Method

Before welding, the samples were polished with sandpapers to remove the oxide film. Welding test was carried out on the butt joint, the butt gap was set as 0.4 mm, the laser was offset and irradiated on the stainless steel. The offset was set as 0.1 mm. Pure argon gas was adopt to maintain the side blowing protection, and

Fig. 1 RC-YLS-2000 fiber laser and manipulator



flow rate of the gas was 10 L/min. Our results of the preliminary experiments showed that welding defects such as macroscopic deformation and abnormal deposition of filler materials appeared in the joint under high welding power. Results conducted at low welding power showed that the penetration depth at the root of the weld was insufficient. When the welding power was set as 1400–1600 W, there were no defects such as macroscopic deformation, undercut, and spatter occurred in the joint. Therefore, the welding parameters used in this study were selected as welding speed, 0.020 mm/s, wire filling rate, 0.015 mm/s and welding power 1400–1600 W. Test results of the laser welding showed that the specimen was corroded with an etching solution of 25 g FeCl₃, 25 mL HCL, 100 mL H₂O for 10–15 s. Scope Axio ZEISS type metallurgical microscope, TESCAN type scanning electron microscope, EDAX type energy dispersive spectrometer and X'pert3 X-ray diffractometer were used here to observe and analyze the interface formation, microstructure and fracture morphology of the welded joint. The standard tensile test was performed using the MT-810 test machine at the displacement rate of 0.8 mm/min. The joints under each process parameter was subjected to three tensile tests, and the average value was taken as the joint tensile force under each parameter. Furthermore, by using the standard DIC test procedures, 2D digital image correlation (DIC) experiments were performed with the shooting spatial resolution of 30 pixels/mm in the position control mode.

3 Results and Discussion

3.1 Temperature Field Analysis

Figure 2a shows that the isotherms on the copper side and the steel side were distributed asymmetrically, and the temperature gradient on the stainless steel side was higher. This is mainly because copper has higher thermal conductivity. The heat-affected zone, weld zone and base metal zone were marked in Fig. 2a. Four characteristic locations were selected as observation points (point 1234), which correspond to the center of the weld, the weld near stainless steel side, the weld near copper side and the copper heat-affected zone. According to the numerical simulation process, the four-point welding process thermal cycle curve was extracted (Fig. 2b). Figure 2b shows that the slopes of the thermal cycle curves at 4 points during the heating process were all large, indicating that the heated area heats up quickly. The peak temperature of points 1 and 2 exceeded 1450 °C (stainless steel melting temperature), and the peak temperature of point 3 exceeded 1083 °C (copper melting temperature), which indicates the melting of copper and stainless steel during heating; The peak temperature of point 4 was between 433.8 °C (copper recrystallization temperature) and 1083 °C. The temperature in the haz on Cu side exceeded the copper recrystallization temperature, which indicates the grain

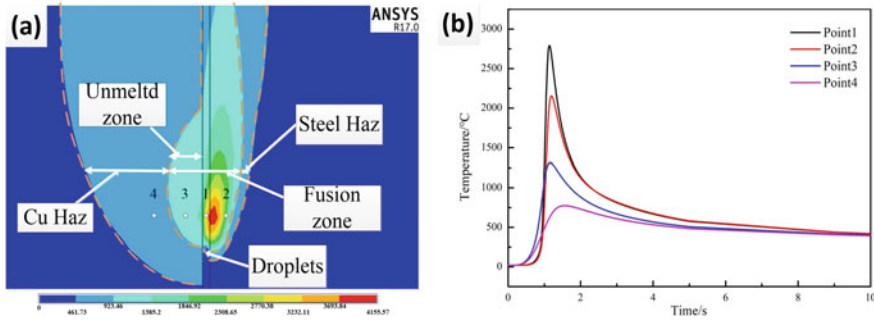


Fig. 2 Temperature field simulation (a) Temperature distribution cloud diagram of temperature field at 3 s (b)

growth in the haz on Cu side compared to the base material. During the cooling process, the temperature at point 3 dropped to the melting point of copper first, which indicates that the weld near copper side solidifies first.

3.2 Joint Microstructure Analysis

The optical micrographs on the copper base metal and the haz has been shown in Fig. 3. Our results showed that copper grains in the heat-affected zone were heated to grow and a large number of twins were formed compared to the copper base material (Fig. 3a). As copper has a better thermal conductivity and a large amount of heat was dissipated from the copper side, the joint produced a wider heat-affected zone at the copper side than that of the stainless steel. It can be seen from our results of analysis in 3.1 that the peak temperature of the copper heat-affected zone increased the recrystallization temperature of copper (433.8 °C). As a result, the heat-affected zone grains recrystallized during the welding process, making

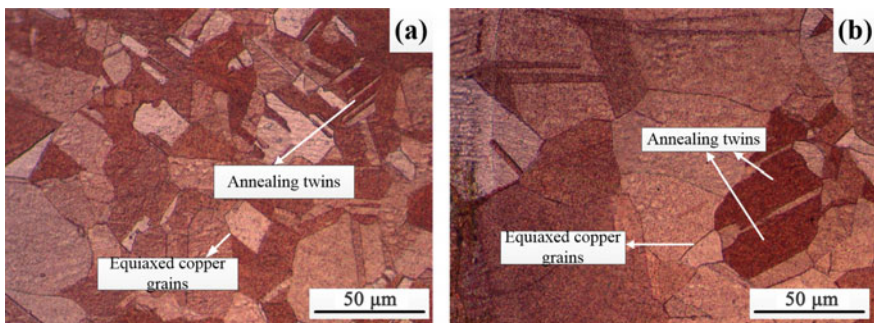


Fig. 3 Optical micrographs of local weld zones: a Cu-BM, b Cu-HAZ

the grains coarser (Fig. 3b). In addition, accidental stacking faults occurred when the interface moved in the recrystallization process of copper grains, and co-lattice twin boundaries were formed. Indicating that coarsening of the grains in the copper heat-affected zone may affect the mechanical properties of the joint.

The optical micrographs on the Cu-weld interface were shown in Fig. 4. Our results showed that the partially melted copper near the fusion line did not blend with the stainless steel base material and the welding wire melted in the molten pool (Fig. 4a). This part of unblent liquid copper re-solidified to form the unblent zone (a thin layer of molten copper) at the joint. Formation of the unblent zone was mainly due to the different chemical composition and solidification sequence between the copper base material and the weld. During the welding process, liquid metal in the molten pool included molten copper, stainless steel and welding wire. Since the main components of welding wire and the stainless steel base metal were exactly the same, it can be suggested that the main constituent elements of the liquid metal in the molten pool were Fe and Ni (stainless steel base material of the welding wire). Cu-Ni and Cu-Fe systems have different surface tensions, and difference in the surface tension results in liquid immiscibility. Analysis of solidification sequence in 3.1 illustrated that the molten copper solidified first during the cooling process of the molten pool, which made the cooling time of the molten pool be shorter. In addition, near the fusion line on the copper side, the unblent area at the root and top of the weld was narrow, while the unblent area at the middle of the weld was wide (Fig. 4a). This may result from that the convection and compression dominate the specific position of weld root and top, promoting the blending of copper and stainless steel in the molten pool. Moreover, the steel swirling into the copper-side matrix weld near the copper-side fusion line, which was caused by the stirring effect of the flow vortex in the molten pool, and it was also one of the reasons for the good mechanical properties of the joint (Fig. 4b–c).

Figure 5 shows the optical micrographs in the fusion zone. It is showed that there was a confluence of solidified grains in the middle of the weld, the grain morphology on the copper side was typical equiaxed dendrites while on the steel side was columnar dendrites (Fig. 5b). This may result from that the solidification rate, local temperature and composition gradient at the copper side and the steel side of the weld were different. The ferrite-rich regions were distributed in the form of

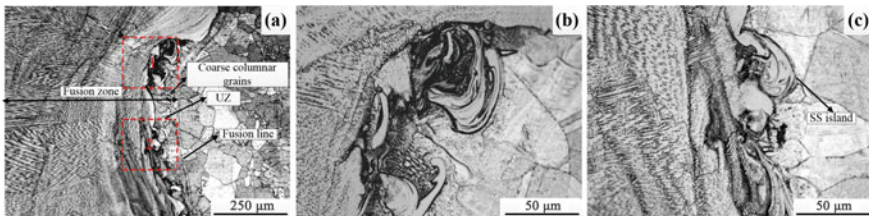


Fig. 4 Optical micrographs of local weld zones: **a** Cu-weld interface, **b** Enlarged view of position 1, **c** Enlarged view of position 2

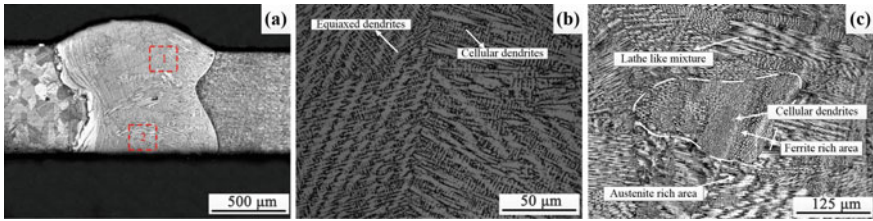


Fig. 5 Optical micrographs of local weld zones: **a** Fusion zone, **b** Enlarged view of position 1, **c** Enlarged view of position 2

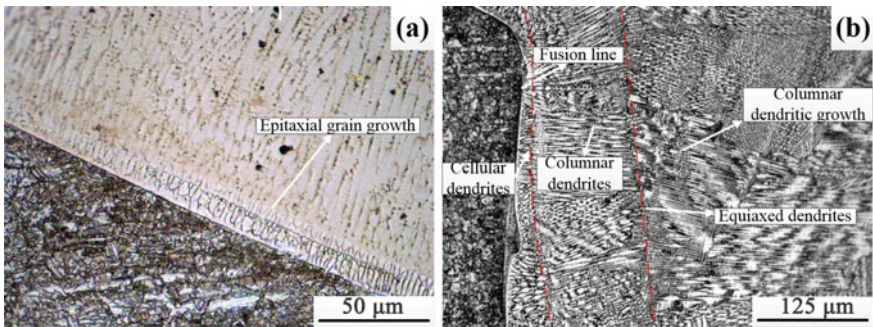


Fig. 6 Optical micrographs of local weld zones: **a** upper side of SS-weld interface, **b** under side of interface

cellular crystals and surrounded by the austenite-rich regions in the form of lath dendrites (Fig. 5c). This was caused by the non-equilibrium rapid cooling of the fusion zone that promoted by the high thermal conductivity of copper and the composition gradient in the weld zone.

The optical micrographs on the SS-weld interface has been presented in Fig. 6. Our results showed that there was a typical epitaxial growth of the cellular grains near the fusion line on the steel side of the weld, and followed by the columnar dendrites (Fig. 6a). And the grain morphology changed from the fusion line to the middle of the molten pool showed the cell crystals, columnar crystals and columnar dendrites (Fig. 6b). Resulting from that the temperature gradient on the stainless steel side decreased while the crystallization rate increases as the solidification proceeded. And increase in segregation of alloying elements further leads to an increase in the component undercooling.

The SEM and corresponding micrographs captured along the Cu⁻ weld interfaces has been illustrated in Fig. 7. Our results showed that the weld interface was clear, and there were no defects near the interfaces on both sides (Fig. 7a); Scan results of EDS line in this study showed that there were two areas with entirely different composition distributions in the weld (Fig. 7b). In area 1, due to the

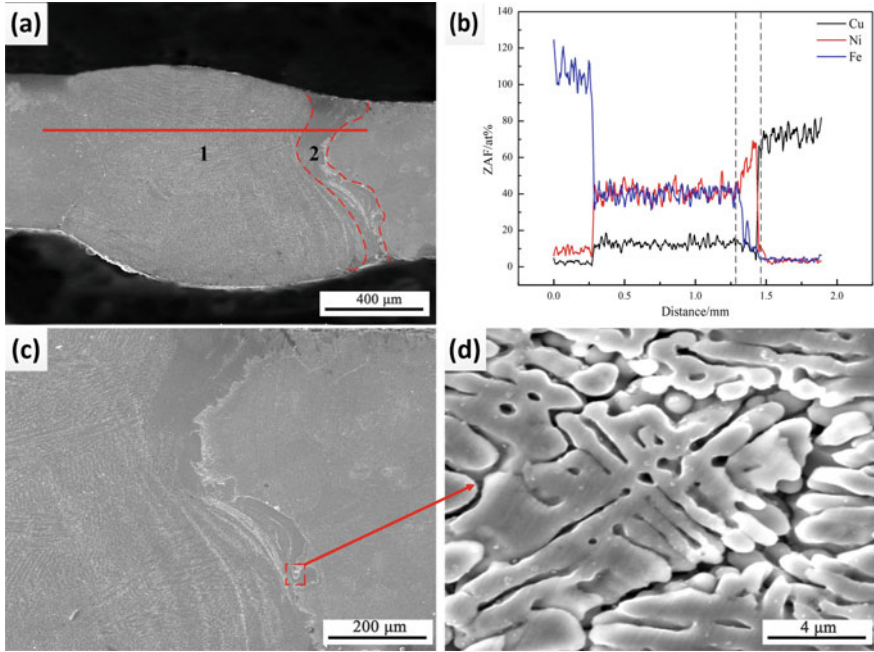


Fig. 7 The SEM and its corresponding SEM micrographs micro morphology of the joint when the welding power is 1600 W. **a** Cross section of joint; **b** EDS line scan result; **c** Micro morphology on copper side interface; **d** Enlarged view in the dotted frame in **c**

dilution of the nickel-based welding wire on the base material of stainless steel 301, content of iron in the weld was much lower than that in the base metal of 301 stainless steel, and the ingredients were evenly distributed (Fig. 7b). Element distributions on the copper interface in area 2 was with different gradient, and the nickel content was much higher than the iron, which confirmed that this area was a nickel-based stainless steel wire without sufficiently blending. And in the microstructure of the weld near the copper side fusion line, the bright characteristic copper element was uniformly distributed, the atomic number of copper was higher than that of the iron and the nickel, so the copper element in the weld had bright characteristics (Fig. 7c). Heat conduction and heat convection made part of the copper base material melt and evenly dispersed into the weld (Fig. 7c); Additionally, there were equiaxed dendrites with primary and secondary dendrite arms at the interface on the copper side, this is because the composition super-cooling of the copper side weld transformed long columnar grains into the equiaxed dendrites (Fig. 7d). These equiaxed dendrite structures have high resistance to the thermal cracking during the solidification of the weld metal.

SEM and corresponding micrographs captured along the Cu⁻ weld interfaces under different powers were represented in Fig. 8. Our results showed that there were obvious micro cracks when the welding power was 1400 W, which was

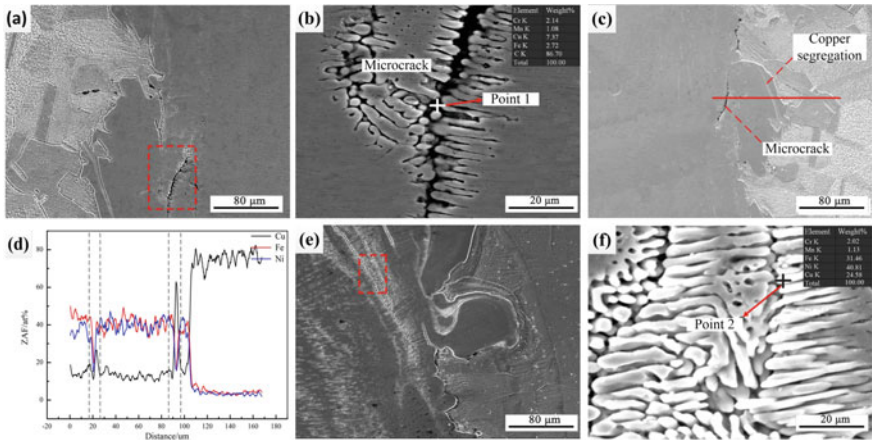


Fig. 8 The SEM and its corresponding SEM micrographs micro morphology of the joint under different power. **a** The micro morphology of the joint when the welding power is 1400 W; **b** The enlarged view of the dotted box in **a**; **c** The micro morphology of the joint when the welding power is 1500 W; **d** EDS line scan results; **e** The micro morphology of the joint when the welding power is 1600 W; **f** the enlarged view of the dotted box in **e**

mainly caused by the large residual stresses after welding, the fast cooling rate of the joint and the insufficient transformation of the weld structure (Fig. 8a). Since the thermal expansion coefficients of copper and stainless steel were totally different, and the obvious stress was concentrated at the interface between the copper and the weld, it is easy to form cracks in this area during the cooling process. And the EDS analysis at a previous point of the microcrack showed that there was a large amount of carbon in the microcrack (Fig. 8b). It can be indicated that when the welding power was low, the cooling rate was fast, and impurity elements such as carbon and phosphorus were segregated at the cracks, which will form a low melting point eutectic. While when the welding power was 1500 W, in addition to the obvious presence of microcracks, there was also copper segregation at the copper side interface (Fig. 8c). And the content of iron, nickel, and copper dropped sharply at the cracks, while the copper content peaked at the copper segregation (Fig. 8d). Segregation of the copper will cause more inhomogeneities and thermal stresses, resulting in more microcracks. When the welding power was 1600 W, there were no micro cracks in the joint (Fig. 8e). The result of EDS analysis showed that Cu-Ni solid solution phase was formed in the weld (Fig. 8f). It is proposed that increasing of the welding power will increase the welding heat input, reduce the cooling rate of the joint, and reduce the temperature gradient on the weld near copper interface, this promotes the transformation of columnar grain to equiaxed grain on the weld near copper interface. So the micro-cracks in the weld were effectively suppressed. Taken together, our results indicated that reducing the strain rate of the weld metal and the transformation of columnar grain to equiaxed grain will effectively suppress microcracks in the weld.

Figure 9 showed the XRD diffraction analysis of the micro area at the interface of the joint. The main structure of the copper side interface was mainly constituted of copper-nickel solid solution (Cu(Ni)) (Fig. 9a), which confirmed the effective diffusion of copper into the weld; And the interface of stainless steel was mainly constituted of iron-nickel solid solution (Fe(Ni)) (Fig. 9b), which confirmed the diffusion between the stainless steel base metal and the weld. Taken together, there was no formation of intermetallic compounds on both sides of the interface, which avoided the formation of cracks in the weld.

Figure 10 showed the EBSD map and high spatial resolution pole map (PF) map of the local welding area. there was obvious epitaxial grains growth on the fusion line(Fig. 10a). The grain growth direction of the columnar crystals was consistent with the flow direction of the heat in the weld and both were perpendicular to the fusion line. Under the combination of the non-uniform nucleation and overcooling of the component, weld zone had elongated columnar grains (Fig. 10a). Due to the difference in spatial resolutions between SEM and EBSD, this morphology can only be observed in EBSD. As the high cooling rate of the laser wire filler occurred in welding process, there was no obvious heat affected zone in the stainless steel base metal. And our results of SS-BM showed that stainless steel base material existed more randomly equiaxed austenite grains instead of the preferentially oriented FCC structure(Fig. 10b).

Our results of tensile strength and elongation showed that the average tensile strength of joint 1, 2, and 3 were 229 MPa, 226 MPa and 224 Mpa, respectively, accounting for 84.8, 83.7 and 82.9% of the tensile strength of copper plates (Fig. 11). The average elongation of the joint was 15.6, 19.4 and 20.6%, respectively (Fig. 11). As the welding power increased, average area of the grains in the copper heat-affected zone increased as well, while the tensile strength of the joint decreased. This may result from that when the heat input increased, average area of

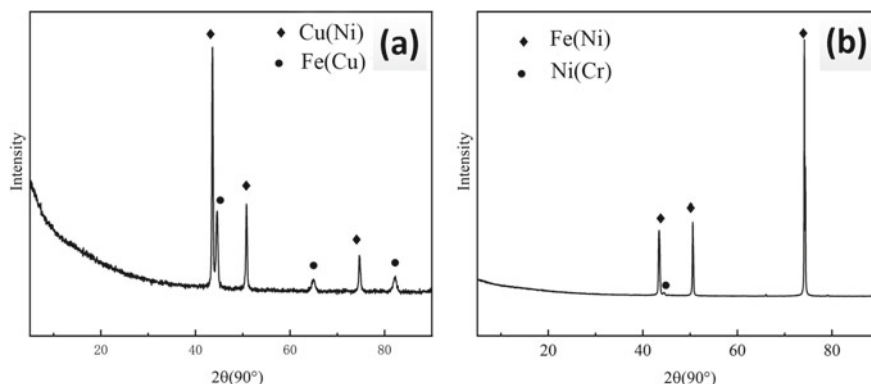


Fig. 9 Micro-area XRD diffraction analysis. **a** Copper side interface XRD; **b** Stainless steel interface XRD

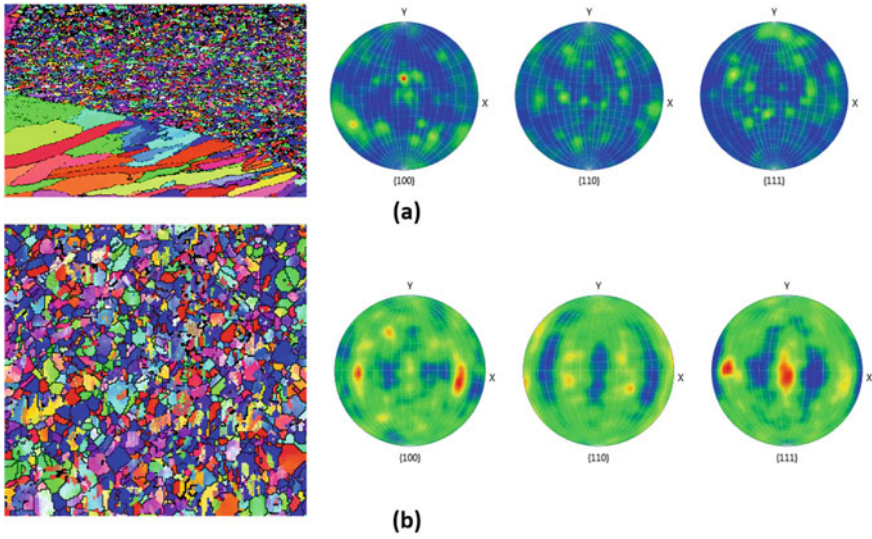
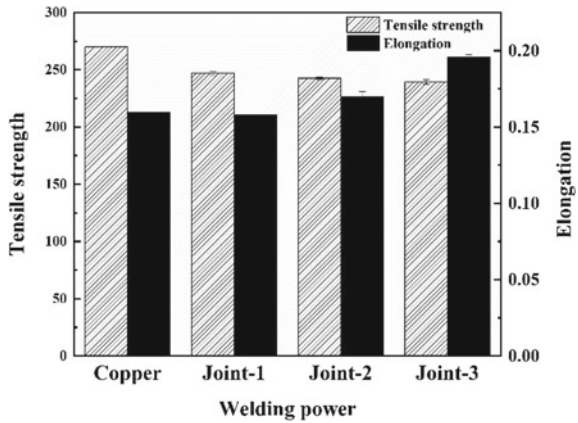


Fig. 10 EBSD-PF micrograph of partial weld sub-area. **a** SS-welding interface; **b** SS-BM

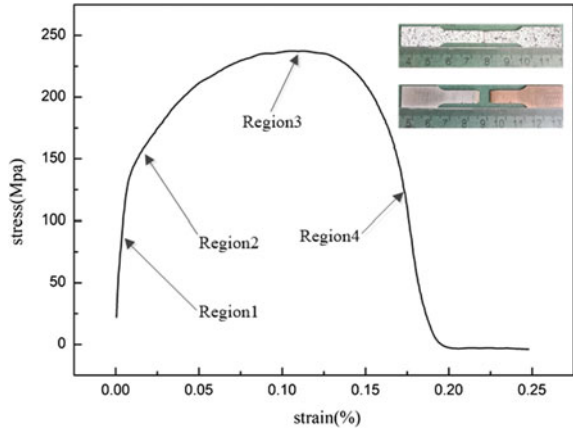
Fig. 11 The tensile strength and elongation of the joint



the grains in the heat-affected zone of the copper base metal increased, which led to an obvious decrease in the tensile strength of the joint.

Furthermore, results of the joint stress-strain curve showed that the joint fractured in a ductile fracture mode (Fig. 12). Four typical moments 1, 2, 3, 4 were selected on the stress-strain curve and digital image correlation (DIC) technology was used to analyze the local mechanical behavior of the joints. Figure 13 showed that at time point 1, the copper/301 stainless steel joint did not show obvious strain localization under low tensile stress (Fig. 13a). At time point 2, plastic deformation and strain localization appeared and the strain field of the copper/301 stainless steel

Fig. 12 Stress-strain curve of the joint



joint was still relatively uniform (Fig. 13b). The necking did not appear until time point 3, localization of the strain was obvious, and Cu-HAZ accumulated a large amount of strain (Fig. 13c). As shown in the red box of Fig. 13, strain localization points of the copper/301 stainless steel joints were all located in the copper heat-affected zone, indicating that the fracture started from the copper haz. And at time point 4, the strain increased and the strain localization phenomenon became more obvious as the tensile test proceed (Fig. 13d). Strain localization point of the copper/301 stainless steel joint reached 0.852, and the joint fractured at the copper heat-affected zone, which also corresponded to the fracture position showed in Fig. 12. All these tensile specimens analyzed in this test fractured in the copper heat-affected zone instead of the weld zone, implying that the copper heat-affected zone was the weak location of the entire welded joint. Moreover, the strain of weld metal was within 0.05 and this trend continued until the specimen get fractured. Therefore, this event clearly demonstrated the sound mechanical behaviour of the weld metal compared to the Cu-BM due to the fine SS grains occupied in the fusion

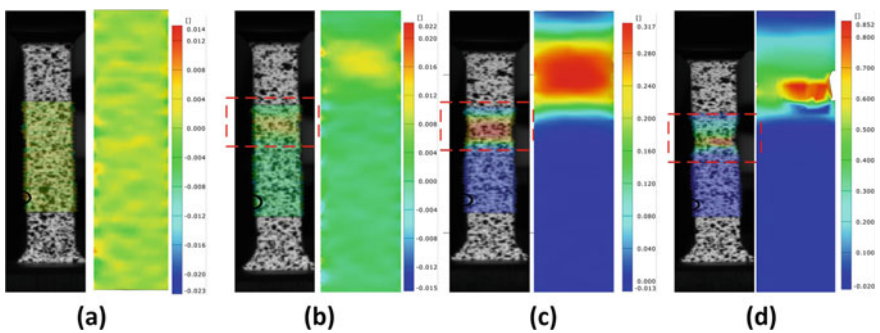


Fig. 13 Sequential strain map obtained through 2D-DIC

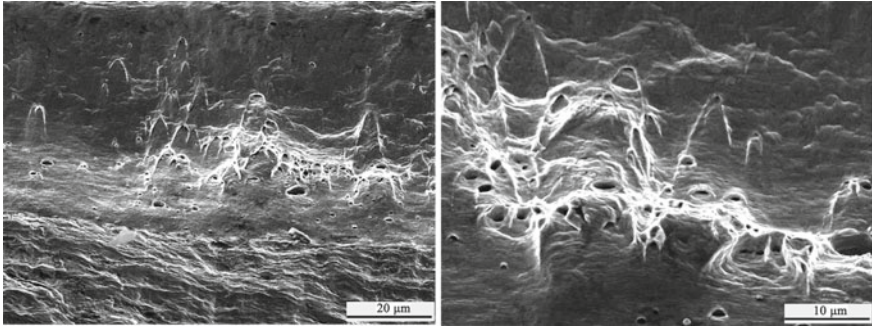


Fig. 14 SEM images of tensile fracture surfaces

zone as observed in the EBSD micrographs. Figure 14 showed that fracture mode of the joint was ductile fracture based on the plastic deformation in the form of dimples.

4 Conclusion

1. The isotherms on the copper side and the steel side were distributed asymmetrically, and the temperature gradient on the stainless steel side was higher. During the cooling process, the weld near copper side solidified first.
2. There existed an obvious grain coarsening in the haz on Cu side and there was an unmixed zone in the weld near the copper side; the composition of the weld near the fusion line on the stainless steel side was evenly distributed, and the structure shows the change of cellular grains, columnar grains and columnar dendrite.
3. As the welding power increased, the cooling rate of the joint decreased, and the temperature gradient of the copper side weld decreased. This promoted the transformation of columnar dendrites in the weld on the copper side to equiaxed dendrites and effectively suppressed microcracks in the weld.
4. With the increase of welding power, the tensile strength of copper/stainless steel joints gradually decreased. All the fracture positions of copper/stainless steel welded joints under different powers were located at the copper heat-affected zone. The fracture mode of the joint was ductile fracture based on plastic deformation in the form of dimples. The maximum tensile strength of the joint was 229 MPa, which is 84.8% of the strength of the copper base metal.

References

1. Cheng, Z., Huang, J., Ye, Z., et al.: Microstructures and mechanical properties of copper-stainless steel butt-welded joints by MIG-TIG double-sided arc welding. *J. Mater. Process. Technol.* **265**, 87–98 (2019)
2. Kar, J., Roy, S.K., Roy, G.G.: Effect of beam oscillation on electron beam welding of copper with AISI-304 stainless steel. *J. Mater. Process. Technol.* **233**, 174–185 (2016)
3. Magnabosco, I., Ferro, P., Bonollo, F., et al.: An investigation of fusion zone microstructures in electron beam welding of copper–stainless steel. *Mater. Sci. & Eng. A* **424**(1/2), 163–173 (2006)
4. Ramachandran, S., Lakshminarayanan, A.K., et al.: An insight into microstructural heterogeneities formation between weld subregions of laser welded copper to stainless steel joints. *Trans. Nonferrous Metals Soc. China* **30**(3), 727–745 (2020)
5. Chen, H., Fu, L., Liang, P., et al.: Microstructure and mechanical properties of friction stir welded butt joints of AlLi alloy ultra-thin sheets. *Alloys Compd.* **692**, 155–169 (2017)
6. Joshi, G.R., Badheka, V.J., et al.: Microstructures and Properties of Copper to Stainless Steel Joints by Hybrid FSW. *Metallogr., Microstruct., Anal.* **6**, 470–480 (2017)
7. Imani, Y., Besharati Givi, M.K., Guillot, M., et al.: Improving Friction Stir Welding between Copper and 304L Stainless Steel. *Adv. Mater. Res.* **409**, 263–268 (2012)
8. Sahlot, P., Nene, S.S., Frank, M., et al.: Towards attaining dissimilar lap joint of CuCrZr alloy and 316L stainless steel using friction stir welding. *Sci. Technol. Weld. Joining* **23**, 715–720 (2018)
9. Zhang, H., Zhao, K.X., Zhang, J.L., et al.: Microstructure and mechanical properties investigations of copper–steel composite fabricated by explosive welding. *Mater. Sci. Eng.* **731**, 278–287 (2018)
10. Durgutlu, A., Gulenc, B., Findik, F., et al.: Examination of copper/stainless steel joints formed by explosive welding. *Mater. Des.* **26**(6), 497–507 (2005)
11. Joshi, R.G., Badheka, V., et al.: Microstructures and properties of copper to stainless steel joints by hybrid FSW. *Metallogr. Microstruct. & Anal.* **6**, 470–480 (2017)
12. Kong, X.F., Li, F., et al.: Fiber Laser Welding of 5083 Aluminum Alloy with Filler Wire. *Chin. J. Lasers* **41**(010), 81–86 (2014)
13. An, N., Zhang, X.Y., Wang, Q.M., Yang, W.X., Xiao, R.S.: Fiber Laser Welding of 2060 Aluminum-Lithium Alloy with Filler Wire. *Chin. J. Lasers* **41**(10), 94–99 (2014)

Research on Ultrasonic Welding of Ultra-Thin Copper and Stainless Steel Dissimilar Metals with Nickel Foil as Intermediate Layer



Xiaoyan Gu and Wei Gao

Abstract A high-power ultrasonic spot welding machine was employed to successfully weld T2 copper and 301 stainless steel dissimilar metals with nickel foil as intermediate layer. The influence of different welding energy on the interface temperature, cross-sectional macroscopic morphology, interface formation and mechanical properties of the joint was analyzed. The ABAQUS finite element numerical simulation software is used to analyze the temperature field of the interface under different welding energy. The study found that the peak temperature, high temperature residence time and the depth of indentation gradually increased with the increasing welding energy and the joint interfaces were relatively straight. There were three types of joint interfaces including copper/nickel, nickel/stainless steel and copper/stainless steel. Each interface department occurred element inter-diffusion. There are diffusion layers. The maximum diffusion distances of copper-nickel elements and nickel-steel elements are 6.39 and 2.22 μm respectively. The maximum tensile shear force increases with the increase of welding energy and the maximum value was 1233.33 N. Welded joints fractured along the interface near the steel side of the base metal.

Keywords Ultrasonic welding · Copper/nickel/steel dissimilar metals · Welding energy · Interfacial stress distribution · Numerical simulation analysis

1 Introduction

In recent years, new energy vehicles have developed rapidly and are expected to gradually take place of traditional fuel-consuming vehicles [1, 2]. The development of new energy vehicles is inseparable from the development of power battery cells. Copper materials have been extensively applied in the field of new energy

X. Gu (✉) · W. Gao

Ministry of Education, College of Materials Science and Engineering, Jilin University, Changchun 130022, China

e-mail: guxiaoyan821@sina.com

© The Author(s), under exclusive license to Springer Nature Switzerland AG 2021

319

L. Zheng et al. (eds.), *Proceedings of MEACM 2020*,

Mechanisms and Machine Science 99,

https://doi.org/10.1007/978-3-030-67958-3_34

batteries due to their good electrical conductivity, thermal conductivity, corrosion resistance, ductility [3], good mechanical properties and processing properties [4]. In addition, it is widely used in the fields of electrical, mechanical manufacturing, national defense and communications [5, 6]. Stainless steel is an alloy steel with high chemical stability and high mechanical properties, and thus it is often used in the manufacture of parts or equipment with special requirements for corrosion resistance, oxidation resistance and high temperature resistance. Since copper and stainless steel are the bipolar materials of the battery cylinder manifold of new energy vehicles, the research of welding of copper and stainless steel is significantly valuable. Due to the large differences in the chemical composition and physical and chemical properties of dissimilar metals, it remains challenging to weld dissimilar metal materials [7]. Moreover, stainless steel is prone to intergranular cracks during the fusion welding process and thus the solid phase welding method-Ultrasonic Welding is used. Ultrasonic metal welding is a special connection and a solid-state welding technology [8–10]. It shows the difference from traditional welding technology in that it does not input current, arc and other high-temperature heat sources to the workpiece, but combines ultrasonic vibration with normal clamping force. The ultrasonic energy is converted into the friction energy between the metal interfaces, and then the temperature is relatively increased. Eventually, a connection technology achieves the bonding of the atoms between two base materials.

With T2 copper, 301 stainless steel and pure nickel foil as the research objects, combined with the temperature distribution at the interface during the welding process, the present study systematically analyzes the interface forming mechanism and the influence of welding energy on the microstructure and mechanical properties of the joint. It provides necessary data references and theoretical supports for the production and application of ultrasonic welding in the field of copper/stainless steel dissimilar metal connection.

2 Experimental Materials and Methods

2.1 *Experimental Materials*

T2 copper plates and 301 stainless steel plates with a thickness of 0.5 mm were used in the current work, and the dimension of plates was 25 mm long and 25 mm wide. Meanwhile, pure nickel foil with a thickness of 0.02 mm was used as the intermediate layer.

2.2 Experimental Equipment

The ultrasonic metal spot welding system is used in the current experiment. Figure 1a shows the size of the indenter. The welder is a Viper-20 ultrasonic metal welder with a rated power of 3 kW, a working frequency of 20.01 kHz, and a welding time of 0.005–9.999 s. The indenter and bottom of the welder are like sharp teeth. The indenter’s height is 0.55 mm with its area of 4.2 mm × 14.0 mm.

2.3 Experimental Method

The welding test was carried out with the overlap method of “copper on nickel under steel”. The main welding parameters of ultrasonic welding include welding amplitude A, static pressure P and energy E. The welding energy exerts an important influence on frictional heat generation and plastic deformation. Through a large amount of test data, it can be concluded that this welding machine has the best joint forming when the welding static pressure is 0.25 MPa and the amplitude is 95 μm. In the present study, the single factor variable method is used to change the corresponding welding energy in the range of 1400–2400 J with an interval of 100 J to investigate the influence of different welding energy on welding formation.

Before welding, 600#, 1000#, 2000# and 3000# sandpaper can be used to polish the sample to remove the oxide film, wipe it with acetone to remove oil stains, then place it in an alcohol solution, and clean it using the H6005 ultrasonic cleaner. A 17 mm × 7 mm welded joint was cut out, inlaid, polished, and corroded to obtain a metallographic specimen. Scope Axio ZEISS type metallurgical microscope, TESCAN type scanning electron microscope and EDAX type energy dispersive spectrometer were employed to observe and analyze the interface formation, microstructure and fracture morphology of the welded joint. X’pert3 Powder X-ray diffractometer was used to analyze the joint the phase composition at the interface and both sides of the fracture are detected and analyzed.

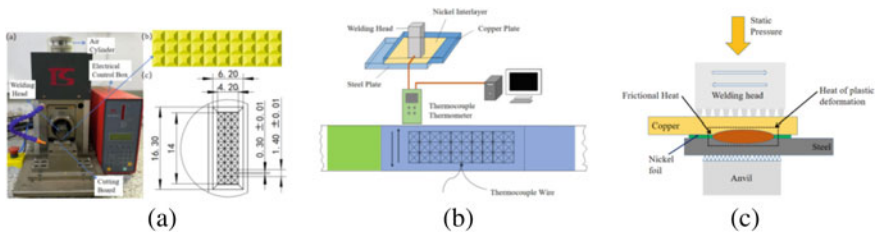


Fig. 1 The diagram of experimental equipment **a** The ultrasonic metal welding machine and detailed knurl pattern of sonotrode (top) and its dimension (bottom), **b** Thermocouple thermometer and temperature measuring position, **c** Schematic diagram of welding assembly

Before welding, draw the profile of the welding head pressing tooth in the center of the copper plate, and process a test hole with a diameter of 0.8 mm at the lower edge of the pressing tooth profile, and subsequently place the thermocouple in the test hole for fixing. Figure 1b and c shows the schematic diagram of machining position and thermocouple temperature measurement. The sampling frequency is 6 points/sec. The temperature data at different times is collected by the UT-325 thermometer so as to complete the welding thermal cycle test.

The tensile and shear force of the copper/steel welded joint specimen was completed on the MTS-810 electro-hydraulic servo universal material testing machine. Figure 2 shows the schematic diagram of the copper/steel lap joint tensile-shear specimen. The tensile loading speed is 0.8 mm/min and the loading load is 1 N. Meanwhile, it should ensure that the upper and lower chucks of the testing machine are clamped in the gasket area. After the chucks are clamped, the preload force value displayed on the electrical controller must be cleared. This study takes the average value of the strength of three joints under each process parameter as the tensile shear force under this parameter.

3 Results and Discussion

3.1 Analysis of Characteristics of Copper/Stainless Steel Ultrasonic Welding Thermal Cycle

Figure 3 shows the temperature distribution cloud diagram at the center of the copper/nickel/steel joint interface when the welding amplitude is 9.5 μm , the



Fig. 2 The schematic diagram of shear model

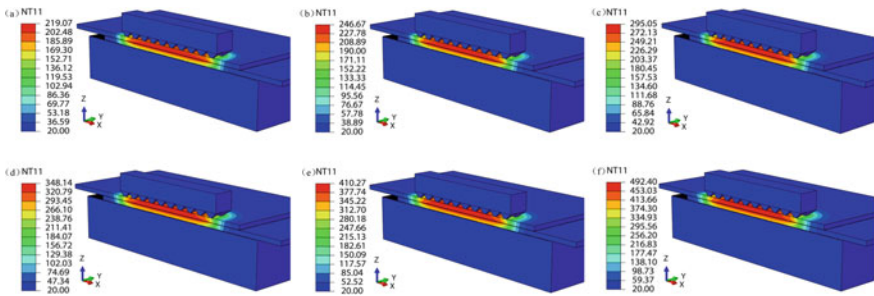


Fig. 3 Temperature field under different welding energy a 1400 J, b 1600 J, c 1800 J, d 2000 J, e 2200 J, f 2400 J

welding static pressure is 0.25 MPa, and the welding energy is 1400, 1600, 1800, 2000, 2200, 2400 J, respectively. The figure obviously shows that when the welding energy increased, the maximum temperature of the interface below the indentation gradually increased. From the distribution cloud diagram under different welding energy, it can be seen that the interface temperature distribution has local inhomogeneity. The high temperature area was mainly concentrated on the corresponding interface under the indentation and gradually decreases to the surroundings. The highest temperature was located slightly away from the tooth tip.

Figure 4a and b show the simulated cloud diagram and temperature change diagram of the steel plate interface temperature along the X axis when the welding energy is 2000 J. Obviously, the temperature distribution was roughly parabolic, which first increased and then decreased along the X axis. The highest temperature in the center of the interface was 357.35 °C. Due to the heat generated by interfacial friction and plastic deformation of materials, the temperature of the interface increased. These two heat sources were difficult to measure directly by employing experimental methods. However, they can be obtained from finite element analysis. The isothermal distribution cloud map of the entire copper plate interface is approximately elliptical. Figure 4c shows the interface friction heat and plastic deformation heat distribution. It can be seen that as the welding progresses, the heat generation of the two heat sources would increase, and the slope of the curve of the heat generated by the interface friction remains almost unchanged, indicating that the frictional heat generation rate remains almost constant. The plastic deformation heat had almost no heat production rate in the first 0.2 s, and the plastic deformation heat production rate slowly increases from 0.2 s to the end of welding. This was mainly due to the small plastic deformation of the copper plate at the beginning of welding. As the welding progresses, the copper plate gradually softens and the plastic deformation heat generation rate accordingly increased. It can be seen from the steep change trend of the temperature curve that the overall thermal cycle at the copper/steel interface had the characteristics of fast heating and cooling as well as short high-temperature residence time. This was mainly related to the pressing of the indenter during the welding process, high-frequency vibration, and a large amount of workpiece friction. The instantaneous frictional heat is related to the higher thermal conductivity of the copper/steel alloy. Induced by Galileo:

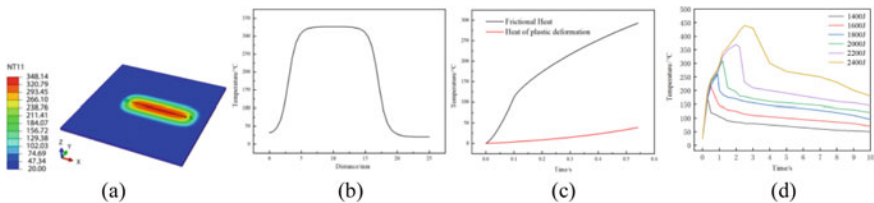


Fig. 4 **a** Thermal analysis of welding interface, **b** Interface temperature change along the X axis, **c** Interface frictional heat and plastic deformation heat distribution, **d** The thermal cycle curve of the interface of thermocouple under different welding energy outside the pressure tooth

$$\mu = \frac{4\pi\varepsilon^t}{\sigma} \quad (1)$$

where μ denotes the friction factor of the material, ε is the surface roughness of the material, t is the temperature of the material, and σ represents the stiffness of the material. It can be seen from this formula that the friction factor is associated with the temperature of the material. The welding heat input under different energies was different, resulting in different temperatures at the interface and different friction. At the same time, the test results demonstrate that as the welding energy increased, the welding time and high-temperature residence time would be prolonged, which would have a great impact on the microstructure and mechanical properties of the joint interface.

When the thermocouple was outside the pressure tooth, the peak temperature at the interface of the copper/steel ultrasonic welded joint under different energy was measured, and the thermal cycle curve measured at the interface of the ultrasonic welded joint (Fig. 4d). The changing trend of the curve shows that the overall thermal cycle at the copper/steel interface had the characteristics of fast heating and cooling speeds and short high-temperature residence time. The peak temperature at the copper/steel interface gradually increased with the increasing welding energy. This is because as the welding energy increases, the high temperature residence time increases, and the frictional heat generation accordingly increases.

3.2 The Influence of Welding Energy on the Macroscopic Morphology of the Cross Section

Figure 5a shows the upper and lower surfaces of the copper/steel ultrasonic welding joint. During the welding process, the welding head and the base leave pyramidal and jagged dents on the surface of the copper plate and the lower surface of the steel plate, respectively. Figure 5b shows the indentation depth of the copper/steel ultrasonic welded joint under different welding energy. Obviously, indentations can be observed on the surface of the copper plate, and there was no obvious change on the surface of the steel plate. Meanwhile, it can be seen that with the increase of welding energy, the thickness of the copper plate directly under the indentation continues to decrease, and the depth of indentation on the base metal continues to increase. This is because with the increase of welding energy, the temperature and stress of the copper interface under the tooth tip of the pressing tooth gradually increase, and thus the plastic flow ability of the material gradually increases. As a result, the depth of the tooth mark continued to increase under the action of welding static pressure. If you continue to increase the welding energy (more than 2400 J), the depth of the tooth marks will continue to increase, and the bearing area at this place will gradually decrease. In comparison with other positions, cracks are likely

to initiate and expand in this place, which is easy to reduce the mechanical properties of the joint.

3.3 The Influence of Welding Energy on the Formation of Joint Interface

Figure 5c shows the microscopic morphology of the joint interface under different welding energy. When the energy was 1800 J, the nickel foil in the middle layer was in good continuous contact with the steel, and the nickel foils on both sides accumulate in the middle, resulting in mountain and plain morphology. With the increasing welding energy, the nickel foil and the copper undergone the plastic deformation near the interface. The degree became larger. Under the action of shearing force, the nickel foil was cut and mixed with the plastic flowing copper. When the energy rose to 2200 J, most of the nickel foil became a discontinuous shape under the action of shearing force, and the copper flowed plastically near the interface.

In the process of ultrasonic welding, the high-frequency friction vibration generated by the workpiece under the action of static pressure and high-frequency ultrasonic vibration caused the contact surface of the workpiece to generate a large amount of friction heat instantly, the temperature of the contact surface of the workpiece rose rapidly, and the yield strength of the material was greatly reduced due to softening. The tendency of plastic deformation was increased, facilitating the exposure and bonding of fresh metal to form fusion between molecular layers. At the same time, both the atomic diffusion activity and the plastic flow ability of the metal will also be improved, which will exert an impact on the joint interface formation, microstructure and mechanical properties. In the state of the highest welding energy, the peak temperature at the interface was still lower than the melting temperature of the base material copper, stainless steel and pure nickel in the intermediate layer, suggesting that the formation mechanism of the copper/steel

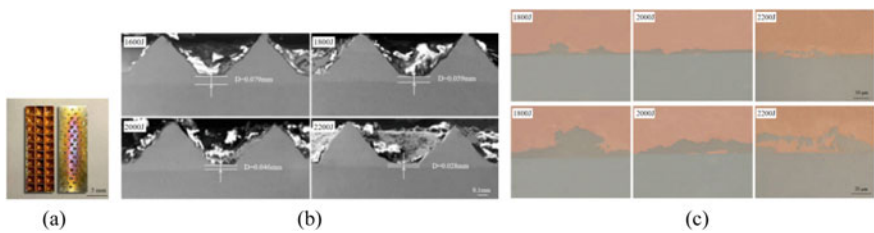


Fig. 5 Macro profiles of the joint under different welding energy **a** Top and bottom surface graphy, **b** Indentation depth at different welding energy, **c** Microstructure of the joints under different welding energy

ultrasonic welded joint interface was a solid state connection based on atomic diffusion.

When the welding energy increased, the welding time and high-temperature residence time would be prolonged, and the yield strength of copper, nickel, and steel would decrease significantly. Under the interaction of welding pressure and ultrasonic vibration, the three had uneven plastic deformation. In addition, the internal stress was unevenly distributed near the welding interface, and the softened base metal undergoes plastic flow under the uneven internal stress, forming a mechanical self-locking. As the welding time increases, the interface temperature increased, the yield strength of copper and nickel decreased, the plastic flow increased, and the mutual embedding depth of copper and nickel accordingly increased, contributing to the improvement of the tensile strength of nickel/copper welded joints.

Figure 6 shows the SEM photograph and EDS line scan analysis result of the welded joint (partial position in the middle of the two pressing teeth). According to the results, there was a diffusion layer at the interface, and as the welding energy increases, the thickness of the diffusion layer increased sequentially. The nickel-copper diffusion distances were 2.31 μm , 3.57 μm , and 6.39 μm . The nickel-steel diffusion distance were 1.73, 1.96, 2.22 μm . Obviously, the diffusion distance of nickel-copper was greater than that of nickel-steel, indicating that the diffusion rate of copper-nickel was greater than that of copper-iron. Figure 6d shows that when the copper-steel interface was bonded, the diffusion distance between the copper-side atoms and the steel-side atoms was small, and the copper-steel was not easy to directly bond.

The increase in the thickness of the diffusion layer with the increasing welding energy was determined by the following factors. First, as the welding energy increased, the welding time increased, and then the atom diffusion time increased. Second, the welding interface temperature increased significantly with the increase

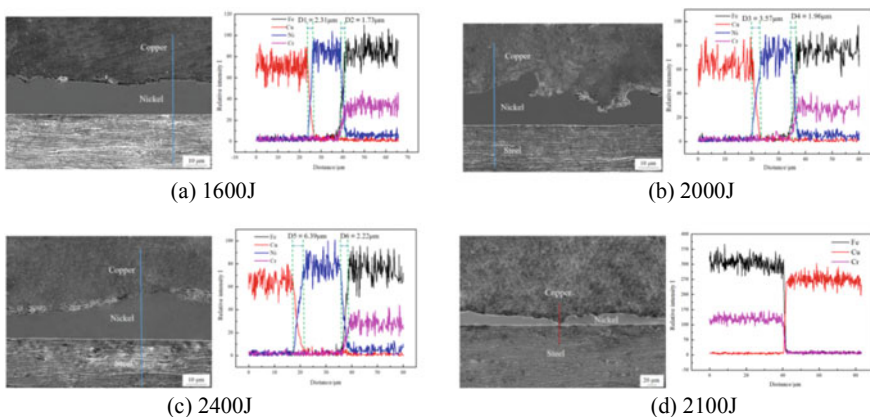


Fig. 6 Results of EDS line scan analysis under different welding energy

in welding time. According to Fick’s law of diffusion, the thickness of the diffusion layer can be analyzed using the following classic formula:

$$x = k_0 \sqrt{t} \exp\left(-\frac{Q}{RT}\right) \tag{2}$$

where k_0 denotes the reaction constant, Q is the diffusion activation energy, R is the gas constant and T is the thermodynamic temperature. It is known that the diffusion coefficient of atoms increases exponentially with temperature. Third, as the welding energy increased, plastic deformation occurs at the interface, resulting in a large number of lattice defects. The diffusion of atoms along dislocations and grain boundaries was the short-circuit diffusion. The diffusion activation energy was low and the diffusion speed was faster.

3.4 The Influence of Welding Energy on the Shear Performance of Joints

Figure 7a shows the curve of shear force change of copper/stainless steel ultrasonic welding joint under different energy. It can be seen from the figure that as the welding energy increases, the shear force of the joint increases first and then decreased. When the welding energy reached 2000 J, the joint shear force reached the maximum, which was 1233.33 N. Figure 7b shows the macroscopic morphology of the cross-section of copper/stainless steel joints with different welding energies after the lap shear tensile test. In addition, all specimens fractured at the interface.

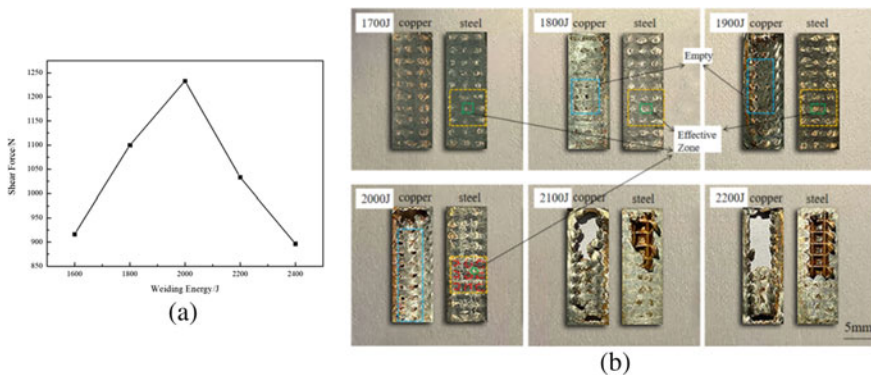


Fig. 7 **a** The shear force of joints at different welding energy, **b** Macro-morphology of fracture surface under different welding energy

From the previous Galileo induction, it can be seen that when the welding energy was low (1700 J), the overall stress of the welding interface was at a low level, the friction at the interface was low, the plastic flow ability of the metal was weak, and the diffusion of atoms at the welding interface was limited. Consequently, the bonding surface was only the small area under and around the tooth tip with high stress forming micro-connections. Therefore, the mechanical properties of the joint were low, and there was no large plastic deformation. With the increase of welding energy, the interface temperature (≥ 400 °C) was greater than the softening temperature of copper 150 °C, the copper base material begins to soften, the stress increased and the welding time was prolonged. In addition, a large amount of friction heat was generated, the temperature rose, and diffusion was promoted. The increase in overall stress caused a greater degree of plastic deformation near the interface. In the meanwhile, the expansion of the plastic zone increased the interface area and the interface diffusion area.

At the same position of the steel side section, a 6 mm \times 6 mm section was selected as a reference to calculate the ratio of the effective bonding area to the total area under different energy. The ratio was defined as the effective binding rate. After the calculation, the effective binding rate was respectively 41.5, 57.8, 72.1 and 82.3% at 1700, 1800, 1900, and 2000 J energy. It could be concluded that as the energy increased, the effective bonding rate increased and the joint strength was improved. However, when the energy exceeded 1800, the upper plate began to be cracked, reducing the mechanical properties. On the copper side, as the energy increases, part of the base material was broken down by the pressure teeth, and voids appear at 1800 J, and part of the copper side base material was completely broken and attached to the steel side at 2100 J.

3.5 Fracture Analysis

Figure 8c and d shows the microscopic morphology of the shear fracture of the copper/steel ultrasonic welded joint when the energy was 2000 J, and Table 1 shows the results of the EDS point scanning analysis corresponding to Fig. 8c and d.

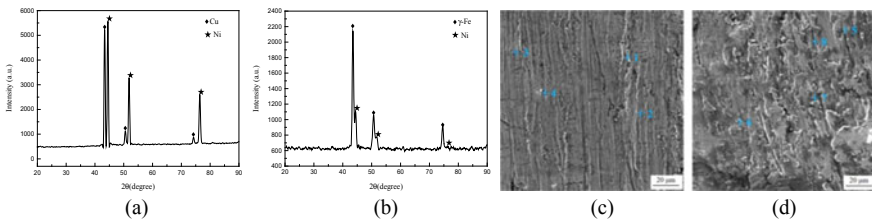


Fig. 8 X-ray diffraction analysis and fracture surface morphology of joints of fractures at 2000 J energy. **a** XRD of copper fracture, **b** XRD of steel fracture, **c** The fracture of copper side, **d** The fracture of steel side

Table 1 EDS analysis of regions scanned as indicated in Fig. 8 (at.%)

Position Serial number	Ni (at.%)	Cu (at.%)	Cr (at.%)	Fe (at.%)
1	93.58	0.56	0.99	4.88
2	95.57	0.74	0.54	3.15
3	98.48	0.28	0.44	0.79
4	93.83	0.33	3.15	2.68
5	6.74	0.35	18.31	74.60
6	8.76	9.33	3.48	78.42
7	23.44	0.38	15.68	60.50
8	56.08	0.52	9.09	34.31

Figure 8c and d shows that the fracture surface of the copper side and the steel side was relatively flat as a whole, consisting many steps of different heights, presenting typical brittle fracture. From the results of energy spectrum analysis, it can be seen that there are mainly nickel atoms at the fracture points 1 and 2 on the copper side, and the content of copper atoms was almost zero, indicating that most of the nickel adheres to the steel side during fracture. At the fracture points 5 and 7 on the steel side at 8, nickel atoms were attached to the steel side with different specific gravity. However, there were only a few copper atoms while at point 6, there was a part of copper atoms, indicating that the copper atoms plastically flow to the steel side during the welding process. Some of the copper/steel welded joint fracture occurred in the copper-side diffusion layer area, and some occurred in the steel-side non-diffusion layer area.

The fracture surface of the joint was analyzed by employing X-ray diffraction. Figure 8a and b shows the XRD analysis result of the joint under an energy of 2000 J. Copper-nickel solid solution appeared on the copper side and Fe-nickel solution appeared on the steel side.

4 Conclusion

- (1) Ultrasonic welding technology was used to achieve the effective connection of T2 copper and 301 stainless steel alloy with pure nickel foil as the intermediate layer. The overall interface was relatively straight, and the local interface had small fluctuations. No defects such as cracks and infusion could be found. Additionally, there existed no obvious reaction layer.
- (2) As the welding energy increases, the thickness of the interface diffusion layer gradually increased, and the nickel-copper diffusion distance was greater than the nickel-steel diffusion distance. When the energy was low, the intermediate layer of nickel foil was in good continuous contact with the steel. As the welding energy increased, part of the nickel foil was sheared under the action of shearing force and mixed with the plastic flowing copper. When the energy rose to 2200 J, the most nickel foils were transformed into discontinuous shapes.

- (3) With the increasing welding energy, the shear performance of joints first increased and then decreased. When the welding energy was 2000 J, the joint shearing force was the largest, which was 1233.33 N.
- (4) The welded joint fractured at the nickel-steel interface under different welding energy, and brittle fracture was the fracture surface.

References

1. Yuan, X., Liu, X., Zuo, J.: The development of new energy vehicles for a sustainable future: A review. *Renew. & Sustain. Energy Rev.* **42**, 298–305 (2015)
2. Kimble, C., Wang, H.: China's new energy vehicles: value and innovation. *J. Bus. Strat.* **34** (2), 13–20 (2013)
3. Lei, L., Shen, Y., Chen, X., et al: Ultrahigh strength and high electrical conductivity in copper. *Science* **304**, 422–426 (2004)
4. Wang, B.W., Wang, T., Lu, J.B., et al: Copper alloy and its processing technology. Chemical Industry Press, Beijing, 1–2 (2007)
5. Pawar, R.P., Gaikwad, D.D., Kauthale, S.S., et al: Application progress of recent advances in some copper catalyzed coupling reactions. *Mini-Rev. Org. Chem.* **10**(3), 232–238 (2013)
6. Miura, S., Honma, H.: Advanced copper electroplating for application of electronics. *Surf. & Coat. Technol.* **169**(22), 91–95 (2003)
7. Liu, W., Li, Q., Jiao, D.Z., et al.: Deformation and strain hardening behaviors of austenitic cold rolled 301L stainless. *Acta Metall. Sin.* **44**(7), 775–779 (2008)
8. Chen, X.F., Ma, Z.W., Zhang, Y.Y.: Analysis on fracture cause for 301 austenitic stainless steel cold drawing deformation. *Chin. Heavy Equip.* **2**, 52–54, 57 (2016)
9. Sireesha, M., Shankar, V., Albert, S.K. et al.: Microstructural features of dissimilar welds between 316LN austenitic stainless steel and alloy 800. *Materials Sci. Engineering A* **292**(1), 74–82 (2000)
10. Vaporization of propane in horizontal smooth mini-channels. *Int. J. Refrig.* **32**(5), 837–845 (2019)

Numerical Prediction of the Permeability Tensor Components for 2D Woven



M. Kiauka , I. Kolodiazhnyj , and A. Borovkov

Abstract The article presents with the method of numerical prediction of the permeability tensor components for 2D woven by CFD. This method allows to assess the permeability using geometric simulation tool TexGen and ANSYS Fluent. The study defines the permeability of the 2D woven unit cell in three significant directions—along the warp, the weft and at the angle of 45° to the warp. According to this data the permeability tensor components in principal axes are calculated for unidirectional flow. We compare the permeability values with experimental data mentioned in the references. The woven unit cell results can be used as the input data for the subsequent impregnation modeling.

Keywords Liquid composite molding · Resin transfer molding · Vacuum infusion · 2Dtextile · Permeability tensor · Principal in-plane permeability · TexGen · CFD · Inter-yarn flow · Intra-yarn flow

1 Introduction

Depending on the field of application, there are many methods of transfer composite molding, which consist of impregnating a dry reinforcing material with a liquid resin, followed by its curing in a special molding tool and getting a finished product.

On the way of liquid resin through a reinforcing material a flow resistance appears. Depending on the way of coping with this resistance, there are two main

M. Kiauka (✉) · I. Kolodiazhnyj · A. Borovkov
Peter the Great St. Petersburg Polytechnic University (SPbPU), St. Petersburg, Russia
e-mail: kiauka_myu@spbstu.ru

I. Kolodiazhnyj
e-mail: kolodyazhnyj_iyu@spbstu.ru

A. Borovkov
e-mail: borovkov@spbstu.ru

penetration methods—due to extra pressure (resin transfer molding, RTM), or due to vacuum (vacuum infusion).

In RTM method a resin goes under pressure to a hermetic cavity, which is formed by punch and die, with prepared dry preform. In vacuum infusion a dry reinforcing material is being set between hermetic film and a die, which is the surface of an item. As a result we have a vacuum bag with the exhaustion inside due to which the binder is pulled in the working area and impregnates the reinforcing material.

The manufacturing process by transfer methods should follow the mathematical (numerical) modeling. The impregnation modelling helps to optimize the technological process, to lower the price of production and reduce the possibility of defects. It is especially important for large-sized composite constructions, where defects result the financial and timeconsuming losses. One of the key characteristics required for impregnation processes modelling in transfer molding methods is the permeability of the reinforcement preform. In such modelling software as PAM-RTM permeability tensor components are used as initial data and need to be entered.

Prediction methods of permeability of reinforcing material are not standardized nowadays and they are based on simple areas impregnation experiments. Among these tasks are impregnation of rectangular disk by line source, 2D and 3D radial impregnation of spherical domain.

In reference [1] Demaria et al. describe the method based on ellipse equation to get the permeability tensor in woven plane using deformed woven unidirectional injection experiment results. Results are being compared with experiments in radial impregnation. In reference [2] Demaria et al. develop the previous work approach and offer the prediction model of in-plane anisotropic permeability characterization of deformed woven fabrics. In Vernet et al. [3] take a step towards standardizing permeability measurements—several research groups have been encouraged to use the same values for parameters such as fiber volume fraction, injection pressure, liquid viscosity to minimize dispersion source in unidirectional injection of woven plane.

Experimental determination of the permeability of engineering textiles is a complicated and expensive procedure, that is why it is important to develop methods of numerical prediction of this parameter.

In reference [4] Belov and Lomov et al. use the Lattice Boltzmann method (LBM) for solving Navier-Stokes equations using own code. Intra-yarn flow is considered by Brinkman equations.

In [5, 6] references Swery et al., using FlowTex and ANSYS CFX solvers, compare predicted permeability values received while modeling, with experimental results [3]. Predicted permeability values of textile model which is close to real structure of woven, were approximately twice higher than experimental data. The solvers' results were a good match.

Numerical prediction of permeability is covered in some thesis works [7, 8, 9].

In reference [10] Cai and Berdichevsky use the analytical model for permeability prediction of yarn in longitudinal and transversal directions. Unit cell contains a

representative yarn surrounded by a liquid. Stokes flow is applied to the liquid domain and Darcy flow is being considered in the yarn area. The authors get the dependencies for permeability prediction using such parameters as the average fiber volume, yarn volume ratio and its size.

In our research for numerical prediction of permeability we have also chosen the scaled experimental textile sample published in reference [3]. For modelling we have chosen the most common and available software: the unit cell is modelled in TexGen; the flow modelling is processed in ANSYS Fluent. The results are being compared and analyzed. The recommendations to improve the accuracy of modelling are proposed.

The method can be useful for engineers to better assessment of the textile permeability before impregnation modelling.

2 Basic Relations of Flow Dynamics on a Porous Medium and Methodology of Reinforcement Textile Permeability

Permeability is a geometric characteristic, connected with the weft structural features on various length scale. In fact liquid molding is a liquid filtration through porous medium which is described by Darcy’s law [11]:

$$\vec{u} = - \frac{1}{\mu\rho} \mathbf{K} \cdot \nabla P \tag{1}$$

where \vec{u} —fluid velocity, μ —resin dynamic viscosity, ρ —resin density, P —pressure, $\langle \rangle$ —volume average index, \mathbf{K} —permeability tensor of porous medium.

Generally the permeability tensor can be presented as following:

$$\mathbf{K} = \begin{bmatrix} K_{xx} & K_{xy} & K_{xz} \\ K_{yx} & K_{yy} & K_{yz} \\ K_{zx} & K_{zy} & K_{zz} \end{bmatrix} \tag{2}$$

For a textile the permeability tensor is orthotropic, where $K_{xy} = K_{yx}$, $K_{xz} = K_{zx}$, $K_{yz} = K_{zy}$ and it’s in the principal axes look like:

$$\mathbf{K} = \begin{bmatrix} K_1 & 0 & 0 \\ 0 & K_2 & 0 \\ 0 & 0 & K_3 \end{bmatrix} \tag{3}$$

K_1 and K_2 components characterize in-plane permeability of textile, K_3 component—in through-thickness direction.

As the basic computational fluid dynamics equation, that is used for simulate the flow through the textile we consider the Navier-Stokes equation:

$$\frac{\partial \vec{u}}{\partial t} = -(\vec{u} * \nabla) \vec{u} - \frac{1}{\rho} \nabla p + \nu \nabla^2 \vec{u} + \vec{F} \tag{4}$$

where u —flow velocity; p —pressure; t —time; ρ —density; ν —kinematic viscosity F —body force field; ∇ —The Hamiltonian operator.

K tensor components are generally defined experimentally. The point of experimental permeability approach is in weight measuring and flow time of resin with the known viscosity through reinforcement preform under the pressure fall [12].

For the steady-state mode of unidirectional flow, when fluid viscosity does not change depending on temperature and time, cross sectional area and permeability index are constant lengthwise, Darcy’s law is written as follows:

$$Q(t) = k \frac{A P_0 - P_1}{\eta \Delta x} \tag{5}$$

where P_0 —initial pressure, Pa; P_1 —final pressure, Pa; Δx —distance between two points, m.

The Eq. (9) does not consider interfacial effects between fiber and resin.

During radial impregnation for isotropic medium the impregnation front will have a circle shape. During radial impregnation for anisotropic medium the impregnation front will have an ellipse shape. It is necessary to set the permeability tensor components in the principal axes for anisotropic medium. For 2D woven the principal axes do not match with warp and weft directions. According to reference [1] fluid front that goes through anisotropic reinforcement preform is shown on Fig. 1.

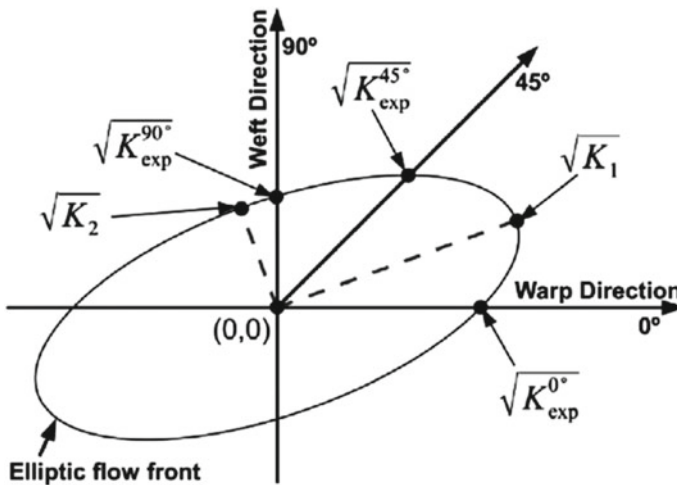


Fig. 1 Reinforcement preform elliptic flow front [1]

Permeability tensor components in the principal axes can be defined as follows [3]:

$$K_1 = K_C^0 \frac{\alpha_1 - \alpha_2}{\alpha_1 - \frac{\alpha_2}{\cos(2\beta)}}; \tag{6}$$

$$K_2 = K_C^{90} \frac{\alpha_1 + \alpha_2}{\alpha_1 + \frac{\alpha_2}{\cos(2\beta)}}; \tag{7}$$

$$\alpha_1 = \frac{K_C^0 + K_C^{90}}{2}; \tag{8}$$

$$\alpha_2 = \frac{K_C^0 - K_C^{90}}{2}; \tag{9}$$

$$\beta = \frac{1}{2} \tan^{-1} \left(\frac{\alpha_1}{\alpha_2} - \frac{\alpha_1^2 - \alpha_2^2}{\alpha_2 * K_C^{45}} \right); \tag{10}$$

That is why the flow modeling through unit cell along the warp, the weft and at the angle of 45° to the warp\weft.

3 Problem Statement and Modeling Example

The textile perform permeability coefficients method using TexGen automated unit cell construction includes the following basic issues: creating a geometric unit cell model in TexGen; exporting a geometric model to one of the mesh generators to prepare for CFD analysis; setting boundary conditions, medium properties, carrying hydrodynamic calculations, analyzing modelling results; calculating of permeability coefficients.

For analytical validation the experimental data of the research have been chosen [3].

3.1 Fabric Pattern

Geometric weaving and fiber parameters were set according to the full-scale measurements showed in reference [3]. In the fabric (400 texG0986 D1200 Carbon 2 × 2 Hexcel twill weave fabric), set in the technological test equipment the fibre volume fraction was $V_f = 0.45$ (Table 1).

The periodic nature of the reinforcement material geometric allows to significantly simplify the calculation models. As a geometric generator we used free special software TexGen, which was developed for reinforcement textiles

Table 1 Geometric weaving parameters 2×2 Twill [3]

Characteristic		
Nominal construction (warp)	tows/cm	3.5
Nominal construction (weft)	tows/cm	3.5
Warp width	mm	2.31
Weft width	mm	2.27
Yarn linear density	kg/m	0.000419
Fibre density	kg/m ³	$1.78 \cdot 10^3$
Fibre diameter	m	$7 \cdot 10^{-6}$
Areal density	kg/m ²	0.284

modeling. The main parameters of geometric unit cell are: fabric thickness, yarn center-to-center distance, number of yarns in different directions, yarn width. According to the research of [13] it is supposed that having V_f under 55% TexGen is able to realistically model the fiber geometry under compression.

To model the unit cell geometry in TexGen the following parameters were set (Table 2).

According to results of the unit cell modeling in TexGen the fibre volume fraction is $V_f = 0.49$ (not considering 10% increase to the cell domain $V_f = 0.54$). With the similar geometric weaving parameters with the real fiber this can be explained by yarn porous structure. «GapSize» parameter, which defines the gap between weaving yarns, which lay on each other at intersections, is equal to 0.03 mm, was set as minimum in order to provide the possibility of generating the fluid domain computational grid model of high quality. The picture of real fiber and the geometric weaving model is shown on Fig. 2.

We used an internal grid generator Ansys Mesher for discretization of calculated volume. This software allows to computerize modeling of various knots of volume. This grid model is designed by a huge amount of tetrahedral unstructured elements, which help to fasten discrete time modeling in condition of various directions of flow, which reduces the advantage of structured hexagrids. The maximum size of the element is 0.05 mm. The curvature element is 18° . While modeling we got two variants of the grid model. A variant for 0° and 90° of flow application to normal and for 45° of flow application to normal. The variant for 0° and 90° has about 4 million computational cells and the variant for 45° —about 18 million elements.

Table 2 Geometric weaving parameters 2×2 Twill in TexGen

Warp yarns	4	
Weft yarns	4	
Yarn spacing	2.95	mm
Yarn width	2.29	mm
Fabric thickness	0.35	mm
Gap size	0.03	mm

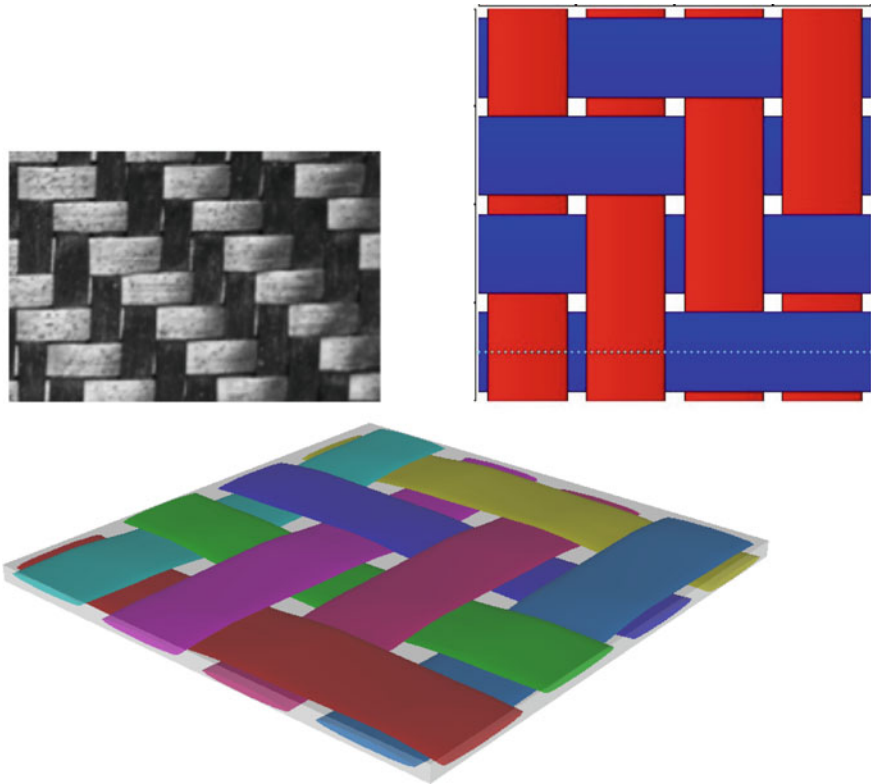


Fig. 2 Geometric unit cell model: real fabric, fabric pattern, and TexGen geometric model

3.2 The Boundary Conditions

ANSYS Fluent numerical prediction of the permeability is calculated according to formula (11), derivative of the formula (5)

$$K = \frac{G\mu L}{A\rho\nabla P}, m^2 \tag{11}$$

where G—mass flow rate, kg/s; μ —dynamic viscosity of resin, Pa·s; L—unit cell length along which the pressure fall appears, m; A—unit cell cross-section area perpendicular to resin flow direction, m^2 ; ρ —resin density, kg/m^3 ; ∇P —pressure gradient, Pa.

On the right side of formula (11) the result of numerical prediction is the mass flow rate G, the other values are the initial data, which is known or assigned. During substitution of all data we define the permeability index in particular direction if the material is anisotropic.

The resin flow mode was assigned laminar according to the Reynolds number calculation ($Re < 1$). As a resin we set a Newtonian fluid with resin properties RTM-6, dynamic viscosity $\mu = 0.1 \text{ Pa}\cdot\text{s}$ and density $\rho = 1110 \text{ kg/m}^3$. The thermal effect were ignored, the dependence of resin viscosity and density on a temperature were not assigned.

The boundary conditions correspond to the experiment conditions described in reference [3] and showed on the Fig. 3. One fiber is supposed to be impregnated, so the «translational periodic» boundary conditions were assigned for the end surface, and in the in-plane permeability of fabric—a «wall no-slip» was set. While modeling we supposed that the fibers are impenetrable for the resin.

To consider the liquid flow inside the weaving fibers, it is necessary to calculate the tensor of the local permeability of the tow K_{tow} . The fibers could be locally approximated as a regular massive cylinder. For the fiber longitudinal permeability and in transversal direction in [4] the following formulas are offered:

$$K_l = \frac{d^2}{32} \left(\ln \frac{1}{V_f^2} - (3 - V_f)(1 - V_f) \right) \tag{12}$$

$$K_t = \frac{4d^2}{9\pi\sqrt{2}} \left(\sqrt{\frac{\pi}{4V_f}} - 1 \right)^{\frac{5}{2}} \tag{13}$$

where V_f —the fiber volume fraction in the tow; d —fiber diameter; K_l —tow longitudinal permeability; K_t —tow permeability in transversal direction. The permeability for the tow is defined in the local coordinate axes and should be recalculated in the global coordinate axes. In general the tow permeability lie in the range 10^{-10} – 10^{-13} m^2 [14].

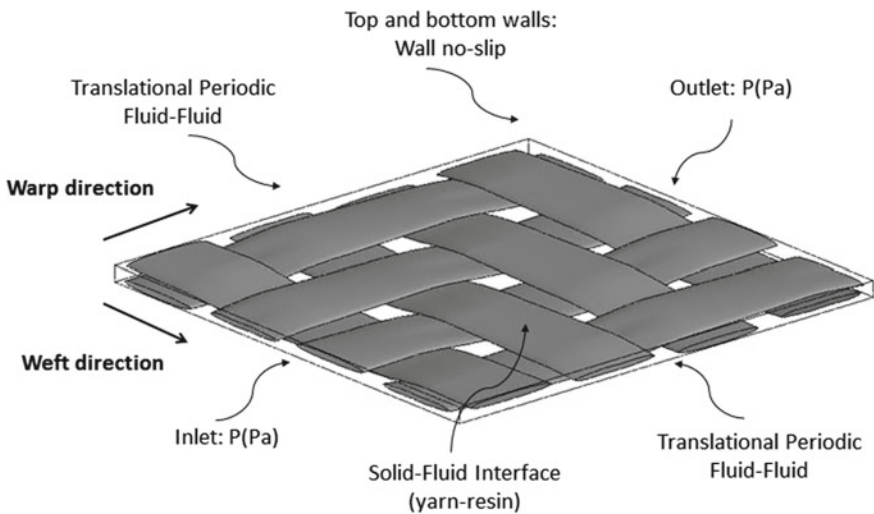


Fig. 3 The boundary conditions for unit cell

4 The Modeling Results

In each case the unit cell impregnation is carried out along the warp (0°), weft (90°), at the angle of 45° to the warp. The flow modeling results of the resin through the unit cell for three specific directions for impregnated yarns are shown on Figs. 4, 5, 6.

The comparison of experiment results [3] and ANSYS Fluent modeling results for the three directions is shown in the Table 3. The comparison used an average calculated during experiments that were carried out by different groups, but following the identical methodology and the approved recommendations.

The modeling results for the FlowTex and Ansys CFX solvers for the same experiment group are presented in reference [6]. The comparative results are shown in a bar chart on Fig. 7. As you can see, in our research, we have managed to achieve a greater permeability convergence with the experiment in the warp direction (0°). On the other hand, the weft permeability (90°), is higher than the warp one (0°) both in experiment [3] and modeling [6].

According to the warp, weft and 45° angle permeability calculation results we have defined the permeability tensor components using formulas (6)–(10). The comparative results with the experimental data are shown in Table 4 [3].

5 Tow Local Permeability Analysis

Local tow permeability K_{tow} in ANSYS Fluent or ANSYS CFX can be considered using “porous medium” model. We can get the porous medium permeability parameters for the tow as a result of the modeling of the resin flow through separate yarns. Besides, we consider a longitudinal and transversal yarn flow. This modeling method is similar to that described for the unit cell on the meso-level. However, in reference [15] they point out the necessity to correct viscous strains on the border of

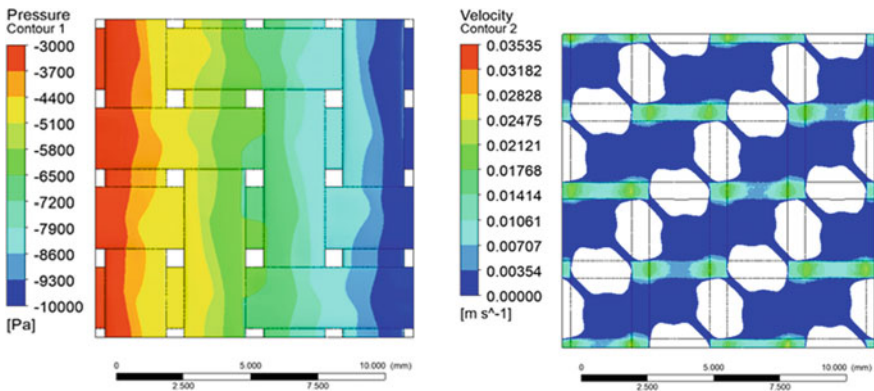


Fig. 4 Pressure and velocity field (section) for the flow in warp direction (0°)

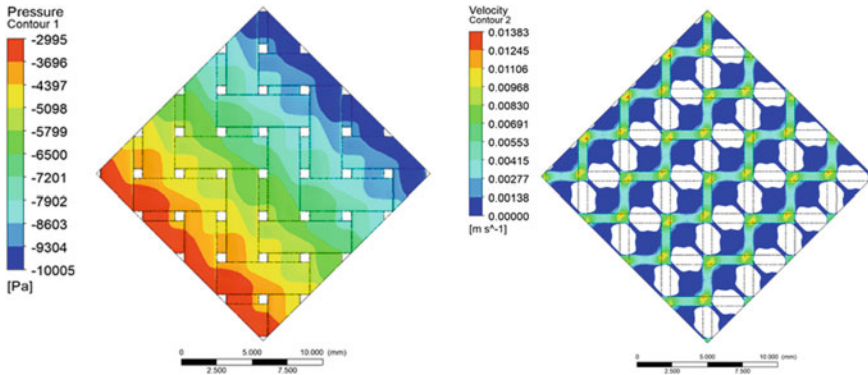


Fig. 5 Pressure and velocity field (section) for the flow at the angle of 45° to the warp/weft

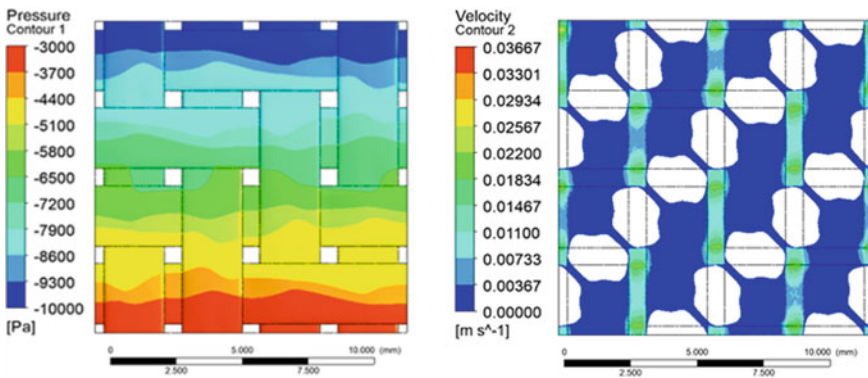


Fig. 6 Pressure and velocity field (section) for the flow in weft direction (90°)

Table 3 Unidirectional flow permeability. Full-scale experiment comparison

Direction	K_c (10^{-10} m^2)	K_{SFF} (10^{-10} m^2)	Difference (%)
0°	0.499	0.807	61.59
45°	0.567	0.861	51.76
90°	0.490	1.311	167.56

porous and fluid regions while modeling in ANSYS Fluent/ANSYS CFX, because there are no physical grounds to set the velocity continuous gradient on the border of the region.

In this research we have assessed the K_{tow} value using formulas (12), (13). We estimate the fiber volume fraction according to theoretical analysis and experimental data.

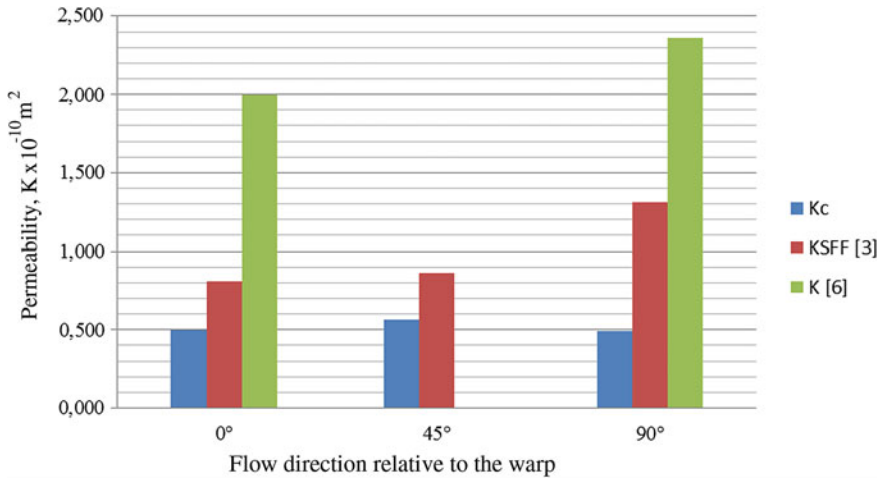


Fig. 7 Permeability comparative results

Table 4 2D permeability tensor components in the principal axes. The comparative results with the experimental data

Parameter	Modeling results	Experimental results [3]
α_1	0.49469E-10	1.0590E-10
α_2	4.7170E-13	-0.25200E-10
β	42.8719°	16.9844°
K1	0.48698E-10, m ²	1.3994E-10, m ²
K2	0.50257E-10, m ²	0.77678E-10, m ²
K1/K2	0.9690	1.8016

In order to get some idea as to the range of constituent volume fractions that may be expected in fiber composites, it is useful to consider representative area elements for idealized fiber-packing geometries such as the square and triangular arrays [16]. For the square array the maximum theoretical value of the fiber volume is $V_{\text{fmax}} = 0.785$. For the triangle array $V_{\text{fmax}} = 0.907$. In a point of fact, it is not possible to get the tight fiber pack, which is needed for this theoretical limitation. In a majority of a continuous fiber composite, the fibers are not ideally spherical and they are being packed randomly, that is why the fiber volume is usually from 0.5 to 0.8 [16].

In this study we have taken the fiber volume of 0.75. For the fiber $d = 7 \cdot 10^{-6}$ m (Table 1) and volume $V_f = 0.75$ we have received the following values: $K_l = 2.6264 \cdot 10^{-14}$ m²; $K_t = 3.9633 \cdot 10^{-16}$ m². The values K_l and K_t can be established in porous medium parameters in ANSYS Fluent or ANSYS CFX in local coordinate system of tow.

As a result, the fiber volume fraction for the unit cell considering the fiber porosity will be $V_f = 0.41$. Taking into consideration the geometry built in TexGen according to real fabric measures the fiber volume is lower than 0.45 measured in the reference [3]. This issue needs a supportive analysis.

6 Conclusions

This article presents the numerical prediction of the permeability tensor components for 2D woven by CFD. The permeability tensor components in the principal axes are determined.

We have assessed the fiber volume fraction of model fabric considering the fiber porosity. The local tow permeability in longitudinal and transversal directions according to analytical dependencies was determined.

In general the modeling results are reliable and similar to the experiment.

For the resin flow in weft direction (90°) the results of numerical prediction and full-scale experiment have the highest difference (more than 1.5 time). Permeability tensor components in the principal axes also have a difference— K_1/K_2 relation for the real fabric is more than 1, despite the fact that the fabric structure in terms of hydrodynamic resistance is identical in the warp and weft. However, it is important to point out that in reference [3] several research groups have received the K_1/K_2 correlation, which was also close to 1, as in the results of our modeling. So, both the efficiency of the experiment (fiber volume control, deformation of fabric, etc.) and a precision of modeling the ideal geometric weaving structure need a further research.

For ANSYS Fluent/ANSYS CFX software, we have to upgrade the methods of geometric models and computational grid by TexGen and universal mesh generators accordingly. While modeling closely to the real fabric geometry, the quality problems of the computational grid appear. On the other hand, we fail to get the assigned fiber volume of the unit cell.

In future research the fibers will be presented by porous medium and the unit cell permeability value will be clarified. The influence of the size of the computational domain (several unit cells in different directions) on the accuracy of the solution will be investigated. Also the warp and weft geometric parameters variability will be introduced in textile geometry in order to control the geometry deviation impact on permeability value.

References

1. Demaria, F.T.C., Edu Ruiz.: In-Plane anisotropic permeability characterization of deformed woven fabrics by unidirectional injection. Part I: experimental results. *Polym. Polym. Compos* **16**(2), 101–113 (2008). Doi: 10.1002/pc
2. Demaria, F.T.C., Edu Ruiz.: In-Plane anisotropic permeability characterization of deformed woven fabrics by unidirectional injection. Part II: prediction model and numerical simulations. *Polym. Polym. Compos.* **16**(2), 101–113 (2008). Doi:10.1002/pc
3. Vernet, N., et al.: Experimental determination of the permeability of engineering textiles: Benchmark II. *Compos. Part A Appl. Sci. Manuf.* **61**, 172–184 (2014). <https://doi.org/10.1016/j.compositesa.2014.02.010>
4. Belov, E.B., et al.: Modelling of permeability of textile reinforcements: Lattice Boltzmann method. *Compos. Sci. Technol.* **64**(7–8), 1069–1080 (2004). <https://doi.org/10.1016/j.compscitech.2003.09.015>
5. Swery, E.E., Meier, R., Lomov, S.V., Drechsler, K., Kelly, P.: Predicting permeability based on flow simulations and textile modelling techniques: comparison with experimental values and verification of FlowTex solver using Ansys CFX. *J. Compos. Mater.* **50**(5), 601–615 (2016). <https://doi.org/10.1177/0021998315579927>
6. Swery, E.E., Meier, R., Lomov, S.V., Hahn, C., Kelly, P., Straumit, I.: Verification of flowtex solver using ANSYS CFX-examining the permeability prediction method on a range of textile architecture models (2014)
7. Karaki, M.: Permeability modeling of engineering (2019)
8. Verleye, B.: Computation of the permeability of multi-scale porous media with application to technical textiles (2008)
9. Xiao, X.: Modeling the structure-permeability relationship for woven fabrics. PhD thesis, Nottingham (2012)
10. Cai, Z., Berdichevsky, A.L.: Estimation of the resin flow permeability of fiber tow preforms using the self-consistent method. *Polym. Compos.* **15**(3), 240–246 (1994). <https://doi.org/10.1002/pc.750150310>
11. Vafai, K.: Handbook of Porous Media, 3rd edin (2015)
12. Ferland, P.: Concurrent methods for permeability measurement in resin transfer molding. *Int. SAMPE Symp. Exhib.* **36**(pt 1), 546–555 (1991). <https://doi.org/10.3139/9781569906200.016>
13. Zeng, X., Brown, L.P., Endruweit, A., Matveev, M., Long, A.C.: Advanced geometry modelling for 3D woven fabrics in composites processing and performance analysis. *JEC Compos. Mag.* **50**(82), 55–60 (2013)
14. Lomov, S., et al.: Permeability of textile reinforcements: efficient prediction and validation. Simbio View project Stochastic Simulation of Composites Manufacturing View project 16 TH International Conference on Composite Materials Permeability of Textile Reinforcements: EF (2007)
15. Degroot, C.: Stress Closure at the Interface Between Fluid and Porous Regions in ANSYS CFX Stress Closure at the Interface Between Fluid and Porous Regions in ANSYS CFX. May 2013, 2018
16. Faulkner, L.L.: 2-Principles of composite material. *Mater. Sci.* **13**, 569 (2012)

Wire Rope Mathematical Model Development



D. A. Lobachev, V. L. Leontiev, Yu. A. Gorskiy,
Ya. A. Belolipeckaya, P. A. Gavrilov, and O. I. Klyavin

Abstract This article is about wire rope simplified model method development. This method allows to carry out calculations of different constructions, the elements of which are cables, without detailed strands modeling, which significantly saves computing resources and time. This work focuses on the usage of experimental data description to validate the material model of the rope, on getting deformation curves under axial tension and bending characteristics, on developing a simplified finite element model of the rope, and, finally, on the implementation of the method in the calculations of real constructions. The result of the research is the developed algorithm of transition from 3D elements to 1D and the creation of mathematical material model, which shows the physical and mechanical properties of steel cables.

Keywords Wire rope · Cable · Validation · Material model · Deformation curve

1 Introduction

Steel cable is one of the wire stranded and braided items which is often the main load-carrying elements of lifting constructions. The key advantages of the wire rope are higher tension capacity, sufficient torsional and small bending stiffness as well as a huge range of standard sizes. These characteristics show the wide range of cable applications: construction engineering, ship, air and ground transportation and many other industries, including oil industry, coal and mining industries. Cable computer modeling is the important task. However, detailed cable modeling is complex and time consuming in terms of computing resources. The fact is that a cable consists of many wires, and it is required not only separately to describe the geometry of each of them, but also to set contact interactions. This problem can be solved by creating a simplified mathematical model that fits well the behavior of the cable.

D. A. Lobachev (✉) · V. L. Leontiev · Yu.A. Gorskiy · Ya.A. Belolipeckaya ·
P. A. Gavrilov · O. I. Klyavin
Peter the Great St. Petersburg Polytechnic University (SPbPU), St. Petersburg, Russia
e-mail: lobachev_da@spbstu.ru

The behavior of wire ropes under loading is described in different sources [1, 2, 3], but there is no unified method of mathematical modeling. And the problem of constructing a proper simplified cable model is of the highest priority in the strength calculation of construction, since the models used today, the behavior of which is close to real, still require more accurate verified data. [4].

There are developments that propose discrete models of high accuracy of rope wires and the rope as a whole using 3D finite elements to rope wires modeling. For example, in [1, 2], a 1 + 6 wire rope with a complex geometry due to the inclusion of double-helical wires is modeled and analyzed using 3D finite elements. In this case, the results of numerical analysis are compared with analytical analysis and experimental results and show a satisfactory correspondence. The article [5] considers a cable containing carbon fibers. The results of 1×7 cable tensile tests are compared with numerical analysis, calculated using a simplified analytical model and a 3D finite element model with tetrahedral finite elements. In the article [6] elastic properties of the rope 1 + 6 are studied. The results are compared with the analytical solution and with the 3D finite element solution. The study [7] is devoted to the analytical models of a 1 + 6 rope consisting of six spiral wires wrapped around a straight core. The solution is compared with solutions calculated using 3D finite elements. In [8], the stress state of a rope with two multi-directional layers of spiral wires wound on an elastic core is analyzed. A simple method is proposed for determining the characteristics of the torque, as well as the distribution of contact stresses between the rope wires. The article [9] proposes a finite element model of the 1 + 6 + 12 rope with 3D finite elements. The results of finite element analysis showed a good correlation with experimental data. In the article [10], a mathematical model of a spiral strand of a 1×7 rope was developed, taking into account the influence of transverse compression of wires and their local contact deformations during flattening. The contact interaction of rope wires is considered as a problem of plane deformation without taking into account friction. In [11], the behavior of the rope during bending is analyzed, and internal force factors are considered. Indentation techniques, which are still being developed, are used to study the properties of deformable solids. In [12], a finite element study is carried out in order to improve the methodology for studying the elastic-plastic properties of a material by means of nanoindenter experiments. It is assumed that the material is isotropic elastic-plastic solid with power-law hardening. The purpose of the article [13] is to create a model of a 1 + 6 wire rope. The proposed model takes into account the effects of friction and sliding. In this case, numerical solutions to the problems of axial loading and rope bending are calculated.

The purpose of this work is to develop a method for simplified cable model construction, which includes not only the transition from three-dimensional finite elements to beam elements, but also the validation of the material model based on reliable experimental data. The approach described in this article will allow to calculate wire ropes of any configuration under various loads, avoiding detailed modeling and significantly saving time and computing resources. In the first stage, the steady-state rope analysis is completed. In this stage movements of the rope with its significant bending and longitudinal deformations with a simplified finite

element model of the rope, local areas of the rope are determined in which significant stress concentrations occur, creating prerequisites for the occurrence and development of cracks, for breaking the rope. At the next stage, it is possible to conduct a detailed study of the stress-strain state of these local areas of the rope using the results of previous calculations and 3D finite elements. Thus, the suggested approach proposes solutions to complex problems of rope dynamics, with the limited resources of computers.

To achieve this goal we had to solve the following tasks:

- 3D cable under tension deformation curve development and validation in normal mode operation (without destruction).
- Mathematical material model validation based on experimental data.
- Getting the bending characteristics of the wire rope also based on experimental data.
- A simplified one-dimensional finite element mathematical cable model development.
- Application of the developed simplified wire rope model to simulate its behavior in real life conditions and compare with the available experimental data.

2 Axial Tension Deformation Curve Estimation

The construction of a simplified wire rope model and the transition to beam elements involves the selection of a new material for these elements. The article [1] describes such a choice and its validation: with the originally used *MAT_CABLE_DISCRETE BEAM b and elements of the beam 6 type, high-amplitude dynamic vibrations appeared in the model, and the compression load was reflected incorrectly, which significantly limited the area of its application. As a result of considering the other types of elements available in the LS-Dyna program, where the wire rope calculations were carried out, it was confirmed that the best result was shown by the beam 2 elements with the material *MAT_166 (or *MAT_MOMENT_CURVATURE_BEAM) [14]. This material model requires the user to define the axial force-strain, curvature moment and torque-moment curves. In this case, only the force-strain and moment-curvature curves included in the material map *MAT_166. Thus, the rope did not work for torsion, and the corresponding data excluded from consideration.

The choice of the rope material parameters is one of the primary tasks set at the beginning of the method development for creating a simplified finite element model of the wire rope. The physical and mechanical properties of the material were described in detail in the article [15], which also contained experimental data that allowed to compare the simulation results with the results of field tests at the initial stage of the study. The finite element model of a wire rope section with a length of 28.75 mm is shown in Fig. 1. Much attention was paid to the choice of the cable length for modeling and analysis [15]. So, for a simple numerical model of a

straight wire strand, the length that provides optimal contact between the central and external wires is 115 mm. Accordingly, at the first stage of the study, it was decided to choose a quarter of this length for consideration.

The finite element model of a cable was calculated with one central and six wires wound around it with a certain angle, consisting of 20-node hexahedral solid-elements (construction 1 + 6). The diameter of external wires is 3 mm, the diameter of the central one is 3.2 mm.

The contacts were set individually for all wires of the strand, the friction coefficient in the contacts was $\mu = 0.115$. This setting is used taking into account the possibility of interaction of each wire with the next one in the cable. Selected [15] physical and mechanical properties of the material are shown in the Table 1.

To get a deformation curve of a small rope, the nodes of the model were rigidly fixed on one side, an axis slide along the rope was set on the other side, rotation is prohibited. The model of loading is shown in Fig. 2.

The calculation was carried out in ABAQUS. Comparison of the axial force arising in the cable attachment from tensile deformation with the experimental data [3] is shown in Fig. 3.

The difference between the finite element modeling results and experimental data by less than 1% allows us to speak about the adequacy of the modeling method used. Consequently, we consider it possible to use this method of getting a deformation curve to determine the characteristics of a full-size rope.

The characteristics of a full-size rope, including the dimensions and number of wires in the cross section, were taken from the technical specifications [16]. Key parameters are shown in the Table 2. The cross-section scheme is in Fig. 4.

The finite element rope model shown in Fig. 5 consists of solid elements. The complete wire rope model deformation curve was defined for solid elements with the length of 150 mm.

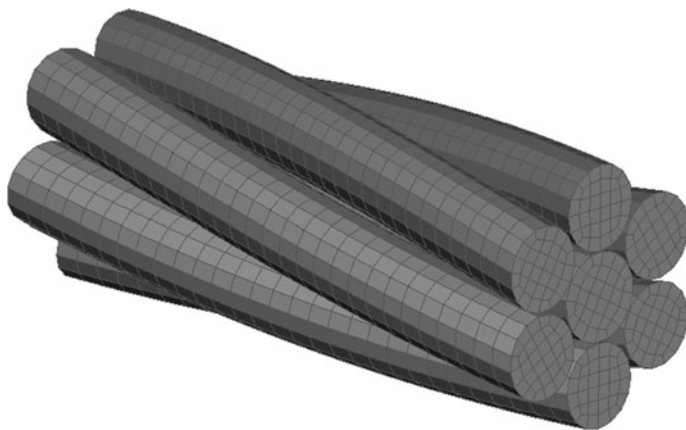


Fig. 1 The wire rope finite element model

Table 1 Physical and mechanical properties of cable material

Yield limit σ_T , MPa	Strength limit σ_B , MPa	Tangent modulus E_t , MPa	Elastic modulus E , MPa	Density ρ , t/mm ³	Poisson's ratio μ
1540	1800	24600	188000	7,85·10-9	0,3

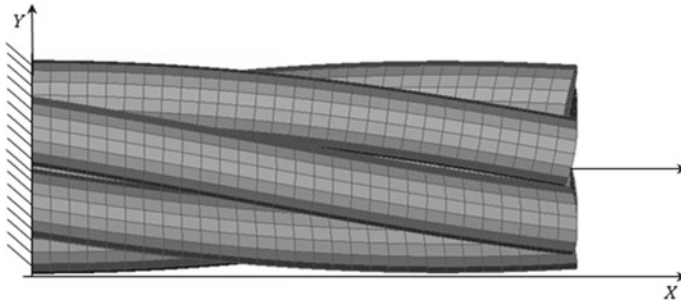


Fig. 2 The fixing and loading the wire rope model

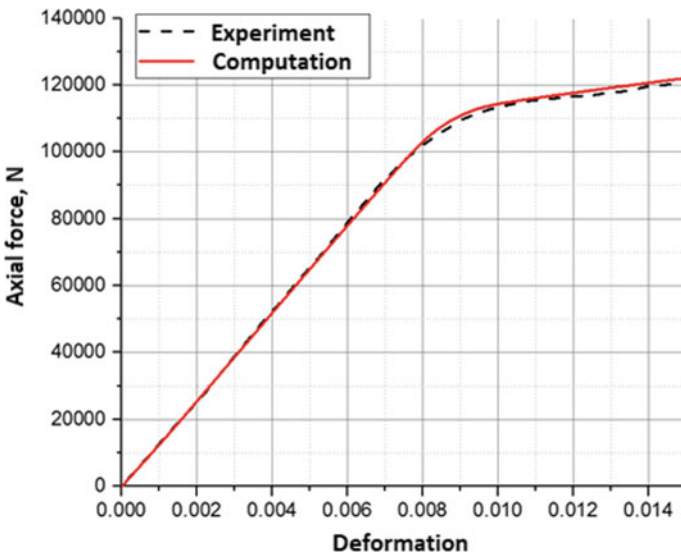


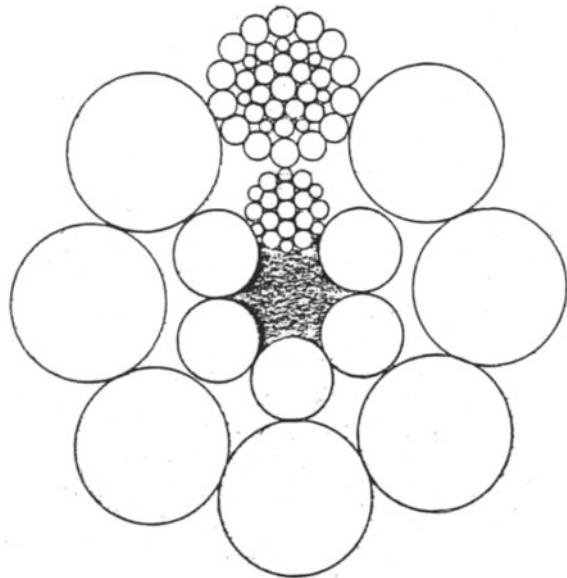
Fig. 3 Model problem and experimental data results comparison

Each wire of the rope $8 \times 36 + 6 \times 19$ has 9 or 16 elements in cross section (tetrahedrons and hexahedrons) depending on the diameter, 1.58 mm long. The total number of elements in the model is 537560. The loading conditions remained the same: rigid fixing on one side and movement along the axis on the other side.

Table 2 Geometric parameters and number of wires in the cross section of a full-size rope

Diameter, mm									
Wire rope	Wires in the strands of the inner layer				Wires in the strands of the outer layer				
	Central	First layer	Second layer		Central	First layer	Second layer		Third layer
36,5	1.30	1.20	1.30	1.00	1.80	1.30	1.30	0.95	1.60
Number of wires, unit									
–	6	36	36	36	8	56	56	56	112

Fig. 4 The cross-section scheme of the wire rope



The resulting dependence is shown in Fig. 6. The deformation values are in the range from 0 to 5% on the diagram, since with further cable tension the total reactive force decreases and this part of the diagram is not considered in this work. The nonlinear section in the diagram shows the moment of the initial rope reduction when a load is applied. This is followed by a linear section, when the deformations increase in proportion to the applied load and the diagram comes to the classic view.

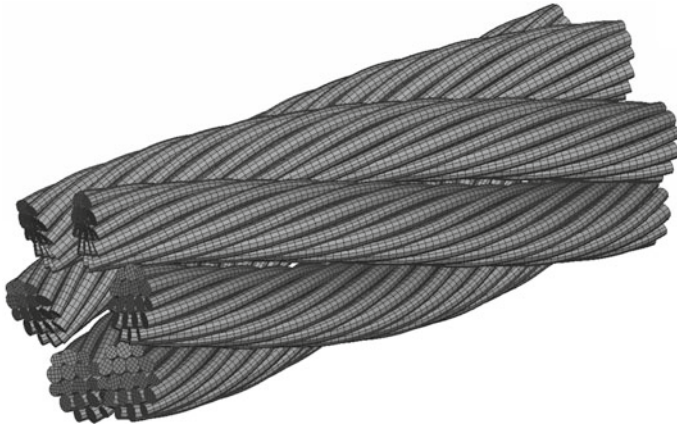


Fig. 5 The finite element wire rope

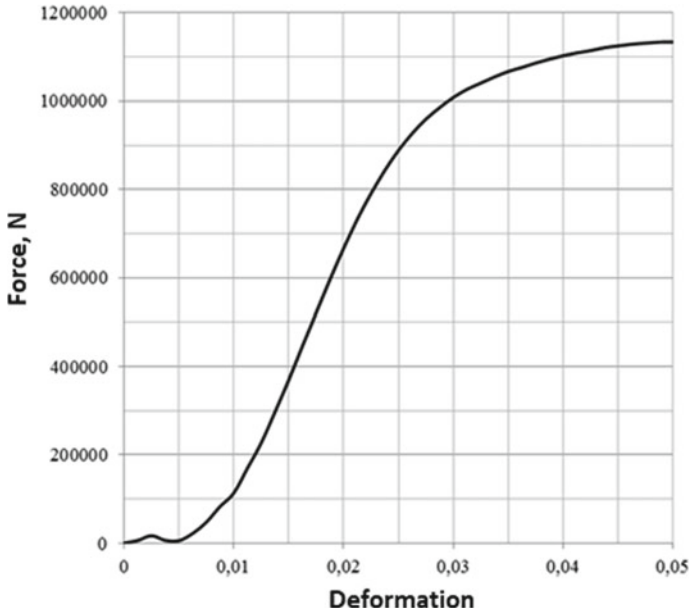


Fig. 6 Full size wire rope deformation curve

3 Material Validation for Transition to Beam Elements

While validating material model we have carried out a series of experiments to get some dependencies, the results of which can be found below. In particular, we run tension tests of wires out of outer strands of wire rope. The deformation curves used

to define Young's modulus, and then the true stresses and strains were calculated and their dependencies were built for different standard sizes of wires. The calculation method is presented here [17]. The true deformation curves and new elastic coefficient were again set for the full-size rope material model in the axial tension task. The comparison of the dependence of force on load for validated and standard materials (for $E = 210$ GPa) is presented in Fig. 7. Here we consider the full deformation curve with the reaction force decrease section, since the breaking tension is compared.

To take into account the plastic flow of the rope, it was required to have a curve representing the stress versus deformation dependence in the plastic deformation area. Usually, such dependences are get experimentally, however, for a wire rope, the test gives inaccurate results, since it is rather difficult to take into account surface hardening, and the deformations are overestimated due to the curvature of the wires. In this work we use the method based on combination of sample surface indentation with the further finite element modeling method. [18]. Based on actual tests we got the indentation curve that is shown in Fig. 8.

Modelling tests were carried out in ABAQUS, Indentation finite element model, which is shown as an indentation process in the diamond pyramid sample is shown in Figs. 9 and 10.

According to the backward simulation method the plastic flow curve was set, and then the indentation curve was chosen iteratively, comparing it experimentally estimated total deviation square of calculated and experimental value. Plastic flow curve is defined be dependence [12]:

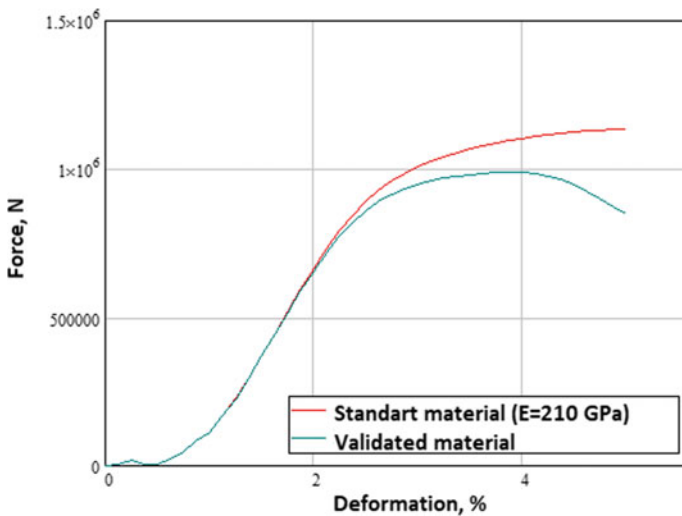


Fig. 7 Force versus load graph

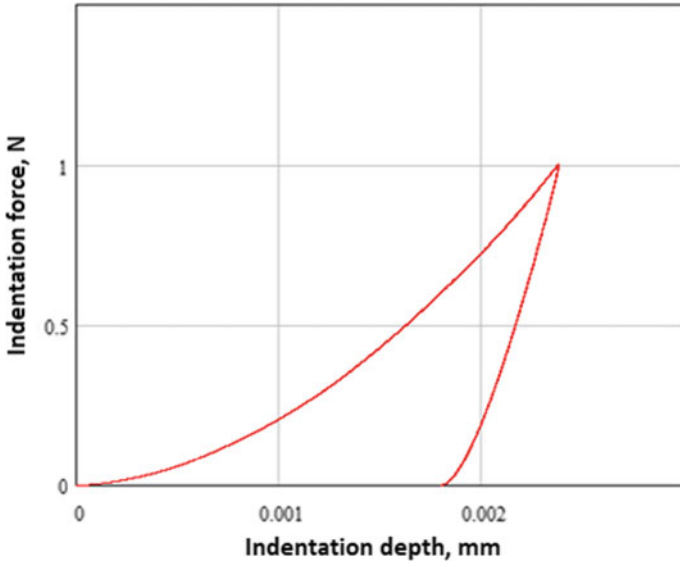


Fig. 8 Experimental indentation curve

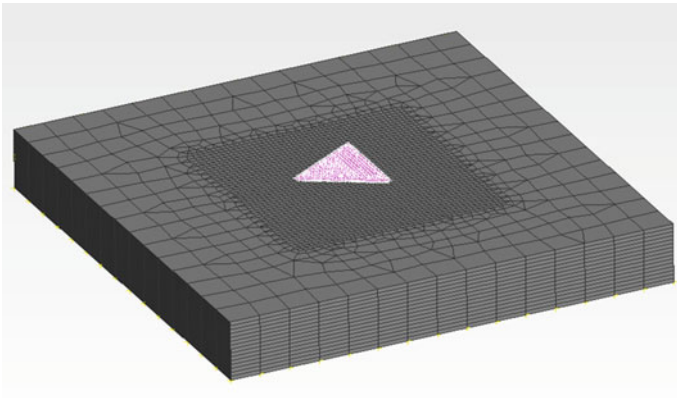


Fig. 9 Finite element model of wire sample indentation

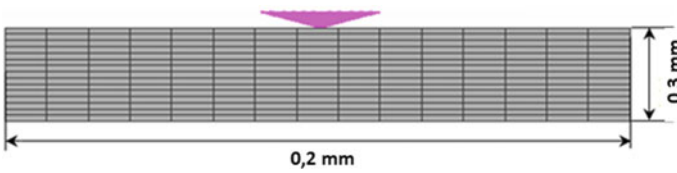


Fig. 10 Finite element model of wire sample indentation with dimensions

$$\sigma = \sigma_0 * \left(1 + \frac{E}{\sigma} \varepsilon\right)^n,$$

σ —flow stress, MPa, σ_0 —yield stress, MPa, E —elastic coefficient, MPa, ε —true strain, n —work-hardening index.

Indentation finite element model has been developed, the contact between sample surface and the pyramid has been changed, the grid was reconfigured. The results of different stages are shown in Fig. 11. It is obvious that the mathematical curve appeared to be rather sensible at the load stage to the work hardening value changes, and then it resulted the yield stress increase.

The plasticity curve calculated with the values of the yield stress and the work hardening value was subsequently substituted into the 1D material model for calculating the rope in tension and getting the dependence of the force on the load.

To adequately identify the properties of the material, it was necessary to calculate the bending stiffness, which is the dependence of the curvature on the bending moment. We carried out tests: a sample of a wire rope was rigidly fixed at one end and loaded at the other. The loose end length was 1 m. Weights of 505, 982 and 1500 g were suspended from one of three points alternatively. We have measured the length from the edge side and the height of the table. The bending stiffness defining scheme is shown in Fig. 12. In this case, the deflections of the ropes h_1, h_2, h_3 were measured at these three points of its axis with coordinates 11, 12, 13.

We have calculated the wire rope model corresponding to the tests: the value of the bending stiffness in the material varied until the minimum error between the calculation and experiment data was obtained. The same way as in experiment the force was applied to the three points of the wire rope alternatively, and after that we measured these points' coordinates. We have also calculated the wire rope free sag data, that means we measured points' coordinates under gravity force only.

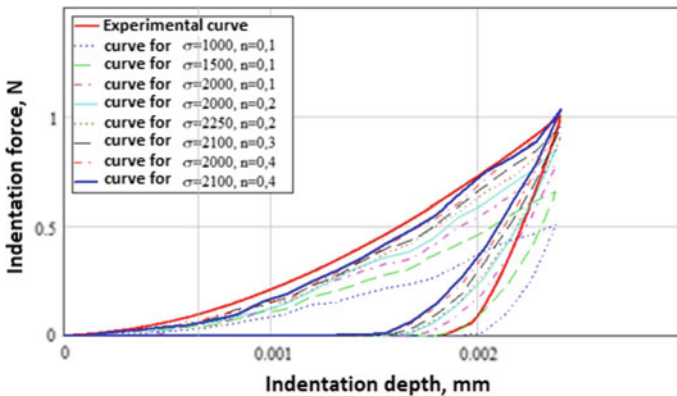


Fig. 11 Indentation curve versus experimental curve

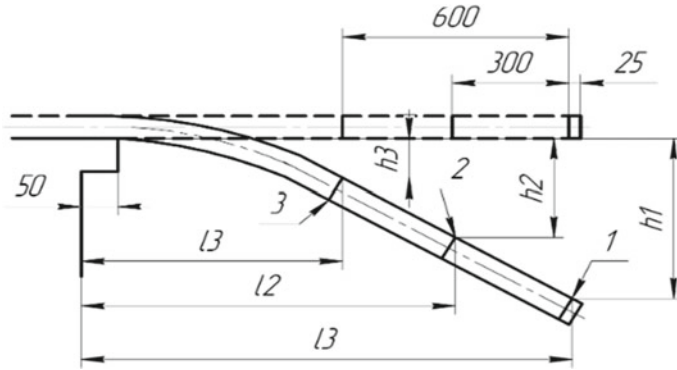
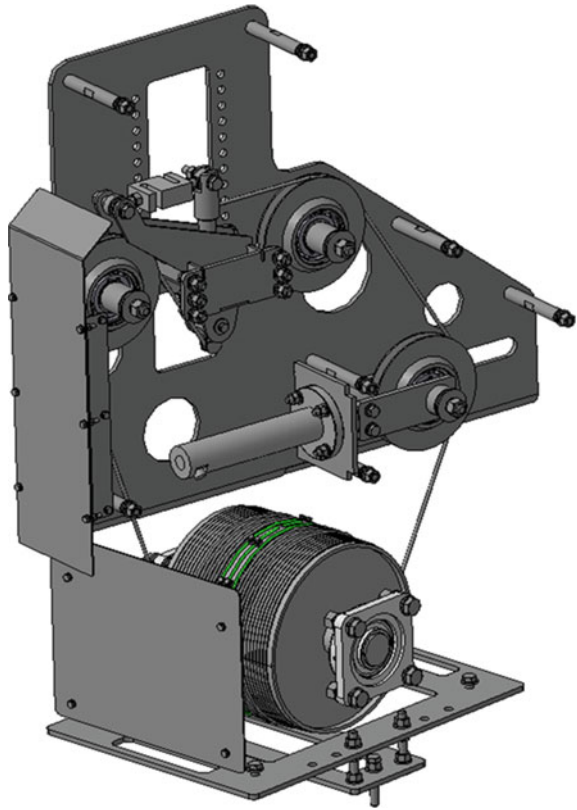


Fig. 12 The wire rope bending stiffness defining scheme

Fig. 13 Tension loader



Fig. 14 Tension loader model (the front cover of frame is hidden)



A comparison of the results of experiments and calculations is shown in Table 3. Taking into account some differences in the coordinates of the forces application points in experiments and calculations, to the conclusion that they are in satisfactory agreement.

4 Validated Wire Rope Model

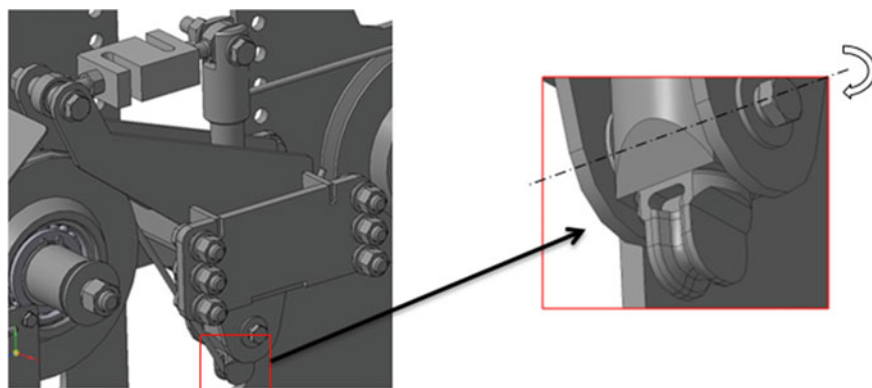
The method of creating a simplified 1D model of a wire rope with a validated material was used to simulate the runner skid rubbing against a wire rope. To carry out field tests we used a loader which was rotated during the test. A fleet wheel and a blocks system were set on the loader, through which the cable was stored. The force was created by hydraulic cylinder block. Test stand runner skid was a scaled aircraft tail hook, connected with the loader holder by the strain gauge. The runner skid holder was adjustable in order to be able to change cable wrapping angle. During the test the friction force of the runner skid against the wire rope was

Table 3 Experiment and calculation data

	h1, mm	L1, mm	H2, mm	L2, mm	H3, mm	L3, mm
Free sag						
Experimental data	255.25	920	198.25	660	80.25	380
Calculation data	228.6	945.4	126.6	663.3	38.3	376.7
505 g weight at point №1						
Experimental data	358.25	870	238.25	640	98.25	375
Calculation data	448.9	849.2	267.3	611.8	104.9	361
982 g weight at point №1						
Experimental data	413.25	850	273.25	630	113.25	370
Calculation data	491.6	818.8	292.2	596.8	4414.61	357
1500 g weight at point №1						
Experimental data	498.25	795	328.25	595	143.25	360
Calculation data	520.95	794.6	309.3	585	121.4	353.9

evaluated at different values of tension force and the wrapping angle. The mounting of the slide and strain gauge on the frame is shown in Fig. 15. The general view and the model are shown on Figs. 13 and 14 accordingly.

The runner skid mount was fixed with bolts to has the required girth angle. The constant pressure in the loader system and the necessary level of rope tension was achieved using a hydraulic cylinder. In this case, we define the rope tension force approximately. In means, we take into account the total force of the hydraulic cylinder and the positions of the blocks, drum, and runner skid with a certain pressure in the hydraulic system. Then this force was used in the next stages. In the experiment, the friction force of the runner skid to the rope was determined at different values of the tension force and the angle of the girth of the runner skid.

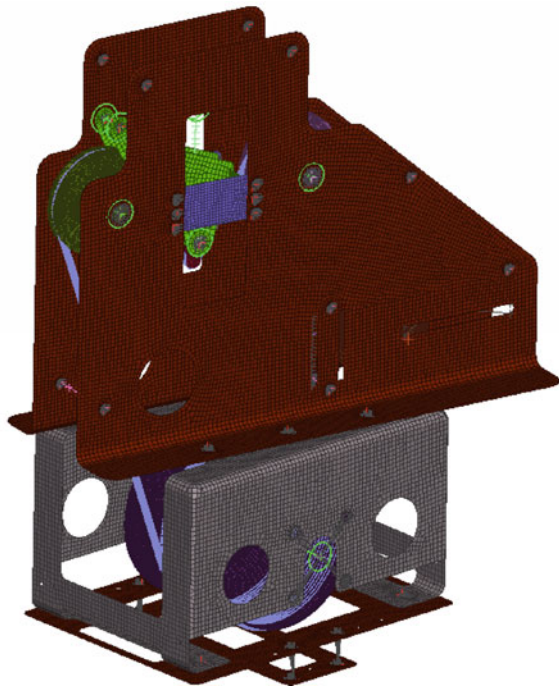
**Fig. 15** The runner skid and strain gauge mounting

The calculation of the friction force of the runner skid against the wire rope was carried out in the finite element model analysis software LS-DYNA. The finite element model has been developed to evaluate the loads to the gear at different operation modes of tension loader. The general view of the finite element model is presented on Fig. 16.

To model the wire rope we used the beam elements and validated *MAT_166 material model. To record the element thickness at contact points of wire rope with the fleet wheel and block the settings were set in contact cards. The internal part of the loader finite element model is shown in Fig. 17. In this model the stress gauge and hydraulic cylinder are modeled with beam elements. The blocks bearings that direct the rope in the loader are modeled as joints. The blocks the runner skid and the drum are modeled with rigid type solid elements. The distribution of equivalent (by Mises) stresses in the body parts of the loader, and the distribution of the rope tension force, is shown in Figs. 18 and 19. The calculated distribution of the cable tension force highlights local areas of stress concentration and permits to simulate these areas of the rope using 3D finite element model. This method allows to has a finite element solution of the occurrence problems and to explore development of cracks in individual wires of the rope.

In the calculations, the values of the axial forces in the finite elements of the stress gauge and tensioner were recorded. In the steady-state mode of cable stretching in the loader, time-averaged forces were calculated. Using these forces,

Fig. 16 Finite element model



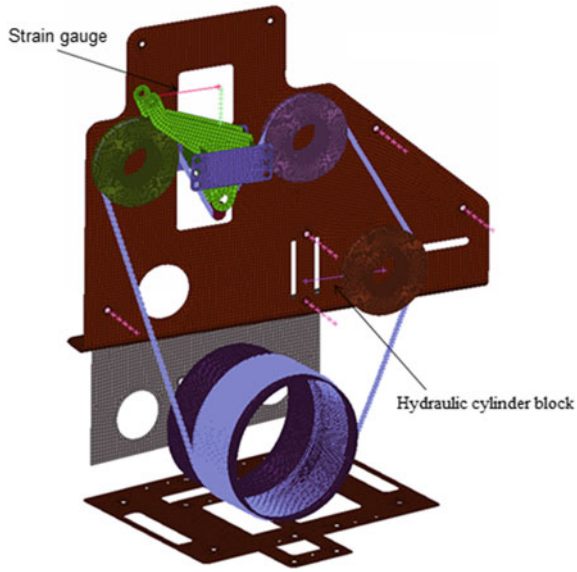


Fig. 17 The internal part of the finite element model of the loader

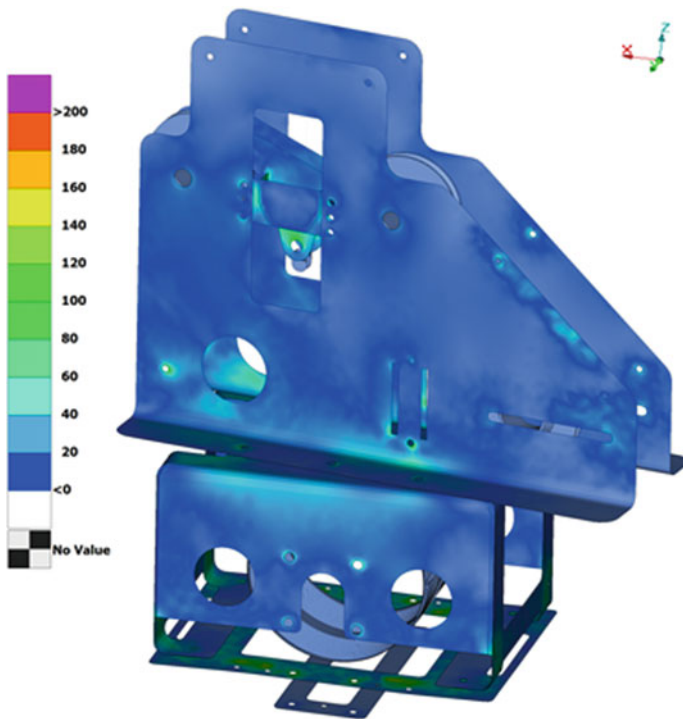


Fig. 18 The distribution of equivalent stresses in the body parts of the loader

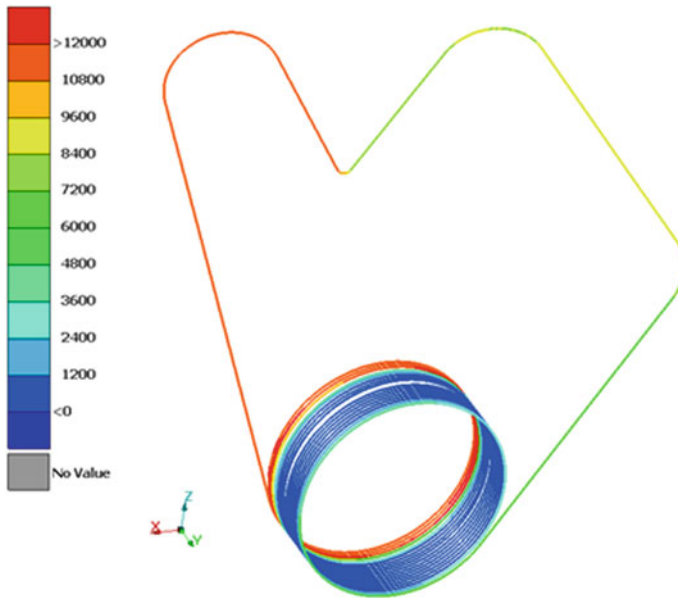


Fig. 19 The distribution of the rope tension force, N

we calculate the empirical coefficient λ . The last one characterizes the friction of the rope on the surface of the slide. On the other hand, coefficient relates the forces F_t and F_n (forces on the stress gauge and tensioner) and is determined by the formula:

$$\lambda = \frac{F_t * \cos(\alpha/2)}{F_n * \cos(\varphi/2)},$$

where α —angle, formed by the branches of the rope from the tension roller, φ —wrap angle of runner skid.

On the other hand, lambda coefficient was calculated in the field tests using the data from a stress gauge and a hydraulic cylinder manometer. In this case, the relationship between the coefficient of friction k and the empirical coefficient λ was determined. The k coefficient is directly defined in the contact settings between the beam elements and the slide surface.

$$k = 0.93 \cdot \lambda$$

The suggested formula can be used for simplified rope modeling. The extension and correction of this generally non-linear relationship can be performed in further development. The results of calculations were close to the results of experiments. It means the presented approach is adequate and can be used in the future in various technical problems.

5 Conclusion

As a result, a method for constructing simplified finite element models of wire ropes has been developed. The proposed algorithm for the transition from 3D finite element to 1D model adequately reflects the physical and mechanical properties of steel cables. It means this method allows to calculate wire ropes of any configuration when applying different loads. Herewith suggested approach doesn't require detailed modeling and permits to save the computational resources. The proposed method highlights the local areas of the rope with significant stress concentrations occur. The last ones creating prerequisites for the occurrence and development of cracks. Then it is possible to calculate a detailed study of the stress-strain state of these local areas of the rope using the results of previous calculations and 3D finite elements.



References

1. Erdonmez, C., Imrak, C.E.: A finite element model for independent wire rope core with double helical geometry subjected to axial loads. *Sadhana* (2011)
2. Imrak, C.E., Erdonmez, C.: On the problem of wire rope model generation with axial loading. *Math. Comput. Appl.* **15**(2), 259–268 (2010)
3. Utting, W.S., Jones, N.: The response of wire rope strands to axial tensile loads: Part I. Experimental results and theoretical predictions. *Int. J. Mech. Sci.* (1987)
4. Stolle, C.S., Reid, J.D.: Modeling Wire Rope Used in Cable Barrier Systems. Midwest Roadside Safety Facility Department of Mechanical Engineering University of Nebraska-Lincoln
5. Luz, F.F., de Menezes, E.A.W., da Silva, L.V., Cimini, C.A., Jr.: Sandro Campos Amico strength analysis of composite cables. *Latin Am. J. Solids Struct.* **15**(4) (2018)
6. Frikha, A., Cartraud, P., Treysède, F.: Mechanical modeling of helical structures accounting for translational invariance. Part I: Static behavior. *Int. J. Solids Struct.* **50**, 1373–1382 (2013)
7. Ghoreishi, S.R., Messenger, T., Cartraud, P., Davies, P.: Validity and limitations of linear analytical models for steel wire strands under axial loading, using a 3D FE model. *Int. J. Mech. Sci.* **49**(11), 1251–1261 (2007)
8. Shibu, G., Parthasarathy, N.S.: An insight of torque and stress balance behaviour of a contrahelically armored cable. In: Proceedings of the World Congress on Engineering, 2008, vol. II, WCE 2008, July 2–4, 2008, London, U.K
9. Shibu, G., Mohankumar, K.V., Devendiran, S.: Analysis of a three layered straight wire rope strand using finite element method. In: Proceedings of the World Congress on Engineering 2011, vol. III, WCE 2011, July 6–8, 2011, London, U.K
10. Argatov, I.: Response of a wire rope strand to axial and torsional loads: asymptotic modeling of the effect of interwire contact deformations. *Int. J. Solids Struct.* **48**, 1413–1423 (2011)
11. Bruski, D.: Determination of the bending properties of wire rope used in cable barrier systems. *Materials* **13**(3842), 22 (2020). www.mdpi.com/journal/materials
12. Heinrich, C., Waas, A.M., Wineman, A.S.: Determination of material properties using nanoindentation and multiple indenter tips. *Int. J. Solids Struct.* **46**, 364–376 (2009)
13. Cengiz Erdonmez, C., Imrak, E.: Modeling and numerical analysis of the wire strand. *J. Naval Sci. Eng.* **5**(1), 30–38 (2009)
14. LS-Dyna Keyword User's Manual Volume 2 Material Models

15. Jiang, W.G., Henshall, J.L.: The analysis of termination effects in wire strand using finite element method (1999)
16. TU-14-4-1549-89. Kanat stal'noj special'nogo naznacheniya. Moscow (1990) (in Russian)
17. Makarov, E.G.: Soprotivlenie materialov s ispol'zovaniem vychislitel'nyh kompleksov: uchebnoe posobie dlya vuzov. Urait, Moscow (2020) (in Russian)
18. Clausner, A., Richter, F.: Determination of yield stress from nano-indentation experiments, Germany

Development of Approaches to Modeling the Processes of Joining Sections and Operation of Drilling Equipment



T. V. Sergeeva , G. V. Monahovskiy , N. A. Kharaldin,
O. I. Klyavin, A. A. Kraev, and O. V. Knyazeva

Abstract The goal of this paper is to develop and test approaches to modeling the processes of joining sections and operating modes of drilling equipment based on using digital modeling. Using this technique made it possible not only to assess the quality of joining the structure of drilling equipment sections, but also to implement the stress-strain state of the structure after joining as the initial conditions for evaluating the design performance under operating conditions. The main method used in this work is all over numerical simulations based on finite-element method. The electricity resistance was measured after a series of simulations to help to understand and estimate the connection tightness between parts. The measured values of electricity resistance calculated by analytical formulas using as background data contact forces values. Achieved values showed their correspondence to real experiment. That results give us better understanding of tightness-dependent values, like electricity resistance and moreover—proved a 3D-modeling approach in sealed-types of connectors.

Keywords Drilling equipment · Digital modeling · Coupling simulation · Contact resistance

T. V. Sergeeva (✉) · G. V. Monahovskiy · N. A. Kharaldin · O. I. Klyavin
CNTI, Peter the Great St.Petersburg Polytechnic University (SPbPU),
195251 St. Petersburg, Russia
e-mail: filina_tv@spbstu.ru

G. V. Monahovskiy
e-mail: monahovskij_gv@spbstu.ru

N. A. Kharaldin
e-mail: kharaldin@spbstu.ru

O. I. Klyavin
e-mail: klyavin_oi@spbstu.ru

A. A. Kraev · O. V. Knyazeva
NOVOBUR LLC, 614000 Perm, Russia
e-mail: kraev.aa@novobur.com

O. V. Knyazeva
e-mail: knyazeva@novobur.com

1 Introduction

The research of drilling processes is widespread and covers a wide range of issues because of the complexity of existing processes and evolving technologies in the field of drilling [1]. In this area, the main tasks and areas of development are the search for optimal technical parameters of drilling (weight, rotation speed, etc.) [2, 3], the study of using various materials for drills and mechanisms of drilling equipment [4], as well as the development of automated systems and hardware simulators for drilling control [5]. Much less scientific research has been carried out in the design of drilling rigs for water wells, as well as research not on the drilling process and the stress state of the drill, and on the process of assembling drilling equipment sections and ensuring the transfer of energy to the tool.

The structure considered in this work uses a method of transferring energy using electric cables passing inside the drill pipes. It is necessary to provide a sufficiently low electrical resistance at the contact points (<0.001 Ohm) for ensuring the reliable and efficient transmission of electricity to the drilling tool. Joining the drilling equipment sections is carried out using rubber-metal joints. The estimation of this type of joint is nontrivial due to the nonlinearity of the properties of rubber bonded to metal components.

The purpose of this work is numerical modeling [6, 7] of the process of joining the drilling equipment sections, as well as an approbation of methods for transferring the stress-strain state (SSS) of the structure between design cases. Because of the design features of joining sections to each other, the listed tasks belong to the class of problems of studying the behavior of sealing joints. Measured parameters: contact pressure at the contact points, stress-strain state of structural parts.

The main feature of this study is using the stress-strain state of the structure after joining as the initial conditions for further virtual tests of the structure under the action of operational loads.

The implementation of the virtual tests described in the work was carried out on the basis of the platform CML-BenchTM (digital platform for the development of digital twins [8] and an activity management system in the field of digital design, mathematical modeling and computer engineering, development of the engineering center CEC SPbPU) using commercial licenses LS-DYNA and computational resources of CNTI.

2 Smart Digital Twin of the Drilling Equipment Section

The design of the drilling equipment sections at the joining area is shown in Fig. 1.

A highly adequate digital model of the drilling equipment section contains:

- Full-scale geometric (CAD) and finite element (CAE) section models;
- Information about all connections (bolts, threads, glue), assembly methods (gluing rubber to steel base) [9];

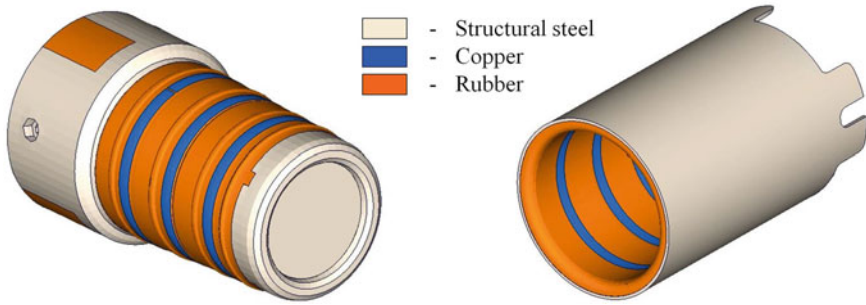


Fig. 1 Structure and material distribution of the indoor and outdoor modules [9]

- Properties of the materials: elastic-plastic characteristics of metals, taking into account the dependence on the rate of deformation, as well as the results of field tests of rubber samples for uniaxial tension (see Fig. 2);
- Information on operating conditions [9]:
 - the value of the internal hydrostatic pressure—75 MPa;
 - vibration (axial/radial)—acceleration amplitude 30 g, frequency 300 Hz;
 - shock impact (axial/radial)—acceleration amplitude 15 g, pulse duration 12 ms;
 - the curvature of the pipe axis of the drilling equipment section—30 mm/m.
- Targets and limitations: for joining—value of interference is not more than 3 mm during joining, the contact resistance is not more than 0.001 Ohm; for mechanical tests—no destruction of parts.

All calculation models were prepared for the LS-DYNA finite element analysis system.

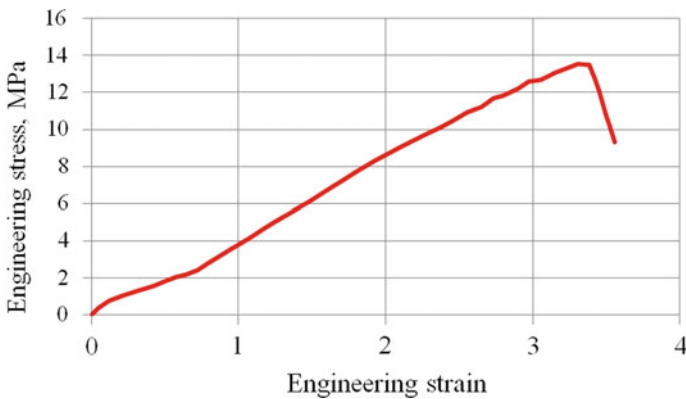


Fig. 2 Results of uniaxial tension full-scale tests of rubber [9]

3 Methods and Approaches

3.1 Material Modeling

The simplest two-parameter Mooney-Rivlin mathematical model (MM) of the rubber was used in this work. Its parameters A and B are defined from the deformation curves of the samples and determine the form of the deformation energy function (see Eq. 1) [10]:

$$W = A(I - 3) + B(II - 3) + \left(\frac{A}{2} + B\right)(III^{-2} - 1) + \frac{A(5\nu - 2) + B(11\nu - 5)}{2(1 - 2\nu)}(III - 1)^2 \quad (1)$$

where

- ν the Poisson's ratio,
- $2(A + B)$ the linear elastic shear modulus,
- I, II, III the invariants of the right Cauchy-Green tensor.

Studies are confirming the possibility of effective use of the two-parameter Mooney-Rivlin MM for modeling the dynamic behavior of seals [11].

The characteristics of MM of the rubber are usually selected based on the results of full-scale tests of elastomer samples for uniaxial tension/compression, biaxial tension/compression and shear, using internal tools of computer simulation software systems (the ANSYS system was used in this work).

An elastic-plastic MM was applied to describe the behavior of metals used in construction (steels and copper) in this work. The main properties of these materials are presented in Table 1.

3.2 Coupling

As a rule, the geometry of the seals reduce the problem of determining their stress-strain state under loading by switching to 2D analysis [12, 13, 14], which decreases the number of required computing resources. However, such a simplification is impossible for this construction and all problems were solved in 3D approach.

Table 1 Basic elastic-plastic properties of metals used in the construction [9]

Material	Young modulus (GPa)	Poisson ratio	Density (kg/m ³)	$\sigma_{0.2}$ (MPa)	σ_B (MPa)
Structural steel	198	0.33	7920	196	510
Copper M1	128	0.4	8940	60	180

The joining process is the connection of parts of adjacent sections of drilling equipment to each other. At the initial moment, parts of the sections (indoor and outdoor modules) are at the distance of 30 mm from each other (this distance is determined from the condition that there are no mutual intersections of undeformed geometries of structural parts at the initial moment). The boundary conditions for the problem of joining sections are presented in Figs. 3, 4. Interference in the joint is created due to additional mutual penetration of parts into each other by up to 3 mm.

Numerical modeling of the joining process was carried out using the implicit dynamic method. Ensuring the convergence of the solution required the following assumptions: the inertial component was not taken into account in the equations of motion; during the numerical simulation, the rotation that occurs in reality due to screwing the screw thread of the parts of the sections was not taken into consideration (only the translational movement was taken into account).

Fig. 3 Boundary conditions of the coupling simulation

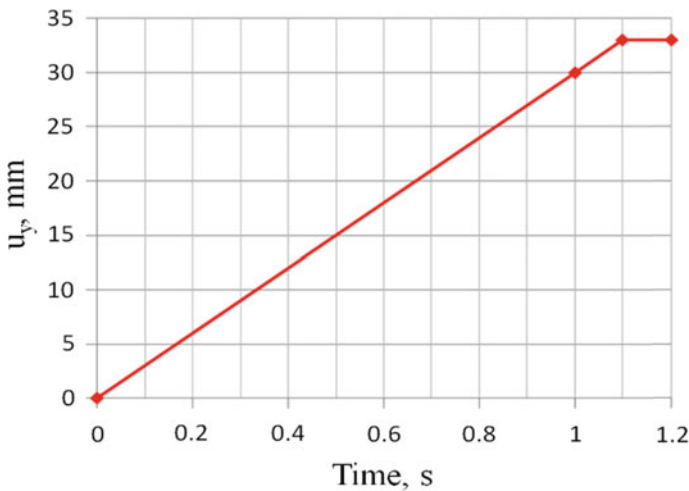
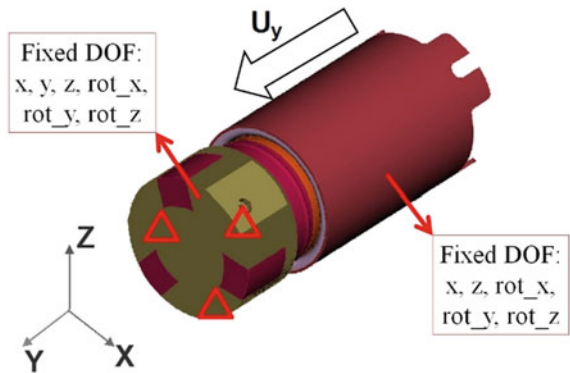


Fig. 4 Time dependence of outdoor unit movement

3.3 *Transfer of SSS Structures*

The transfer of the design SSS from one estimation (joining) to another (simulation of operational mode) in the LS-DYNA software system was performed by:

- updating the coordinates of construction nodes according to their final position in the previous estimation,
- transfer of residual stresses. In this case, for metal parts (steel, copper), the transfer was performed by explicitly specifying the stress tensor components for each finite element using the *INITIAL_STRESS_SOLID tool. For rubber elements, this method is not available because of the nonlinearity of the elastic behavior of the material, therefore, the stress transfer was carried out by specifying the initial position of the nodes of the elements (*INITIAL_FOAM_REFERENCE_GEOMETRY), the resulting stresses were functions only of deformation gradients [15]

$$F_{ij} = \frac{\partial x_i}{\partial X_j} \quad (2)$$

where x_i —the deformed configuration, X_j —the undeformed configuration.

3.4 *Dynamic Structural Analyses (Operational Load)*

The design assessment of the drilling equipment section under the influence of operational loads was carried out using the example of modeling axial vibration according to the loading parameters specified in paragraph 1.

Boundary conditions were applied to the ends of the model, which are the midpoints of the respective connected drilling equipment sections. The applied constraints and loads for the axial vibration problem are shown in Figs. 5, 6.

The entire FE model had an initial velocity in the direction opposite to the action of acceleration to avoid the impact of the structure at the initial moment of the action of the vibration load.

4 Results

4.1 *Material Modeling*

The parameters of MM of the rubber were evaluated from the experimental data of tensile tests of the rubber and publicly available data on deformations in compression of the similar material [16] and are equal to $A = 0.54$ MPa,

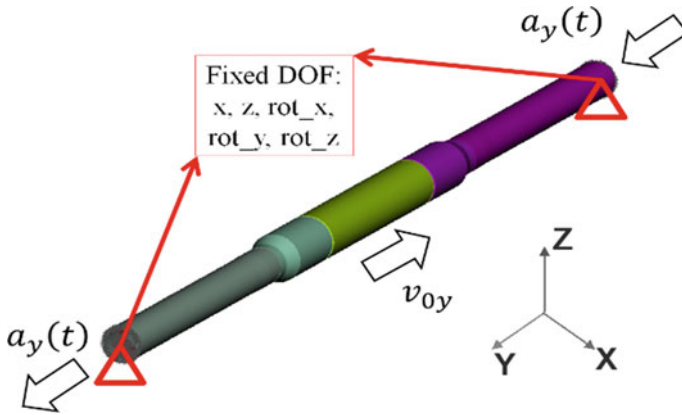


Fig. 5 Graphical interpretation of the axial vibration problem formulation

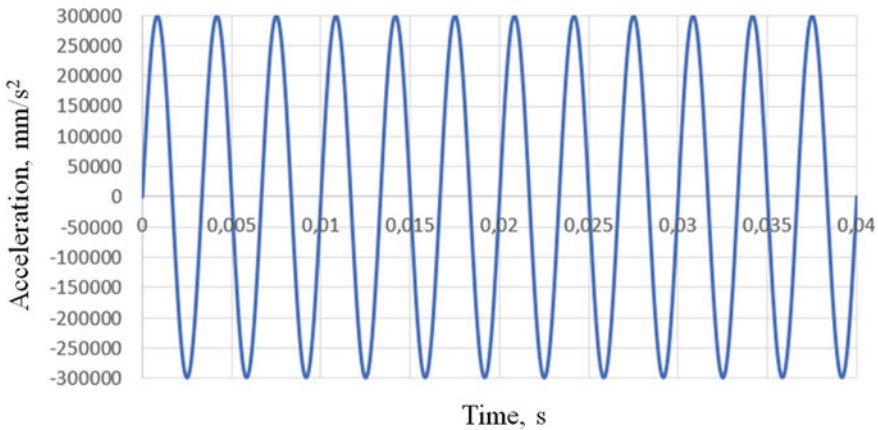


Fig. 6 Dependence of acceleration on time at vibration loadcase

$B = 0.75 \text{ MPa}$. The comparison of deformation curves of the generated MM with input data is presented in Fig. 7.

4.2 Coupling

When joining is modeled, all metal parts of the structure are in the zone of elastic deformation, and large compressive stresses occur locally in the rubber. Dangerous areas from this point of view are the ones associated with the contact copper rings, as well as the end rubber part of the External module, which is significantly

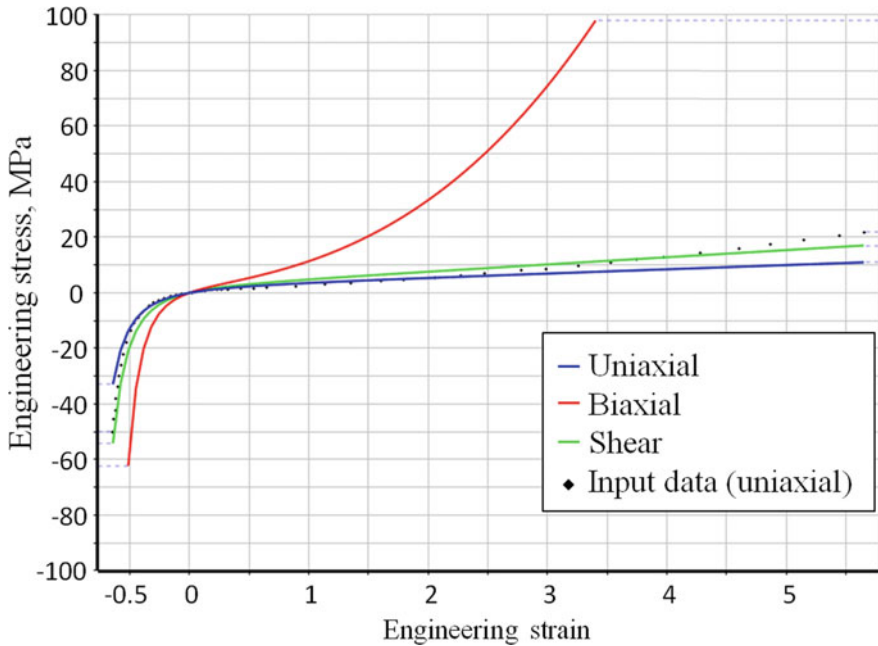


Fig. 7 Comparison of the strain curves of the rubber with the input data

deformed under interference. However, the obtained results do not give grounds for an unambiguous conclusion about the destruction of the rubber composition, since the criteria for the destruction of the elastomer at various stress states is unknown.

Next, the estimation of the contact electrical resistance after joining sections is presented.

The average contact pressure in the copper rings (see Fig. 8) at the final time (interference 2 mm) for slip rings is 3.5 MPa, 4 MPa and 4 MPa, respectively.

Based on the assessment of the areas of the contacting surfaces of the rings and the empirical formula for estimating the electrical resistance [9]

$$R_n = \frac{\rho}{2\sqrt{\frac{S_k}{\pi}}} + \frac{k_{nx}}{(0.102P_k S_k)^{0.6}} \tag{3}$$

where

R_n the transition resistance, Ohm,

S_k the contact area, m^2 ,

P_k the contact pressure between copper rings, N/m^2 ,

ρ the material resistivity at 0 °C (for copper $1.62 \cdot 10^{-8}$ Ohm·m),

k_{nx} The coefficient depending on the material and quality of the contacting surfaces (for copper $0.24 \cdot 10^{-3}$).

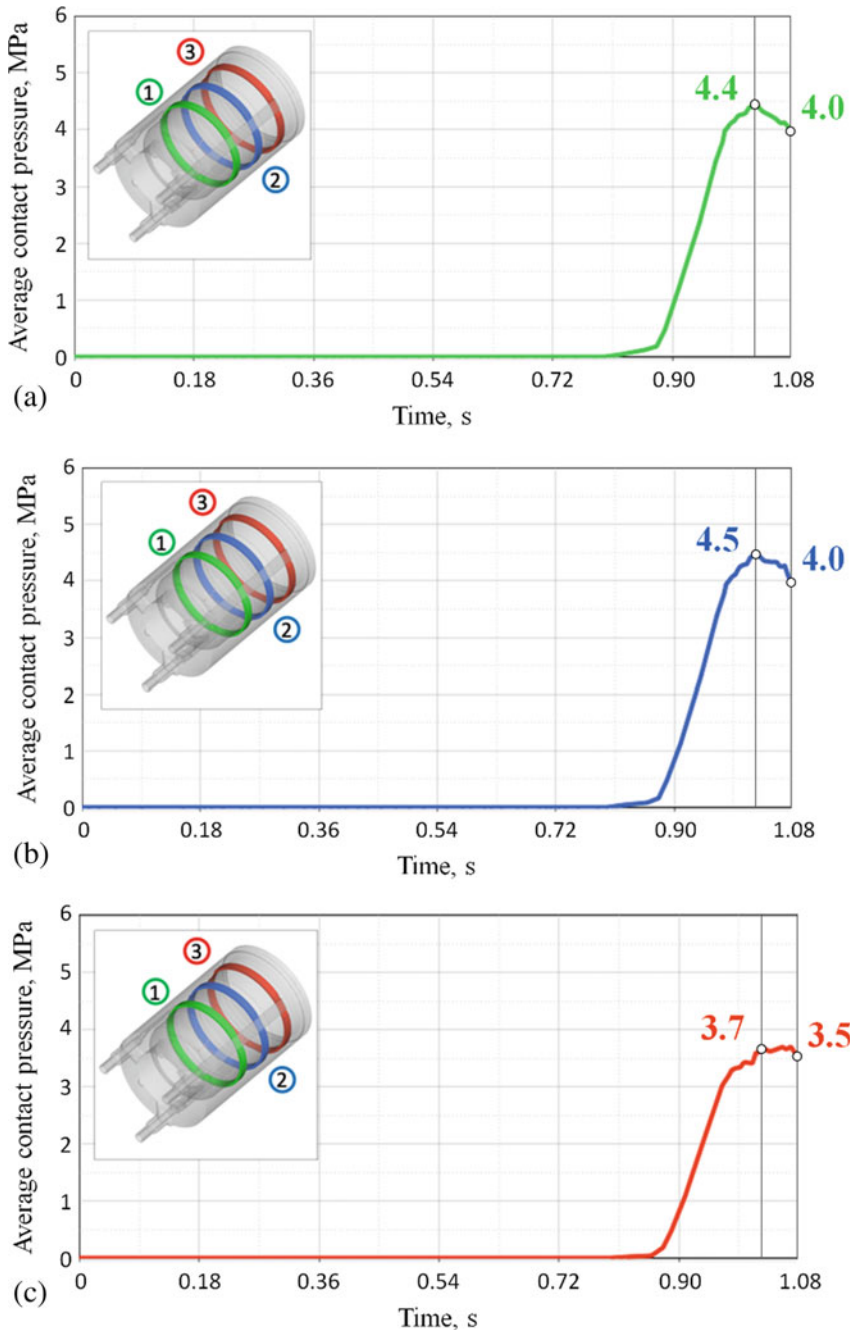


Fig. 8 Contact pressures during joining in the copper rings

The estimated values of the contact resistances of the slip rings after joining are, respectively $R_1 = 6.6 \cdot 10^{-6}$ Ohm, $R_2 = 6.2 \cdot 10^{-6}$ Ohm, $R_3 = 6.3 \cdot 10^{-6}$ Ohm, that is, do not exceed the target value of 0.001 Ohm.

The performance of the electrical system of the drilling equipment after joining the sections is confirmed by the results of full-scale tests.

4.3 Dynamic Structural Analyses (Operational Load)

The most important result of this stage is the reproduction of the level of contact pressures at the first steps of the estimation, achieved during joining (Fig. 8c). Subsequently, the contact pressures, which ensured reliable power transmission, increased because of the internal pressure acting on the structure (Fig. 9).

5 Discussion

The mathematical model of the rubber developed and used in this study is a reasonable compromise between the requirements for the accuracy of the results and the incompleteness of the available initial data. The studies show that the attempt to improve the accuracy of the rubber modeling and switch to the material model with a larger number of parameters (among the Mooney-Rivlin models, the results that are closest to the experimental data are given by MM with five parameters [17]) in the presence of initial information only about uniaxial loading

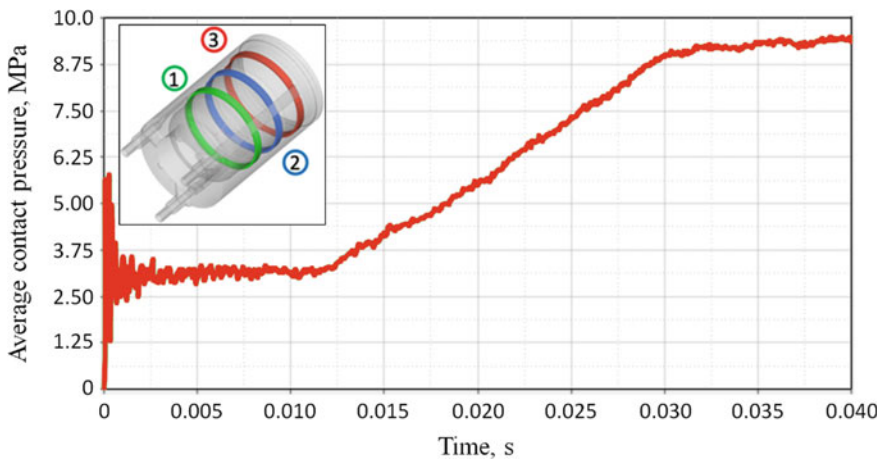


Fig. 9 The contact pressure of the third ring during virtual axial vibration test

leads to non-physical results. Thus, the need for additional full-scale tests of rubber samples (biaxial loading, shear) was revealed for further research.

The results of numerical simulations drilling equipment sections joining show that stress-strain state of structural parts meet the strength conditions. Besides, the structure provides required level of the electrical conductivity in terms of the interaction of contact rings, which is confirmed by full-scale tests of the structure operability after assembly.

The operability of the applied method of transferring the stress-strain state of a rubber-metal structure between virtual tests was confirmed in the course of the test design evaluation of the structure under the action of axial vibration. In the future, this would take into account the contribution of SSS that occurs in the rubber-metal structure during assembly in final SSS caused by the action of operational loads. The assessment of the quantitative characteristics of the structural stress-strain state and the degree of compliance of the results of virtual mechanical tests with reality only after full-scale tests.

This work did not touch upon the topics of assessing the thermally stressed state of the structure in the absence of initial data, which is relevant for rubber-metal products and operating conditions of drilling equipment (temperature range from -40 to 100 °C), as well as validation of the created digital model of the structure based on the results of full-scale tests.

6 Conclusion

The method tested in this study can be used to assess the stress-strain state of various non-axisymmetric rubber-metal joints or sealed-type connectors during assembly and subsequent operations. Also, this method can provide better understanding of tightness-dependent values like contact pressure between any contact surfaces in connected parts during the simulation. Subsequently, this study can be extended by thermal-stress analysis, which can be applied alongside with mechanical operational conditions.

References

1. Current problems of scientific research in priority areas of science, technology and engineering of the Russian federation. Saint-Petersburg Mining University, St. Petersburg (2017). (in Russian) https://www.spmi.ru/sites/default/files/imci_images/aspirant/pdf/Актуальные%20проблемы.pdf. Last Accessed on 15 Sept 2020
2. David, H., Saeed, S., Fatemeh, K.S.: An integrated approach for drilling optimization using advanced drilling optimizer. *J. Petrol. Eng.* **2015**, 1–12 (2015)
3. Vijayaraghavan, A., David, A.D.: Automated drill modeling for drilling process simulation. *J. Comput. Inf. Sci. Eng.* **7**(3), 276–282 (2007)

4. Asit, K.P.: Simulation and experimental investigation of drilling of Ti-6Al-4 V alloy. *Int. J. Lightweight Mater. Manuf.* **1**(3), 197–205 (2018)
5. Hong-Chih, C., Melissa, M.L., Gurtej, S.S., Mitch, P., Eric, V.O.: Development and validation of a scenario-based drilling simulator for training and evaluating human factors. *J. IEEE Trans. Human-Mach. Syst.* **50**(4), 327–336 (2020)
6. Borovkov, A.I., Maruseva, V.M., Ryabov, Y.A.: «Smart» digital twins are the basis of a new paradigm of digital design and modeling of globally competitive products of a new generation. *J. Springboard Success* **13**, 22–27 (2018). (in Russian) http://assets.fea.ru/uploads/fea/news/2018/04_april/12/tramplin-uspeha_13-16.pdf. Last Accessed on 15 Sept 2020
7. Borovkov, A.I., Maruseva, V.M., Ryabov, Y.A.: A new paradigm of digital design and modeling of globally competitive products of a new generation digital production: methods, ecosystems, technologies: working report of the corporate training, pp. 24–35. Department of the Moscow school of management SKOLKOVO), Moscow (2017) (in Russian)
8. Borovkov, A.I., Ryabov, Y.A., Gamzikova, A.A.: Digital twins in oil & gas engineering. *J. Neftegaz. ru* **6**(102), 30–36 (2020). (in Russian) https://assets.fea.ru/uploads/fea/news/2020/06_june/29/neftgaz-18-21.pdf. Last Accessed on 15 Sept 2020
9. Data provided by NOVOBUR LLC
10. LS-DYNA® Keyword User's Manual R10.0, vol. II, p. 266
11. Silvestri, M., Prati, E., Tasora, A.: Dynamic seals behaviour under effect of radial vibration tribology and lubrication engineering. In: 14th International Colloquium Tribology, vol. 2, pp. 1247–1255 (2004)
12. Chilou, Z., Guohua, C., Shu, X., Zhengli, H., Chaohua, G.: Study on fretting behavior of rubber O-ring seal in high-pressure gaseous hydrogen. *Int. J. Hydrogen Energy* **44**(40), 22569–22575 (2019)
13. Zhang, Y., Zhang, X., Yang, L., Yu, X.: Optimization design for downhole dynamic seal based on response surface method. *J. Adv. Mech. Eng.* **11**(2), 1–10 (2019)
14. Hu, G., Wang, G., Dai, L., Zhang, P., Li, M., Fu, Y.: Sealing failure analysis on V-shaped sealing rings of an inserted sealing tool used for multistage fracturing processes. *J. Energies* **11**(6), 1432 (2018)
15. LS-DYNA® Keyword User's Manual R10.0, vol. I, p. 2065
16. <https://www.predictiveengineering.com/consulting/ls-dyna/o-ring-analysis-using-advanced-elastomeric-material-laws-ls-dyna-0>. Last Accessed on 15 Sept 2020
17. Sukumar, T., Ramesh Babu, B.R., Durga Prasad, D.: Numerical and experimental evaluation of hyperelastic material parameters. *J. Adv. Mater. Metall.* 485–494 (2018)

Research and Application of Quality Control Strategy for CNC Workshop



Qing Gao, Zhengming Tang, Tianfu Liu, Weiyi Wang,
and Meilan Luo

Abstract In order to improve the product quality of the manufacturing enterprise in the multi-variety and small-batch production mode, take the K-factor S-CN machining workshop as the carrier, analyze and summarize the quality problems existing in the parts production process, and propose the operator from the management level. Seven-step inspection method, nine red lines of technology, equipment inspection, and three quality control methods, and established a real-time fault processing platform, which can respond to and analyze the quality problems in time. Subsequent practice applied to the workshop, the results show that the product qualification rate of the workshop has increased from 3.8 levels before application to 4.5 levels, and the relevant quality indicators have met the specified requirements, which proves the advanced and practical value of the quality control strategy.

Keywords CNC · Workshop · Quality control · Production operation · Process

1 Foreword

As development of science and technology, new products emerge in endlessly. The market demand is increasingly personalized and diversified. The multi-variety and small-batch production model has gradually occupied an increasingly important position in manufacturing enterprises [1, 2]. Due to the short production cycle and the difficulty in batch automatic production, ensuring the quality of such products is the key to maintain the company's market share and sustainable development [3]. If enterprises want to occupy a favorable position in the global market economy, it is necessary to deeply discuss and study the construction of quality management system under the mode of multi-variety and small-batch production [4]. With Motorola, Honeywell, Toshiba, etc. as a representative of advanced manufacturing

Q. Gao (✉) · Z. Tang · T. Liu · W. Wang · M. Luo
Chengdu Aircraft Industry (Group) Co., Chengdu, China
e-mail: g17360132308@163.com

technology of the world top 500 enterprises, their strategic management and product quality has already entered into a state of calm and transparent. Most domestic enterprises is still in the risk in the process of production with abnormalities in the control stage. As a result, level of the gap can not be ignored, which leading to many varieties of small batch manufacturing quality management level and the foreign advanced enterprise management level [5].

The reason is that there is a serious lack of empirical research on quality control in domestic enterprises. Also, they have not obtained an appropriate management control system (MCS) to support the advantages of quality management [6]. In this case, this paper takes the 2015 annual production situation of S nc machining under workshop of K factory (referred to as “nc workshop”) as the research object. Analyzing problems in quality management of this workshop, it has three quality control strategies. It builds a real-time processing platform. After application worked to this workshop in practice from 2015 to 2017, the rate of unqualified products in the workshop decreased significantly, which proves that the series of quality management and control strategies provided in this paper are effective. That also can provide reference for enterprises with similar processing workshops.

2 Numerical Control Workshop of Internal Quality Problems

2.1 Macro Analysis of Production Project Quality

According to the tracking the failure parts of the 2015 annual production project of the nc workshop. The statistics of a total of 296 failed parts occurred in the production process of project A, B, C and D in the whole year of the workshop, which was accounting for 84.1% of the total failure parts of all projects. The annual quality indicators such as the qualified rate of the internal loss products, the qualified rate of the first delivery inspection, the qualified rate of the out-of-tolerance parts, and the qualified rate of Product qualification, which are shown in Table 1. It can be seen that all the indicators of the project did not reach the expected value. The quality indicators of project B and project C were seriously low. There was still a big gap between the internal quality loss rate of the product, the out-of-tolerance parts should be less than 0.02%, the qualified rate of the first inspection and the quality level of the product qualified rate should be greater than 99.98%.

Table 1 Statistics on quality indicators in 2015

Project name	Index	Internal quality loss rate (%)	First time yield (%)	Excess rate of clearance (%)	Pass-rate of production (%)
	Require	≤ 0.02	≥ 99.99	≤ 0.02	≥ 99.98
Project A	Result	0.05	99.9	0.04	99.04
	Conclusion	Instability	Instability	Instability	Instability
Project B	Result	0.22	99.43	0.06	98.72
	Conclusion	Instability	Instability	Instability	Instability
Project C	Result	0.05	98.90	0.04	98.44
	Conclusion	Instability	Instability	Instability	Instability
Project D	Result	0.05	99.21	Irrelevant	99.36
	Conclusion	Instability	Instability	Irrelevant	Instability

2.2 Micro Analysis of Production Project Quality

The macro analysis shows that there are quality problems in nc workshop, while the micro analysis is to find out the fundamental problems. In 2015, there were 154, 113 and 19 faults caused by production operation, which were technological technology, and machine, and tool equipment, which was accounted for 52.0%, 38.2% and 6.4% respectively, and 10 parts faults caused by other aspects, which was accounted for 3.4%. It can be seen that the fault causes of parts are relatively concentrated, and the specific situation is as follows:

Production operation. Due to the management did not formulate strict operation of specifications before the workers machining, the workers were negligent in some link of preparation before the machining. The whole production process is not under stable control, and the fault is difficult to be found and eliminated in time. After statistical analysis of specific on-site faults in 2015, this paper selected major fault points [7, 8]. According to the principle of “important minority and unimportant majority” in quality management, as shown in Table 2, seven types of key fault causes and typical events occurred during the operation of workers.

Table 2 Key failure points of production operation and typical events

Key failure points	Typical events
Fixture	Fixture installation error
Origin	Error setting
Semifinished prouduct	Installation error of semifinished prouduct
Knife	Knife specification discrepancy/Knife setting is not in line with actual
Mirror	Forget to add or unmirror
Procedure	Transfer error
Making zero	The pendulum angle of machine were not zero

Technological technology. The faults are as followings; the variety of products, the complex working procedures of some parts, the incomplete consideration of the process personnel, the process personnel to effectively coordinate the operation. According to the screening principle mentioned above, the key fault causes of the process technology are summarized as shown in Table 3.

Machine equipments. Mainly inspection regulation in the machine tool is not clear. The operator inspection consciousness is not sufficient. Resulting in the point inspection execution is not ideal. The main failure points of machine tools are shown in Table 4.

3 Quality Control Strategy

The foregoing is only from a single point to find the cause of the fault, but do not systematically solve the quality problem. According to relevant studies, only 15% of quality problems in enterprises are caused by improper operation, and 85% are caused by system errors due to poor management [9]. Starting from the management level, referring to the main fault causes of process technology, production operation and machine tool equipment, this paper puts forward three strategies of

Table 3 Key failure points of process technology and typical events

Key failure points	Typical events
Origin	Ununified origin
Simulation	Disagreement between simulation and actual design
Simulation of five-seater machine	Installation error of semifinished product
Verification block	Failure to simulation by using verification block
Blind hole	The hole depth was not carefully examined during finishing, resulting in knife damage.
Lovercut	Overcutting of parts
Procedure optimization	Procedure optimization error
Size	Important size were substandard

Table 4 Key failure points of machine and typical events

Key failure points	Typical events
Spindle system	Foreign matter
Lubricating system	Insufficient lubricating fluid
Hydraulic system	Abnormal leakage
Refrigeration system	System temperature beyond normal range
Automatic tool magazine	Automatic tool magazine pause
Chip removal system	Abnormal noise

“nine red lines of process”, “seven-step inspection method” and “equipment spot inspection” respectively to standardize the inspection program of staff. Therefore, realizing the product quality control and establishing a real-time fault processing platform for quality control strategy, the fault is in a stable and controlled state, and eventually an evaluation system is provided for the fault processing results.

3.1 Production Expectations of Quality Control

Specification should be from the top quality intentions to corresponding plans, standards and measures, and then extended to enterprises in various sectors to individuals. They are committed to continuously improve, but not limited to the workers. Lastly, focusing on the process of source and helping staff and production workers [10]. Under varieties of small batch production conditions, the requirements of workers should be able to master a variety of operational skills. They adapt to the requirements of multiple varieties and periodic production changes. However, due to the increasing number of key links and key points affecting quality in the whole product process, human operation errors are inevitable [11]. Therefore, the quality control strategy formulated in this paper, which aims to further standardize the operation, minimize the manual fault of parts and thus improve the qualified rate of products.

Seven-step inspection method of operator’s. According to the production process, the control of quality problems caused by the operation of workers can be divided into pre-processing control, in-processing control and post-processing inspection. Statistical analysis found that the numerical control workshop machining operation fault is mainly manifested in the former workers as followings; the state of fixture, the origin, parts machining surface profiling, tool specifications, procedure calls, mirror set equipment, equipment angular of seven aspects, such as back to zero. As shown in Table 5, in view of the above on-site operation problems, this paper formulated the inspection route corresponding to seven steps. According to the processing process, providing an important inspection point for the on-site operators’ pre-processing inspection.

Eight-step equipment point inspection. As an advanced means of equipment maintenance and Management, equipment point inspection is the process of Total Productive Management (TPM) of all employees. they refers to the inspection of important feature points of equipment in a certain frequency [12]. In order to prevent product quality problems caused by equipment problems, statistical analysis was carried out on the problems. According to the principle of “80/20”, characteristics of equipment parts affected by high frequency were extracted. Corresponding codes were carried out, and inspection at different frequency and time periods were arranged. As shown in Table 6, according to the feature points of the machine tool, it is the point inspection standard table and corresponding point

Table 5 Seven-step inspection method of pre-processing

Part number	Quality number	step	machine	date
Inspection step of pre-processing	<p>1、 check fixture status; Check that fixture position and straightness is or not correct; yes <input type="checkbox"/> no <input type="checkbox"/></p> <p>2、 check the origin X__Y__Z__ Origin position is__</p> <p>3、 check the left and right parts of this process, quality of frontage and reverse side Producing part is : left <input type="checkbox"/> right <input type="checkbox"/> Machined surface is: left <input type="checkbox"/> right <input type="checkbox"/></p> <p>4、 Check tool specifications Total number of tool specifications categories required in this process is__. Does specifications satisfy require after re-inspecting.</p> <p>5、 Checking mirror status of machine pane. Does this process require mirroring? yes <input type="checkbox"/> no <input type="checkbox"/> Is there a mirror in the machine settings? yes <input type="checkbox"/> no <input type="checkbox"/></p> <p>6、 Checking program. Is there any other part program in the machining program directory? yes <input type="checkbox"/> no <input type="checkbox"/></p> <p>7、 Check the pendulum instructions at the beginning of the NC program for five-seat machine tools. Is there zero instruction by checking procedure head swing? yes <input type="checkbox"/> no <input type="checkbox"/> Check that the angle on the machine panel is or not zero? yes <input type="checkbox"/> no <input type="checkbox"/></p> <p style="text-align: right;">Operator</p>			
	re-inspect	re-inspector		
	special inspection	specialist inspector		

inspection record table of nc workshop L machine tool. At the same time, it enhances the operators’ awareness of spot inspection, optimizes the route of spot inspection, implement spot inspection and ensures the execution degree of spot inspection.

Nine red lines of the process. The “nine red lines of the process” is a valid way to realize the controllability and accuracy of the process and reduce the artificial faults by implementing normative self-checking and proofreading standards. In order to realize one-to-one effective control of typical fault problems, this paper focuses on the key points of technical fault mentioned above, and puts forward the contents that must be checked for the nine process self-inspection and proofreading in the process development process, which is namely “the nine red lines of the process”, as shown in Table 7.

Table 6 Eight-step machine tool point inspection standard table

Checking point	Point inspection	Inspection cycle	Point inspection standard
①	Main spindle cone	Per day	Check no oil stains, content in, aluminum chi
②	Bottom of table	Per day	Is there any turning of the exchange table bottom There is no abnormal noise and alarm on the switching platform
③	Electric air conditioning cabinet filter screen	Per day	The filter screen shall be ventilation effect
④	Lubricant tank, hydraulic unit	Per week	Pressure gauge and Lubricant level shall be within the scale range
⑤	Compressed air, coolant unit, chip enclosure, liquid level	Per day	Cotton filter shall be clean, and oil skimmer be free from drainage. All motor fans shall be clean, and chip cleaner level at: 6–8, coolant tank level at: 75–100
⑥	Cutter collection, cutter chain, Cutter-change arm	Per week	Mechanical arm shall be clean, cutter chain shall operate normally
⑦	Smog-inhale device, internal filter mesh	Per week	Smog-inhale device shall be in normal condition, the internal filter mesh shall be replaced and cleaned
⑧	Machine, working area, oil-gas separator	Any time	The machine shall be clean in appearance, no abnormal noise and alarm, no crack and leakage

Table 7 Nine red lines of the process

Number	Check content	Check the result
1	Origin unity review	Technologist/ proofreader
2	Whether the simulation adds Fixture and press plate as required by the manual.	Technologist/ proofreader
3	Checking the simulation of Five-Code Machines	Technologist/ proofreader
4	Milling damage check of verify block	Technologist/ proofreader
5	Check the depth of drilling chambering reaming and boring for blind hole	Technologist/ proofreader
6	Overcut inspection of damaged type	Technologist/ proofreader
7	Comparison and simulation between new and old and new in program optimization	Technologist/ proofreader
8	Inspection of asymmetrical tolerance dimensions	Technologist/ proofreader
9	Inspection of important dimensions	Technologist/ proofreader

3.2 *Fault Treatment System*

In order to facilitate the timely treatment of the fault problems found in the production process, it is necessary to establish a fault treatment system to timely handle and track the problems to zero. As a result, it prevents the occurrence of repetitive quality problems. The fault handling system is divided into real-time problem handling system and quality improvement proposal management system. Carry out real-time problem responses management. Displaying important indicators such as timely return to zero rate through information tools such as dashboards, and real-time monitor PDCA of process problems. “Real-time demand information” and “real-time customer satisfaction feedback” can be visualized. According to the on-site demand, staff in each position will try their best to support the on-site production in the first time to ensure the quality and progress of the on-site production. Through DNC monitoring and analysis, the empirical judgment is transformed to data analysis, and the process stability is transformed from focusing on the real substance quantity of products. After the problem is solved, the problem handler returns to zero. Finally, the initiator evaluates the systems.

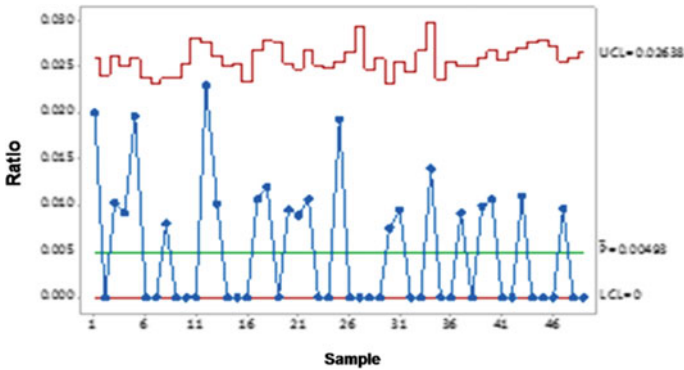


Fig. 1 The P control chart of the number of unqualified products

4 Application of Quality Control Strategy

After the trial application exploration period from 2016 to 2017, this paper conducted A survey on the application effect of quality control strategy in S CNC workshop of K factory in 2018. By sampling different quantities of products in project A, B, C and D of the workshop every week, the sample results of fault parts in 2017 were obtained. The MINITAB sample Statistical Process Control (SPC) chart was used to monitor the product [13], and the P Control chart of the number of unqualified products as shown in Fig. 1 was obtained. It can be seen that the failure rate of the whole process has been controlled, and the product quality of the CNC workshop is in a statistically controllable state. In addition, the workshop produces about 7400 pieces of products in items A, B, C and D every year. According to the six sigma management statistics method, the qualified rate of products in the workshop has increased from 3.25 α in 2015 to 4.5 α in 2018. It has effectively reducing the failure parts.

5 Conclusion

In conclusion, in the face of the lack of empirical research on quality control methods in China, this paper takes S nc machining workshop of K factory as the research object. It analyzes and summarizes the quality problems existing in the process of parts production. Finally, It points out the key failure points of process preparation, production operation and machine tool equipment. In view of this, looking forward the operator’s seven-step inspection method, nine red lines of the process, equipment point inspection three quality control, which set up the real time fault processing platform, to the quality of the emergence of timely response and

analysis to solve the problem. After practical application in the workshop, the number of failures was effectively reduced. The qualified rate of products was increased by 1.15. The research shows that the quality control strategy provided in this paper is helpful for the enterprises of multi-variety and small-batch NC machining. It reduces product failures and improves comprehensive competitiveness.

References

1. Zhong, X.Y.: Key Working Procedure in Multiple Varieties and Small Batch Production Identification and Quality Control, Research and Application. Chongqing University (2017)
2. Zhang, Y.-Z.: Many varieties, small batch production process study. *J. Combination Mach. Tools Autom. Process. Technol.* (6), 76–77 (2006)
3. Chengxuan, S., Ji, W.-X.: For many varieties of small batch machining workshop working procedure quality control method research. *J. Combination Mach. Tools Automatic Process. Technol.* (6), 172–176 (2018)
4. Zhou, B., Shi, L., Ju, W., Wang, H., Cui, Y.: Analysis and research on quality management system in multi-variety and small-batch production and management. *China New Technol. New Prod.* (02), 127–128 (2017)
5. He, Z.: Six Sigma Management. Renmin University of China, Beijing (2017)
6. Wen, D., Chen, S., Pan, F.: Performance effect of total quality management should be: a structural equation model study. *J. Manage. Sci.* **11**, 79–96 (2014)
7. Gong, Y.: Modern Quality Management. Tsinghua University Press (2007)
8. Zhang, G.-B., NiLin, YuNing.: Modern Quality Engineering. Mechanical industry publishing house (2015)
9. Cai, S.-Q., Shang, Y., Wang, Q., Zhou, Y.-H., Liang, K.-C.: *China management science* (2), 116–121 (2017)
10. Zhang, X., Hu, X.: *Business management* (7), 77–79 (2017). *China soft science* (08), 71–75 (2001). Ding, X.: Spot inspection maintenance system and equipment management modernization
11. Su, Q., Guo, T.: Establishment and evolution of enterprise quality environment integrated system. *China Soft Sci.* (08), 71–75 (2001)
12. Ding, X.: Spot inspection maintenance system and equipment management modernization. *Coal Technol.* (12), 110–111 (2003)
13. Di, S.: Design of dynamic SPC quality control system for engine cylinder processing. *Integr. Mach. Tool Autom. Process. Technol.* (02), 115–117 (2015)

Research on Teaching Design of Machining Technology in Higher Vocational Education



Danqing Liu

Abstract Higher vocational education is a type and level of higher education in the national education system. According to the needs of social posts, it trains practical talents at the front line. The mechanical industry shoulders the responsibility of providing various technical equipment for the material life and production of human beings. The improvement of mechanical design and manufacturing level can ensure the sustained and high-speed development of national economic construction. Machining is the basic technology, which plays an important role in the mechanical industry [1]. The design of mechanical processing technology in higher vocational education aims at training practical talents and serving the machinery industry better. The traditional teaching mode of machining technology is no longer suitable for the concept of education. Mechanical technology can not be lost, it needs to be developed and designed. How to teach, how to learn, we combine boring theory and practice. The team of teachers designed and developed the “teaching carrier” and adopted project-based teaching. Mechanical technology points are infiltrated into each subtask. We should increase the process assessment, pay attention to the cultivation of professional quality, improve the teaching environment, and integrate “teaching, learning and doing”. After three rounds of teaching implementation, the teaching effect is remarkable, students quickly adapt to the needs of the mechanical technology industry, social recognition is very high.

Keywords Higher vocational education · Machining technology · Instructional design · Teaching carrier · Professionalism

D. Liu (✉)

School of Electronics and Automation, Beijing Information Technology College,
Beijing, China

e-mail: 9323332@qq.com

1 The Significance of Vocational Education

Higher vocational education is a type and level of higher education in the national education system. Higher vocational education is higher education of different types and levels with higher undergraduate education. Different from the emphasis on discipline in undergraduate education, it is classified according to occupation. According to the requirements of the actual scope of business activities of a certain professional post (Group), higher vocational education cultivates the first-line practical (technical application or professional) talents. This kind of education emphasizes the vocational pertinence and the cultivation of vocational skills and abilities, which is the employment education oriented by the demand of social talent market. In the past 40 years of reform and opening-up, China has established the largest education system in the world, formed the basic framework of modern vocational education system with Chinese characteristics, improved the overall level of school running, and coordinated development of industry and education. There are more than 1400 vocational education groups in China, covering more than 90% of Vocational Colleges and more than 100 industry departments. Higher vocational education has local characteristics, which has trained a number of first-line practical talents for all walks of life [2].

2 Analysis on the Position of Machining Industry in the Industrial Chain

Machinery industry has made positive contributions to the development and construction of national economy in China, and has played a better role as a pillar industry. With the implementation of some policies and measures, the operating environment of machinery industry economy will be improved and the vitality of enterprise development will be further released. Specific policy measures include: pushing to tap the potential of the domestic market, expanding and expanding final consumption, stabilizing investment in the manufacturing sector, upgrading the capacity of the industrial base and the level of the industrial chain, and implementing the policy of reducing taxes and fees. From another angle can also reflect the importance of the state to the machinery industry.

China is in the process of accelerating industrialization. Manufacturing is an important pillar and foundation of the national economy. We should follow the trend of "Internet+" and take the integration of informatization and industrialization as the main line. It will focus on developing the following ten major areas: new-generation information technology, high-end CNC machine tools and robots, aerospace equipment, marine engineering equipment and high-tech ships, advanced rail transport equipment, energy-saving and new energy vehicles, electric power equipment, new materials, biomedicine and high-performance medical equipment, agricultural machinery and equipment. We will strengthen the basic industrial

capacity, improve the level of technology and product quality, and promote intelligent manufacturing and green manufacturing. These ten fields basically belong to the integration of high-tech industry and modern manufacturing industry. Through the definition of the ten fields, it points out the way for the modernization and scientization of modern industry in China, and also points out the direction for optimizing the upgrading of industrial structure. All these are inseparable from the basic industry of machinery manufacturing. Therefore, we should pay attention to it. We should not forget the basic technology and ignore the importance of basic technology when we have new technology. Only by laying a solid foundation can we bid farewell to the national economic structure characterized by heavy chemical industry, and move forward to the direction of high-end, energy-saving, environmental protection and high-tech.

3 The Importance of Machining Technology

3.1 Machining Technology Is the Foundation of Machinery Industry

Mechanical processing technology is to support and promote the skills, knowledge and professional quality of skilled personnel in the production line, such as the operation of mechanical processing equipment, maintenance of mechanical equipment, production process design and product quality inspection and so on.

The machinery industry shoulders an important responsibility to provide various technical equipment for the material life and production of human beings. The production level of the machinery industry is an important symbol of the modernization construction of a country. The improvement of the mechanical design and manufacturing level can ensure the sustained and rapid development of China's economic construction. Therefore, machining technology is an indispensable and important technical work, which occupies a very important position in mechanical engineering.

3.2 Application Scope of Machining Technology

In machining, different machining methods can be selected according to the material and requirements of the machined workpiece. We can choose different machining methods according to the requirements. Common machining methods include turning, milling, planing, grinding, drilling, boring, tooth surface machining, complex surface machining, EDM, ECM, laser machining, ultrasonic machining, etc.

It is widely used in national infrastructure construction, some national defense design institutes and military enterprises [3]. The application scope of machining includes:

1. Processing of various metal parts.
2. Sheet metal, box and metal structure.
3. Mechanical processing of titanium alloy, high temperature alloy and non-metal.
4. Design and manufacture of wind tunnel combustion chamber.
5. Design and manufacture of non-standard equipment.
6. Design and manufacture of mold.

3.3 The Necessity of Machining Technology

In the process of traditional professional transformation, basic technology is easy to ignore. Although it is a new era and digital technology covers many industries, the basic industry cannot be lost, and the spine industry cannot be absent. For the development of our country, we should dedicate our strength from different angles. Contribute to the development of the country from different angles. This is the age of intelligent manufacturing, robotics, but it's all based on the idea of machinery that allows for high-end design and application, so mechanical processing technology is indispensable. We also hope that the society, especially the educators in the education industry, especially in higher vocational colleges, attach importance to the inheritance and application of machining technology. We can't ignore the fundamental. Just like the State advocates paying attention to basic education, the foundation is the foundation. As long as the foundation is firmly laid, high-rise buildings can be built.

4 How to Design the Course of Machining Technology to Better Serve the Society, Taking the Course Design of “Machining and Assembly” as an Example Is Analyzed

The learning and application of a technology is inseparable from the “teaching” and “learning” in the school. It is the teacher's responsibility and responsibility to design a course well. How to integrate technology into the curriculum, and how to transform the boring single technology into a vivid and interesting learning process. These requires good design. To conform to the learning psychology and characteristics of contemporary students, designing suitable learning methods and teaching strategies, and effectively improving the teaching quality, these are the fundamental objectives of teaching. Taking the course design of “machining and

assembly” as an example, this paper analyzes how to effectively run through the course of mechanical processing technology and better serve the society.

4.1 Analysis of the Nature of Curriculum

This course is the professional core course of mechanical specialty. Through the study of this course, students can master the relevant knowledge and ability of mechanical processing technology, such as the preparation of machining process specification documents of mechanical parts, the basic operation of ordinary turning and milling machine, the processing and assembly of simple parts and the detection of parts, and cultivate the relevant professional quality of students. This course is at the forefront of the curriculum system chain of mechanical specialty, and is the key course for the formation of core professional ability. Its previous courses include: mechanical drawing, mechanical manufacturing foundation, etc. And its follow-up courses include: NC machining and assembly, CAM and NC machining, mechanism design and processing, etc. The technical knowledge is paved and spiral upward, laying the foundation for improving the NC machining ability.

4.2 Analysis of Design Ideas

This course emphasizes “working process” as the main learning method of students. The project of “Manual eccentric wheel transmission mechanism” is adopted as the carrier. Integrating “teaching, learning and doing”, students can “do in learning and learn by doing”. By completing the actual machining tasks independently, students can master the preparation method of mechanical parts processing technology, machining operation skills, parts assembly and disassembly skills. At the same time, in the process of typical products processing, students’ professional quality and professional skills are cultivated, which can better meet the requirements of manufacturing industry for high skilled talents.

Through the learning and production process of teaching carrier “Manual eccentric wheel transmission mechanism”, students can master the following skills: basic operation of general turning and milling, preparation of mechanical processing technology of simple parts, processing and assembly of mechanical parts and detection of parts. This typical task is broken down into five teaching projects, as follows.

1. The basis of processing technology of mechanical parts.
2. Preparation and processing of turning parts processing technology documents.
3. Preparation and processing of milling parts processing technology documents.
4. Preparation and processing of sheet metal parts processing process documents.
5. Assembly and debugging of “Manual eccentric wheel transmission mechanism”.

4.3 Advantages of Introducing “Teaching Carrier”

According to the research, the first-line enterprises need the ability of corresponding posts. The teaching content is set up with the workpiece as the carrier and the situation as the guide. In situational teaching, it embodies the integrity of the working process (obtaining information, planning, implementation, evaluation, etc.) and the comprehensiveness of elements (tasks, working objects, tools, working methods, labor organization, staff and work results).

From the German IHK exchange, the idea comes from the project teaching and establishes the ultimate goal. In the process of realizing the task, the new technology is introduced. In the process of learning, training and practical operation, the theory and practice will be organically combined. “Do every step well, learn every technical point well”, this idea runs through all the time. From the teaching links of mechanism design, processing, quality inspection, assembly and debugging, students achieve the ultimate goal. Just like a philosophy of German Enterprises: it is not necessary to highlight personal achievements, as long as we do a good job in each job, and then link through. It is the best production line, which is to achieve a good working state. This concept is worth thinking about and using. In fact, we can use this concept to teach students how to learn technology.

4.4 How to Design “Teaching Carrier”

Based on the needs of machining technology points, a “Project” or “Teaching carrier” is designed in teaching. The technical points are reflected in different design and processing angles, and further learning is carried out. For example, the design of “Manual eccentric wheel transmission mechanism”. Relying on such a teaching carrier, project-based teaching is carried out, which decomposes the large organization into a sub task, and then decomposes the sub tasks into knowledge points and technology points, breaking them into parts and breaking them down. From complex tasks to simple and easy tasks, from simple to difficult, progressive.

For example, the “Movable Ejector” part in the design of “Manual eccentric wheel transmission mechanism”. From the mechanical design and drawing, we should consider the dimension length, size, shape and position tolerance, surface roughness, etc. How to realize the key assembly size design and processing technology, and finally how to check whether the dimensions meet the standard. According to this idea, the sub tasks are designed with reasonable time arrangement and processing sequence. It is necessary to show that technology is a “spiral up” state. In the learning process, students can constantly receive new theories and new technologies, and then infiltrate new theories and new technologies in the review and consolidation, so as to achieve the progressive effect. After the completion of sub task design and processing, assembly design is carried out, and the quality of each component is checked again. When the mechanical structure components are

installed, the mechanism can work normally, which is to achieve the design function. At the same time, we also check whether our technical indicators are up to standard [4].

4.5 Teaching Organization

Project teaching method is adopted to integrate “teaching, learning and doing”. There are 4–5 students in a project team. In order to carry out the study, the division of labor is reasonable and the work is coordinated. For example, there are 32 students in a class, and the students are divided into 8 groups. Two teachers are teaching, and two practical instructors are added for guidance and processing. Eight class hours of teaching content are arranged every week, “2 + 6” mode, 2 K theory teaching and 6 K practice teaching. The teaching environment is alternately carried out in the machine tongs processing training room and classroom. The required teaching facilities and environment are as follows:

1. Ordinary turning, common milling machine and drilling machine are used as machining machines.
2. Fitter workbench facilities are assembled
3. A large number of factory actual parts samples are analyzed for machining process.
4. Multi function computer with network for information inquiry and processing demonstration cases.
5. Use projection equipment to help explain [5].

4.6 Evaluation of Teaching Process

Process evaluation and final evaluation are used in the teaching process. At the same time, various evaluation methods such as individual evaluation, group mutual evaluation and teacher evaluation are adopted. Let students grow up in the process of self cognition and improvement. In the process of teaching, teachers should encourage and affirm students in time, so that students can find problems in time, correct problems and improve their skills [6]. At the same time, it also increases the evaluation of “professional quality”, such as safety production, flexible thinking, logical expression, autonomous learning, team cooperation, etc. In the teaching, we have carried on the training and evaluation of students’ occupation related aspects, such as professional ethics, professional skills, professional behavior, professional style and professional consciousness. All these assessments are designed to enable students to have solid skills and good professional quality, so as to lay a foundation for future work in advance.

4.7 Analysis of Teaching Effect

After three rounds of teaching implementation, the development and design course takes “Manual eccentric wheel transmission mechanism” as the teaching carrier. The cultivation of mechanical processing technology is more effective than before. Students’ interest in learning is stronger and the learning goal is more clear. The quality of learning has been significantly improved. The professional quality of students has been recognized by the needs of social enterprises, and good feedback from enterprises has been obtained in the work after graduation. The changes before and after the teaching design reform are compared as shown in the Table 1.

Table 1 Comparison of changes before and after teaching design reform

Observation angle	Teaching design reform	
	Before	After
Teaching model	Traditional teaching	Adopt “Teaching carrier” project design
Leading position in teaching	Teacher	Student
Students’ learning initiative	Passive	Active
Teaching carrier	Nothing	Manual eccentric wheel transmission mechanism
Teaching objectives	Clear, not easy to reflect	Clear, there are places to check
Technical knowledge	Scattered	Task clues run through and knowledge points are clear
Teaching time	The arrangement is scattered	Time concentration, can complete a sub project
Teaching carrier materials	Aluminium	Steel, closer to actual production demand
Use of teaching materials	General teaching materials	Self developed teaching materials and corresponding guidance books
Task completion form	Personal	Team, exercise the ability of coordination and cooperation, help each other
Process assessment	Nothing	Various evaluation methods are adopted: self evaluation, mutual evaluation and teacher evaluation
Information teaching means	Not used	Adopt, vivid and vivid
Students’ interest in learning	Commonly	Proactive and interested
Professional quality evaluation	Nothing	With professional quality evaluation, students are more active in training
Enterprise feedback	Commonly	Excellent

5 Conclusion

The traditional machining technology has a certain role in ensuring the development of the people. It is an important pillar and foundation of the national economy, which can not be ignored with the development of science and technology, but should still be taken seriously. The country needs the front-line manufacturing talents to serve the society and cultivate the practical talents. It needs the deep thinking design of higher vocational colleges.

In the environment of continuous change of social form and rapid development of information, it is necessary to reform and innovate the teaching mode for traditional machining technology. For example, teaching mode reform and innovation ideas, curriculum design should reflect the expression and expansion of knowledge and technology, knowledge and interest, system and applicability. We should guide and attract students to study in fun, pay attention to the cultivation of professional quality while training technology, so that students can better adapt to the development of society, so as to promote the social and economic development of the country.

References

1. Investment analysis and prospect forecast report of China's machinery industry from 2020 to 2024. <http://www.ocn.com.cn/reports/2006260jixie.shtml>. Latest revision 4/2020
2. Investment analysis and Prospect Forecast of China's higher vocational education industry from 2020 to 2024. <http://www.ocn.com.cn/reports/2009904gaodengzhiyejiaoyu.shtml>. Latest revision 10/2019
3. Machining method and application scope. <http://www.dgmachining.com/cn/new/method.html>. Last accessed 16 Oct 2020
4. Fan, S.: Application of CPS in machining industry. *Text. Sci. Res.* (10), 54–58 (2020)
5. Xia, T.: Exploration of modular teaching reform strategy for mechanical design, manufacturing and automation specialty. *Mod. Agri. Mach.* (6), 35 (2020)
6. Lin, H.: Discussion on interactive network classroom teaching reform of "mechanical innovative design". *China Equipment Eng.* **20**, 220–222 (2020)

Microstructure and Mechanical Properties of CuCrZr Alloy at High Temperature



Wenjing Zhang, Zongwu Li, Haofeng Xie, Zhen Yang, Guojie Huang, Xue Feng, Xujun Mi, Limin Wang, Lijun Peng, and Yu Hou

Abstract The tensile properties and microstructure evolution of Cu–0.2Cr–0.08Zr alloy during high temperature tensile process were investigated. The results showed that with the test temperature increasing, both strength and elongation decreases slowly, the addition of Zr can improve the high temperature properties due to the small precipitates in the matrix. The high temperature fracture mechanism of this alloy was ductile fracture. With the test temperature increasing, the reduction of area decreased, less shallow dimples and more large voids can be observed on the fracture surface of sample.

Keywords Cu–0.2cr–0.08zr alloy · Microstructure evolution · High temperature tensile property · Fracture mechanism

1 Introduction

CuCrZr alloy has good mechanical property, electrical conductivity, high temperature softening resistance and other comprehensive properties, which has been widely used in electric rail transportation, electronic industry, national defense

W. Zhang (✉) · H. Xie · Z. Yang · G. Huang · X. Feng · X. Mi · L. Peng · Y. Hou
State Key Laboratory of Nonferrous Metals and Processes, GRIMAT Engineering Institute Co., Ltd., Yanqi Economic Development Zone, No. 11 XinKe East Street, Beijing 101400, China
e-mail: wenjingzhang1987@163.com

W. Zhang · Y. Hou
General Research Institute for Nonferrous Metals, No. 2, Xinjiekouwai Street, Xicheng District, Beijing 100088, China

W. Zhang · L. Wang
GRIPM Advanced Materials Co. Ltd., Yanqi Economic Development Zone, Beijing 101400, China

Z. Li
Hunan Weapons Technology Center Co. Ltd, Changsha 41000, China

industry and other fields [1–4]. Due to their excellent high temperature properties, CuCrZr is considered as a promising material for critical applications such as combustion chamber liner of the cryogenic rocket engine, mold lining and integrated lead frame [5]. As the high temperature stressed components, CuCrZr alloys are facing the challenge of the stability of alloy performance at high temperature. On the one hand, it is required that the material has higher mechanical strength while maintaining high conductivity. On the other hand, it is more and more concerned about high temperature softening, creep and fatigue. A great deal of researchers had systematically studied the element contents, preparation process, phase transformation, microstructural characteristics and their effects on the mechanical properties of CuCrZr alloys [4, 6–9]. Less work has been done to study the high temperature performance of this alloy. Hence, taking the cue of these viewpoints above, in this paper, a kind of CuCrZr alloy was produced, and the microstructures and high temperature tensile properties were examined. In addition, the relationship between high temperature property and microstructure of CuCrZr alloy was analyzed.

2 Experimental

The composition of CuCrZr alloy used in this study contains 0.2% Cr and 0.08% Zr. The ingot was melted by vacuum induction furnace under argon atmosphere. Firstly, the as-cast ingot was milled with a lathe to remove the oxide layer and impurities on the surface, the ingot diameter for subsequent processing was 82 mm. Then, the ingot was extruded on UBE 2500 mm horizontal extruder at 900 °C for 2 h with 78% reduction in dimension. The extruded bar was solution treated at 950 °C for 1 h and aged at 450 °C for 3 h.

The tensile specimens with a gage length of 50 mm were tensiled at 300, 400, 500, 600 °C on an AG-IS250kN/SHIMADZU testing machine. Three specimens were tested to get an average. Microstructures were observed by an Axiovert 200 MAT type Zeiss metallographic microscope (OM), JSM-7001F scanning electron microscope (SEM), JEM2100 transmission electron microscopy (TEM). The samples for microstructural observation were cut near the fracture of the tensile specimens. Thin foils for TEM observations were prepared from discs sectioned normal to the stress axis of the tensile samples. These foils were prepared by twin-jet thinning technique using a 25% nitric acid in methanol solution at about –40 °C.

3 Results and Discussion

3.1 High Temperature Tensile Results

Figure 1 shows the tensile properties of the investigated alloy at high temperature (from 300 to 600 °C). It is obvious that the variation of tensile temperature has great influence on tensile properties. With the test temperature increasing, both strength and elongation decreases slowly. When the deformation temperature increases from 300 to 600 °C, the value of ultimate tensile strength (UTL) and yield strength (YS) decrease from 176 MPa, 123 MPa to 168 MPa, 114 MPa respectively. The decrease of tensile strength can be attributed to that the atomic diffusion ability and movement of boundaries become easier with the deformation temperature increasing, which will reduce the strengthening effects of solution atom and boundaries [10–15]. This alloy has excellent high temperature plasticity, and the elongation (EL) of this alloy is over 20% when the tensile temperature exceeds 300 °C.

3.2 Microstructures Evolution

Figure 2 shows the microstructure of CuCrZr alloy aged and after tensile test at 600 °C. From Fig. 2a, it can be seen that the aging microstructure of this alloys is inhomogeneous, which is mainly manifested in disordered grain boundaries,

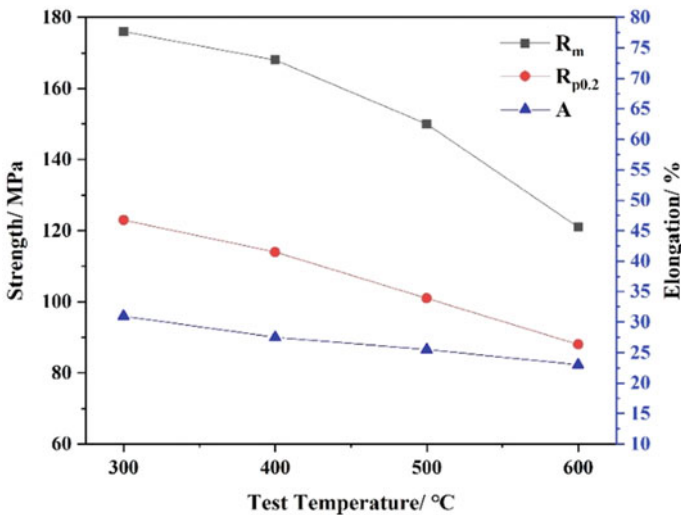


Fig. 1 High temperature tensile strength of CuCrZr alloy

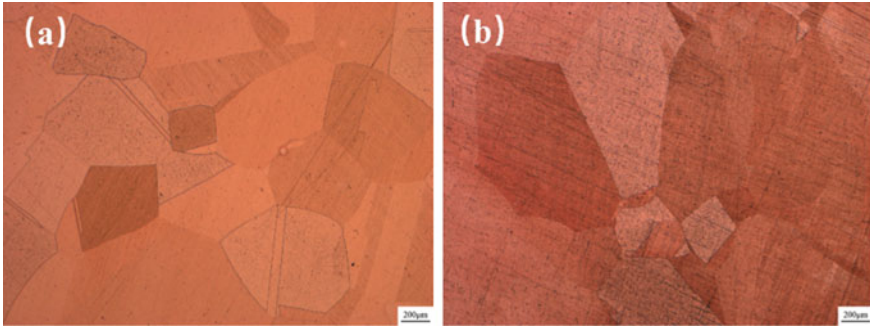


Fig. 2 Microstructures of CuCrZr alloy **a** before and **b** after tensile tests at 600 °C

irregular grain shape and large size difference. At the same time, the existence of annealing twins can be observed in the microstructure, which exist at the intersection of grain boundaries, run through the whole grain and terminate in the grain at one end. The formation of twinning is closely related to stacking fault. The lower the stacking fault energy is, the easier to form twins.

Compared with the microstructure of CuCrZr alloy before tensile test, the grain size increases, which is caused by the short heat preservation process during the tensile test. The high temperature environment provides conditions for the growth of the grains, but the grains do not coarsen obviously due to the short heat preservation time. Meanwhile, the grains are elongated along the tensile direction.

Figure 1 shows that with the tensile temperature rising, the strength decreases slowly, indicating that the addition of Zr is beneficial to improve the high temperature strength. In order to further research the effect of Zr in maintaining the high temperature strength of the materials, TEM analysis is carried out to observe the tensile sample of CuCrZr at 500 °C, as shown in Fig. 3. During the high temperature tensile process, small precipitates are precipitated in the matrix, which is beneficial to improve the high temperature properties of the alloy.

3.3 Fracture Behavior

The fracture morphology of CuCrZr alloy at 300 and 500 °C are shown in Fig. 4. The fracture mechanism of this alloy can be determined as ductile fracture. The reduction area of tensile fracture at 300 °C is significantly greater than that at 500 °C. Meanwhile, larger voids can be observed on the fracture surface of the 500 °C sample. There are more shallow dimples on the fracture surface at 300 °C, and the number of dimples is more than that of 500 °C. In the 500 °C sample, there are more voids with the size of 5–20 µm, and the dimples are not obvious. The results indirectly indicate that the plasticity of the alloy decreases with the increase of temperature.

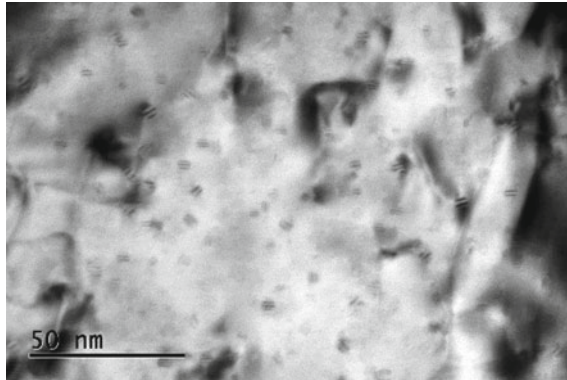


Fig. 3 TEM image of CuCrZr alloy after 500 °C tensile test

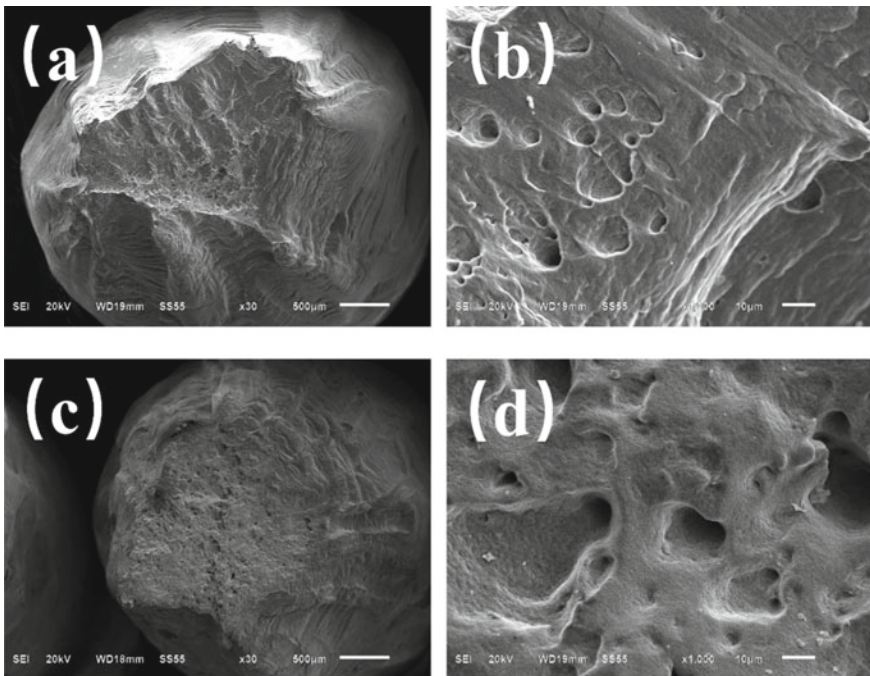


Fig. 4 Tensile fracture morphology of CuCrZr alloy at 300 and 500 °C: a, b 300 °C, c, d 500 °C

4 Conclusion

The Cu–0.2Cr–0.08Zr alloy was tensile tested at 300, 400, 500, 600 °C to study the tensile properties, microstructure evolution and fracture behavior. The following conclusions are made:

1. With the test temperature increasing, both yield strength and ultimate tensile strength decrease slowly. When the deformation temperature increases from 300 to 600 °C, the value of ultimate tensile strength (UTL) and yield strength (YS) decrease from 176 MPa, 123 MPa to 168 MPa, 114 MPa, respectively. The addition of Zr can promote the precipitation of fine precipitates during high temperature tensile process, which improves the high temperature properties.
2. Tensile temperature influences the plasticity and fracture behavior of CuCrZr alloy. The elongation decreases with the tensile temperature increasing. Compared with the sample at 300 °C, more large voids and less shallow dimples on the fracture surface of the 500 °C sample.

Acknowledgements This work was financially supported by National Key Research and Development Program of China (No. 2016YFB0301400) and the technological innovation 2025 and Major special project of NingBo (No. 2018B10030 and 2019B10088). The authors gratefully acknowledge the assistance of persons who dedicated themselves to this paper.

References

1. Liu, Q., Zhang, X., Ge, Y., Wang, J., Cui, J.: Effect of processing and heat treatment on behavior of Cu–Cr–Zr alloys to railway contact wire. *Metallurgical & Materials Transactions A* **37**(11), 3233–3238 (2006)
2. Feng, H., Jiang, H., Yan, D., Rong, L.: Effect of continuous extrusion on the microstructure and mechanical properties of a CuCrZr alloy. *Mater. Sci. Eng., A* **582**, 219–224 (2013)
3. Sun, L., Tao, N., Lu, K.: A high strength and high electrical conductivity bulk CuCrZr alloy with nanotwins. *Scripta Mater.* **99**, 73–76 (2015)
4. Mishnev, R., Shakhoba, I., Belyakov, A., Kaibyshev, R.: Deformation microstructures, strengthening mechanisms, and electrical conductivity in a CuCr–Zr alloy. *Mater. Sci. Eng., A* **629**, 29–40 (2015)
5. Li, Z., Xie, H., Huang, G., Feng, X., Peng, L., Yang, Z., Mi, X., Yin, X.: Study on high temperature properties of CuCrAg alloy. *Mater. Sci. Forum* **921**, 141–146 (2018)
6. Zhang, Y., Volinsky, A., Tran, H., Chai, Zh, Liu, P., Tian, B., Liu, Y.: Aging behavior and precipitates analysis of the Cu–Cr–Zr–Ce alloy. *Mater. Sci. Eng., A* **650**, 248–253 (2016)
7. Xia, C., Jia, Y., Zhang, W., Zhang, K.: Study of deformation and aging behaviors of a hot rolled– quenched Cu–Cr–Zr–Mg–Si alloy during thermomechanical treatments. *Mater. Des.* **39**, 404–409 (2012)
8. Vinogradov, A., Patlan, V., Suzuki, Y., Kitagawal, Kopylovvi.: Structure and properties of ultra-fine grain Cu–Cr–Zr alloy produced by equal-channel angular pressing. *Acta Mater.* **50**, 1639–1651 (2002)
9. Peng, L., Xie, H., Huang, G., Yang, Z., Mi, X., Xiong, B.: Dynamic of phase transformation in Cu–Cr–Zr alloy. *Adv. Mater. Res.* **887–888**, 333–337 (2014)
10. Abib, K., Azzeddine, H., Tirsatine, K.: Thermal stability of Cu–Cr–Zr alloy processed by equal-channel angular pressing. *Mater. Charact.* **118**, 527–534 (2016)
11. Hamilton, C.H., Ghosh, A.K., Mahoney, M.M.: In: Hamilton, C.H., Hasson, D.F. (eds.) *Advanced Processing Methods for Titanium*, pp. 129–144. TMS-AIME, Warrendale, PA (1982)
12. Zhang, C.: Study on high temperature tensile properties of Cu–Zr and Cu–Ag–Zr. *China Technol.* (13), 276 (2014)

13. Chatterjee, A., Mitra, R., Chakraborty, A.: Comparative study of approaches to assess damage in thermally fatigued Cu–Cr–Zr alloy. *J. Nucl. Mater.* **474**, 120–125 (2016)
14. Krishna, S., Rao, G., Jha, A.: Strengthening in high strength Cu–Cr–Zr–Ti alloy plates produced by hot rolling. *Mater. Sci. Eng., A* **674**, 164–170 (2016)
15. Pond, R., Clark, W., King, A.: Boundaries and interfaces in materials: The David A. Smith symposium [C]. *Materials Week 97, Indianapolis, IN (United States), 14–18 Sep 1997 (1998)*

Size Effect Study of Tensile Strength and Elongation of Copper Foil



Yu Hou, Haofeng Xie, Xujun Mi, Wenjing Zhang, Zhen Yang, Guojie Huang, Xue Feng, Lijun Peng, Shuihui Huang, and Dongmei Liu

Abstract In order to study the effect of dimensional parameters on the tensile strength and elongation of metallic foil, unidirectional tensile tests are carried out at room temperature with copper foil of different thickness and grain size. The results show that the tensile strength and elongation of copper foil are affected by both the thickness and grain size. The tensile strength varies with grain size ratio with different thickness. The elongation decreases with the decrease of the grain size ratio at the same thickness. Scanning electron microscope analysis of tensile fracture shows that the sudden drop of the elongation of foil with the decrease of thickness is related to the change of fracture mechanism.

Keywords Size effect · Pure copper foils · Mechanical properties · Deformation behavior · Free surface grain

1 Introduction

Foil is a thin metal sheet with a thickness of 0.01 ~ 0.5 mm. With the development of science and technology, the demand of copper foil for electronic materials, micro-electro-mechanical products, construction and decoration materials is increasing day by day. According to the different production process, copper foil is divided into calendared copper foil and electrolytic copper foil two categories. Compared with electrolytic copper foil, calendared copper foil is mainly used in microelectronic products, transformers, lithium batteries and high frequency

Y. Hou · H. Xie · X. Mi · W. Zhang (✉) · Z. Yang · G. Huang · X. Feng · L. Peng · S. Huang · D. Liu

State Key Laboratory of Nonferrous Metals and Processes, GRIMAT Engineering Institute Co., Ltd., Yanqi Economic Development Zone, No. 11 XingKe East Street, Beijing 101400, China

e-mail: wenjingzhang1987@163.com

Y. Hou · W. Zhang

General Research Institute for Nonferrous Metals, No. 2, Xinjiengkouwai Street, Xicheng District, Beijing 100088, China

high-speed transmission, fine lines of printed circuit boards due to its high strength, toughness, elongation and high-density advantages [1, 2], and the crystalline forms range from monocrystalline to polycrystalline. Due to the size, the molded quality and basic properties of the micro-formed part change. This variation differs from a class of materials that includes crystalline and amorphous metals [3]. It is mentioned in the literature that mechanical properties change when the material has a clear critical size point, i.e., a grain size less than 500 nm, a specimen size less than 100 μm [4]. The reason of “smaller and weaker” in uniaxial tensile of nickel foil and other materials is often attributed to the fact that the specimen surface is free and has no hindrance to dislocation slip. The “smaller is stronger” in micro-bending is caused by strain gradient hardening effect [5]. The experimental results in recent years show that when the thickness of thin plate is kept constant, the yield stress and the reciprocal of the square root of grain size no longer change linearly, but change slope.

A number of experimental studies on the dimensional effects of flow stress in microscopic rough deformation were conducted by Geiger et al. [6] and a surface model was proposed to explain this phenomenon. Kals, Li, and Engel [7, 8], through a series of tensile and flanging experiments on geometrically similar parts, performed experiments on two kinds of brass. They propose a “surface model” where, when the microstructure of the specimen remains unchanged, as the specimen size decreases, the ratio of surface layer grains to inner layer grains increases, dislocations cannot accumulate on the specimen surface, and the work-hardening ability of the material decreases, resulting in a decrease in the flow stress of the material. Lee and Yu et al. [9, 10] conducted tensile tests on 0.1 ~ 8 μm thick aluminum and copper films, the test results show that as the thickness decreases, the yield strength gradually increases, as “the smaller the stronger”, but the elongation is rapidly decreasing, and in the thickness unchanged, the smaller the grain size, the smaller the elongation. In general, if a material’s dimensional change is brought about by plastic deformation, its internal grain size will change as well. This is where the effect of grain refinement on strength is intertwined with the specimen size. Simple experimental comparisons cannot reveal the effect of size.

In this work, copper foils with different thicknesses and grain sizes are investigated experimentally by tensile tests to study the effects of thickness and grain size on mechanical properties such as tensile strength and elongation, respectively. The effect of the size effect on the flow stress curve is clearly demonstrated, and the theory of the size effect is improved through the analysis of its fracture behavior.

2 Experimental

Copper foils were deformed from commercial cathode copper (Jiangxi Copper Groups), the thickness of the original copper foils was 500 μm . Preparation of copper foils with thicknesses ranging from 125 to 500 μm by calendaring. The use of wire-cutting processed dimensions as shown in Fig. 1, the specimen tensile

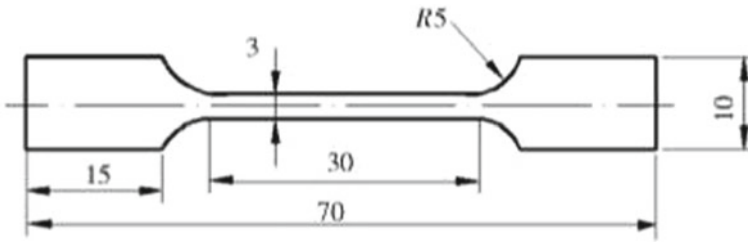


Fig. 1 Geometry of the tensile specimen

direction and the same direction as the rolling direction. The tensile tests were performed on an Instron testing machine at a low strain rate of five mm/min, using ASTM E8/E8M-13a as standards. Samples of copper foil of 99.93 wt% purity were annealed in vacuum for one hour at temperatures of 500, 600, 700, and 850 °C to obtain different grain sizes. Microstructural observations were made with an optical microscope. Fracture is the material basis for the diagnosis of fracture failure mechanism, as well as an important basis for judging the fracture failure mechanism and plasticity index of materials. The fracture morphology of tensile specimens was observed by 6500 °F scanning electron microscope, and the experimental results were analyzed by the fracture morphology.

3 Results and Discussion

3.1 *The Tensile Tests of Copper Foils*

The tensile strengths of the specimens at different temperatures and specimen sizes are shown in Fig. 2. The decrease in thickness brings about a significant decrease in the tensile strength of the specimens, and this decrease is more pronounced for higher annealing temperatures and larger grain sizes. According to the traditional theory of fine grain reinforcement, an increase in grain size results in a decrease in the tensile strength of the specimen. The barrier hardening of fine grains is more significant than that of coarse grains, because the finer the grains are, the smaller the dislocation slip distance will be, and the fewer the number of dislocation plug will be when hardening occurs. Due to the resistance of grain boundary to deformation, the hardness in the vicinity of grain boundary must be higher than that in grain, so the strength of course-grain sample is lower than that of fine-grain sample.

Figure 3 shows that for a given foil thickness, the smaller the grain size, the greater the elongation at break; Similar to tensile strength, it is the combined effect of grain size and thickness size that makes the elongation of copper foil significantly different from that of ordinary metal sheet. For a given annealing temperature, i.e., a given grain size, the elongation is positively correlated with the

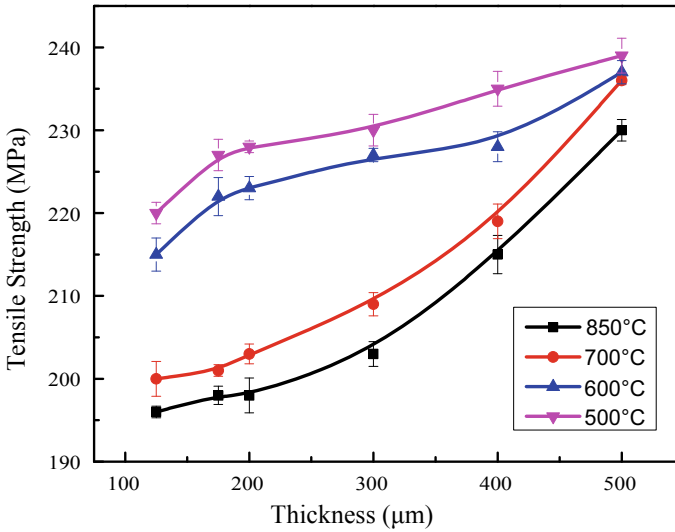


Fig. 2 Tensile strength of specimens with different specimen and grain sizes

thickness. This is because the larger the number of grains involved in the cross-sectional deformation, the greater the coordinated deformation between the grains, which delays the onset of fracture [11–13].

3.2 Analysis of Fracture Behavior

In order to further investigate the size effect of elongation, the tensile fracture analysis is used to explain the size effect of elongation. Figure 4 shows the tensile fracture morphology of the larger grain size (850 °C treatment) specimens with different thicknesses, respectively.

The tensile fractures were all plastic fractures, but their fracture mechanisms were obviously different from each other. Figure 4a, b is the thickness of 500 and 400 μm sample fracture, the fracture on both sides is irregularly undulating slip fragmentation pattern, the center is the ligament fossa band, ligament fossa size with the thickness decreases and becomes smaller, in addition, Fig. 4a in some of the larger ligament fossa also exists in some holes, fracture belongs to the slip separation and ligament fossa cracking the mixed fracture. Figure 4d–f is the thickness of 200, 175 and 125 μm sample fracture, the fracture in the middle of a sharp cleavage, the two sides of the serpentine slip pattern clearly visible, is a typical slip separation fracture [14, 15].

From the fracture, we can infer the fracture process of different thicknesses of copper foil, the thicker copper foil is first deformed by sliding to produce a neck

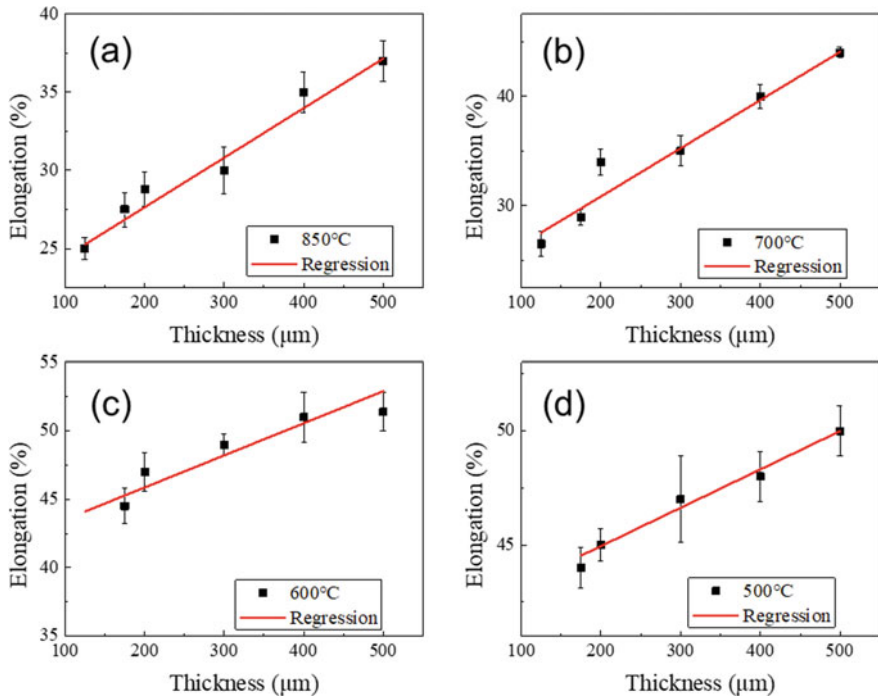


Fig. 3 Tensile elongation of specimens with different thickness

contraction, when the neck contraction is reduced to a certain extent, a hole appears in the neck contraction site, the hole gradually grows up with the increase of deformation, when the holes are connected to each other, fracture occurs; while the thinner copper foil has been deformed by sliding to produce a neck contraction, and finally separated to form a sharp cleavage [16, 17]. From this we can see that the copper foil fracture mechanism with the changes in the thickness of the plate is also changing, and the size and number of tenuous fossae with the thickness of the decreasing gradually become smaller and reduced until the disappearance.

4 Conclusion

The effects of thickness and grain size on tensile strength and elongation of copper foil and copper sheet with different thickness and grain size were studied by tensile tests at room temperature. The experimental results show that the tensile strength and elongation of copper foil have obvious size effect.

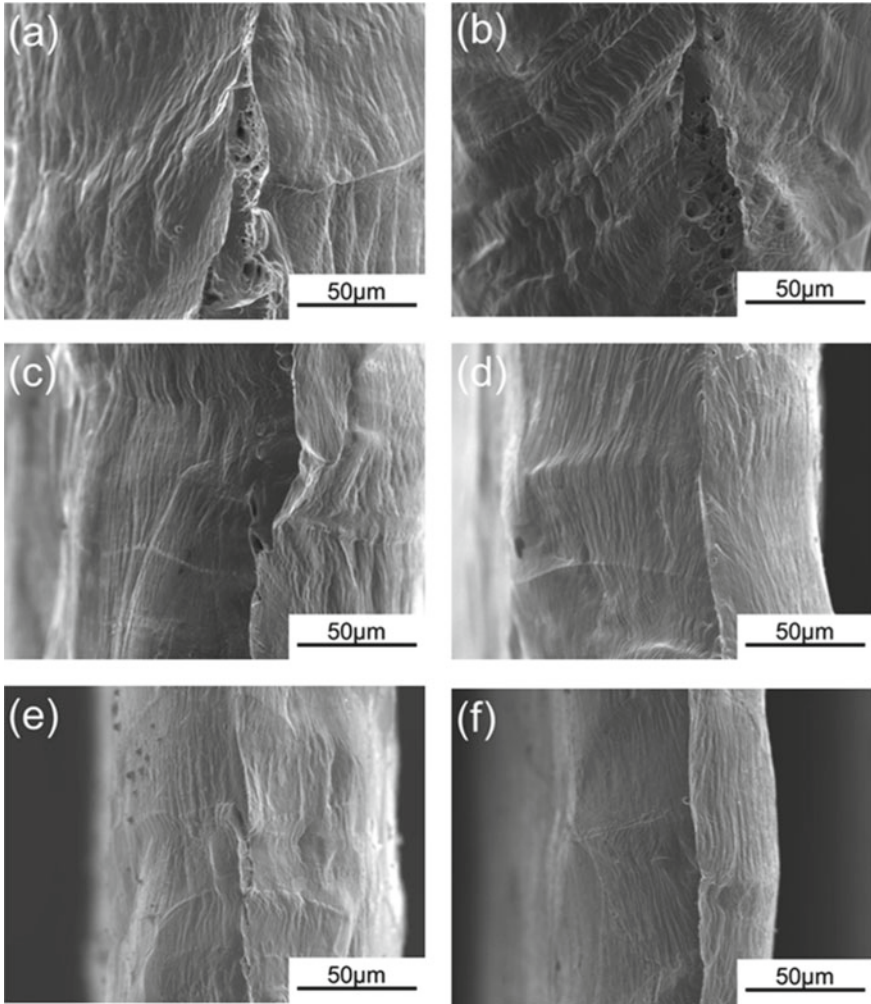


Fig. 4 Fracture morphology of tensile specimens of different thicknesses. **a** 500 μm . **b** 400 μm . **c** 300 μm . **d** 200 μm . **e** 175 μm . **f** 125 μm

1. The tensile strength increases with the decrease of grain size at constant thickness. The smaller the thickness is, the greater the influence of grain size on the tensile strength. This phenomenon is caused by the joint action of grain deformation hardening and surface layer grains.
2. The effect of thickness on the elongation was significant. At the same grain size, the elongation decreased with the decrease of thickness, the relationship varies linearly over the 500–125 μm thickness range. The smaller the grain size is, the larger the elongation is.

3. Tensile fracture scanning electron microscopy (SEM) analysis showed that: The linear relationship of elongation with thickness is related to the variation of the fracture mechanism, when the thickness is large, the fracture is a mixed fracture of slip separation and tough nest cracking, while the thickness of 175 and 125 μm sample fracture is a single slip separation fracture, low hardening index. The low hardening exponent and surface grain together inhibit the growth of the voidage, making the elongation much lower than the sample with larger thickness.

Acknowledgements This work was financially supported by National Key Research and Development Program of China (No. 2016YFB0301400) and the technological innovation 2025 and Major special project of NingBo (No. 2018B10030 and 2019B10088). The authors gratefully acknowledge the assistance of persons who dedicated themselves to this paper.

References

1. Acharya, A., Beaudoin, A.J.: Grain-size effect in viscoplastic polycrystals at moderate strains. *J. Mech. Phys. Solids* **48**(10), 2213–2230 (2000)
2. Bittencourt, E.: Interpretation of the size effects in micropillar compression by a strain gradient crystal plasticity theory. *Int. J. Plasticity* (2009)
3. Chen, S.H., Wang, T.C.: A new hardening law for strain gradient plasticity. *Acta Mater.* **48** (16), 3997–4005 (2000)
4. Haouala, S., Lucarini, S., Llorca, J., Segurado, J.: Simulation of the Hall-Petch effect in FCC Polycrystals by means of strain gradient crystal plasticity and FFT homogenization. *J. Mech. Phys. Solids* (2019)
5. Jian, H.G., Du, M.X., Jiang, F., Yin, Z.M.: Fatigue characteristic of aluminum alloy plates with different thickness. *Appl. Mech. Mater.* **477–478**, 1284–1287 (2013)
6. Engel, U., Eckstein, R.: Microforming—from basic research to its realization. *J. Mater. Process. Tech.* **125**(2), 35–44 (2002)
7. Geiger, M., Vollertsen, F., Kals, R.: Fundamentals on the manufacturing of sheet metal microparts. *CIRP Annals—Manuf. Technol.* **45**(1), 277–282 (1996)
8. Kals, T.A., Eckstein, R.: Miniaturization in sheet metal working. *J. Mater. Process. Tech.* **103**(1), 95–101 (2000)
9. Lee, H., Lim, M.G., Kim, J.H., Adams, B.L., Wagoner, R.H.: Simulation of polycrystal deformation with grain and grain boundary effects. *Int. J. Plast.* **27**(9), 1328–1354 (2011)
10. Yu, D.Y.W., Spaepen, F.: The yield strength of thin copper films on kapton. *J. Appl. Phys.* **95**(6), 2991–2997 (2004)
11. Nix, W.D., Gao, H.: Indentation size effects in crystalline materials: a law for strain gradient plasticity. *J. Mech. Phys. Solids* **46**(3), 411–425 (1998)
12. Raabe, D., Ma, D., Roters, F.: Effects of initial orientation, sample geometry and friction on anisotropy and crystallographic orientation changes in single crystal microcompression deformation: a crystal plasticity finite element study. *Acta Mater.* **55**(13), 4567–4583 (2007)
13. Shan, D.B., Wang, C.J., Guo, B., Wang, X.W.: Effect of thickness and grain size on material behavior in micro-bending. *T. Nonferr. Metal. Soc.* **19**(S2), s507–s510 (2009)
14. Velayarce, J.R., Zamanzade, M., Abad, O.T., Motz, C.: Influence of single and multiple slip conditions and temperature on the size effect in micro bending. *Acta Mater.* **154** (2018)

15. Wang, Y., Fu, R., Lei, J., Li, Y., Sang, D.: Grain refinement and nanostructure formation in pure copper during cryogenic friction stir processing. *Mater. Sci. Eng. A*, **703**(Aug 4), 470–476 (2017)
16. Yu, D.Y.W., Spaepen, F.: The yield strength of thin copper films on kapton. *J. Appl. Phys.* **95** (6), 2991–2997 (2004)
17. Wang, C., Guo, B., Shan, D., Sun, L.: Effects of specimen size on flow stress of micro rod specimen. *T. Nonferr. Metal. Soc.* **19**(s2), s511–s515 (2009)

Analysis of the Influence of Different Mechanical Delaminating Process on the Electrochemical Performance of MXene Films



Xingmin Liu and Yi Qu

Abstract MXene is a new type of two-dimensional nanomaterials with good electrochemical properties, which can be used as electrode materials for supercapacitors. And the electrochemical performance of the few-layered MXene is better than that of the multilayered MXene. The differences in the microstructure and electrochemical properties of the thin films obtained by three different mechanical layering methods, namely, hand-shaking treatment, ultrasonic treatment and step-by-step ultrasonic treatment, were studied. The results show that the ultrasonic treatment of MXene is not only simple and efficient, but also the self-supporting film of MXene prepared by vacuum assist has the advantages of low density and high conductivity. Compared with the other two methods, the electrochemical performance of the thin film prepared by ultrasonic treating is also the best. The oxidation peak is obvious in cyclic voltammetry test, the voltage drop is small when the constant current is charged and discharged, the energy conversion is high, the impedance spectrum shows the internal impedance is the smallest, and the ion diffusion rate is the largest. The comparison results show that the ultrasonic treatment can be used as a stable process for delaminating MXene, which provides a reference for the subsequent MXene composite experiments.

Keywords MXene · Electrochemical performance · Delaminate · Self-supporting film

1 Introduction

With the rapid economic development and social progress, people have higher and higher requirements for energy storage in electronic products. As a new type of energy storage device, supercapacitor combines the advantages of traditional

X. Liu (✉) · Y. Qu

School of Materials Science and Engineering, Shenyang Aerospace University,
Shenyang, Liaoning, China
e-mail: xmliusy@163.com

capacitors and chemical batteries [1]. It has the advantages of fast charge and discharge rate, high power density long cycle-life and fast recharge ability, and has become a kind of energy storage equipment that has attracted much attention [2–4]. Due to its unique layer structure and surface hydrophilicity, the two-dimensional MXene material increases the contact area between the electrode and the electrolyte, and has good electrochemical properties [5], and can be used as an electrode material for supercapacitors. In addition, MXene can also be applied to many fields such as photocatalysis [6], adsorption, energy storage [7] and polymer composite preparation [8]. The MAX phase of the two-dimensional MXene material is a ternary carbon-nitrogen compound and a precursor of MXene. Its general chemical formula can be expressed as $M_{n+1}AX_n$ ($n = 1, 2, 3$), where “M” is a transition-metal element, “A” is an element of group III or group IV in the periodic table, and “X” represents C or N or CN [9, 10].

When using the safest and most environmentally friendly mixture of LiF and HCl as the etching solution, the “A” layer in the MAX phase will be removed by chemical extraction. But at this time, there is van der Waals force between the MXene flakes, so that the flakes are not completely separated, but present an accordion-like structure. Therefore, it is necessary to divide multilayered flakes into few-layered flakes in order to obtain a better composite effect. The MXene was layered without intercalating agent, and the colloidal solution was vacuum-assisted suction filtration to obtain self-supporting films. The advantages and disadvantages of the three layering methods are compared and analyzed.

2 Experimental Section

2.1 Synthesis of Ti_3AlC_2

The MXene nanosheets were obtained by etching the Al in MAX materials based on minimally intensive layer delamination (MILD) method. The 3.2 g LiF (Sinopharm Chemical Reagent Co., Ltd, China) was added to 9 M 40 mL HCl (Sinopharm Chemical Reagent Co., Ltd, China). After mixing the two completely, the 2 g high purity Ti_3AlC_2 powder (Jinlei, Ningbo) was added slowly and the solution was stirred and etched at room temperature (RT) for 24 h, sealed. After the reaction, the liquid in the beaker was centrifuged and repeated washing with deionized (DI) water. After centrifugation, the transparent supernatant in the test tube was poured out, and then deionized water was added for centrifugal washing until the upper liquid appeared dark green. The pH value of supernatant reached about 6.

2.2 Three Ways to Delaminate MXene Materials

Delaminate MXene by hand-shaking treating. Continue to add deionized water to the centrifuge tube to wash the remaining sediment in the tube. Mixtures of deionized water with MXene was hand-shaken for 5 min and sonicated for 10 min. Then, the solutions were centrifuged at 3500 rpm for 5 min, and collected the upper dispersion liquid of the centrifuged liquid. Then repeated the above operation while depositing the sediment in the tube until the colour of the upper liquid after centrifugation become lighter. In order to facilitate comparison with the other two delamination methods, control the total volume of the upper layer solution to approximately 500 mL. Then, the solutions were centrifuged at 3500 rpm for 1 h, and the black supernatants were decanted and used for further investigation.

Delaminate MXene by ultrasonic treating. The precipitate was added to 500 mL of deionized water, treated by ultrasonic in an ice bath, the protective gas is argon, centrifugation parameters 80 W 4 h. After the ultrasonic treatment, the upper layer solution was centrifuged at 3500 rpm for 1 h.

Delaminate MXene by step-by-step ultrasonic treating. 125 mL of deionized water was added to pre-cleaned mixtures, and ultrasonic treatment under the protection of an ice bath and rare gas. After 1 h, the upper layer solution was centrifuged with a parameter of 3500 rpm for 30 min. The supernatant after centrifugation was collected for subsequent experimental steps usage, and 125 mL of deionized water was added to the precipitate to disperse with the same parameters. Repeat the above-mentioned ultrasonic and centrifugal steps.

After cleaning, the few-layered $\text{Ti}_3\text{C}_2\text{T}_x$ MXene colloidal solutions obtained by the above three delamination methods were vacuum-assisting suction filtered into thin films and dried; the remaining precipitate after delaminating was dispersed in an evaporating dish and freeze-dried for 24 h to obtain dry MXene powders.

3 Characterization

3.1 The Difference of MXene Liquid

The few-layered $\text{Ti}_3\text{C}_2\text{T}_x$ MXene colloidal solution obtained by the above three delamination methods is vacuum-assisting suction filtered into thin films with a thickness of 6 μm and the dispersion concentration was calculated. The concentration of the dispersion obtained by hand shaking is only about 0.22 mg/mL, while the concentration of the colloidal solution by the other two methods can reach about 0.6 mg/mL (Table 1). If a high-concentration $\text{Ti}_3\text{C}_2\text{T}_x$ dispersion is required in subsequent experiments, in addition to adding deionized water to the $\text{Ti}_3\text{C}_2\text{T}_x$ powder for ultrasonic treatment or step-by-step ultrasonic treatment can be used to obtain a high-concentration dispersion. But the other two delamination methods

Table 1 Comparison of colloidal solutions

Delamination method	Volume of colloidal solution (mL)	Film quality (mg)	Concentration of colloid (mg/mL)
Hand-shaking treatment	80	17.2	0.215
Ultrasonic treatment	30	17.5	0.583
Step-by-step ultrasonic treatment	30	18.4	0.613

also have drawbacks. The multi-layer MXene precipitate obtained by centrifugation was freeze-dried, and the obtained powder contained a small amount of gray impurities, which was presumed to be MAX that was not completely etched.

3.2 Characterization of Thin Films

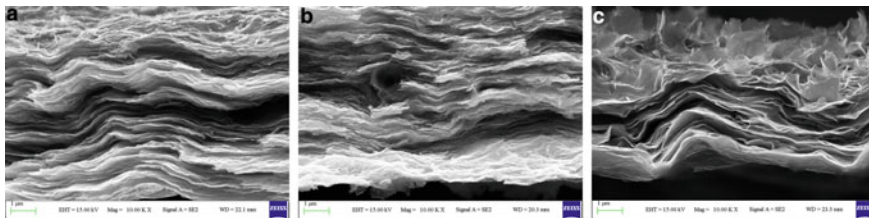
Take different volumes of the dispersion liquid into a thin film with a thickness of 9 μm . After weighing it, the density can be calculated and its conductivity can be measured. The density and conductivity of the films prepared by the hand-shaking treatment and the ultrasonic treatment are not much different, while the film density obtained by the step-by-step ultrasonic treatment is higher than the other two methods, and the conductivity is lower. This is because the process of layering MXene by hand shaking is relatively gentle, and the resulting single-layer MXene sheet has a larger surface area. Therefore, MXene sheets may be curled and folded during the suction process. This phenomenon causes the distance between the sheets to increase and the density of the film to decrease. However, due to the long time of the ultrasonic treating, some of the MXene sheets were broken into MXene sheets with a small surface area. In the suction filtration process, the small flakes and the large flakes formed a certain angle of stacking. And the large surface area of the sheet has also been folded, which makes the spacing between the sheets larger, which leads to a decrease in density. The difference is that after the step-by-step ultrasonic treating, only the small surface area MXene flakes of the upper layer of the solution are collected, and the multi-layer or large surface area MXene flakes of the lower layer are re-probe ultrasonically processed. As a result, the surface area of the resulting MXene sheets is relatively small, and they will be denser when stacked together.

In the same treatment method, as the density of the film increases, the internal resistance generated by the internal structure increases, so the conductivity is also lower. But when the density is not much different, the conductivity of the film obtained by the ultrasonic treatment is higher than the other two groups (Table 2).

As shown in Fig. 1, the diameter of MXene sheets and the interlayer spacing of MXene films treated by hand shaking and ultrasonic treatment are larger, and the film stacked by step-by-step ultrasonic treatment is denser, leaving only a small amount of pores.

Table 2 Comparison of films conductivity

Delamination method	Density of film (g/cm^3)	Electrical conductivity of the film (S/cm)
Hand-shaking treatment	2.31	884.314
Ultrasonic treatment	2.36	889.114
Step-by-step ultrasonic treatment	2.50	678.557

**Fig. 1** SEM images of few-layered $\text{Ti}_3\text{C}_2\text{T}_x$ MXene films. **a** Hand-shaking treatment, **b** ultrasonic treatment, and **c** step-by-step ultrasonic treatment

The bottom broken line in Fig. 2 is the XRD pattern of Ti_3AlC_2 powder before etching. There are two obvious and sharp peaks at 9.5° and 39° , which are (002) peak and (008) peak, respectively. The remaining three broken lines represent the XRD patterns of the films obtained by the three delaminating methods. It can be clearly observed that the peaks relative to Ti_3AlC_2 did not appear. Instead, peaks appeared at 7° and 16° . The reason that the peak angle becomes smaller is that the functional groups with negative ions exist on the surface of the etched MXene sheet, and they repel each other, which causes the layer spacing to increase. The XRD pattern of the film obtained by analyzing the three groups of different delaminating methods through Debye Scherer's formula shows that the step-by-step ultrasonic treatment has the smallest film layer spacing.

4 Electrochemical Performance Testing

Figure 3 is a graph of the cyclic voltammogram of the film obtained by three delamination methods at a scan rate of $5 \sim 100 \text{ mV}/\text{s}$, and the voltage window is $-0.2 \sim 0.4 \text{ V}$. The curve has a certain degree of symmetry and is accompanied by obvious peaks, indicating that the hydrogen ions in the electrolyte circulate between the MXene flakes during the detection, and loss of electrons will produce a reversible redox reaction. Most of the capacitance comes from the pseudocapacitance generated by this reaction. At low (less than $50 \text{ mV}/\text{s}$) scanning rate, the hydrogen ions in the electrolyte diffuse sufficiently, so it shows the maximum

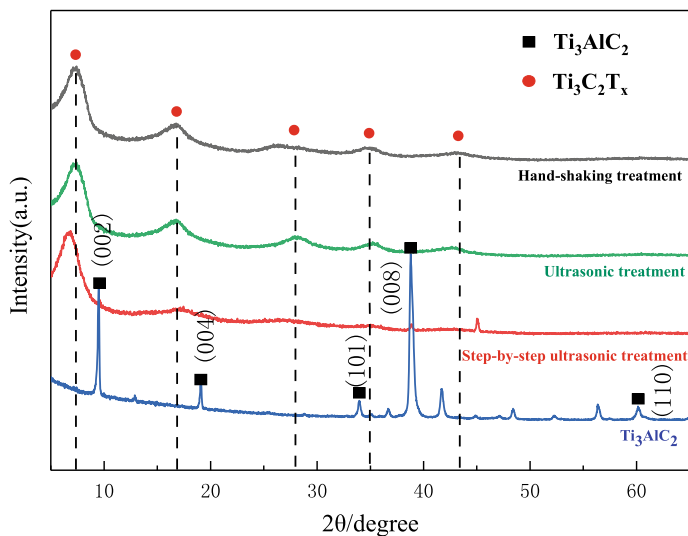


Fig. 2 XRD patterns of $\text{Ti}_3\text{C}_2\text{T}_x$ films and Ti_3AlC_2 powder

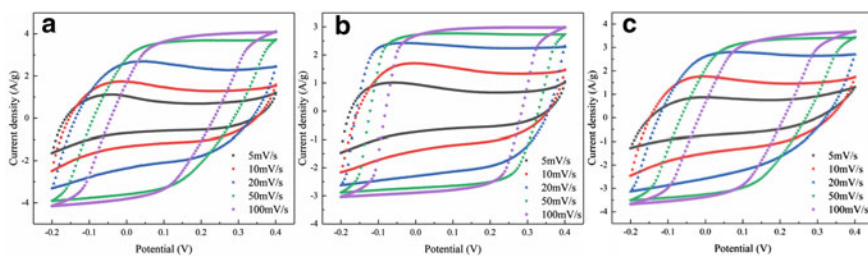


Fig. 3 CV curves of $9 \mu\text{m}$ $\text{Ti}_3\text{C}_2\text{T}_x$ films. **a** Hand-shaking treatment, **b** ultrasonic treatment, and **c** step-by-step ultrasonic treatment

capacitance. As the scanning rate increases (more than 50 mV/s), the oxidation peak is no longer obvious, and there is a deviation between the shape of the entire cyclic voltammetry curve and the original. This is because when the scan rate is increased, the hydrogen ions in the electrolyte diffuse to a lower degree, do not fully enter the internal structure of the film, and the redox reaction is incomplete, so the capacitive performance is far inferior to that of the scan at low rates.

Figure 4a is the cyclic voltammogram of the three mechanical layering methods at a scan rate of 5 mV/s . The closed loop areas of the three curves in the figure are not much different. However, it can be observed that the oxidation peak of the hand-shaking treatment and the step-by-step ultrasonic treatment appears at about -0.05 V , and the oxidation peak of the ultrasonic treatment is near -0.1 V . Moreover, the oxidation potential range of the former is larger than the latter, and the intensity of the oxidation peak is also stronger. Figure 5b is the cyclic

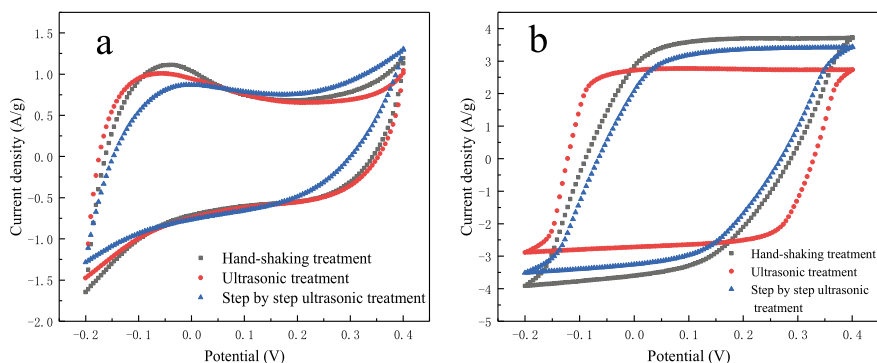


Fig. 4 CV curves of $\text{Ti}_3\text{C}_2\text{T}_x$ films at different scan rates. **a** 5 mV/s, **b** 50 mV/s

voltammogram of the film at a scanning rate of 50 mV/s. The oxidation peaks of the redox reaction curves of the three methods are no longer obvious. Among them, The gain and loss of the electronic process range of the ultrasonic treatment is wider than the other two, but the current density is not as high as the other two groups.

As the scan rate increases, the specific capacitance also decreases. When the rate is increased from 5 to 50 mV/s, the specific capacitance of hand-shaking treating drops from 133.5 to 42.9 F/g, and the coulombic efficiency is 32.1%; the specific capacitance of ultrasonic treating drops from 134.5 to 40 F/g, and the coulombic efficiency is 29.7%; the specific capacitance of step-by-step ultrasonic treating drops from 119.7 to 34.6 F/g, and the coulombic efficiency is 28.9%. By comparison, it is found that the film obtained by the hand shake delaminating method has higher stability under high-speed scanning (Table 3).

Figure 5 shows the constant current charge and discharge curves of the thin film prepared by the three mechanical layering methods as the working electrode when the current density is 0.25, 0.5 and 1 A/g. The initial discharge voltage of the three sets of curves will be lower than the charge termination voltage. This part of the voltage drop comes from the internal impedance of the film. At a current density of 0.25 A/g, the voltage drop of the hand shaking treatment, the ultrasonic treatment and the step-by-step ultrasonic treatment are 0.03 V, 0.015 V and 0.02 V,

Table 3 Cyclic voltammetry measures the specific capacitance of films

Scan rate (mV/s)	Specific capacitance (F/g)		
	Hand-shaking treatment	Ultrasonic treatment	Step-by-step ultrasonic treatment
5	133.5	134.5	119.7
10	114.8	117.2	119.0
20	90.6	94.0	92.3
50	42.9	40.0	34.6
100	17.2	17.4	12.5

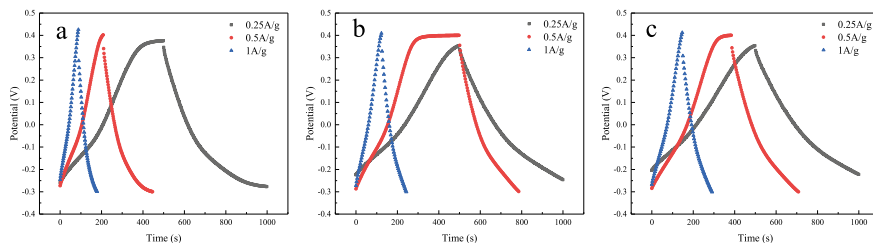
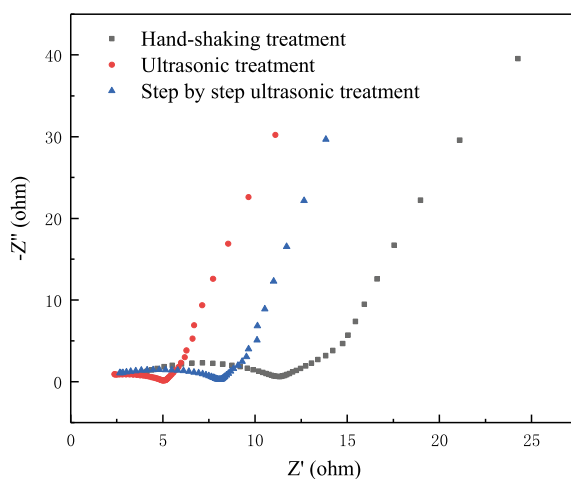


Fig. 5 GCD curves of $9 \mu\text{m Ti}_3\text{C}_2\text{T}_x$ films. **a** Hand-shaking treatment, **b** ultrasonic treatment, and **c** step-by-step ultrasonic treatment

respectively. Ultrasonic treating is the group with the smallest voltage drop among the three groups. Under the same conditions, the conductivity of this group is also the highest, its own loss is also smaller, and the energy conversion rate is higher.

Figure 6 is the electrochemical impedance spectra, also known as Nyquist chart, which of MXene films was prepared by different mechanical layering methods. The larger the radius of the semicircle of the spectrum, the greater the impedance of the film itself. The slope of the straight line represents the degree of diffusion of electrolyte ions, the greater the slope, the better the degree of diffusion. The frequency range of this test is 0.01 Hz–100 kHz. The three curves in the figure show similar changing trends, which is that there is a semicircle located in the high-frequency region and a straight line located in the low-frequency region. It is found by comparison that among the three curves, the radius of the ultrasonic treating is the smallest, which means that the internal impedance is smaller, the conductivity is larger, and the constant current charging and discharging voltage drop is smaller, which is consistent with the results obtained from other tests above.

Fig. 6 EIS spectra of all electrodes
(100 kHz ~ 0.01 Hz)



5 Conclusions

In this study, three delaminating methods were successfully used to obtain MXene dispersion, and the dispersion was suction filtered into a film for characterization and electrochemical detection. The density, conductivity and electrochemical performance of the film after delaminating were compared and analyzed. The comprehensive analysis obtained the following conclusions: When the thickness of the film obtained by dispersive suction filtration is consistent, the density of the film obtained by the hand shaking treatment is the smallest, and the film density obtained by the step-by-step ultrasonic treatment is the largest. The conductivity and electrochemical performance of the film obtained by the ultrasonic treatment are the best among the three methods, and the operation is simple and convenient, and a higher concentration dispersion can be prepared. The method of controlling the experimental parameters in the ultrasonic treating process can be used as a stable process for preparing a few layers of MXene.

References

1. Pandolfo, A.G., Hollenkamp, A.F.: Carbon properties and their role in supercapacitors [J]. *J. Power Sources* **157**(1), 11–27 (2006)
2. Aricò, A.S., Bruce, P., Scrosati, B., et al.: Nanostructured materials for advanced energy conversion and storage devices [J]. *Nat. Mater.* **4**(5), 366–377 (2005)
3. Liu, C., Li, F., Ma, L.P., et al.: Advanced materials for energy storage [J]. *Adv. Mater.* **22**(8), E28–E62 (2010)
4. Rakhi, R.B., Chen, W., Cha, D., et al.: Nanostructured ternary electrodes for energy-storage applications [J]. *Adv. Energy Mater.* **2**(3), 381–389 (2012)
5. Naguib, M., Mochalin, V.N., Barsoum, M.W., et al.: 25th anniversary article: MXenes: a new family of two-dimensional material [J]. *Adv. Mater.* **26**(7), 992–1005 (2014)
6. Guo, Z., Zhou, J., Zhu, L., Sun, Z.: MXene: a promising photocatalyst for water splitting [J]. *J. Mater. Chem. A* **4**(29), 11446–11452 (2016)
7. Lukatskaya, M.R., Mashtalir, O., Naguib, M., et al.: Cation intercalation and high volumetric capacitance of two-dimensional titanium carbide [J]. *Science* **341**(6153), 1502–1505 (2013)
8. Xiao, L., Zhu, J., Wenling, W., et al.: Hierarchical architecture of PANI@TiO₂/Ti₃C₂T_x ternary composite electrode for enhanced electrochemical performance [J]. *Electrochim. Acta* **228**, 282–289 (2017)
9. Haddad, T., Mahmoud, K.A., Ali, A., et al.: Transport properties of a highly conductive 2D Ti₃C₂T_x MXene/graphene composite [J]. *Appl. Phys. Lett.* **109**(112), 32006–43109 (2016)
10. Tang, Q., Zhou, Z., Shen, P.: Are MXenes promising anode materials for Li ion batteries computational studies on electronic properties and Li storage capability of Ti₃C₂ and Ti₃C₂T_x (X=F, OH) monolayer [J]. *J. Am. Chem. Soc.* **134**(40), 16909–16916 (2012)

Effect of Solution Heat Treatment on Microstructures and Stress Rupture Properties of DZ406 Alloy



Wei jie Xing, Changkui Liu, Xiaotong Guo, Gang Zhu, Wenxia Zhao, Xinlang Zuo, and Zhen Zheng

Abstract The heat treatment process is one of the keys factors for the microstructure and mechanical properties of superalloys, while there are few reports on the heat treatment of DZ406 alloy. In this paper, three different solution heat treatment processes were used to study the microstructure and stress rupture properties. DZ406 alloy contains γ' phase, γ/γ' eutectic and carbides in the as-cast state. After the heat treatment at 1265, 1275 and 1285 °C, the γ' phase changed to be cubic shape, and the eutectic structure is reduced to 12.46, 6.27 and 5.8%. The stress rupture test indicates that the crack originates from the interfaces of carbide/matrix and γ/γ' eutectic/matrix. With the increase of temperature of solution heat treatment, the content of γ/γ' eutectic decreased, and resulting the gradually increased stress rupture properties.

Keywords Superalloy: DZ406 alloy · Solution heat treatment · Microstructure · Creep · Stress rupture property

1 Introduction

Nickel-base superalloy has always been the preferred material for aero-engine, which benefits from its excellent corrosion resistance and mechanical properties. DZ406 alloy is a Ni-based precipitation hardening directionally solidified superalloy with Re 3 wt% in composition. The design service temperature of DZ406

W. Xing · C. Liu (✉) · W. Zhao · Z. Zheng
AECC Beijing Institute of Aeronautical Materials, Beijing 100095, China
e-mail: changkuiliu621@163.com

X. Guo · G. Zhu · X. Zuo
China Electronic Product Reliability and Environmental Testing Research Institute,
Guangzhou 510610, China
e-mail: zhugang05020129@163.com

© The Author(s), under exclusive license to Springer Nature Switzerland AG 2021
L. Zheng et al. (eds.), *Proceedings of MEACM 2020*,
Mechanisms and Machine Science 99,
https://doi.org/10.1007/978-3-030-67958-3_43

alloy is 30 °C higher than the first-generation directionally solidified superalloys and is equivalent to that of the first generation of single crystal superalloys.

The excellent properties are attributed to the addition of refractory elements such as Ta and Re, but the addition of refractory elements is very unfavorable to the solidification segregation behavior of the alloy, which is reflected in the formation of more eutectic structure in the interdendritic region [1]. The existence of the eutectic structure and the inhomogeneity of the composition will greatly reduce the creep properties of the alloy, so proper solution heat treatment is the key to achieve the best performance of the alloy [2]. Heat treatment is an essential process after alloy production. It can reduce the element segregation and eutectic structure content in the casting process. Lamei Cao et al. [3] have shown that increasing the solution temperature can avoid the undesirable microstructure and greatly enhance the structural stability. In addition, for CMSX series alloys, researchers have given a solution heat treatment temperature of 1365 °C for more than 45 h to obtain good solution effect [4–6].

Therefore, the solution temperature is much important for the mechanical properties of directionally solidified superalloy, but the research on this topic of DZ406 superalloy is rarely reported. Therefore, this study takes it as the research object, carries out different heat treatment temperatures, and studies the microstructure and mechanical properties of the alloy, aiming to provide a reference for the engineering application of the alloy.

2 Experimental

The blank is solidified in a vacuum directionally and cast into a solid bar with a total length of 200 mm. All samples are sliced in the same batch to ensure the accuracy of the conclusion. The composition of the material is measured by a chemical method, and the results are shown in Table 1.

To reveal the impact of solution heat treatment temperature on DZ406 alloy. The solution heat treatment temperature was adjusted based on the standard solution heat treatment. The solution temperatures were set as 1265, 1275 and 1285 °C. Table 2 lists the detailed information of heat treatment.

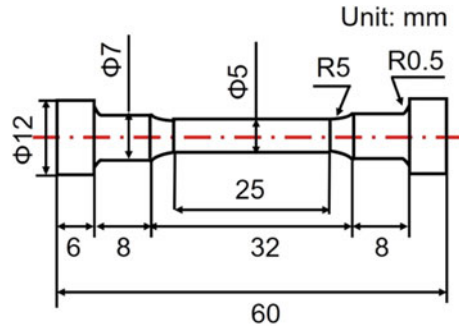
The stress rupture tests were conducted at 980 °C and 275 MPa in air according to Chinses standard GB/T 15974-2008. Figure 1 depicts the size of the specimen. The temperature variation in the gauge zone was within 3 °C during stress rupture tests, and the furnace door was opened quickly to cool the specimens. At least five specimens were tested for each condition to get one statistical result.

Table 1 Chemical composition of DZ406 alloy measuring using chemical method (wt%)

Co	Cr	Ta	Al	W	Re	Mo	Hf	C	B	Ni
11.98	6.77	6.28	6.02	4.84	2.92	1.53	1.48	0.12	0.014	Bal.

Table 2 Solution heat treatment of the DZ406 alloy

Number	Detail information
1	1265 °C/1 h + 1120 °C/4 h + 1080 °C/4 h + 870 °C/16 h (air cooling)
2	1275 °C/1 h + 1120 °C/4 h + 1080 °C/4 h + 870 °C/16 h (air cooling)
3	1285 °C/1 h + 1120 °C/4 h + 1080 °C/4 h + 870 °C/16 h (air cooling)

Fig. 1 Size of the stress rupture specimen

Samples were sectioned, ground and polished for microstructural characterization. The γ matrix was removed to observe γ' precipitates by electrochemical etching in a chemical solution of 6 ml phosphoric, 20 ml nitric and 24 ml sulfuric acid at 3 V for 5 s [7]. A chemical etchant consisting of 20 g copper sulfate, 5 ml sulfuric acid, 100 ml hydrochloric acid, 80 ml water was employed to observe the carbide and grain boundary. A FEI Nova Nano 450 microscope was adopted to observe the microstructures. The interdendritic γ' precipitates showed similar morphologies to that in the dendrite core regions in DZ406 alloy, and the γ' in dendrite core regions is more sensitive to heat exposure. Therefore, we measured the area fraction in the dendrite core regions to evaluate the microstructure degradation γ' precipitates. The standard point counting method is adopted. Five representative sites were adopted to quantify the area fraction of γ' precipitates. The average particle size is defined as the equivalent diameter of γ' particles according to the following formula:

$$D = \sqrt{\frac{4S}{\pi}} \quad (1)$$

where D means the equivalent diameter, S means the area.

The area fraction of the γ' precipitates and γ/γ' eutectic were measured using Image Pro software as Eq. (1). Five representative locations and three consecutive images were used to get one result.

The segregation degree of alloying elements was investigated, and the compositions of interdendritic region and dendrite core region were determined at least 10 positions randomly selected from each sample by JXA-8100 electron probe

microanalyzer (EPMA). The test point does not include γ/γ' eutectic pool or carbide. The solidification segregation coefficient K_i can be defined as follows [8]:

$$K_i = \frac{C_{dendrite}^i}{C_{interdendrite}^i} \quad (2)$$

where, $C_{interdendrite}$ and $C_{dendrite}$ is the mass fraction of element i in the dendrite stem and the mass fraction between dendrites, respectively. $K_i > 1$ indicates that alloy element i segregates in dendrite core, while $K_i < 1$ indicates that alloy element i segregates between interdendritic region [8].

3 Results

3.1 The as-Cast Microstructure of DZ406 Superalloy

The as-cast structure of DZ406 alloy is shown in Fig. 2. Figure 2a, b are OM images showing the dendrite morphology, which presents cross shape as previously reported, and primary dendrite spacing is about 289 μm . γ/γ' eutectic (Fig. 2b) in sunflower shape formed in the interdendritic regions during the casting process, The γ/γ' eutectic content is about 14.06%. Figure 2c shows the microstructure of γ' precipitates in the dendrite cores, and exhibited approximately cubic. The area fraction and average size was 59.3% and 0.54 μm , respectively (Table 3). It is worth noting that the morphologies of γ' precipitates were similar in both the interdendritic and dendrite core regions [9]. Script-like MC_1 and granular MC_2 carbides distributed in the interdendritic regions (Fig. 2d). MC_1 and MC_2 carbides distributed in the interdendritic regions, and the main difference is that MC_1 was rich in Ta, while MC_2 carbides was rich in Hf. The composition characteristics of MC carbides accord well with the typical characteristics of Hf rich superalloys [10, 11].

3.2 Microstructure Characteristics After the Solution Heat Treatment

The microstructure of γ' phase in the dendrite core area is shown in Fig. 3, and Table 3 lists the corresponding statistical area fraction and the average size of γ' phase. Figure 3 illustrates that after the different solution heat treatment, the γ' phase are still maintain a relatively cubic shape [5, 6].

After the Num.1 heat treatment, the area fraction and the size of γ' particles increased to 65.78% and 0.63 μm (Table 3). Increasing the solution heat treatment temperature, the area fraction and size of γ' precipitates did not change

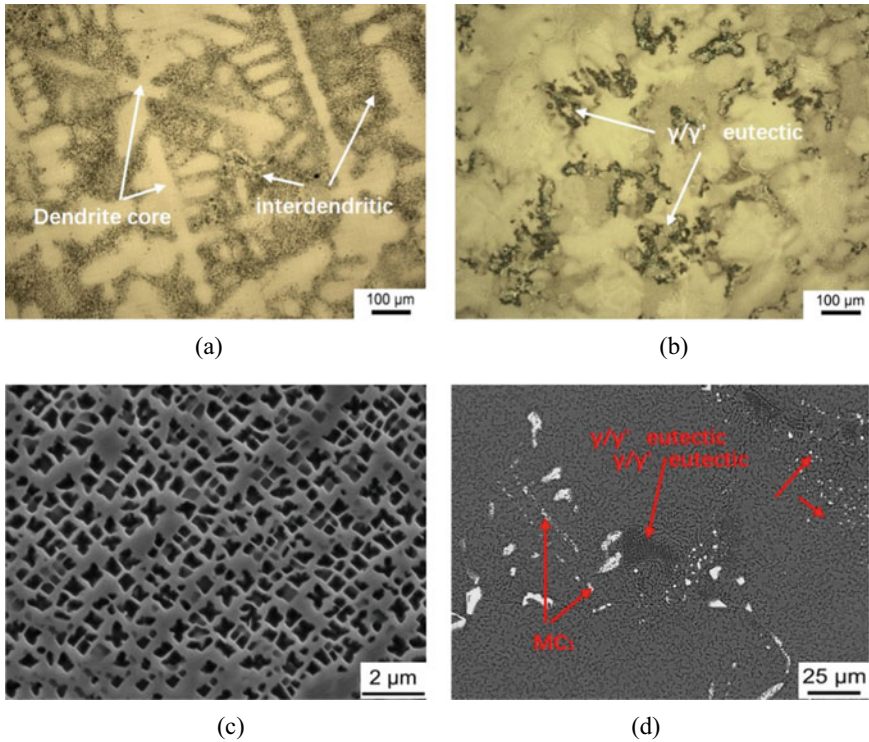


Fig. 2 The as-cast microstructure of DZ406 superalloy

Table 3 Measured area fraction and average size of γ' precipitates in the dendrite core regions, area fraction the interdendritic γ/γ' eutectic, MC carbides of DZ406 alloy after solution heat treatment

Solution heat treatment condition (°C)		As-cast	1265	1275	1285
γ/γ' eutectic (%)		14.06 ± 1.17	12.46 ± 1.85	6.27 ± 0.54	5.80 ± 0.65
MC carbides (%)		1.47 ± 0.44	1.48 ± 0.64	1.24 ± 0.31	1.37 ± 0.17
γ' phase	Area fraction (%)	59.3 ± 2.1	65.78 ± 2.6	65.38 ± 2.6	63.22 ± 1.9
	Average size (μm)	0.54 ± 0.061	0.63 ± 0.067	0.62 ± 0.055	0.64 ± 0.055

significantly, which changed to 65.38%, 0.62 μm at Num.2 and 63.22%,0.64 μm at Num.3 respectively, (Fig. 3b, c). The results clear that γ' phase is not very sensitive to the three kinds of solution heat treatment, which is in consistent with previous studies [5, 12].

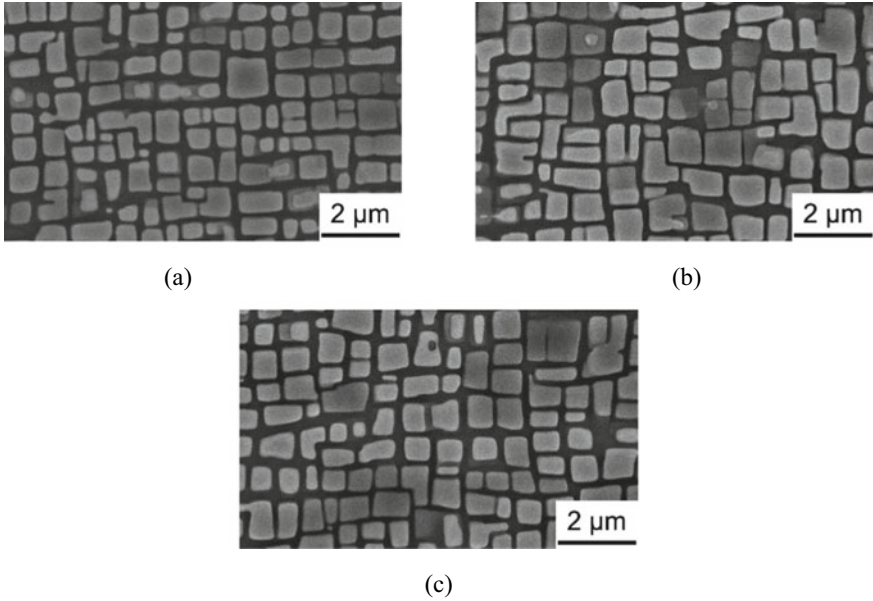


Fig. 3 SEM-SE images of γ' precipitates in the dendrite cores after solution heat treatment: **a** Num. 1, **b** Num. 2, **c** Num. 3

Figure 4 is the OM image showing the γ/γ' eutectic morphology after the different solution heat treatment systems (Table 2). At solution temperature 1265 °C, the γ/γ' eutectic area fraction is 12.46%, and the area fraction of carbides is 1.47%. And there are micro porosity at 1265 °C. When the solution temperature increases to 1275 and 1285 °C, the eutectic content decreases to 6.27 and 5.8%, and the area fraction of carbides is 1.24 and 1.31%. It is worth mentioning that the area of micro porosity is also increasing. It is obvious that the increase of solution temperature lead to the decrease of the area fraction of γ/γ' eutectic, but the effect of solution temperature on carbides is not obvious. In addition, the area of micro holes gradually increases with increasing of heat treatment temperature, which is obviously related to eutectic dissolution [13].

3.3 Stress Rupture Property After the Solution Heat Treatment

The stress fracture characteristics of DZ406 alloy after heat treatment were tested at 980 °C/225 MPa, and Fig. 5 shows the curves of stress rupture lives, elongation and reduction of area vs solution heat treatment temperatures. It is surprising that the stress rupture lives increased with the increase of solution temperature, and were

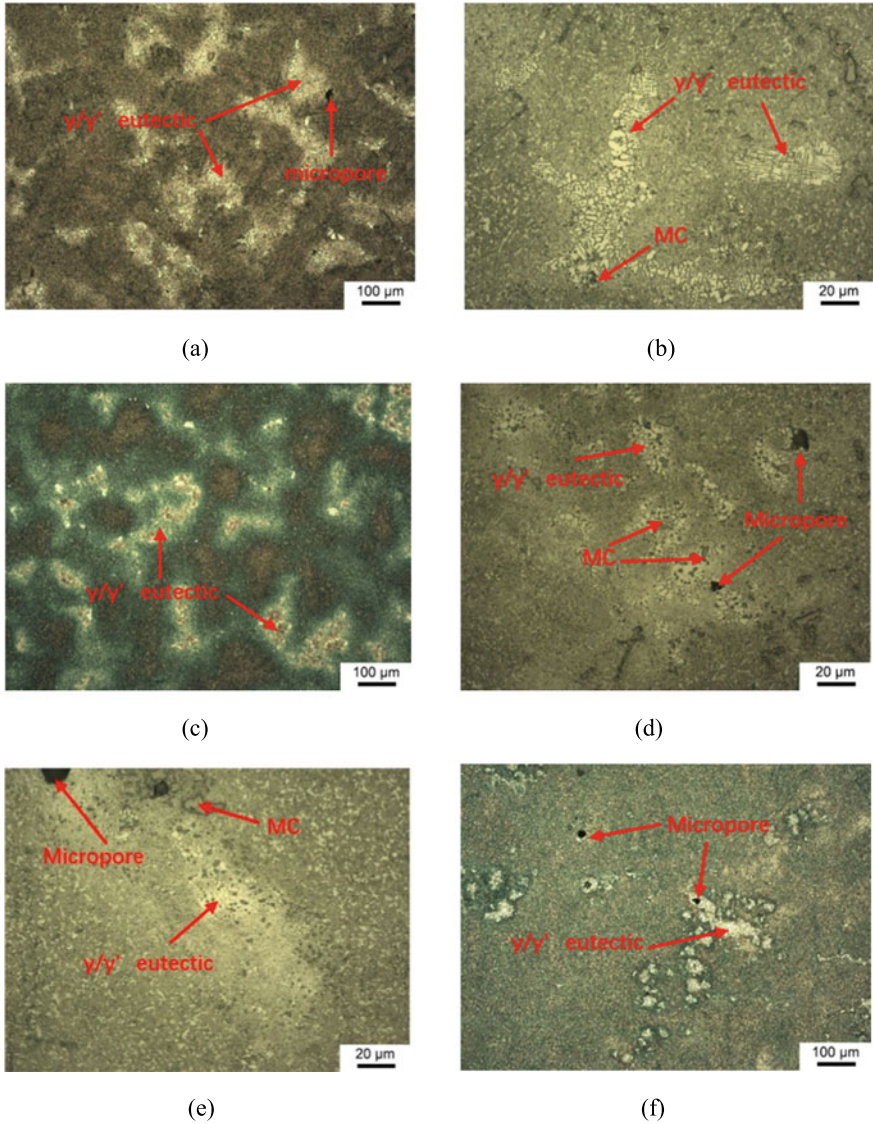


Fig. 4 SEM images of interdendritic γ' eutectic: **a** and **b** 1265 °C; **c** and **d** 1275 °C; **e** and **f** 1285 °C

between 55 and 60 h (Fig. 5a). At solution temperature 1265 °C, the rupture life is 57.6 h. With the temperature rising to 1275 and 1285 °C, the rupture life increased to 59 and 60 h. Meanwhile, Fig. 5b depicts that the reduction of area and elongation after solution heat treatment were also close. The results show that the effect of solution temperature on the stress rupture property is not very significant, the

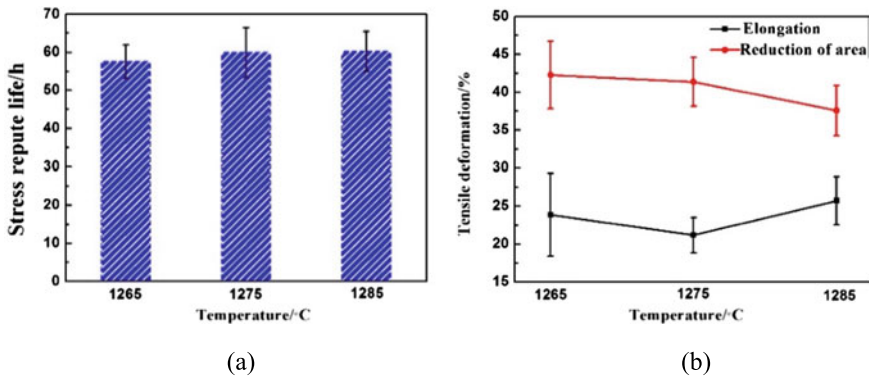


Fig. 5 The curves of stress rupture lives (a), elongation and reduction of area (b) as a function of the different temperature of DZ406 alloy under 980 °C/275 MPa

impact is limited. This is inconsistent with the previous reports on single crystal superalloys [4, 13–15].

There is no significant difference in fracture mode, macro and micro morphology after different solution heat treatment, and Fig. 6 reveals the morphology of microcracks in stress ruptured specimens under solution heat treatment at Num.3 (Table 2). Figure 6a is the SEM-SE image showing the macro fracture surface, and Fig. 6b shows that during the fracture process, obvious oxidation reaction occurs on the fracture surface, and a large amount of oxidation products are attached to the fracture surface. Figure 6c indicates that the fracture mode is dimple morphology, which conforms to the fracture characteristics reported by predecessors. Figure 6d, e are SEM-BSE images depicting the longitudinal interface. It can be seen that the small cracks originate at the interfaces of eutectic structure/ γ matrix, and carbide/ γ matrix. The results show that the interface between carbide and matrix and eutectic structure are the weak position of the alloy, which is easy to fracture.

4 Discussion

4.1 Solution Heat Treatment Effect on the Microstructural Evolution

During the solidification process, γ dendrites precipitated from the liquid phase and grows up during the whole process. Refractory elements Re and W segregate to the γ dendrites [16, 17], while Al and Ta segregate to the interdendritic regions. With the solidification of interdendritic phase, the γ/γ' eutectic structure is shaped due to the variation in the liquid component. The amount of eutectic reflects segregation degree in the solidification process to a certain extent. The more eutectic content

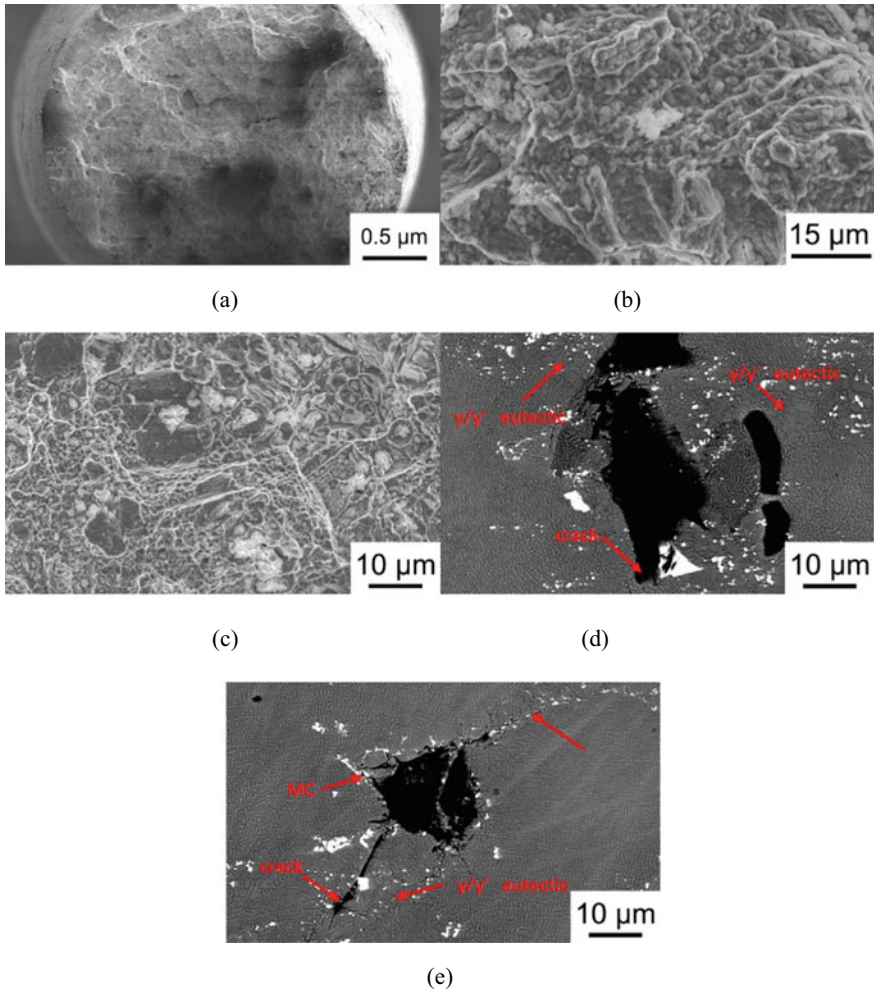


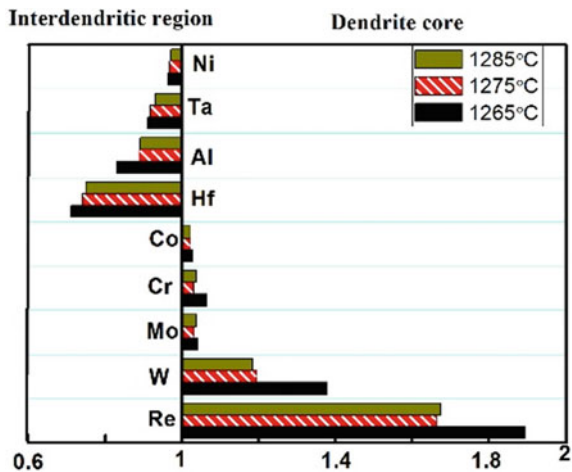
Fig. 6 SEM-SE images of the fracture surfaces of transverse stress ruptured specimens at a low **a** and high **b, c** magnification; SEM-BSE images of cracks at the longitudinal cross sections in the fractured specimen, close to the surface **d**, the γ/γ' eutectic **e** and the interdendritic MC carbides of DZ406 alloy under 980 °C/275 MPa after solution heat treatment at Num. 3

indicates that the alloy has serious component segregation, otherwise, it indicates that the alloy has small component segregation [17–19]. After Num.1, Num.2 and Num.3 heat treatment, coarse γ' phase and γ/γ' eutectic dissolve into the γ matrix in the as-cast alloy, promoting the full diffusion of the insoluble alloy elements, reducing the solidification segregation, and finally reduce the segregation degree of the interdendritic regions specially for the low melting point elements [1, 13, 18, 20].

In this study, about 14.06% of γ/γ' eutectic exists after casting (Fig. 2b), and the element segregation is also serious. However, area fraction of γ/γ' eutectic reduce significantly (Table 3) after Num.1, Num.2 and Num.3 heat treatment. The degree of segregation of various elements is shown in Fig. 7. It can be found that the segregation degree decreases with increasing the solution temperature.

During castings solidification process of superalloy, because of the continuous growth of the first solidified dendrites and their contact with each other, a closed micro liquid pool is often shaped in the interdendritic region. When the liquid metal in the micro liquid pool condenses into a solid phase, it shrinks and fails to get feeding, thus causing shrinkage cavity. Due to the unbalanced solidification, eutectic reaction occurs when the liquid between dendrites reaches the eutectic composition point in the later stage of solidification and crystallization [14–16, 21]. Therefore, the solidification shrinkage cavity is mainly distributed in the interdendritic and eutectic areas in the late solidification stage. In this study, there are irregular holes in the as-cast statue, and mainly formed around γ/γ' eutectic structure (Fig. 5). The above results show that a large number of solution micropores are produced in the alloy during solution heat treatment, which can be explained by the micropore formation caused by the Kirkendall effect in the process of element diffusion between dendrites and dendrites. The solute redistribution makes that Re and W are segregated in the dendrite, while Al and Ta are segregated in the interdendritic regions during solidification [22, 23]. During the following solid solution heat treatment process, there are two diffusion flows with different diffusion rates: the diffusion flow of enriched elements from dendrites to dendrites and the diffusion flow of enriched elements from dendrites to dendrites. The diffusion rate of the former is smaller than that of the latter, and this unbalanced diffusion mechanism will lead to the accumulation of vacancies and the formation of micropores.

Fig. 7 Elements segregation coefficient of DZ406 alloy after Num. 1, Num. 2, Num. 3 solution heat treatment



4.2 Effect of Solution Heat Treatment on the Fracture Property of DZ406 Alloy

Previous studies confirmed that the creep rupture resistance of Ni-based superalloys are attributed to the area fraction and morphology of γ' phase, the γ channel width, solution strengthening the effect, micropores and interdendritic γ/γ' eutectic [4, 24]. Our results reveal that the solution heat treatment has no significant effect on the microstructure stability of γ' phase, but influence obviously on the solution strengthening effect and γ/γ' eutectic. The main factors that affect the performance are discussed respectively.

4.2.1 Solid Solution Strengthening Effect of Elements

Ni-based superalloy always contains Re, Cr Mo and Mo as the solid solution strengthening elements, and Re shows the greatest impact on creep rupture resistance. Re is enriched in γ matrix and easy to form short-range ordered re clusters of about 1 nm [17]. This kind of cluster has better strengthening effect than the traditional solid solution method. This is because when the dislocation moves through the cluster, it will destroy the ordered region of Re atom and enhance the resistance of dislocation movement. Cr, Mo and W are mainly distributed in the matrix, and strengthened the matrix due to solution enhancement, thus the stress rupture life is significantly increased [23, 25].

In this study, the dendrite has a good solution strengthening effect, but the dendrite becomes the weak areas due to the poor solution strengthening effect, which is easy to cause crack initiation and propagation. Increasing the solution heat treatment temperature, the segregation degrees of Re, W, Mo and Cr decreased, the interdendritic regions thus contained more strengthening elements and get better solution strengthening effect to improve the stress rupture properties.

4.2.2 Effect of Eutectic on Stress Rupture Properties

Wilson et al. [13] found that the eutectic structure with incomplete solid solution between dendrites can significantly reduce the creep properties of CMSX-4 alloy. P. Caron et al. [26] considered that micropores were the most effective crack sources in the absence of brittle eutectic and local primary melting. Fritzemeier et al. [21] considered that micropores are the main source of failure cracks in the single crystal superalloys. A much better high temperature rupture property was achieved by reducing the micropore content.

The thermal expansion coefficient of γ/γ' eutectic structure is different from that of γ matrix [16], and the interface of γ/γ' eutectic structure and γ matrix can produce large thermal stress. The γ/γ' eutectic structure is easy to separate from matrix and become the initiation locations of crack initiation. Improving the

solution treatment temperature and gradually decreases the content of γ/γ' eutectic structure, and increase the relative proportion of micropores. However, the γ/γ' eutectic content is high and the micropore content is very small after Num.1 heat treatment, the creep property are the worst in comparison with other solution conditions, indicating that the effect of a small number of micropores is not necessary to introduce a worse creep property. Therefore, the stress rupture property was improved as the temperature of the solution increased.

5 Conclusions

1. The γ/γ' eutectic structure is easily affected by solution heat treatment, while the microstructures other precipitates including γ' precipitates and carbides basically didn't change at the three kinds of solution temperatures.
2. The area fraction of eutectic decreases with the increase of solution temperature.
3. A higher the solution temperature can reduce the element segregation degree, and finally enhance the stress rupture property.

References

1. Rowland, L.J.: Creep and microstructural stability of ruthenium-containing nickel-base single crystal superalloys (2005)
2. Khajavi, M.R., Shariat, M.H.: Failure of first stage gas turbine blades. *Eng. Fail. Anal.* **11**(4), 589–597 (2004)
3. Cao, L.M., Li, X.H., Chen, J.Y., et al.: Influence of solution heat treatment temperature on the microstructure of the third generation Ni-based single crystal superalloy DD10 **59**(10), 23–27 (2011)
4. Fuchs, G.E.: Improvement of creep strength of a third generation, single-crystal Ni-base superalloy by solution heat treatment. *J. Mater. Eng. Perform.* **11**(1), 19–25 (2002)
5. Rzyankina, E., Pytel, M., Mahomed, N., et al.: Solution heat treatment of single crystal castings of CMSX-4 nickel-base superalloy. In: *Proceedings of the International Conference on Competitive Manufacturing* (2016)
6. Fuchs, G.E.: Solution heat treatment response of a third generation single crystal Ni-base superalloy. *Mater. Sci. Eng.* **300**(1–2), 52–60 (2001)
7. Zheng, Z., Zhou, J.Y., Zhao, W.X., et al.: Service temperature evaluation of cast K465 superalloy turbine vane based on microstructural evolution. *Mater. Sci. Forum* **944**, 411–420 (2019)
8. Wang, A., Lv, J., Chen, C., et al.: Effects of heat treatment on microstructure and high-temperature tensile properties of nickel-based single-crystal superalloys. *Mater. Res. Exp.* **6**(12) (2019)
9. Gasson, P.C.: *The superalloys: fundamentals and applications* Reed R. C. Cambridge University Press, The Edinburgh Building, Shaftesbury Road, Cambridge, CB2 2RU, UK, 2006. 372pp. Illustrated. 80. ISBN 0-521-85904-2. **112**(1131), 372-291 (2008)
10. Huang, Z.H., Tan, Y.N., Jia, X.Y., et al.: Study on long-term aging of the second generation DS superalloy DZ406. *J. Mater. Eng.* (2009)

11. Sims, C.T., Stoloff, N.S., Hagel, W.C.: *Superalloys II: High-Temperature Materials for Aerospace and Industrial Power* (1987)
12. Hobbs, A.R.: *Solidification characteristics, microstructural stability and creep behaviour of advanced ruthenium-bearing nickel-base single crystal superalloys*. University of Cambridge (2006)
13. Wilson, B.C., Hickman, J.A., Fuchs, G.E.J.J.: The effect of solution heat treatment on a single-crystal Ni-based superalloy. *JOM* **55**(3), 35–40 (2003)
14. Kaiser, R., Williamson, K., O'Brien, C., et al.: Effects of hot isostatic pressing and heat treatment on cast cobalt alloy. *Mater. Sci. Technol* **31**(11), 1298–1304 (2015)
15. Proebstle, M., Neumeier, S., Feldner, P., et al.: Improved creep strength of nickel-base superalloys by optimized γ/γ' partitioning behavior of solid solution strengthening elements. *Mater. Sci. Eng.* **676**(Oct 31), 411–420 (2016)
16. Heckl, A., Neumeier, S., Goken, M., et al.: The effect of Re and Ru on γ/γ' microstructure, γ -solid solution strengthening and creep strength in nickel-base superalloys. *Mater. Sci. Eng. A-Struct. Mater. Prop. Microstruct. Process.* **528**(9), 3435–3444 (2011)
17. Neumeier, S., Pyczak, F., Goken, M.: Influence of rhenium and ruthenium on the local mechanical properties of the γ and γ' phases in nickel-base superalloys. *Mater. Sci. Eng.* **91** (33), 4187–4199 (2011)
18. Yang, D.Y., Jin, T., Zhao, N.R., Wang, Z.H., et al.: Microstructure Evolution of a Single Crystal Nickel-Base Superalloy During Heat Treatment and Creep **025**(5), 80–82 (2004)
19. Fuchs, G.E., Boutwell, B.A.: Modeling of the partitioning and phase transformation temperatures of an as-cast third generation single crystal Ni-base superalloy. **333**(1–2), 72–79 (2002)
20. Yu, X., Liang, F., Li, A., et al.: Creep behavior of a single crystal nickel-based superalloy containing 4.2% Re (2012)
21. Fritzscheier, L.G.: *The Influence of High Thermal Gradient Casting, Hot Isostatic Pressing and Alternate Heat Treatment on the Structure and Properties of a Single Crystal Nickel Base Superalloy* (1988)
22. Chen, J.Y., Zhao, B., Feng, Q., Cao, L.M., et al.: Improvement of stress–rupture property by Cr addition in Ni-based single crystal superalloys. **528**(10–11), 3791–3798 (2011)
23. Faehrmann, M., Fratzl, P., Paris, O., et al.: Influence of coherency stress on microstructural evolution in model Ni-Al-Mo alloys. *Acta Metall. Mater* **43**(3), 1007–1022 (1995)
24. Ali, L., Ghauri, K.M., Hasan, F.: *Cracking Failure in GAS-Turbine Blades* (2011)
25. Rowland, L.J., Feng, Q., Pollock, T.M.: Microstructural stability and creep of Ru-containing Nickel-base superalloys. *Mater. Sci.* (2004)
26. Caron, P., Naveos, S., Khan, T.: Improvement of creep strength in a nickel-base single-crystal superalloy by heat treatment. *Mater. Sci. Eng.* **61**(2), 173–184 (1983)

Design of Embedded Intelligent Online Monitoring System of OLTC Based on Vibration Analysis



Changqing Peng, Rongyan Shang, Wenquan Huang, Min Deng,
and Ruiming Fang

Abstract Most of the traditional intelligent monitoring systems of on-load tap-changer (OLTC) are PC-based, which is expensive, high in power loss, complex in deployment, and large in space. A small, low-cost and low-power-loss embedded intelligent online monitoring system of OLTC based on vibration analysis is designed. The system uses an equal-integral-bandwidth feature extraction method of vibration signal based on fast Fourier transform (FFT), which solves the problems of difficulty in implementation and insufficient computing power in embedded systems. First, the FFT-based equal-integral-bandwidth feature extraction of vibration signal is discussed in detail. Then, a method applying fault diagnosis based on support vector machines (SVM) to the embedded system is proposed, and the framework of the intelligent online monitoring system of OLTC is given. Finally, the fault diagnosis experiments of OLTC are carried out. The experimental results show that after adopting the embedded system, it takes a very short time and the fault diagnosis is accurate, which can meet the needs of intelligent online monitoring of OLTC.

Keywords Vibration analysis · Feature extraction · Embedded system · OLTC · Fault diagnosis

1 Introduction

The vibration signal of mechanical equipment contains a large amount of status information. The rapid and effective extraction of fault characteristic information from the vibration signal and the in-depth research of equipment condition monitoring and fault diagnosis technology have extremely important practical signifi-

C. Peng · R. Shang (✉) · W. Huang · R. Fang
Huaqiao University, Xiamen 361021, China
e-mail: Shangry@hqu.edu.cn

M. Deng
Red Phase Co., Ltd, Xiamen 361005, China

cance for ensuring the safe operation of equipment [1–3]. An on-load tap changer (OLTC) is one of the most error-prone parts in the transformer. When a fault occurs, it threatens the safe and stable operation of the power transformer [4]. Statistics show that transformer accidents caused by OLTC account for more than 20%, and they are mainly mechanical faults [5, 6]. It is necessary to develop the online monitoring and fault diagnosis of the internal mechanical state of the OLTC without stopping or disassembling based on vibration analysis. This not only greatly improves the work efficiency of maintenance personnel and the accuracy of fault diagnosis, effectively reducing the power outage time of the equipment, but also makes it possible to find faults in the early stage, and prevents problems before they occur.

At present, the hardware implementation of the monitoring system is as follows: (1) Using single-chip microcomputer (SCM), digital signal process (DSP) or advanced RISC machines (ARM) as the slave computer, responsible for signal conditioning, data acquisition and sending data to the host computer; Personal computer (PC) as the host computer, responsible for receiving the data transmitted from the slave computer, And analyze, diagnose, display and store the data [7]. (2) Using the data acquisition card as the data acquisition core, and the PC as the monitoring system of the hardware platform to analyze the collected data [8, 9]. The PC-based monitoring system is expensive, high in power loss, complicated to deploy, large in space, and demanding on the operating environment and maintenance.

The requirements for miniaturization, distribution, and low power loss of equipment have increased with the wide range of application scenarios of online monitoring and intelligent diagnosis systems. Embedded system can meet the above needs, but it also has shortcomings [10]. On the one hand, the current various feature extraction algorithms have complex principles, cumbersome processing, and large amounts of calculation. If an embedded system is adopted, the threshold for programming is very high and the processing speed cannot meet the real-time requirements [11, 12]. On the other hand, the development of the Internet of Things in Electricity also puts forward new requirements for monitoring and diagnosis systems [13]. Balancing of operation of data in the local environment and in the cloud is very important. A large amount of basic collected data can only be stored locally, but key feature information and diagnosis results must be pushed to the cloud.

Therefore, how to simplify the frequency domain feature extraction of vibration signals, improve the accuracy of fault diagnosis, and then realize intelligent online monitoring of OLTC in the embedded system are the core objectives of this study. The rest of this study is organized as follows. In Sect. 2, the FFT-based equal-integral-bandwidth feature extraction method is discussed. In Sect. 3, a method applying fault diagnosis based on support vector machines (SVM) to the embedded system is proposed, and the framework of the intelligent online monitoring system of OLTC is given. The fault diagnosis experiments of OLTC are carried out in Sect. 4. Finally, conclusions are drawn, and potential areas for future research are highlighted in Sect. 5.

2 FFT-Based Equal-Integral-Bandwidth Feature Extraction Method

2.1 Feature Extraction Process of Vibration Signal

The FFT-based equal-integral-bandwidth feature extraction process of vibration signal is shown in Fig. 1.

It can be seen from Fig. 1 that the output signal of the vibration sensor is adjusted by the sampling circuit and converted into the original discrete digital signal. First, preprocess the collected original data of the vibration signal, such as filtering, trimming, etc., to obtain relatively pure data information. Second, the preprocessed signal is transformed from time domain to frequency domain to obtain its spectrum information. Third, the frequency spectrum is segmented according to the amplitude integral value to obtain the bandwidth information of each segment. Finally, the bandwidth information is converted to obtain the feature value required for fault diagnosis.

2.2 Data Preprocessing

The measured waveform of vibration signal during normal action of OLTC collected by the slave computer is shown in Fig. 2.

It can be seen from Fig. 2 that the vibration signal of OLTC was divided into a starting segment AB, an energy storage segment BC, a switching segment CD, and a stopping segment DE according to the action process. Among them, the signal of starting segment AB and a stopping segment DE is very random. It is difficult to effectively extract the fault feature information, and even cause interference problems. Therefore, it needs to be trimmed during preprocessing to obtain a “pure” effective signal segment BD.

The time of energy storage segment BC was relatively long, and the signal was relatively stable. The frequency characteristics are concentrated in the middle and low frequency components, and the high frequency components are very few. The switching segment CD was a sudden change in waveform with a wide frequency domain distribution. These two segments were suitable for vibration analysis, but if energy storage segment and the switching segment do not extract the features separately, fault features of the switching segment will be completely annihilated.

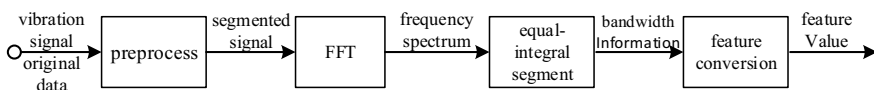


Fig. 1 The FFT-based equal-integral-bandwidth feature extraction process of vibration signal

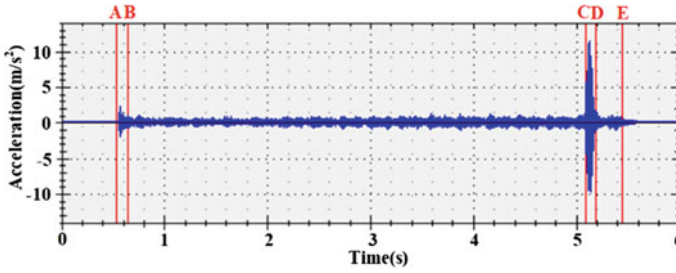


Fig. 2 Measured waveform of vibration signal during normal action of OLTC

Therefore, it is necessary to preprocess the vibration signals in segments and extract the fault feature information of the energy storage segment and the switching segment separately.

2.3 Transform Signal from Time Domain to Frequency Domain

If only the time domain is used, the information that OLTC vibration signals can extract is limited, and it is far from satisfying the need for mechanical condition monitoring based on vibration signals. Only through the frequency domain of the vibration signal, the key feature information can be truly extracted, and then accurate mechanical fault diagnosis be performed.

After the vibration signal is transformed by FFT, the required “frequency point-amplitude” spectrogram can be obtained. The frequency spectrum of the energy storage segment BC and the switching segment CD are shown in Fig. 3a, b respectively.

2.4 Divide Frequency Spectrum into Several Segments According to Equal Integral

According to amplitude $A(n)$ in Fig. 3 (where n is the frequency point, A is the spectral amplitude), the integral sum σ is obtained, as shown in Eq. (1).

$$\sigma = \sum A(n) \quad (1)$$

The number of segments was set to m ; then, the integral sum of each segment was as shown in Eq. (2).

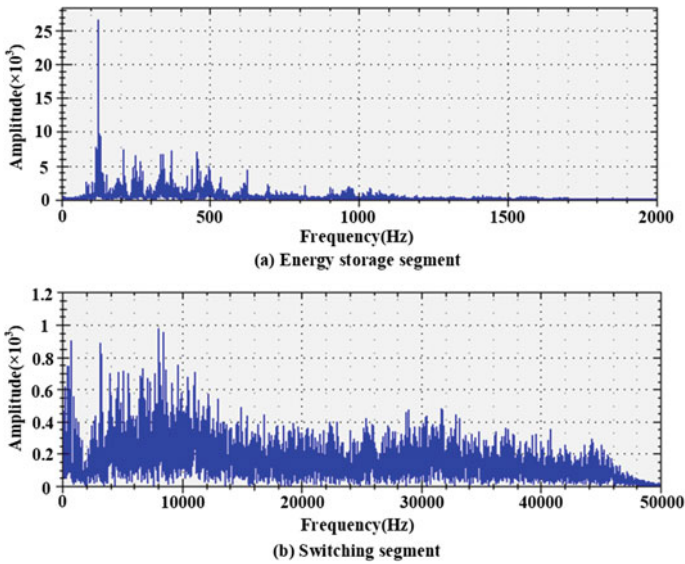


Fig. 3 The frequency spectrum of vibration signal

$$\sigma' = \frac{\sigma}{m} \tag{2}$$

The frequency spectrum is divided into m segments according to the integral sum equal to σ' , and the frequency points F_j ($j = 0, 1, \dots, m$) of each segment point are obtained. Then the bandwidth $b(i)$ ($i = 0, 1, \dots, m - 1$) of each segment is calculated, as shown in Eq. (3).

$$b(i) = F_{i+1} - F_i \tag{3}$$

2.5 Feature Conversion

According to Sect. 2.4, for a segment, the larger the spectrum amplitude of the vibration signal, the smaller the bandwidth $b(i)$. Due to the weight inversion, it is very unfavorable in the fault diagnosis system. Therefore, it is necessary to perform a normalization operation on the bandwidth first. Second, take the reciprocal of the normalized value. Third, calculate its natural logarithm. Finally, normalize again to obtain the feature value.

The bandwidth coefficient $b^*(i)$ after normalization is calculated as shown in Eq. (4).

$$b^*(i) = \frac{b(i)}{\sum b(i)} \tag{4}$$

The conversion coefficient $b'(i)$ of each segment is calculated, as shown in Eq. (5).

$$b'(i) = \ln \frac{1}{b^*(i)} \tag{5}$$

The conversion coefficient is normalized again to get the feature value $b'^*(i)$ as shown in Eq. (6).

$$b'^*(i) = \frac{b'(i)}{\sum b'(i)} \tag{6}$$

3 Design of the Intelligent Online Monitoring System

3.1 Method of Applying Fault Diagnosis Based on SVM to the Embedded System

SVM has the advantages of rigorous theory, strong adaptability, global optimization, high training efficiency and good generalization performance. It has extremely high application value [14]. This paper uses SVM classifier to realize the intelligence diagnosis of mechanical failure of OLTC.

Before using SVM for data diagnosis, it is necessary to train the model first, and the training model requires a large number of typical sample support. The establishment process of a complete SVM-based fault diagnosis system is shown in Fig. 4.

However, due to the limited computing power of the embedded system and the inconvenience of interactive operations, it is recommended that the model training work be arranged on a computer with a Windows operating system. After the model

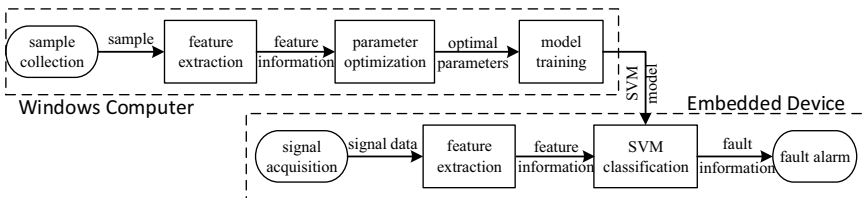


Fig. 4 The establishment process of a complete SVM-based fault diagnosis system

training is completed, it is transplanted to the embedded system for use, which can greatly improve the efficiency of model training and reduce the difficulty of model training.

3.2 The Framework of the Intelligent Online Monitoring System

The framework of the embedded intelligent online monitoring system of OLTC based on vibration analysis is shown in Fig. 5.

The core feature information of the system is the frequency domain feature of the main vibration signal. In order to improve diagnosis accuracy, some time-domain characteristics of vibration signals are introduced as SVM input vectors, such as energy storage duration, average vibration acceleration of energy storage segment, and so on. In order to further improve the diagnostic accuracy, the drive motor current signal and the drive shaft angle signal are introduced as auxiliary criteria, and the time domain characteristics are mainly extracted as the SVM input vector, such as driving current duration, driving current average value, and so on.

The intelligent online monitoring system of OLTC can be operated as a single machine offline to realize functions such as signal acquisition, feature extraction, fault diagnosis, fault alarm, and alarm linkage.

In terms of system expansion, after the intelligent online monitoring system of OLTC is connected to the Internet of Things, it can actively push alarm information and regular statistical reports through the gateway through mobile phone text messages, emails, etc. The centralized control server can simultaneously connect multiple online monitoring systems in the same Internet of Things, collect and save the data collected on site, the extracted feature values, the diagnosis results, etc., and the running status and real-time diagnosis results of each monitoring device are dynamic displayed on the large monitor screen in the duty room. Users can

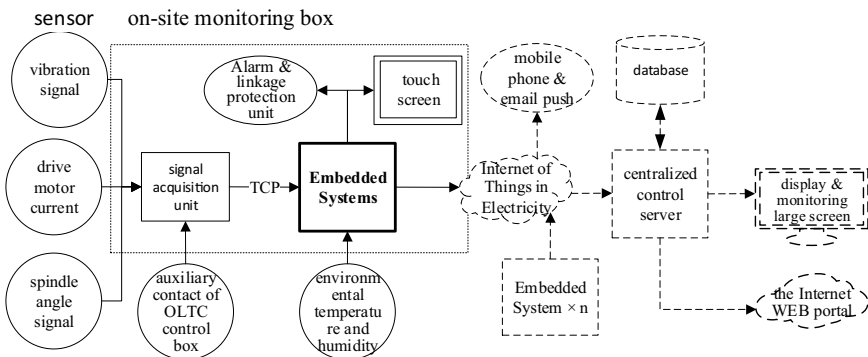


Fig. 5 The framework of the embedded intelligent online monitoring system of OLTC

remotely view detailed information through a Web browser. With more advanced functions, the centralized control server can perform longitudinal mining on the historical data of a single monitoring device in the background, as well as horizontal mining on the same period related data of multiple monitored objects of the same model, conduct in-depth trend analysis and analogy discrimination, and discover potential risk of failure.

4 Experimental Study

The physical object of the intelligent online monitoring system of OLTC is shown in Fig. 6, and it is operated as a single machine offline. In this system, the signal acquisition unit is temporarily replaced by the Red Phase TCD-200, and the data source is the offline experimental data stored in the device. The object of this batch of data acquisition is an OLTC of type Huaming CMIII 600Y/126C-10193W. The collected signal includes one current signal and one main vibration signal, and the sampling rate is 100Ksa/s. The type of the vibration acceleration sensor used is LC0103TB-50, sampling time is about 6 s per action. The hardware of the embedded system uses the popular RaspBerry 4 Pi model B as the implementation platform.

After actual testing, the signal takes about 0.4 s from the start of preprocessing after acquisition to the completion of feature extraction. After feature extraction, it takes about 0.3 s to call libSVM for diagnosis and recognition. There is room for further optimization, which can fully meet the needs of field applications.

In order to verify the feasibility of the FFT-based equal-integral-bandwidth feature extraction method described in this paper, the test samples shown in Table 1

Fig. 6 The physical object of the intelligent online monitoring system of OLTC

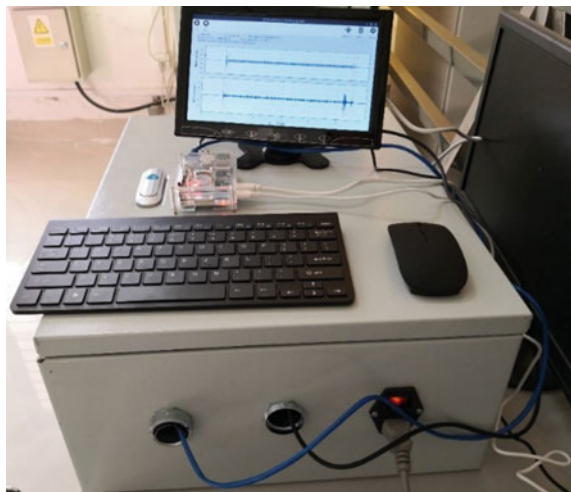


Table 1 The test samples

Fault type	Total number of samples	Number of training samples	Description
Normal	90	60	No fault. A total of three tests, 28 samples twice, 34 samples once. Disassemble and reassemble at least once during each test
Abnormal switching	28	20	The position of the switch was adjusted so that it was offset by a certain angle
Spring fatigue	28	20	The main spring was shortened by four turns
	44	20	The main spring was shortened by two turns
Contact wear	28	20	The surface of a group of four moving and static transition contacts was artificially roughened to simulate the fault that the contacts were burned by the ar
	44	20	The surface of 16 A-phase moving contacts was artificially roughened to simulate the fault that the contacts were burned by the arc
Curved plate falling off	28	20	The entire curved plate of phase A was removed
Curved plate loosening	28	20	The screws of the A-phase curved plate were loosened
Contact loosening	28	20	The pressure spring of the selector switch contact was cut off for one turn
Contact falling off	28	20	One set of three selector switch contacts was removed
Jamming	50	30	Sawdust was added to the gearbox. A total of two tests, the number of samples were 12 and 38, and the amount of sawdust was different

are used to perform experiments. The total number of samples is 424, and the number of samples used for training is 270.

The verification content includes parameter optimization test and generalization test, and libSVM is used for multi-class test. First, optimize the parameters of the training samples, and record the optimal parameters and optimal accuracy. Second, use the parameters and training samples to train and generate the SVM model. Finally, use the model to classify and identify all samples (including training samples), and record the generalization accuracy.

Taking into account the need to compare with other methods, and in order to improve the efficiency of the verification, the verification work is completed on a computing workstation installed with the Windows operating system. Under Windows and Linux, the implementation of FFT-based equal-integral-bandwidth mouthed uses exactly the same source code, and libSVM also uses the same underlying code, only the compilation target is different, so the impact of different

hardware devices and operating systems on the diagnostic accuracy should be ignored.

(1) Compared with EMD and WPD

Verification scheme: The FFT-based equal-integral-bandwidth feature extraction method takes the number of segments as $m = 8$, and uses the eight feature values as the main SVM input vector. The EMD- (Empirical mode decomposition) method decomposes into 10 IMF (intrinsic mode function) components to obtain energy entropy, and takes the first 8 components as the main SVM input vector. The WPD- (wavelet packet decomposition) method uses DB3 wavelet basis to perform four-layer decomposition, and then take the first 8 components as the main SVM input vector.

Accuracy of parameter optimization and verification are shown in Table 2.

It can be seen from Table 2 that FFT-based equal-integral-bandwidth feature extraction method has a higher diagnostic accuracy.

(2) Compare the accuracy before and after adding time domain features

Verification scheme: In the scheme of the pure frequency domain feature, The FFT-based equal-integral-bandwidth feature extraction method takes the number of segments as $m = 8$, and uses the eight feature values as the main SVM input vector. The comparison scheme adds the average value of vibration acceleration as the input vector.

The accuracy before and after adding time domain features are shown in Table 3.

It can be seen from Table 3 that the accuracy is higher after adding the time domain feature.

(3) Compare the accuracy before and after multi-signal fusion

Verification scheme: In the scheme of the frequency domain and time domain feature, The FFT-based equal-integral-bandwidth feature extraction method takes

Table 2 Accuracy of parameter optimization and verification

Accuracy of	WPD	EMD	FFT-based equal-integral-bandwidth
Parameter optimization	84.51% (228/270)	72.54% (196/270)	95.54% (258/270)
Verification	90.80% (385/424)	87.50% (361/424)	96.70% (410/424)

Table 3 Accuracy before and after adding time domain features

Accuracy of	Before	After
Parameter optimization	95.54% (258/270)	98.51% (266/270)
Verification	96.70% (410/424)	99.29% (421/424)

Table 4 Accuracy before and after adding the energy consumption index of the drive motor

Accuracy of	Before	After
Parameter optimization	98.51% (266/270)	99.63% (269/270)
Verification	99.29% (421/424)	99.76% (423/424)

the number of segments as $m = 8$, and uses the eight feature values and the average value of vibration acceleration as the main SVM input vector. The comparison scheme adds the energy consumption index of the drive motor on this basis (the square of the drive current multiplied by the duration) as the input vector.

The accuracy before and after adding the energy consumption index of the drive motor are shown in Table 4.

It can be seen from Table 4 that multi-signal fusion can further improve the accuracy.

5 Conclusion

The FFT-based equal-integral-bandwidth feature extraction method is used to extract the characteristic information of the vibration signal, which is used as the main fault characteristic solution for fault diagnosis. It is easy to implement in the embedded system, the performance can meet the application needs, and the recognition accuracy is ideal. In order to improve the diagnostic accuracy, it is recommended to focus on the frequency domain characteristics of the vibration signal, supplemented by the time domain characteristics of the vibration signal. If possible, it is recommended to add the current signal characteristics of the drive motor and the angle signal characteristics of the drive shaft as the auxiliary criterion (input vector), which can further improve the diagnostic accuracy.

The shortcomings of the current system: (1) The system currently does not have the function of multi-fault concurrent identification; (2) It is necessary to further study multi-vibration signal sensor fusion to eliminate transformer body vibration and external vibration interference; (3) Due to the inherent characteristics of different OLTC there are differences in the characteristics of the vibration signal itself, and it is necessary to in-depth study the subject of reuse of fault samples of the same type of equipment.

Acknowledgements This study was supported in part by the Industry–University Research Project of Xiamen under Project 3502Z20203036 and Project 3502Z20193032 and the Natural Science Foundation of Fujian Province under Project 2012J01223.

References

1. Yang, Q., Ruan, J., Zhuang, Z.: Fault diagnosis of circuit breakers based on time–frequency and chaotic vibration analysis. *IET Gener. Transm. Distrib.* **14**(7), 1214–1221 (2020)
2. Ali, M.Z., Shabbir, M.N.S.K., Liang, X., et al.: Machine learning-based fault diagnosis for single- and multi-faults in induction motors using measured stator currents and vibration signals. *IEEE Trans. Ind. Appl.* **55**(3), 2378–2391 (2019)
3. Nayana, B.R., Geethanjali, P.: Analysis of statistical time-domain features effectiveness in identification of bearing faults from vibration signal. *IEEE Sens. J.* **17**(99), 5618–5625 (2017)
4. Yang, R., Zhang, D., Li, Z., et al.: Mechanical fault diagnostics of power transformer on-load tap changers using dynamic time warping. *IEEE Trans. Instrum. Meas.* **68**(9), 3119–3127 (2019)
5. Zhou, X., Wang, F.H., Fu, J., et al.: Mechanical condition monitoring of on-load tap changers based on chaos theory and K-means clustering method. *Proc. CSEE* **35**(6), 1541–1548 (2015)
6. Kang, P.J., Birtwhistle, D.: Condition monitoring of power transformer on-load tap-changers. Part I: condition diagnostic. *Gener., Transm. Distrib. IEE Proc.* **148**(4), 301–306 (2001)
7. Xue, Z.Y., Zheng, X.C., Qiu, X., et al.: The online diagnosis method of marine induction motor bearing fault based on SVM. *Ship Ocean Eng.* **49**(5), 1–5 (2020)
8. Li, Z.X., Chen, Z.Y., Xue, H.T.: Online diagnosis method for mechanical fault of in-wheel motor based on DBNs. *J. Vibr., Measur. Diagonosis* **40**(4), 643–649 (2020)
9. Lei, Y.F.: Research on industrial internet plus condition monitoring and fault diagnosis system for hydraulic system of hydraulic servo motor. Ph.D thesis, Yanshan University, Qinhuangdao, China (2020)
10. Ge, N., Pantel, M., Nakajima, S.: Online diagnosis of accidental faults for real-time embedded systems using a hidden Markov model. *Simulation* **91**(10), 851–868 (2015)
11. Lu, J., Zhang, M., Zhao, H.F., et al.: Design of power transformer condition monitoring system based on the vibration signal. *Proc. CSU-EPSCA* **28**(4), 73–77 (2016)
12. Poza, F., et al.: Programmable electronic instrument for condition monitoring of in-service power transformers. *IEEE Trans. Instrum. Meas.* **55**(2), 625–634 (2006)
13. Ding, E.J., Yu, X., Liao, Y.B., et al.: Key technology of mine equipment state perception and online diagnosis under Internet of Things. *J. China Coal Soc.* **45**(6), 2308–2319 (2020)
14. Fang, R.M.: Support vector machine theory and its application analysis, 1st edn. China Electric Power Press, Beijing (2007)

Management Strategy Under the Intelligent Manufacturing Initiative of Chinese Coal Machine Equipment Enterprises



Peng He, Lixia Zeng, and Jie Dai

Abstract Equipment manufacturing industry is the basic industry of national economy, and its development level determines China's economic strength. Coal machine equipment manufacturing industry is a strategic industry providing technology and equipment for the modernization construction of coal industry and an important guarantee for the upgrading and technological progress of coal industry. In recent years, the intelligent manufacturing initiative for China's coal machine equipment enterprises has triggered a new round of reform reflection. Based on the analysis of the characteristics of China's coal machine equipment manufacturing industry, this paper points out that the key tasks of developing coal machine intelligent manufacturing include: standardization and modularization of products and data; Promote safe production management and build intelligent manufacturing production chain. This paper concludes that China's coal machinery equipment manufacturing industry needs policy support for technological innovation incubation to realize digitalization and intelligentization.

Keywords Manufacturing industry · Coal equipment · Intelligent manufacturing · China

1 Introduction

China is the world's largest coal producer, consumer and net importer [1]. Especially since 2000, with the strong recovery of China's coal industry, the scale of the coal machine manufacturing market most closely related to China has also

P. He
College of Cultural Industries and Tourism, Xiamen University of Technology, Xiamen, China

L. Zeng (✉)
College of Economics and Management, Xiamen University of Technology, Xiamen, China
e-mail: 2011110102@xmut.edu.cn

J. Dai
Institute for Advanced Studies, University of Malaya, Kuala Lumpur, Malaysia

expanded rapidly, attracting a large number of funds from outside the industry, and many new coal machine enterprises have been born. Although the development and utilization of renewable energy has become the consensus of all countries, at present the livelihood and industry development of the Chinese people is still mainly supported by coal resources [2–5]. Even coal is likely to make up the bulk of China's energy mix for centuries to come. By the end of 2050, coal is still expected to account for more than half of China's total energy demand. Therefore, at present, although the coal industry is temporarily in the stage of excess demand, the coal machinery equipment industry market still has great potential.

China has made rapid progress in coal mining equipment since the reform and opening up. China has established a complete modern coal equipment manufacturing system, making it the world's largest producer and user of coal equipment. Especially since the 18th National Congress of the COMMUNIST Party of China (CPC), the level of coal equipment manufacturing has improved significantly, and the gap between coal equipment manufacturing and foreign advanced equipment has been gradually narrowed, with some equipment reaching the international leading level. Some of the equipment has reached the international leading level, realizing leapfrog development from introduction, absorption and following to independent innovation. However, in the current trend of rapid development of industry 4.0 and intelligence, "intelligent manufacturing" of coal machine equipment has become a hot topic in recent years. Intelligent manufacturing, derived from the research of artificial intelligence, has been pushed to the forefront since China proposed the "Made in China 2025" strategy [6, 7]. As an innovative project integrating new generation of information technology and manufacturing equipment, intelligent manufacturing is not only a breakthrough point in the deep integration of IT application with industrialization. It is estimated that in the next 20 years, it will bring us \$3 trillion in GDP growth, 20% increase in enterprise efficiency, 20% reduction in cost, and 10% reduction in energy conservation and emission reduction. It can be said that intelligent manufacturing foreshadows the new industrial revolution, marking that China's manufacturing industry is officially marching toward high quality and high level.

In 2020, the intelligent manufacturing of coal machine equipment has been mentioned many times on various platforms in China [7]. On October 30, 2020, the 18th China International Coal Mining Technology Exchange and Equipment Exhibition was held in Beijing on November 2. The intelligent equipment of coal mine became the highlight of this exhibition. Among them, there are not only large-sized mining equipment suitable for annual production of 10 million tons, but also intelligent mining equipment suitable for thin coal seam mining. There are not only the demonstration of trans-boundary mining intelligent hydraulic support with large expansion ratio, right-angle turning conveyor, tunnel repair machine, saw cutting roadheader and heavy-duty flatbed vehicle, but also the application of shield tunneling machine, UAV and other new technologies in the coal mining industry. It has not only intelligent transportation, intelligent fans, robots, roof cutters, but also digital mining construction technology and equipment such as automatic control system, 5G centralized control and intelligent control terminal. Not only green

remanufacturing technology display, but also pure water support, explosion-proof lithium electric trolley, electric unmanned wide-body dump truck and other clean energy technology equipment.

At present, the mechanization degree of coal mining in China is close to 80%, and the mechanization degree of large-scale coal mining is as high as 95%. China's coal mining requires increasingly higher degree of mechanization. Even though China's current coal mining industry has been developed to some extent and its technical level has been improved, there is still a long way to go to realize intelligent manufacturing [8]. Through the study of this paper, we find that China's independent innovation ability needs to be improved, the level of intelligence is low, the dependence on import of key core technologies and equipment is high, the level of industrial structure is backward and other problems are more prominent. The "Made in China 2025" manufacturing strategy proposed by China and the 2016–2020 Smart Manufacturing Development Plan put forward the "three-step" strategy mean that China's manufacturing industry is undergoing supply-side structural reform, hoping to create new competitive advantages for China's manufacturing industry and achieve manufacturing power. The new thinking triggered by the intelligent manufacturing initiative provides new possibilities for solving the problems of China's coal machine equipment, such as the surplus of medium and low-end products, the shortage of high-end high-reliability products, and the lack of core competitiveness and innovation ability. This paper hopes to provide reference for reliability and intelligent innovation of coal machine equipment products in China and promote the transformation from traditional coal machine manufacturing to intelligent coal machine manufacturing.

2 Analytical Framework

2.1 PEST Model

PEST represents four major environmental factors: politics/law (P), economy (E), society/culture (S) and technology (T). PEST is a combination of the first letters of four English words. PEST analysis process is as follows: The first step is to analyze the current situation of the research object in terms of politics, economy, society and technology, etc., and to extract the part that has a great impact on it. The second step is to further analyze the four factors and discuss their influence on the development strategy of the research object. The third step is to evaluate the influence degree of each factor objectively and find out the key strategy on this basis.

2.2 SWOT

SWOT, on behalf of Strengths, Weaknesses, Opportunities and Threats, analyzes the internal and external environment of an enterprise from four different angles respectively, and thus summarizes the strategic measures taken by the enterprise to respond to the internal and external environment. SWOT analysis method is widely used in strategic or competitive analysis, is an important strategic management analysis tool. Opportunities and threats belong to external environmental factors, and any company is in a certain external environment, which inevitably will be deeply influenced by them. These influences may be good or bad, but they all exist objectively. Most of these influences are macroscopic, such as politics, economy, culture and so on. Advantages and disadvantages belong to internal environmental factors. In the process of continuous development, a company will also have its own favorable and unfavorable factors, which can be actively intervened. This part of the impact is mostly micro, such as the company's internal management, organizational structure, business model and so on. Taking the above factors into comprehensive consideration, poundage can obtain the following four strategic countermeasures: WT strategy (defensive strategy): that is, the strategy of directly overcoming internal weaknesses and avoiding external threats. WO strategy (torsional strategy): A strategy that exploits external opportunities to improve internal weaknesses. ST strategy (diversified business strategy): that is, make use of the advantages of enterprises; To avoid or mitigate external threats. SO strategy (growth strategy): the strategy that relies on internal advantages to seize external opportunities.

3 Analysis Results

3.1 Lack of Indigenous Innovation

Continue the train of thought provided by PEST. We find that in terms of technology (T), although China's coal mining equipment manufacturing industry has made great progress in recent years, even some mining equipment manufacturing level has been among the world's advanced. For example, hydraulic support, shearer, scraper conveyor and other products complete, machine performance and overall parameters have reached the international advanced level. However, from the point of view of the whole coal machine manufacturing industry in China, there are still many problems. These problems will have a great impact on the coal machine equipment manufacturing industry, and may even affect the sustainable development of the entire coal industry, one of the main performance points is the lack of innovation ability. This can be discussed from the three perspectives of P, E and S.

Economically, most coal machine manufacturing enterprises in China have small capital scale, low technology investment ratio and rely on scientific research institutes for technological innovation. Product development is mainly the introduction, tracking imitation. So the lack of innovation and independent intellectual property rights. In terms of manufacturing technology, compared with developed countries, there is still a certain gap, and the vast majority of key technologies are mainly imported. Only a few key technologies have their own intellectual property rights, and only focus on structural design for technological breakthroughs. Less money has been invested in integration technology research. However, the reasons for these are largely political (P). China's coal machine manufacturing enterprises are mainly small and medium-sized enterprises, which do not have strong financial strength and are unable to invest a large amount of funds in the development of machinery. At present, coal machine manufacturing process mainly relies on state support, which further limits the innovation ability of private enterprises. In addition, As the largest carbon emitter, China also has a large number of energy conservation and emission reduction tasks. In recent years, China has invested heavily in new energy resources, and most local governments are ambivalent about coal mining. This has allowed less money to flow into technological innovation in coal mines. Even in recent years, China's coal machine enterprises have developed rapidly, and some of the technical products have reached the international leading level. However, due to the incomplete technology and lack of innovative capital investment in the industrial chain, the key technologies of mine mining are still controlled by foreign enterprises, and the key coal machine products still need to be imported from foreign countries. In particular, there is a big gap between the core components in terms of service life and reliability. Finally, on the cultural level (Society, S), we believe that a considerable part of coal machine equipment enterprises can only produce low-technology products, and have no ability to innovate and develop new products. They did not grasp the core technology in the process of imitation and unable to form a benign production process. In China's development over the past few decades, the inertia of low-quality production has been strong, creating a cultural atmosphere that is difficult to improve in the short term.

3.2 Low Intelligence Level

To solve the problem of low level of intelligence is the key to develop coal mine machinery and equipment. Computer technology has penetrated into all aspects of people's production and life, and coal mine machinery and equipment also have a certain fusion with computer technology, but the current level of intelligence of coal mine machinery and equipment in China is still relatively low. In the use of coal mine machinery and equipment, operators are still required to carry out manual control, which not only needs to improve the professional technical level and ability of operators, work safety is not easy to be guaranteed [9–11]. Through thinking

with PEST model, we think that the current problems restricting the intelligent construction of coal mine are concentrated in a series of technical aspects, such as high-efficiency communication, intelligent equipment and intelligent decision-making. Due to insufficient data, staff members are often in a state of lack of information, also known as “information island”. Restricted by the traditional management of coal mine, the construction of each information system lacks unified planning, the data between departments and majors are independent, and the lack of unified data interface and standard makes the data unable to realize effective association and interaction. Not only that, generally speaking, the information amount of data is small, low precision and single type, so it is difficult to support the application requirements of big data mining, early warning analysis, high-precision 3D model, artificial intelligence computing and other technologies. Taking stope face as an example, it is restricted by wired network layout and mobile communication. It can only transmit very little information such as mine pressure, gas, dust and fully-mechanized mining equipment. Besides, each monitoring system is independent, with fewer points and longer transmission time interval. There is still a certain distance from the expected intelligent management. All these reflect the inadequacy of information digitization. In addition to the lack of digital processing, the reliability of information acquisition equipment and sensing precision problems are also relatively obvious. Large mining equipment operation machinery, lack of flexibility, low level of intelligence. The collection data of a large number of sensors arranged for safe operation are relatively single, with low accuracy, poor anti-interference ability and single use. Moreover, the sensors only have the function of data collection without the ability of data analysis. All of these problems pose major security risks, especially in the area of disaster occurrence or early warning. At present, subject to the above factors, disaster monitoring lacks an effective early warning mechanism, most judgments are only based on rules and institutional constraints, and disaster warning is passive and post-response. Moreover, most emergency plans are relatively simple and broad, lacking specific operation and technical content, and the on-site adaptability is not strong. The above three points also create obstacles to the formulation of enterprise management decisions. Without the help of intelligent means, enterprise analysis mostly relies on experience judgement and simple statistical analysis. Therefore, there is a great uncertainty in decision-making, make it difficult to provide effective decision support for mining operation and management.

4 Discussion

4.1 Innovation Suggestions

The government and relevant departments need to increase investment and policy guidance in the development of coal mining machinery, which will help ensure that

coal mining machinery in the future market can meet the needs of relevant industries, and resist the competition pressure of imported products. In addition, it is necessary to reform the education industry. Colleges and universities should develop specialized courses related to coal mine machinery and equipment, increase the investment of education fund, and strengthen the reserve of coal machinery talents. Scientific research talents can provide a steady stream of power for the innovative research, development and manufacturing of national coal mine machinery and equipment. In recent years, relevant units have sent professional researchers to developed countries for in-depth study to improve their professional knowledge and skills [12–14]. However, the application of advanced technology in the research and development of coal mine machinery and equipment in China is relatively low. In addition, China's coal mining machinery and equipment are usually developed by universities or specialized machinery research institutions [15, 16]. Therefore, the government and relevant departments should further establish the coal mine machinery innovation department, which is dedicated to the innovation and research and development of coal-related machinery and equipment, and conduct in-depth exploration of key technologies, so as to promote the research and development of coal mine machinery and equipment, and make the equipment play a better role. At the same time, the department needs researchers as well as coal mining professionals. This is because professional coal mining personnel will have a detailed understanding of coal mining work, such as mining technology and process, etc., not only that, but also know the actual mining work related to the needs of coal mining machinery and equipment. It can be said that the cooperation between scientific researchers and coal mining professionals provides a solid guarantee for the innovation and research and development of coal mining machinery and equipment to better meet the needs of China's coal mining work.

4.2 Intelligentization Suggestions

We believe that intelligent production process should be realized by constructing networked distributed production facilities of intelligent production system, and then intelligent factories should be built based on CPS and industrial Internet, including physical layer, information layer, big data layer, industrial cloud layer and decision layer. The physical layer contains the hardware equipment of each layer in the factory, from the minimum production unit to the assembly unit, from logistics to storage and management, and realizes the interconnection of the whole factory, so as to build a “measurable and controllable, production-manageable” vertical integration environment. Through intelligent manufacturing, on the one hand, it guarantees the safety of coal mine construction personnel; on the other hand, it also provides the possibility for the realization of green manufacturing through intelligent means. Implementing the low-carbon economic concept of energy conservation and consumption reduction in the whole process of intelligent manufacturing of coal machine can control the consumption of environment and resources in the

manufacturing process of coal machine and contribute to energy conservation and emission reduction. Because green manufacturing need fully consider the use cycle of coal machine products, from the design of coal machine to production, transportation, scrap, and also have to consider raw materials and energy consumption. With the combination of advanced intelligent manufacturing technology and green concept, we can control the use of raw materials in the production process of coal machine products intelligently, and also have the opportunity to provide intelligent assistance for the recycling, regeneration and reuse of materials.

5 Conclusion

Equipment manufacturing industry is the basic industry of national economy [17], and its development level determines China's economic strength. The intelligent manufacturing initiative for China's coal machine equipment enterprises has triggered a new round of re-form reflection. Based on the analysis of the characteristics of China's coal machine equipment manufacturing industry, this paper points out that the key tasks of developing coal machine intelligent manufacturing include: standardization and modularization of products and data; Promote safe production management and build intelligent manufacturing production chain. This paper concludes that China's coal machinery equipment manufacturing industry needs policy support for technological innovation incubation to realize digitalization and intelligentization.

References

1. Lin, B.Q., Liu, J.H.: Estimating coal production peak and trends of coal imports in China. *Energy Policy* **38**(1), 512–519 (2010)
2. Pan, X., Zhang, W., Chou, L.: The theory on the environmental emission trading under the concept of two-tired earning. *Ekoloji* **28**(107), 1659–1663 (2019)
3. Xu, R., Chou, L.C., Zhang, W.H.: The effect of CO₂ emissions and economic performance on hydrogen-based renewable production in 35 European Countries. *Int. J. Hydrogen Energy* **44** (56), 29418–29425 (2019)
4. Wang, J., Yu, B., Kang, H., Wang, G., Mao, D., Liang, Y., Jiang, P.: Key technologies and equipment for a fully mechanized top-coal caving operation with a large mining height at ultra-thick coal seams. *Int. J. Coal Sci. Technol.* **2**(2), 97–161 (2015)
5. Dong, L., Mingyue, R., Guoying, M.: Application of internet of things technology on predictive maintenance system of coal equipment. *Proc. Eng.* **174**, 885–889 (2017)
6. Li, L.: China's manufacturing locus in 2025: with a comparison of "Made-in-China 2025" and "Industry 4.0". *Technol. Forecasting Social Change* **135**, 66–74 (2018)
7. He, G., Dang, Y., Zhou, L., Dai, Y., Que, Y., Ji, X.: Architecture model proposal of innovative intelligent manufacturing in the chemical industry based on multi-scale integration and key technologies. *Comput. Chem. Eng.* **141**, 106967 (2020)
8. Zhu, T., Bian, W., Zhang, S., Di, P., Nie, B.: An improved approach to estimate methane emissions from coal mining in China. *Environ. Sci. Technol.* **51**(21), 12072–12080 (2017)

9. Wang, G., Xu, Y., Ren, H.: Intelligent and ecological coal mining as well as clean utilization technology in China: Review and prospects. *Int. J. Mining Sci. Technol.* **29**(2), 161–169 (2019)
10. Wang, J., Huang, Z.: The recent technological development of intelligent mining in China. *Engineering* **3**(4), 439–444 (2017)
11. Lin, H.C., Chou, L.C., Zhang, W.H.: Cross-Strait climate change and agricultural product loss. *Environ. Sci. Pollut. Res.* 1–14 (2019)
12. Chou, L.C., Zhang, W.H.: The effect of democracy on energy efficiency in European countries. *Econ. Res.-Ekonomiska Istraživanja* **33**(1), 3476–3491 (2020)
13. Chou, L.C., Zhang, W.H., Wang, M.Y., Yang, F.M.: The influence of democracy on emissions and energy efficiency in America: new evidence from quantile regression analysis. *Energy Environ.* **31**(8), 1318–1334 (2020)
14. Li, Z., Li, A., Dai, X.Z., Dai, J.: Impact of public participation on coastal pollution emissions under the growth of personal income. *J. Coastal Res.* **109**(SI), 39–44 (2020)
15. Li, C.M., Nie, R.: An evaluating system for scientific mining of China's coal resources. *Resour. Policy* **53**, 317–327 (2017)
16. Peng, B., Guo, D., Qiao, H., Yang, Q., Zhang, B., Hayat, T., Ahmad, B.: Bibliometric and visualized analysis of China's coal research 2000–2015. *J. Clean. Prod.* **197**, 1177–1189 (2018)
17. Dong, Y., Yang, J., Hu, P., Chou, L.: A study on the relationship between economic production performance and pollution in Chinese Coastal Cities: an analysis of the undesired output. *J. Coastal Res.* **96**(SI), 21–25 (2019)

Study on the Thermodynamic Calculation Model and Solution Method Along the Steady Operation of Long Transport Pipeline



Yin De, Yi Zhao, Rongqiang Zhong, Lirong Yao, and Ying Xu

Abstract The thermal variation of long-distance heat transfer oil pipeline directly determines the gathering and transportation heat consumption. Accurate calculation of temperature variation along the route is the key to energy conservation and consumption reduction. In this paper, a mathematical model of thermal calculation for steady-state operation is established for different buried modes of long-distance transport pipelines, and the calculation method of soil temperature field and total heat transfer coefficient is given. The numerical solution is carried out by using the finite difference method. The test loop of gathering and transport operation was set up, and the steady-state operation test was carried out to verify the correctness of the model and the solution method.

Keywords Long distance pipeline · Steady state operation · Numerical simulation · Thermodynamic calculation

1 Preface

Since most of the crude oil produced in China is high grade crude oil, heating is often used to reduce the viscosity and improve the fluidity of crude oil in the transportation process. Therefore, the proportion of heat consumption in the oilfield production process is increasing constantly. For the oil pipeline transported by heating, the temperature along the pipeline keeps decreasing during the process of crude oil transportation, so as to accurately obtain the temperature change rule along the pipeline and control the temperature rise range, which is the key technology of oil field production and energy saving gathering and transportation.

Y. De · Y. Zhao · R. Zhong · L. Yao (✉)
SINOPEC Northwest Oilfield Company, Urumqi 830011, Xinjiang, China
e-mail: yaolr.xbsj@sinopec.com

Y. Xu
Northeast Petroleum University, Daqing 163318, China

According to the laying method, oil pipelines can be roughly divided into three categories: overhead pipelines, underwater pipelines and buried pipelines [1, 2]. Since the temperature of atmosphere and water is little affected by the heat dissipation of pipelines, the external heat transfer of the first two types of pipelines (namely the heat transfer of pipelines in environmental media) is relatively simple compared with buried pipelines. For buried hot oil pipelines, the external heat transfer is the transfer process of heat in semi-infinite soil medium [3–5]. The external heat transfer of buried pipelines is complicated because the soil thermal and physical property parameters vary with the types, porosity, humidity and temperature of soil, the change of atmospheric temperature will cause the change and delay of soil temperature field, and there are also radiation and convection heat exchange between the surface and the atmosphere.

In the early studies on heat transfer of buried geothermal oil pipelines [6], more analytical methods were used to solve the problem. Because the analytical solution needs to simplify the problem, there is a significant deviation between the solution result and the reality. To numerically solve the heat transfer in soil, the semi-infinite soil medium needs to be transformed into a finite solution domain.

In the past, the average temperature method was used in the process calculation of hot oil pipeline, ignoring the influence of the change of physical property with oil temperature and friction heat, so the result error was relatively large. In literature [7, 8], the influence of these two factors on process calculation was fully considered, and the thermodynamic and hydraulic calculation equation was established. Simpson quadrature method was adopted to solve the equation, and the results could meet the general engineering requirements.

In this paper, a mathematical model of thermal calculation along the steady operation of long-haul pipeline and different pipeline laying modes will be established, and the model solving method will be studied. At the same time, the experimental platform was built to complete the temperature test along the running line, which was used to verify the correctness of the model and the solution method.

2 Mathematical Model for Axial Thermal Calculation in Steady State Operation of Pipeline

When the hot oil pipeline is running, it is assumed that the oil is Newtonian fluid and the influence of radial temperature drop on the physical properties of the oil is ignored. The average flow rate and average oil temperature were used, and the frictional heat generation was considered. The oil in the pipe is simplified to a one-dimensional stable flow process. A micro element pipe section is taken to establish a thermal balance equation that is included in the heat of friction based on the thermal balance relationship of the hot oil pipe:

$$K(T)\pi D(T - T_0)dl = -q_m c(T)dT + q_m g i(T)dl \quad (1)$$

Boundary conditions:

$$T|_{l=0} = T_R$$

where: T —Oil flow temperature in the tube, °C; l —Axial distance of pipeline, m; V —Average flow rate of oil products, m/s; $K(T)$ —Heat transfer coefficient, W/(m² °C); T_0 —The medium temperature around the pipeline under natural conditions, °C; $c(T)$ —Specific heat of oil, J/(kg °C); D —Pipe outside diameter, m; g —Acceleration due to gravity, m/s²; $i(T)$ —Hydraulic slope of oil flow, m/m; q_m —Oil mass flow rate, kg/s; T_R —Oil outlet temperature, °C.

In the Eq. (1), the left side of medium size is the heat dissipated from oil to the outside through the pipe wall, the first item on the right side is the change of the internal energy of the pipe, and the second item is the heat generated by friction.

Under different laying methods, T_0 in Eq. (1) has three different access methods.

For buried pipelines, T_0 is the natural temperature of soil buried deep in the pipeline, which can be obtained from Eq. (2). When the pipe is overhead, T_0 is atmospheric temperature; When the pipe crosses the river, T_0 is the water temperature of the river.

3 Calculation Method of Relevant Parameters

3.1 Natural Temperature of Soil Buried Deep in Pipe

The natural temperature of the soil deep in the pipeline is affected by the annual cycle of the earth temperature, so it also changes in the annual cycle, and causes time delay, which leads to the periodic change and delay of the oil temperature of the pipeline. According to reference [9], The specific calculation method of natural temperature field of soil annual cycle change is as follows:

$$T(\tau, y) = T_A + \left(TA_{Amax}()^{-\sqrt{\frac{\pi}{\alpha\tau_0}y}} \cos\left(\frac{2\pi\tau}{\tau_0} - y\sqrt{\frac{\pi}{\alpha\tau_0}} - \psi\right) \right) \quad (2)$$

$$\varphi = \left[1 + 2\frac{\lambda_t}{\alpha} \sqrt{\frac{\pi}{\alpha\tau_0}} + 2\left(\frac{\lambda_t}{\alpha} \sqrt{\frac{\pi}{\alpha\tau_0}}\right)^2 \right]^{-0.5} \quad (3)$$

$$\psi = tg^{-1}\left(\frac{1}{1 + \frac{\alpha}{\lambda_t} \sqrt{\frac{\alpha\tau_0}{\pi}}}\right) \quad (4)$$

where: T_A —Atmospheric annual average temperature, °C; T_{Amax} —Atmospheric annual maximum temperature, °C; τ —The time from the maximum temperature, s; τ_0 —Annual fluctuation period of atmospheric temperature, $\tau_0 = 3.156 \times 10^{17}$ s; λt —Soil thermal conductivity around the pipe, W/(m °C); y —Buried depth of pipeline, m; a —Soil temperature conductivity coefficient, m^2/s ; α —The convective heat transfer coefficient between surface and atmosphere, W/(m^2 °C).

3.2 Calculation of the Total Heat Transfer Coefficient

The formula for calculating the total heat transfer coefficient between the oil flow inside the tube and the external environment is shown in (5):

$$\frac{1}{KD_e} = \frac{1}{\alpha_1 d} + \sum \frac{\ln\left(\frac{D_{i+1}}{d_i}\right)}{2\lambda_i} + \frac{\ln\left(\frac{d}{d_L}\right)}{2\lambda_L} + \frac{1}{\alpha_2 D_w} \quad (5)$$

where: D_e —Calculate the diameter, m, take the average inside and outside diameter of the insulation layer for the insulation pipeline, and take the outside diameter of the asphalt layer for the buried pipeline without insulation; D_w —The outermost diameter of the pipeline, m; α_1 —Heat transfer coefficient of oil flow and inner wall surface of pipe, W/(m^2 °C); α_2 —The heat release coefficient between the outer wall of the tube and the surrounding medium, W/(m^2 °C); λ_i —The corresponding thermal conductivity of layer i , W/(m °C); $d_i D_i$ —The inner and outer diameter of layer i of the pipeline, m; d —Pipe diameter, m; d_L —Tube diameter after waxing, m.

To calculate the total heat transfer coefficient K , the internal heat transfer coefficient α_1 , the thermal conductivity resistance from the pipe wall to the outermost diameter of the pipe, and the heat release coefficient α_2 from the pipe wall or the maximum periphery to the surrounding environment should be calculated respectively.

(1) Internal heat transfer coefficient α_1

If the flow state of crude oil is known, according to reference [10], the heat transfer coefficient can be calculated by the correlation formula.

In laminar flow state ($Re < 2000$)

When the $Gr \cdot Pr < 500$,

$$Nu_y = \frac{\alpha_1 d}{\lambda} = 3.65 \quad (6)$$

When the $Gr \cdot Pr > 500$,

$$Nu_y = \frac{\alpha_1 d}{\lambda} = 0.15 Re_y^{0.33} \cdot Pr_y^{0.43} \cdot Gr_y^{0.1} \left(\frac{Pr_y}{Pr_g} \right)^{0.25} \tag{7}$$

In the intense turbulent state ($Re > 104$), $P < 2500$,

$$\alpha_1 = 0.021 \frac{\lambda}{d} Re_y^{0.8} \cdot Pr_y^{0.44} \cdot \left(\frac{Pr_y}{Pr_g} \right)^{0.25} \tag{8}$$

In ($2000 < Re < 104$), the oil flow exothermal intensity has increased, there is no formula for calculation of reliable estimate can be reference to the next type:

$$Nu_y = K_0 \cdot Pr_y^{0.43} \cdot Gr_y^{0.1} \left(\frac{Pr_y}{Pr_g} \right)^{0.25} \tag{9}$$

where, the coefficient K_0 is a function of Re , which is determined by Table 1.

In the above categories, $Re = \frac{v \cdot d}{\nu}$ is the Reynolds number; $Nu = \frac{\alpha_1 d}{\lambda}$ is the Nussle number; $Pr = \frac{v \rho c}{\lambda}$ is Prandtl number; $Gr = \frac{d^3 g \beta (t - t_g)}{\nu^2}$ is grashchev criterion. In Eqs. (6) to (9), “y” in the middle corner indicates that the qualitative temperature of each parameter is the average oil temperature, while “g” indicates that the qualitative temperature of the physical parameter is the pipe wall temperature.

Where: v —Flow velocity of oil, m/s; λ —Thermal conductivity of oil, W/(m K); ν —Kinematic viscosity of oil, m^2/s ; ρ —Oil density, kg/m^3 ; β —The volume expansion coefficient of oil, $1/K$; t, t_g —the temperature of oil flow and the inner wall of the pipe, $^{\circ}C$; g —The acceleration due to gravity, m/s^2 .

(2) Thermal resistance of each pipe wall

This part of the thermal resistance includes the thermal resistance of the steel pipe, the anticorrosive layer and the insulation layer. The thermal conductivity of the steel pipe λ_g was about $45 \text{ W/(m } ^{\circ}C)$, and its thermal resistance was negligible. The thermal conductivity of coal tar enamel anti-corrosion layer was about $1.1 \text{ W/(m } ^{\circ}C)$, and the thermal conductivity of yellow jacket insulation material λ_f was about $0.04 \text{ W/(m } ^{\circ}C)$.

For uninsulated hot oil pipelines with δ_g thick and δ_f thick coal tar enamel anticorrosion coating, the thermal resistance calculation formula is as follows:

$$\sum \frac{\delta_i}{\lambda_i} \approx \frac{\delta_g}{\lambda_g} + \frac{\delta_f}{\lambda_f} \tag{10}$$

Table 1 Relationship between coefficient K_0 and Re

$Re \times 10^{-3}$	2.2	2.3	2.5	3.0	3.5	4.0	5.0	6.0	7.0	8.0	9.0	10
K_0	1.9	3.2	4.0	6.8	9.5	11	16	19	24	27	30	33

Generally, the influence of steel tube and anticorrosive layer on the total heat transfer coefficient is very small.

For the insulated pipe, the thermal resistance of the insulation layer determines the influence. Therefore, the thermal resistance calculation formula of heat preservation oil pipeline with wall thickness δ_g and outsourcing heat preservation material δ_b is as follows:

$$\sum \frac{\ln\left(\frac{D_i}{d_i}\right)}{2\lambda_i} \approx \frac{\ln\left(\frac{D_b}{d_b}\right)}{2\lambda_b} \tag{11}$$

(3) The heat release coefficient K from the outer wall of the pipeline or the maximum periphery to the surrounding environment α_2

① α_2 of underground pipeline

α_2 of underground pipeline can be obtained from Eq. (12):

$$\alpha_2 = \frac{2\lambda_t}{D_w \cdot \ln \left[\frac{2h_0}{D_w} + \sqrt{\left(\frac{2h_0}{D_w}\right)^2 - 1} \right]} \tag{12}$$

If $\frac{h_0}{D_w} > 3 \sim 4$, then it can be simplified as

$$\alpha_2 = \frac{2\lambda_t}{D_w \cdot \ln \frac{4h_0}{D_w}} \tag{13}$$

where: λ_t —Soil thermal conductivity, W/(m K); h_0 —Buried depth of pipeline center, m; D_w —Maximum peripheral diameter of pipeline, m.

② α_2 of the overhead pipeline

α_2 of the overhead pipeline can be obtained from Eq. (14):

$$\alpha_2 = \alpha_2^0 + 7\sqrt{w_B} \tag{14}$$

where: α_2^0 —The external heat release coefficient of the hot oil pipeline to the atmosphere when there is no wind, W/(m² K); For hot tubing: α_2^0 can be approximated as: $\alpha_2^0 = 11.6$ W/(m² K); w_B —wind velocity, m/s.

③ α_2 of river pipeline can be obtained from Eq. (15)

$$\alpha_2 = 0.25 \left(\frac{\lambda_0}{D_n} \right) \text{Re}_0^{0.6} \text{Pr}_0^{0.38} \left[\frac{\text{Pr}}{\text{Pr}_w} \right]^{0.25} \tag{15}$$

where: Re_0 —The Reynolds number of water, $Re_0 = \frac{vD_0}{\nu_0}$; v —The velocity of water, m/s; ν_0 —Kinematic viscosity of water, m^2/s ; Pr_0 —The Prandtl number of waters with water temperature as the qualitative temperature, and the water temperature is taken as the water temperature far away from the pipe wall; Pr_w —The Prandtl number of waters with the average temperature of the tube wall as the qualitative temperature.

4 Solution Method of Axial Temperature

The finite difference method is used to solve the axial oil temperature. Take a pipe segment of a unit length as the control volume, and its energy balance relationship is shown in Fig. 1.

Q_1 —Net energy flowing into and out of the control body; Q_2 —Heat is dissipated from the micro-element segment to the surrounding environment; Q_3 —Heat generated by friction.

Ignoring the heat conduction of axial oil flow, the energy balance equation of oil flow is:

$$\frac{\partial T_y}{\partial t} = v \frac{\partial T_y}{\partial z} - \frac{4\alpha_y(T_y - T_w)}{\rho_y c_y d} + \frac{f}{2C_y} |V|^3 \tag{16}$$

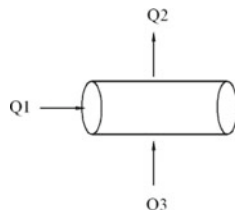
It is expanded as an implicit difference scheme

$$\begin{aligned} \frac{T_{yi}^{n+1} - T_{yi}^n}{d\tau} &= V_i^{n+1} \frac{T_{yi-1}^{n+1} - T_{yi+1}^{n+1}}{2h} \\ &- \frac{4\alpha_{li}^{n+1}}{\rho_{yi}^{n+1} c_{yi}^{n+1} d} (T_{yi}^{n+1} - T_{bi}^{n+1}) + \frac{f_i^{n+1}}{2c_{yi}^{n+1} d} |V_{yi}^{n+1}|^3 \end{aligned} \tag{17}$$

After finishing to

$$T_{yi}^{n+1} = \frac{\frac{T_{yi}^n}{d\tau} + V_i^{n+1} \frac{T_{yi-1}^{n+1} - T_{yi+1}^{n+1}}{2h} - \frac{4\alpha_{li}^{n+1} T_{bi}^{n+1}}{\rho_{yi}^{n+1} c_{yi}^{n+1} d} + \frac{f_i^{n+1}}{2c_{yi}^{n+1} d} |V_{yi}^{n+1}|}{\frac{1}{d\tau} + \frac{4\alpha_{li}^{n+1}}{\rho_{yi}^{n+1} c_{yi}^{n+1} d}} \tag{18}$$

Fig. 1 Energy balance diagram of oil flow



The implicit difference scheme has the advantages of unconditional convergence and good stability of solutions. However, due to the need for iteration, and each iteration of each section requires solving the radial temperature field to determine the inner wall temperature of the tube, so the calculation amount is large.

The radial temperature field is solved as follows:

$$n = \sum_{j=1}^M \sum_{i=1}^N k_{ij} \tag{19}$$

where: k_{ij} —Step i time, the number of solutions required to reach the convergence conditions in step 1 space.

5 Experimental Verification and Analysis

The running test was carried out on the 304 m circular gathering and transportation laboratory bench. The pipeline flow diagram was shown in Fig. 2. The pipe specification was DN100 stainless steel pipe, the length was 304 m, and the outside was 40 mm thick polyethylene foam insulation. The selected test pipeline had four temperature transmitters on the pipeline, which were located at the inlet and outlet of the pipeline and at the distance of 93 and 211 m respectively.

The medium used was crude oil from the second oil recovery plant of Daqing Oilfield. After the produced oil-gas-water mixture was separated by the oil-gas-water separator, the separated oil products were heated to the temperature required by the test through the flow meter and enter the test pipeline for testing.

Part of the natural gas separated from the oil-gas-water separator was used for heating oil in the heating furnace, and the other part was used for boiler heating; The water separated from the oil-gas and water separator went directly into the sewage pipe for retreatment.

It can be seen from the Fig. 3 that the terminal temperature of the pipeline was 48.71 °C, and the absolute error was 0.11 °C, and the relative error was 0.23%,

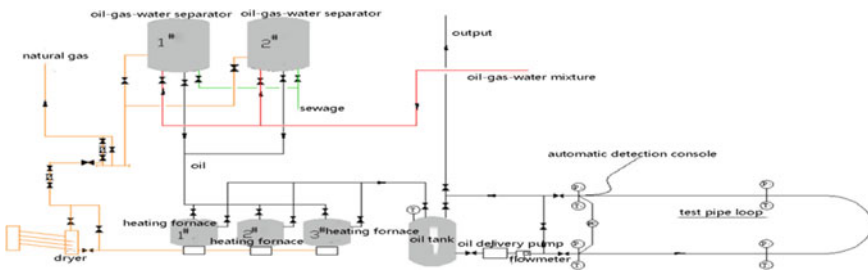


Fig. 2 Schematic diagram of experimental pipeline flow

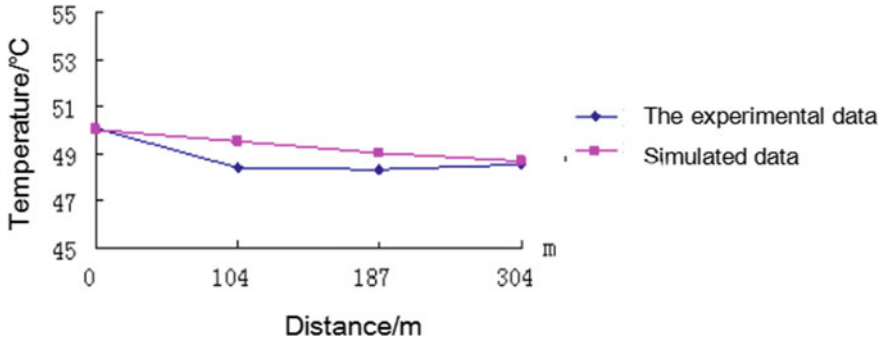


Fig. 3 Comparison of experimental and simulation results

compared with the measured terminal temperature value of the pipeline was 48.60 °C. This was because in the process of solving the model, the changes of oil properties and total heat transfer coefficient with temperature are considered. The maximum absolute error was 104 m, the absolute error value was 1.4 °C, and the relative error was 2.81%. It can be seen that the model established in this paper and its solution method have good accuracy, which can be used to analyze the temperature variation law along the pipeline.

6 Conclusions

The mathematical model of thermal calculation along the steady operation of the pipeline was established, and the calculation method of relevant parameters was given. The finite difference method was used to solve the problem discretely. The simulation results were compared with the experimental results to verify the correctness of the model and its solution method.

References

1. Xu, Y., Cheng, Q.L., Liu, X.Y., et al.: Effects of crude oil's variable physical properties on temperature distribution in a shutdown pipeline. *Adv. Mech. Eng.* **9**(4), 1–9 (2017)
2. Yang, X.Z.: Experiment study on heat transfer of submarine oil pipeline[D], pp. 35–44. Daqing Petroleum institute, Daqing (2007)
3. Xu, Y., Nie, X., Dai, Z.H., et al.: Heat transfer analysis of waxy crude oil under a new wide phase change partition model. *Numer. Heat Trans., Part A: Appl.* **10** (2019)
4. Zhu, X.J.: Study on Temperature Drop of Waxy Crude in Pipe. Dong Ying, China University of Petroleum, pp. 22–25 (2009)
5. Li, C.J., Ji, G.F., Wang, Y.C.: Fhermal calculation of heated crude oil pipeline at shutdown. *J. Southwest Pet. Inst.* **22**(2), 84–88 (2000)

6. Dai, Zhonghua: Analysis on influencing factors of buried hot oil pipeline. *Case Stud. Therm. Eng.* **16**, 1–6 (2019)
7. Wang, Y.: Numerical calculation of hot oil pipeline technology. *J. Fushun Pet. Inst.* **16**(4), 71–75 (1996)
8. Hong, Q.J., Li, W.F., Min, J.L., et al.: A pore-scale visualized study of melting heat transfer of a paraffin wax saturated in a copper foam: effects of the pore size. *Int. J. Heat Mass Transf.* **112**, 39–44 (2017)
9. Xing, X.K., Zhang, G.Z.: Study on shutdown and restart process of buried geothermal oil pipeline. *Pet. Planning Eng.* **12**(3), 21–23 (2001)
10. Yang, X.H., Zhang, G.Z.: *Pipeline Design and Management*. Petroleum University Press, Shan Dong (1996)

Effect of Hot Isostatic Pressing on Microstructure of 24CrNiMo Steel Produced by Selective Laser Melting



Jing Liang, Ziyang Lin, Xiuyuan Yin, Suiyuan Chen,
Changsheng Liu, Yang Guo, Shixing Yan, and Shiyun Dong

Abstract 24CrNiMo alloy steel samples were fabricated by Selective Laser Melting (SLM), performed Hot Isostatic Pressing (HIP) at the temperature of $\alpha + \gamma$ coexistence region. The macrostructure of SLM-24CrNiMo steel was composed of two zones. Heat Affected Zone (HAZ) was composed of lath bainite, granular bainite, and tempered martensite, while As Fabricated (AS) composed of lath martensite, acicular bainite, lath bainite, and a small amount of retained austenite. The microstructure of HIPped SLM-24CrNiMo steel was granular pearlite with discontinuous carbide size about 100–300 nm, massive bainite, polygonal ferrite with less than 100 nm carbides, and a small amount of retained austenite. Nano-sized carbides as reinforcement phase promoted the uniformity of microstructure and ensured the stability of microstructure. The average density of the HIPped sample was 99.50%, which increased 0.4–0.9% than that of the SLM-24CrNiMo sample. In this paper, uniform and dense microstructure were obtained, which provided reference for the application of high-speed train brake disc.

Keywords Selective laser melting · Hot isostatic pressing · 24CrNiMo alloy steel

1 Introduction

Brake disc is an important part to ensure the safe operation of high-speed train, and becomes the last safety guarantee [1]. When the train is running at high speed, the instantaneous temperature produced by braking is between 350 and 500 °C, but the

J. Liang (✉) · Z. Lin · X. Yin · S. Chen · C. Liu · Y. Guo

Key Laboratory for Anisotropy and Texture of Materials, Ministry of Education, Key Laboratory for Additive Manufacturing and Remanufacturing Materials, School of Materials Science and Engineering, Northeastern University, Shenyang 110819, Liaoning, China
e-mail: liangj@atm.neu.edu.cn

S. Yan · S. Dong

Academy of Army Armored Forces, Beijing, China

© The Author(s), under exclusive license to Springer Nature Switzerland AG 2021

467

L. Zheng et al. (eds.), *Proceedings of MEACM 2020*,

Mechanisms and Machine Science 99,

https://doi.org/10.1007/978-3-030-67958-3_47

cast brake pads generally lose braking performance when the temperature exceeds 400 °C. The higher the vehicle speed is, the faster the temperature rises during braking, and the more unstable the microstructure is, which will greatly affect the properties. Therefore, in order to obtain the brake disc with a stable structure, it is necessary to improve the material [2].

Selective Laser Melting (SLM) is a kind of Laser Additive Manufacturing (LAM) technology, which has the advantages of one-step near-final forming, short preparation cycle, low production cost and easy to improve material performance [3]. Tucho et al. [4] studied and proved that increasing the laser energy density controlled the porosity of SLM-316L stainless steels and increased the density. Hu et al. [5] also used SLM to prepare 17-4PH stainless steel, as the laser scanning speed increased, the density of the sample first increased and then decreased. Different laser processes caused changes in the size and shape of the pores. In the process of preparing steels by SLM, the defects such as tiny pores and cracks existed between the cladding layers. Therefore, in order to obtain a densely structured alloy steel, the process needs to be improved [6].

Hot Isostatic Pressing (HIP) is to densify the sample under the action of high temperature and high pressure [7]. Cai et al. [8] prepared Ti6Al4V by LAM and HIP, which showed fewer pores, higher strength and better elongation. Han et al. [9] used LAM to prepare the nickel-based superalloy Hastelloy X, then followed HIP. The pores of the sample were reduced after HIP, but the yield strength and tensile strength of the sample are about 130 and 60 MPa lower than that of the deposited sample, respectively.

24CrNiMo steel is one of the High Strength Low Alloy (HSLA) steels. With high ultimate tensile strength, good fracture toughness and thermal stability, it was widely used in the manufacture of brake discs [10]. In this paper, 24CrNiMo alloy steel for high-speed train brake discs was prepared by SLM followed HIP. Comparing the microstructure changes of SLM-24CrNiMo and HIPped samples, this paper provided a theoretical basis for obtaining alloy steel with stable and uniform microstructure.

2 Material and Experimental Procedure

The average particle size of 24CrNiMo alloy steel powder was 46.3 μm , the shapes were spherical or ellipsoid. The microstructure of the powder was shown in Fig. 1 and the chemical composition was shown in Table 1.

Using EOS M290 Metal 3D printer for SLM, powder layer with thickness of 20–100 μm was deposited on Q235 substrate. The 24CrNiMo sample was prepared by SLM with laser power 320 W, scanning speed 950 mm/s, scanning distance 110 μm and spot diameter 75 μm , which protected by argon (oxygen content 0.05%). Take the middle part of the sample and performed HIP under the temperature of $\alpha + \gamma$ coexistence region, the pressure of 100–200 MPa for 1–4 h.

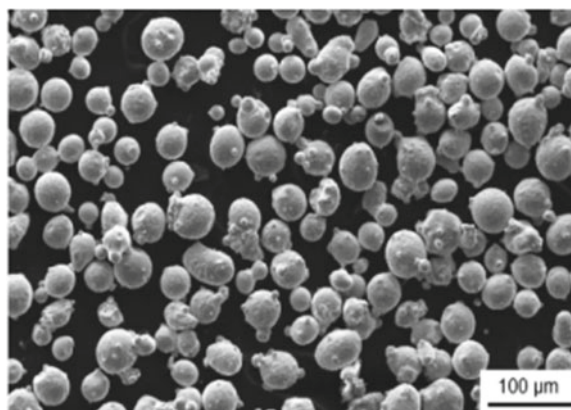


Fig. 1 The SEM micrograph of 24CrNiMo alloy steel powders

Table 1 The chemical compositions of 24CrNiMo alloy steel powders (mass fraction) %

C	Cr	Ni	Mo	Si	Mn	V	S	O	Fe
0.26	0.84	0.89	0.56	0.17	0.76	0.05	0.008	0.046	Bal.

The density test used the “immersion” method. The phase of the samples was analyzed by X-ray diffraction analysis instrument (SmartLab-9000), the parameters were: Cu target K_{α} line ($\lambda = 1.5406 \text{ \AA}$), tube flow was 40 mA, tube pressure was 40 kV, scanning speed was $3^{\circ}/\text{min}$, and the scanning angle range was 20° to 120° . The macrostructure of the samples was observed by the inverted optical microscope (OLYMPUS-GX71) and the microstructure was observed by JSM-7001F field emission Scanning Electron Microscope (SEM). The target scanning voltage of the scanning electron microscope was 15 kV, the current was 10 A, and the vacuum degree was 5.1×10^{-4} Pa. Samples point scanning were observed through the JXA-8530F Electron Probe Micro-analyzer (EPMA), which scanning voltage was 30 kV, the working distance was 11 mm, and the secondary electron resolution was 3 nm. The samples were observed and analyzed by Transmission Electron Microscope (TEM) of TECNAIG220. The Twin-jet used 7% perchloric acid solution (7% HClO_4 + 93% absolute ethanol), the parameters were dual injection voltage 22 V and current 20 mA.

3 Results and Analysis

3.1 Density Analysis

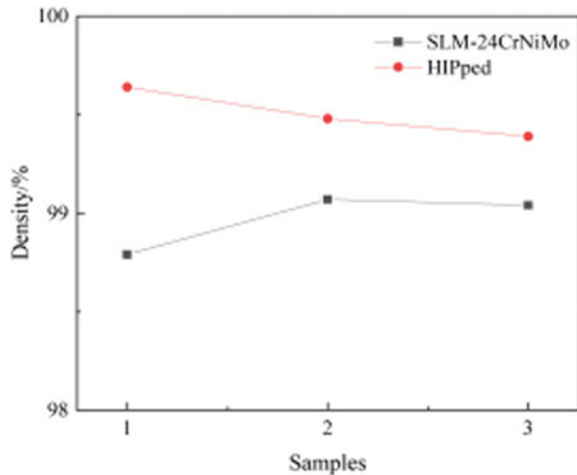
The relative density compared with forge samples for the SLM and SLM + HIP samples were shown in Fig. 2.

After HIPping, the relative density of SLM samples increased 0.4–0.9%, the average density of SLM-24CrNiMo sample was 98.97%, while the HIP one was 99.50%. In the processing of SLM-24CrNiMo steel, the powder was rapidly melted and solidified under the scanning of high-energy laser beam. Pores were occasionally formed at the overlap between the melt channels and junction area between the layers. The existence of hollow void in the powder materials also led to the formation of porosity. The SLM-24CrNiMo alloy steel samples in this study had good formability and high relative density after HIP, which met the requirements of high-speed train brake disc.

3.2 Phase Analysis

Figure 3a showed the X-ray diffraction result of SLM-24CrNiMo sample and HIPped sample. SLM-24CrNiMo sample mainly composed of BCC α -Fe and a small amount of FCC retained austenite. Two diffraction peaks for M(101) and M(110) of martensite $C_{0.08}Fe_{1.92}$ were found at $2\theta = 44.02^\circ$ and $2\theta = 44.84^\circ$ respectively, the diffraction peak of retained austenite $\gamma'(111)$ occurred at $2\theta = 43.7^\circ$. As low-carbon alloy steel with 0.26% carbon content, 24CrNiMo had less carbide, so no diffraction peak of carbide was found in the XRD results.

Fig. 2 The relative density of SLM-24CrNiMo and HIPped SLM-24CrNiMo samples



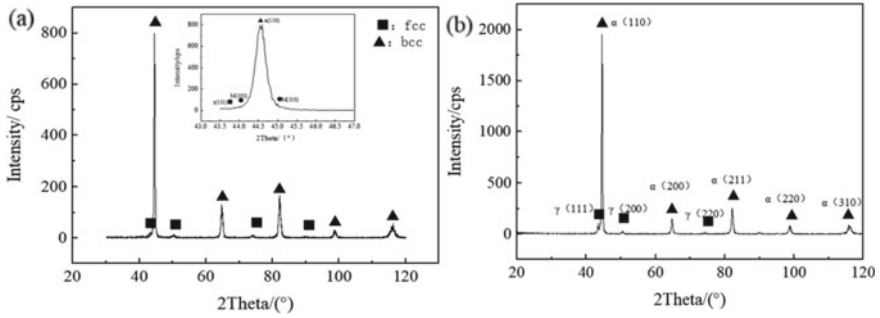


Fig. 3 The X-ray diffraction analysis of samples, **a** SLM-24CrNiMo, **b** HIPped SLM-24CrNiMo

The HIPped SLM-24CrNiMo sample was mainly composed of BCC α -Fe and a small amount of FCC retained austenite, as shown in Fig. 3b. The holding temperature of HIP was in the $\alpha + \gamma$ coexistence area, which was higher than A_{c3} of the 24CrNiMo alloy steel, so the sample was austenitized during the heating and holding process.

3.3 OM and SEM Analysis

Figure 4a, b showed the OM images of SLM-24CrNiMo, which were obviously divided into two areas: dark gray and light gray two areas. The dark gray area defined as Heat Affected Zone (HAZ) marked in Fig. 4a was generated due to the thermal effects on the former layer when the scanning laser forming the present layer upon it. The light gray area was directly formed without phase transition caused by subsequent heat input during the laser scanning cycles, which was defined as the As Fabricated (AS) area. As shown in Fig. 4c, 24CrNiMo powder was melted by high-energy laser beam and then rapidly cooled. At top of the formed sample, the molten pool produced by SLM solidified through thermal radiation and convection in the air and along the substrate which led to high cooling

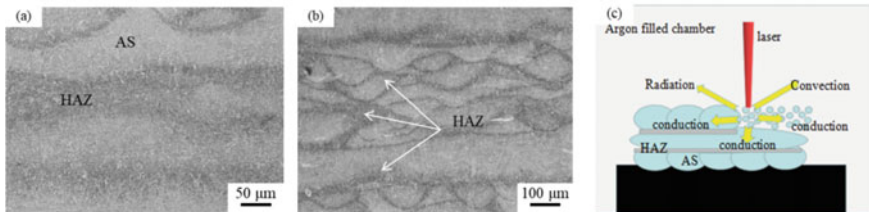


Fig. 4 The OM images of SLM-24CrNiMo sample and schematic diagram, **a**, **b** macrostructure of the sample, **c** schematic diagram of SLM

rate. When laser scanning to form present layer, the heat induced re-austenitized the layers formed under it and transformed the HAZ previous martensite into tempered martensite.

HAZ in Fig. 5a consisted of Lath bainite (LB), Granular bainite (GB), and Tempered martensite (TM). The lath width of lath bainite was about 1 μm , and that of tempered martensite was about 200 nm. The AS in Fig. 5b consisted of lath martensite, acicular and lath bainite. The acicular bainite size was 200 nm, and the lath bainite in AS was smaller than that in HAZ. A small number of fine carbides embedded in granular bainite at about 100 nm were observed in Fig. 5c. A large number of dispersed second phases were observed in the ferrite area in Fig. 5d.

After HIP the microstructure of the sample no longer had the dark gray and light gray as found in SLM-24CrNiMo samples. HIPped sample was composed of granular pearlite, massive bainite and polygonal ferrite, as shown in Fig. 6a, b. Two different morphologies of carbide precipitates were observed in Fig. 6c.

Figure 6c showed that spherical carbide precipitated with less than 100 nm size in the interior of the polygonal ferrite. Due to the presence of unmelted carbides in the austenite grain boundaries during the austenitization, which remained in the austenite carbon-poor zone, such as Carbide1. The austenite C-rich zone formed pearlite when it was cooled to a high temperature, and formed massive bainite when it continued to cool to medium temperature, finally formed a uniform two-phase region of granular pearlite and massive bainite. The carbides in the granular pearlite structure were intermittent granular with 100–300 nm, such as Carbide2. A thin film of retained austenite was observed. Two different nano carbides presented a fine dispersion distribution, which increased the stability and uniformity of the structure.

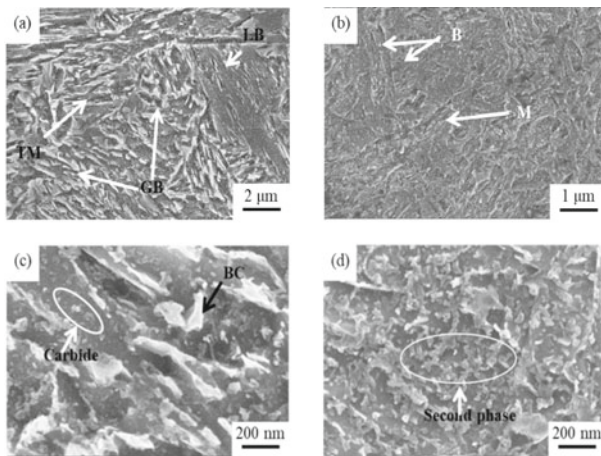


Fig. 5 The SEM of HIPped sample, **a** HAZ, **b** AS, **c** HAZ carbide, **d** AS second phase

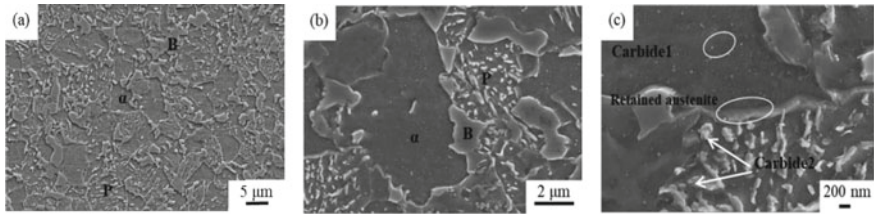


Fig. 6 The SEM of HIPped SLM-24CrNiMo sample, **a** and **b** P + B+a phase region, **c** carbides

3.4 EPMA Analysis

The Electron Probe Micro-analyzer (EPMA) was performed on the circular areas at different positions in Fig. 7 to determine the C element content in the HIPped SLM-24CrNiMo sample, as shown in Table 2. Among them, points 2 and 4 were polygonal ferrite, because the carbon content of ferrite was low. Points 1 and 3 were C-rich massive bainite, point 5 was high intermittent granular carbides in granular pearlite of C.

The proportion of each phase in the HIPped sample was counted, the contents of granular pearlite, massive bainite, polygonal ferrite and were 65.06, 19.74 and 15.2%, respectively. The increase of granular pearlite and nano-carbide made the microstructure uniform and dense, which provided conditions for improving the performance of the brake disc.

3.5 TEM Analysis

Figure 8 showed the transmission morphology and electron diffraction spots of SLM-24CrNiMo alloy steel. Figure 8a was determined as BCC martensite $C_{0.12}Fe_{1.88}$ along the $[\bar{1}11]$ crystal belt axial. The martensite width was less than 1 μm. There was a layer of black thin layer with nanometer thickness at the boundary of martensite strip, which was the residual austenite. Figure 8b showed the martensite $C_{0.08}Fe_{1.92}$ along the $[13\bar{1}]$ crystal belt axial and retained austenite

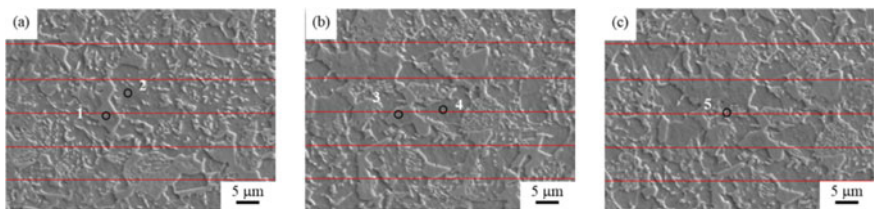


Fig. 7 The EPMA point of 24CrNiMo steel samples after HIP, **a** Field 1, **b** Field 2, **c** Field 3

Table 2 The EPMA result of 24CrNiMo steel samples after HIP (mass fraction) %

Element	Fe	C	Cr	Ni	Mo	Mn	Si	V
Point 1	95.657	0.479	0.466	0.457	0.510	0.805	0.149	0.002
Point 2	98.424	0.065	0.522	0.590	0.525	0.744	0.123	–
Point 3	95.901	0.436	0.488	0.505	0.524	0.668	0.120	0.018
Point 4	96.914	0.134	0.681	0.367	0.573	0.726	0.158	0.005
Point 5	94.881	1.517	0.464	0.484	0.555	0.672	0.188	0.032

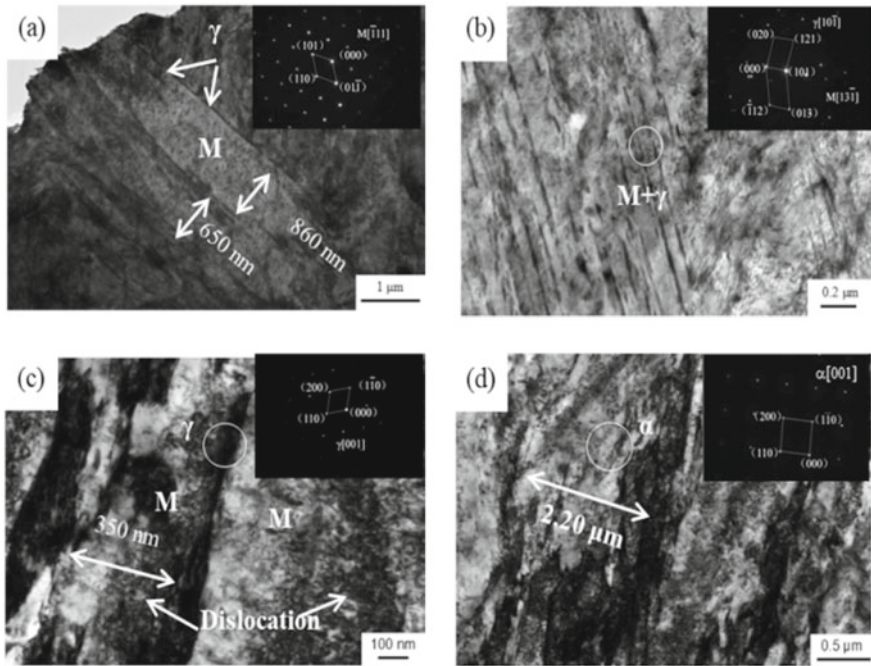


Fig. 8 The TEM image of SLM-24CrNiMo steel sample, **a** M, **b** M + γ , **c** γ , **d** α

along the $[10\bar{1}]$ crystal belt axial. Figure 8c was lath martensite along the $[001]$ crystal belt axial with dislocation substructure in the interior. Black residual austenite thin layers were observed on the edge of lath martensite in Fig. 8a–c, which thickness was about 25–30 nm. The residual austenite film between lath martensites made the adjacent two lath martensites separated, which alleviated the deformation stress of lath martensite, so it hindered the interaction of martensite under external stress and prevented the crack from spreading among martensite strips. Figure 8d was the ferrite along the $[001]$ crystal belt axial.

Figure 9 showed the TEM images and diffraction patterns of HIPped SLM-24CrNiMo sample. Figure 9a showed BCC ferrite along the axis of $[\bar{1}13]$

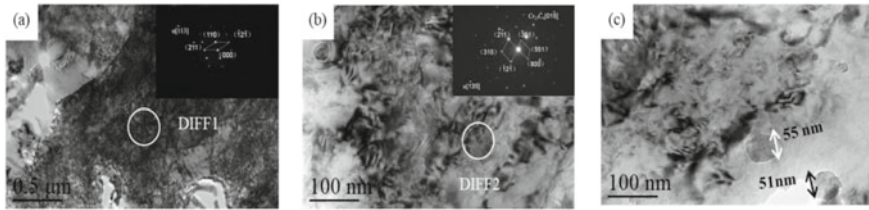


Fig. 9 The TEM of 24CrNiMo steel samples after HIP, **a** α , **b** and **c** Cr_{23}C_6

crystal band. Figure 9b showed BCC ferrite and FCC Cr_{23}C_6 with $[0\ 1\ \bar{5}]$ crystal band axis. Cr_{23}C_6 with the nano-size was the carbide formed in the high temperature region during HIP cooling, as shown in Fig. 9c. Fine carbides were dispersed on the granular pearlite, and the morphology of carbides was mostly spherical and ellipsoidal. There was no sharp corner to split the matrix when the sample was under tension, which improved the properties of the material. The second phase was strengthened by the dispersed nano carbides. The carbide particles worked on the dislocation stress, resulting in the interaction between solute atoms and dislocations, which hindered the movement of dislocations and improved the deformation resistance of alloy steel samples.

4 Conclusion

The macrostructure of SLM-24CrNiMo alloy steel samples was divided into AS and HAZ regions. The HAZ region composed of lath bainite, granular bainite and tempered martensite, while AS region consisted of lath martensite, acicular and lath bainite, and a small amount of retained austenite. HIPped processing for SLM-24CrNiMo was in the $\alpha + \gamma$ coexistence region. The HIPped sample composed of granular pearlite with discontinuous carbide size about 100–300 nm, massive bainite, polygonal ferrite with less than 100 nm nano carbides participated on, and a small amount of retained austenite. The sample microstructure was uniform and dense after HIP, and the relative density of HIPped sample increased 0.4–0.9% than that of SLM-24CrNiMo sample.

Acknowledgements This work was financially supported by the National Key R&D Program of China (2016YFB1100203), Joint Funds of NSFC-Liaoning (U1508213) and Funds of Green Manufacturing System Integration Project of the Industry and Information Ministry of China (2017).

References

1. Wei, M.W., Chen, S.Y., Xi, L.Y., et al.: Selective laser melting of 24CrNiMo steel for brake disc: fabrication efficiency, microstructure evolution, and properties. *Opt. Laser Technol.* **107**, 99–109 (2018)
2. Cao, L., Chen, S.Y., Wei, M.W., et al.: Effect of laser energy density on defects behavior of direct laser depositing 24CrNiMo alloy steel. *Opt. Laser Technol.* **111**, 541–553 (2019)
3. Tomasz, K., Konrad, G., Wojciech, S., et al.: Correlation between process parameters, microstructure and properties of 316 L stainless steel processed by selective laser melting. *Mater. Sci. Eng., A* **718**, 64–73 (2018)
4. Tucho, W.M., Lysne, V.H., Austb, H., et al.: Investigation of effects of process parameters on microstructure and hardness of SLM manufactured SS316L. *J. Alloy. Compd.* **40**, 910–925 (2018)
5. Hu, Z.H., Zhu, H., Zhang, H., et al.: Experimental investigation on selective laser melting of 17-4PH stainless steel. *Opt. Laser Technol.* **87**, 17–25 (2017)
6. Chlebus, E., Gruber, K., KuNicka, B., et al.: Effect of heat treatment on the microstructure and mechanical properties of Inconel 718 processed by selective laser melting. *Mater. Sci. Eng., A* **639**, 647–655 (2015)
7. Lavery, N.P., Cherry, J., Mehmood, S., et al.: Effects of hot isostatic pressing on the elastic modulus and tensile properties of 316L parts made by powder bed laser fusion. *Mater. Sci. Eng., A* **693**, 186–213 (2017)
8. Cai, C., Gao, X.Y., Teng, Q., et al.: A novel hybrid selective laser melting/hot isostatic pressing of near-net shaped Ti-6Al-4 V alloy using an in-situ tooling: interfacial microstructure evolution and enhanced mechanical properties. *Mater. Sci. Eng., A* **717**, 95–104 (2018)
9. Han, Q.Q., Raya, M., Maria, L., et al.: Laser powder bed fusion of Hastelloy X: effects of hot isostatic pressing and the hot cracking mechanism. *Mater. Sci. Eng., A* **732**, 228–239 (2018)
10. Kang, X.L., Dong, S.Y., Men, P., et al.: Microstructure evolution and gradient performance of 24CrNiMo steel prepared via laser melting deposition. *Mater. Sci. Eng., A* **777**, 139004 (2020)

Numerical Simulation of Melting Flow in Crude Oil Water Based on Fluent



Yi Zhao, Deyin Zhao, Rongqiang Zhong, Lirong Yao,
and Xiaoqing Li

Abstract Multiphase flow is an important problem in crude oil transportation because crude oil transportation involves the flow of crude oil and water in pipelines. Transportation of crude oil involves safety, efficiency and cost. Fluent software was used for numerical simulation in this paper. The melting flow characteristics of crude oil in pipelines under different flow rates and water temperatures. The changes of temperature and liquid phase ratio at the center point of crude oil with time were monitored and analyzed.

Keywords Multiphase flow · Numerical simulation · Crude oil · Water temperature · Flow rate

1 Introduction

Safety is the most important factor in the transportation of crude oil [1], and on this basis, efficiency and cost savings should be improved [2]. As for the transportation of crude oil in pipelines, scholars have done a lot of researches, and numerical simulation is an important research method [3, 4]. Many scholars use fluent software to carry out numerical simulation [5–7]. Lu et al. [8] assumed that the solidification region of crude oil was a dynamic porous medium region composed of solid and liquid phases, proposed the heat transfer model of the mass, momentum and energy equation of crude oil and the energy equation of soil and pipeline, and carried out numerical simulation of the temperature drop during the shutdown process of buried crude oil pipelines. The temperature field, solidification interface and natural convection of crude oil during the shutdown period are described. Xu et al. [9] applied the mathematical model of partition method and equivalent

Y. Zhao · D. Zhao · R. Zhong · L. Yao (✉)
Sinopec Northwest Oil Field Company, Wulumuqi City, China
e-mail: yaolr.xbsj@sinopec.com

X. Li
School of Civil and Engineering, Northeast Petroleum University, Daqing 163318, China

specific heat capacity method to deal with the latent heat of wax extraction, and put forward the judgment basis for the total condensation of crude oil in the pipeline in order to determine the final solidification position. Du et al. [10] analyzed the influence of latent heat on temperature drop of crude oil when studying the temperature rule during pipeline shutdown, used enthalpy model to simulate the temperature drop rule of crude oil in underwater pipeline, and recorded the positions of solid phase, mixed phase and liquid phase of crude oil in pipeline at different times. Chen et al. [11] used Fluent software to simulate the temperature drop process of submarine pipeline shutdown, analyzed the temperature drop process under different initial oil temperatures and different ambient temperatures, and obtained a temperature drop curve that was in good agreement with the actual situation.

At present, the solidification process of gelled crude oil is the main research direction, and study of the temperature and interface changes of condensate crude oil after pipeline shutdown. In this paper, the effects of hot water temperature and water flow velocity on the melting flow characteristics of spherical gelled crude oil in pipelines are studied through numerical simulation research.

In recent years, scholars have studied a variety of auxiliary methods for non-heating gathering and transportation, including natural non-heating oil collecting auxiliary, warm water adding auxiliary and chemical auxiliary. However, difficulties have also been encountered in the process of gathering and transportation without heating. When the temperature of crude oil is lower than its freezing point temperature, it will produce structural solidification and become a gelatinization state, which will greatly reduce the fluidity of crude oil and cause problems such as blocked pipelines and normal production. For this reason, Liu et al. [12] studied the shear fluidization treatment system of water-gelled crude oil to change the gelled crude oil into particle state and realize the water-gelled crude oil particle transport without heating hydraulic suspension. However, when it transports crude oil over a long distance or for a long time, the terminal concentration or wellhead pressure will increase. In order to analyze this problem, numerical simulation method is adopted in this paper to study the melting characteristics of spherical colloidal crude oil, so as to provide technical help for solving the problem of crude oil terminal accumulation and reducing energy consumption in the future.

2 Physical Model and Physical Property Parameters

The melting of crude oil is a phase transition process. At present, the commonly used method for the melting of phase change materials is to use fluent software for numerical simulation. A physical model of the melting of colloidal crude particles in hot water was established, and the VOF model and solidification and melting model in fluent software were used for numerical simulation. The effects of water velocity and water temperature on the melting flow characteristics of crude oil are analyzed.

The gelled crude oil was fluidized into a sphere and a two-dimensional physical model was established as shown in Fig. 1. The square with side length of 100 mm was filled with hot water, ignoring the effect of wall thickness, and spherical gel crude oil was put into the square, and the temperature of crude oil was lower than the temperature of hot water. Assuming that the crude oil particles are always at this position, the upper and lower boundaries are adiabatic boundaries, the left boundary is the inlet of constant temperature and constant flow velocity of hot water, and the right boundary is the outlet of hot water. Heat is transferred first by convection and then by conduction into the interior of the oil. To facilitate the analysis of the simplified physical model, the following assumptions are made: isotropy of crude oil; The thermal property parameters, density, specific heat capacity and thermal conductivity of crude oil are constants that do not change with time. No heat dissipation between the system and the outside world. The physical parameters of crude oil are shown in Table 1.

Fig. 1 Physical model

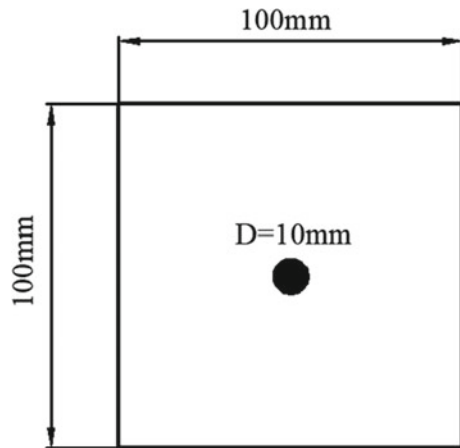


Table 1 Physical parameters

Physical property parameter	Parameter
Density (kg/m ³)	870.2
Specific heat (J/kg K)	2100
Thermal conductivity (W/m K)	0.2
Kinematic viscosity (kg/m s)	0.05
Molecular weight (kg/kg mol)	18
Standard enthalpy of state (J/kg mol)	-2.86 × 10 ⁸
Latent heat (kJ/kg)	30
Phase transition temperature range (K)	303.15–333.15

3 Effect of Hot Water Velocity on Crude Oil Melting

Set a gel crude oil with a radius of 5 mm, latent heat of phase change of 30000 J/kg, phase change temperature range of 30–60 °C, and initial temperature of 10 °C. Hot water with initial temperature of 70 °C and flow rate of 0.1 m/s was set. Set the above data as raw data. In the boundary conditions of Fluent, the flow rate was changed to 0.15, 0.2, 0.25 and 0.3 m/s in turn, and then numerical simulation was carried out.

As shown in Fig. 2, the faster the flow velocity at the same time, the higher the central temperature of crude oil. The higher the slope of the curve, the faster the oil melts. The higher the water velocity is, the stronger the heat exchange capacity is and the shorter the melting time is. So, other things being equal, the higher the flow rate, the faster the melting speed.

Figure 3 shows the variation curve of liquid phase ratio of crude oil with time at different flow rates. It can be seen from the figure that when the flow rate is 0.1 m/s, the liquid phase ratio of crude oil is 1, that is, the complete melting time of crude oil is 12.33 s. At a flow rate of 0.15 m/s, it took 8.88 s for the crude to melt completely. At the flow rate of 0.2 m/s, the time was 6.84 s. At the flow rate of 0.25 m/s, the time was 5.69 s. At a flow rate of 0.3 m/s, the time was 4.90 s.

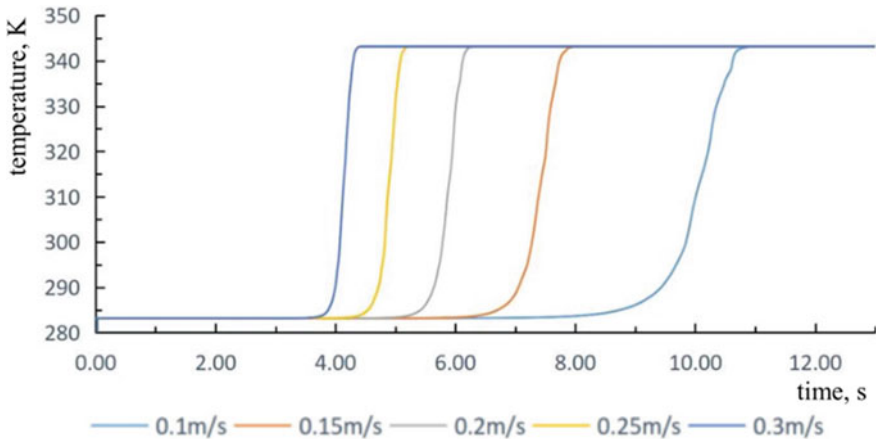


Fig. 2 Central point temperature of different flow rates

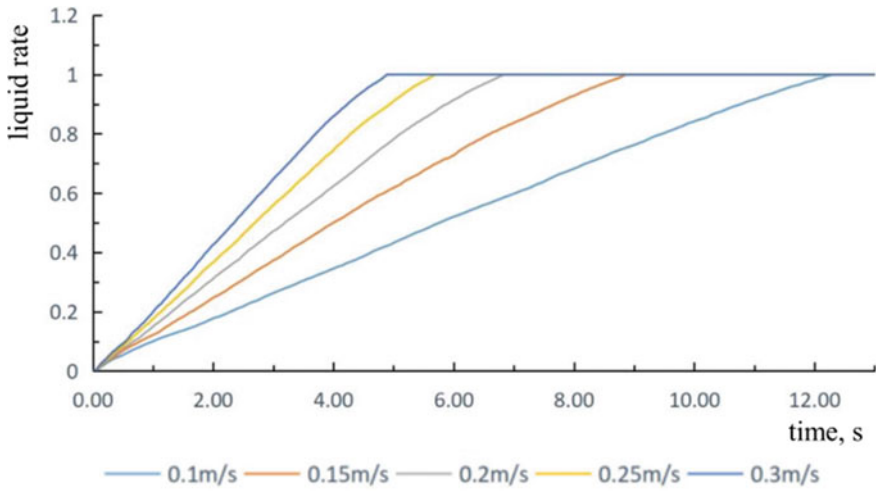


Fig. 3 Liquid phase rates of different flow rates

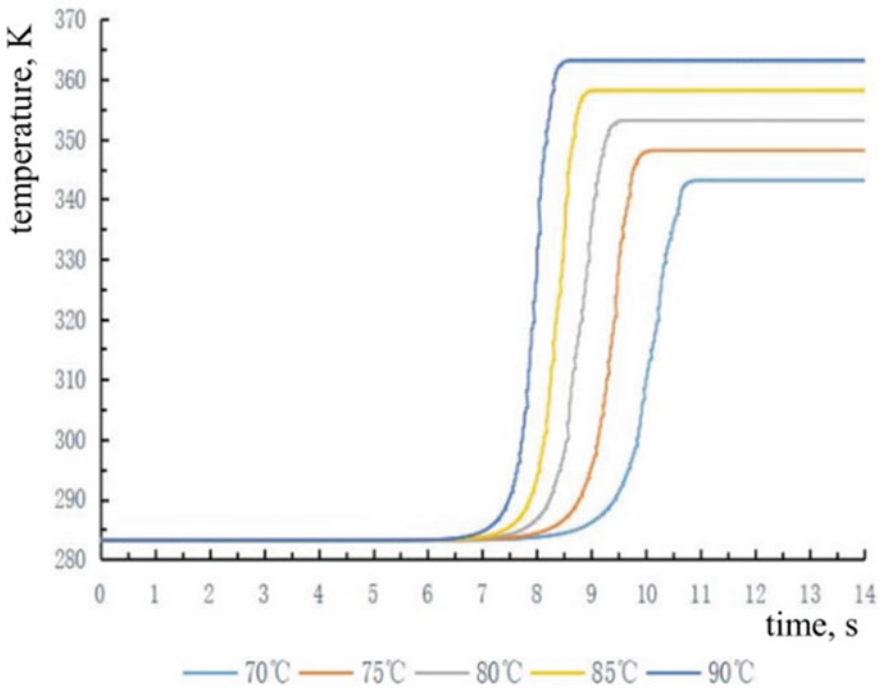


Fig. 4 Central point temperature of different water temperature

4 Effect of Water Temperature on the Melting of Crude Oil

The original data above was selected to simulate the melting of crude oil with a radius of 5 mm and initial temperature of 10 °C in hot water with a flow velocity of 0.1 m/s. The water temperature is 70, 75, 80, 85 and 90 °C.

Figure 4 shows the change of center temperature with time under different water temperature. The higher the temperature of the water at the same time, the higher the temperature at the center. The higher the slope of the curve, the faster the oil melts. The higher water temperature increases the heat exchange between the hot water and the crude oil, reducing the time it takes for the crude oil to melt completely.

Figure 5 shows the change curve of liquid phase ratio of crude oil at different water temperatures. This figure can reflect the relationship between hot water temperature and melting rate. Other things being equal, the higher the water temperature, the faster the oil melts.

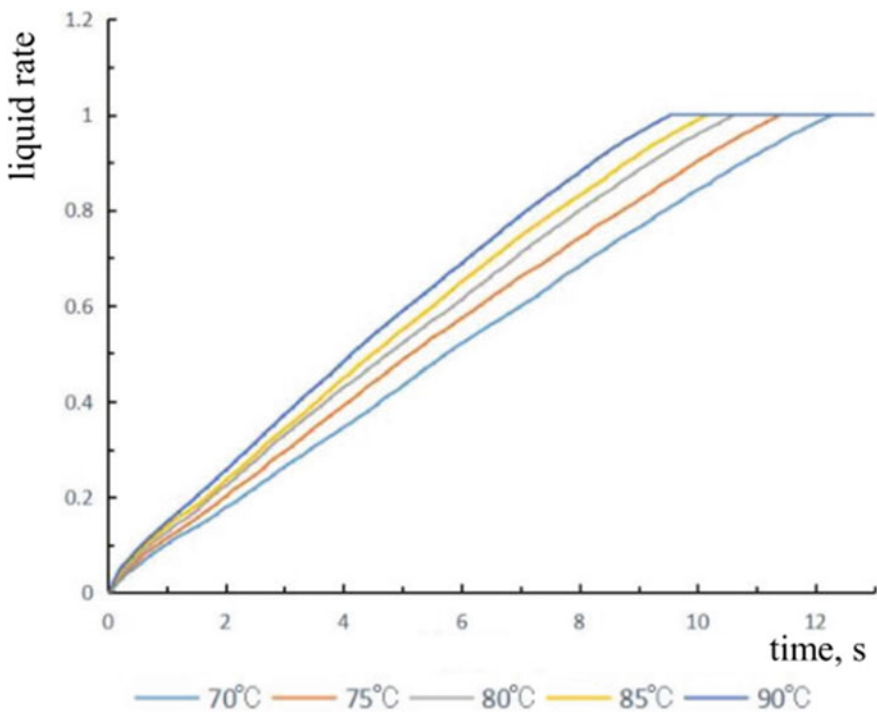


Fig. 5 Liquid phase rates at different water temperatures

5 Conclusion

In this paper, a model of spherical gel crude oil melted in hot water is built in a square container. The melting flow characteristics of crude oil were studied by Fluent. The effects of flow rate and water temperature on the melting characteristics of crude oil are analyzed by using the control variable method. The affirmative conclusions are drawn as follows:

- (1) When other factors remain unchanged, the greater the flow rate of hot water, the shorter the total melting time of crude oil and the faster the melting rate of crude oil.
- (2) When other conditions remain unchanged, the larger the temperature difference between oil and water is, the faster the crude oil melts.

References

1. Li, P., Zhou, X., Wang, D., et al.: Design discussion on the flow assurance for transportation pipelines of high pour point crude oil. *Oil-Gas Field Surf. Eng.* **37**(02), 52–55 (2018)
2. Cheng, Q., Liu, Y., Liu, X.: Energy use description and energy consumption evaluation in the transportation process of waxy crude oil pipeline. *Oil Gas Storage Transp.* **36**(6), 617–623 (2017)
3. Gan, Y., Cheng, Q., Wang, Z., et al.: Molecular dynamics simulation of the nucleation and gelation process for a waxy crude oil multiphase system under different physical-chemical influencing factors. *Energy Fuels* **33**(8), 7305–7320 (2019)
4. Gan, Y., Cheng, Q., Wang, Z., et al.: Molecular dynamics simulation of the microscopic mechanisms of the dissolution, diffusion and aggregation processes for waxy crystals in crude oil mixtures. *J. Petrol. Sci. Eng.* **179**, 56–69 (2019)
5. Jiang, L., Wei, L., Jingwei, Q.: Accidental consequence analysis of buried crude oil pipeline leakage based on Fluent. *J. Saf. Environ.* **17**(1), 199–203 (2017)
6. Wang, P.: Simulation on shutdown process of buried waxy crude oil pipeline based on Fluent software. *Liaoning Chem. Ind.* **45**(7), 966–967, 971 (2016)
7. Xiaoyan, L., Wang, L., Yang, L., et al.: Numerical investigation of waxy crude oil paste melting on an inner overhead pipe wall. *Appl. Therm. Eng.* **131**, 779–785 (2018)
8. Lu, T., Jiang, P.: Heat transfer model and numerical simulation of temperature decreasing and oil solidifying of buried crude pipeline during shutdown. *J. Therm. Sci. Technol.* **4**(04), 298–303 (2005)
9. Xu, Y., Nie, X., Dai, Z., et al.: Analysis of heat transfer based on the change rule of the highest temperature point for shutdown. *J. Eng. Thermophys.* **41**(03), 685–691 (2020)
10. Du, M., Ma, G., Su, K.: Numerical simulation of petrol temperature drop in pipelines during stopping transportation under water. *J. Liaoning Shihua Univ.* **30**(03), 51–54 (2010)
11. Chen, J., Fu, X.: Numerical simulation of the temperature drop in submarine oil pipeline during shutdown based on Fluent. *J. Petrochem. Univ.* **27**(02), 93–96 (2014)
12. Liu, X., Chen, W., Gao, H., et al.: Experimental study on fluidization of water-gelled crude oil two-phase flow. *J. Eng. Thermophys.* **34**(03), 480–483 (2013)

Effects of Nickel on Microstructure and Properties of Direct Laser Deposited 00Cr25-xNiMo4 Duplex Stainless Steel



Jing Liang, Lizhao Wang, Yunfei Gao, Suiyuan Chen,
Changsheng Liu, Chuang Li, Shixing Yan, and Shiyun Dong

Abstract In this study, the 00Cr25-xNiMo4 Duplex Stainless Steel (DSS) was fabricated by Direct Laser Deposition (DLD) using a YSL-1000 W fiber laser, and the influence of different nickel contents ($x = 7.0, 8.0, 9.0,$ and 10.0 wt%) on the microstructure and properties of the DLDed 00Cr25-xNiMo4 samples were studied. Optimized laser processing parameters were obtained with the laser power 650 W, scanning velocity 6 mm/s. The microstructure of the samples was composed of ferrite and austenite. The percentage of austenite phases in the DLDed 00Cr25Ni9Mo4 DSS samples reached the highest value of 41.8%, which led to the highest tensile strength of 1084 MPa. The yield strength and microhardness of them were 720 MPa and 294.9 HV_{0.2} respectively. The self-corrosion potential of the DLDed 00Cr25Ni9Mo4 DSS samples was -0.228 V, and the self-corrosion current density was 6.410×10^{-7} A/cm². Excellent mechanical properties and corrosion resistance with a balance of ferrite and austenite phases were obtained in the DLDed 00Cr25Ni9Mo4 DSS.

Keywords Direct laser deposition · 00cr25-xNiMo4 duplex stainless steel · Microstructure · Mechanical properties · Corrosion resistance

J. Liang (✉) · L. Wang · Y. Gao · S. Chen · C. Liu · C. Li
Key Laboratory for Anisotropy and Texture of Materials, Ministry of Education,
Key Laboratory for Additive Manufacturing and Remanufacturing Materials,
School of Materials Science and Engineering, Northeastern University,
Shenyang 110819, Liaoning, China
e-mail: liangj@atm.neu.edu.cn

S. Yan · S. Dong
Academy of Army Armored Forces, Beijing, China

1 Introduction

Duplex Stainless Steel (DSS) consisting of nearly equal amount ferrite and austenite phases was widely used in the application of propellers, ship impellers, and valve bodies, etc. DSS had better plasticity and toughness than ferritic stainless steel did, which strength was as twice as that of the austenitic stainless steel, meanwhile, its corrosion resistance was excellent [1]. The casting was the main fabricating method for DSS components. The mold design and manufacturing of complex DSS components was difficult. Nonuniformity and defects were easy to appear in some thin-wall parts. DLD used laser directly scanning the feeding powder mixtures to fabricate fully dense metal samples layer by layer without shape limits. According to the characteristics of DLD, complex parts could be fabricated by this method more flexibly [2].

Many researchers had studied the microstructure and properties of DLDED stainless steel recently. Juntao Zhang et al. study the tensile strength (632 MPa) and elongation (46.9%) of the DLDED 304L stainless steel samples under the optimized process parameters were significantly higher than that of the casting samples (tensile strength 485 MPa, elongation 35%) [3]. Zhuqing Wang et al. studied that the grain size (21 μm) of DLDED 304L stainless steel samples under the laser power of 2300 W was smaller than that of the samples under the laser power of 4000 W [4]. Michael A. Melia et al. found that chemical segregation was avoided by increasing the cooling rate or reducing the heat input during the process of direct laser deposition [5].

Peng Guo et al. studied the tensile strength and elongation of the DLDED 316L stainless steel samples with an angle (η) of 0° between the tensile direction and deposition plane were higher 130 MPa and 2.5% than that of the samples with $\eta = 90^\circ$ [6]. Aref Yadollahi et al. found that the microstructure of DLDED 316L SS with longer interlayer time intervals was more uniform [7].

At present, most researches on DLDED stainless steel were concentrated on 316L and 304L SS, while only a few studies were on direct laser deposition of duplex stainless steel. C. J. Wang et al. studied the effects of molybdenum on the properties of DLDED 15Cr21Ni7-xMo (Mo contents were 0, 1, 2, 3, 4 wt%, respectively) DSS. The microhardness of the DLDED 15Cr21Ni7Mo3 DSS samples was the highest (350 HV_{0.2}), and the self-corrosion potential of the samples was the lowest of -142.26 mV [8]. C. Zhang et al. used laser additive manufacturing technology and N-containing 2205 DSS powder to repair large structural parts of the ships and marine equipment. The yield strength and tensile strength of the repaired samples were higher 210 and 240 MPa than that of the original used EQ56 structural steels respectively [9].

Researches showed that the ratio of ferrite to austenite in the DLDED duplex stainless steel was difficult to balance because of the fast cooling rates during the DLD process. In the paper, more nickel (one of the austenite forming elements) was added in the DLD processing to adjust the ratio of ferrite to austenite phases. The influences of nickel contents on the microstructure and properties of the DLDED

samples were discussed in detail, and the optimized alloy composition was obtained.

2 Experimental Details

Q 235 steel plates were used as the substrate for the DLD. The element powder mixture with the designed composition (according to the SAF 2507 duplex stainless steel as reference) and particle size ranged from 140 to 200 μm was used. The powder mixture was ball milled for 10 h at a speed of 350 r/min to ensure uniform dispersion of each element. The composition of the powder mixture used in the DLD experiment was shown in Table 1.

A YSL-1000 fiber laser was used for the DLD with argon protection during the processing. The laser spot diameter was 1.8 mm and the overlap rate of each path was 50%. The optimized experimental parameters with the laser power of 650 W, the scanning rate of 6 mm/s were used to fabricate DSS specimens. They were etched with 5 g FeCl_3 + 50 ml HCl + 100 ml H_2O solution.

The OLYMPUS-GX71 inverted optical microscope (OM), the JM-6510A scanning electron microscope (SEM), and the TECNAIG220 transmission electron microscope (TEM) were used to analyze the microstructure. Phases identification of the deposited layer was carried out using an X-ray diffractometer (X'PertProMPD-PW3040/60) with Cu target K_α radiation ($\lambda = 1.5406 \text{ \AA}$) at 40 kV, 200 mA, the scanning speed $3^\circ/\text{min}$, and the diffraction angle range $20^\circ\text{--}120^\circ$. The microhardness was measured by Wilson Wolpert 401MVD digital Vickers hardness tester with the interval distance of 0.2 mm, the load of 200 g, and the loading time of 10 s. The AG-X100KN electronic universal testing machine was used for the tensile test with the tensile speed of 0.5 mm/min. The electrochemical workstation was used for the test of corrosion resistance with the test solution of 3.5% NaCl solution. The test parameters involved scanning range -0.2 to 0.4 V, frequency $10^{-2}\text{--}10^5$ Hz, and the rate 0.5 mV/s.

3 Results and Discussion

Figure 1 showed that DLDED 00Cr25-xNiMo4 DSS was composed of ferrite and austenite. No other phase in the DLDED 00Cr25-xNiMo4 DSS samples was found through XRD analysis because the cooling rate was very fast during the DLD

Table 1 Chemical composition of Cr-Ni duplex stainless steel alloy powder (mass fraction) %

Element	C	Cr	Ni	Mo	Mn	Si	Fe
00Cr25-xNiMo4	0.03	25.00	7.0/8.0/9.0/10.0	4.00	1.20	0.80	Bal.

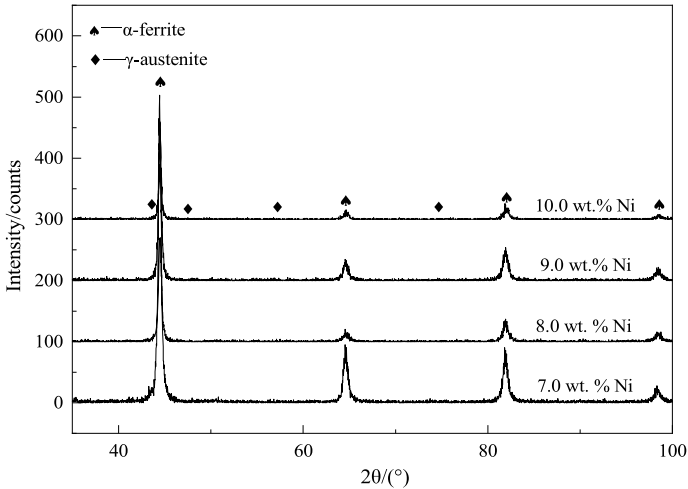


Fig. 1 XRD patterns of DLDed 00Cr25-xNiMo4 DSS with different nickel additions

process, which was on the left of the TTT curve of the precipitated phases according to the research presented by Feng Shang et al. [10]. With the nickel contents increased, the intensity of ferrite peak ($2\theta = 82.335^\circ$) in XRD patterns overall decreased, which indicated the amount of ferrite decreased while the austenite increased.

Figure 2 showed that with the increase of nickel contents, the percentage of gray phases increased while the white phases decreased. According to the results of XRD analysis, the bright white phases and gray phases were identified as ferrite and austenite respectively. The dendritic austenite was distributed in the ferrite phase boundary. The austenite of Fig. 2c, d were blocky and lamellar respectively.

The amount of ferrite, austenite was roughly analyzed by the grid counting method and the grain sizes of the sample with different amounts of nickel additions were showed in Fig. 3. The amount austenite of the samples reached the highest value of 41.8% when the nickel additions of 9.0 wt%. The grain size of 00Cr25Ni10Mo4 samples (Fig. 2d) was smaller than that of 00Cr25Ni9Mo4 samples (Fig. 2c).

Figure 4 showed SEM images of DLDed 00Cr25-xNiMo4 DSS with different nickel additions. The samples were composed of ferrite (dark gray phases) and austenite (bright white phases). The ferrite was first formed during the solidification of the molten pool. With the temperature decreased, the liquid phase completely transformed into the ferrite and the last austenite precipitated near the ferrite. Under the high cooling rate of the DLD, the nickel additions expanded and stabilized the region of austenite phases. The amounts of nickel at the phase boundary between the ferrite and the austenite were higher than that in the ferrite according to the research presented by V. J. Gadgil et al. [11]. Nickel element diffused from high concentration to lower one which was the driving force for interface movement,

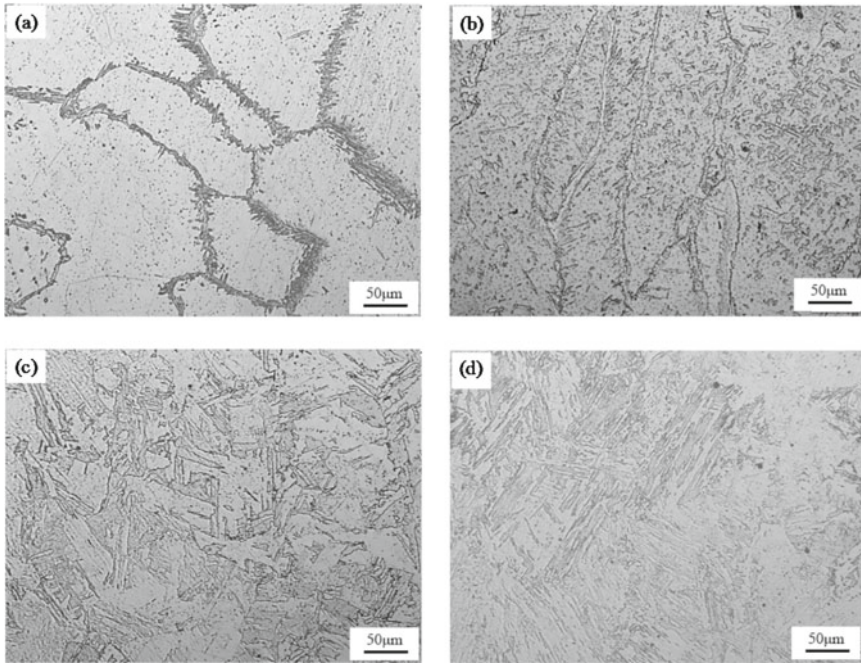


Fig. 2 The morphologies of DLDED 00Cr25-xNiMo4 DSS with different nickel additions: **a** 00Cr25Ni7Mo4 **b** 00Cr25Ni8Mo4 **c** 00Cr25Ni9Mo4 **d** 00Cr25Ni10Mo4

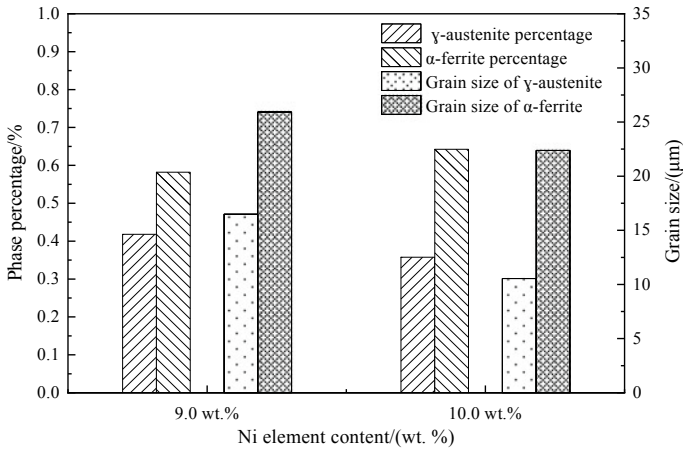


Fig. 3 Phase percentage and grain sizes of DLDED 00Cr25-xNiMo4 DSS with the nickel additions of 9.0 and 10.0 wt%

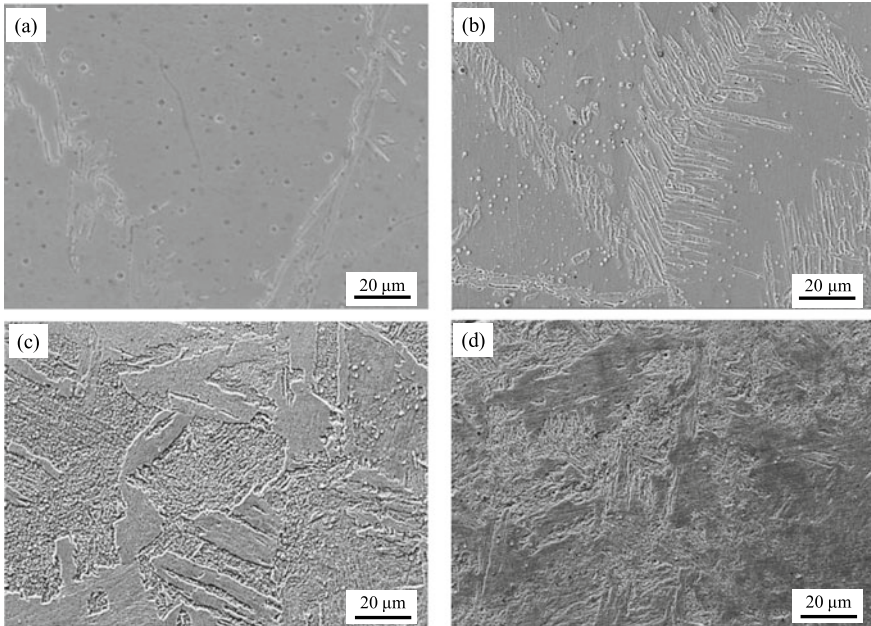


Fig. 4 SEM images of DLDED 00Cr25-xNiMo4 DSS with different nickel additions: **a** 00Cr25Ni7Mo4 **b** 00Cr25Ni8Mo4 **c** 00Cr25Ni9Mo4 **d** 00Cr25Ni10Mo4

so the austenite grew into the ferrite. Increasing the nickel contents in the samples increased the amount of the austenite phases of the DLDED 25Cr-xNi4Mo DSS samples.

It showed in Fig. 5a, a lot of dislocations were found in the DLDED 00Cr25Ni10Mo4 DSS samples. As reported, the dislocations were caused by the fast cooling rate in the direct laser deposition processing. Figure 5b showed the standard electron diffraction patterns of zone axis $[011]$ of ferrite (body-centered cubic), so A region (black lamellar structure) was lamellar ferrite.

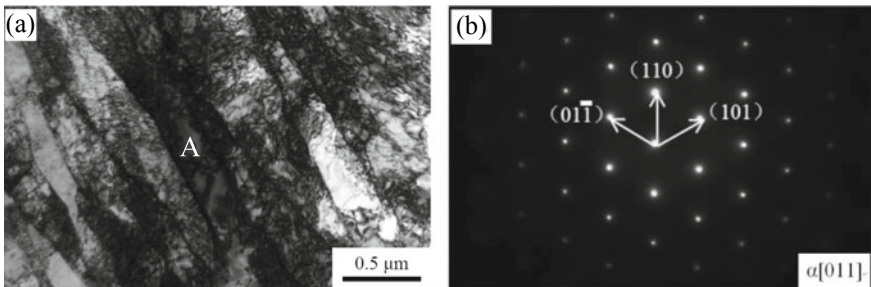


Fig. 5 TEM morphology and electron diffraction pattern of DLDED 00Cr25Ni10Mo4 duplex stainless steel

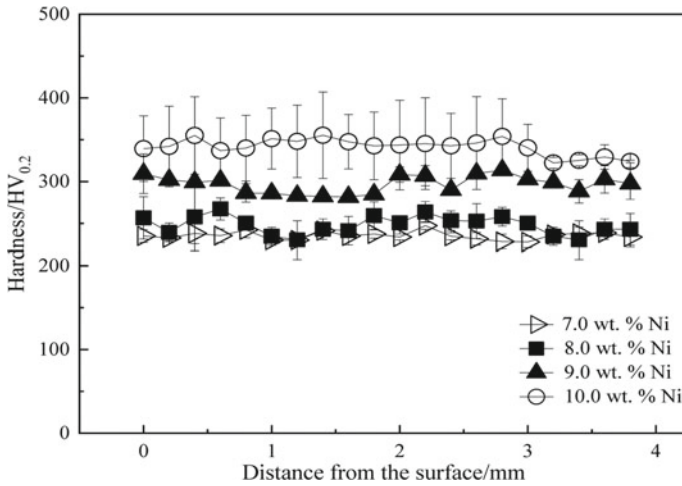


Fig. 6 Variation in Vickers hardness values of DLDED 00Cr25-xNiMo4 DSS with nickel additions of 7.0, 8.0, 9.0, and 10.0 wt%

Figure 6 showed the microhardness distribution of the cross-section to the laser scanning direction of the DLDED samples. With the distance from the deposited layer to the substrate changed, the microhardness of the samples also changed because the DLD process produced the tempering effects on the previous layer when the latter layer was fabricated. The uneven heat diffusion of each layer led to uneven stress distribution. The average microhardness of the DLDED 00Cr25Ni9Mo4 samples was 294.9 HV_{0.2}.

Stress-strain curves of the DLDED samples with different nickel contents were showed in Fig. 7. The increase of nickel contents improved the yield strength of the samples because more nickel dissolved in the austenite to form the solution strengthening. Due to the different atomic radius of nickel and iron, nickel replaced the iron in the crystal lattice and caused the lattice distortion. The lattice distortion stress field interacted with the dislocations, hindered the movement of the dislocations, and improved the strength of the samples. The austenite was hard phases, which benefited for the high tensile strength and yield strength. The tensile strength 1084 MPa and the yield strength 720 MPa of the DLDED 00Cr25Ni9Mo4 samples (Fig. 8) with the highest austenite percentage (41.8%) were higher than that of casting DSS.

Potential polarization curves of DLDED 00Cr25-xNiMo4 DSS with different nickel additions were showed in Fig. 9. The samples with nickel contents of 8.0, 9.0, and 10.0 wt% had obvious passivation areas, and the dense passive films were formed on the surface of the samples in the corrosive liquid of 3% NaCl solution. Nickel improved the corrosion resistance of DSS because nickel formed a denser oxide layer than that formed by iron in corrosive solution according to the research

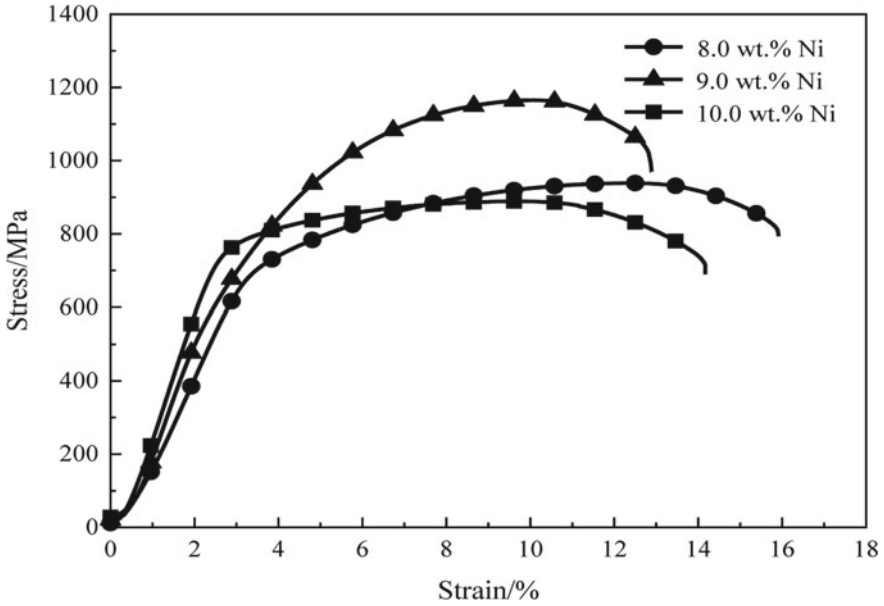


Fig. 7 Tensile stress-strain curves of DLDed 00Cr25-xNiMo4 DSS with nickel additions of 8.0, 9.0, and 10.0 wt%

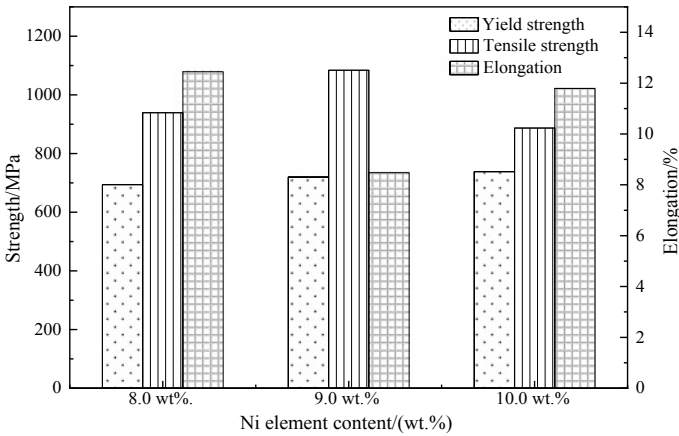


Fig. 8 Tensile properties of DLDed 00Cr25-xNiMo4 DSS with nickel additions of 8.0, 9.0, and 10.0 wt%

presented by X. H. Ma et al. [12]. Figure 10 showed the DLDed 00Cr25Ni9Mo4 samples had the highest self-corrosion potential (-0.228 V) and the lowest self-corrosion current density (6.41×10^{-7} A/cm²).

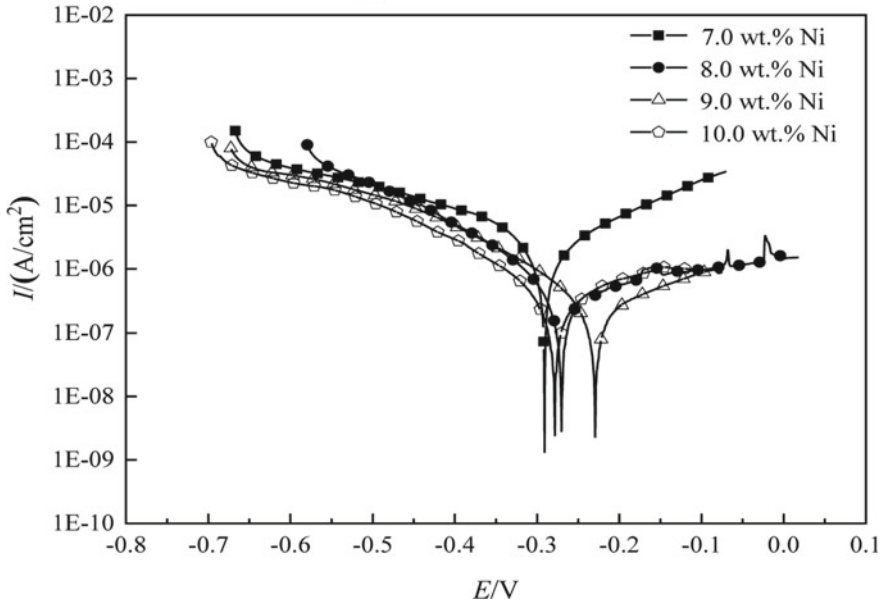


Fig. 9 Tafel curves of DLDed 00Cr25-xNiMo4 DSS with different nickel additions of 7.0, 8.0, 9.0, and 10.0 wt%

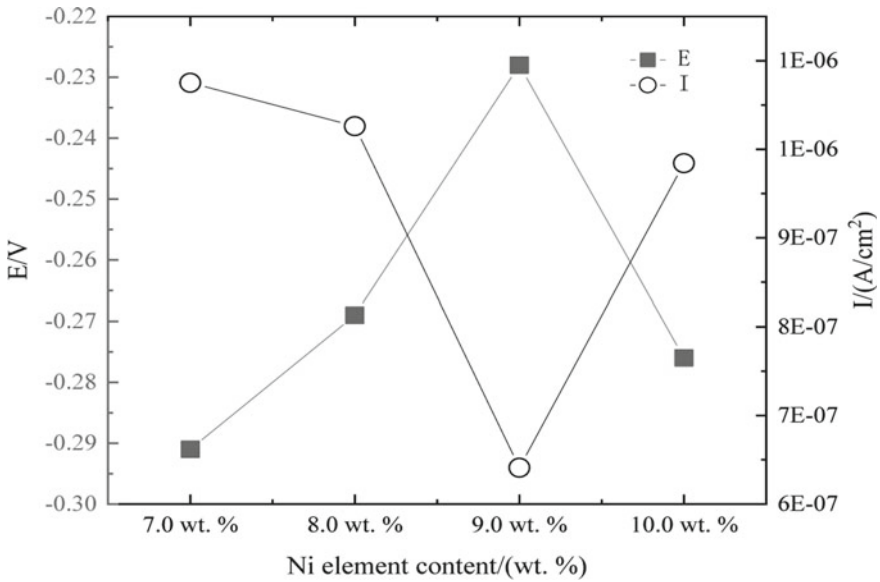


Fig. 10 The self-corrosion potential and the self-corrosion current density of DLDed 00Cr25-xNiMo4 DSS with different nickel additions of 7.0, 8.0, 9.0, and 10.0 wt%

With the increasing of nickel compositions, the corrosion resistance of samples first increased and then decreased. The additions of nickel increased the percentage of austenite and overall refined the grain sizes of ferrite. Nickel was beneficial to the formation of austenite, and the austenite with the face-centered cubic lattice accommodated more alloying elements, thus nickel additions increased the electrode potential of austenite. When the nickel contents of the samples were 9.0 wt%, the balance of austenite and ferrite phases was obtained, and the corrosion resistance of the samples was the highest.

4 Conclusions

The DLDed 00Cr25-xNiMo4 ($x = 7.0, 8.0, 9.0,$ and 10.0 wt%) DSS samples were obtained under optimization processing parameters with laser power of 600 W and laser scanning speed of 6 mm/s.

The DLDed 00Cr25Ni9Mo4 DSS was composed of austenite (percentage of 41.8%) and ferrite (percentage of 58.2%). It had good mechanical properties with the tensile strength of 1084 MPa, yield strength of 720 MPa, elongation of 8.48%, and microhardness of 294 HV_{0.2}. The corrosion resistance of DLDed 00Cr25Ni9Mo4 DSS was the best among these 00Cr25-xNiMo4 ($x = 7.0, 8.0, 9.0,$ and 10 wt%) samples with the self-corrosion potential -0.228 V and the self-corrosion current density 6.410×10^{-7} A/cm².

Acknowledgements This work was financially supported by the National Key R&D Program of China (2016YFB1100203), Joint Funds of NSFC-Liaoning (U1508213), and Green Manufacturing System Integration Project of the Industry and Information Ministry of China (2017).

References

1. Huang, H., Xu, L., Jing, H., Lv, X.: Droplet transfer characteristics of SAF 2507 super duplex stainless steel CMT + P. *Trans. China Weld. Inst.* **40**(10), 127–136 (2019)
2. Cheng, Y., Zhao, L., Zhou, K.: Precision casting of 2205 duplex stainless steel inducer. *Foundry Equip. Technol.* **4**, 20–22 (2018)
3. Zhang, J., Zhang, W., Li, Y., Songhao, H., Huang, S., He, T., Liu, Y.: Laser deposition additive/subtractive hybrid manufacturing process for stainless steel powder based on DMG MORI LASERTEC 65 3D. *Mater. Sci. Eng. Powder Metall.* **23**(4), 368–374 (2018)
4. Wang, Z., Palmer, T.A., Beese, A.M.: Effect of processing parameters on microstructure and tensile properties of austenitic stainless steel 304L made by directed energy deposition additive manufacturing. *Acta Mater.* **110**, 226–235 (2016)
5. Melia, M.A., Nguyen, H.-D.A., Rodelas, J.M., Schindelholz, E.J.: Corrosion properties of 304L stainless steel made by directed energy deposition additive manufacturing. *Corros. Sci.* **152**, 20–30 (2019)

6. Guo, P., Zou, B., Huang, C., Gao, H.: Study on microstructure, mechanical properties and machinability of efficiently additive manufactured AISI 316L stainless steel by high-power direct laser deposition. *J. Mater. Process. Technol.* **240**, 12–22 (2017)
7. Yadollahi, A., Shamsaei, N., Thompson, S.M., Seely, D.W.: Effects of process time interval and heat treatment on the mechanical and microstructural properties of direct laser deposited 316L stainless steel. *Mater. Sci. Eng., A* **644**, 171–183 (2015)
8. Wang, C., Liang, J., Chen, S., Liu, C., Shang, S., Chen, Y.: Study on microstructures and properties of direct laser deposited 15Cr21Ni7-xMo stainless steels. *Appl. Laser* **37**(1), 11–16 (2017)
9. Zhang, C., Zhang, Z., Li, S., Qiu, C., Zhu, S.: Mechanical and corrosion properties of Nitrogen Bearing Duplex stainless steel Sample prepared by laser forming. *China Surf. Eng.* **32**(2), 163–169 (2019)
10. Shang, F., Chen, X., Wang, Z., Ji, Z., Ming, F., Ren, S., Xuanhui, Q.: The microstructure, mechanical properties, and corrosion resistance of UNS S32707 hyper-duplex stainless steel processed by selective laser melting. *Metals* **9**(9), 1012 (2019)
11. Gadgil, V.J., Sasse, A.G.B.M., Swens, J.J., Kolster, B.H.: Effect of cooling rate on the austenite-ferrite phase boundary composition of a duplex stainless steel. *J. Mater. Eng.* **13**, 291–297 (1991)
12. Ma, X.H., Zhang, L., Yang, X.H., Li, Q., Huang, Y.D.: Effect of Ni addition on corrosion resistance of FePC bulk glassy alloy. *Corros. Eng. Sci. Technol.* **50**(6), 433–437 (2015)